CENTRAL RESEARCH LIBRARY

ORNL-5105

Cy 1

Mechanical Properties Test Data for Structural Materials Quarterly Progress Report for Period Ending April 30, 1975

[redacted]

OAK RIDGE NATIONAL LABORATORY
CENTRAL RESEARCH LIBRARY
DOCUMENT COLLECTION
LIBRARY LOAN COPY
DO NOT TRANSFER TO ANOTHER PERSON
If you wish someone else to see this document, send in name with document and the library will arrange a loan.
UCN-7969
(3 3-67)

OAK RIDGE NATIONAL LABORATORY
OPERATED BY UNION CARBIDE CORPORATION • FOR THE U.S. ATOMIC ENERGY COMMISSION

Printed in the United States of America. Available from
the Energy Research and Development Administration,
Technical Information Center
P.O. Box 62, Oak Ridge, Tennessee 37830
Price: Printed Copy $10.60 ; Microfiche $2.25

This report was prepared as an account of work sponsored by the United States Government. Neither the United States nor the Energy Research and Development Administration, nor any of their employees, nor any of their contractors, subcontractors, or their employees, makes any warranty, express or implied, or assumes any legal liability or responsibility for the accuracy, completeness or usefulness of any information, apparatus, product or process disclosed, or represents that its use would not infringe privately owned rights.

ORNL-5105
UC-79b, -h, -k
(Liquid Metal Fast
Breeder Reactors)

Contract No. W-7405-eng-26

METALS AND CERAMICS DIVISION

MECHANICAL PROPERTIES TEST DATA FOR STRUCTURAL MATERIALS QUARTERLY PROGRESS REPORT FOR PERIOD ENDING APRIL 30, 1975

Aerojet Nuclear Company

Argonne National Laboratory

Oak Ridge National Laboratory

Naval Research Laboratory

Hanford Engineering Development Laboratory

Westinghouse Advanced Reactors Division

University of Cincinnati

University of California at Los Angeles

General Electric Company

Compiled by M. R. Hill

JUNE 1975

OAK RIDGE NATIONAL LABORATORY
Oak Ridge, Tennessee 37830
operated by
UNION CARBIDE OCRPORATION
for the
U.S. ENERGY RESEARCH AND DEVELOPMENT ADMINISTRATION

FOREWORD

This is the seventh in a series of progress reports, the purpose of which is to record and distribute quarterly the collected results of all structural materials mechanical properties test programs sponsored by the Reactor Research and Development Division of the USERDA.

To be useful as resource documents, the reports in this series must be published and distributed in a timely manner to those in the reactor design and materials technology community who have a need of mechanical property test data for nuclear reactor and power plant applications. A test and material index is included to increase the effectiveness of the report.

Reports previously issued in this series are as follows: ORNL-4936, period ending October 31, 1973; ORNL-4948, period ending January 31, 1974; ORNL-4963, period ending April 30, 1974; ORNL-4998, period ending July 31, 1974; ORNL-5103, period ending October 31, 1974; and ORNL-5104, for period ending January 31, 1975. The next quarterly report will be for the period ending July 31, 1975, and contributions are due at ORNL by August 15, 1975.

W. R. Martin
Metals and Ceramics Division
Oak Ridge National Laboratory

CONTENTS

SUMMARY ix

1. AEROJET NUCLEAR COMPANY 1

1.1 INTRODUCTION 1

1.2 FATIGUE TESTS ON CLADDING AND STRUCTURAL MATERIALS . . 2

1.2.1 Tensile Properties of Interrupted Fatigue Specimens 2

1.3 INCONEL 718 MECHANICAL PROPERTY PROGRAM 11

1.3.1 Development of New Heat Treatment for Weldments 11

1.3.2 Strain-Age Cracking of Inconel 718 12

1.3.3 Optimization of INEL Heat Treatment 15

1.4 REFERENCES 19

2. ARGONNE NATIONAL LABORATORY 21

2.1 INTRODUCTION 21

2.2 FRACTURE AND FATIGUE STUDIES ON STAINLESS STEEL . . . 21

2.2.1 Effects of Surface-Roughness and Strain Range on the Low-Cycle Fatigue Behavior of Type 304 Stainless Steel 21

2.2.2 Microstructural Effects in Low-Cycle Fatigue. . 32

2.2.2.1 Experimental 34

2.2.2.2 Results. 39

2.2.2.3 Future Research 50

2.3 SODIUM EFFECTS ON LMFBR MATERIALS 52

2.3.1 Influence of Sodium Environment on the Uniaxial Creep-Rupture Properties of Austenitic Stainless Steels 52

2.3.2 Influence of Sodium Environment on the Low-Cycle Fatigue Behavior of Austenitic Stainless Steels 61

2.4 REFERENCES 64

3. OAK RIDGE NATIONAL LABORATORY 67

3.1 INTRODUCTION 67

3.2 MECHANICAL PROPERTIES AND BEHAVIOR FOR STRUCTURAL MATERIALS 67

3.2.1 Mechanical Property Characterization of Type 304 Stainless Steel Reference Heat 67

3.2.1.1 Creep and Rupture Properties of the 2-in. (51-mm) Plate of Reference Heat. 67

3.2.1.2 Tensile Tests Following Periods of Creep 68

3.2.2 Heat-to-Heat Variation of Mechanical Properties of Types 304 and 316 Stainless Steel 91

3.2.2.1 Long-Term Creep Tests in Heat-to-Heat Variation Study of Type 304 Stainless Steel 91

3.2.2.2 Heat-to-Heat Variation and Its Relation with Chemical Composition . . 95

3.2.2.3 Relation Between Creep-Rupture and Short-Term Tensile Properties 101

3.2.2.4 Relation Between Tensile Properties in the As-Received (Mill-Annealed) and Reannealed (Laboratory-Annealed) Conditions for Types 304 and 316 Stainless Steel 102

3.2.2.5 Effect of Aging on Tensile and Creep Properties of Types 304 and 316 Stainless Steel 112

3.2.3 Materials Behavior in Support of Development and Evaluation of Failure Criteria for Materials . 141

3.2.4 Material Data Processing 164

3.2.5 Elastic Properties of Engineering Materials . . 172

3.2.5.1 Elastic Properties Determined by Dynamic Tests 173

3.2.5.2 Elastic Properties Determined by Static Tests 173

3.3 MECHANICAL AND METALLURGICAL BEHAVIOR OF WELDMENTS FOR LMFBR 174

3.3.1 Creep and Creep-Rupture Characterization of Type 16-8-2 Stainless Steel Weld Metal 174

3.3.2 Effect of Thermal Aging on the Creep and Creep-Rupture Behavior of CRE Type 308 Stainless Steel SMA Welds 178

3.3.3 Creep-Rupture Behavior of Gas Tungsten-Arc Types 308, 316, and 16-8-2 Stainless Steel Welds Made with Special Filler Materials . . . 182

3.4 MECHANICAL PROPERTIES OF STEAM GENERATOR AND HEAT EXCHANGER MATERIALS 187

3.4.1 Strain Rate Effects on the Tensile Properties of Annealed 2 1/4 Cr-1 Mo Steel 187

3.4.2 Effect of Sodium on Mechanical Properties of 2 1/4 Cr-1 Mo Steel 196

3.4.3 Heat-to-Heat Variation of 2 1/4 Cr-1 Mo Steel . 197

3.4.4 Fatigue Behavior of 2 1/4 Cr-1 Mo Steel 200

3.4.4.1 Low- and High-Cycle Fatigue 202

3.4.4.2 Creep-Fatigue Interactions 211

3.4.4.3 Creep-Fatigue Data Analysis 215

3.4.4.4 Microstructural Studies of Fatigue Specimens 221

3.4.4.5 Subcritical Crack Growth of 2 1/4 Cr-1 Mo Steel 226

3.4.5 Mechanical Property Correlations of 2 1/4 Cr-1 Mo Steel for LMFBR Steam Generators. 231

3.4.6 Mechanical Properties of Weld-Overlaid Stainless Steel Forging 232

3.5 HIGH-TEMPERATURE DESIGN. 241

3.5.1 Exploratory Studies in Support of Structural Design Methods 241

3.5.1.1 Characterization of the Product Forms of the Reference Heat of Type 304 Stainless Steel 242

3.5.1.2 Tensile Testing of 1-in. (25-mm) Plate of the Reference Heat of Type 304 Stainless Steel. 245

3.5.1.3 Creep-Rupture Testing of the 1-in. (25-mm) Plate of the Reference Heat of Type 304 Stainless Steel 246

3.5.1.4 Strain Cycling Tests of Type 304 Stainless Steel 250

3.5.1.5 Exploratory Testing of 2 1/4 Cr-1 Mo Steel 250

3.5.2 Investigations of Creep Failure Under Uniaxial and Multiaxial Conditions 252

3.5.2.1 Constant-Load Uniaxial Tests 252

3.5.2.2 Step-Load Uniaxial Tests 253

3.5.2.3 Interrupted Uniaxial Tests 253

3.5.2.4 Biaxial Test 258

3.5.2.5 Loading Strains 258

3.5.2.6 Inconsistent Microstructure 259
3.5.2.7 Machine/Specimen Differences 260
3.5.2.8 Modified Reanneal 263
3.6 MECHANICAL PROPERTIES OF HTGR STEAM GENERATOR AND PRIMARY CIRCUIT MATERIALS 267
3.6.1 Tensile Testing 267
3.6.2 Environmental Creep Testing 267
3.6.3 Subcritical Crack Growth Studies 269
3.6.4 Fatigue Life Tesing 270
3.7 REFERENCES 270
4. NAVAL RESEARCH LABORATORY 281
5. HANFORD ENGINEERING DEVELOPMENT LABORATORY 283
6. WESTINGHOUSE ADVANCED REACTORS DIVISION 285
6.1 INTRODUCTION 285
6.2 BASIC SPECIMEN TESTING 285
6.2.1 Uniaxially Loaded Specimen Models with Nonuniform Gage Section 285
6.2.1.1 Test Piece Description (304 SS Heat 9T2796) 285
6.2.1.2 Current Results 285
6.2.2 Eccentrically Loaded Specimens with Uniform Gage Section (304 SS Heat 9T2796) 293
6.2.2.1 Test Piece Description 293
6.2.2.2 Current Results 293
6.2.3 Specimens with Welds (304 SS, Heat 9T2796) . . 295
6.2.3.1 Test Piece Description 295
6.2.3.2 Current Results 295
6.3 TUBULAR SPECIMEN TESTING 297
6.3.1 Test Piece Description 297
6.3.2 Test Matrix 297
6.3.3 Test Equipment, Specimens, and Measurement . . 297
6.3.3.1 Test Equipment 297
6.3.3.2 Test Specimens 300
6.3.3.3 Test Measurements and Data Records . . 300
6.3.3.4 Microstructural Characterization of the Post-Test Specimens 300

6.3.4 Data Reduction 306
6.4 REFERENCES 307
7. UNIVERSITIES 311
7.1 UNIVERSITY OF CINCINNATI 311
7.1.1 Introduction 311
7.1.2 Experimental Program 311
7.1.2.1 Characterization of the Creep and Tensile Substructure of 304 Stainless Steel, Reference Heat 9T2796) . . 312
7.1.2.2 Characterization of the Substructure During Early Stages of Creep of 304 Stainless Steel. 316
7.1.2.3 Change in Stress Experiments on 304 Stainless Steel, Reference Heat 9T2796 322
7.1.2.4 Subgrain Misorientation Observation in Incoloy 800 Tested in the Fatigue Mode 324
7.1.2.5 Second Phase Particles and Their Influence on the Mechanical Behavior of Incoloy 800 Tested in the Fatigue Mode 330
7.1.3 REFERENCES 339
7.2 UNIVERSITY OF CALIFORNIA, LOS ANGELES 341
7.2.1 Microstructure and High Temperature Deformation of Cr-Mo Steels for LMFBR Heat Exchanger . . . 341
7.2.1.1 Introduction 341
7.2.1.2 Microstructure-Creep Properties Correlations 342
7.2.1.3 Temperature Dependence of Creep . . . 342
7.2.1.4 Stress Dependence of Creep 347
7.2.1.5 References 365
8. GENERAL ELECTRIC COMPANY 369
8.1 INTRODUCTION 369
8.2 MECHANICAL PROPERTIES OF STAINLESS STEEL IN CARBURIZING SODIUM 369
8.2.1 Background 369
8.2.2 Current Progress 376

8.3 DECARBURIZATION KINETICS AND DESIGN METHODS VERIFICATION TESTING 382

8.3.1 Background 382

8.3.2 Current Progress 384

8.4 REFERENCES 385

INDEX 389

SUMMARY

1. AEROJECT NUCLEAR COMPANY

Tensile tests of fatigue specimens following fatigue and creep-fatigue cycling have been performed to evaluate the degradation of mechanical properties as a function of cyclic life. Reductions in ductility and the presence of surface cracks were observed at relatively low fractions of anticipated cyclic life.

Work is continuing to improve the mechanical properties of Inconel 718 welds through heat treat modifications. An INEL Heat Treatment is proposed and investigations regarding heat treat cracking with respect to material process history are reported.

2. ARGONNE NATIONAL LABORATORY

The low-cycle fatigue behavior of Type 304 stainless steel (Heat 9T2796) that has a well-characterized initial surface roughness has been studied at 593°C (1100°F). The fatigue tests were performed in air at a strain rate of 4×10^{-3} sec^{-1} and total strain ranges between 0.5 and 2.0%. The results were compared with similar data obtained from smooth specimens. The extent of the reduction in crack-initiation life that results from both an initial surface roughness and an increase in the applied strain range as well as the relation between fatigue life and crack-initiation life has been discussed quantitatively.

Low-cycle fatigue tests at 593°C have been conducted on three high-purity Fe-20Cr-Ni austenitic alloys to determine the influence of microstructure on fatigue life. Alloys in the as-cast condition exhibit lives 2 to 20 times longer than those in the wrought condition and in conventional Type 304 stainless steel. Insertion of a 1-min tension hold time into the loading cycle causes fatigue life to decrease, but the as-cast materials remain the most resistant to fatigue failure. Striation counting on fracture surfaces indicates that in excess of 75% of fatigue life is spent in crack initiation. The alloys with the longest fatigue lives are those most resistant to surface rumpling through inter- and intragranular deformation.

Uniaxial creep-rupture tests are being conducted on Type 304 stainless steel specimens after exposure to flowing sodium of controlled, nonmetallic element concentrations. The results at 700°C indicate that the minimum creep rates at an applied stress of 90 MPa (13 ksi) are 0.086 and 0.218%/hr for the annealed condition and after 1512-hr exposure to flowing sodium, respectively. A comparison of the calculated and measured values of strain indicated an absence of grain-boundary sliding and negligible grain-boundary migration in specimens exposed to sodium at 700°C.

Fatigue tests in sodium are being conducted to investigate the effect of the high-temperature sodium environment on the low-cycle fatigue behavior of Types 304 and 316 stainless steel in the annealed, annealed and aged, and sodium-exposed conditions. Results on the strain range versus cycles to failure for annealed Type 316 stainless steel indicate a factor of four increase in the time to failure for specimens tested in sodium compared with similar specimens tested in air. The carbon concentration in sodium in the range 0.03-0.3 ppm was shown to have no significant effect on the fatigue lifetime for the mechanical test conditions used.

3. OAK RIDGE NATIONAL LABORATORY

Elevated-temperature creep testing of the ORNL reference heat of type 304 stainless steel is continuing, and data have been updated. Some tests have exceeded 21,000 hr.

The literature on effect of prior creep deformation on tensile properties of various metals and alloys was reviewed. Data available to date on tensile properties following periods of creep have been treated in great detail. The prior creep deformation lowers the residual tensile ductility, measured as ε_u (true uniform elongation), e_t (engineering total elongation), and D_t^* [true tensile ductility, ln 100/(100-RA)]. Fractional prior creep elongation $\varepsilon_c/(D_c-\varepsilon_l)$ was shown to best describe the changes in residual tensile ductility. A creep strain of 1 to 2% brought the residual tensile ductility below 10% in the range 482 to 593°C (900 to 1100°F). The data comparison to date indicated that the effect of prior creep strain on residual tensile ductility is far greater than that produced by thermal aging. Various possible damage functions for creep and tensile summations are suggested.

Creep data have been updated for ten long-term (50,000 hr) creep tests. The heat-to-heat variation in long-term stress-rupture data are presented for ORNL and literature data for test times approaching 66,000 hr. The stress exponents, n_m (stress-minimum creep data) and n_r (stress-rupture data), for strong heats were much greater than for weak heats. The high stress exponents for strong heats indicate a high internal back stress in these heats.

Chemical analyses for Nb, V, Ti, Ta, and W were repeated on 20 heats of type 304 stainless steel. A systematic analysis on the distribution of 20 heats as a function of time to rupture and various chemical elements showed that niobium appeared to be responsible for heat-to-heat variation. Heats were then classified as weak, medium, and strong, and they contained respectively 26, 96, and 160 ppm of niobium. Niobium increased the stress exponents by raising the internal back stress, which reduces the effective creep stress.

The relation between creep rupture and ultimate tensile strength developed last quarter was extended to the time-to-rupture plot. For a fixed stress and temperature, time to rupture increased with increasing

ultimate tensile strength. The importance of elevated-temperature ultimate tensile strength in selecting a new heat of austenitic stainless steel is pointed out.

Quantitative relations of the form, P(reannealed) = $A + BP$(as-received) have been developed between the tensile properties (0.2% yield, ultimate tensile strength, and uniform elongation) for various product forms of types 304 and 316 stainless steel in the as-received (mill-annealed) and reannealed (laboratory-annealed) conditions. The Hall-Petch relation was used to show that constant A describes the straightening stress for for products if grain size remains unchanged on reannealing. The constant B accounts for the effect of grain growth on the change in property on reannealing.

Stress-strain curves showing the effect of 10,000 hr aging at various temperatures are presented. The influence of aging temperature for an aging time of 4000 hr on yield, ultimate tensile strength, and reduction of area for several other heats is also presented. Thermal aging in the reannealed condition changed yield strength even at 482°C (900°F); a similar effect occurred at 593°C (1100°F) for aging in the as-received condition. The large reduction of area obtained for heat 807 is associated with the transformation of δ-ferrite to sigma phase.

The ORNL and HEDL results on effects of aging temperature and time on uniform elongation of types 304 and 316 stainless steel are compared. The differences observed were explained on the basis of an opposite strain rate dependence of the uniform and total elongation for the aged and unaged material.

Relations of time to rupture and time to onset of third-stage creep with ultimate tensile strength are presented for the unaged and aged conditions. The long-term tests on annealed and annealed-and-aged specimens of the reference heat of type 304 stainless steel are compared.

Optical, scanning, and transmission electron micrographs are shown for creep specimens of heat 926 of type 304 stainless steel, tested at 593°C (1100°F) and 30 ksi (207 MPa) in unaged and aged conditions. An aging temperature of 593°C (1100°F) and higher resulted in a transition from grain boundary to twin boundary cavaties. A tentative mechanism has been suggested for twin boundary cavitation.

A previously reported method for parametric correlation and extrapolation of creep ductility data has now been applied to five different heats of types 304 and 316 stainless steels. Ductility increases as stress and temperature increase.

The data base for the Mechanical Properties Data Storage and Retrieval System (DSRS) has been expanded to include the results from over 5000 mechanical property tests. In addition, software developments are continuing. The Automatic Data Acquisition System (ADAS) continues to operate and expand.

Dynamic elastic constant measurements on several alloys in various conditions are in various stages of data processing, measurement, and specimen preparation. Preparations for static measurements on 2 1/4 Cr-1 Mo steel and type 304 stainless steel are in an advanced state, and the first data on isothermally annealed 2 1/4 Cr-1 Mo steel containing 0.136% C are presented.

Characterization of the creep and creep-rupture behavior of commercial 16-8-2 weld metal for potential LMFBR structural applications is continuing. A series of welds made by manual gas tungsten-arc, manual shielded metal-arc, and automatic gas tungsten-arc processes was tested at 649°C (1200°F). Creep strains before tertiary creep less than 1% were observed; also, total strains and reductions of area for the automatic weld consistently decreased with increasing rupture time. The range of rupture times observed at any stress was about equal to the range of times expected for type 316 stainless steel base metal.

Type 308 CRE shielded metal-arc welds that are prototypic of the longitudinal seam and girth welds in the FFTF vessel are being aged at 482, 593, and 649°C (900, 1100, and 1200°F). Aging is almost complete to 20,000 hr. Creep and creep-rupture data for specimens aged 10,000 hr and then tested at the aging temperature are presented together with data from comparable unaged specimens. The most significant effect is an 80 to 90% decrease in rupture time after aging at 482°C (900°F) for either 4000 or 10,000 hr; this aging had previously been shown to cause changes in the carbides present in the weld metal and to reduce the ultimate tensile strength in tests performed at 482°C (900°F).

We are creep-rupture testing at 649°C (1200°F) types 308, 316, and 16-8-2 stainless steel weldments made by the gas tungsten-arc (GTA) process. Filler materials were fabricated at ORNL and contained varying levels of boron, phosphorous, and titanium. Preliminary results show that the additions of 0.5% Ti, 0.042% P, and 0.006% B to types 308 and 316 stainless steel GTA weld deposits produce the greatest enhancement of creep strength and long-time ductility.

High-strain-rate tensile tests were conducted on annealed 2 1/4 Cr-1 Mo steel at 204 and 371°C (400 and 700°F). With the completion of these tests and some recently completed tests at 2.67×10^{-6}/sec, it was possible to describe the tensile behavior of this material as a function of strain rate from 2.67×10^{-6} to 144/sec at 25, 204, 371, 454, 510, and 566°C (75–1050°F). Three-dimensional plots of yield stress, ultimate tensile strength, total elongation, and reduction of area are presented.

The metallurgical characterization of the annealed 2 1/4 Cr-1 Mo steel as annealed, after aging for 26,500 hr at 566°C, and after decarburization by sodium for 26,500 hr is complete. The change in microstructure and carbide content has been summarized, and conclusions have been drawn concerning the decarburization process and the effect of decarburization and aging on elevated-temperature mechanical properties.

Tensile tests over the range 25 to 566°C (75—1050°F) were made on 2 1/4 Cr-1 Mo steel specimens taken from two VAR forgings and an ESR plate; the specimens were tested in the as-received condition. The properties are somewhat above those previously presented for these same materials after an identical isothermal anneal.

Results are reported on the fatigue, creep-fatigue, and subcritical crack growth studies presently being conducted on 2 1/4 Cr-1 Mo steel. Continuous cycling tests have been conducted at 316 and 371°C (600 and 700°F) in both the low- and high-cycle regimes. At 371°C (700°F), evidence of dynamic strain aging was found in that fatigue life reduced with a decrease in test frequency. Results of creep-fatigue (strain hold time) tests are summarized, and several damage summation and prediction techniques were employed in correlating the data. Progress in characterizing fatigue crack growth behavior including the influence of mean stress and environment is discussed.

Development of mechanical property correlations for annealed 2 1/4 Cr-1 Mo steel continued, including investigations of Charpy impact energy and ductile-brittle transition temperature, and a revision of earlier results for 0.2% offset yield strength and ultimate tensile strength.

With the exception of several continuing long-term creep-rupture tests, the experimental phase of the creep-rupture studies on the type 308 stainless steel weld metal has been completed. Creep-rupture results have been collected to determine the effect of specimen orientation and location in the overlaid forging at 482, 538, and 593°C (900, 1000, and 1100°F); the results are summarized and discussed.

The status of the creep-rupture characterization tests on the different product forms of the reference heat of type 304 stainless steel is reported. Values for the 1000-hr rupture strength at 593°C (1100°F) range from 22.70 ksi (156 MPa) to 24.47 ksi (169 MPa). Rupture strength and strain component data are reexamined on the basis of modulus-compensated true stresses and true strains for the 1-in. (25-mm) plate of the reference heat of type 304 stainless steel. Rupture data are correlated with the Barrett-Ardell-Sherby parameter. A method of correlating the true linear creep components is examined and found to provide a fair approximation to data behavior in the range 482 to 649°C (990—1200°F) for two heats of type 304 stainless steel.

Creep-rupture lives of 21,500, 37,400, and 67,400 hr are estimated for tests still in progress at 16, 17, and 18 ksi (110, 117, and 124 MPa) of type 304 stainless steel heat 9T2796 5/8-in. (16-mm) bar. Life fractions for step-load uniaxial tests have been recalculated. Progress is described on interrupted uniaxial tests and biaxial tests. Microstructural instability and differences in testing procedure and specimens are being investigated as contributors to scatter in creep results.

Tensile, creep, and subcritical crack growth rate testing of HTGR structural alloys has continued, and low-cycle fatigue life testing has begun. Results of tensile tests of Hastelloy X are presented, and the

matrix of environmental creep tests on 2 1/4 Cr-1 Mo steel, 9 Cr-1 Mo steel, and Hastelloy X is presented and discussed. Progress in environmental crack growth studies on 2 1/4 Cr-1 Mo steel is also reviewed.

4. NAVAL RESEARCH LABORATORY

(No Report)

5. HANFORD ENGINEERING DEVELOPMENT LABORATORY

(No Report)

6. WESTINGHOUSE ADVANCED REACTORS DIVISION

Creep testing of bar- and plate type specimens was continued using material from the ORNL type 304 stainless steel reference heat (9T2796). Tests were performed on a notched bar base metal specimen with current results indicating double the rupture life of plane stress specimens. Results from a notched bar weld specimen also indicate a large rupture life increase when compared to an unnotched weld test. A second eccentrically loaded base metal plate test was performed and creep data for the first 2500 hours are reported. Results are also reported for an axial weld specimen containing a central hole entirely with the weld metal.

Creep testing of tubular specimens from the ORNL type 304 stainless steel reference heat (9T2796) continued with short-term testing and metallographic examination of specimens that had been previously exposed to creep conditions. Multiaxial creep test data have been examined to evaluate an equation for prediction of creep behavior.

7. UNIVERSITIES

UNIVERSITY OF CINCINNATI

Work on the analysis of the creep and tensile test results and its correlation with the corresponding substructure characteristics of AISI 304 stainless steel reference heat (9T2796) is nearing completion. These specimens were tested at temperatures ranging from 538 to 816°C and strain rates from 1.22×10^{-7} sec^{-1} to 8.33×10^{-2} sec^{-1}. Preliminary TEM observations suggest that the typical substructure consists of subgrains with well-defined subboundaries at modulus compensated stress levels below about 6×10^{-3}. At stress levels above this initial critical value the substructure consists of cells where the walls are diffused tangles of dislocations. For the specimens tested at the fastest strain rate, i.e., 8.33×10^{-2} sec^{-1}, the substructure consists of cells with incomplete cell walls and patches of dislocations lying along the traces of {111} planes.

TEM evaluations of the substructure were performed on a set of specimens of 304 stainless steel tested in creep to study the development of the substructure as a function of creep strian. On initial loading the dislocations are generated in large numbers and tangles are formed. With increasing strain, the dislocations tend to segregrate into areas of high dislocation density. At the end of primary creep, the substructure takes the shape of cells and during steady state the rearrangement of cell walls continues with a very small change in the cell/subgrain size and total dislocation density. The misorientation angle between adjacent cells or subgrains seems to increase during primary and secondary stages of creep reaching more or less a saturation value at rupture.

A family of creep tests has been performed on 304 stainless steel reference heat (9T2796) in which the stresses were changed during steady state creep to obtain the strain-time behavior after the stress changes. Subsequent TEM will be performed to help develop a better understanding of the substructure and its correlation to the internal stresses.

Work is continuing on the development of the microstructure of 304 stainless steel tested in the fatigue mode at 650°C. These tests were conducted at ANL under a Thesis Parts Program.

The influence of plastic deformation at elevated temperatures on subgrain misorientation angles and also the effects of fatigue test temperatures on second phase particles in alloy Incoloy 800 are presented. The technique of determining the misorientation angles between adjacent subgrains is outlined and the preliminary observations suggest that the misorientation angles between the cells is much smaller than that between the well developed subgrain. The second phases that were developed in alloy Incoloy 800 during the fatigue tests were identified utilizing high resolution dark field and diffraction pattern analysis. The influence of these second phases, viz., γ', $(Fe, Cr)_{23}C_6$ and TiN on the cyclic stress strain behavior is also being evaluated. Preliminary observations suggest that the enhanced elevated temperature mechanical properties of Incoloy 80(could be attributed to the presence of second phases.

UNIVERSITY OF CALIFORNIA, LOS ANGELES

Creep data on 2 1/4 Cr-1 Mo steel are correlated in terms of various theoretical and empirical models. The temperature dependence is consisten with diffusion control in the range 449 to 566°C (930–1050°F) but not at lower temperatures. Various relations between creep rate and stress appea to apply only over limited ranges of stress.

8. GENERAL ELECTRIC COMPANY

Programs for defining the effects of high temperature sodium environments on the mechanical properties of 2¼Cr-1Mo steel and stainless steels were initiated. The effect of a carburizing sodium environment on creep

rupture, creep rate, and creep-fatigue properties of Type 316 stainless steel is being determined. The test facilities for automatic load interruptions and data accumulation have been completed. In addition, the effect of carburizing sodium on the fatigue crack propagation rate will be determined using a fracture mechanics approach. Pre-exposed specimens will be subjected to continuous carburization during testing. A matrix of tests to be conducted in this program is presented; currently, the fabrication of the experimental apparatus is nearing completion, and specimens are being pre-exposed in Loop A.

The effect of decarburization on creep and creep-fatigue properties of 2¼Cr-1Mo base metal and weld metal is being studied. Uniaxial testing of sodium and gas filled pipe samples is underway. The test facility for the determination of creep-fatigue interaction effects under decarburizing sodium is virtually complete. Effects of cycling on the rupture life of 2¼Cr-1Mo tubing and weld metal will be determined in this rig.

1. AEROJET NUCLEAR COMPANY

D. D. KEISER

1.1 INTRODUCTION

Aerojet Nuclear Company is conducting mechanical properties investigations under two programs sponsored by ERDA Division of Reactor Research and Development. Program 06031, Fatigue Tests on Cladding and Structural Materials, involves experimental fatigue tests on stainless steel Types 304 and 316 as well as Type 304/308 weldments. These tests are intended to determine the influence of irradiation, cold work, heat treatment, heat-to-heat property variations, and temperature on fatigue behavior. Irradiated, thermal control, as-received, and annealed specimens are being tested at 427 to 700°C (800 to 1292°F). Current work on irradiated material is reported in the Semi-Annual Progress Report for the Irradiation Effects on Reactor Structural Materials Program compiled at HEDL. Unirradiated work reported in this document involves tensile testing of fatigue specimens cycled to some fraction of their fatigue life short of failure.

Program 06084, Inconel 718 Mechanical Property Program, has as its primary objective the acquisition of the necessary mechanical property data to permit safe, efficient use of this material in LMFBR service. The specific immediate application is for selected structural components of the Clinch River Breeder Reactor Project. Other reactor service applications which require high levels of mechanical properties at temperatures up to 649°C (1200°F) are also expected to make use of this material.

What have been considered standard heat treatments for Inconel 718 have not consistently yielded acceptable ductility values for the welded material. Current work involves scoping tests on material subjected to modified thermal treatments in an effort to optimize the heat treatment that will yield the best mechanical properties of both base and weld metal.

1.2 FATIGUE TESTS ON CLADDING AND STRUCTURAL MATERIALS - G. E. Korth and M. D. Harper

1.2.1. Tensile Properties of Interrupted Fatigue Specimens

An investigation has been undertaken to evaluate changes in tensile properties after fatigue or creep-fatigue cycling. Hourglass fatigue specimens of Type 304 and 316 stainless steel were cycled to some fraction of their anticipated fatigue life and then tensile tested. Although total elongation and reduction in area of hourglass specimens do not compare exactly with standard uniform gage tensile specimens, the values are relatively close and are valid in establishing trends and changes. Uniform strain, yield strength, and ultimate strength of hourglass specimens can be compared directly with uniform gage tensile data. Specimens were tested in air in strain control with a ramp waveform for the fatigue portion of the test and strain control with a constant strain rate to failure for the tensile part of the test. The axial strain rate for both fatigue and tensile tests was $4 \times 10^{-3}\ s^{-1}$. Results are reported in Table 1.1 where:

$\Delta\varepsilon_t$ = total strain range

$\Delta\varepsilon_p$ = plastic strain range

$\Delta\sigma$ = stress range

σ_t = tensile stress amplitude at peak strain

$\sigma_{t,min}$ = tensile stress amplitude at end of hold time

N = number of cycles

N_f = cycles to failure

σ_{ys} = 0.2% yield strength

σ_{uts} = ultimate tensile strength

ε_u = uniform elongation

ε_t = total elongation

R.A. = reduction in area

Plots of ductility vs cycle life (Figures 1.1-1.3) show that

Table 1.1 Tensile Property Data of Type 304 and 316 Stainless Steel Tensile Tested after an Interrupted Fatigue or Creep-Fatigue Test[a]

Specimen No.	Material & Condition[b]	Tensile Hold, hr	Conditions at Last Full Cycle: $\Delta\varepsilon_t$, %	$\Delta\varepsilon_p$, %	$\Delta\sigma$, ksi	σ_t, ksi	$\sigma_{t,min}$ ksi	Cycle Test Stopped, N	Fraction of Cycle Life, N/N_f	σ_{ys}, ksi	σ_{uts}, ksi	ε_u, %	ε_t, %	R.A. %	Test Temp, °C
D-57[c]	316,1A	0	1.51	1.03	117.2	57.5	--	1,505	1.0	--	--	--		--	427
D-55[c]	316,1A	0	1.00	0.63	83.1	40.9	--	7,660	1.0	--	--	--		--	427
D-56[c]	316,1A	0	.76	0.42	76.6	35.6	--	13,302	1.0	--	--	--		--	427
D-53[c]	316,1A	0	0.50	0.27	70.3	36.0	--	23,679	1.0	--	--	--		--	427
D-58	316,1A	0	1.00	0.62	87.4	41.8	--	3,830	0.5	43.5	75.1	19.0	28.6	25.0	427
D-59	316,1A	0	1.00	0.64	81.1	39.9	--	5,745	0.75	41.6	74.9	21.2	34.4	50.0	427
D-60	316,1A	0	0.51	0.23	70.2	33.8	--	11,840	0.50	37.9	79.3	30.0	77.1	57.5	427
D-54	316,1A	0	0.50	0.22	66.9	31.4	--	18,000	0.75	32.0	76.7	35.4	75.1	67.5	427
BP-35[d]	304,2B	-	--	--	--	--	--	--	0	26.7	68.1	30.6	50.3	62.5	427
BP-38[d]	304,2B	-	--	--	--	--	--	--	0	24.5	68.0	32.5	56.9	60.0	427
BP-17	304,2B	0	1.98	1.47	129.0	63.5	--	171	0.25	61.9	78.6	25.2	66.2	57.5	427
BP-18	304,2B	0	2.00	1.48	124.7	60.9	--	342	0.50	59.1	70.1	28.2	45.2	47.5	427
BP-26	304,2B	0	2.00	1.44	125.0	61.3	--	513	0.75	56.9	77.3	18.8	45.2	50.0	427
BP-16	304,2B	0	1.01	0.66	82.8	40.8	--	950	0.25	42.5	86.0	31.0	65.9	65.0	427
BP-12	304,2B	0	1.00	0.68	78.4	38.5	--	1,900	0.50	40.0	71.1	24.0	40.5	50.0	427
BP-28	304,2B	0	1.00	0.66	77.1	37.4	--	2,850	0.75	37.7	72.1	22.9	41.9	47.5	427
BP-22	304,2B	0	0.50	0.26	58.9	28.7	--	7,000	0.25	31.0	70.1	28.2	45.2	47.5	427
BP-31	304,2B	0	0.51	0.23	63.7	30.6	--	14,000	0.50	29.4	72.6	32.7	54.1	60.0	427
BP-32[d]	304,2B	0	0.50	0.24	62.9	29.9	--	21,000	0.75	32.6	72.5	33.3	48.0	55.0	427
BT-44[d]	304,2B	-	--	--	--	--	--	--	0	37.7	66.5	39.7	69.4	68.0	593
BT-46[d]	304,2B	-	--	--	--	--	--	--	0	22.7	60.0	33.3	65.9	66.4	593
BT-48[d]	304,2B	-	--	--	--	--	--	--	0	26.2	58.8	32.9	73.9	65.8	593
BT-39	304,2B	0	0.4	0.15	54.3	25.2	--	20,000	0.5	27.2	61.1	30.1	77.2	62.8	593
BT-37	304,2B	0	0.4	0.12	52.4	22.3	--	30,000	0.75	29.4	61.2	30.6	75.3	66.4	593
BT-38	304,2B	0	1.00	0.61	93.9	47.5	--	1,100	0.50	36.9	61.2	24.4	57.8	53.8	593
BT-50	304,2B	0	1.00	0.55	85.6	44.0	--	1,650	0.50	34.4	58.3	21.0	46.1	45.2	593
BT-51	304,2B	0.1	1.00	0.50	85.5	40.2	37.8	300	0.50	--	--	--	--	--	593
BT-56[e]	304,2B	0.1	1.00	0.58	87.1	41.9	34.4	150	0.25	--	--	--	--	--	593
BT-58[e]	304,2B	0.1	1.00	0.50	85.5	40.2	37.4	300	0.50	--	--	--	--	--	593
BT-54[e]	304,2B	0.1	1.00	0.65	83.3	40.3	31.4	450	0.75	--	--	--	--	--	593
BT-55[e]	304,2B	0.1	1.00	0.66	84.5	41.4	43.3	450	0.75	54.7	65.0	32.0[f]	39.8[f]	41.9[f]	593
BT-35	304,2B	0.1	1.00	0.69	85.2	41.8	33.3	300	0.5	34.6	60.4	25.9	47.5	49.6	593
BT-34	304,2B	0.1	1.00	0.67	83.3	39.8	33.7	450	0.75	36.7	56.9	19.0	31.0	29.4	593
BT-41	304,2B	0.1	1.00	0.58	84.5	41.3	33.8	450	0.75	35.5	60.3	24.0	49.9	43.7	593
BT-49	304,2B	0.5	1.00	0.60	84.1	40.6	33.8	147	0.25	34.2	60.2	24.9	44.4	53.8	593
BT-52	304,2B	0.5	1.01	0.61	83.0	39.6	33.8	206	0.30	--	60.4	18.8	40.5	40.0	593
BT-36	304,2B	0.5	1.00	0.69	76.8	35.8	27.2	294	0.50	35.6	55.3	13.6	25.7	24.3	593
8-30[d]	304,3C	--	--	--	--	--	--	--	0	20.3	55.0	20.9	70.9	64.0	593
8-35[d]	304,3C	--	--	--	--	--	--	--	0	23.3	54.9	28.1	42.6	70.0	593
8-34	304,3C	0.1	1.00	0.72	78.7	37.7	32.4	427	0.25	35.1	58.2	27.9	84.6	63.0	593
8-32[e]	304,3C	0.1	1.00	0.69	81.6	39.2	34.6	427	0.25	--	--	--	--	--	593
8-31[e]	304,3C	0.1	1.00	0.63	78.3	37.1	34.1	854	0.50	--	--	--	--	--	593
8-33	304,3C	0.1	1.00	0.63	78.5	37.9	35.0	854	0.50	37.7	57.7	30.0	65.8	58.0	593
E2-62[d]	316,4D	--	--	--	--	--	--	--	0	57.9	75.9	15.5	72.4	69.0	593
E2-3[d]	316,4E	--	--	--	--	--	--	--	0	51.1	68.2	11.3	51.7	75.0	593
E2-69	316,4D	0.1	1.00	0.58	105.1	49.7	39.6	510	0.5	40.2	62.0	10.4	26.2	25.0	593
E2-68	316,4D	0.1	1.00	0.65	89.5	41.0	34.2	762	0.75	37.9	55.5	6.9	10.8	18.0	593
E2-80	316,4E	0.1	1.01	0.68	83.9	40.8	35.9	700	0.25	38.2	60.9	19.3	57.6	73.0	593
E2-82[e]	316,4E	0.1	1.00	0.64	82.3	41.4	35.9	719	0.25	--	--	--	--	--	593
E2-83	316,4E	0.1	1.00	0.61	85.2	41.2	37.4	1441	0.50	37.6	62.2	21.6	76.7	67.5	593
E2-81[e]	316,4E	0.1	1.00	0.60	83.8	40.3	32.6	1441	0.50	--	--	--	--	--	593

[a] Both tensile and fatigue testing conducted in strain control at $4\times10^{-3}s^{-1}$ strain rate.
[b] Condition legend: 1A = Ht. 65808, annealed, aged 410°C for 1096 hours.
2B = Ht. 600414, as received (mill anneal).
3C = Ht. 8043813, aged 1000 hours at 593°C.
4D = Ht. 81583, 20% CW
4E = Ht. 81583, 20% CW plus 1000 hours at 593°C.

[c] Fatigue tested to failure to establish failure curves.
[d] Tensile tested without any prior cycling.
[e] Used for metallography after cycling.
[f] Gage section ground to remove all surface cracks.

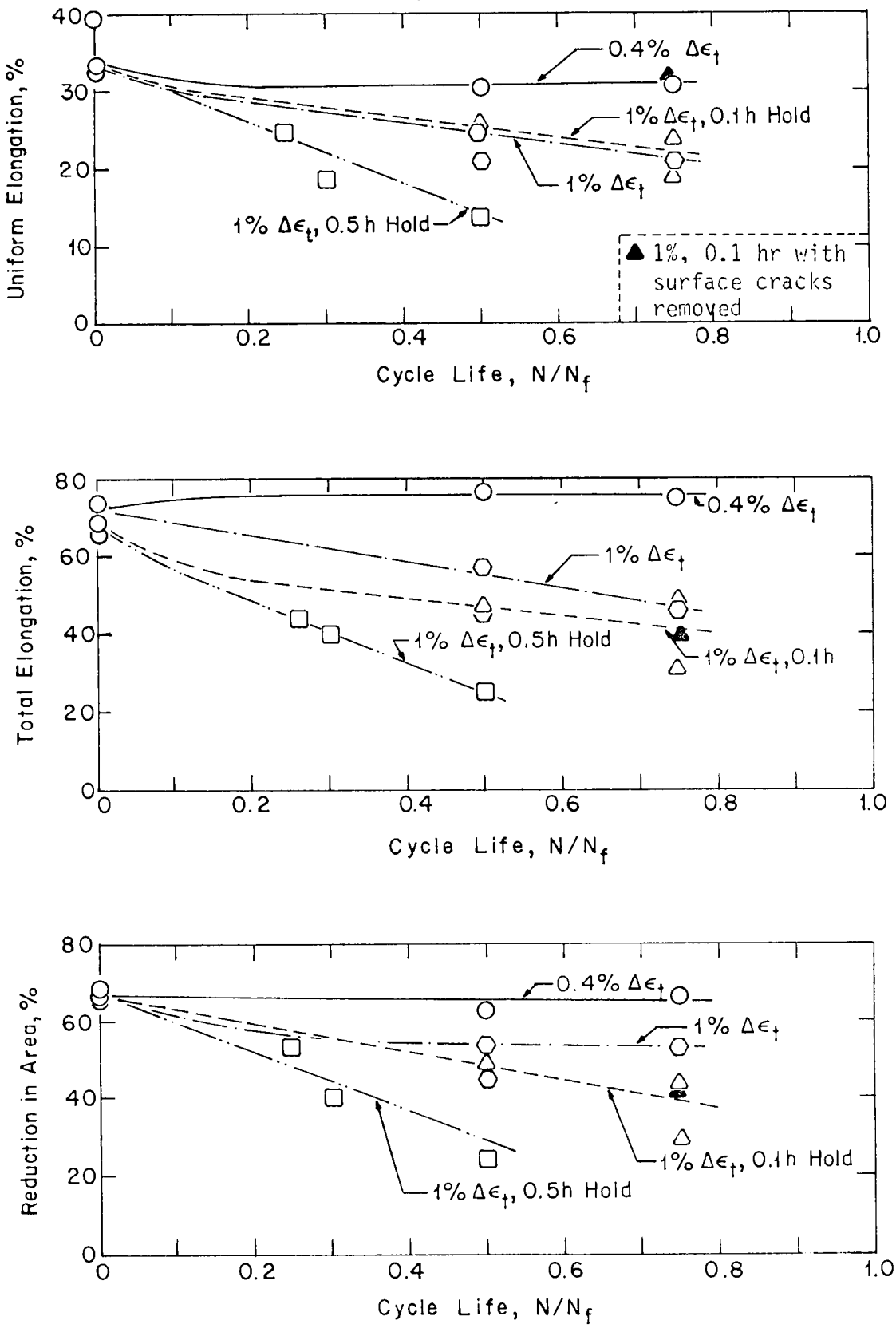

Figure 1.1 Tensile ductility of interrupted fatigue tests vs. cycle life of Type 304 stainless steel (Ht. 600414) at 593°C (1100°F).

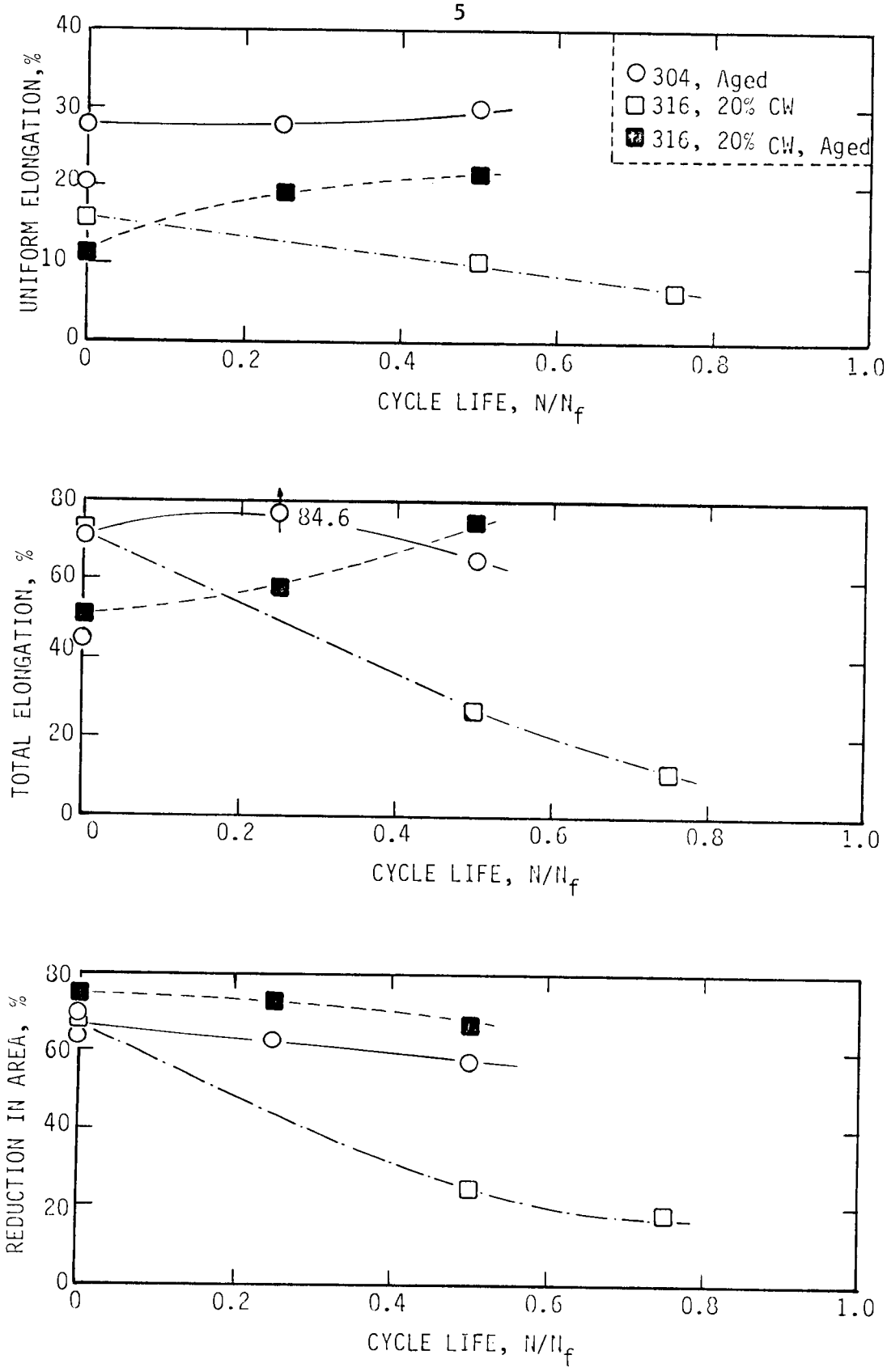

Figure 1.2 Tensile ductility of interrupted fatigue tests vs. cycle life of Type 304 and 316 stainless steel at 593°C (1100°F). Fatigue cycling was at 1% total strain range with 0.1 hr tensile hold.

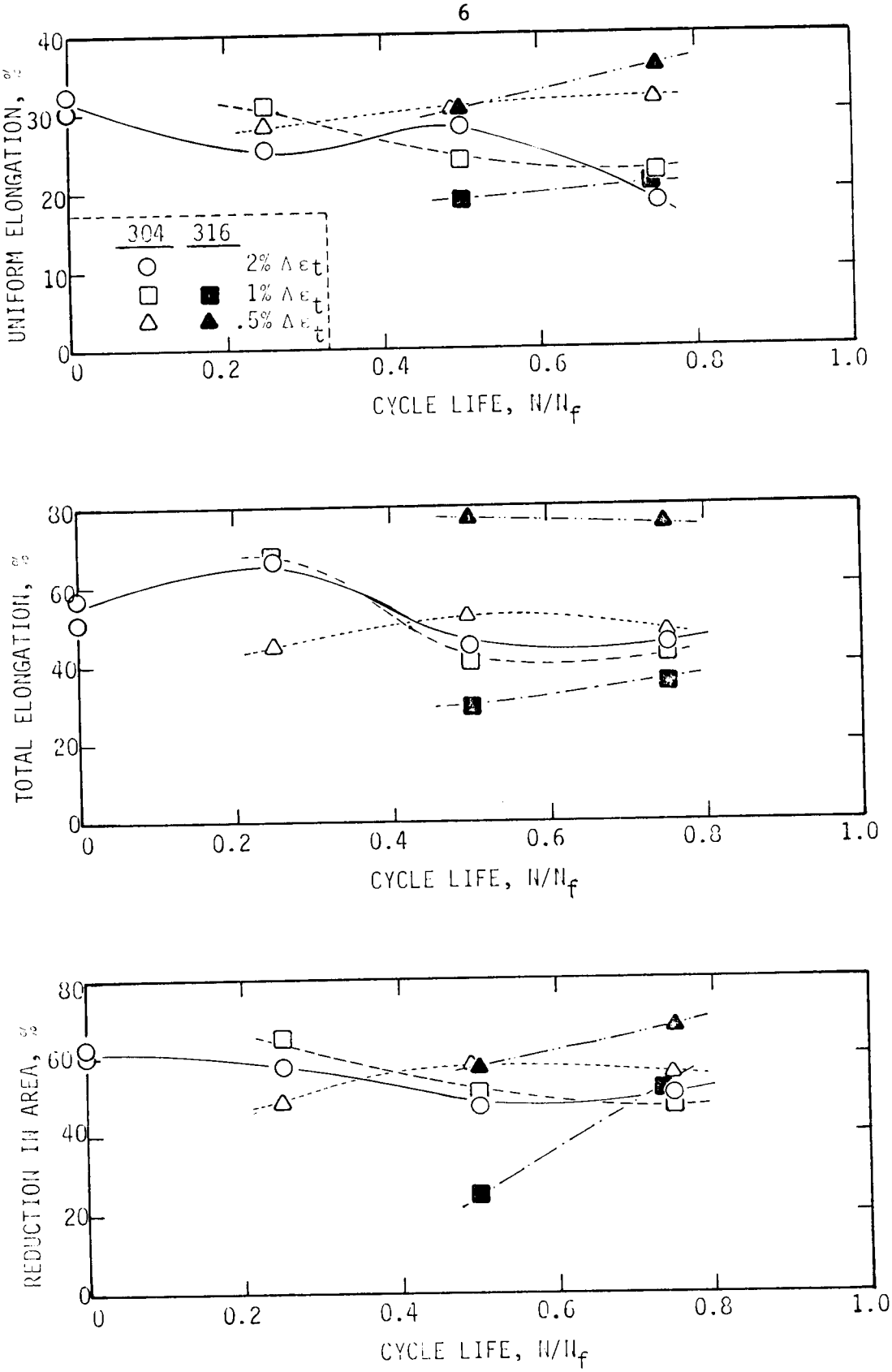

Figure 1.3 Tensile ductility of interrupted fatigue tests vs. cycle life of Type 304 and 316 stainless steel tested at 427°C (800°F).

ductility of Type 304 stainless steel (Heat 600414) was unchanged at 593°C (1100°F) out to 3/4 cycle life when the strain range was relatively low ($\Delta\varepsilon_t$ = 0.4%). But after cyclic periods of 1% total strain range, the ductility was significantly reduced, especially with a 0.5 hour tensile hold period incorporated into each cycle. Yield strength exhibited the expected cyclic hardening of previously cycled material but ultimate tensile strength remained unchanged regardless of cyclic history. Another heat of Type 304 stainless steel (Heat 8043813) which has been shown[1] to have superior creep-fatigue resistance exhibited less tensile ductility reductions after cycling than Heat 600414. Heat 81583 (Type 316 20% CW) which had also been shown[2] to be relatively creep-fatigue resistant in the aged condition was tensile tested after interrupted fatigue and this material also showed less tensile ductility reductions. Thus there appears to be a correlation that when superior creep-fatigue resistance is exhibited, the tensile ductility will be damaged less after interrupted creep-fatigue cycling. Tensile ductility at 427°C (800°F) did not appear to be significantly changed after an interrupted cycling period in both Type 316 and 304 stainless steel as shown in Figure 1.3.

The gage section of specimens given an interrupted cycling period were observed to contain what looked like surface cracks as shown in Figure 1.4. Sectioning and subsequent metallography confirmed the fact that surface cracks and surface cold work were indeed present even though the specimen had been cycled to only a fraction of its anticipated fatigue life. Specimen BT-54 which had experienced 3/4 cycle life at 1% total strain range with a 0.1 hour hold time exhibited surface cracks of up to 0.28mm (0.011 inches) deep (Figure 1.5a) and yet no measurable drop in load range had been observed. Further metallographic examination showed smaller surface cracks were present when a specimen was cycled to only 1/4 of its anticipated cycle life as shown in Figure 1.5b. Figure 1.5c-g are surface sections of other specimens which show the degree of surface cracks is related to the change in ductility as noted in Figures 1.1 and 1.2. To evaluate the effects of the surface damage as opposed to bulk material damage, a specimen (BT-55) was cycled to 3/4 fatigue life at 1% strain range with a 0.1 hour hold (compare with BT-54). Specimen BT-55 was then ground and polished in

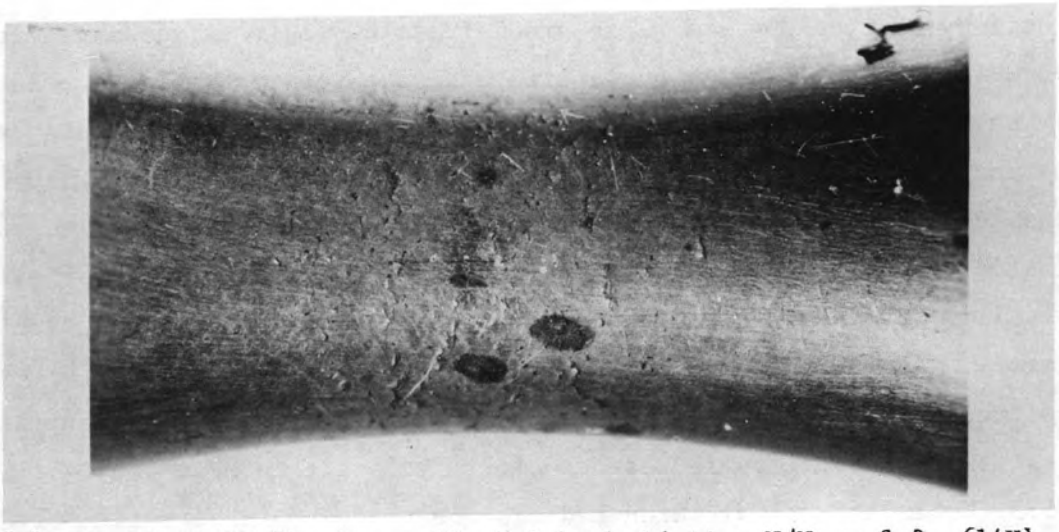

(a) Specimen BT-52, $\Delta\varepsilon_t$ = 1%, 0.5 hr hold time N/N_f = 0.3 (14X)

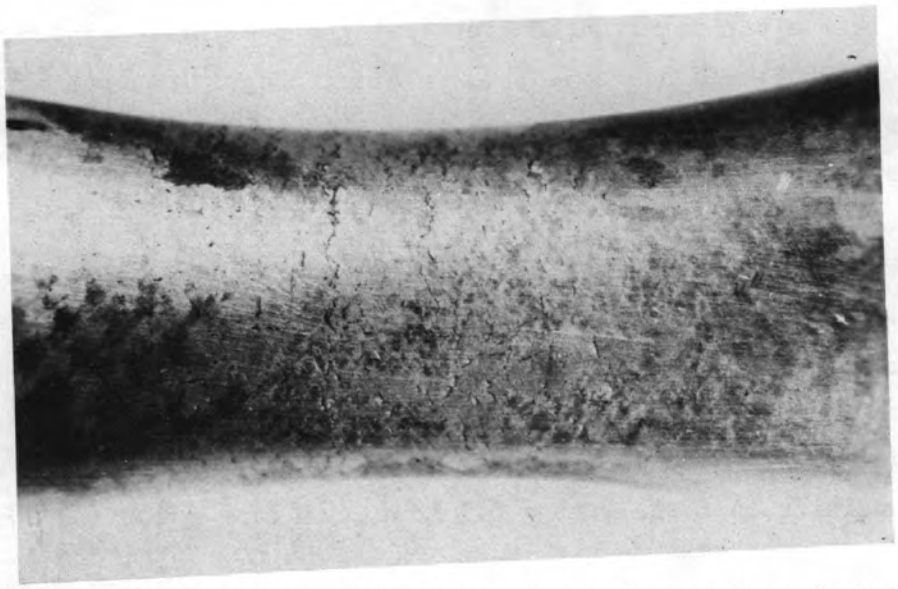

(b) Specimen BT-58, $\Delta\varepsilon_t$ = 1%, 0.1 hr hold time, N/N_f = ½ (14X)

Figure 1.4 - Macrographs of Type 304 hourglass fatigue specimens cycled at 593°C (1100°F) and stopped prior to failure.

(a) Specimen BT-54, 3/4 N/N_f (300X)

(b) Specimen BT-56, 1/4 N/N_f, 200X

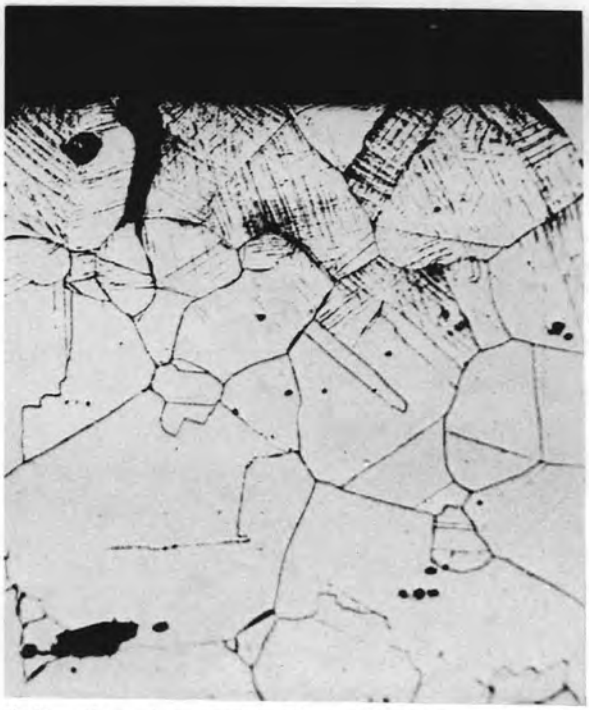

(c) Specimen BT-58, 1/2 N/N_f, 200X

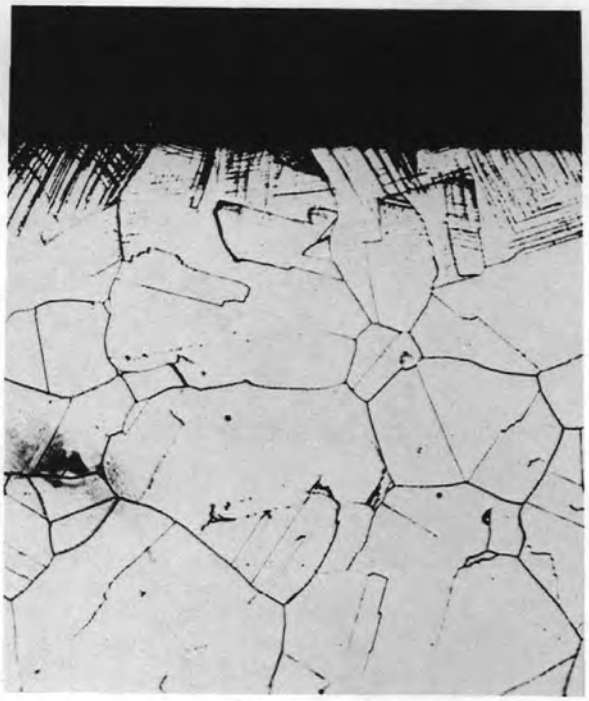

(d) Specimen 8-32 1/4 N/N_f, 200X

Figure 1.5 - Micrographs of sections taken from interrupted fatigue specimens showing surface cracks and other surface damage. All specimens tested at 1% $\Delta\varepsilon_t$ with 0.1 hr tensile hold at 593°C (1100°F).

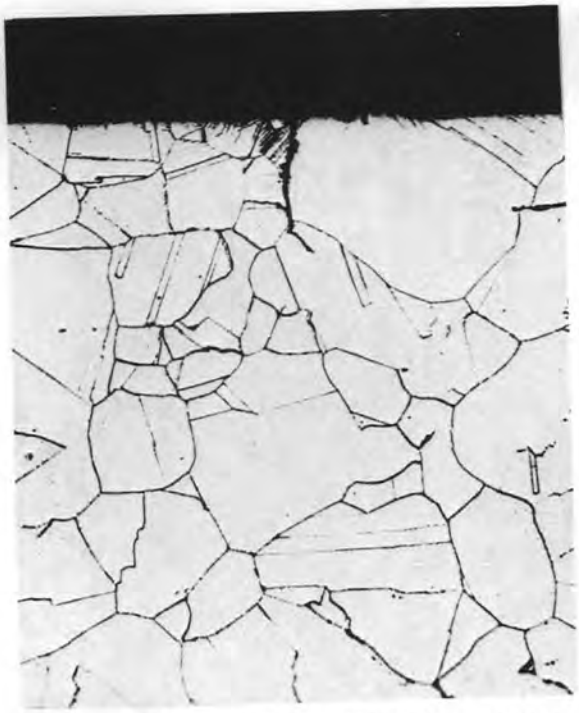

(e) Specimen 8-31, 1/2 N/N_f, 200X

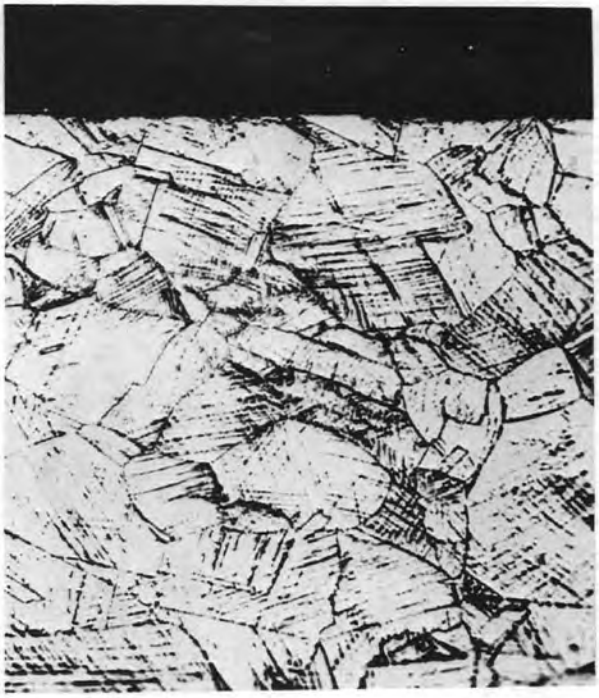

(f) Specimen E2-82, 1/4 N/N_f, 200X

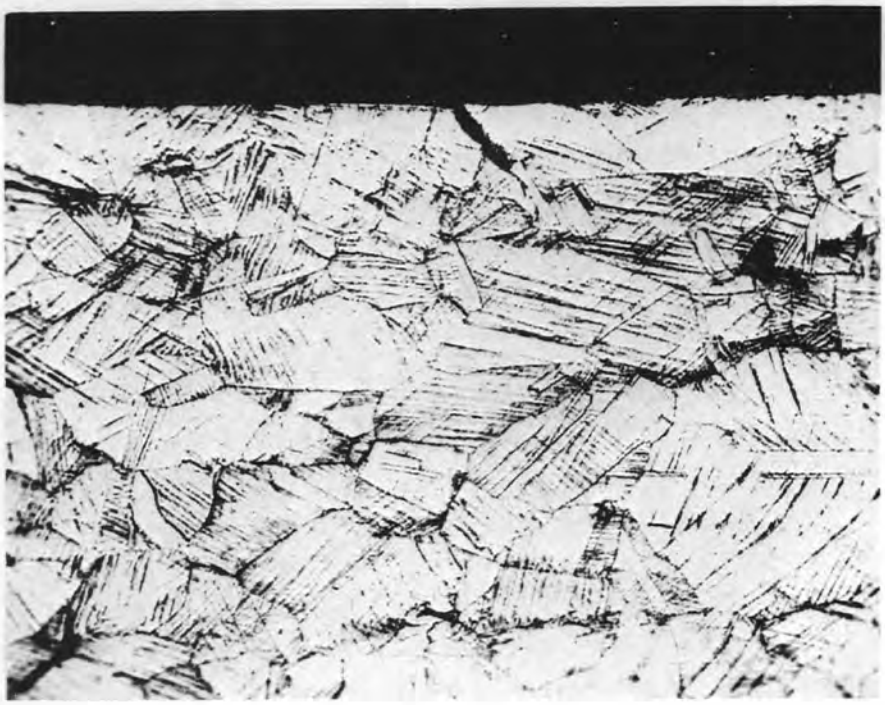

(g) Specimen E2-81, 1/2 N/N_f, 200X

Figure 1.5 (continued)

the gage section until dye penetrant inspection indicated no further surface cracks. Surface material had to be removed to a depth of 0.32mm (0.0125 inch) to eliminate all cracks. Although the ductility of this specimen was still not equivalent to uncycled material, a considerable improvement was shown which indicated the surface cracks and/or other surface damage played a significant role in the reduced tensile ductility.

From this investigation the following conclusions can be drawn:

1. Fatigue cycling in the creep regime of Type 304 and 316 can cause reductions in tensile ductility at relatively low fractions of expected cycle life.
2. The incorporation of tensile hold times (creep-fatigue damage) results in further decreased tensile ductility of interrupted fatigue cycling.
3. A significant amount of the reduced ductility is due to surface cracks and/or other surface damage.
4. Cracks initiate in the surface as low as 0.25 of the cycle life.
5. Material showing superior creep-fatigue resistance also exhibits less tendency toward ductility degradation with cycle life and is slower to initiate surface cracks during cycling.

1.3 INCONEL 718 MECHANICAL PROPERTY PROGRAM - G. E. Korth and G. R. Smolik

1.3.1 Development of New Heat Treatment for Weldments

In order to obtain consistently acceptable values for weld ductility (>12-15% elongation) a new heat treatment for Inconel Alloy 718 has been developed. This new heat treatment has been designated as the INEL Heat Treatment and is recommended for the post heat treatment for Inconel 718 weldments. The INEL Heat Treatment is described as follows:

2000°F solution anneal for 1 hour
Slow cool to <1000°F at 100°F/hr
Duplex age at 1325°F for 4 hours and
1150°F for 16 hours

The 2000°F solution anneal is required to dissolve the undesirable Laves phase found in the weld deposit. Although the high solution anneal temperature causes some grain growth, the enchanced weld ductility more than offsets the undersirable effects of larger grains. With the slow cool and duplex age, typical room temperature mechanical properties for either base or weld metal are shown in Table 1.2.

Table 1.2 - Typical Room Temperature Tensile Properties of Inconel 718 Base or Weld Metal given the INEL Heat Treatment

Yield Strength - 145-155 ksi
Ultimate Tensile Strength - 190-200 ksi
Total Elongation - 15-25%
Reduction in Area - 25-40%

1.3.2 Strain-Age Cracking of Inconel 718

After a 2000°F solution anneal an elevated temperature ductility minimum observed in Inconel 718 between 1350 to 1500°F is seen to become worse. Experience with PBF welded components has shown that if this minimum ductility was in the range of 4-5% elongation the component would crack during the heat treating cycle. Evaluation of this cracking showed evidence of a heat-to-heat variation in response and therefore, seven different heats of Inconel 718 from two different suppliers with two different process histories were tested between 1200 and 1600°F in the solution annealed condition with two cooling rates. The results are shown in Figures 1.6 and 1.7. There is considerable data scatter but two conclusions may be drawn from the tests:

1. The fast cooling rate (1200°F/hr) which corresponds to an air cool resulted, on the average, in lower ductility values at the minimum than the furnace cooling rate

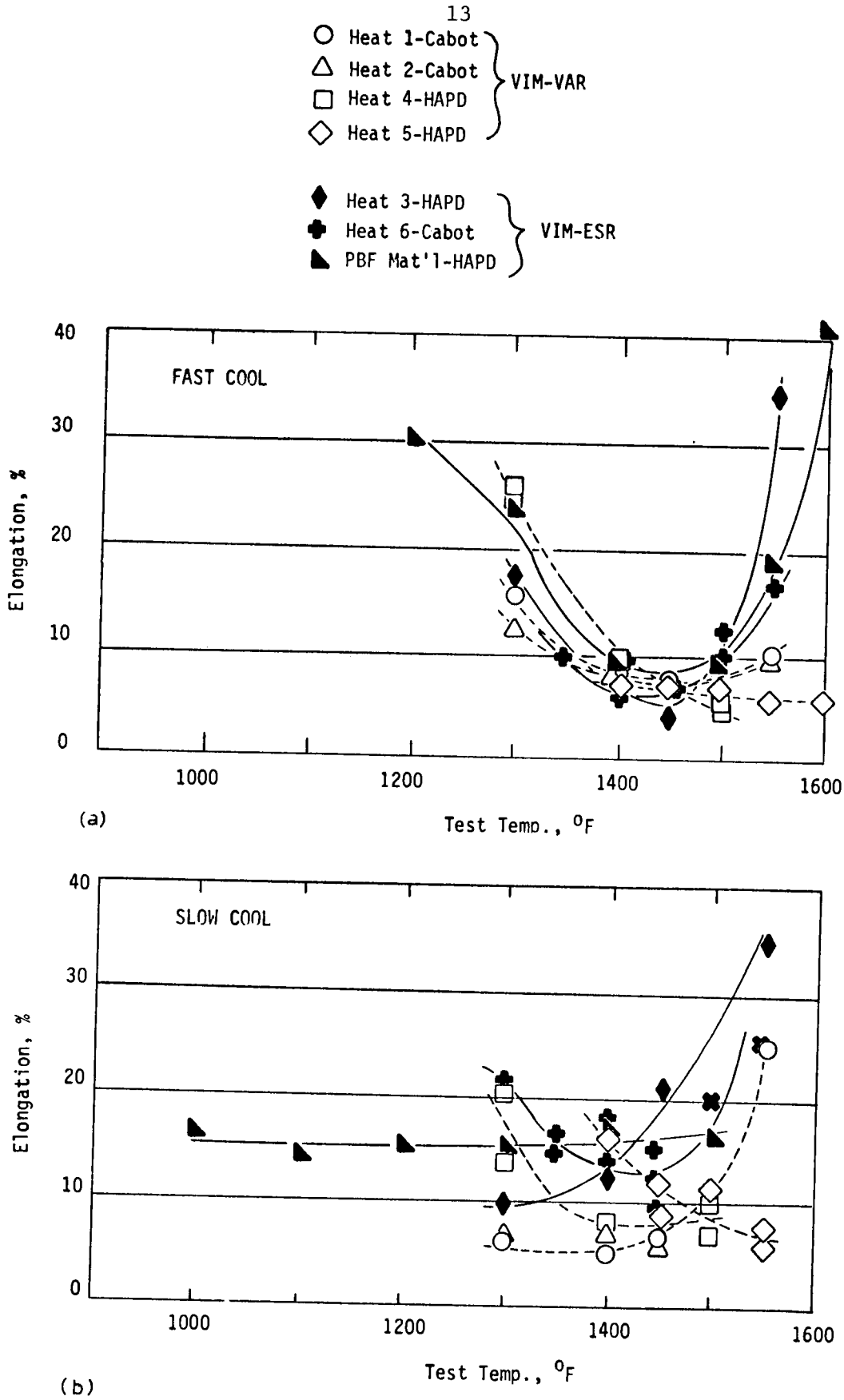

Figure 1.6 Elongation (1 in.) vs. Test Temperature for Inconel 718 Solution Annealed at 2000°F and Cooled at 1200°F per hour (a); and 100°F/hr (b).

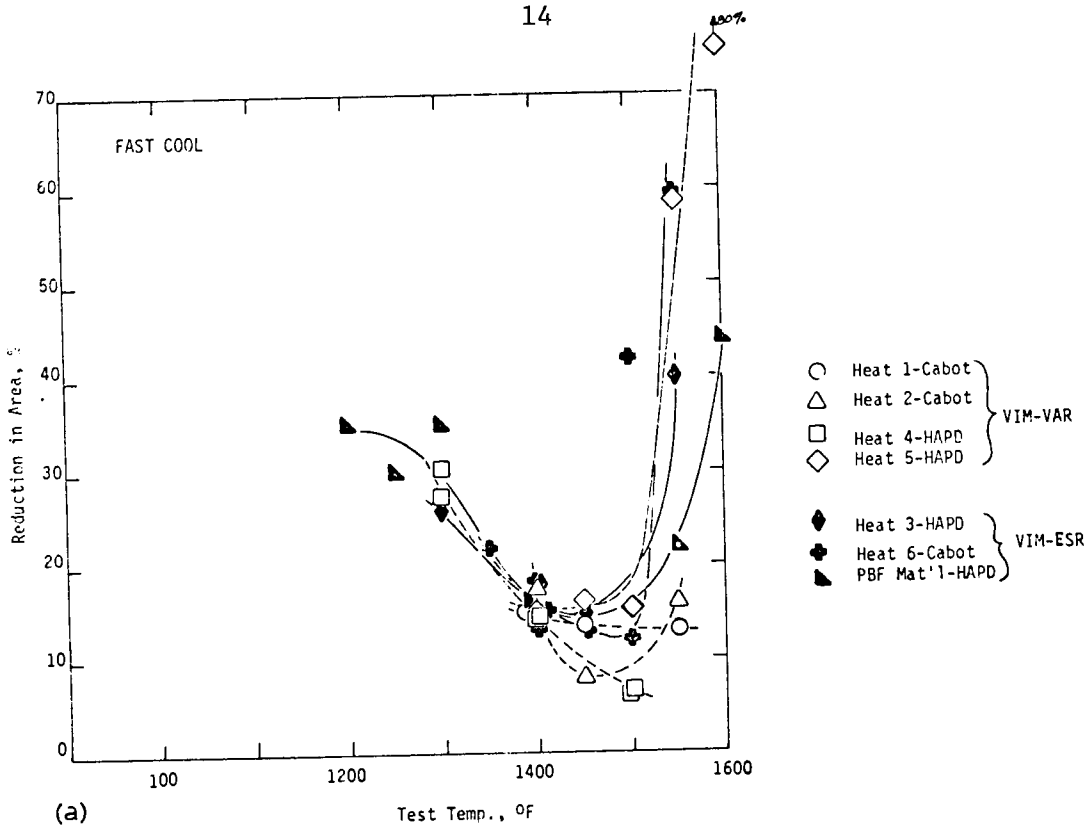

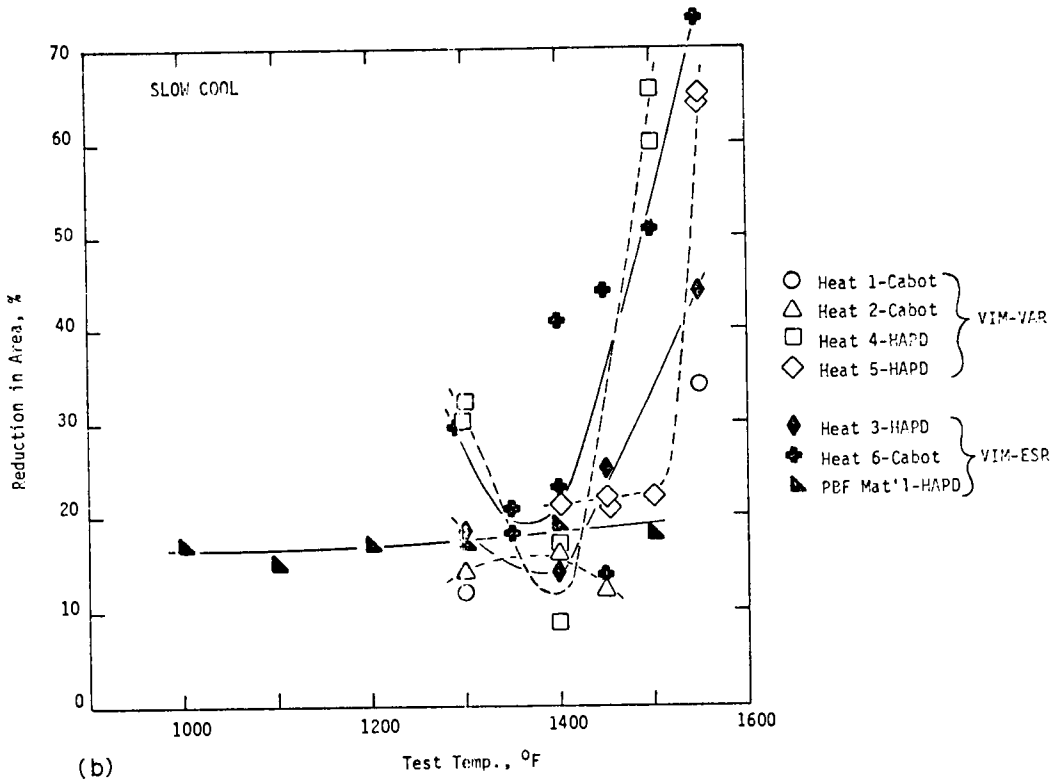

Figure 1.7 Reduction in Area vs. Test Temperature for Inconel 718 Solution Annealed at 2000°F and cooled at 1200°F per hour; (a); and 100°F/hr (b).

($100^{\circ}F/hr$).

2. The VIM-ESR (Vacuum Induction Melt-Electroslag Remelt) consistently yielded higher ductility values than the VIM-VAR (Vacuum Induction Melt-Vacuum Arc Remelt) process history regardless of supplier.

A further investigation of the INEL Heat Treatment with respect to the elevated temperature ductility minimum was undertaken by solution annealing a series of specimens from two heats and quenching at various points during the $100^{\circ}F/hr$ cool. These specimens were tested at the Wright-Patterson Air Force Laboratory for ANC at $1400^{\circ}F$ in solution annealed condition. The test temperature was chosen to approximate the ductility minimum as seen in Figures 1.6 and 1.7. The results are shown in Figure 1.8 where elongation and reduction in area are plotted as a function of quench temperature. The results indicate that the metallurgical condition at the $1850^{\circ}F$ quench was the most detrimental to the hot ductility and recovery was not marked until the cooling had progressed to approximately $1500^{\circ}F$ or lower. All the ramifications of these results are not clearly understood at the present time, but the type, location, and size of the precipitates present at any time undoubtedly are the controlling parameters.

1.3.3 Optimization of INEL Heat Treatment

The INEL Heat Treatment employs the $2000^{\circ}F$ solution anneal to dissolve the Laves phase but an examination of the time-temperature-precipitation curve shows that a cooling curve at $100^{\circ}F/hr$ cuts through the nose of the Laves phase precipitation curve (see Figure 1.9). In an attempt to evaluate the effects of cooling so as to not cut through the Laves precipitation curve, two step-type cooling curves were evaluated on a composite weld-heat affected zone-base metal tensile specimens and compared with the standard INEL Heat Treatment. The orientation of the test specimen with respect to the weldment is shown in Figure 1.10 and the results of the tests are listed in Table 1.3.

Specimens with the INEL Heat Treatment failed in the weld metal while the fracture for the two step-type cooling curves was located

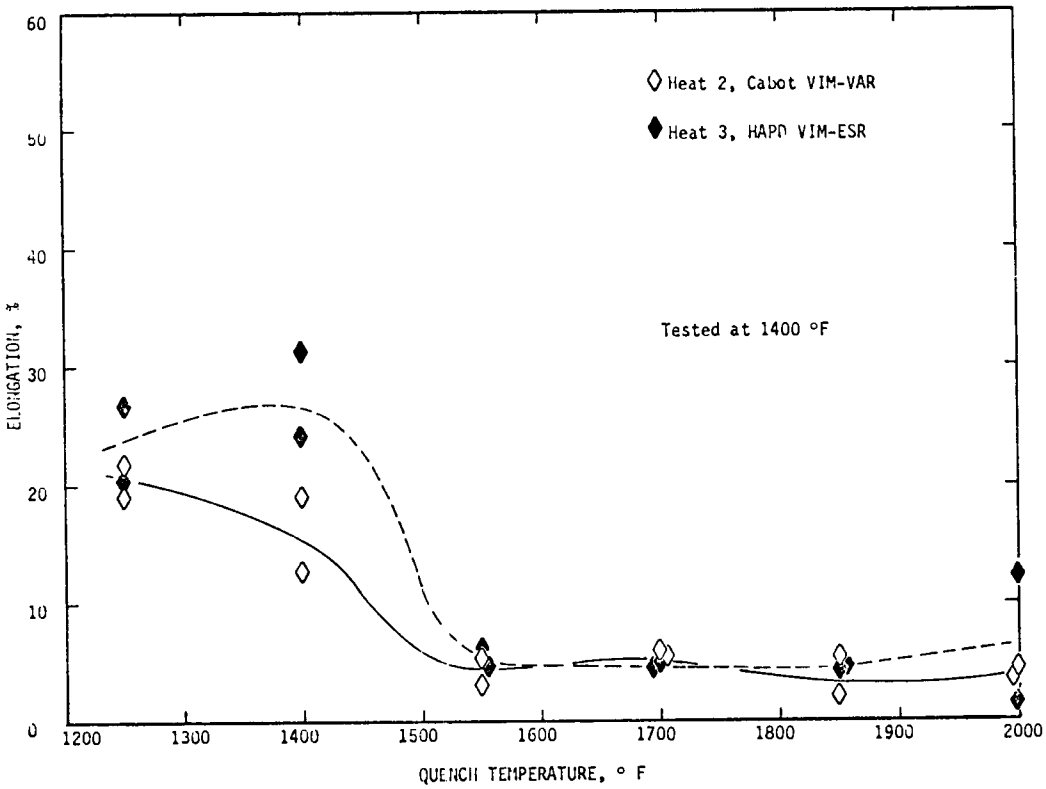

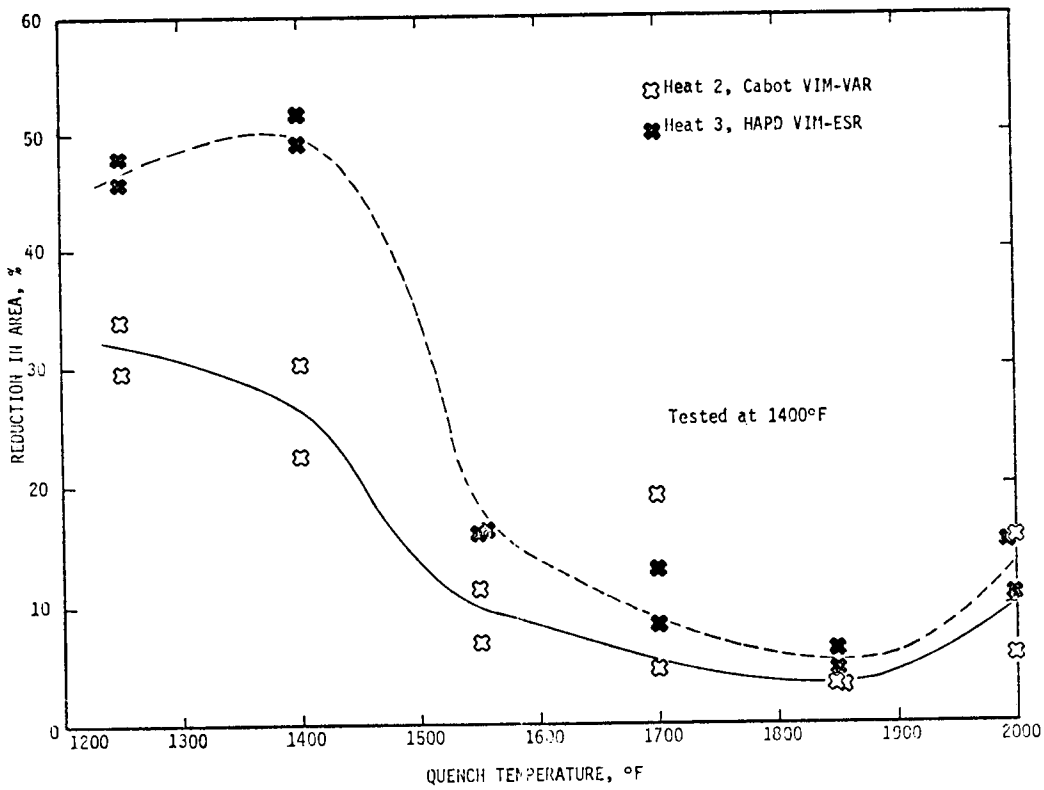

Figure 1.8 Ductility of 1400°F tensile tests of Inconel 718 at various stages of the INEL Heat Treatment solution anneal. (2000°F anneal and cooled at 100°F/hr to quench temperature.)

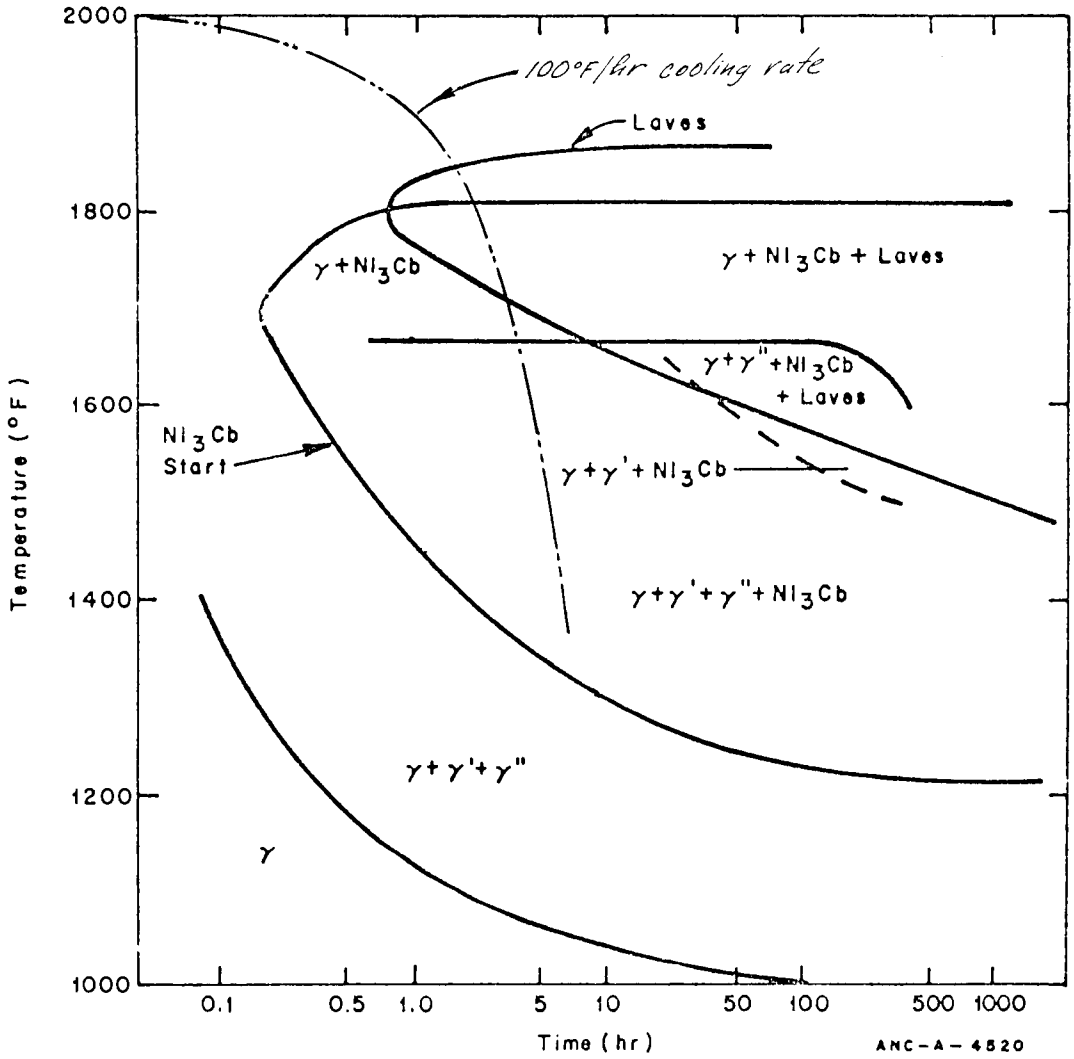

Figure 1.9 Time-temperature-precipitation curves for Inconel 718.

TABLE 1.3 ROOM TEMPERATURE TENSILE PROPERTIES OF INCONEL 718

WELDMENT WITH VARIOUS HEAT TREATMENTS

Specimen No.	Heat Treat	σ_{ys}, ksi	σ_{uts}, ksi	Elong %	R.A., %
5-5-22A	A	154.2	206.4	17.5	28.0
5-5-22B	A	156.1	204.8	----	24.2
5-5-22C	A	157.6	207.3	16.5	25.7
5-8-21B	B	161.8	199.6	16.6	41.6
5-8-21C	B	160.9	204.7	18.0	39.8
4-8-10A	B	162.9	205.9	24.9	34.9
5-7-22A	C	149.5	203.1	----	23.3
5-7-22B	C	146.3	198.5	13.2	15.7
5-7-22C	C	142.2	200.0	24.9	34.0

A - INEL heat treatment (2000°F solution anneal; 100°F/hr cool to 1000°F, air cool, aged)

B - 2000°F solution anneal; 1200°F/hr cool to 1600°F then 400°F/hr to 1000°F, air cool, aged

C - 2000°F solution anneal; 1200°F/hr cool to 1600°F then 100°F/hr to 1000°F, air cool, aged

A, B, C - Aged 1325°F 4 hours and 1150°F for 16 hours

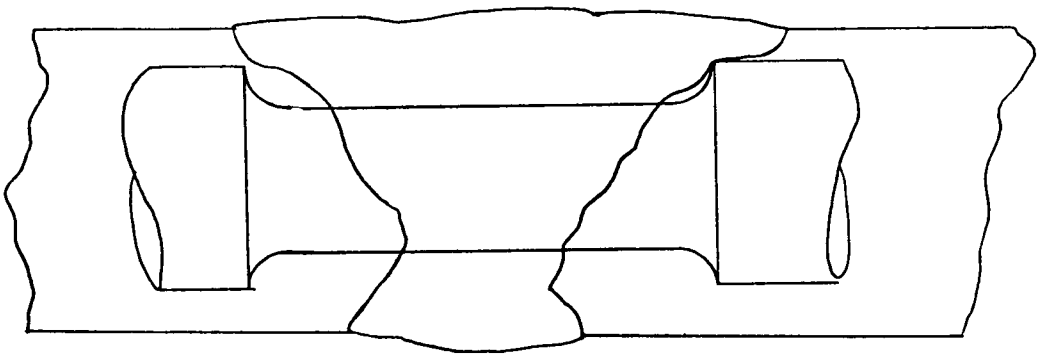

Figure 1.10 Orientation of gage section (0.5 inch) of tensile specimens with respect to weldment.

in the base metal as shown in Figure 1.11. The step-type cooling curves may yield superior mechanical properties but this type cooling is probably not compatible with massive welded components requiring large heat treating furnaces not capable of such step-type cooling rates.

1.4 REFERENCES

1. C. R. Brinkman and G. E. Korth, J. Nucl. Mats. 48 (1973) 293-306.
2. G. E. Korth and M. D. Harper, ANC Contribution to Mechanical Properties Quarterly Progress Report ending July 31, 1974, ORNL-4998.

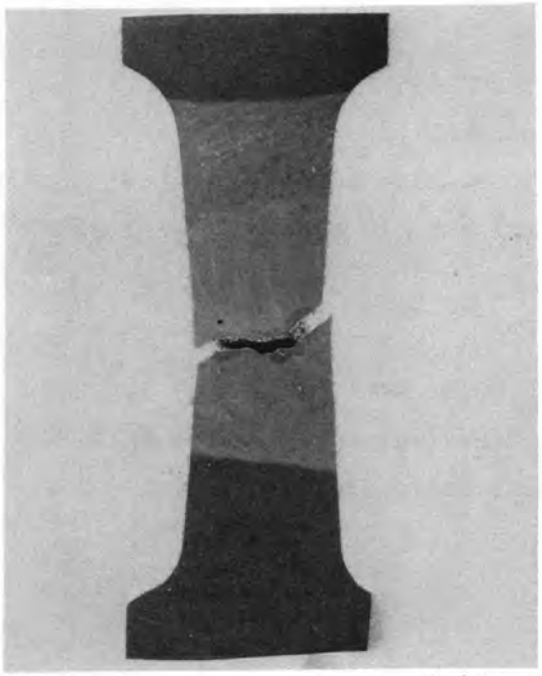

3.4X

100X

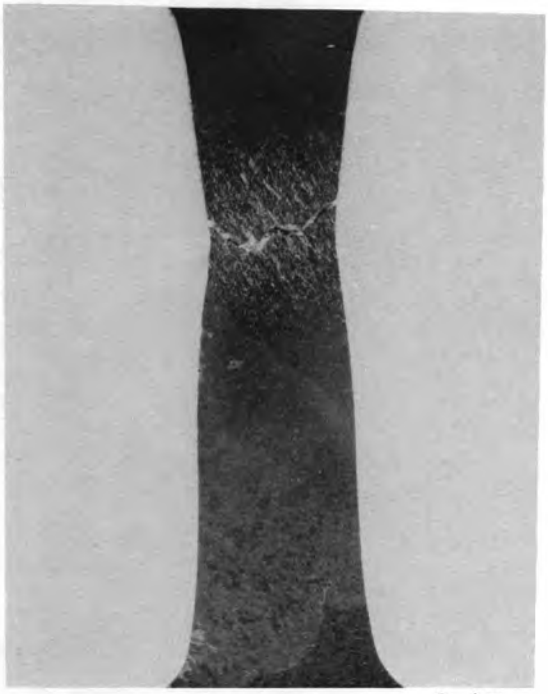

3.4X

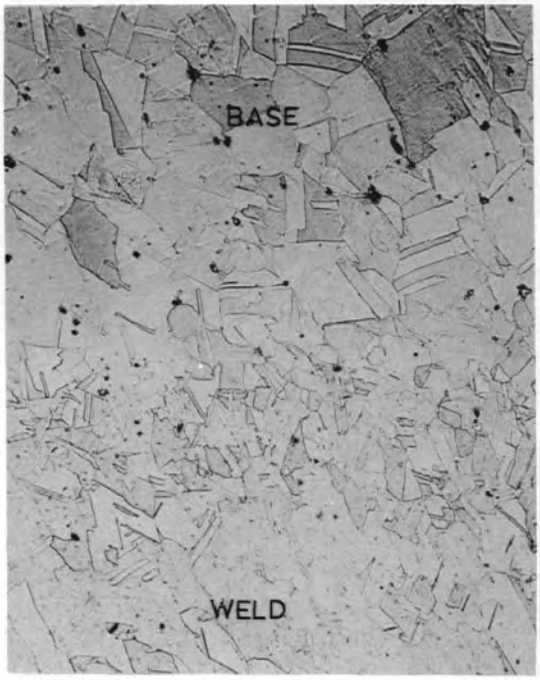

100X

Figure 1.11 Macrograph and fusion line micrograph of Inconel 718 tensile specimens (a) Specimen 5-5-22A (INEL Ht. Tr.), (b) Specimen 5-8-21B (Step-type cooling from solution anneal).

2. ARGONNE NATIONAL LABORATORY

R. W. Weeks

2.1 INTRODUCTION

Argonne National Laboratory (ANL) is conducting an extensive program to provide low-cycle, high-temperature fatigue data on Types 304 and 316 stainless steel in support of LMFBR component design, as outlined in a previous report.[1] The present report describes a further analysis of surface effects on the low-cycle fatigue life of Type 304 stainless steel, some preliminary work on microstructural effects on low-cycle fatigue in Fe-Cr-Ni alloys, and the effects of sodium exposure on the creep and low-cycle fatigue behavior of Types 304 and 316 stainless steel.

2.2 FRACTURE AND FATIGUE STUDIES ON STAINLESS STEEL -- D. R. Diercks

2.2.1 Effects of Surface-roughness and Strain Range on the Low-cycle Fatigue Behavior of Type 304 Stainless Steel -- P. S. Maiya

The present report is concerned with the low-cycle fatigue behavior of Type 304 stainless steel (Heat 9T2796) that has a well-characterized surface roughness initially introduced in smooth specimens by a silicon carbide technique. The results are compared with similar data obtained earlier[2] from smooth specimens prepared by a mechanical polishing technique. The extent of reduction in crack-initiation life that results from both an initial surface roughness and an increase in the applied strain range as well as the relation between fatigue life and crack-initiation life has been discussed quantitatively.

The hourglass-shape specimens of stainless steel used in the present study had a surface finish (parallel to longitudinal axis) better than $R = 0.3$ μm, where R is the root-mean-square (rms) value for the depth of the surface grooves. All specimens were given the same aging heat treatment as described previously.[2] In addition, a surface roughness of $R \approx 2.9$ μm was introduced circumferentially along the gauge length of fatigue specimens by a controlled silicon carbide grinding technique.[3,4] The low-cycle fatigue properties of these specimens were then determined in air in axial strain control at a strain rate of 4×10^{-3} sec^{-1} at

593°C. To compare the present fatigue results with the smooth specimen data reported elsewhere,[2] the same total strain ranges ($\Delta\varepsilon_t$) were selected, namely, 0.5, 0.75, 1.0, and 2.0%. The procedure for estimating the number of cycles to initiate a crack length of one grain diameter ($\approx$ 0.1 mm) is based on fatigue-striation spacing measurements[4,5] and on the validity of the crack-growth relation[2,4] $\ln a = KN$, where a is the crack length, N is the number of strain cycles, and K is a constant. The procedure for estimating crack-initiation life has been described elsewhere.[4]

The decrease in fatigue life that results from surface roughness at different strain ranges is conveniently described by the quantity $N_f(R)/N_f(S)$, where $N_f(R)$ is the fatigue life of a specimen with R $\approx$ 2.9 μm, and $N_f(S)$ is the fatigue life of the smooth (mechanically polished) specimens. The results listed in Table 2.1 show that surface roughness decreases the fatigue life. Furthermore, they suggest a trend that surface-roughness effects on fatigue become more important as the strain range decreases. These results can be understood by a simple analysis based on crack-initiation and crack-propagation considerations.

Table 2.1. Low-cycle Fatigue-life Data for Type 304 Stainless Steel at 593°C as Affected by Surface Roughness[a]

Total Strain Range, %	Cycles to Failure for Smooth Specimens $N_f(S)$	Cycles to Failure for Specimens with R $\approx$ 2.9 μm $N_f(R)$	$\frac{N_f(R)}{N_f(S)}$
0.5	31,896	10,084	0.32
0.75	8,827	4,005	0.45
1.0	4,014	2,224	0.55
2.0	700	332	0.47

[a]The reproducibility of $N_f(S)$ or $N_f(R)$ is within 10-15%. The smooth-specimen data are obtained from Ref. 2.

The relation between the decrease in fatigue life $N_f(R)/N_f(S)$ and the decrease in crack-initiation life $N_o(R)/N_o(S)$ that results from surface roughness, following the formalism of Grosskreutz, is given by[3]

$$N_f(R)/N_f(S) = 1 + \beta[N_o(R)/N_o(S) - 1], \tag{1}$$

where β is the crack-initiation life in a smooth specimen $N_o(S)/N_f(S)$. The magnitude of the observed decrease in fatigue life at various strain ranges listed in Table 2.1 can now be explained by using Eq. (1). A plot of $N_f(R)/N_f(S)$ versus $N_o(R)/N_o(S)$ is constructed for arbitrarily chosen values of β, as shown in Fig. 2.1. It shows quantitatively how surface roughness affects fatigue life and, as explained below, how surface-roughness effects tend to become more important at lower strain ranges. The value of $N_o(R)/N_o(S)$, determined previously[3,4] for $\Delta\varepsilon_t = 1\%$

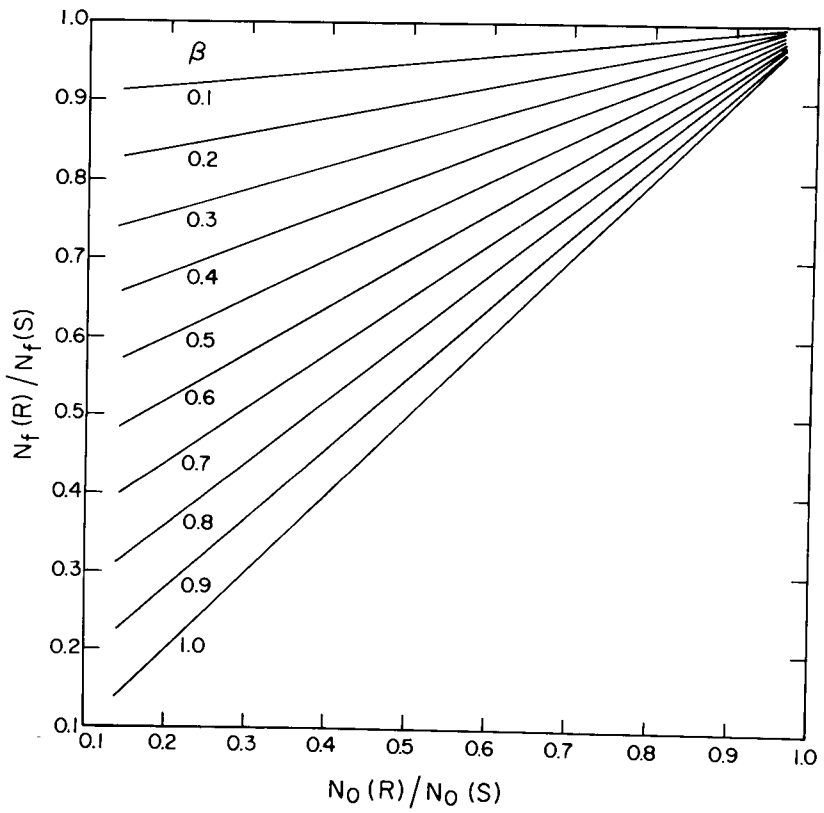

Fig. 2.1. Plot of Decrease in Fatigue Life with Decrease in Crack-initiation Time Constructed from Eq. (1) for Different Values of β. $\beta \leq 1.0$.

and R = 2.9 μm, is 0.25. Let us suppose that the quantity $N_o(R)/N_o(S)$, which is a measure of the decrease in crack-initiation time that results from surface roughness, depends only on R and not on the applied strain range. Then it is clear that, at the lowest strain range $\Delta\varepsilon_t = 0.5\%$ for which $\beta \approx 0.90$,[2] the reduction in fatigue life read from Fig. 2.1 is ~ 0.33, which is close to the result observed experimentally (Table 2.1). The above results have been further substantiated by determining the number of cycles to initiate a crack length of 0.1 mm as a function of strain range.

The fractured surfaces have been examined by scanning-electron microscopy, and, from the fatigue striation-spacing measurements, plots of ln a versus N were constructed as shown in Fig. 2.2. At lower strain ranges ($\Delta\varepsilon_t \leq 0.75\%$), a straight-line relationship is obtained between ln a and N, as in the case of smooth specimens. At total strain ranges $\geq 1\%$, we find

$$\left(\frac{d \ln a}{dN}\right)_{a \leq 1\text{-}2\text{mm}} < \left(\frac{d \ln a}{dN}\right)_{a \geq 1\text{-}2\text{mm}} \tag{2}$$

Although it is difficult to comprehend this crack-growth behavior from a mechanistic viewpoint, the plots of ln a versus N provide a convenient method of estimating $N_o(R)$ associated with a crack of a specified length. This crack length is assumed to be equal to 1 grain diameter ($\approx$ 0.1 mm), which is consistent with our previous studies.[2-4]

The fatigue life $N_f(R)$ is given by

$$N_f(R) = N_o(R) + N_p(R), \tag{3}$$

where $N_o(R)$ is the number of cycles to crack initiation, and $N_p(R)$ is the number of cycles to propagation. The variation of $N_o(R)$ and $N_p(R)$ with strain range follows the form of the Coffin-Manson relations

$$N_o(R) = A' \, (\Delta\varepsilon_p)^{-\alpha'}, \tag{4}$$

and

$$N_p(R) = C' \, (\Delta\varepsilon_p)^{-\gamma'}, \tag{5}$$

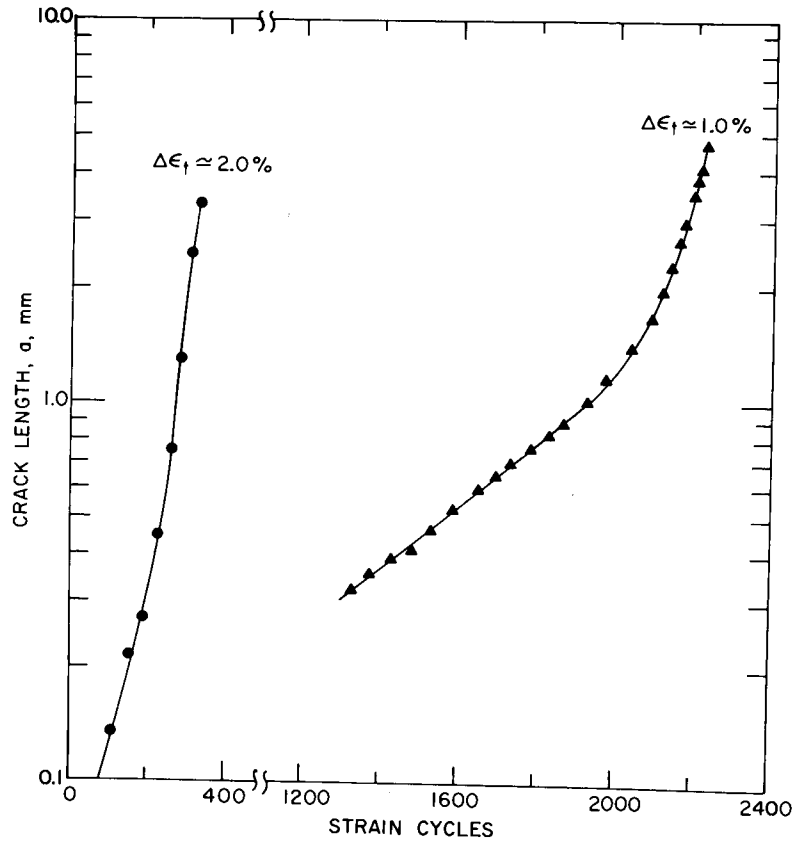

(a)

Fig. 2.2 Semilogarithmic Plots of Crack Length for Different Strain Ranges in Type 304 Stainless Steel. R $\approx$ 2.9 μm.

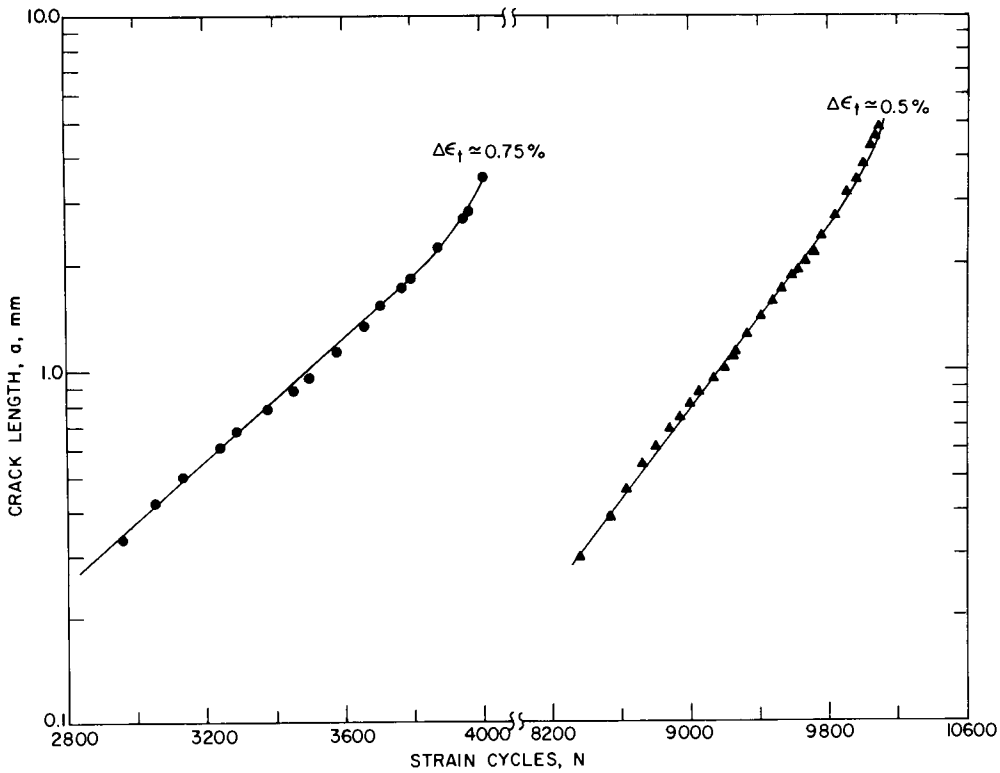

(b)

where A', α', C', and γ' are constants, and $\Delta\varepsilon_p$ is the plastic strain range. The values of the constants determined from the least-squares fit of the data are 1.511, 2.627, 1.247, and 1.33, respectively. We have reported[2] similar constants for the smooth specimens. For the case of smooth specimens, we write the analogous equations

$$N_f(S) = N_o(S) + N_p(S), \tag{6}$$

$$N_o(S) = A\ (\Delta\varepsilon_p)^{-\alpha}, \tag{7}$$

and

$$N_p(S) = C\ (\Delta\varepsilon_p)^{-\gamma}. \tag{8}$$

A comparison of Eqs. (4) and (7) is shown in Fig. 2.3, where it can be seen that $\alpha \approx \alpha'$, and the quantity $N_o(R)/N_o(S)$ is insensitive to changes in the strain range, a result which will be discussed later.

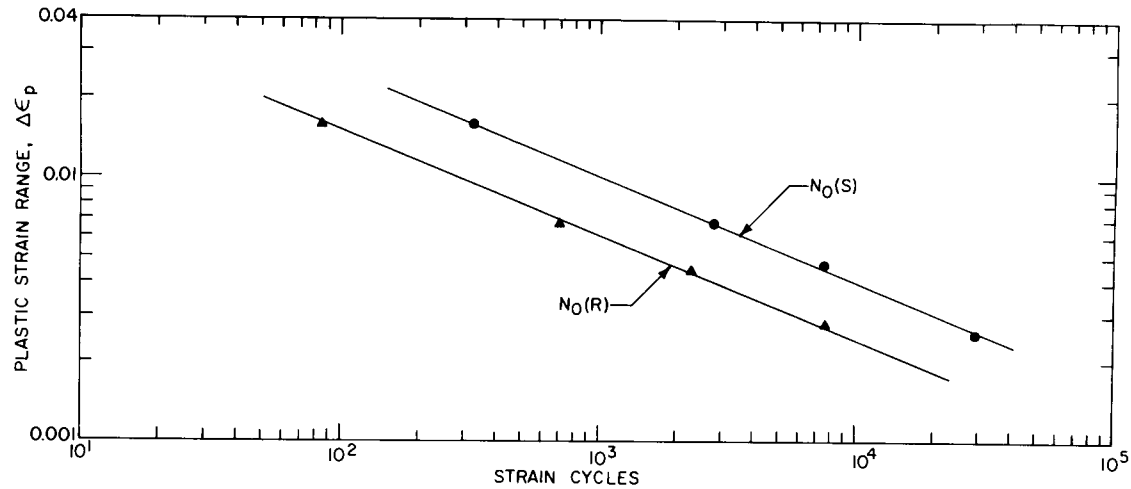

Fig. 2.3. Crack Initiation as Influenced by Plastic Strain Range and Surface Roughness in Type 304 Stainless Steel.

Phenomenologically, the fatigue lives $N_f(R)$ and $N_f(S)$ can be described by Eqs. (3)-(8), and the representation of total life in terms of crack initiation and crack propagation is shown in Fig. 2.4. The results show that surface roughness affects N_o and not N_p for all strain ranges investigated.

Inasmuch as surface roughness affects only the crack-initiation life, it is meaningful to define a fatigue-strength reduction or plastic-strain concentration factor K_f based on N_o and not on the overall fatigue life N_f. We use the same definition for crack-initiation life for both the smooth specimens and specimens with roughness R. The term K_f can then be defined as the ratio $(\Delta\varepsilon_p)_S/(\Delta\varepsilon_p)_R$ at the same cycle-to-crack initiation. The terms $(\Delta\varepsilon_p)_S$ and $(\Delta\varepsilon_p)_R$ are the strain ranges applied to the smooth specimen and the specimen with roughness R, respectively, to obtain the same number of cycles to crack initiation. For the above case,

$$N_o(R) = N_o(S), \tag{9}$$

and

$$A' \, [(\Delta\varepsilon_p)_R]^{-\alpha} = A \, [(\Delta\varepsilon_p)_S]^{-\alpha}, \tag{10}$$

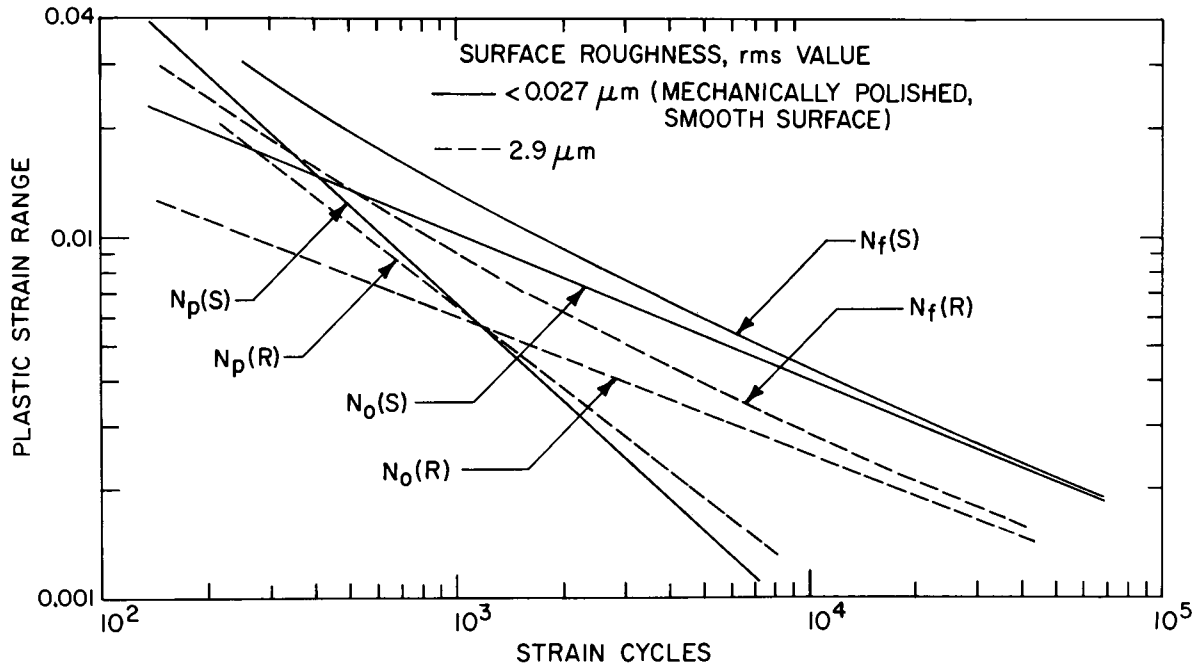

Fig. 2.4. Crack Initiation and Crack Propagation as a Function of Plastic Strain Range in Type 304 Stainless Steel.

and, from Eq. (10) and from the definition of K_f, it follows that

$$N_o(R) = A\ (K_f\ \Delta\varepsilon_p)^{-\alpha}. \tag{11}$$

Equation (11) relates the crack-initiation life for specimens with surface roughness R to the smooth specimen constants through K_f. It is important to point out that K_f depends only on surface roughness and remains unaffected by different strain ranges for a fixed surface roughness. Therefore, in fatigue experiments, if $\Delta\varepsilon_p$ is held constant and R is varied, we observe that

$$N_o(R) = (\text{constant})(K_f)^{-\alpha}, \tag{12}$$

where K_f is related to the geometrical parameters of surface roughness. Recently, the author has examined the validity of Eq. (12) in greater detail.[6]

A comparison of the crack-initiation life in smooth specimens and specimens with R $\approx$ 2.9 μm has been made (Fig. 2.5). It is clear that the percent of life in crack initiation decreases from 46 to 26% at the largest strain range and from 91 to 75% at the smallest strain range used in the present work by introducing an initial surface roughness. The significant point of this comparison is that crack initiation occupies a major portion of the total life at lower strain ranges, even when the surface contains irregularities of the kind described in the present report.

Finally, we would like to discuss the relation between fatigue life and crack-initiation time in smooth specimens. Several years ago, Manson[7] hypothesized crack initiation and proposed an equation of the following form for estimating $N_o(S)$ in a ductile material:

$$N_f(S) - N_o(S) = N_p(S) = PN_f^{\,c}(S), \tag{13}$$

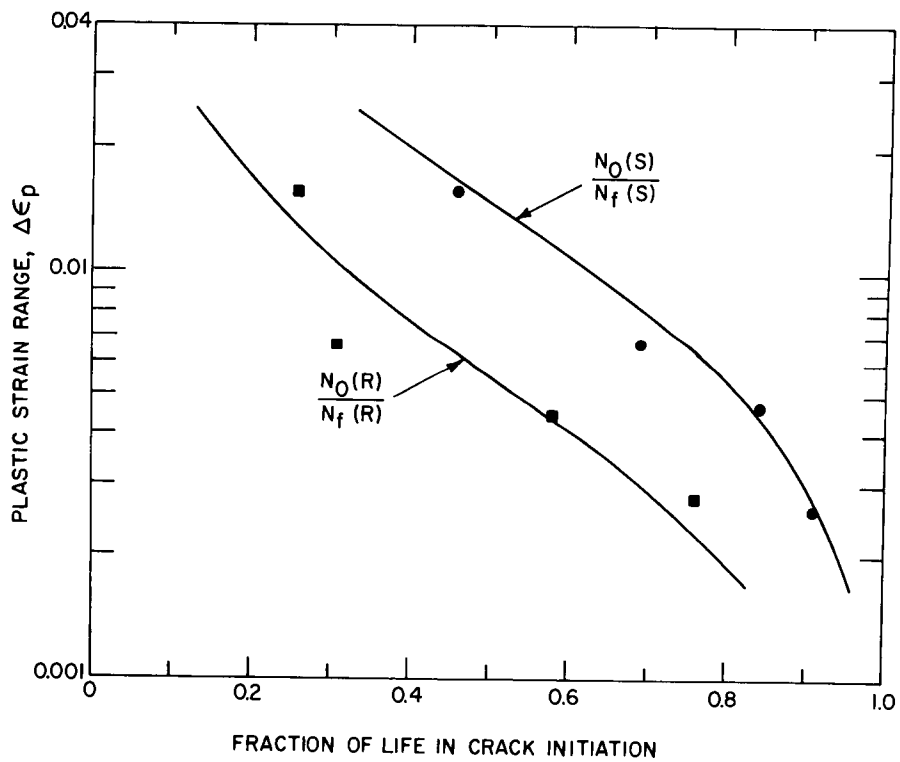

Fig. 2.5. Effect of Plastic Strain Range on the Fraction of Life Spent in Crack Initiation.

where P and c are adjustable constants. On the other hand, other investigators[8] have suggested the following relation based on their crack-initiation data:

$$N_o(S) = a\ N_f^{\ b}(S), \tag{14}$$

where a and b are material constants. Neither Eq. (13) nor Eq. (14) follows from the description of fatigue life in terms of crack intiation and crack propagation contained in Eqs. (6)-(8). It can be shown from Eqs. (6)-(8) that the fatigue life and crack initiation are related by

$$N_f(S) = N_o(S) + B\ N_o^{\ d}(S), \tag{15}$$

where $B = C/A^{\gamma/\alpha}$ and $d = \gamma/\alpha$. The crack-initiation data generated for smooth specimens of Type 304 stainless steel can be fit to Eq. (15) to obtain

$$N_f(S) = N_o(S) + 31.52\ N_o^{\ 0.44}, \tag{16}$$

and the experimental points follow the prediction reasonably well (Fig. 2.6). It is also observed that the crack-initiation data obtained by other investigators for several materials (e.g., annealed and aged Type 304 stainless steel, annealed Fe-Cr-Ni austenitic alloys, annealed Al, and annealed as well as prestrained Ni) can be described by a form of Eq. (15), as shown in Fig. 2.7. The surface roughness, strain-rate, and hold-time effects are not taken into account in this correlation. However, the correlation suggests that crack initiation and crack propagation obey the same kinetic laws in several materials. It should also be pointed out that all equations which describe the relation between N_o and N_f, although they serve as predictive tools, do not shed light on the crack-initiation mechanisms.

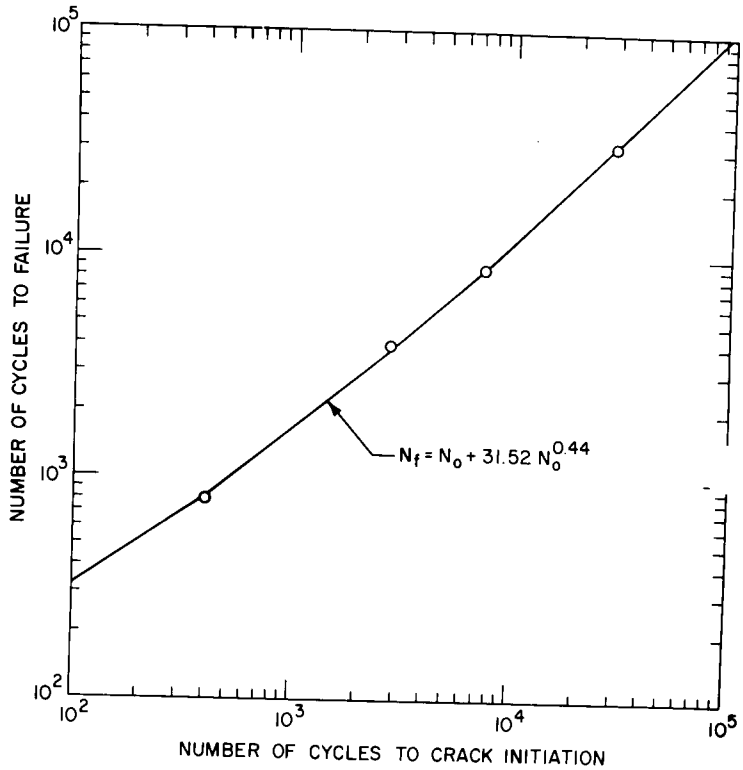

Fig. 2.6. Relation between Fatigue Life and Crack-initiation Life for Smooth Specimens of Type 304 Stainless Steel at 593°C.

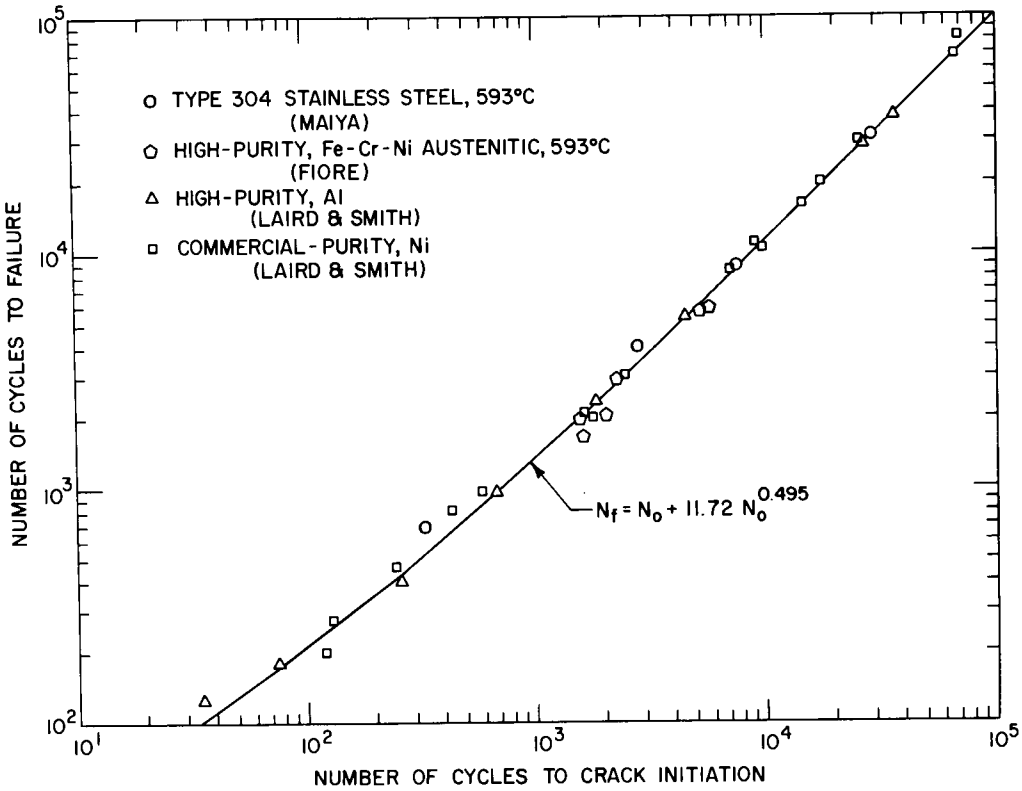

Fig. 2.7. Correlation between Fatigue Life and Crack-initiation Life for Several Materials. Crack-initiation data for Al and Ni have been kindly furnished by Laird[9] and for Fe-Cr-Ni alloys by Fiore.[10]

2.2.2 Microstructural Effects in Low-cycle Fatigue -- N. F. Fiore (Visiting Scientist; Univ. of Notre Dame) and D. R. Diercks

Low-cycle fatigue tests are being conducted on three high-purity Fe-20 wt% Cr-Ni austenitic alloys in an effort to determine the influence of certain microstructural and submicrostructural parameters on fatigue life.

The alloys, the compositions of which are listed in Table 2.2, have been vacuum melted and vacuum chill-cast at the U. S. Steel Research Laboratories and have been used in studies at the University of Notre Dame. They represent a particularly attractive system for low-cycle fatigue research for a number of reasons:

Table 2.2. Chemical Composition of High-purity Fe-Cr-Ni Austenites

Element	Alloy A (γ = 10 ergs/cm^2)	Alloy B (γ = 20 ergs/cm^2)	Alloy C (γ = 30 ergs/cm^2)
Nickel	10.03	14.35	18.83
Chromium	17.87	17.64	17.75
Carbon	0.01%	0.01%	0.01%
Manganese	<0.01	<0.01	<0.01
Phosphorus	<0.005	<0.005	<0.005
Sulfur	0.015	0.007	0.010
Silicon	0.04	0.03	0.04
Molybdenum	<0.01	<0.01	<0.01
Aluminum	0.008	0.005	0.01
Nitrogen	0.0051	0.012	0.0094
Oxygen	0.046	0.051	0.038

(a) The gross compositions of these alloys span the range of Cr and Ni content of the 300 series of austenitic stainless steels used in LMFBR applications. Moreover, their high purity minimizes problems in interpretation of fatigue behavior that arise from the presence of minor alloying elements and second-phase particles.

(b) In the chill-cast condition, the heavily cored, directional-dendritic microstructure simulates that of the thick-plate weld beads and centrifugally cast, thick-walled stainless pipe used in the LMFBR.

(c) In the chill-cast condition, alloy A, which contains only 10 wt% Ni, exhibits a duplex microstructure consisting of cored austenite dendrites enveloping interdendritic δ-ferrite. Alloys B (15 wt% Ni) and C (20 wt% Ni) consist of cored austenitic dendrites. Comparisons of the fatigue life of the three alloys in the cast condition may delineate the role of δ-ferrite in crack initiation and growth, an important area in practice, since δ-ferrite is a constituent in the E-308 weldments employed in the LMFBR.

(d) Alloy A, which has a low Ni content, forms the σ-phase during elevated-temperature exposure, whereas alloys B and C remain σ-free.

Fatigue tests on aged chill-cast specimens of the three alloys may define the effect of σ-phase on fatigue life, another important practical area, since cast and welded reactor components may develop σ-phase during their operation.

(e) In the wrought condition, the alloys are single-phase austenites in which the Ni content varies from 10 to 20 wt%; thus, they allow the study of the influence of this solid-solution strengthening element on fatigue life. Moreover, because Ni decreases[11,12] the stacking-fault energy γ in Fe-Cr-Ni alloys, the effect of this parameter on fatigue life can be investigated. Table 2.2 lists the estimated values of γ as a function of Ni content for the three alloys. The values range from 10 ergs/cm^2 for alloy A to 30 ergs/cm^2 for alloy C. Variations in γ within this range have been found to exert a strong influence on crack initiation[13] and propagation[14] in high-cycle fatigue; therefore, the influence on low-cycle fatigue is worthy of study.

(f) The austenitic alloys can be processed to exhibit a wide range of grain sizes. Because of the relatively high grain-boundary mobility due to the absence of impurity-grain-boundary and precipitate-grain-boundary interactions, the wrought microstructures may be altered in a straightforward manner. The role of grain boundaries in failure under creep-fatigue loading conditions may be studied systematically.

(g) Single crystals of the alloys, produced at the University of Notre Dame, provide model systems for the study of basic deformation and fracture mechanisms in low-cycle fatigue.

Table 2.3 summarizes the microstructural conditions developed in the alloys and the possible microstructure-fatigue-life relations that may be uncovered by the testing program.

2.2.2.1 Experimental

To conserve the high-purity materials, coupons of the test alloys have been welded into end pieces of conventional Type 304 stainless steel stock. The welded composite is then machined into a 0.38-cm-dia

Table 2.3. Possible Microstructure-Fatigue-life Interactions in High-purity Fe-20 wt% Cr-Ni Alloys

Microstructural Condition	Effect on Fatigue Life
As-cast	Effect of δ-ferrite in crack initiation and propagation. Effect of solidification substructure and texture on fatigue life.
Aged	Effect of σ-phase in crack initiation and propagation.
Wrought and Single Crystalline	Effect of bulk Ni content on fatigue life of samples with constant grain size. Effect of stacking-fault energy on deformation and fracture process. Effect of grain size on fatigue life.

hourglass-gauge section fatigue specimen that incorporates the standard button-head ends employed at ANL (Fig. 2.8). Prior to testing, the gauge section of each test specimen is mechanically polished to a mirror finish to eliminate surface finish as a test variable.

Material for the gauge section of the as-cast specimens is cut from ingots so that the specimen axis coincides with the solidification direction. The microstructure of the cast specimens consists of ∿ 5 dendritic grains running the length of the hourglass. Figure 2.9 shows the microstructures of alloys A, B, and C in the as-cast condition.

For the tests in which the influence of σ-phase on fatigue life is to be investigated, fabricated and polished specimens of as-cast A, B, and C are sealed in quartz capsules under an atmosphere of 50-cm high-purity argon and then annealed at 700°C for 100 hr. This treatment is optimum[15] for the development of σ-phase in austenitic stainless steels.

To develop the wrought microstructures, slugs 1.8 by 1.8 by 8 cm in length are cut parallel to the solidification direction of the ingots.

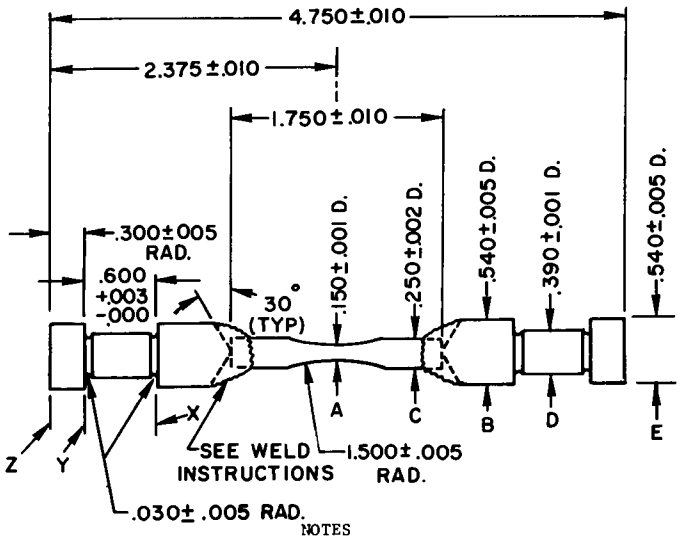

NOTES

1. Centers in ends of specimen permissible.
2. Surfaces X and Y to be parallel to surface Z within 0.0005 total indicator reading (TIR).
3. Surface Z to be perpendicular to center line of specimen within 0.0005 TIR.
4. Surfaces X, Y, Z to be free of burrs. Corner radius not to exceed 0.005.
5. Diameters B, C, D, E to be concentric with Diameter A within 0.001 TIR.
6. Contoured center portion to have a 16√ or better. Finish grinding the final 0.010 from the diameter of the contoured center portion in the axial direction, completely removing all transverse marks.
7. Machining methods to be used that leave a minimum of residual stress in contoured center portion.

Welding Instructions - Wrought End Piece to Weldment Center Piece

a. Use Type 308 stainless steel welding rod.
b. Copper chill blocks must be used on specimen gauge blank to minimize temperature. Intermediate water quenching is permissible if specimens are thoroughly dried before additional welding.
c. Welding must be done using low heat input rate to minimize specimen temperature during welding.
d. Intermediate machining is permitted to maintain alignment.
e. Maintain all orientation marks during welding. Mark may be located on end or side of blank as needed during fabrication.

Fig. 2.8. Welded Hourglass Low-cycle Fatigue Specimen. All measurements are in inches unless noted otherwise.

(a)
Alloy A
Fe-20 Cr-10 Ni

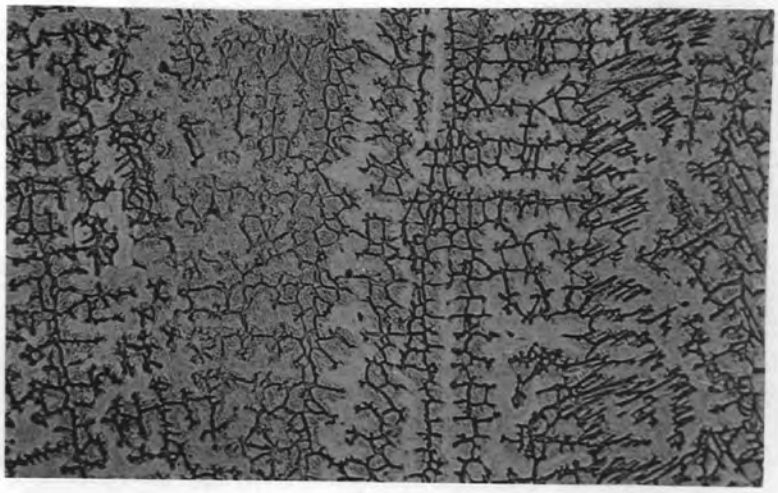

(b)
Alloy B
Fe-20 Cr-15 Ni

(c)
Alloy C
Fe-20 Cr-20 Ni

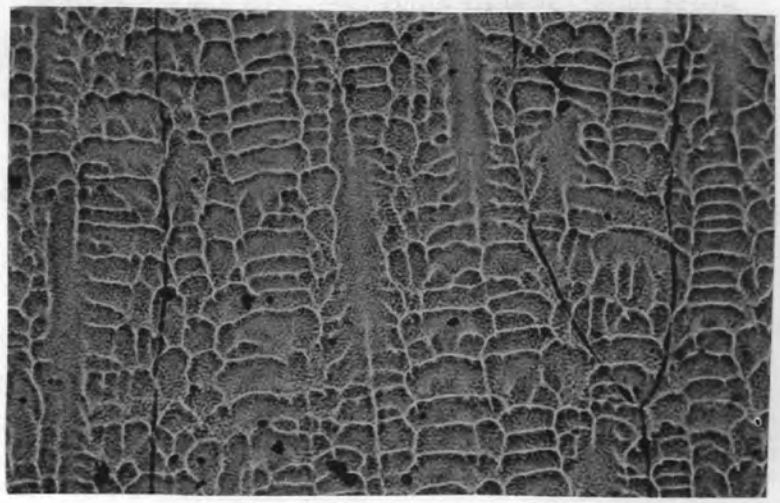

Fig. 2.9. Microstructures of As-cast Alloys. Mag. 70X.

The slugs are hot-rolled at 1100°C to 1.3-cm-dia rods and then homogenized in quartz tubes under 25 cm of argon at 1300°C for 24 hr. The homogenized rods are cold rolled to a 0.89-cm dia and swaged to 0.78 cm to provide round, straight lengths for the hourglass sections of the specimens.

The cold-rolled rods are annealed at 800°C for 4 hr to produce a fully recrystallized,[16] fine-grained austenitic microstructure in each of the three alloys. The recrystallized rods are cut into the appropriate lengths for welding into the Type 304 stainless steel end pieces and machining into the standard test specimens.

Most of the tests on wrought materials have been conducted on machined and polished specimens that have been resealed in quartz capsules and annealed under 50 cm of argon at 1092°C for 30 min. This treatment is the standard solutionizing anneal employed prior to testing Types 304 and 316 stainless steel at ANL. The anneal not only eliminates fabrication stresses introduced during specimen preparation but also develops a standardized microstructure for comparison with the commercial alloys tested. No carbide-precipitation aging treatment is employed before testing because the alloys have such low carbon content.

Some of the tests on wrought materials are being conducted to establish the role of grain size in fatigue behavior. These tests are made on specimens of alloy B that have been subjected to various grain-growth treatments. Some as-fabricated and polished samples are given an additional 30-min anneal at 800°C to relieve fabricating stresses. Others are given various grain-growth anneals at 1092 and 1200°C. The microstructures of the alloys consist of equiaxed grains ranging in size from about ASTM 8 (20 μm) to ASTM 2 (150 μm).

The single-crystal samples are grown by techniques described elsewhere.[17] The as-grown crystals are sealed in quartz capsules under 25-cm purified argon and homogenized at 1300°C for 48 hr.

Fatigue testing is conducted at 593°C in servohydraulic machines under axial strain control. A constant strain rate of 4×10^{-3}/sec is employed, with total strain range varying from 0.5 to 1%. In certain tests, a tension hold time of 1 min is inserted into the program cycle.

Since the entire research program is in its initial stages and the extent of the influence of each of the microstructural parameters is unknown, the tests described in the present report are of a scoping nature. In general, extreme values of the test variables have been employed to bracket the magnitude of the effects on fatigue life or to indicate whether any such effects exist.

2.2.2.2 Results

2.2.2.2.1 Lifetime of As-cast Materials. In Fig. 2.10, the fatigue life of as-cast A and C is compared with that of solution-annealed Type 304 stainless steel in a logarithmic plot of number of cycles to failure (N_f) as a function of total strain range ($\Delta\varepsilon_t$). The as-cast materials have lifetimes from 3 to 20 times longer than conventional material. In addition, alloy A, which contains interdendritic δ-ferrite, has a longer lifetime than alloy C.

A scanning-electron-micrograph composite of a typical fracture surface of an as-cast sample is shown in Fig. 2.11. No obvious connection exists between fracture and microstructural characteristics. Fatigue striations

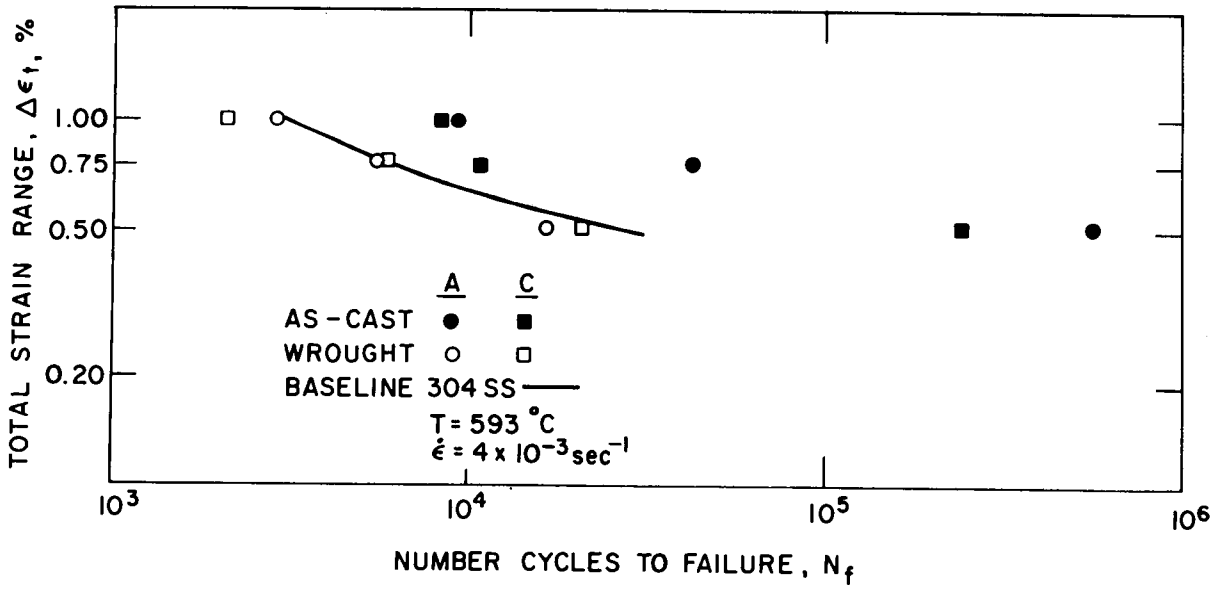

Fig. 2.10. Cycles to Failure (N_f) as a Function of Total Strain Range ($\Delta\varepsilon_t$).

Fig. 2.11. Striated Fracture Surface of As-cast Alloy C. Mag. 220X.

are evident on the surface, with their width increasing as specimen failure is approached. If it is assumed that the widest striation marks the position of the major fatigue crack at failure (i.e., at N_f cycles) and if the striations are counted back toward the crack-initiation site (with each striation representing one cycle of life), then the finest striation resolvable defines the number of cycles necessary to initiate a measurable crack.[4,18] Such striation counting in as-cast materials indicates that from 75 to 95% of the sample lifetime is spent in crack initiation and a much smaller portion is spent in crack propagation.

Figure 2.12a shows a typical scanning-electron micrograph of the external surface of the hourglass of an as-cast sample near the crack-initiation site. The surface shows no evidence of rumpling nor deformation-band formation. Evidently surface relief does not develop readily during the cycling of cast materials, so that long cycling times are necessary to produce the surface irregularities which serve as fatigue-crack initiators. This observation is consistent with the conclusion that most of the fatigue life of the as-cast material must be spent in crack initiation and suggests that the inherent low-cycle fatigue resistance of as-cast materials should be of interest to the designer.

2.2.2.2.2 Lifetime of Solution-annealed Equiaxed Grain Materials. Figure 2.10 shows that alloys A and C in the solution-annealed condition have only two-thirds the fatigue life of the baseline Type 304 stainless steel and only about one-fifth that of the cast material. Moreover, alloy A has a lifetime equal to alloy C, in contrast to the marked superiority of alloy A when both alloys are in the as-cast condition. Since the microstructures of the two alloys are identical in the wrought condition and differ in the cast condition only in that δ-ferrite is present in alloy A, it appears that δ-ferrite improves fatigue life.

As was the case with cast materials, inspection of the fracture surfaces of the wrought samples failed to disclose an obvious connection between microstructure and failure. On the other hand, an examination of the external surfaces of samples A and C does provide an explanation for

(a)
As-cast
Alloy A

(b)
Wrought
Alloy A

(c)
Wrought
Alloy C

Fig. 2.12. External Surfaces of Low-cycle Fatigue Specimens. Mag. 200X.

the drastic decrease in fatigue life of wrought alloys. It is evident from Figs. 2.12b and 2.12c that extensive surface rumpling and slip-band formation occurs during cycling of the wrought material. The deformation is more intense and on fewer slip systems in alloy A. This is to be expected since alloy A, with lower γ, should have a tendency to deform by planar slip, because extended dislocations resist cross slip. An irregular surface is generated with ease in the wrought materials. Fatigue cracks initiate at these surface irregularities, and failure occurs.

The importance of the crack-initiation stage of fatigue failure in smooth specimens is reemphasized by the results of striation counting. Over 75% of fatigue life is spent in crack initiation in both the wrought and cast materials.

Figure 2.13 and Table 2.4 summarize striation-counting results for wrought alloys A and C tested at 0.5, 0.75, and 1% total strain range. As has been observed,[18] striations widen monotonically as fracture is approached. In the early stages of crack propagation, striation width, i.e., incremental increase in crack length per cycle, is constant. More interestingly, the six crack-growth curves are almost identical. This indicates that bulk Ni content and stacking-fault energy have little influence on crack propagation. Moreover, for a given $\Delta\varepsilon_t$, total fatigue life is independent of composition.

The parameter that does appear to influence fatigue life is $\Delta\varepsilon_t$ because it determines N_o, the number of cycles necessary to initiate a crack. As $\Delta\varepsilon_t$ increases N_o decreases, and, since the propagation stage for all samples is similar, N_f decreases. These data provide quantitative evidence of the importance of crack initiation in governing fatigue life in smooth samples.

2.2.2.2.3 <u>Hold-time Tests on Cast and Wrought Materials</u>. The conventional fatigue tests have indicated that bulk Ni content and stacking-fault energy have little influence on fatigue life. The phenomenon that apparently establishes fatigue life in smooth specimens is the formation

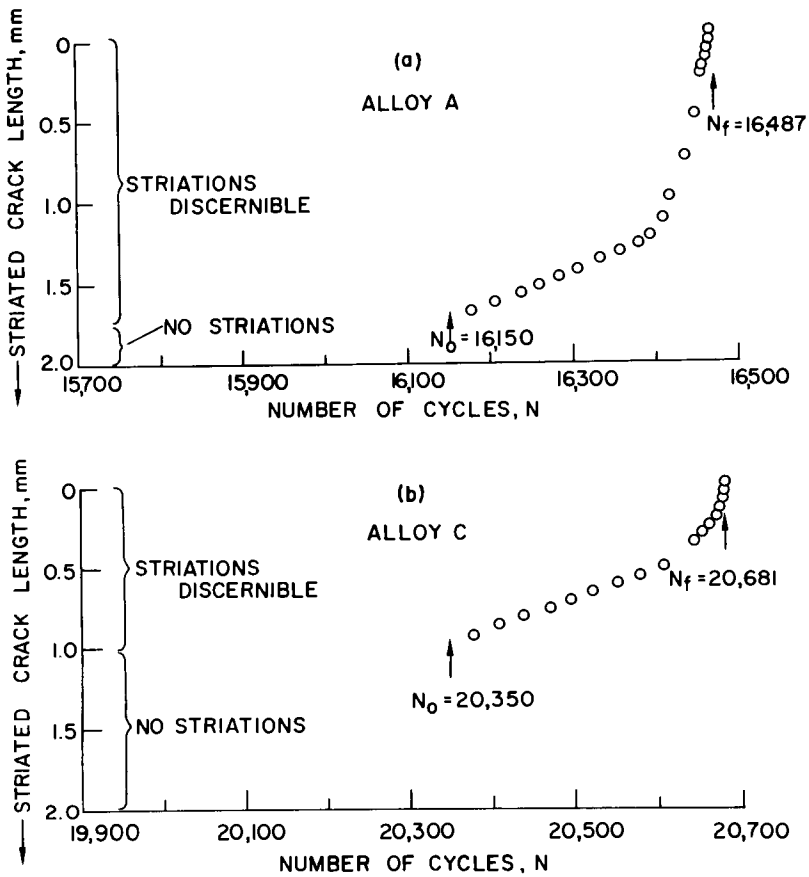

Fig. 2.13. Crack-growth Plots for Wrought Alloys A and C Tested at 593°C with $\dot{\varepsilon} = 4 \times 10^{-3}$ sec^{-1}. (a) and (b) $\Delta\varepsilon_t = 0.5\%$, (c) and (d) $\Delta\varepsilon_t = 0.75\%$, (e) and (f) $\Delta\varepsilon_t = 1.0\%$.

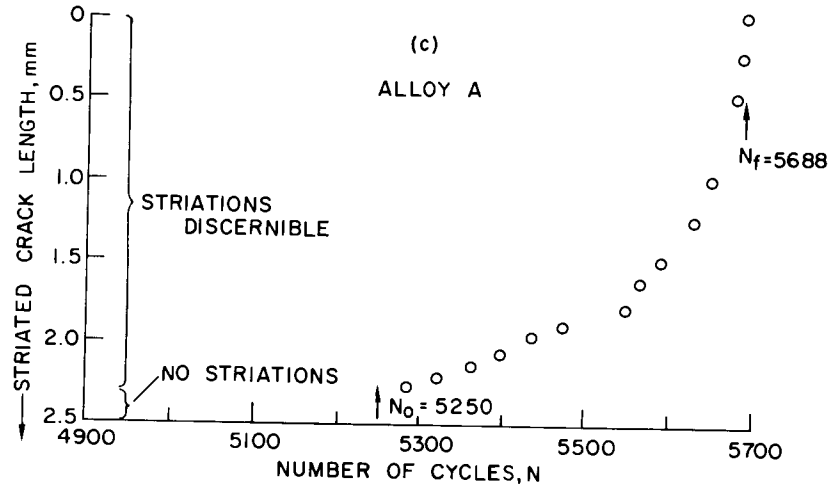
(c)
ALLOY A
STRIATIONS DISCERNIBLE
NO STRIATIONS
N_o = 5250
N_f = 5688
STRIATED CRACK LENGTH, mm
NUMBER OF CYCLES, N
0
0.5
1.0
1.5
2.0
2.5
4900
5100
5300
5500
5700

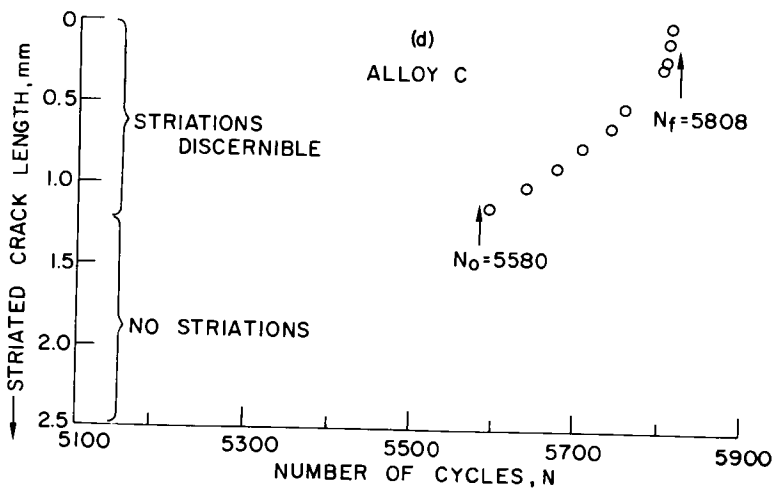
(d)
ALLOY C
STRIATIONS DISCERNIBLE
NO STRIATIONS
N_o = 5580
N_f = 5808
STRIATED CRACK LENGTH, mm
NUMBER OF CYCLES, N
0
0.5
1.0
1.5
2.0
2.5
5100
5300
5500
5700
5900

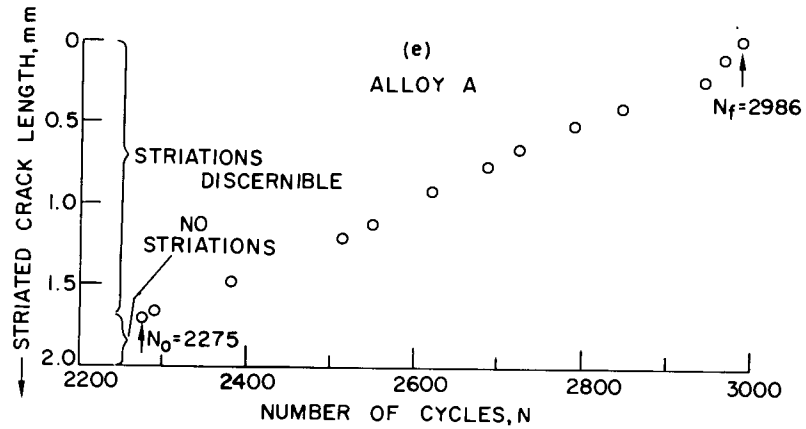
(e)
ALLOY A
STRIATIONS DISCERNIBLE
NO STRIATIONS
N_o = 2275
N_f = 2986
STRIATED CRACK LENGTH, mm
NUMBER OF CYCLES, N
0
0.5
1.0
1.5
2.0
2200
2400
2600
2800
3000

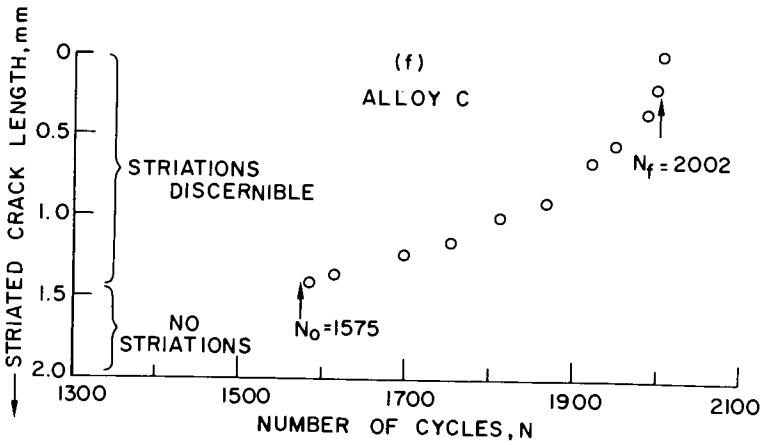
(f)
ALLOY C
STRIATIONS DISCERNIBLE
NO STRIATIONS
N_o = 1575
N_f = 2002
STRIATED CRACK LENGTH, mm
NUMBER OF CYCLES, N
0
0.5
1.0
1.5
2.0
1300
1500
1700
1900
2100

Table 2.4. Striation-counting Results on Wrought Samples

$T = 593°C \qquad \dot{\varepsilon} = 4 \times 10^{-3}\ sec^{-1}$

Alloy	Total Strain Range $\Delta\varepsilon_t$, %	Cycles to Failure N_f	Cycles to Initiation N_o	Fraction of Life Spent in Initiation
A	0.5	16,467	16,150	0.98
C	0.5	20,681	20,350	0.98
A	0.75	5,688	5,250	0.92
C	0.75	5,808	5,580	0.96
A	1.0	2,986	2,275	0.75
C	1.0	2,002	1,570	0.78

of surface crack-initiation irregularities. These irregularities form more easily in wrought materials than in cast materials, so the wrought materials have a much shorter fatigue life. For some reason, the cast alloy that contains δ-ferrite shows maximum fatigue life.

Since austenitic alloys that have LMFBR applications will be subjected to periods of tension hold time interjected during periodic cycling, a series of tests have been undertaken to establish the influence of microstructure on fatigue life when hold times are present. The results of the hold-time tests are summarized in Table 2.5. As with the straight fatigue tests, the cast high-purity alloys have a longer fatigue life than conventional wrought material, which, in turn, lasts longer than the wrought high-purity alloys. The marked superiority of as-cast alloy A is lost when hold times are introduced, whereas as-cast C performs at least as well under hold-time conditions as under straight fatigue. For the wrought alloys, including standard Type 304 stainless steel, introduction of the tension hold time reduces fatigue life by a factor of two to five.

A possible explanation for the deleterious effect of hold time on fatigue life may be found in the scanning-electron micrographs of the as-tested hourglass surfaces as presented in Fig. 2.14. In contrast to the smooth surfaces present in cycled as-cast A, the surface of the hold-time cast sample shows interdendritic grooves and tears. The grooves, which probably arise through grain-boundary sliding during the hold-time portion of the loading cycle, can serve to initiate cracks and decrease fatigue life. Evidently, interdendritic δ-ferrite causes accelerated intergranular deformation, and the resultant rumpled surface is responsible for the loss of some of the effectiveness of as-cast alloy A as a fatigue-resistant material. The absence of extensive rumpling and tearing in cast alloy C (Fig. 2.14b) is responsible for its superiority to cast alloy A, the wrought high-purity alloys, and the conventional material.

The reason for the poor performance of the wrought high-purity alloys also is suggested by Fig. 2.14. Considerably less intragranular

Table 2.5. Fatigue Life during Hold-time Tests

$T = 593°C \qquad \Delta\varepsilon_t = 0.75\% \qquad \dot{\varepsilon} = 4 \times 10^{-3}$

Material	Microstructural Condition	N_f (No Hold Time)	N_f (Hold Time)
304 SS	Solution Annealed - 1092°C - 30 min	9,000	3,500
A	Solution Annealed - 1092°C - 30 min	5,688	799
B	Solution Annealed - 1092°C - 30 min	-	2,077
C	Solution Annealed - 1092°C - 30 min	5,808	1,156
A	As-cast	40,809	3,489
B	As-cast	-	5,710
C	As-cast	10,290	23,478

(a) As-cast Alloy A

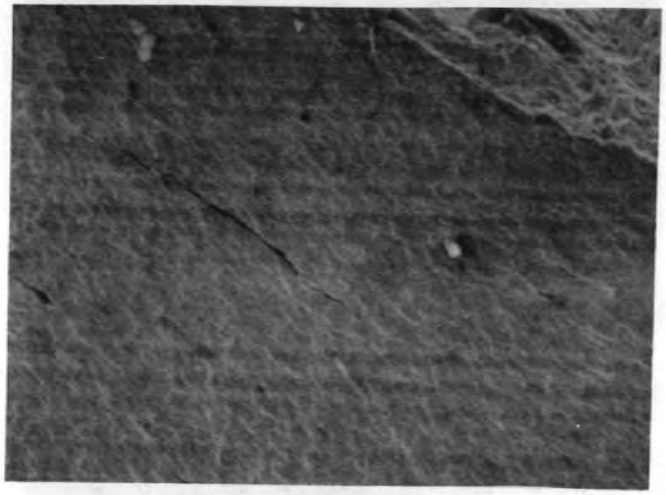

(b) As-cast Alloy C

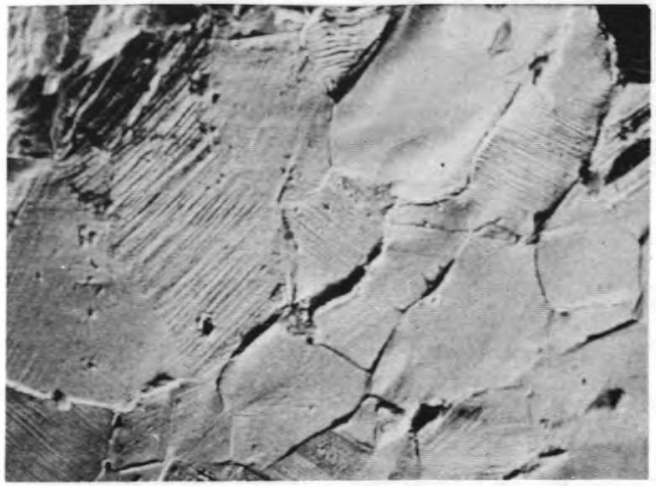

(c) Wrought Alloy A

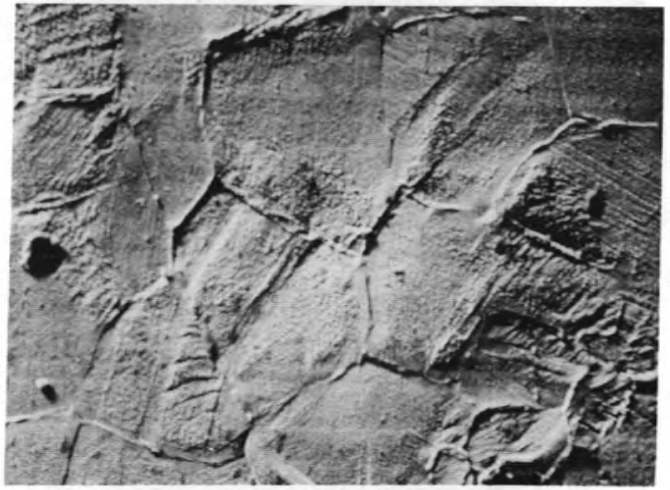

(d) Wrought Alloy C

Fig. 2.14. External Surfaces of Hold-time Test Specimens. Mag. 200X.

deformation is evident after hold-time testing than after straight cycling (compare with Fig. 2.12b and c); however, grain-boundary sliding is obvious. The resultant intergranular surface grooves may be crack initiators, which are responsible for shortening the fatigue life.

The influence of intergranular deformation in wrought materials subjected to tension hold times is shown in Fig. 2.15. The obvious intergranular fracture mode and the absence of striations indicate that the wrought material literally separates at its seams during the hold-time segment of the cycle.

It follows that if the microstructure is adjusted to decrease grain-boundary (including interdendritic) area, then fatigue life under creep-fatigue conditions will increase. Tests on wrought material of various grain sizes and on single crystals will provide a test of this hypothesis.

2.2.2.3 Future Research

The results to date indicate that microstructure has a marked influence on fatigue life under both straight fatigue and hold-time conditions. The influence appears to be most strongly associated with crack initiation. The following test programs will be continued in an effort to document and to provide an understanding of the structure-property relations revealed by the preliminary tests:

1. The influence of σ-phase on crack initiation and growth on aged samples will be investigated.
2. The influence of grain size on fatigue life under both straight low-cycle and hold-time fatigue conditions will be studied.
3. Single-crystal tests will be conducted to provide additional information as to the role of grain boundaries. The tests will also serve as the focal point of studies of the basic deformation processes leading to crack initiation and growth.

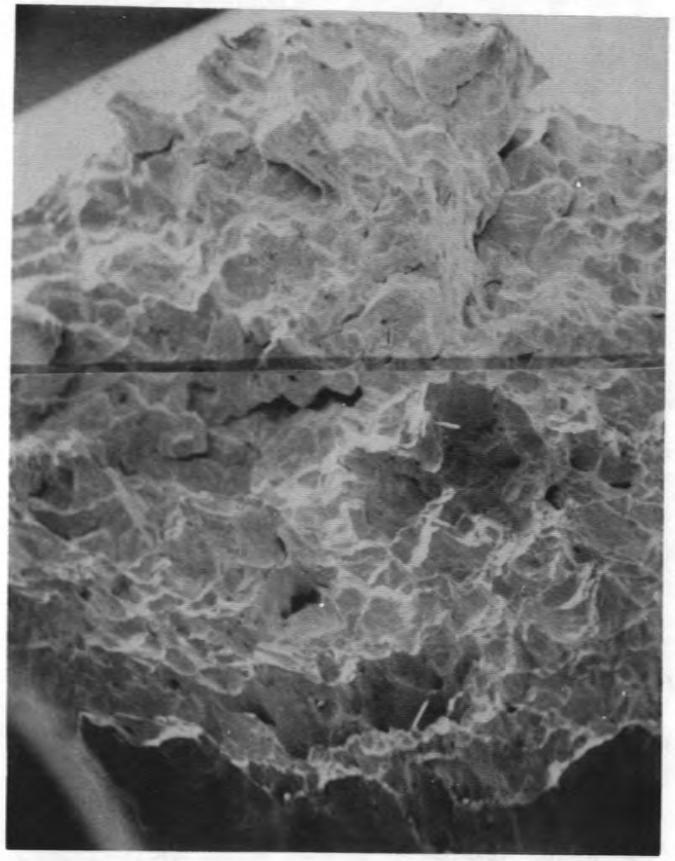

(a) Mag. 50X

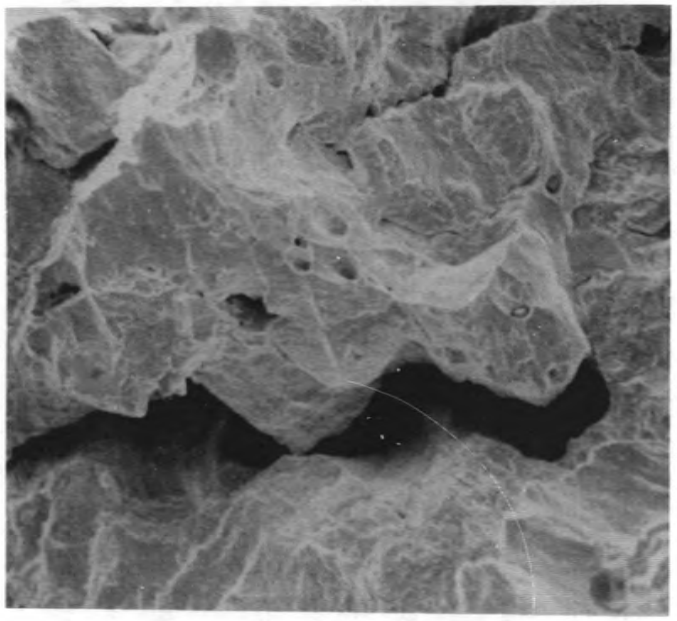

(b) Mag. 200X

Fig. 2.15. Fracture Surface of Wrought Alloy C Tested under Hold-time Conditions.

2.3 SODIUM EFFECTS ON LMFBR MATERIALS -- T. F. Kassner

2.3.1 Influence of Sodium Environment on the Uniaxial Creep-rupture Properties of Austenitic Stainless Steels -- K. Natesan and O. K. Chopra

The effect of carburization on the creep-rupture properties of Types 304, 316, and Ti-modified 316 stainless steel, after exposure to well-characterized sodium at temperatures between 550 and 700°C, is being determined. Since composition and microstructure of the material in the vicinity of the sodium-steel interface can have a strong influence on crack initiation and propagation, the degree of carburization resulting from the sodium environment needs to be correlated with the mechanical-property changes in the material.

Uniaxial creep-rupture specimens of Type 304 stainless steel were exposed to flowing sodium at 700, 650, and 600°C for 120 to 5012 hr to yield carbon penetration depths between ∿4 and 15 mils. The 15-mil-thick specimens were subsequently used in uniaxial creep-rupture tests to obtain the creep curves and creep-rupture life. The creep-rupture life and the minimum creep rate calculated from the test results for various sodium exposure and testing conditions are listed in Table 2.6. The results show that, for a given sodium-exposure condition, the creep-rupture life increases, whereas the minimum creep rate decreases as the applied stress decreases. The results at 700°C also indicate that the minimum creep rate increases, whereas the creep-rupture life decreases as the sodium-exposure period increases. For example, at an applied stress of 90 MPa (13 ksi), the minimum creep rate increases from 0.086%/hr for material in the solution-annealed condition to 0.218%/hr for specimens after 1512-hr exposure to flowing sodium. For the same cases, the creep-rupture life decreases from 324.2 to 135.5 hr. Figures 2.16 and 2.17 show the variation of minimum creep rate and rupture life, respectively, with applied stress at 700°C for specimens in the solution-annealed, aged (1000 hr at 650°C), and sodium-exposed conditions. A similar comparison of creep test results at 650 and 600°C will be made subsequent to conducting more tests.

Table 2.6. Creep-rupture Behavior of AISI Type 304 Stainless Steel (Heat 9T2796) upon Exposure to Sodium Environment

Temperature, °C	Heat Treatment	Na-exposure Time, hr	Carbon Penetration Depth, mils	Applied Stress, MPa (ksi)	Rupture Life, hr	Minimum Creep Rate, %/hr	Strain at Rupture, %
700	Annealed	0		90 (13)	324.2	0.086	34.3
				138.5 (20)	8.6	3.11	44.1
	Annealed & Aged[a]	0		138.5 (20)	15.6	2.05	46.9
	-	120	~4	62.5 (9)	4902.7	0.002	19.4
				76.5 (11)	1052	0.0113	22.9
				90 (13)	678	0.0145	17.2
				125 (18)	125.5	0.134	16.4
	-	504	~8	55.5 (8)	2418[b]	0.0097	33.0
				69.5 (10)	600.8	0.045	42
				90 (13)	159.5	0.190	44
				111 (16)	36.5	0.925	52.4
				125 (18)	12.5	2.498	47
	-	1512	~15	55.5 (8)	2338[b]	0.011	31.9
				69.5 (10)	822	0.043	42.6
				76.5 (11)	182.2	0.128	35.6
				90 (13)	135.5	0.218	44
650	Annealed	0		138.5 (20)	68.3	0.291	27.1
	Annealed & Aged[a]	0		138.5 (20)	57.9	0.448	41.6
	-	312	~4	104 (15)	760.5	0.023	19.8
				208 (30)	22.9	1.00	28.3
	-	1512	~8	83 (12)	(c)	0.0056	(c)
				104 (15)	493.6	0.0424	28.3
				173 (25)	39.9	0.515	31.2
600	Annealed	0		138.5 (20)	(c)	0.0122	(c)
	Annealed & Aged[a]	0		138.5 (20)	(c)	(c)	(c)
	-	1512	~4	152.5 (22)	(c)	0.0011	(c)
				173 (25)	631.4	0.0146	13.2
				208 (30)	250.8	0.024	9.5
				242.5 (35)	34.7	0.326	14.9

[a]Aged 1000 hr at 650°C.

[b]Specimen rupture life was incorrectly stated in ORNL-5104, p. 42.

[c]Test in progress.

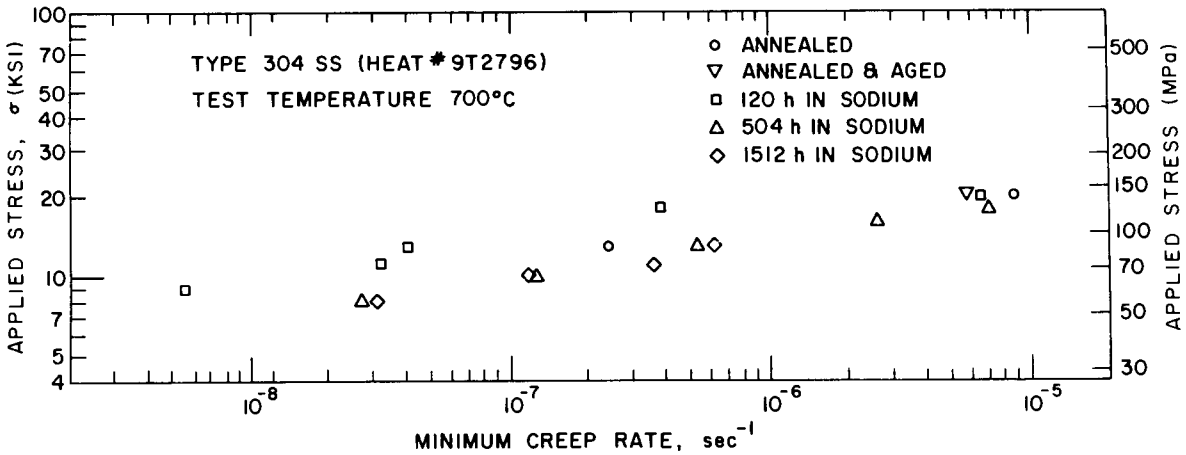

Fig. 2.16. Stress vs Minimum Creep Rate for Type 304 Stainless Steel (Heat 9T2796) in the Annealed, Aged, and Sodium-exposed Conditions.

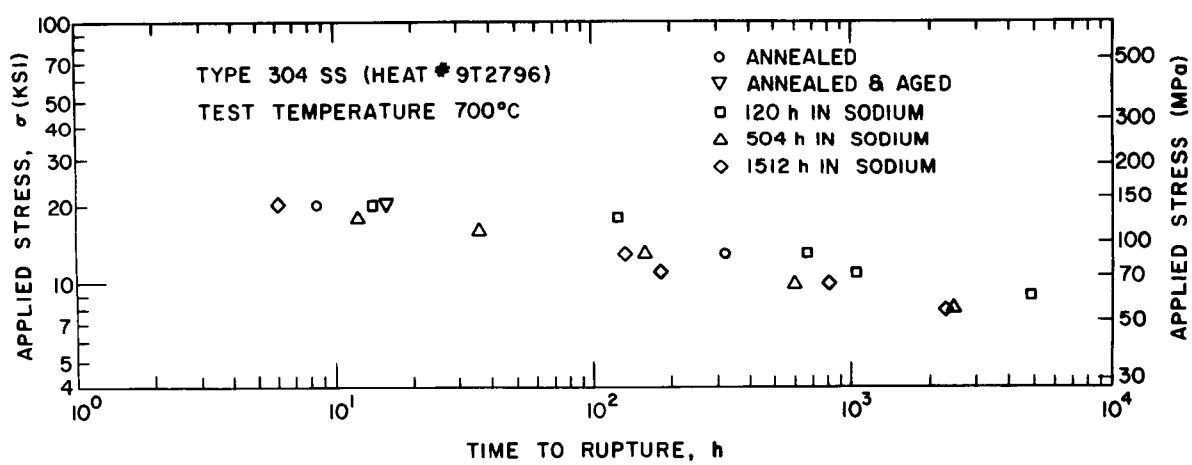

Fig. 2.17. Stress vs Rupture Life for Type 304 Stainless Steel (Heat 9T2796) in the Annealed, Aged, and Sodium-exposed Conditions.

The surface carbon concentrations in the mechanical test specimens were determined from combustion analyses of 2-mil-thick foils of the same material equilibrated in sodium during the specimen-exposure period. The values for Type 304 stainless steel ranged from 0.04 to 0.06 wt% at 700°C, 0.25 to 0.30 wt% at 650°C, and 0.30 to 0.40 wt% at 600°C. The surface carbon concentration values are being used with a kinetic analysis for carbon diffusion[19] and carbon activity-concentration data for commercial austenitic stainless steels[20] to obtain carbon-concentration profiles and average carbon concentrations in the specimens after exposure to sodium. The mechanical-property data will be correlated, at a later date, with the depth of carbon penetration, surface carbon concentration, and temperature.

Microstructural examination of the sodium-exposed specimens before and after testing is being conducted using optical metallography and scanning- and transmission-electron microscopy techniques. Figure 2.18 shows the fracture surfaces of annealed and sodium-exposed specimens creep tested at an applied stress of 90 MPa (13 ksi) at 700°C. It is evident that the fracture is completely ductile in all cases, and no apparent change in the mode of fracture could be seen.

The microstructure of the sodium-exposed specimens (in the axial direction) before and after creep testing at an applied stress

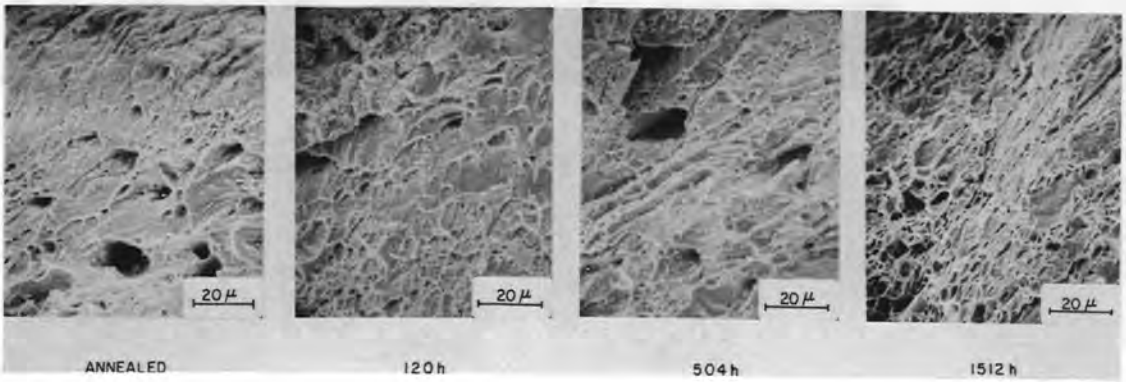

Fig. 2.18. Fracture Surface of Type 304 Stainless Steel Specimens Creep Tested at an Applied Stress of 90 MPa (13 ksi) in the Annealed Condition and after Exposure to Flowing Sodium for 120, 504, and 1512 hr at 700°C.

of 90 MPa (13 ksi) at 700°C is shown in Fig. 2.19. The strains at rupture in these specimens were 17.2, 44, and 44% after sodium-exposure periods of 120, 504, and 1512 hr, respectively. Figure 2.19B shows that the specimens with larger rupture strain have grains elongated significantly in the axial direction. The higher magnification micrographs of the creep-tested specimens show that carbide particles preferentially precipitate at the grain boundaries. Furthermore, the size of the carbide particles in the specimen with longer sodium exposure is larger, which indicates growth of these particles with time. The precipitate morphology in these specimens should inhibit grain-boundary sliding and migration during the testing period. The respective contributions of grain elongation and relative grain movements to the deformation were determined

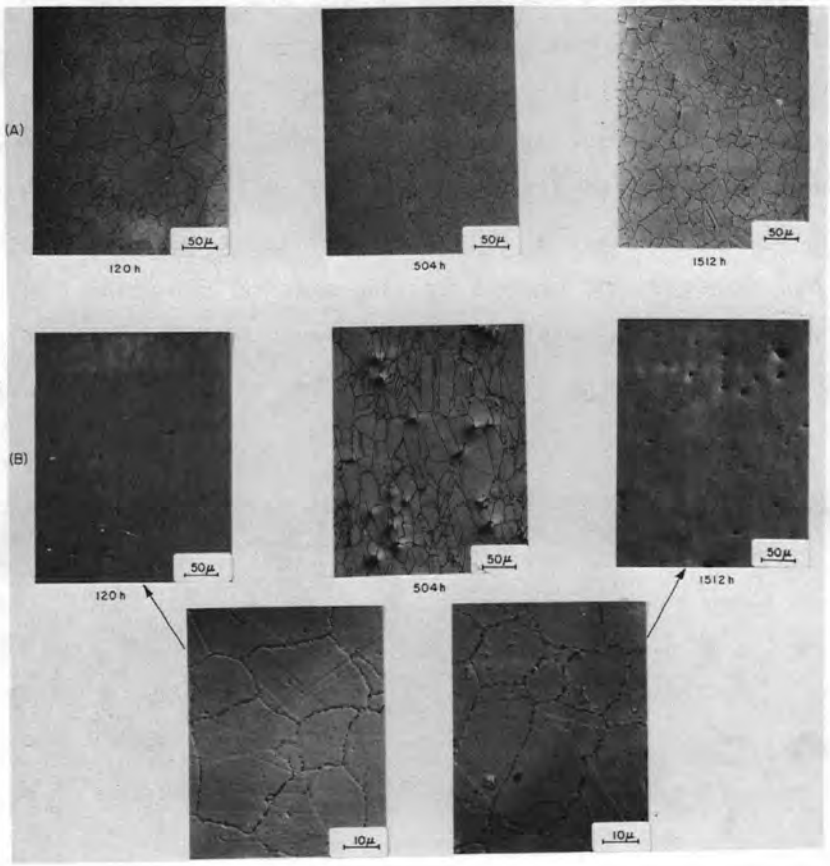

Fig. 2.19. Photomicrographs of Type 304 Stainless Steel Creep Specimens Exposed to Sodium for 120, 504, and 1512 hr. (A) Before and (B) after testing at an applied stress of 90 MPa (13 ksi) at 700°C.

in these specimens by evaluating the change in shape of internal grains and computing the intragranular deformation.[21] The intragranular elongation ε_g and grain-growth factor K are given by

$$\varepsilon_g = \left(\frac{\ell}{w} \cdot \frac{w_o}{\ell_o}\right)^{2/3} - 1, \tag{17}$$

and

$$K = \left(\frac{\ell\, w^2}{\ell_o\, w_o^2}\right)^{1/3}, \tag{18}$$

where ℓ_o/w_o and ℓ/w are the average length-to-width ratios in the sodium-exposed specimens before and after testing, respectively; ℓ is measured parallel with and w transverse to the stress axis. The contribution of grain-boundary sliding can then be determined from the total creep strain ε_t by

$$\varepsilon_{gb} = \varepsilon_t - \varepsilon_g. \tag{19}$$

The measured and computed values shown in Table 2.7 indicate absence of grain-boundary sliding and migration. The influence of carbide morphology is also reflected in the shape of the grains in the sodium-exposed specimens.

Table 2.7. Comparison of Measured and Computed Values of Grain Elongation in Creep-tested Specimens

Na-exposure Time, hr	Applied Stress, MPa (ksi)	Na Exposure and Test Temperature, °C	Calculated		Measured
			ε_g	K	ε_t
120	90 (13)	700	0.208	1.01	0.172
1512	90 (13)	700	0.426	0.98	0.440
1512	242.5(35)	600	0.161	1.08	0.150
1512	173 (25)	600	0.114	1.02	0.132

Figure 2.20 shows the results of the grain-shape measurements on specimens solution-annealed and exposed to sodium at 600 and 700°C. A Gaussian distribution with a peak at six-sided grains was obtained for specimens exposed to sodium at 600°C, irrespective of exposure time. At 700°C, the peak shifts to between the four- and five-sided grains, which indicates pinning of the boundaries by carbide precipitation at a relatively early stage of sodium exposure.

The mechanical-property samples are also being examined by transmission-electron microscopy and electron microprobe to identify the morphology of carbides and intermetallic compounds that form during sodium-exposure and creep-testing periods. The specimen surfaces were polished and then etched, using a preferential potentiostatic etching technique, with a 10% Na_2CO_3 aqueous electrolyte to reveal only the carbides in the sample. Carbon-extraction replicas of these surfaces

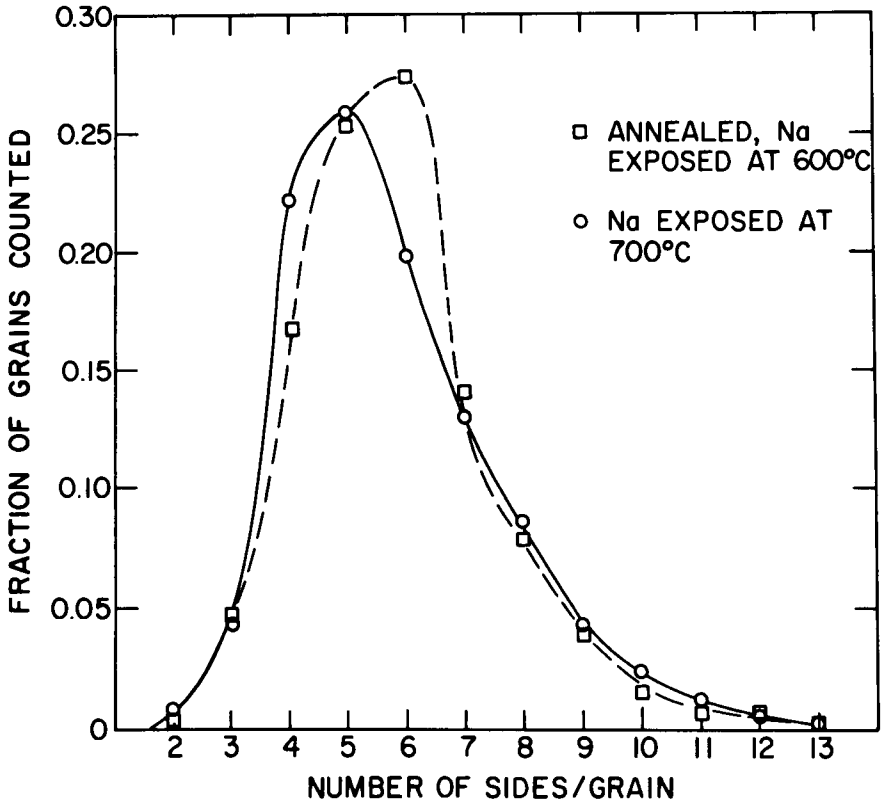

Fig. 2.20. Grain-shape Distribution for Type 304 Stainless Steel Specimen in Annealed Condition and after Exposure to Sodium at 600 and 700°C.

are being obtained by carbon deposition on the surface and subsequent dissolution of the matrix phase in a 10% bromine-methanol solution. A typical area of the surface replica for a specimen exposed to sodium at 650°C for 312 hr is shown in Fig. 2.21. The relative composition of the particles, obtained with an energy-dispersive X-ray analyzer, is also shown in Fig. 2.21. In general, a high ratio of Cr/Fe was observed for most of the particles. The same replica was also examined in the transmission-electron microscope, and the micrographs

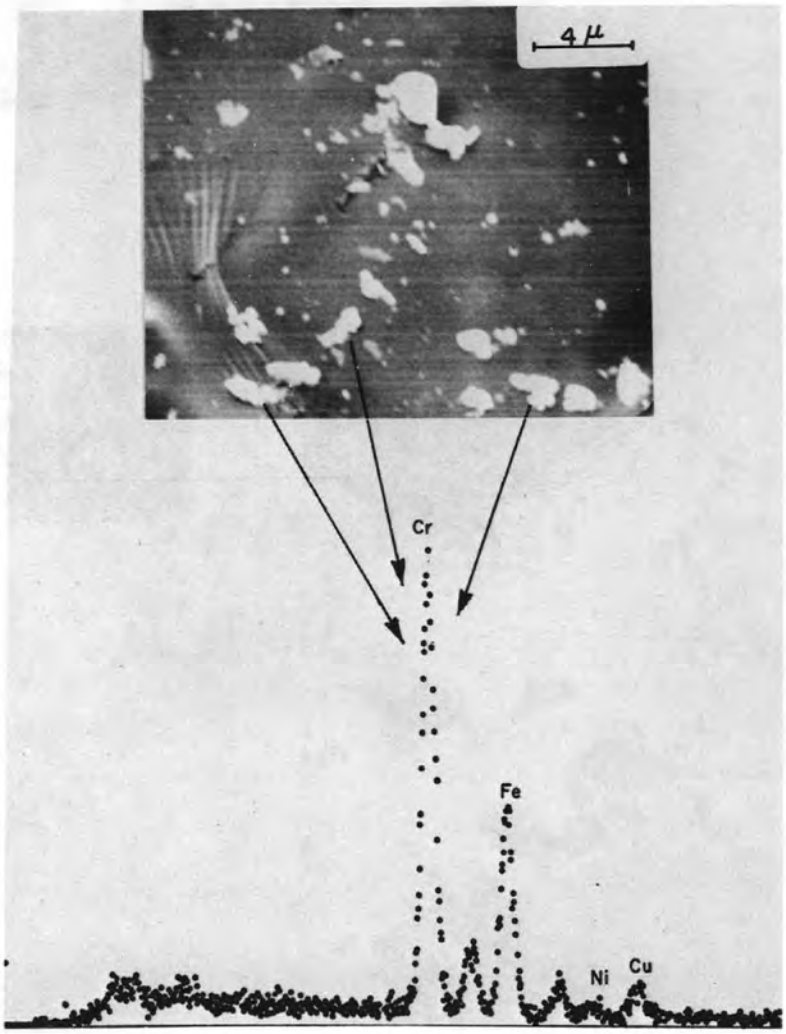

Fig. 2.21. Scanning-electron Micrograph of a Carbon Replica of the Surface of a Specimen Exposed to Flowing Sodium at 650°C for 312 hr.

of particles in different regions are shown in Fig. 2.22. An analysis of the diffraction patterns of a number of different particles in the replica indicated that particles smaller than 1 μm have an $M_{23}C_6$-type structure, irrespective of whether the carbides were located at the grain boundary or in the matrix. The large particles that were

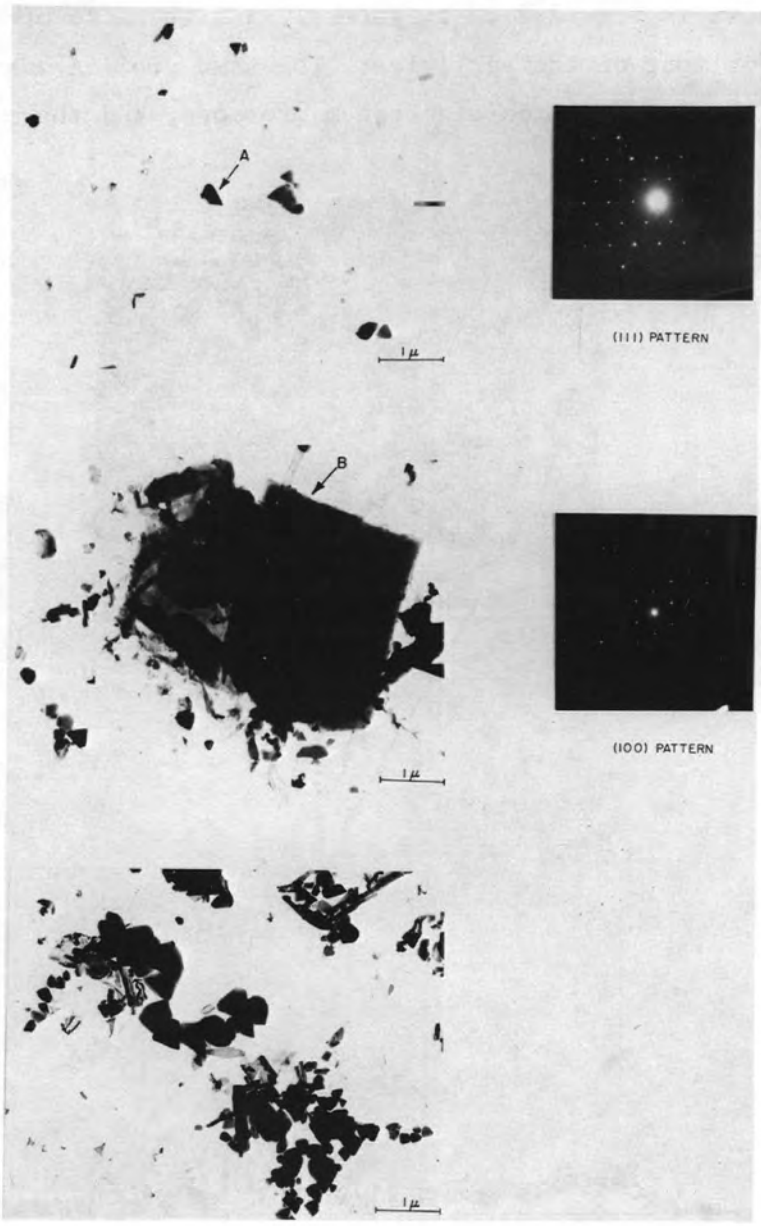

Fig. 2.22. Transmission-electron Micrographs of the Surface of a Specimen Exposed to Flowing Sodium at 650°C for 312 hr. The diffraction patterns correspond to particles identified as A and B in the micrographs.

predominantly present at the grain-boundary regions were identified as sigma phase with a tetragonal structure. Diffraction patterns of carbide and sigma-phase particles, identified as A and B, respectively, are also shown in Fig. 2.22. Similar examinations are being performed on specimens after exposure to sodium and testing at other temperatures.

The effect of test temperature on the creep behavior of sodium-exposed specimens is being determined to substantiate the increased creep rate observed with an increase in sodium-exposure period. Testing of 50-mil-thick Type 304 stainless steel specimens that have been exposed to sodium has been initiated. Types 316 and Ti-modified 316 stainless steel specimens that have been exposed to flowing sodium will be tested upon completion of the test program on Type 304 stainless steel.

2.3.2 Influence of Sodium Environment on the Low-cycle Fatigue Behavior of Austenitic Stainless Steels -- D. L. Smith and G. J. Zeman

Fatigue tests in sodium are being conducted to investigate the effect of the high-temperature sodium environment on the low-cycle fatigue behavior of Types 304 and 316 stainless steel in the annealed, annealed and aged, and sodium-exposed conditions. The major effects of the sodium environment on the fatigue properties of austenitic stainless steels relate to nonmetallic-element interactions. The low-oxygen potential present in sodium (of the order of 10^{-40} torr) is not only much lower than that of air but is substantially lower than the oxygen potentials typical of either high-vacuum or inert-gas environments. Therefore, enhanced crack-propagation rates, as a result of oxidation at the crack tip, are less likely to occur in sodium than in other environments. Carbon interactions in the stainless steel-sodium system can contribute to two phenomena that may affect the fatigue life of the steel. First, carburization or decarburization of steel at the crack tip during the fatigue test may affect the crack-propagation rate. Second, long-term exposure to sodium can result in carburization or decarburization of the surface of stainless steel

and substantially change the mechanical properties of the surface region. The low-cycle fatigue tests conducted in this program are designed to identify the relative importance of these effects for the range of conditions appropriate for LMFBR applications.

The test materials, the facilities for fatigue testing in sodium (FFTS), and the test procedure have been described in a previous report.[22] During the present report period, as-received Type 316 stainless steel specimens in the annealed condition have been fatigue tested at 600°C in air to confirm the validity of the test procedure. Figure 2.23 is a plot of strain range versus cycles to failure for tests conducted at a strain rate of 4×10^{-3} sec^{-1} with a fully reversed triangular waveform under stroke-control operation. The total strain range $\Delta\varepsilon_t$ agrees well with the data of Brinkman et al.,[23] which were obtained from annealed Type 316 stainless steel specimens at 593°C in air. The plastic strain-range data obtained in the present investigation are slightly lower than the literature data.

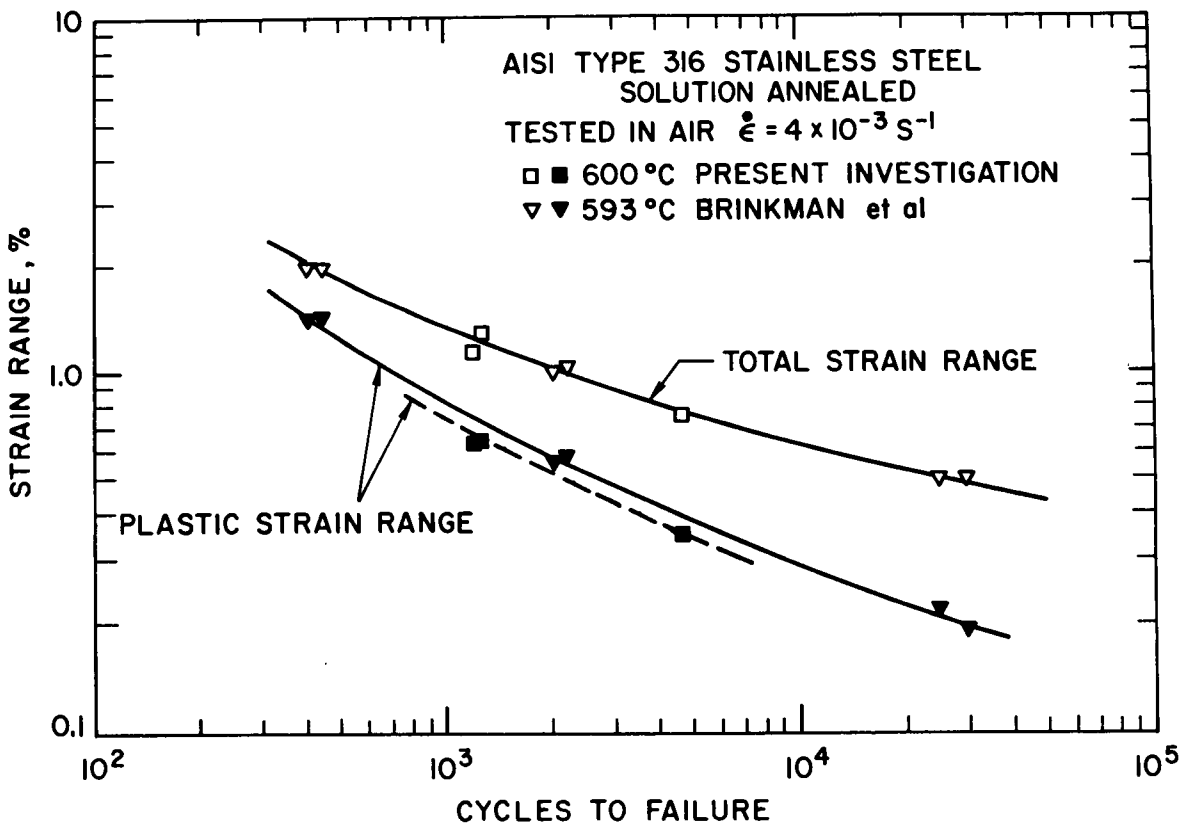

Fig. 2.23 Strain Range vs Cycles to Failure for Type 316 Stainless Steel Tested in Air at Elevated Temperature.

Several fatigue tests have been conducted at 600°C in sodium on as-received Type 316 stainless steel in the annealed condition. The oxygen concentration of the sodium was maintained at 1.0 ± 0.2 ppm, and the hydrogen in sodium was controlled at a level corresponding to a hydrogen partial pressure of 5×10^{-4} torr. These values are typical of those expected in an LMFBR. Tests were conducted at three carbon levels in sodium (0.03, 0.06, and 0.3 ppm) that are in the range of interest for LMFBR applications. The three carbon concentrations in sodium are (a) slightly decarburizing to, (b) approximately in equilibrium with, and (c) carburizing to Type 316 stainless steel at 600°C. The results plotted in Fig. 2.24 show approximately a factor of four increase in the time to failure for the samples tested in sodium compared with similar samples tested in air. However, no significant effect of carbon concentration in sodium, between 0.03 and 0.3 ppm, was observed on the fatigue lifetime for the mechanical test conditions used. Additional tests are in progress on samples that have been exposed to 600°C sodium for periods sufficient to produce a 0.1-mm carbon penetration depth into the sample.

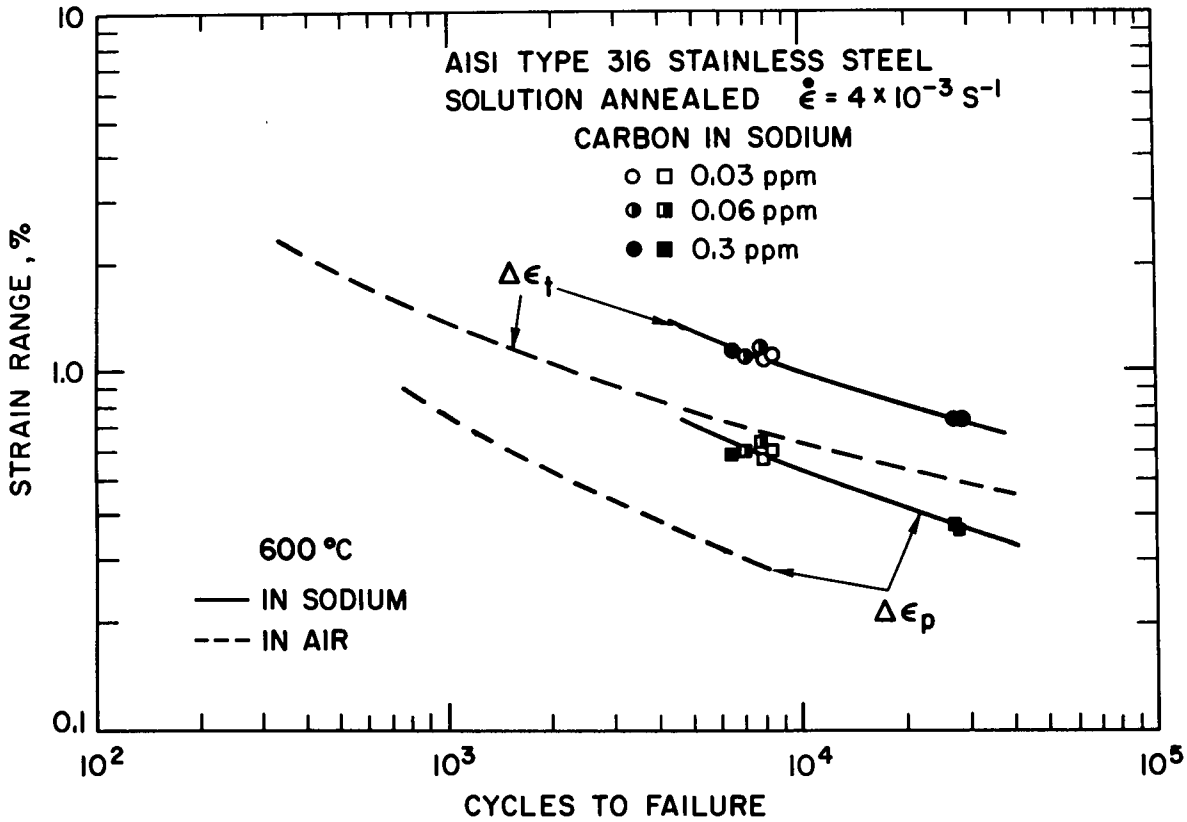

Fig. 2.24. Strain Range vs Cycles to Failure for Type 316 Stainless Steel Tested in Sodium and Air Environments at 600°C. (Air curves from data in Fig. 2.23.)

2.4 REFERENCES

1. Mechanical Properties Test Data for Structural Materials Quarterly Progress Report for Period Ending October 31, 1973, Oak Ridge National Laboratory, ORNL-4936, pp. 15-33.

2. Mechanical Properties Test Data for Structural Materials Quarterly Progress Report for Period Ending January 31, 1975, Oak Ridge National Laboratory, ORNL-5104, pp. 13-22.

3. Mechanical Properties Test Data for Structural Materials Quarterly Progress Report for Period Ending April 30, 1974, Oak Ridge National Laboratory, ORNL-4963, pp. 23-37.

4. P. S. Maiya and D. E. Busch, "Effect of Surface Roughness on Low-cycle Fatigue Behavior of Type 304 Stainless Steel," submitted to Met Trans.

5. C. Laird, ASTM STP 415, Philadelphia, Pa., 1967, p. 131.

6. P. S. Maiya, "Geometrical Characterization of Surface Roughness and Its Application to Fatigue-crack Initiation," to be published.

7. S. S. Manson, Intl. J. Fracture Mechanics 2, 327 (1966).

8. K. Iida, Trans. Japan Welding Soc. 2, 86 (1971).

9. C. Laird and G. C. Smith, Phil. Mag. 8, 1945 (1963).

10. N. F. Fiore, Argonne National Laboratory, private communication (1975).

11. P. R. Swann, Corrosion 19, 102t (1963).

12. D. L. Douglass, A. Thomas, and W. R. Roser, Corrosion 20, 15t (1964).

13. C. Laird and D. J. Duquette, Corrosion Fatigue, NACE-2, 88 (1972).

14. J. C. Grosskreutz, Phys. Stat. Sol. (b) 47, 359 (1971).

15. B. Weiss and R. Stickler, Met. Trans. 3, 851 (1972).

16. J. E. Spruell, J. A. Scott, C. S. Ary, and R. L. Hardin, Met. Trans. 4, 2535 (1973).

17. M. C. Mangalick, Ph.D. Thesis, University of Notre Dame (1969).

18. C. Laird, ASTM STP 415, Philadelphia, 1967, p. 121.

19. R. B. Snyder, K. Natesan, and T. F. Kassner, "Kinetics of the Carburization-Decarburization Process of Austenitic Stainless Steels in Sodium," J. Nucl. Mater. 50, 259-274 (1974).

20. K. Natesan, Argonne National Laboratory, unpublished work.

21. R. N. Stevens, "Grain-Boundary Sliding in Metals," Met. Rev. 11, 129-142 (1966).

22. Mechanical Properties Test Data for Structural Materials Quarterly Progress Report for Period Ending October 31, 1974, Oak Ridge National Laboratory, ORNL-5103, pp. 13-17.

23. C. R. Brinkmann, G. E. Korth, and R. R. Hobbins, Nucl. Technol. 16, 297(1972).

3. OAK RIDGE NATIONAL LABORATORY

W. R. Martin

3.1 INTRODUCTION

The ORNL mechanical properties effort comprises several programs. The program Mechanical Properties and Behavior for Structural Materials deals with materials of general applicability to the LMFBR program. Other programs are concerned with the mechanical properties of weldments in LMFBR components, the specific materials of interest for LMFBR steam generators, collection and correlation of mechanical data needed for design on high-temperature LMFBR systems, and materials for the primary circuit and steam generators of HTGR systems.

3.2 MECHANICAL PROPERTIES AND BEHAVIOR FOR STRUCTURAL MATERIALS — C. R. Brinkman

The objective of this program is to collect mechanical property data and material behavior for LMFBR structural and component materials. Included in the scope of this effort are the following: (1) basic tensile, creep, creep-rupture, and relaxation base-line data that are directly applicable to design criteria and methods for types 304 and 316 stainless steel reference heats and cyclic stress-strain tests performed with emphasis on loading and aging history effects, (2) variations in properties for several heats of types 304 and 316 stainless steel determined to allow establishment of minimum and average values of specific properties and the equation parameters required for design purposes. This work will include determination of property variation of samples from different mill products within a given heat of stainless steel.

3.2.1 Mechanical Property Characterization of Type 304 Stainless Steel Reference Heat — V. K. Sikka

3.2.1.1 Creep and Rupture Properties of the 2-in. (51-mm) Plate of Reference Heat

Several creep tests on 2-in. (51-mm) plate of the reference heat of type 304 stainless steel (9T2796) continued. The test times and creep

strains for all tests have been updated and summarized in Table 3.1. Three tests have exceeded test times of 21,000 hr and several others have exceeded 15,000 hr. All creep tests are progressing smoothly and will be continued during the next quarter. The creep test duration achieved during next quarter will also permit updating the isochronous stress-strain curves.

3.2.1.2 Tensile Tests Following Periods of Creep

The literature was searched in the area of influence of prior creep deformation (low-strain-rate deformation) on the short-term tensile properties of types 304 and 316 stainless steel and other metals and alloys. The summary of the literature search is presented here along with the progress made in the ORNL test program.

The data available from the literature regarding this subject are scarce. In fact, the only available results on the effect of prior creep on tensile properties of types 304 and 316 stainless steel are due to Lovell, Blackburn, and Holmes.[1] Their investigation was limited to only four tensile tests following prior creep on type 304 stainless steel and five on type 316. Their work indicated that prior creep deformation can significantly reduce the residual tensile elongation of these alloys.

The amount of creep strain required to reduce the tensile elongation to the 10% level was determined[1] for various test temperatures. Only 4% prior creep strain was found necessary to reduce the tensile elongation to the 10% level at 538°C (1000°F), whereas at 593°C (1100°F) and higher temperatures the creep damage effect was not a significant factor.

Paxton[2] investigated the effect of prior creep strain on residual mechanical properties of 20%-cold-worked type 316 stainless steel. The results showed that for low creep strain (<2%) the engineering tensile strength was lowered whereas the ductility increased. For large creep strains (>10%), the engineering tensile strength and ductility values both decreased.

Most of the earlier literature[3—6] on the effect of prior creep on tensile properties refers to aluminum, its alloys, and precipitation hardenable stainless steel. The investigation of Beck[3] on aluminum-clad alloy 2024-T3 suggested the following:

Table 3.1. Creep Tests on Type 304 Stainless Steel Reference Heat 9T2796 2-in.-thick (51-mm) Plate[a]

Test	Temperature		Stress		Time in Test	Strain, %		Ratio of Creep Stress to Yield Stress[b]	Comments[c]
	(°C)	(°F)	ksi	MPa	(hr)	Loading	Creep		
11595	427	800	20.0	138	15,572	2.67	0.073	1.57	
12368	427	800	18.0	124	12,540	1.91	0.099	1.42	
12472	427	800	16.0	110	11,671	1.17	0.063	1.26	
12570	427	800	14.0	97	11,343	0.83	0.040	1.10	
11569	482	900	20.0	138	15,455	3.27	0.141	1.70	Discontinued
12375	482	900	18.0	124	12,376	2.40	0.072	1.53	
11675	482	900	16.0	110	2,451	1.48	0.032	1.36	Discontinued
11693	482	900	14.0	97	2,202	0.92	0.14	1.19	Discontinued
11830	482	900	12.0	83	1,682	0.35	0.04	1.02	Discontinued
13152	482	900	10.0	69	9,544	0.089	0.085	0.85	
13020	482	900	10.0	69	10,208	0.085	0.029	0.85	
10489	538	1000	20.0	138	20,577	3.80	0.650	1.80	
12250	538	1000	18.0	124	13,042	2.62	0.283	1.62	
11625	538	1000	16.0	110	15,437	1.79	0.252	1.44	
10491	538	1000	14.0	97	20,598	1.16	0.254	1.26	
12444	538	1000	14.0	97	12,035	1.18	0.192	1.26	
12445	538	1000	14.0	97	4,498	1.17	0.090	1.26	Discontinued
11568	538	1000	12.0	83	15,684	0.53	0.112	1.08	
11626	538	1000	10.0	69	15,445	0.071	0.095	0.90	
11641	538	1000	8.0	55	3,170	0.040	0.027	0.72	Discontinued
10853	593	1100	18.0	124	4,547	2.84	5.94	1.65	Ruptured
10852	593	1100	16.0	110	14,647	2.29	3.55	1.47	Ruptured
13947	593	1100	16.0	110	5,346	2.13	1.289	1.47	
10554	593	1100	14.0	97	8,710	1.40	0.65	1.28	Discontinued

Table 3.1. (Continued)

Test	Temperature (°C)	Temperature (°F)	Stress ksi	Stress MPa	Time in Test (hr)	Strain, % Loading	Strain, % Creep	Ratio of Creep Stress to Yield Stress[b]	Comments[c]
11596	593	1100	12.0	83	15,540	0.52	0.420	1.10	
10490	593	1100	10.0	69	20,576	0.22	0.365	0.92	
13710	593	1100	10.0	69	2,010	0.096	0.204	0.92	Discontinued
14163	593	1100	10.0	69	4,578	0.228	0.110	0.92	
11227	593	1100	8.0	55	6,103	0.041	0.080	0.73	Discontinued
12459	593	1100	5.0	34	11,780	0.024	0.106	0.46	
10855	649	1200	16.0	110	304	2.41	12.0	1.57	Ruptured
10854	649	1200	14.0	97	761	1.60	13.0	1.37	Ruptured
11563	649	1200	12.0	83	2,674	0.59	13.4	1.18	Ruptured
11226	649	1200	10.0	69	7,278	0.18	7.0	0.98	Ruptured
10851	649	1200	8.0	55	18,753	0.044	2.38	0.78	
12255	649	1200	5.0	34	992	0.030	0.08	0.49	Discontinued
12443	649	1200	5.0	34	11,735	0.024	0.153	0.49	
12460	649	1200	3.0	21	11,752	0.020	0.208	0.29	
10856	704	1300	10.0	69	568	0.067	15.6	0.90	Ruptured
11562	704	1300	10.0	69	653	0.12	22.5	0.90	Ruptured
11222	704	1300	8.0	55	2,760	0.031	16.4	0.72	Ruptured
12254	704	1300	5.0	34	12,928	0.030	1.781	0.45	
12461	704	1300	3.0	21	11,750	0.018	0.380	0.27	
12462	704	1300	2.0	14	11,565	0.010	0.228	0.18	

[a]Annealed 0.5 hr at 1093°C before testing. All tests loaded at a strain rate of 0.004/min.

[b]Yield stresses used in this ratio were 12,700 psi (88 MPa) at 427°C (800°F), 11,800 psi (81 MPa) at 482°C (900°F), 11,100 psi (77 MPa) at 538°C (1000°F), 10,900 psi (75 MPa) at 593°C (1100°F), 10,200 psi (70 MPa) at 649°C (1200°F), 11,100 psi (77 MPa) at 704°C (1300°F).

[c]Unless otherwise noted, tests in progress.

1. Elongation at fracture was not significantly affected by prior creep deformation at 260°C (500°F), T/T_m = 0.57.

2. In tests at 260°C (500°F), prior creep deformation of 1.5% in 20 hr produced higher ultimate tensile and yield strengths than did exposure to temperature without stress for the same period before tensile testing.

Gluck et al.[4] investigated the effect of prior creep deformation up to 2% at 176, 204, and 260°C (350, 400, and 500°F) (T/T_m = 0.48–0.57) in 10, 50, and 100 hr on short-term tensile properties of 2024-T86 aluminum alloy. Some work was also performed[4] on 17-7PH alloy after creep exposures at 316 to 482°C (600–900°F), T/T_m = 0.36–0.47. The results obtained provided the following conclusions.

1. Short-time strengths may be either raised or lowered by prior exposure to temperature, with or without stress. Changes in strength may be as much as 50% of the original value. The direction and magnitude of the changes depend on the material, test temperature, creep-exposure conditions, and property being measured.

2. Exposure to temperature in the absence of applied stress had approximately the same magnitude of effect on subsequent properties as did the added effect of creep during the exposure period. In most cases, longer exposure times and larger amounts of deformation during the exposure resulted in greater changes in mechanical properties.

3. For the 2024-T86 alloy tests, compression properties showed a greater sensitivity to tension exposure conditions than did tensile properties. Tension-impact strength was relatively insensitive to prior creep exposure.

4. The most important changes are a large drop in the strength of alloy 2024-T86 after prior creep exposure for time periods of 10 to 100 hr and an apparent decline in room-temperature ductility of 17-7PH (TH 1050) after prior creep exposure for 100 hr near 316°C (600°F), T/T_m = 0.36.

Bogardus et al.[6] investigated the effect of prior creep deformation on tensile properties of cold-worked unalloyed aluminum and made the following conclusions.

1. Small amounts of creep strain are generally associated with small changes in tensile properties.

2. Creep strains developed in short periods of exposure appeared to be effective in cold working the material and may even be associated with increases in the tensile and yield strength.

3. The amount of prior creep cannot be used alone as a measure of associated losses in tensile strength, since, for any given temperature the amount of loss is also dependent on the length of exposure and the creep stress.

4. The residual tensile properties after a creep exposure are directly related to the exposure temperature; a given amount of prior creep, developed during a given exposure, is associated with increasing losses in strength as the temperature increases.

A limited amount of data[7] on the influence of prior creep deformation on short-term tensile properties of INOR-8 suggested the following:

1. Yield strength increases, while ultimate tensile strength and total elongation decrease.

2. For a fixed stress, prior creep for short times decreases the total elongation, whereas for long times it starts to show an increase.

The ORNL data on influence of prior creep deformation on all tensile properties (0.2% yield, ultimate tensile strength, uniform and total elongations, and reduction of area) of type 304 stainless steel, along with HEDL[1] data on type 316 are described here.

Creep data on the reference heat 9T2796 of type 304 stainless steel before tensile testing are summarized in Table 3.2 and the tensile data following periods of creep are summarized in Table 3.3. Tensile data were calculated from original (precreep) specimen dimensions. Reduction of area was calculated from both the pre- and postcreep dimensions.

3.2.1.2.1 Stress-Strain Curves. Engineering stress-strain curves showing the effect of prior creep deformation are presented in Figs. 3.1 and 3.2. The sum of creep and tensile elongation is in most cases less than the tensile elongation without any prior creep, indicating thereby a loss in tensile elongation due to prior creep deformation. The prior

Table 3.2. Creep Data on the Reference Heat 9T2796[a] of Type 304 Stainless Steel Before Tensile Test

Test	Temperature		Stress		Duration (hr)	Strain, %		Creep Stage
	(°C)	(°F)	(ksi)	(MPa)		Creep	Total	
11830[b]	482	900	12	83	1682.0	0.04	0.39	1
11693[b]	482	900	14	97	2690.0	0.14	1.06	1
11675[b]	482	900	16	110	2451.0	0.032	1.51	1
11641	538	1000	8	55	3170.0	0.027	0.067	1
8973	538	1000	10	69	5035.0	0.045	0.095	1
14974	538	1000	12	83	500.0	0.10	0.809	1
12445	538	1000	14	97	4498.0	0.090	1.26	1
9314	538	1000	15	103	5058.0	0.2625	1.44	2
13996	538	1000	20	138	97.5	0.056	4.43	2
8938	538	1000	30	207	1171.0	1.225	9.525	2
13710[b]	593	1100	10	69	2009.6	0.060	0.156	2
10554[b]	593	1100	14	97	8710.0	1.306	2.706	2
13755	593	1100	20	138	100.0	0.536	4.24	2
13946	593	1100	20	138	99.4	0.545	4.17	2
13853	593	1100	20	138	500.0	1.200	4.92	2
12255	649	1200	5	34	992.0	0.080	0.11	1
13951	649	1200	12	83	98.6	0.59	1.528	2
13824	649	1200	16	110	102.2	2.80	5.110	2
13764[c]	649	1200	16	110	244.9	14.53	16.95	Ruptured

[a]Annealed for 0.5 hr at 1093°C (2000°F) before testing.

[b]Specimen taken from the center of 2-in. (51-mm) plate. All other specimens were from the bottom level of the plate.

[c]Test was intended to be discontinued after 500 hr.

Table 3.3. Tensile Properties on Reference Heat 9T2796[a] of Type 304 Stainless Steel After Creep Tests

Tensile Test	Creep Test	Temperature °C(°F)		Proportional Limit		Strength, ksi(MPa)		Elongation, %		Reduction of Area, %	
		Creep	Tensile	(ksi)	(MPa)	Yield	Ultimate Tensile	Uniform	Total	Overall	Residual[b]
14977			482(900)	5.28	36.4	11.0(75.8)	55.7(384.1)	38.3	44.9	68.9	68.9
13978			482(900)	6.50	44.8	11.8(81.4)			42.2	66.8	66.8
11798[c]			482(900)	6.10	42.0	12.2(84.1)	55.8(384.7)	43.5	53.6	71.4	71.4
14981	11830	482(900)	482(900)			19.4(133.8)	54.9(378.5)		41.6	69.3	69.2
13701	11693	482(900)	482(900)	7.12	49.1	15.7(108.3)	56.95(392.7)	38.5	43.9	63.4	63.2
13702	11675	482(900)	482(900)	12.40	85.5	21.7(149.6)	55.4(382.0)	34.2	39.3	68.1	67.9
13979			538(1000)	7.3	50.0	10.6(73.1)	51.9(357.9)	37.6	42.5	63.6	63.6
11795			538(1000)	5.6	39.0	11.0(75.8)	47.4(326.8)			71.1	71.1
14978	11641	538(1000)	538(1000)	3.6	24.8	12.2(84.1)	53.8(371.0)	36.0	41.0	70.9	70.9
15021	8973	538(1000)	538(1000)	7.4	51.0	12.3(84.8)	53.1(366.1)	36.7	33.1	67.4	67.4
15064	14974	538(1000)	538(1000)	9.2	63.4	12.4(85.5)	57.0(393.0)	36.5	47.1	67.1	66.8
15022	9314	538(1000)	538(1000)	12.6	86.9	17.3(119.3)	54.6(376.5)	30.4	36.3	61.6	61.3
15020	8938	538(1000)	538(1000)	26.4	182.0	31.3(215.8)	51.4(354.4)	22.0	26.0	44.9	39.5
14976			593(1100)	5.6	38.6	9.5(65.5)	47.3(326.1)	37.5	43.7	66.9	66.9
13980			593(1100)	5.9	40.7	10.2(70.3)			43.4	67.8	67.8
21163[c]			593(1100)			9.5(65.5)	47.2(325.4)	37.8	39.1	66.3	66.3
13787	12445	538(1000)	593(1100)	8.2	56.5	13.7(94.5)	46.3(319.2)	31.9	37.2	64.5	64.3
13983	13710	593(1100)	593(1100)	4.4	30.3	14.3(98.6)	46.8(322.7)	34.1	40.1	57.9	57.9
14980	10554	593(1100)	593(1100)	13.3	91.7	20.2(139.3)	43.7(301.3)	15.2	16.8	28.9	26.9
13788	13755	593(1100)	593(1100)	13.9	95.8	21.2(146.2)	45.2(311.7)	29.2	34.0	60.5	57.6
13982	13946	593(1100)	593(1100)	13.2	91.0	21.1(145.5)	46.5(320.6)	31.6	35.9	55.6	53.2
13984	13853	593(1100)	593(1100)	18.4	126.9	23.3(160.7)	45.2(311.7)	21.8	24.3	45.1	42.4
13981			649(1200)	4.5	31.0	9.5(65.5)	39.4(271.7)	32.4	41.5	47.2	47.2
14150	13996	538(1000)	649(1200)	14.3	98.6	19.05(131.4)	39.08(269.5)	28.0	38.7	46.7	44.7
14979	12255	649(1200)	649(1200)	5.0	34.5	13.9(95.8)	41.6(286.8)	29.1	38.9	52.9	52.9
14149	13951	649(1200)	649(1200)	12.8	88.3	15.8(108.9)	35.6(245.5)	31.1	40.9	43.2	42.5
13869	13824	649(1200)	649(1200)	18.5	127.6	20.05(138.2)	37.6(259.3)	21.5	25.8	38.2	35.0

[a]Annealed for 0.5 hr at 1093°C (2000°F) before creep and tensile testing.

[b]All properties were based on precreep dimensions. Residual reduction of area was based on postcreep diameter.

[c]Specimen gage length 5 times diameter for these specimens; all other specimens 9 times.

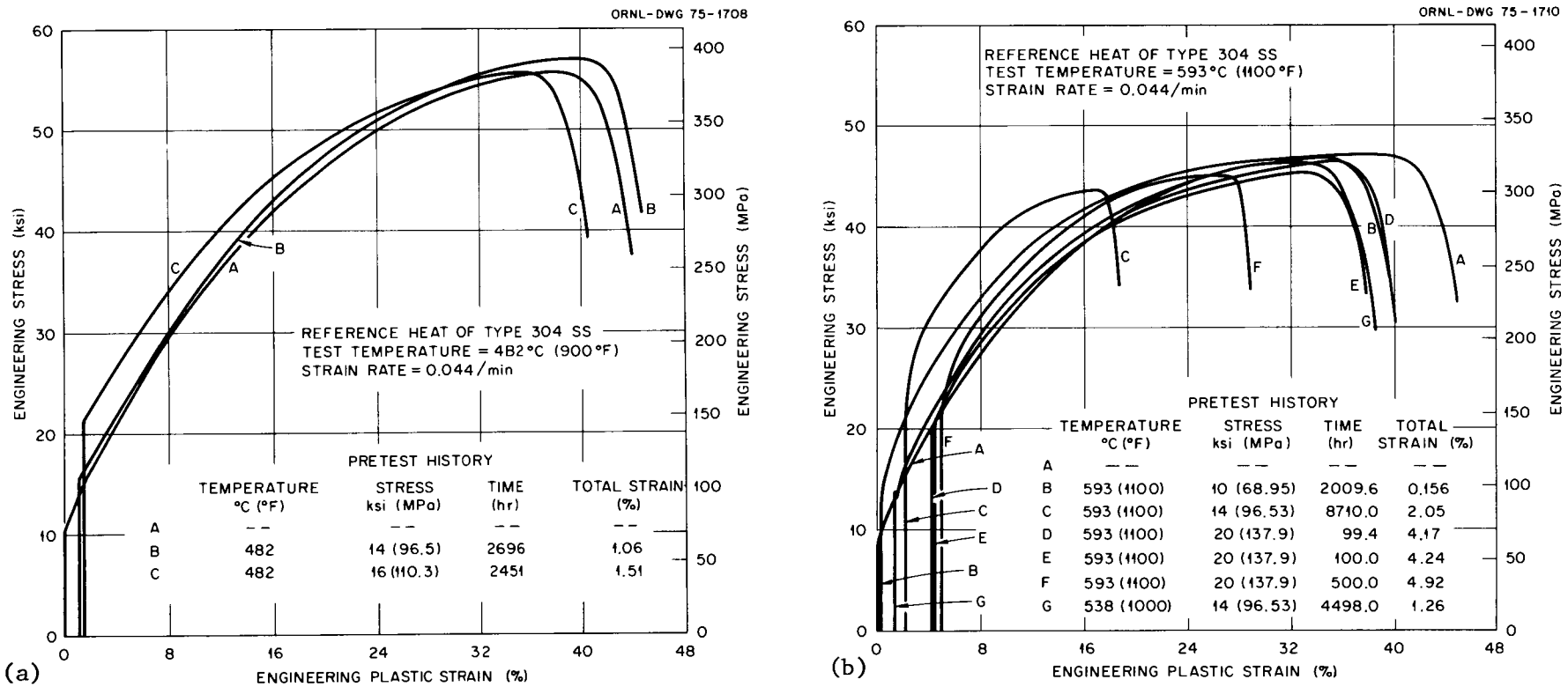

Fig. 3.1. Stress-Strain Curves for Type 304 Stainless Steel After Prior Creep Deformation at (a) 482°C (900°F), (b) 593°C (1100°F). The specimen for curve C in (b) was also exposed to a thermal transient of about 167°C (301°F) before the test was discontinued.

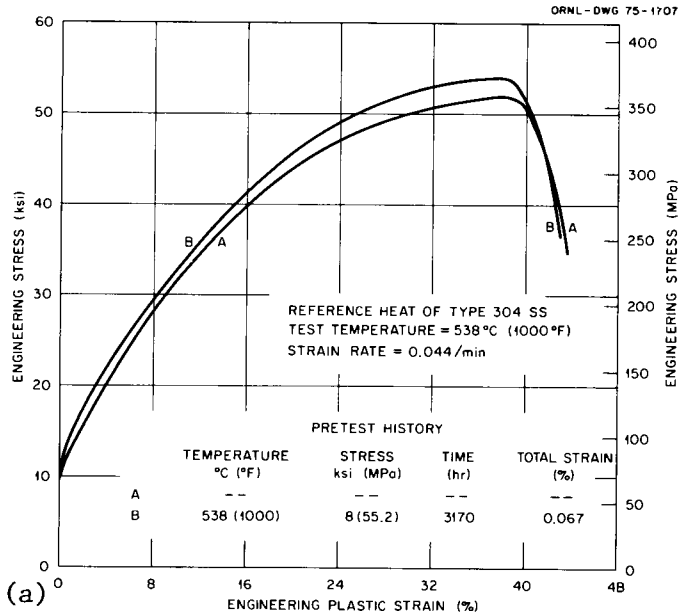

(a)

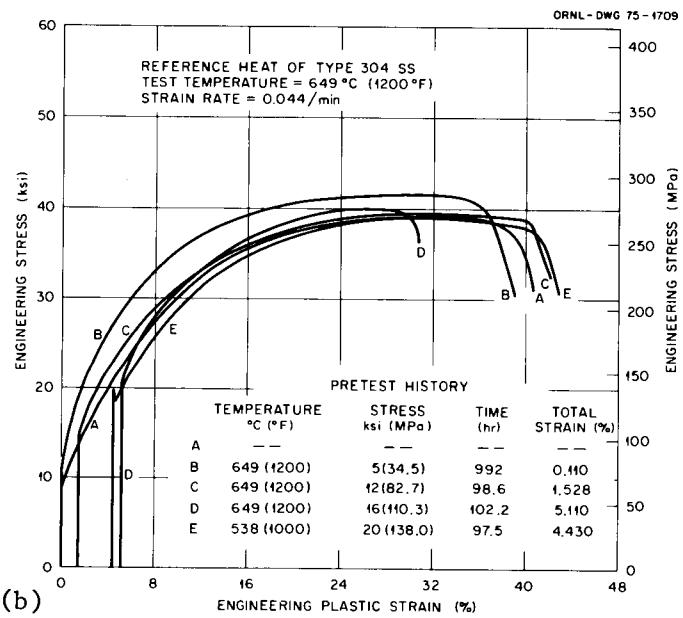

(b)

Fig. 3.2. Stress-Strain Curves for Type 304 Stainless Steel After Prior Creep Deformation at (a) 538°C (1000°F), (b) 649°C (1200°F).

creep deformation also tends to increase yield strength and lower ultimate tensile strength, uniform elongation, and reduction of area.

3.2.1.2.2 <u>0.2% Yield Strength</u>. Figure 3.3 shows the effect of prior true creep stress on the 0.2% yield strength of types 304 and 316 stainless steel. The ORNL and HEDL data on types 304 and 316 stainless steel can be represented by the following equations:

type 304 stainless steel, ORNL data:

$$S_y = 9.67 + 0.612\sigma_c,\ 482\text{–}649°C,\ T/T_m\ 0.44\text{–}0.54; \quad (1)$$

type 304 stainless steel, HEDL data:

$$S_y = 15.58 + 0.551\sigma_c,\ 538\text{–}649°C,\ T/T_m\ 0.48\text{–}0.54; \quad (2)$$

type 316 stainless steel, HEDL data:

$$S_y = 17.76 + 0.615\sigma_c,\ 538\text{–}649°C,\ T/T_m\ 0.48\text{–}0.54; \quad (3)$$

where S_y is 0.2% yield stress and σ_c is true prior creep stress.

In Fig. 3.4, 0.2% yield stress is plotted as a function of total prior strain (loading plus creep) and compared with the corresponding values from the stress-strain curves. It can be noted in Fig. 3.4 that the specimens first crept to small strains show a large increase in 0.2% yield strength as compared with the strains produced during the tensile tests. At larger strains, the effectiveness of prior creep strain decreases such that the yield strength values fall below the corresponding tensile values. The large initial increase in yield strength due to prior creep strain is possibly associated with dislocations produced during loading becoming decorated with precipitates produced during creep. In tensile tests the strain rate is so high that time does not permit the decoration of dislocations, at least for test temperatures of 482 and 538°C (900 and 1000°F), where no serrations were observed during the tensile tests. For test temperatures of 593 and 649°C (1100 and 1200°F), serrations were observed during the tensile test, indicating a fast migration of atoms. Thus, for specimens first crept at 593 and 649°C (1100 and 1200°F), although dislocations produced on loading were decorated with precipitates

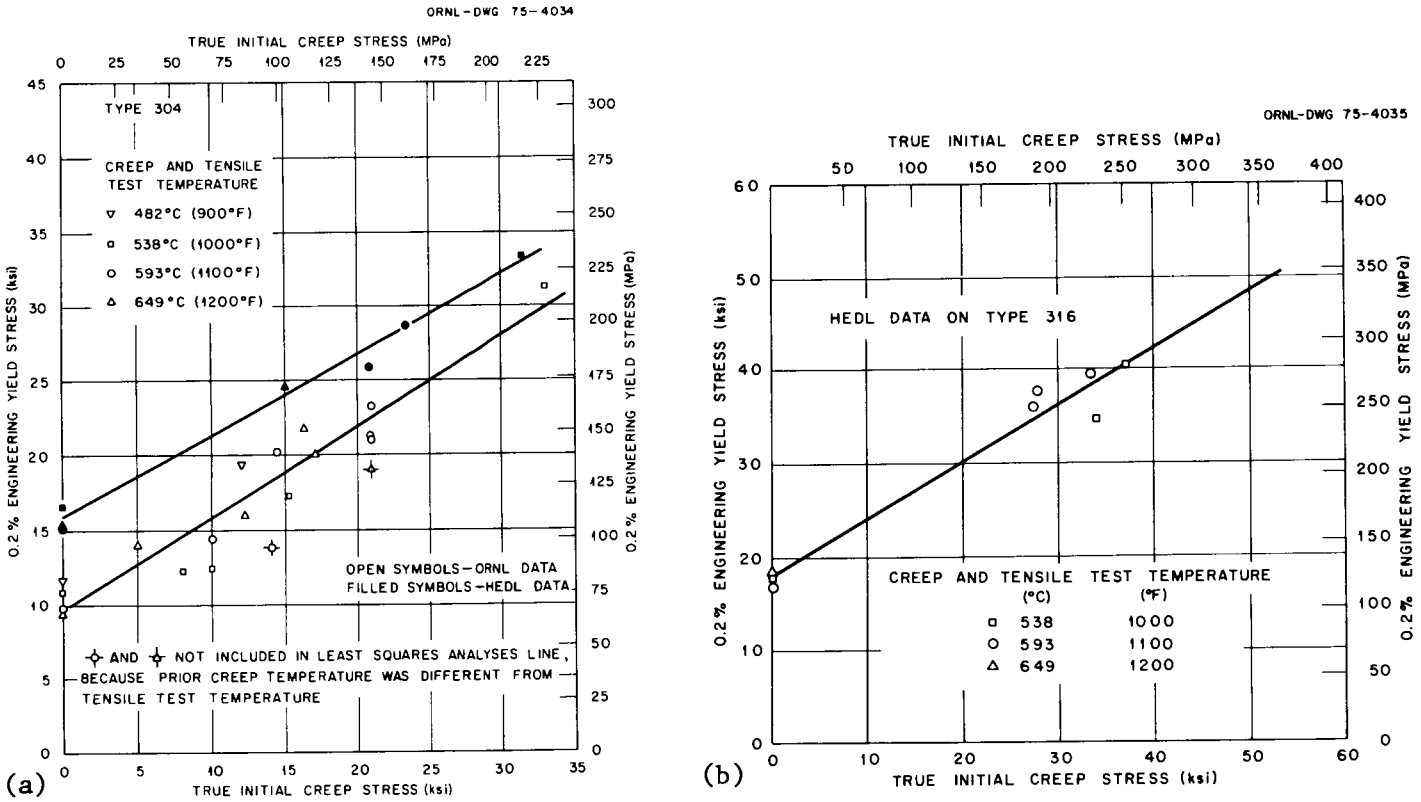

Fig. 3.3. The Influence of Prior Creep Stress on 0.2% Yield Strength of Stainless Steel. (a) Type 304. (b) Type 316.

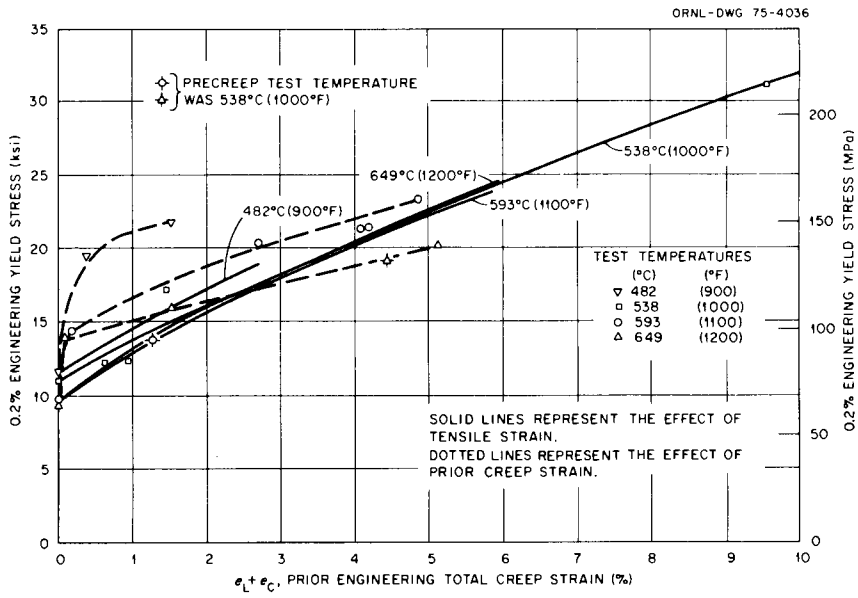

Fig. 3.4. Comparison Between the Influence of Prior Creep Strain (Creep and Loading) and Tensile Strain on the Tensile Yield Strength (0.2%) of Type 304 Stainless Steel at Several Temperatures.

(possibly $M_{23}C_6$ type), they grew rapidly to produce an overaging condition so that their effectiveness in strengthening was possibly lost. Transmission electron microscopy will be performed to check the above suggested mechanism.

3.2.1.2.3 Ultimate Tensile Strength. Prior creep deformation can result in grain boundary cavities (see Fig. 3.5, specimen tested at 593°C and 14 ksi and discontinued after 8710 hr) and thus lower the effective load carrying area[8] with a resultant decrease in uniform elongation and ultimate tensile strength. Plots showing the influence of life fraction used during prior creep and fractional prior creep elongation are shown in Figs. 3.6 and 3.7. The results in Fig. 3.7 show that the true ultimate tensile strength ratio can reach a value of approximately 0.6 for a value of life fraction used during prior creep approaching 0.85. The value of $\sigma_u/\sigma_u(0) = 0.60$ is in remarkably good agreement with results calculated by Scott et al.[8] on RR58 alloy, in which creep cracks were estimated to cover approximately 60% of the ruptured surface area. Thus, the lowering of ultimate tensile strength ratio observed in prior creep-deformed specimens must be associated with creep cracks.

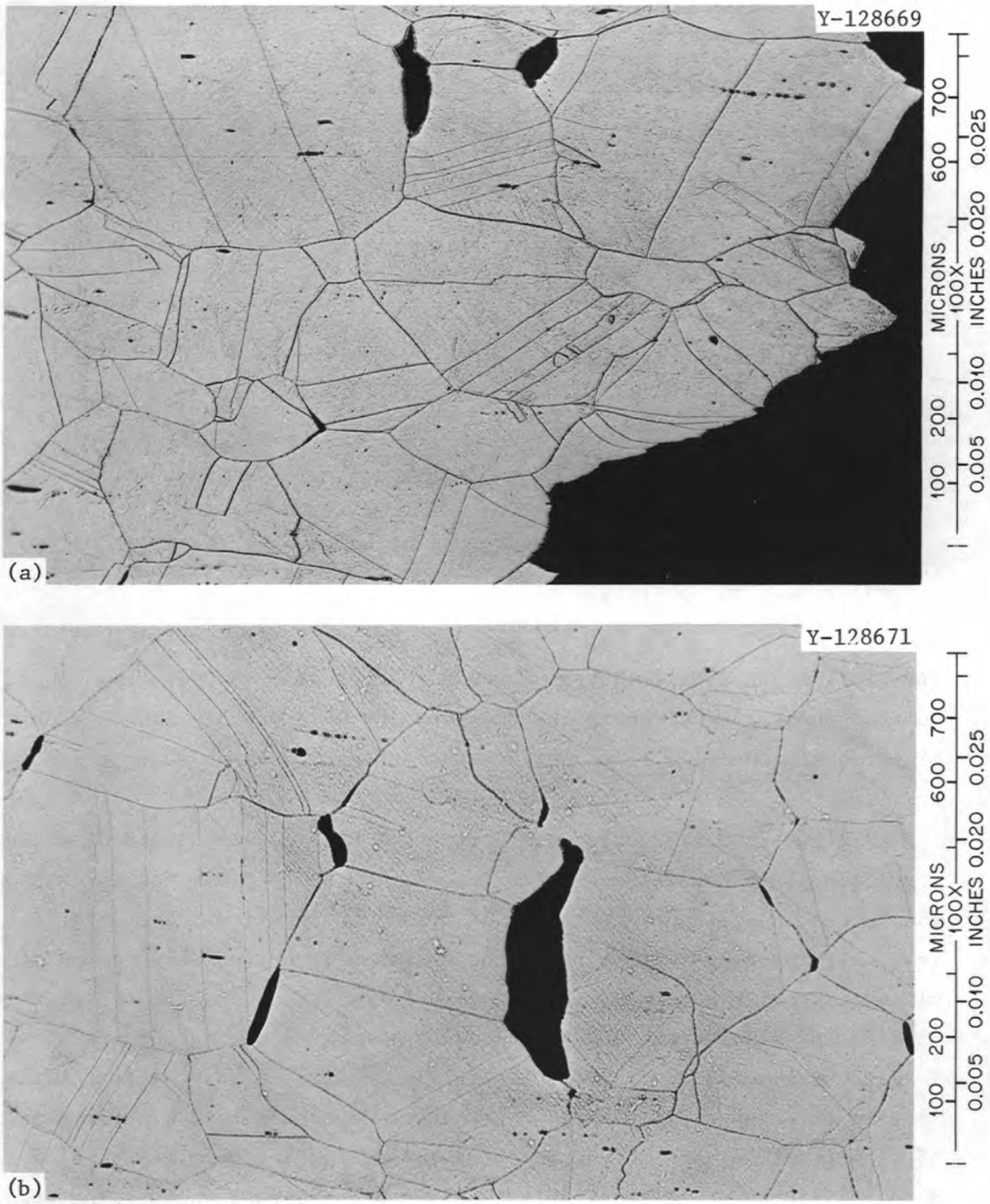

Fig. 3.5. Microstructure Showing Grain Boundary Cavities the Reference Heat (9T2796) of Type 304 Stainless Steel. The specimen was tensile tested at 593°C (1100°F) and a strain rate of 0.040/min, following creep for 8710 hr at 14 ksi (96 MPa) and 593°C (1100°F). (a) Fracture. (b) Gage section remote from the fracture.

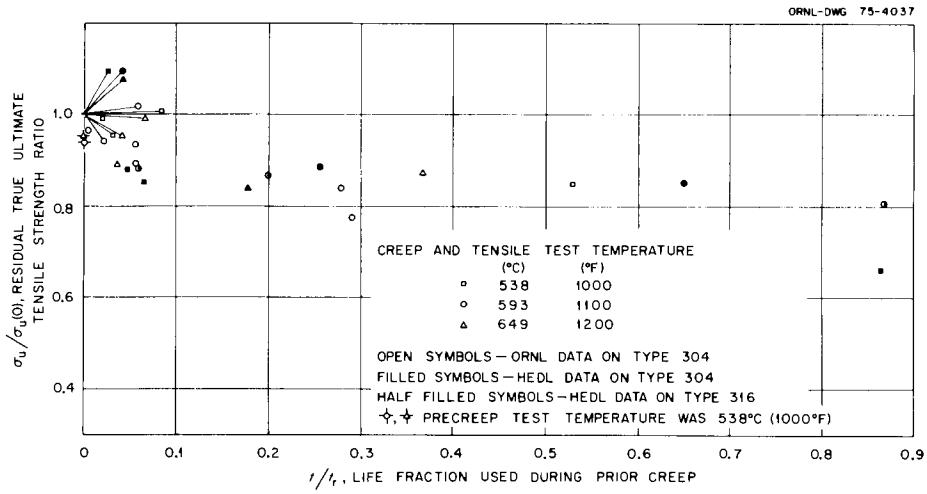

Fig. 3.6. The Influence of Life Fraction Used During Prior Creep on Residual True Ultimate Tensile Strength Ratio.

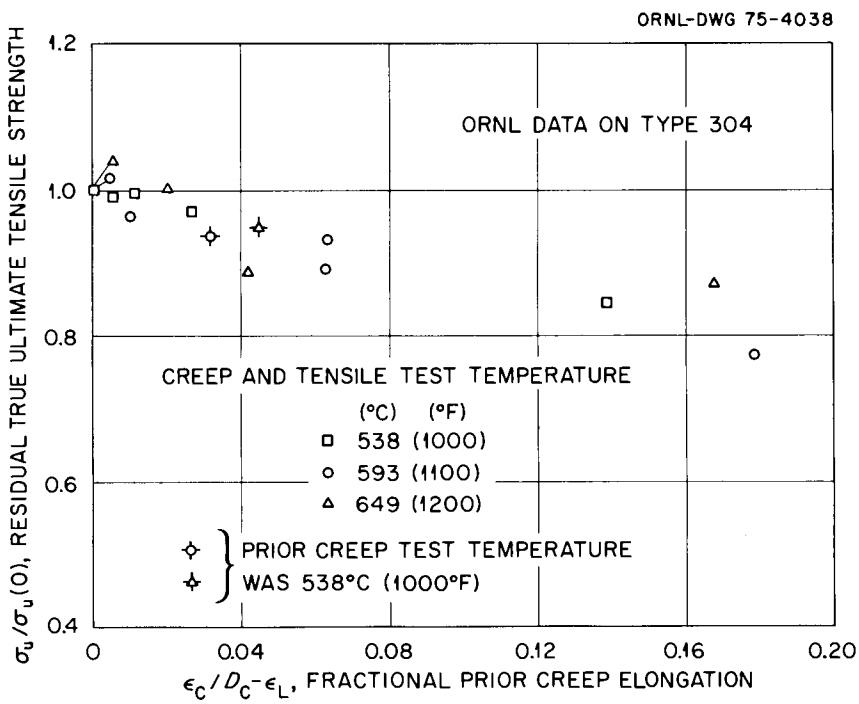

Fig. 3.7. The Influence of Fractional Prior Creep Elongation on True Ultimate Tensile Strength Ratio.

3.2.1.2.4 Uniform Elongation. The following definitions were used to examine the influence of prior creep deformation on short-term tensile uniform elongation.

$$\text{True Prior Creep Strain} = \varepsilon_c$$
$$\varepsilon_c = \ln[(1 + e_L + e_c)/(1 + e_L)] \ ,$$

where e_L and e_c are engineering loading and creep strains, respectively.

$$\text{True Residual Uniform Elongation} = \varepsilon_u$$
$$\varepsilon_u = \ln[(1 + e_L + e_c + e_u)/(1 + e_L + e_c)] \ ,$$

where e_u = engineering uniform elongation.

$$\text{True Creep Rupture Ductility} = D_c$$
$$D_c = \ln[100/(100 - \text{RA})] \ ,$$

where RA = reduction of area.

$$\text{Fractional Prior Creep Elongation} = \varepsilon_c/(D_c - \varepsilon_L) \ ,$$

where $\varepsilon_L = \ln(1 + e_L)$ = true loading strain.

Residual true uniform elongation is plotted as a function of true prior creep strain in Fig. 3.8. The residual true uniform elongation, ε_u, is shown as a function of t/t_r and $\varepsilon_c/(D_c - \varepsilon_L)$ in Figs. 3.9 and 3.10. This property shows a rather scattered decrease with increasing ε_c and t/t_r; however, it shows a linear decrease as a function of $\varepsilon_c/(D_c - \varepsilon_L)$, as shown in Fig. 3.10.

3.2.1.2.5 Total Elongation. The change in engineering residual total elongation as functions of e_c and $\varepsilon_c/(D_c - \varepsilon_L)$ is shown in Figs. 3.11 and 3.12, respectively. Both figures show a linear decrease in ε_T with e_c and $\varepsilon_c/(D_c - \varepsilon_L)$.

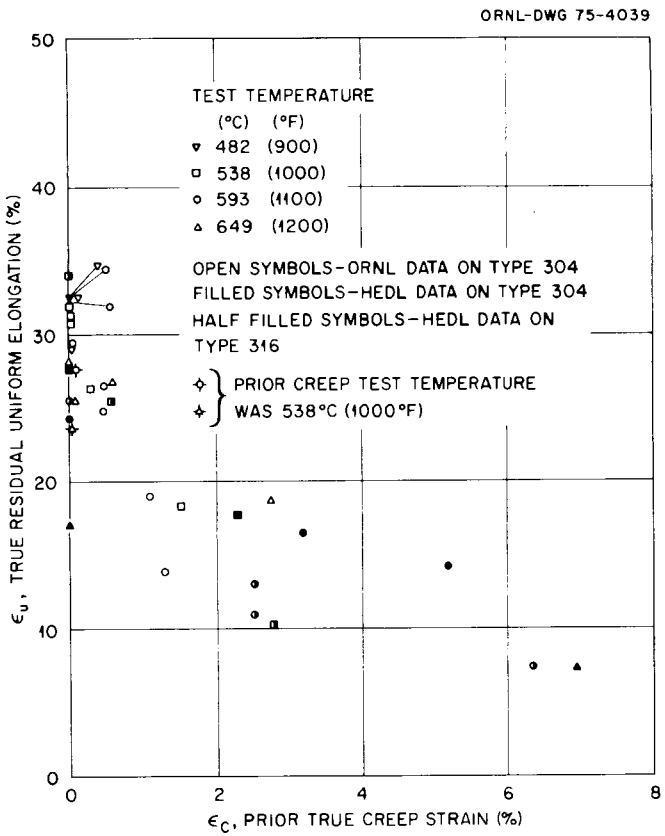

Fig. 3.8. The Influence of Prior Creep Strain on Residual True Uniform Elongation.

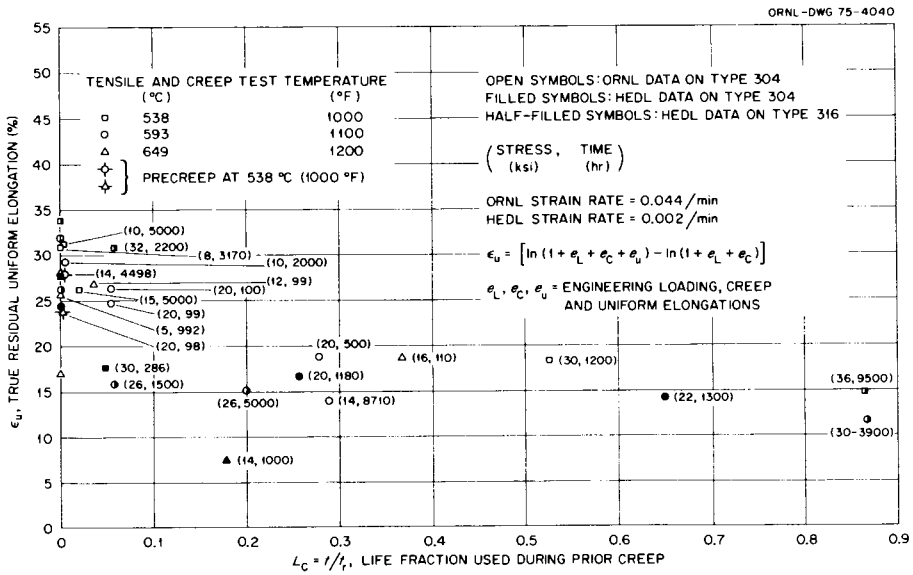

Fig. 3.9. The Influence of Life Fraction Used During Prior Creep on Residual True Uniform Elongation.

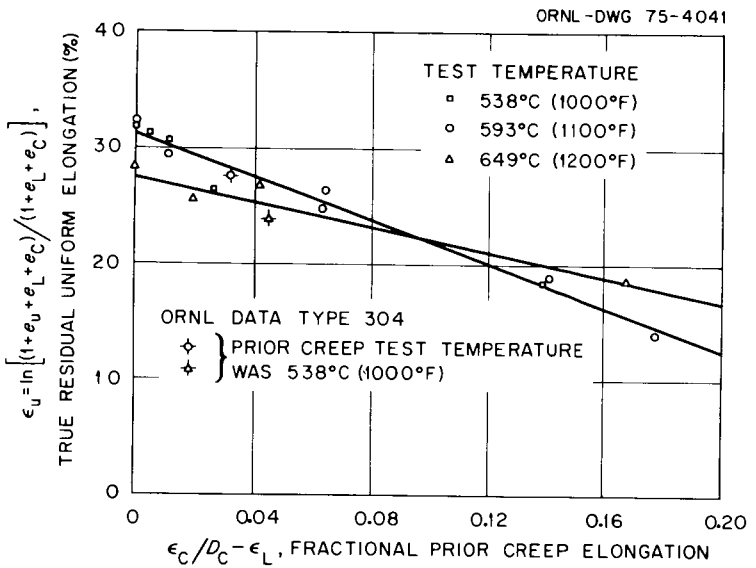

Fig. 3.10. The Influence of Fractional Prior Creep Elongation on Residual True Uniform Elongation.

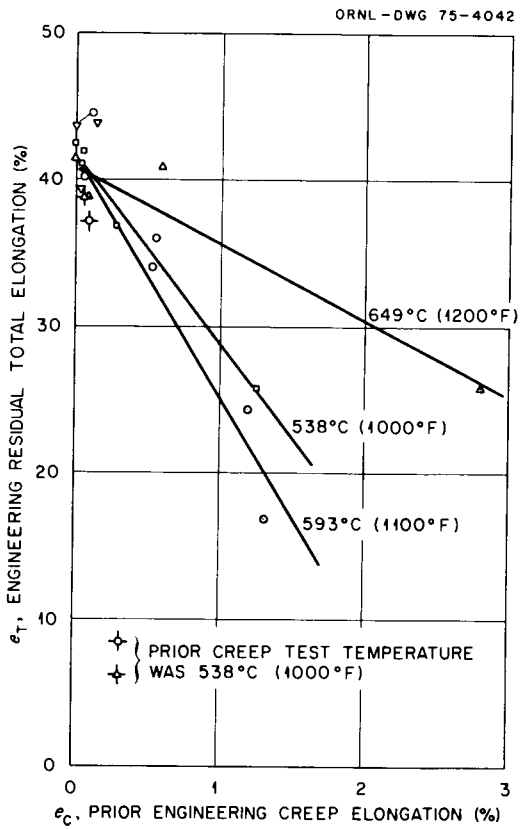

Fig. 3.11. The Influence of Engineering Prior Creep Elongation on Engineering Residual Total Elongation.

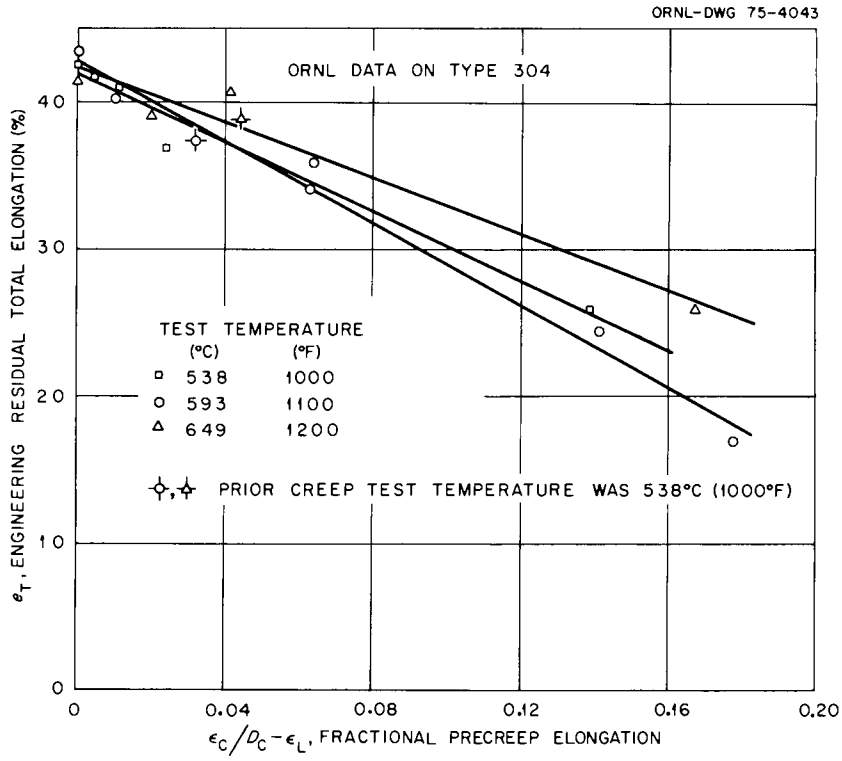

Fig. 3.12. The Influence of Fractional Prior Creep Elongation on Engineering Residual Total Elongation.

3.2.1.2.6 <u>True Residual Ductility</u>. The true residual ductility was defined as follows:

$$D_T' = \ln[100/(100 - \mathrm{RA})] \ ,$$

and RA was calculated from postcreep and tensile dimensions. This quantity is plotted as a function of ε_c, $\varepsilon_c/(D_c - \varepsilon_L)$, and t/t_r in Fig. 3.13.

The true residual ductility decrease due to thermal aging and prior creep time is shown in Fig. 3.14. It can be noted from the figure that for the same time, aging under stress (prior creep deformation) produces a much larger reduction in D_T' than does only thermal aging (no stress).

From the linear relationships for various ductility measures, we have calculated the prior creep deformation for 10% residual tensile

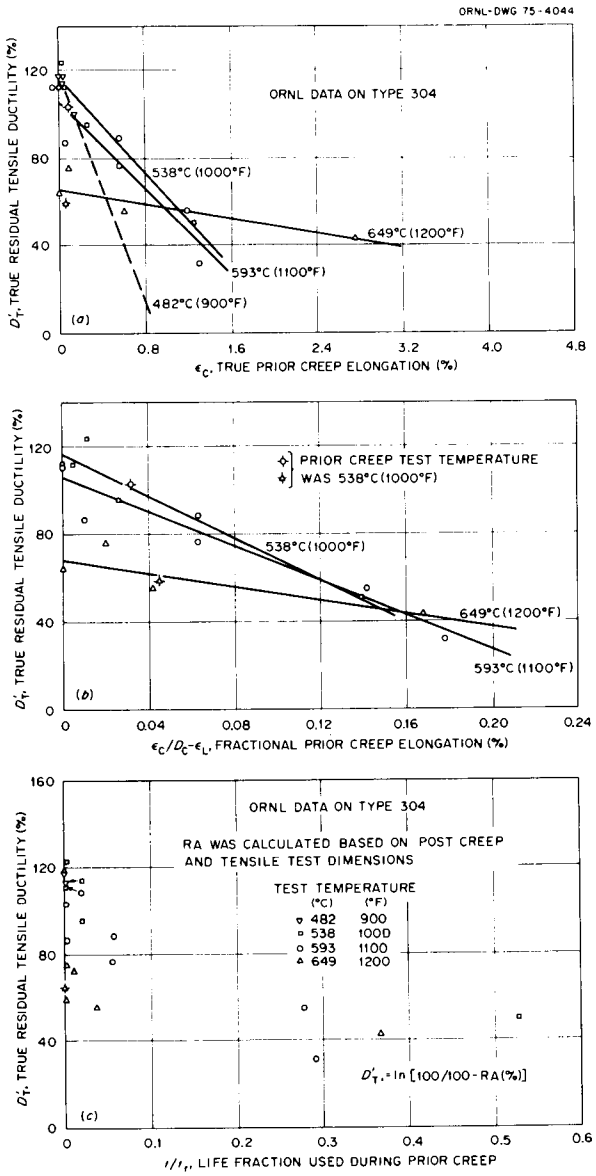

Fig. 3.13. The Influence on True Residual Tensile Ductility of (a) True Prior Creep Elongation, (b) Fractional Prior Creep Elongation, and (c) Life Fraction Used During Prior Creep.

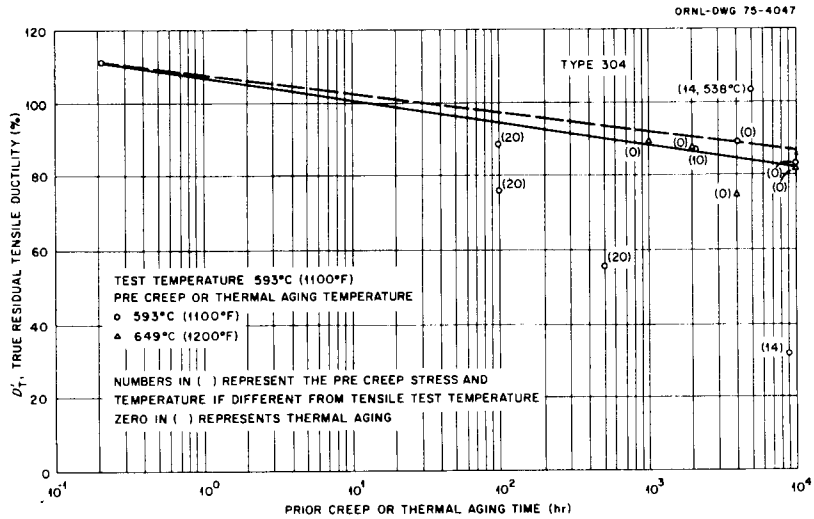

Fig. 3.14. The Influence of Prior Creep or Thermal Aging Time on True Residual Tensile Ductility.

ductility at various test temperatures, and the results are summarized in Fig. 3.15. It can be noted from the figure that in the range 482 to 593°C (900–1100°F), 1 to 2% prior creep strain can result in a residual tensile ductility less than 10%.

We tried to check if creep and tensile damage is additive and obeys the linear summation law. The following linear summations were tried:

$$\frac{\varepsilon_c}{D_c - \varepsilon_L} + \frac{D_T - \varepsilon_c}{D_T(0)} = 1 \ , \tag{4}$$

$$\frac{t_c}{t_r} + \frac{D'_T}{D_T(0)} = 1 \ , \tag{5}$$

$$\frac{t_c}{t_r} + \frac{t_i}{t_t} = 1 \ , \tag{6}$$

where D_T = true total ductility after prior creep deformation,

$D_T(0)$ = true tensile ductility without prior creep,

D'_T = true residual tensile ductility,

$D_T - \varepsilon_c$ = true total tensile ductility, including the loading strain,

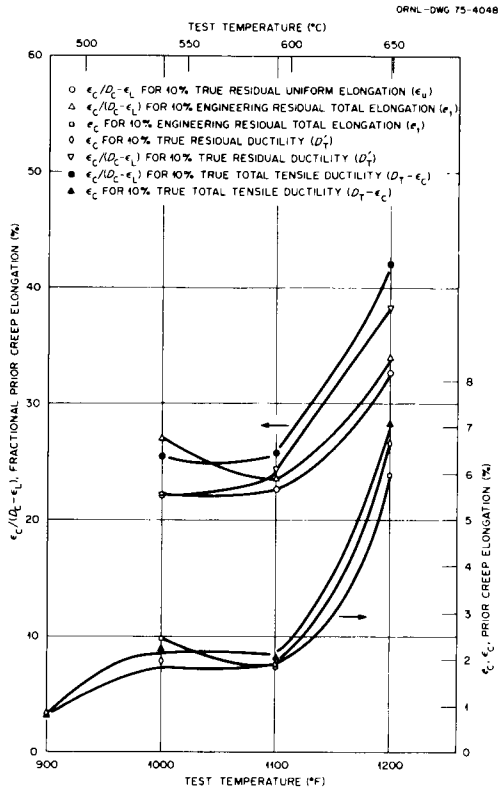

Fig. 3.15. Prior Creep Deformation Necessary for 10% Residual Tensile Ductility as a Function of Test Temperature.

t_c = prior creep period,

t_r = time to rupture during creep,

t_i = tensile test time after creep,

t_t = time to rupture during tensile testing.

The results of various linear summations are presented in Figs. 3.16 and 3.17. These figures show that the linear summation rules in Eqs. (4) through (6) are not obeyed and thus need modification. One way to modify is to replace unity in these equations by ϕ_1, ϕ_2, and ϕ_3, such that:

$$\frac{\varepsilon_c}{D_c - \varepsilon_L} + \frac{D_T - \varepsilon_c}{D_T(0)} = \phi_1 \ , \qquad (7)$$

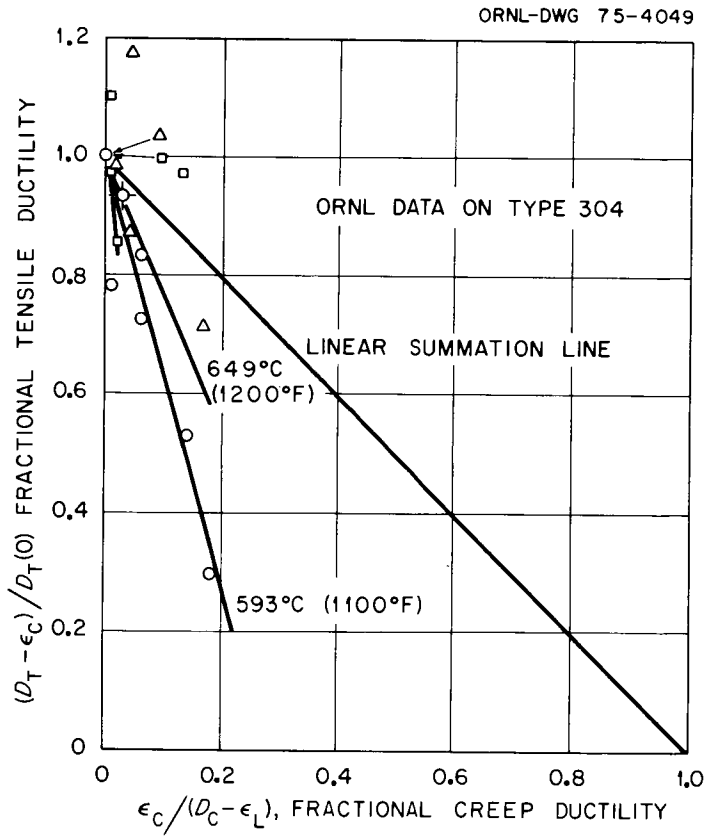

Fig. 3.16. Tensile and Creep Damage Summation: Fit to Eq. (4).

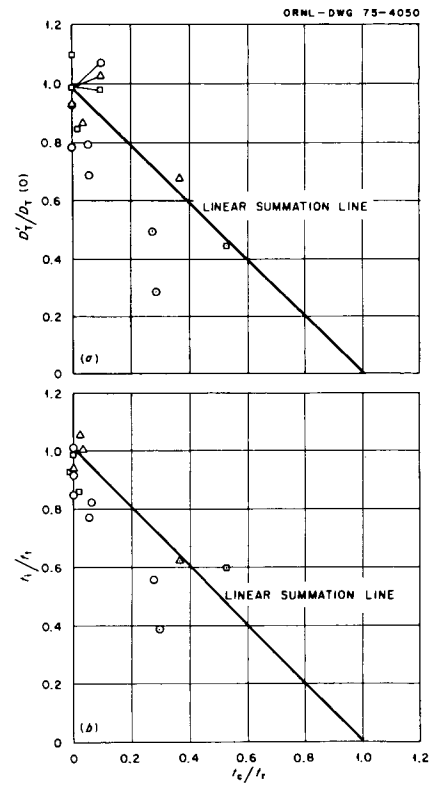

Fig. 3.17. Tensile and Creep Damage Summation: Fits to (a) Eq. (5) and (b) Eq. (6).

$$\frac{t_c}{t_r} + \frac{D_T'}{D_T(0)} = \phi_2 \ , \tag{8}$$

$$\frac{t_c}{t_r} + \frac{t_i}{t_t} = \phi_3 \ . \tag{9}$$

The influence of prior creep deformation on ϕ_1, ϕ_2, and ϕ_3 is shown in Figs. 3.18 and 3.19. The deviation from unity is a measure of net damage produced by prior creep. In general, the deviation of damage summation ϕ_1, ϕ_2, and ϕ_3 from unity increases with the increase in prior creep deformation or life fraction used during prior creep. The damage summation values greater than unity are hard to explain but could result from errors in extrapolated values of time to rupture. More data are needed to determine a summation method other than the linear summation.

Work is in progress on tests to be discontinued after very long prior creep periods and will be reported as they become available.

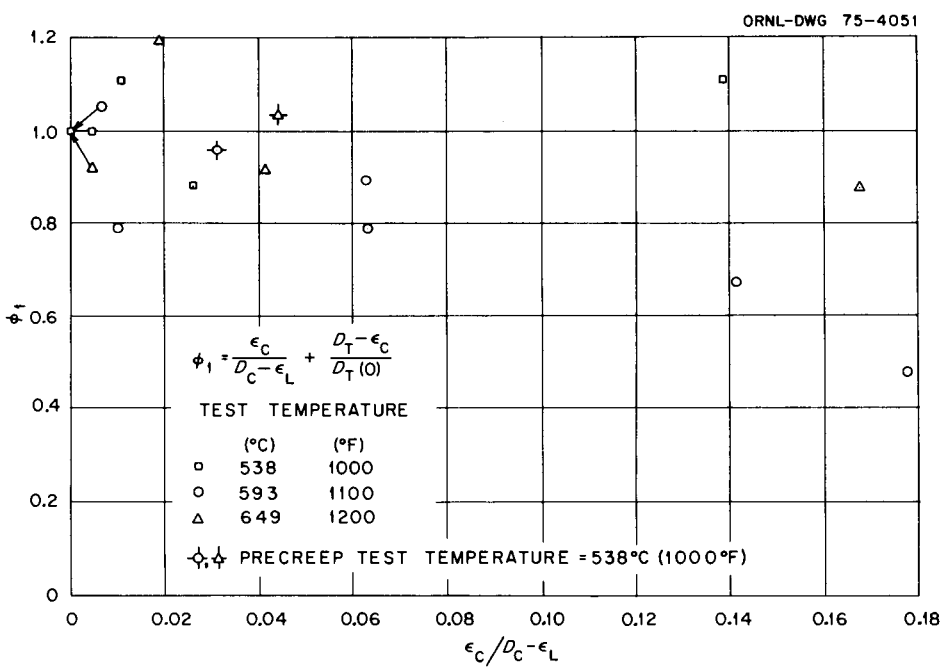

Fig. 3.18. Influence of Prior Creep on Damage Summation ϕ_1.

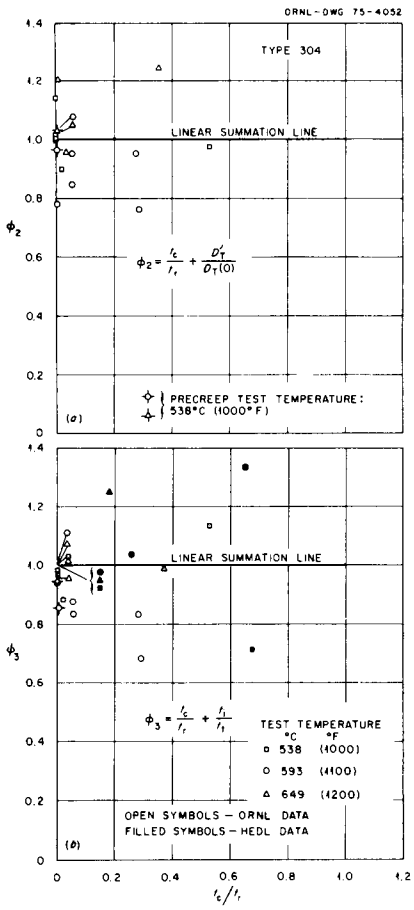

Fig. 3.19. Influence of Prior Creep on Damage Summations (a) ϕ_2 and (b) ϕ_3.

3.2.2 Heat-to-Heat Variation of Mechanical Properties of Types 304 and 316 Stainless Steel — V. K. Sikka

3.2.2.1 Long-Term Creep Tests in Heat-to-Heat Variation Study of Type 304 Stainless Steel

Ten long-term creep tests have been in progress on several heats of type 304 stainless steel at 593°C (1100°F). One more test ruptured during this quarter after 26,875 hr, leaving five still continuing. The creep curve for this long-term test is shown in Fig. 3.20. The updated data on the long-term tests are summarized in Table 3.4. The creep data on additional long-term tests on weak, medium, strong, and reference heats will be updated during the next quarter.

The ORNL long-term stress-rupture data (≈30,000 hr) and the longest time (≈66,000 hr) data available in the literature on various heats of type 304 have been plotted in Fig. 3.21. The ASME Code Case 1592 minimum

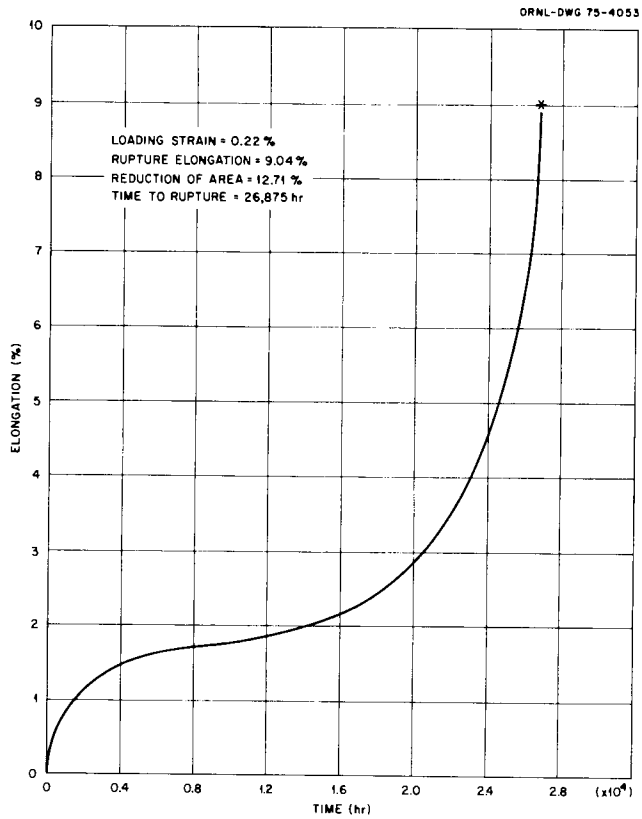

Fig. 3.20. Creep Curve for Heat 544 in As-Received Condition Tested at 593°C (1100°F) and a Stress of 17 ksi (117 MPa).

value curve has also been included. For a fixed test temperature, 593°C (1100°F), creep-rupture properties of various heats of type 304 stainless steel vary widely. The 10^4-hr creep-rupture strength for various heats varies from 16.5 to 28.5 ksi (113.8–196.5 MPa). The stress exponent, n_r, ($1/t_r = A\sigma^{n_r}$), for stress-rupture data of various heats was calculated. The values of n_r varied from 8.2 to 14.45 for weak to strong heats. The plot of minimum creep rate for various heats is shown in Fig. 3.22. Note the wide variation in minimum creep rate observed for various heats. The stress component for the minimum creep rate, n_m ($\dot{\varepsilon}_m = B\sigma^{n_m}$), ranged from 9.6 to 16.5 for weak to strong heats. In general, the stress exponents n_r and n_m were low for the weak heats and high for the strong heats. McLauchlin[9] has shown that the stress exponent is directly proportional to the internal back stress, σ_i, thought to arise largely from the presence of particles in the alloy, and that the magnitude and temperature dependence

Table 3.4. Status of Several Long-Term Creep Tests of Type 304 Stainless Steel at 593°C (1100°F)

Test	Heat	Condition[a]	Stress, (ksi)	Stress, (MPa)	Test Time[b] (hr)	Strain, % Loading	Strain, % Creep	Minimum Creep Rate (%/hr)	Time to Rupture (hr)
10396	60551	A 479	25.0	172	Ruptured	1.81	6.31	1.4×10^{-4}	19,180
10395	346845	A 240	25.0	172	Ruptured	1.37	11.35	1.4×10^{-4}	14,077
9499	300380	Reannealed	17.0	117	27,277	0.72	1.03	~0	
9483	600414	Reannealed	17.0	117	27,350	1.49	0.98	1.1×10^{-5}	
9464	337330	A 240	17.0	117	27,611	−0.20	0.18	5.5×10^{-6}	
9446	9T2796	A 479	17.0	117	27,449	0.13	2.28	2.1×10^{-5}	
9443	337187	A 240	17.0	117	Ruptured	0.47	10.18	9.7×10^{-5}	22,622
9371	55697	A 479	17.0	117	Ruptured	0.62	8.27	1.4×10^{-4}	25,823
9221	600414	A 240	17.0	117	29,759	0.18	0.79	1.0×10^{-5}	
9508	346544	A 240	17.0	117	Ruptured	0.22	9.04	4.5×10^{-5}	26,875

[a]As received per indicated specification or reannealed 0.5 hr at 1065°C (1950°F).

[b]Unless otherwise noted tests are in progress.

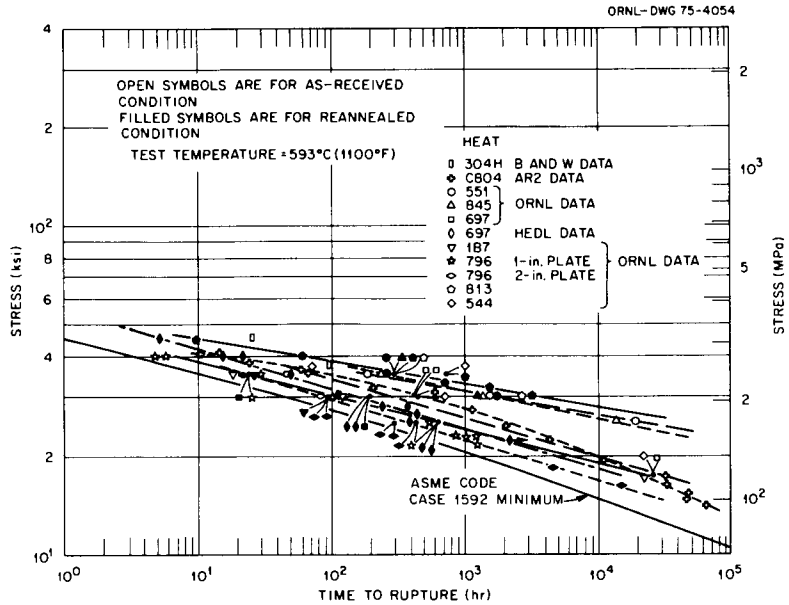

Fig. 3.21. Heat-to-Heat Variation in Long-Term Creep-Rupture Data for Type 304 Stainless Steel at a Test Temperature of 593°C (1100°F).

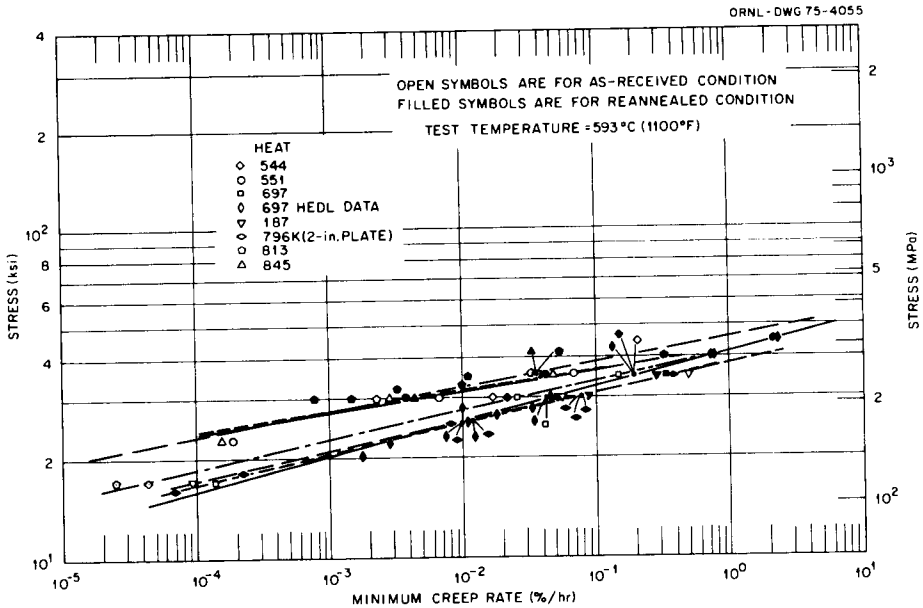

Fig. 3.22. Heat-to-Heat Variation in Minimum Creep Rate Data at a Test Temperature of 593°C (1100°F).

of the exponents arise from the magnitude and dependence on temperature of σ_i. Thus, it is quite possible that the strong heats contain more particles than the weak heats or the particles in the strong heat are fine and uniformly distributed. In the next section we show that strong heats contain more niobium than weak heats and also the stress exponents increase with increasing niobium content.

The observed relations between n_m and n_r and niobium content and their direct proportionality to σ_i indicate that niobium may be responsible for increasing the internal back stress.

3.2.2.2 Heat-to-Heat Variation and Its Relation with Chemical Composition

In a continuing effort to understand heat-to-heat variation in tensile and creep properties of 20 heats of type 304 stainless steel, chemical analyses for impurity elements Nb, V, Ti, Ta, and W were repeated. The results of the new chemical analyses along with previously reported contents of other elements are summarized in Table 3.5. The new chemical analysis of the impurity elements had a precision of ±30% or better. Histograms showing the distribution of 20 heats as a function of time to rupture are presented in Fig. 3.23. A similar histogram showing distribution of heats as a function of niobium content is presented in Fig. 3.24. The times to rupture for 20 heats yield three distinct peaks. These peaks for both as-received and reannealed conditions occur at 68—72, 283—336, and 745—1195 hr for a stress of 35 ksi (241 MPa) and a test temperature of 593°C (1100°F). Similar peaks for 30 ksi (207 MPa) and 593°C (1100°F) occur at 125—128, 400—430, and 1920—2030 hr. A comparison of Fig. 3.23 with Fig. 3.24 shows that the peaks observed in time to rupture are reflected by similar peaks in the niobium content distribution.

Thus, 20 heats can be classified into three categories of weak, medium, and strong, and they contain 26, 96, and 160 ppm, respectively, of niobium. In view of the results in Figs. 3.23 and 3.24, 20 heats were ranked according to increasing time to rupture and niobium content.

The long-term tests were ranked according to strain accumulated after 15,000 and 5000 hr, and the heats included were again ranked according to niobium content. The creep rankings are plotted as a function of niobium

Table 3.5. Summary of Chemical Analysis of 20 Heats of Type 304 Stainless Steel

Heat Symbol	Content, %																				
	C	N	P	B	O	H	Ni	Mn	Cr	Si	Mo	S	Nb	V	Ti	Ta	W	Cu	Co	Pb	Sn
796	0.047	0.031	0.029		0.0110	0.0006	9.58	1.22	18.5	0.47	0.10	0.012	0.008	0.037	0.003	<0.0005	0.022	0.10	0.05	0.01	0.02
807	0.029	0.021	0.024	0.0005	0.010	0.0012	9.67	1.26	18.8	0.50	0.20	0.023	0.0015	0.012	0.002	<0.0005	0.020	0.11	0.03	0.01	0.01
797	0.059	0.055	0.028	0.0020	0.0075	0.0007	9.78	1.49	18.3	0.60	0.30	0.110	0.0050	0.020	0.005	0.0005	0.050	0.30	0.07	0.002	0.005
283	0.043	0.025	0.018	0.0003	0.0140	0.0009	9.12	1.32	18.2	0.45	0.30	0.020	0.0030	0.030	0.0010	<0.0005	0.021	0.14	0.05	0.01	0.01
926	0.053	0.041	0.020		0.0084	0.0007	9.79	1.16	19.0	0.68	0.10	0.025	0.0180	0.050	0.0100	0.0010	0.030	0.070	0.05	0.010	0.02
187	0.068	0.031	0.018		0.0042	0.0005	9.43	0.83	18.2	0.59	0.07	0.008	0.0020	0.060	0.003	<0.0005	0.015	0.15	0.05	0.01	0.02
697	0.057	0.034	0.016		0.0150	0.0005	9.38	0.91	18.5	0.50	0.05	0.037	0.0030	0.030	0.002	<0.0005	0.011	0.10	0.05	0.01	0.02
866	0.044	0.022	0.023	0.0002	0.0096	0.0010	8.98	1.51	18.5	0.47	0.2	0.007	0.0010	0.018	0.0005	0.0005	0.007	0.13	0.04	0.01	0.01
544	0.063	0.019	0.23	0.0002	0.0081	0.0006	9.12	0.99	18.4	0.47	0.2	0.006	0.0050	0.025	0.017	0.0006	0.026	0.12	0.05	0.01	0.01
330	0.068	0.031	0.018		0.0042	0.0005	9.43	0.83	18.2	0.59	0.07	0.008	0.0100	0.025	0.002	<0.0005	0.0060	0.15	0.05	0.01	0.02
845	0.057	0.024	0.023	0.0002	0.0092	0.0013	9.28	0.92	18.4	0.53	0.10	0.006	0.0100	0.050	0.008	<0.0005	0.007	0.11	0.07	0.01	0.01
779	0.065	0.023	0.024	0.0002	0.0056	0.0009	9.46	0.94	18.1	0.47	0.20	0.005	0.0035	0.029	0.010	0.0020	0.043	0.16	0.02	0.01	0.01
390	0.066	0.086	0.018	0.0020	0.0052	<0.0001	8.75	1.57	18.6	0.60	0.30	0.006	0.0160	0.020	0.001	0.0006	0.043	0.20	0.07	0.0007	0.002
414	0.073	0.058	0.016		0.0190	0.0004	9.52	0.94	18.7	0.69	0.10	0.015	0.0100	0.025	0.002	<0.0005	0.027	0.10	0.05	0.01	0.02
551	0.043	0.027	0.022	0.0010	0.0220	0.0013	9.40	1.20	18.5	0.59	0.30	0.018	0.0140	0.050	0.025	<0.0005	0.049	0.25	0.08	0.01	0.01
737	0.064	0.075	0.026	0.00005	0.0072	<0.0001	9.01	1.71	18.3	0.50	0.30	0.012	0.0140	0.031	0.001	<0.0005	0.016	0.50	0.07	<0.0003	0.0050
380	0.063	0.068	0.018		0.0260	0.0009	8.30	0.97	18.4	0.55	0.07	0.010	0.0100	0.028	0.004	<0.0005	0.016	0.10	0.05	0.01	0.02
086	0.050	0.043	0.025		0.0091	0.0005	9.46	1.23	18.4	0.53	0.20	0.016	0.0030	0.019	0.006	<0.0005	0.021	0.10	0.05	0.01	0.02
813	0.062	0.033	0.044	0.0003			8.95	1.87	17.8	0.48	0.32	0.004	0.0200	0.022	0.002	<0.0005	0.02				
121	0.065	0.140	0.019	0.00005	0.0026	0.0011	9.19	1.92	18.1	0.30	0.14	0.010	0.0010	0.035	0.016	<0.0005	0.015	0.07	0.07	<0.0003	0.002

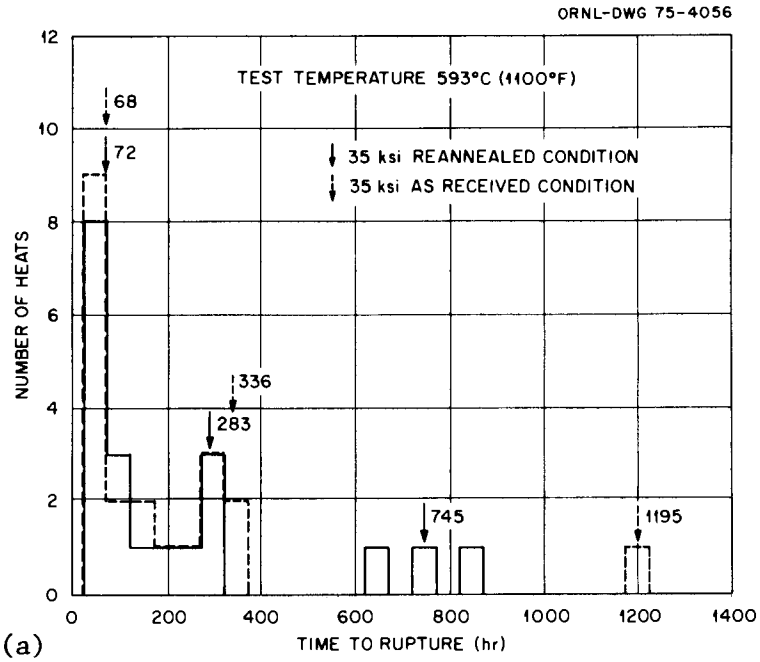

(a)

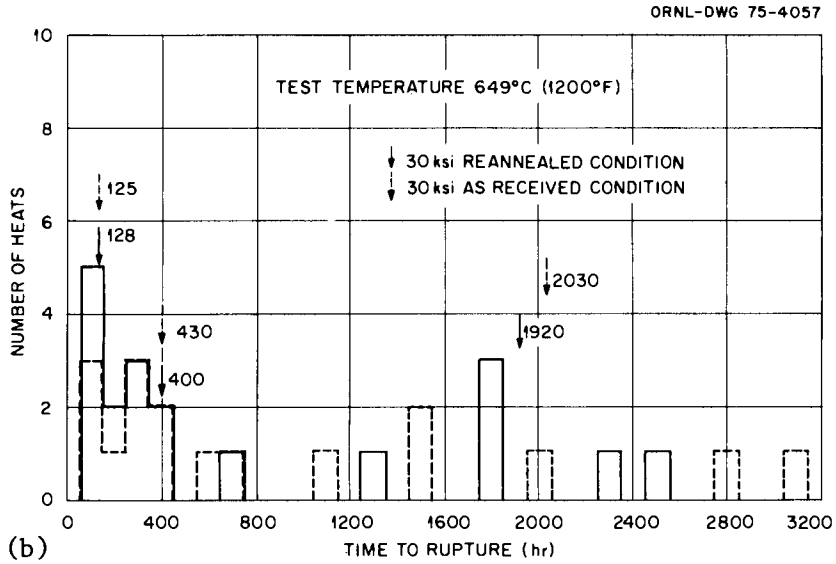

(b)

Fig. 3.23. Distribution of 20 Heats of Type 304 Stainless Steel As A Function of Time to Rupture. Numbers indicated by arrows are the average values of each peak. Tested at (a) 593°C (1100°F) and 35 ksi (241 MPa); (b) 649°C (1200°F) and 30 ksi (207 MPa).

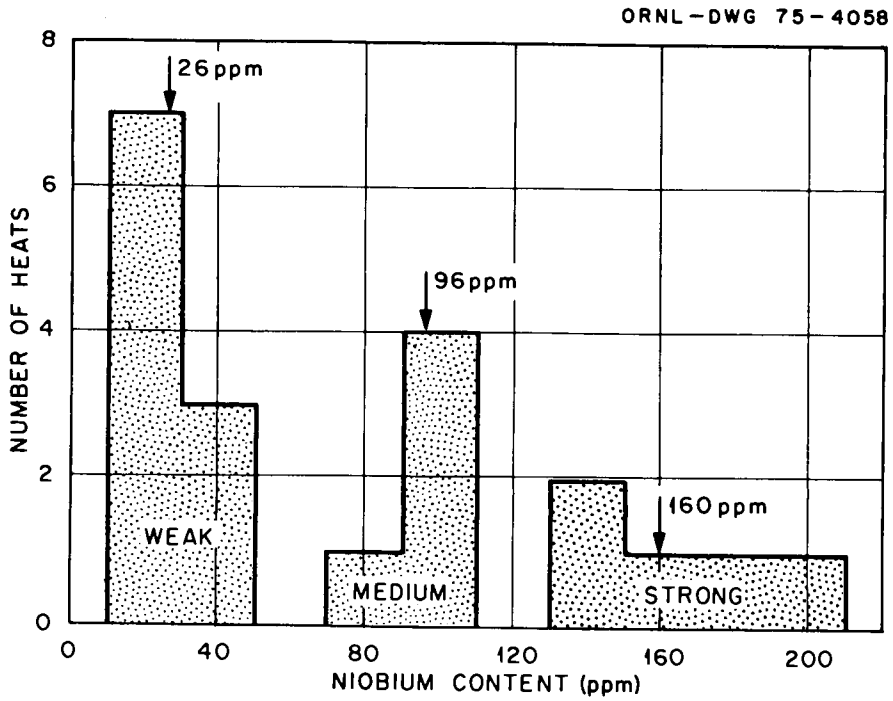

Fig. 3.24. Distribution of 20 Heats of Type 304 Stainless Steel as a Function of Niobium Content. Numbers indicated by arrows are the average values of each peak.

ranking in Fig. 3.25. It can be noted that increasing niobium rank increases the creep ranking for most of the heats. The only exception to creep ranking as a function of niobium ranking is heat 121, which contains 0.14% N. Thus, the higher rank of this heat as compared with one based on only niobium must result from additional strengthening due to nitrogen. Stone[10] suggested that if precipitation plays a dominant role, the strength should show a peak at the stoichiometric Nb:(C + N) value. In view of this, creep ranking was determined as a function of Nb:(C + N) and is shown in Fig. 3.26. It should be noted that Nb:(C + N) ranking does take into account the high-nitrogen heat.

Shinoda et al.[11] pointed out that in 18 Cr-8 Ni austenitic stainless steel the coexistence of titanium and niobium, even in very small amounts, with proper amounts of carbon makes the dispersion of $M_{23}C_6$ finer and more stable, and thus increases the rupture strength. Following the same line of argument, relations observed in Figs. 3.25 and 3.26 are easy to understand.

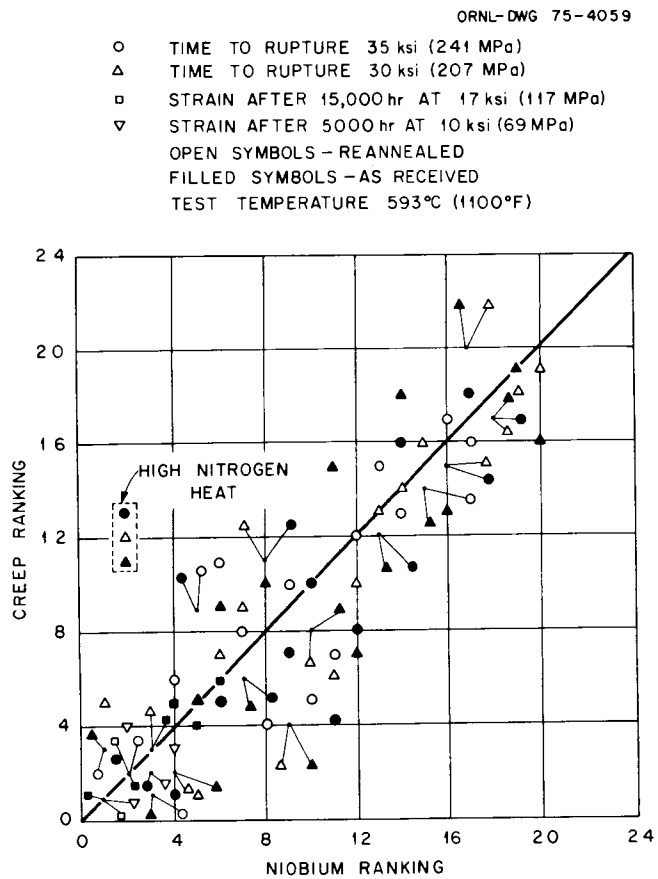

Fig. 3.25. Creep Ranking As A Function of Niobium Ranking for 20 Heats of Type 304 Stainless Steel.

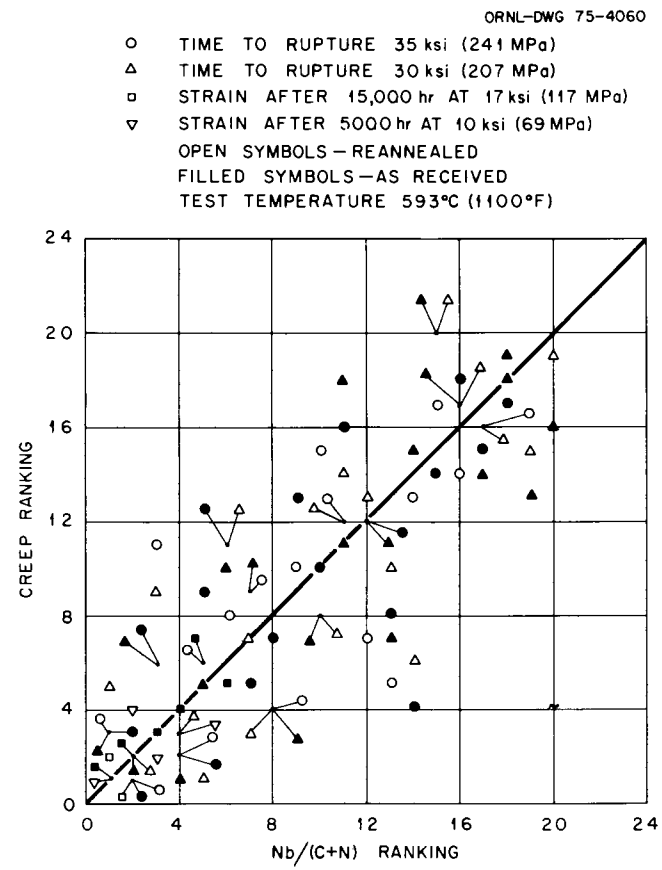

Fig. 3.26. Creep Ranking As A Function of Nb/(C + N) Ratio Ranking for 20 Heats of Type 304 Stainless Steel.

The stress exponents for the minimum creep rate, n_m, and time to rupture, n_r, have been plotted as functions of niobium content in Fig. 3.27. Least squares analysis gave following equations for the two exponents:

$$n_m = 6.22(\mathrm{Nb})^{1/5.96} ,$$

$$n_r = 4.04(\mathrm{Nb})^{1/4.18}$$

where (Nb) is the niobium content, expressed as ppm by weight.

The increasing values of n_m and n_r with niobium content suggest that niobium is probably responsible for increasing the internal back stress, σ_i (resistance of the metal to deformation), which reduces the effective stress, σ_{eff}, and makes the heat stronger. The effective stress, σ_{eff}, is defined as:

$$\sigma_{eff} = \sigma_A - \sigma_i ,$$

where σ_A is the applied stress.

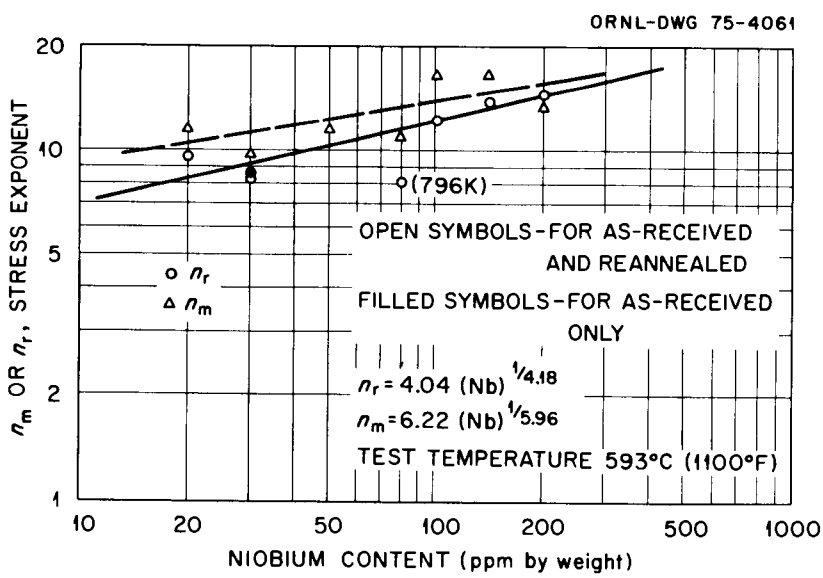

Fig. 3.27. Stress Exponents as Functions of Niobium Content for Various Heats of Type 304 Stainless Steel. The point marked (796K) was not included in the least squares analysis.

Transmission electron microscopy will be performed during the next quarter to determine if indeed the $M_{23}C_6$ dispersion is finer in high-niobium-content heats or if niobium increases the internal back stress by some other mechanism.

3.2.2.3 Relation Between Creep-Rupture and Short-Term Tensile Properties

Last quarter[12] creep-rupture strength, S_R^t, and ultimate tensile strength, S_u^R, were related for several heats of types 304 and 316 stainless steel by a relation of the form:

$$S_R^t = \alpha \exp(\beta S_u^R) \ , \tag{10}$$

where α and β are material constants.

We are continuing to seek relations between creep and short-term tensile properties. Plots of time to rupture for 20 heats of type 304 stainless steel, in both as-received and reannealed conditions, as functions of ultimate tensile strength at the creep test temperature are shown in Fig. 3.28. An exception to the trend of increasing time to rupture with increasing ultimate tensile strength is heat 121, which contains 0.14% N. The isolation of the high-nitrogen heat from average-nitrogen heats is not quite clear, but it could be related to a stronger strain-rate sensitivity of ultimate tensile strength for this heat.

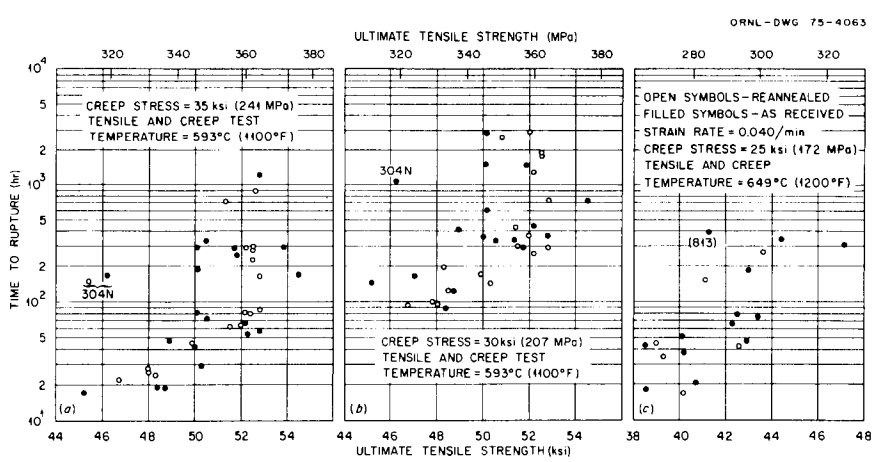

Fig. 3.28. Time to Rupture as a Function of Ultimate Tensile Strength for 20 Heats of Type 304 Stainless Steel.

The increase in ultimate tensile strength produces an exponential increase in time to rupture for austenitic stainless steels, whereas similar relations cited in the literature[13–15] on 2 1/4 Cr-1 Mo are for room-temperature tensile strength and are linear. Reasons for such differences in relations between the two materials are not clear, except that 2 1/4 Cr-1 Mo steel can be heat-treated to produce very large increases in ultimate tensile strength.

In general, heats with high ultimate tensile strength have long times to rupture, and thus elevated-temperature ultimate tensile strength can be used as a method to select a new heat for applications in which creep is important. Work will continue in this area to examine similar relations for not only time to rupture but other creep properties — e.g., minimum creep rate and rupture elongation.

3.2.2.4 Relation Between Tensile Properties in the As-Received (Mill-Annealed) and Reannealed (Laboratory-Annealed) Conditions for Types 304 and 316 Stainless Steel — V. K. Sikka, R. W. Swindeman, and T. L. Hebble*

Mechanical property data are frequently reported on structural materials in the laboratory-annealed condition, although they will be used in the as-received condition (mill annealed). The difference between these conditions is that the mill-annealed material contains straightening stresses, which result in higher strength and lower ductility properties. We have determined quantitative relations between the tensile properties in the as-received and reannealed conditions for various product forms of types 304 and 316 stainless steel.

The tensile properties — 0.2% yield strength, ultimate tensile strength, and uniform elongation — for reannealed material were plotted as functions of the same property as the as-received condition for test temperatures from room temperature to 649°C (1200°F) for types 304 and 316 stainless steel and are shown in Figs. 3.29 through 3.31. The results were fitted to linear relations of the form:

---

*Mathematics Research Staff.

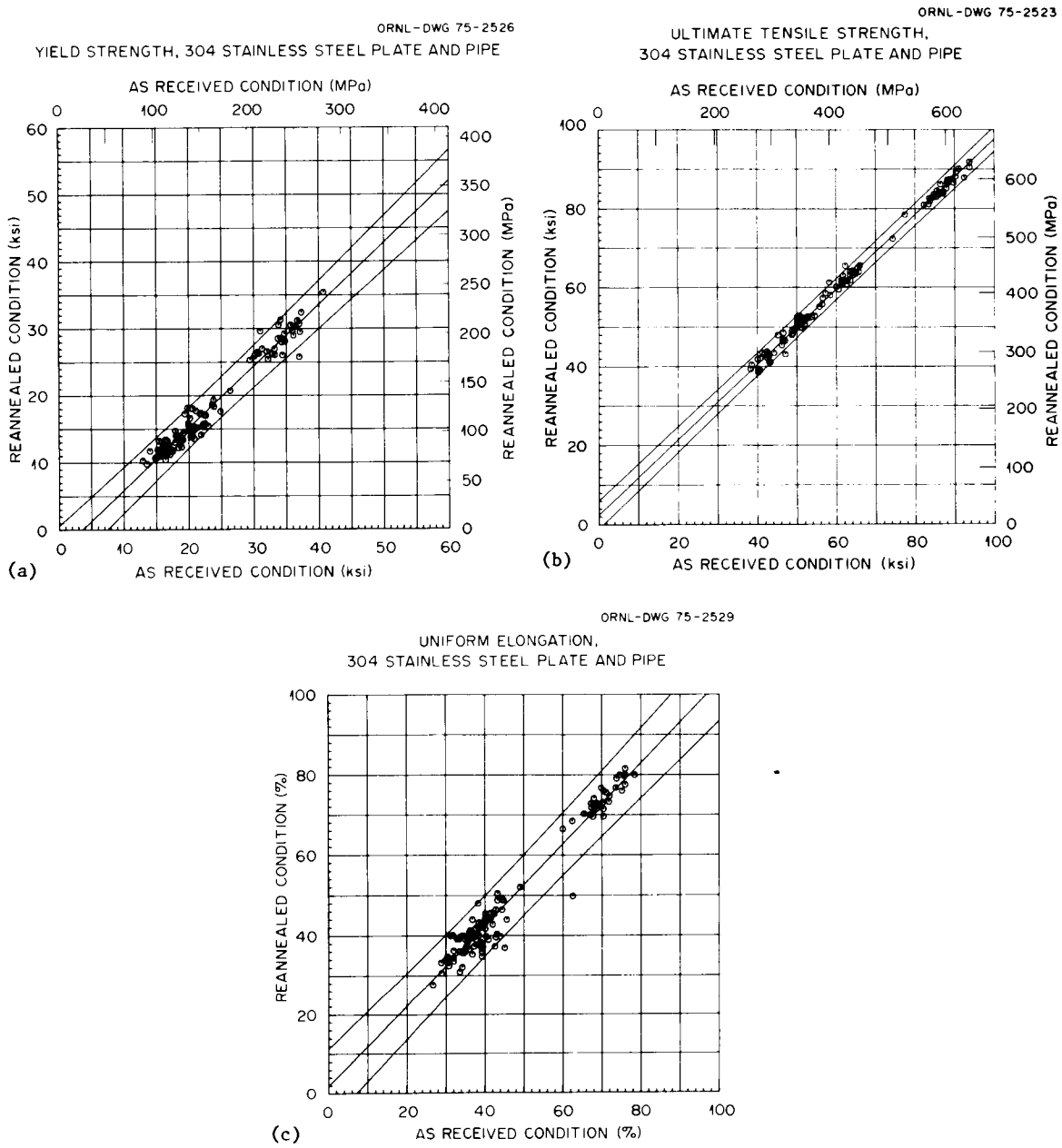

Fig. 3.29. Relation Between Tensile Properties of Plate and Pipe Products of Several Heats of Type 304 Stainless Steel in the As-Received (Mill-Annealed) and Reannealed (Laboratory-Annealed) Conditions. (a) 0.2% offset yield strength. (b) Ultimate tensile strength. (c) Uniform elongation.

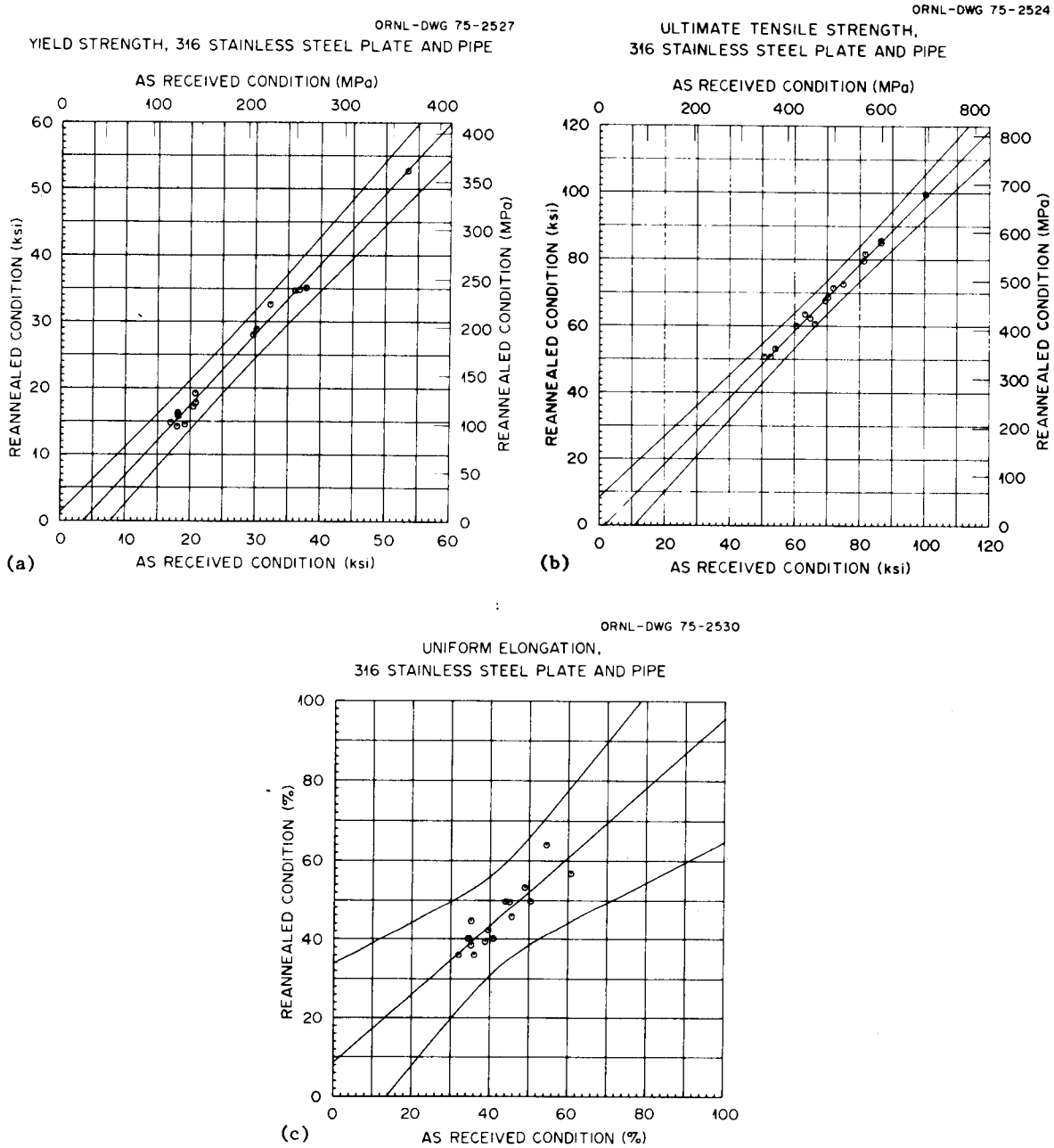

Fig. 3.30. Relation Between Tensile Properties of Plate and Pipe Products of Four Heats of Type 316 Stainless Steel in the As-Received (Mill-Annealed) and Reannealed (Laboratory-Annealed) Conditions. (a) 0.2% offset yield strength. (b) Ultimate tensile strength. (c) Uniform elongation.

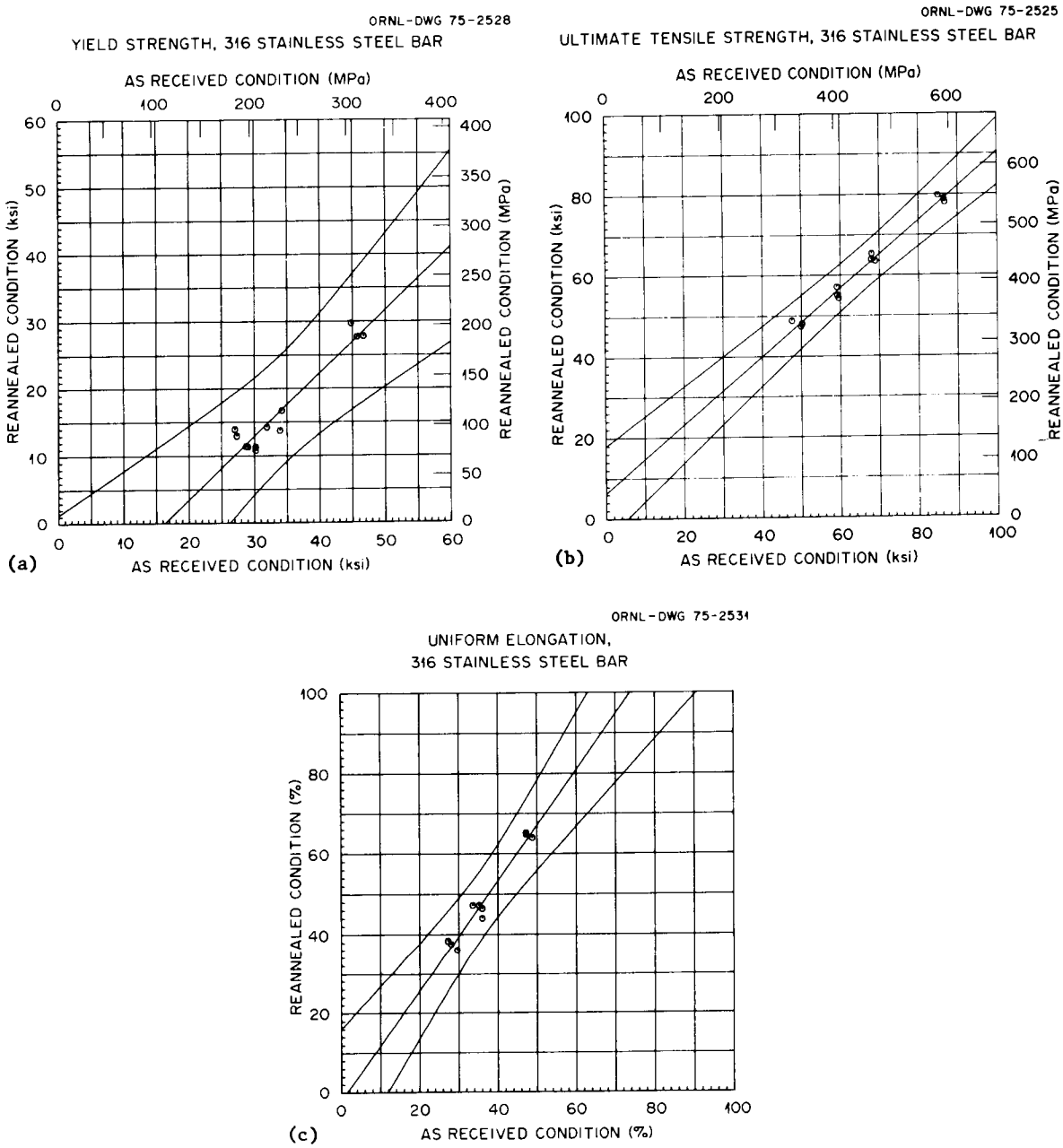

Fig. 3.31. Relation Between Tensile Properties of Three Heats of Type 316 Stainless Steel Bar in the As-Received (Mill-Annealed) and Reannealed (Laboratory-Annealed) Conditions. (a) 0.2% offset yield strength. (b) Ultimate tensile strength. (c) Uniform Elongation.

$$P(\text{reannealed}) = A + BP(\text{as-received}) \ , \qquad (11)$$

where P stands for the tensile properties.

Constants A and B for several product forms of types 304 and 316 stainless steel are presented in Table 3.6. The 95% confidence limits for each property are also shown in the figures. Figures 3.29 through 3.31 and constants in Table 3.6 show that reannealing lowers the yield and ultimate tensile strengths but increases uniform elongation. For type 316 stainless steel reannealing lowered the room-temperature yield strength of the bar by approximately 40%, compared with only 5% for the plate and pipe. For type 304 stainless steel reannealing lowered the room-temperature yield strength of the plate and pipe by approximately 17%. For type 316 stainless steel reannealing increased the room-temperature uniform elongation of the bar by approximately 34%, compared with only 1% for the plate and pipe. For type 304 stainless steel reannealing increased the room-temperature uniform elongation of the plate and pipe by approximately 4%. Thus, it was noted that the bar product of type 316 stainless steel showed rather large changes in tensile properties on reannealing, as opposed to small changes for plate and pipe products of types 304 and 316 stainless steel.

To determine the reasons for the large changes observed in tensile properties of type 316 stainless steel bar as opposed to plate and pipe, microstructures of various products were examined in both the as-received and reannealed conditions, and their micrographs are shown in Figs. 3.32 through 3.34. The average grain intercepts were determined for microstructures in the as-received and reannealed conditions and are given for each micrograph in Figs. 3.32 through 3.34. It can be noted from the figures that while only small changes occurred in the grain intercept of the plate and pipe, it approximately doubled for the bar.

The yield strength dependence on grain size is commonly expressed by a Hall-Petch relationship of the form:

$$S_y = S_0 + k_y d^{-1/2} \ , \qquad (12)$$

Table 3.6. Summary of Constants for the Relation Between Tensile Properties in the Reannealed[a] and As-Received Conditions for Types 304 and 316 Stainless Steel

Property	Material	Constants[b] and Standard Error Limits	
		A	*B*
Yield Strength	20 heats of type 304 plate and pipe		
ksi		−3.30 ± 0.44	0.922 ± 0.018
MPa		−22.8	
Ultimate tensile strength			
ksi		2.48 ± 0.45	0.950 ± 0.007
MPa		17.1	
Uniform elongation, %		1.87 ± 1.06	1.014 ± 0.021
Yield strength	4 heats of type 316 plate and pipe		
ksi		−3.81 ± 0.74	1.062 ± 0.026
MPa		−26.3	
Ultimate tensile strength			
ksi		−1.78 ± 2.0	1.005 ± 0.027
MPa		−12.3	
Uniform elongation, %		8.55 ± 5.03	0.87 ± 0.117
Yield strength	3 heats of type 316 bar		
ksi		−15.26 ± 3.11	0.939 ± 0.089
MPa		−105.2	
Ultimate tensile strength			
ksi		6.38 ± 2.16	0.840 ± 0.032
MPa		44.0	
Uniform elongation, %		−1.98 ± 3.46	1.382 ± 0.093

[a]0.5 hr at 1065°C (1950°F).

[b]$\ln P(\text{reannealed}) = A + BP(\text{as received})$.

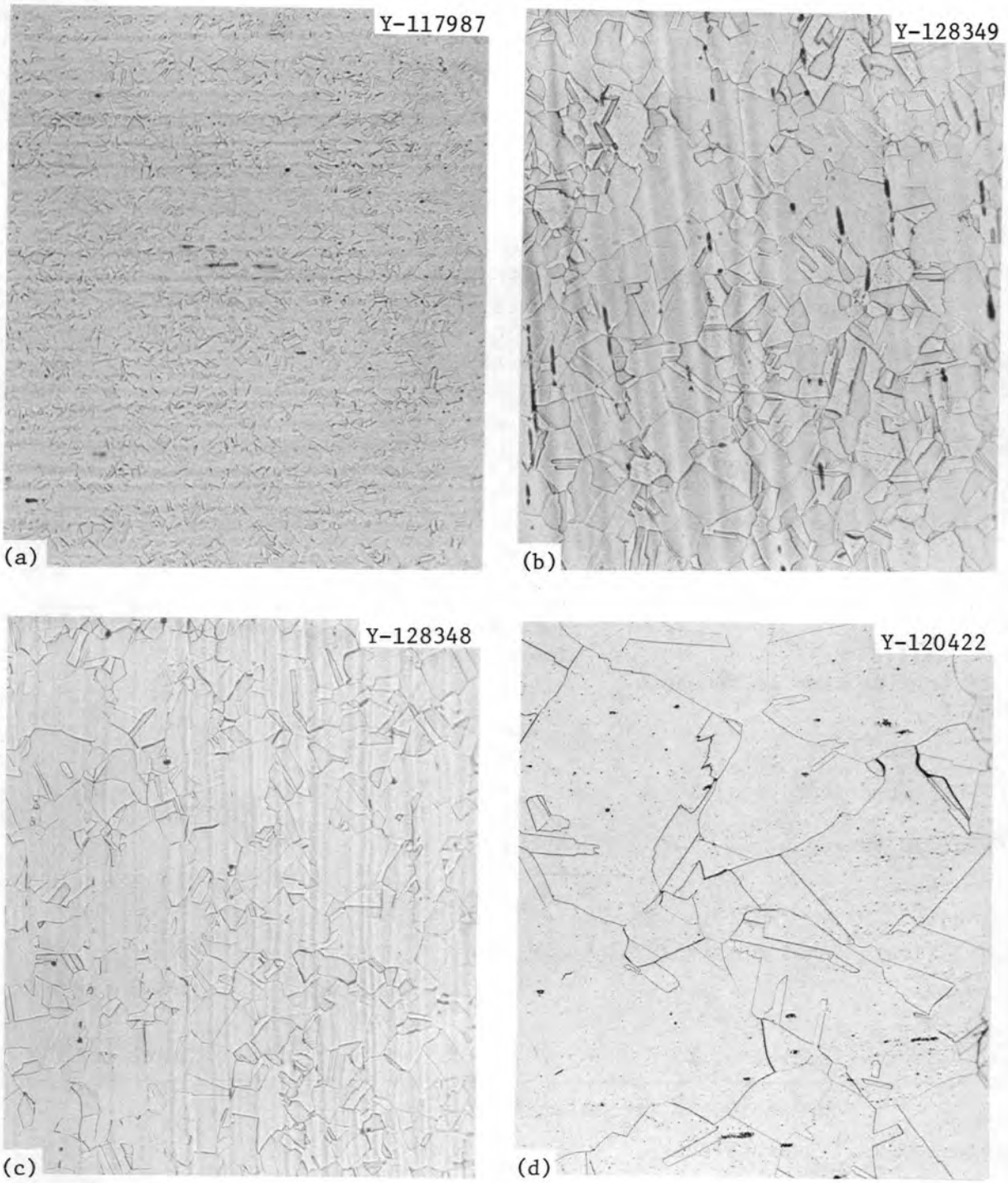

Fig. 3.32 Typical Microstructures for As-Received Plate and Pipe of Four Heats of Type 316 Stainless Steel. Etched with glyceria regia. 100×. (a) Heat 686 plate, intercept grain size ASTM 10, 8 μm. (b) 613 plate, ASTM 6.0, 39 μm. (c) 212 plate, ASTM 6.5, 33 μm. (d) 509 pipe, ASTM 4.0, 78 μm.

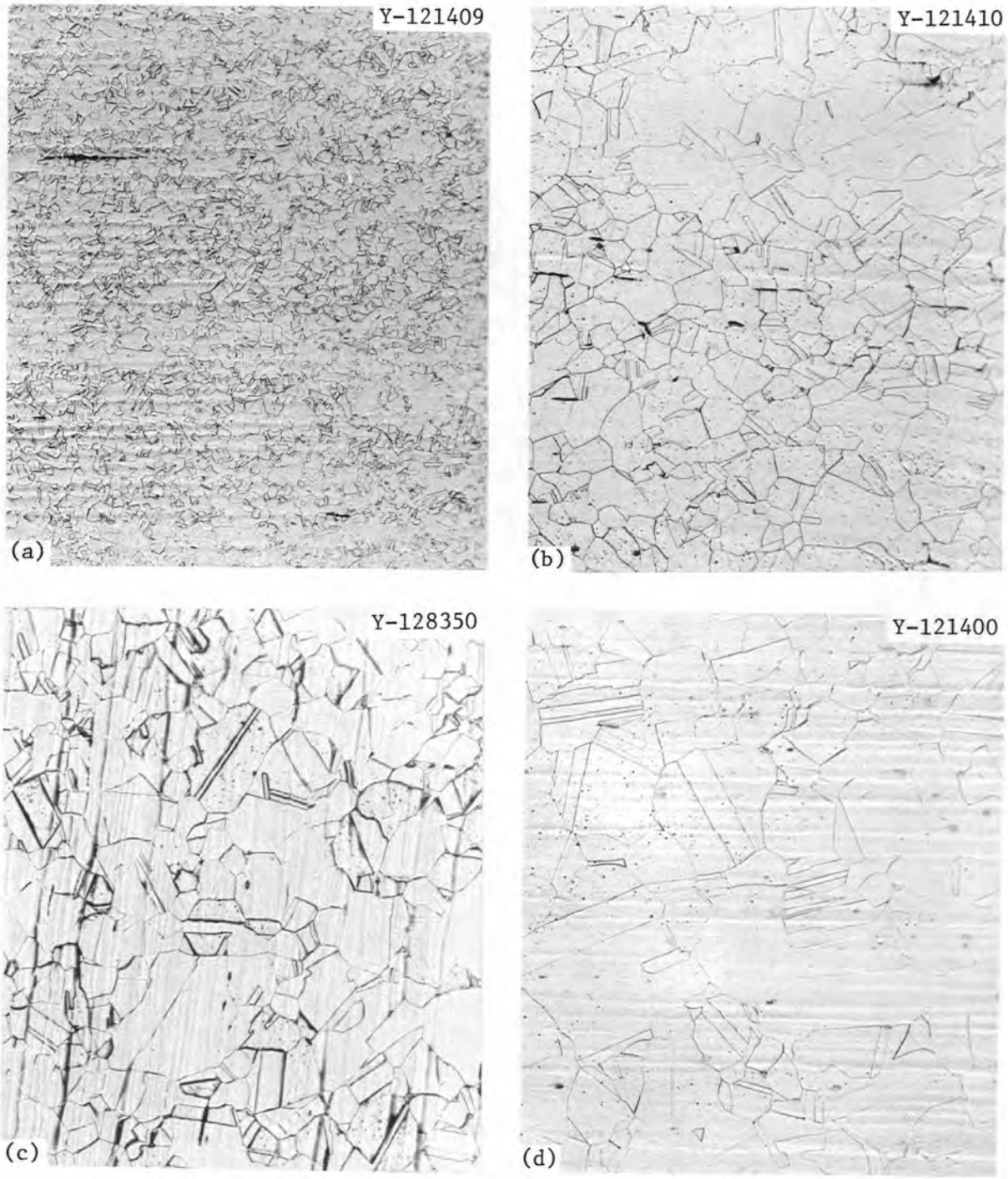

Fig. 3.33. Typical Microstructure for Reannealed Plate and Pipe of Four Heats of Type 316 Stainless Steel. Etched with glyceria regia. 100×. (a) Heat 686 plate, intercept grain size ASTM 10, 8 μm. (b) 613 plate, ASTM 6.4, 34 μm. (c) 212 plate, ASTM 4.8, 60.0 μm. (d) 509 pipe, ASTM 4.8, 60.0 μm.

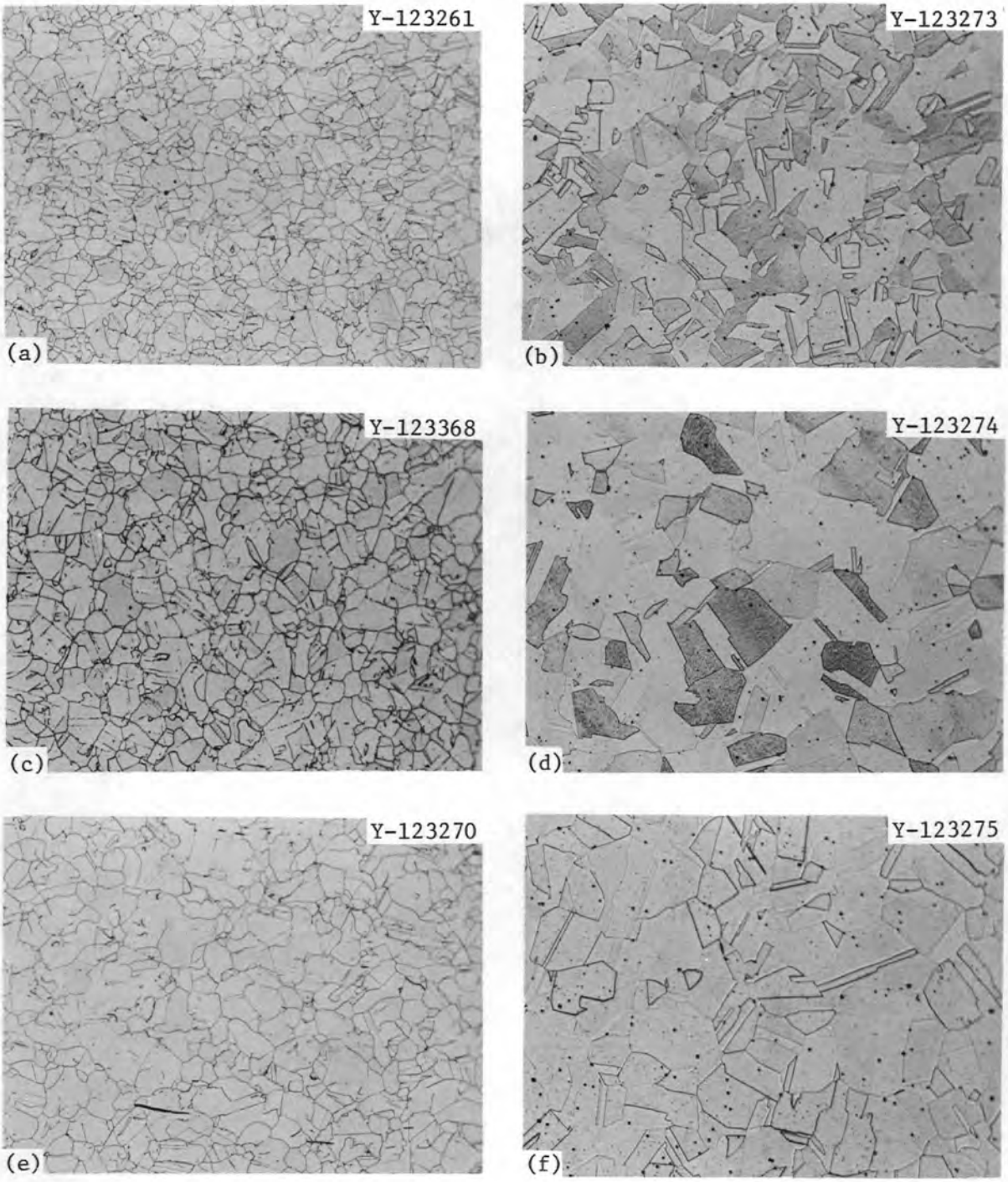

Fig. 3.34. Typical As-Received (Left) and Reannealed (Right) Microstructures of Three Heats of Type 316 Stainless Steel Bar. Etched with glyceria regia. 100×. (a,b) Heat 160; (c,d) 694; (e,f) 695. Grain sizes by intercept method are: (a) ASTM 9, 14.5 μm. (b) ASTM 6.8, 29 μm. (c) ASTM 7.4, 24 μm. (d) ASTM 5.4, 48 μm. (e) ASTM 7.5, 23 μm. (f) ASTM 5.3, 50 μm.

where d = average grain intercept,

S_0 = frictional stress opposing the motion of dislocations, and

k_y = measure of extent to which dislocations are piled at the grain boundaries.

Equation (12) can be rewritten for the yield strength for the as-received, S_y^{AR}, and reannealed, S_y^{RA}, conditions as follows:

$$S_y^{AR} = S_0^{AR} + k_y d_{AR}^{-1/2} , \tag{13}$$

$$S_y^{RA} = S_0^{RA} + k_y d_{RA}^{-1/2} , \tag{14}$$

where S_0^{AR} and S_0^{RA} = frictional stress in the as-received and reannealed conditions, respectively, and d_{AR} and d_{RA} are the grain intercepts in the two conditions.

For type 316 stainless steel[12] k_y was essentially the same for yield and ultimate tensile strength correlation with $(C + N)$-compensated grain size $[(C + N)/\sqrt{d}\,]$, thus indicating that k_y is not a strong function of strain, so that its value is the same for as-received and reannealed conditions. Eliminating k_y from equations (13) and (14) gives:

$$S_y^{RA} = [S_0^{RA} - S_0^{AR}(d_{AR}/d_{RA})^{1/2}] + S_y^{AR}(d_{AR}/d_{RA})^{1/2} . \tag{15}$$

Equation (11) for the yield strength can be written as:

$$S_y^{RA} = A + B\, S_y^{AR} . \tag{16}$$

A comparison of Eqs. (15) and (16) yields

$$S_0^{RA} - S_0^{AR}(d_{AR}/d_{RA})^{1/2} = A , \tag{17}$$

$$(d_{AR}/d_{RA})^{1/2} = B . \tag{18}$$

Thus, constants A and B in Eq. (11) and Table 3.6 have been shown to represent the amount of cold work and change in grain size on reannealing.

For plate and pipe products of type 316 stainless steel, $d_{RA} \approx d_{AR}$, giving rise to $B \approx 1$, in excellent agreement with the observed value of 1.062 in Table 3.16. Thus, for plate and pipe $A = S_0^{RA} - S_0^{AR}$, which is the difference in frictional stresses in the as-received and reannealed conditions and must represent the straightening stresses or the amount of cold work.

For the case of bar product, $d^{RA} \approx 2d^{AR}$, giving rise to $B \approx 0.71$, as compared with an observed value of 0.94. Thus, for the bar product, the cold work is not only $S_0^{RA} - S_0^{AR}$, but is modified by the changes in grain size.

For the plate and pipe of type 304 stainless steel, $d^{RA} \approx d^{AR}$, which gives $B \approx 1$, in reasonable agreement with an observed value of 0.92.

Thus, in general for small changes in grain size on reannealing, constant A in Eq. (16) and Table 3.6 gives the amount of decrease in yield strength due to the recrystallization process. For the case where significant grain growth takes place on reannealing, constants A and B both describe the decrease in yield strength due to recrystallization and grain growth.

The present work on relations between tensile properties in the as-received and reannealed conditions has clearly shown that the bar product in the mill-annealed condition has much greater straightening stresses than the plate and pipe products. This is further supported by the grain growth observed in microstructure of the reannealed bar (see Fig. 3.34), which generally results from a critical amount of cold work present in the material (see Fig. 3.35 for the effect of cold work on grain growth in type 316 stainless steel).

3.2.2.5 Effect of Aging on Tensile and Creep Properties of Types 304 and 316 Stainless Steel

3.2.2.5.1 Tensile Properties. In the previous quarter[16] we reported the effect of aging temperature and time on uniform elongation of various

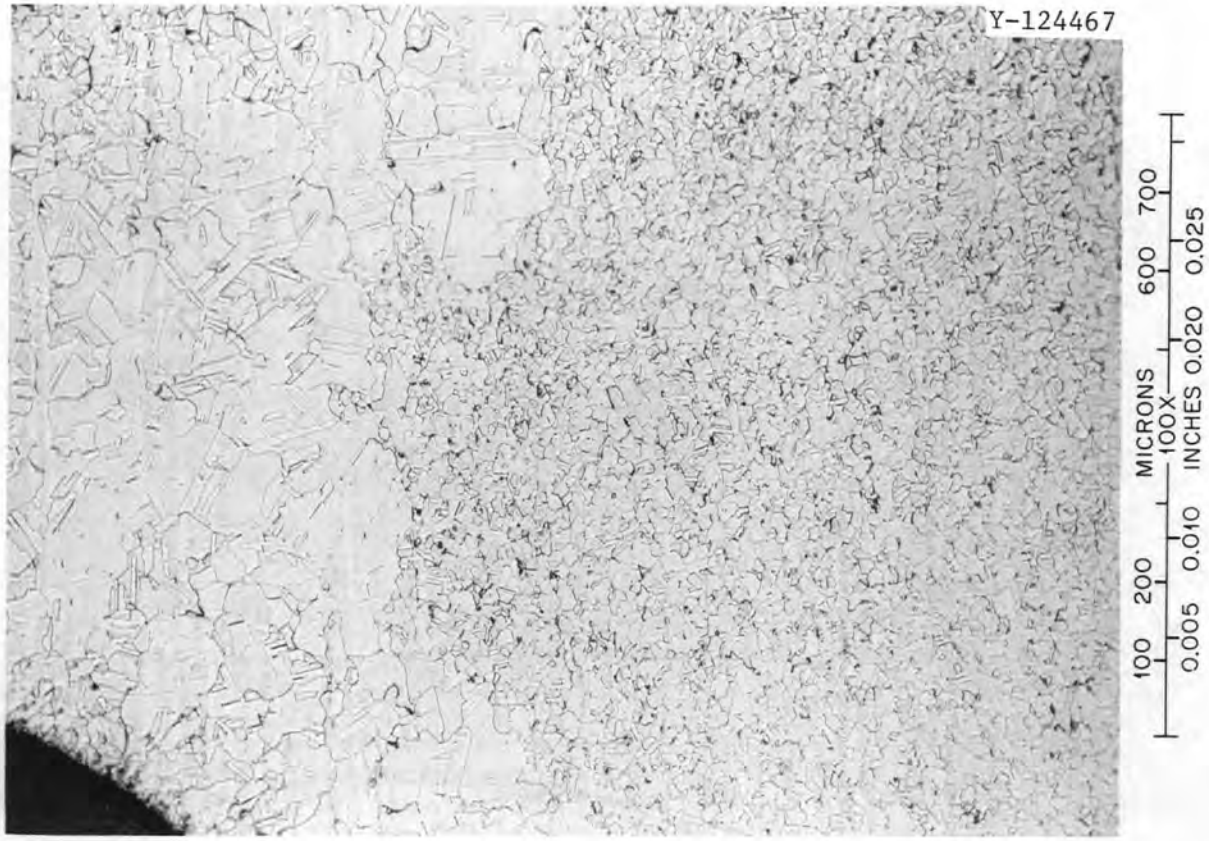

Fig. 3.35. Microstructure of Specimen Head Showing the Effect of Cold Work on Grain Growth in Heat 686 of Type 316 Stainless Steel. The grain growth shown on the left resulted from the cold work introduced by machining threads on the specimen; part of a thread shows in the lower left. Heat treated for 0.5 hr at 1100°C (2012°F). Etched with a solution of lactic acid, methanol, and HCl (45, 45, and 10 ml).

heats of type 304 stainless steel. We have now examined the influence of 10,000 hr aging on stress-strain curves of the weak, reference, and two strong heats of type 304 stainless steel. Stress-strain curves for these heats aged for 10,000 hr at 482, 593, and 649°C (900, 1100, and 1200°F) are presented in Figs. 3.36 and 3.37.

The tensile curves for the as-received and reannealed conditions are included in these figures for comparison. For all heats reannealing decreased yield and ultimate tensile strengths but increased total elongation. Heat 807 and the reference heat, which were aged in the reannealed condition, showed increases in flow stress even for an aging temperature of 482°C (900°F), whereas heats 845 and 926, aged in the as-received condition, did not show any change. For heat 807, which contained δ-ferrite

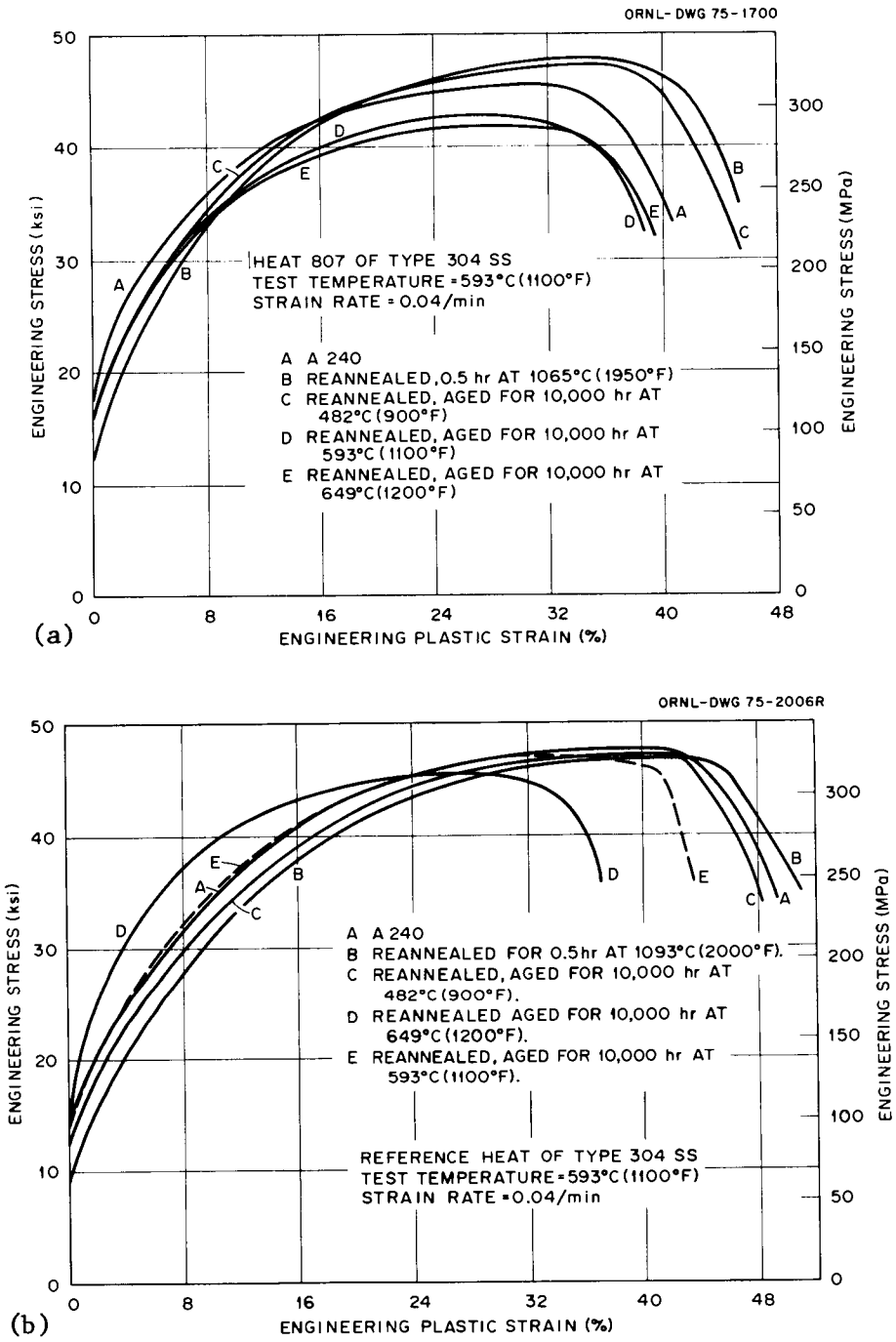

Fig. 3.36. Stress-Strain Curves for Type 304 Stainless Steel at 593°C (1100°F) After Aging for 10,000 hr at Several Temperatures. (a) Heat 807. (b) Reference heat.

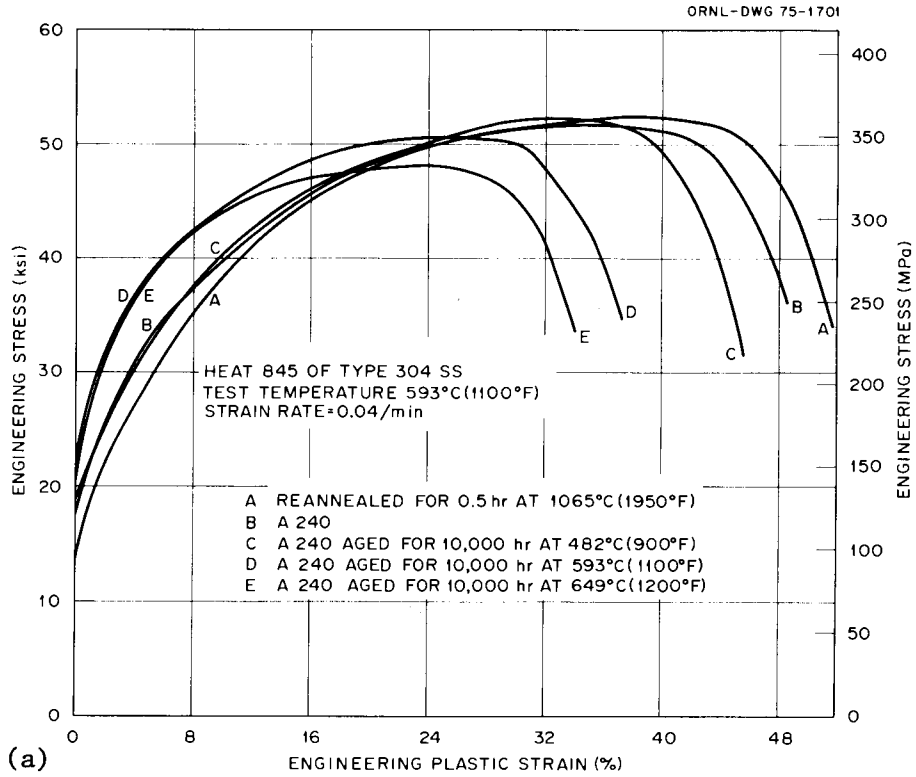

(a)

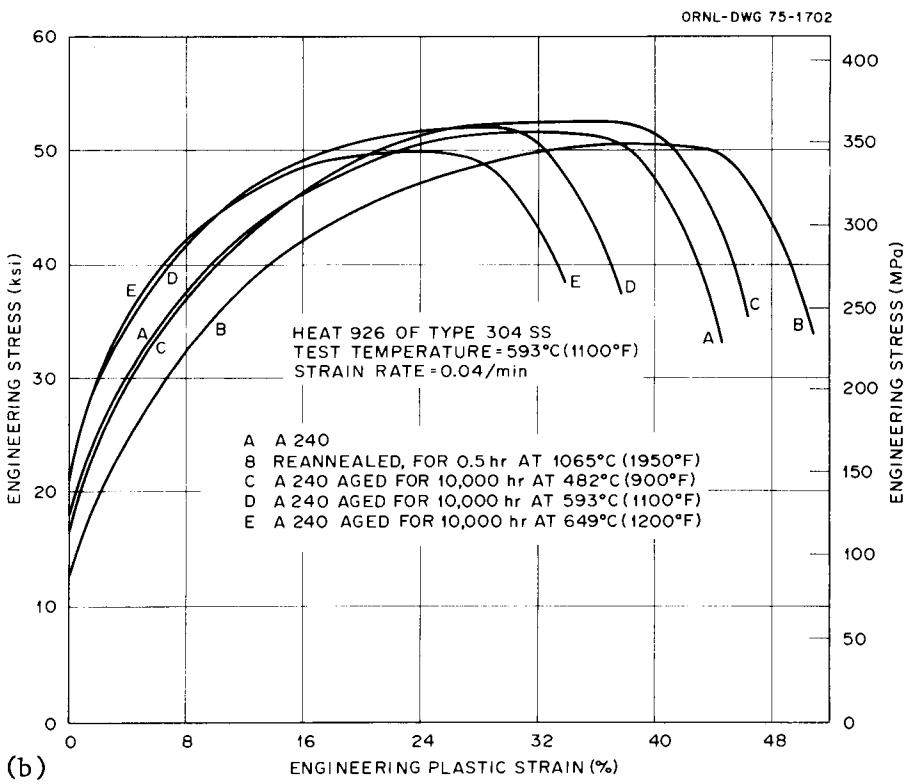

(b)

Fig. 3.37. Stress-Strain Curves for Type 304 Stainless Steel at 593°C (1100°F) After Aging for 10,000 hr at Several Temperatures. (a) Heat 845. (b) Heat 926.

in the unaged condition — see Fig. 3.38 — the change in flow stress up to 5% strain after 10,000 hr was independent of aging temperature. The ultimate tensile strength showed a large decrease on aging, and it varied with the aging temperature. For the strong heats, 845 and 926, total elongation decreased with increasing aging temperature. The maximum loss in total elongation for heats 845 and 926 and the reference heat was about 14%, compared with only about 8% for heat 807.

The influence of aging for 4000 hr at several temperatures on various heats is presented in the following figures for comparison with 10,000-hr data presented in Figs. 3.36 and 3.37. Figure 3.39 shows the influence of aging temperature on the yield strength of various heats aged in both as-received and reannealed conditions. It can be noted that aging in the reannealed condition increases the 0.2% yield strength for all aging temperatures, 482, 593, and 649°C (900, 1100, and 1200°F). Aging performed in the as-received condition produced no change for an aging temperature of 482°C (900°F), whereas the yield strength increased for aging at 593 and 649°C (1100 and 1200°F).

The ultimate tensile strength data are plotted as functions of aging temperature in Fig. 3.40. Aging in the as-received condition caused almost no change in ultimate tensile strength, whereas aging in the reannealed condition lowered it. This lowering occurred for aging at 482°C (900°F) and is quite similar to the change observed in the yield strength, shown in Figs. 3.36, 3.37, and 3.39.

The influence of aging temperature on reduction of area of various heats in the as-received and reannealed conditions is presented in Fig. 3.41. Most of the heats showed no change in reduction of area for aging below 593°C (1100°F). Thermal aging at 649°C (1200°F) lowered the reduction of area for all heats. Heat 807 showed a large decrease in reduction of area for all aging temperatures from 482 to 649°C (900–1200°F). The influence of aging time at 649°C (1200°F) on reduction of area is shown in Fig. 3.42. It should be noted that the loss in reduction of area is greater for heat 807 than for other heats. The greater loss in reduction of area for heat 807 can be explained by the microstructural changes observed in Fig. 3.38. The elongated light areas in (a) and (b) were

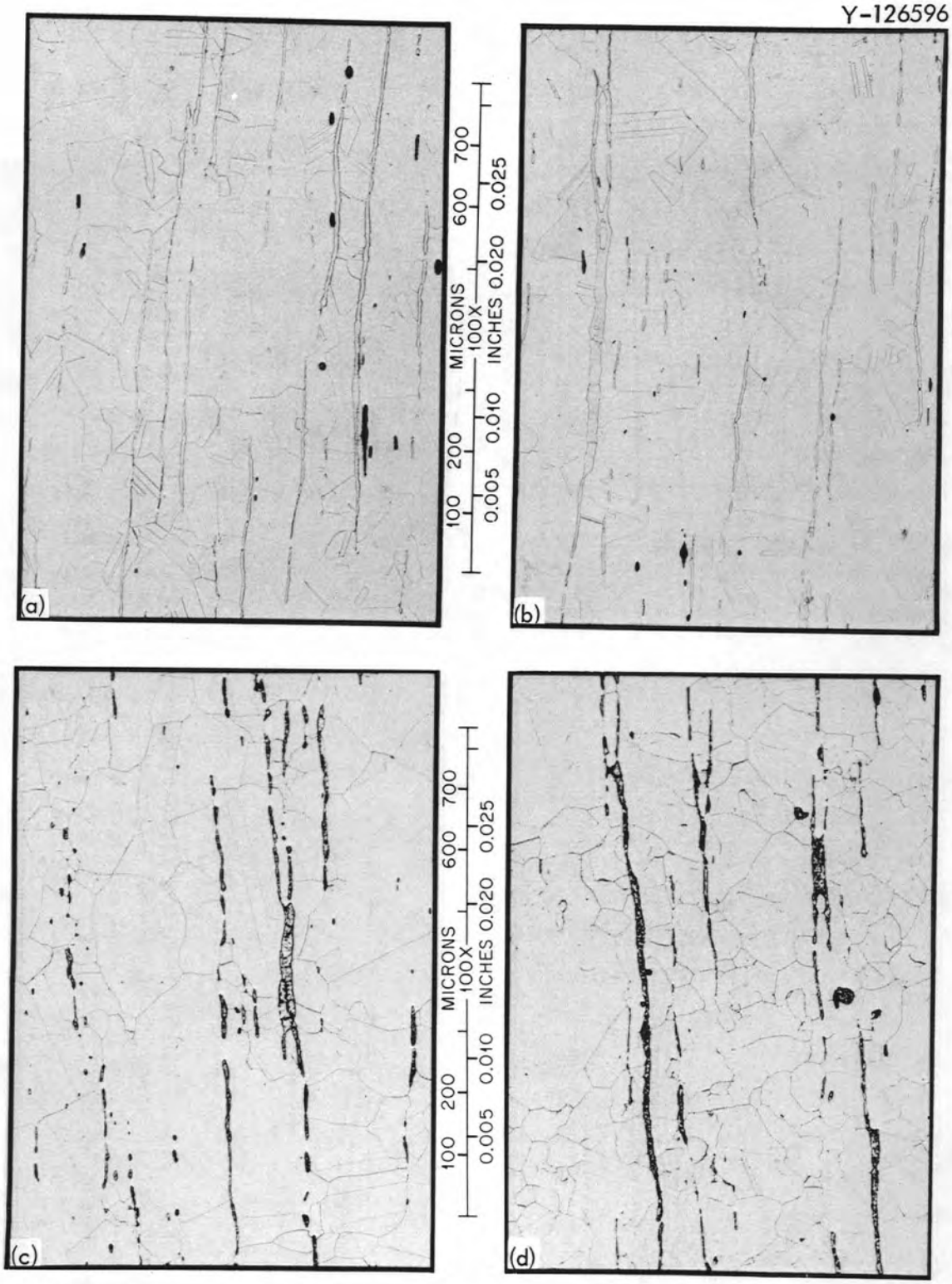

Fig. 3.38. Typical Microstructures Showing Effects of Aging for Heat 807 of Type 304 Stainless Steel. Etched. (a) As received. (b) Aged 4000 hr at 482°C (900°F); (c) at 593°C (1100°F); (d) at 649°C (1200°F).

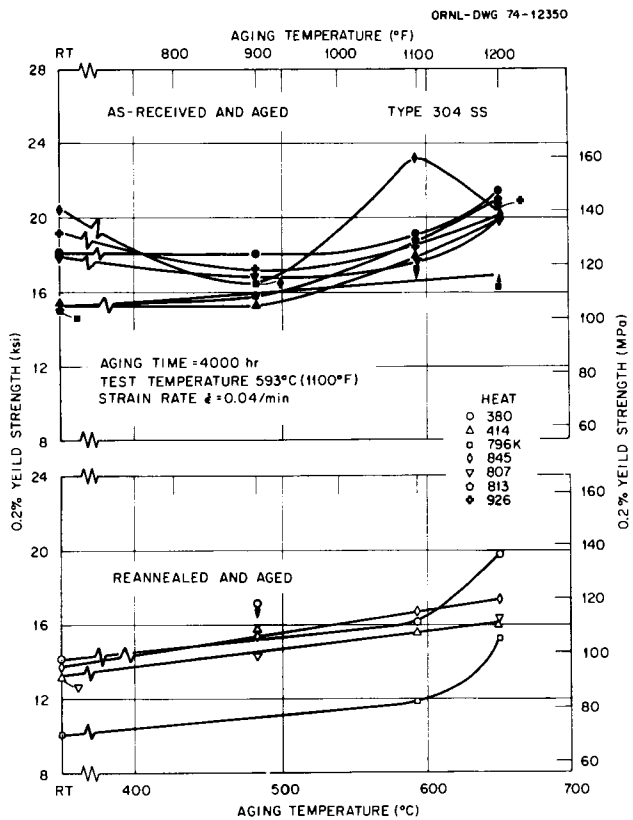

Fig. 3.39. Effect of Aging Temperature on 0.2% Yield Strength of Several Heats of Type 304 Stainless Steel Aged for 4000 hr and Tested at 593°C (1100°F).

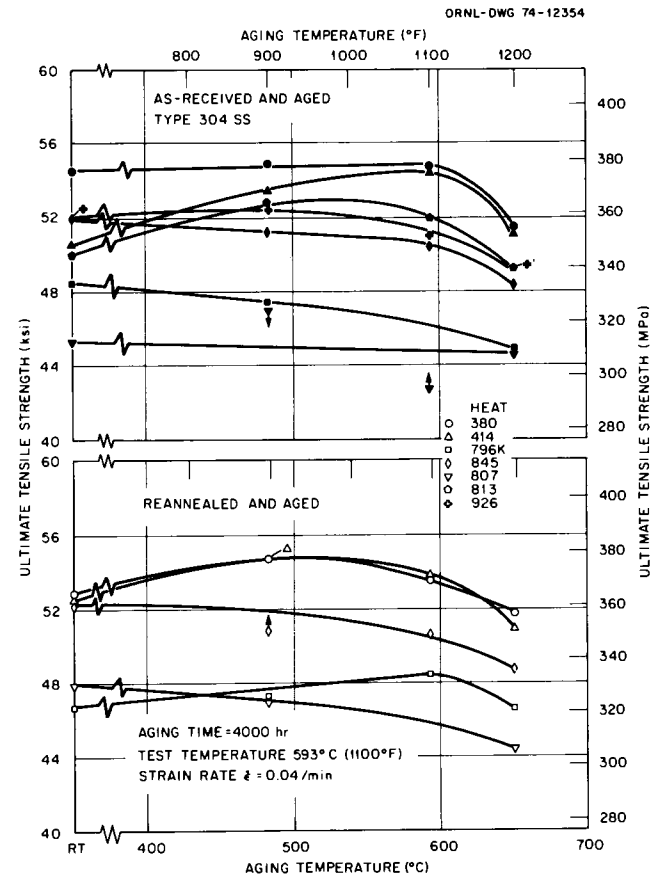

Fig. 3.40. Effect of Aging Temperature on Ultimate Tensile Strength of Several Heats of Type 304 Stainless Steel Aged for 4000 hr and Tested at 593°C (1100°F).

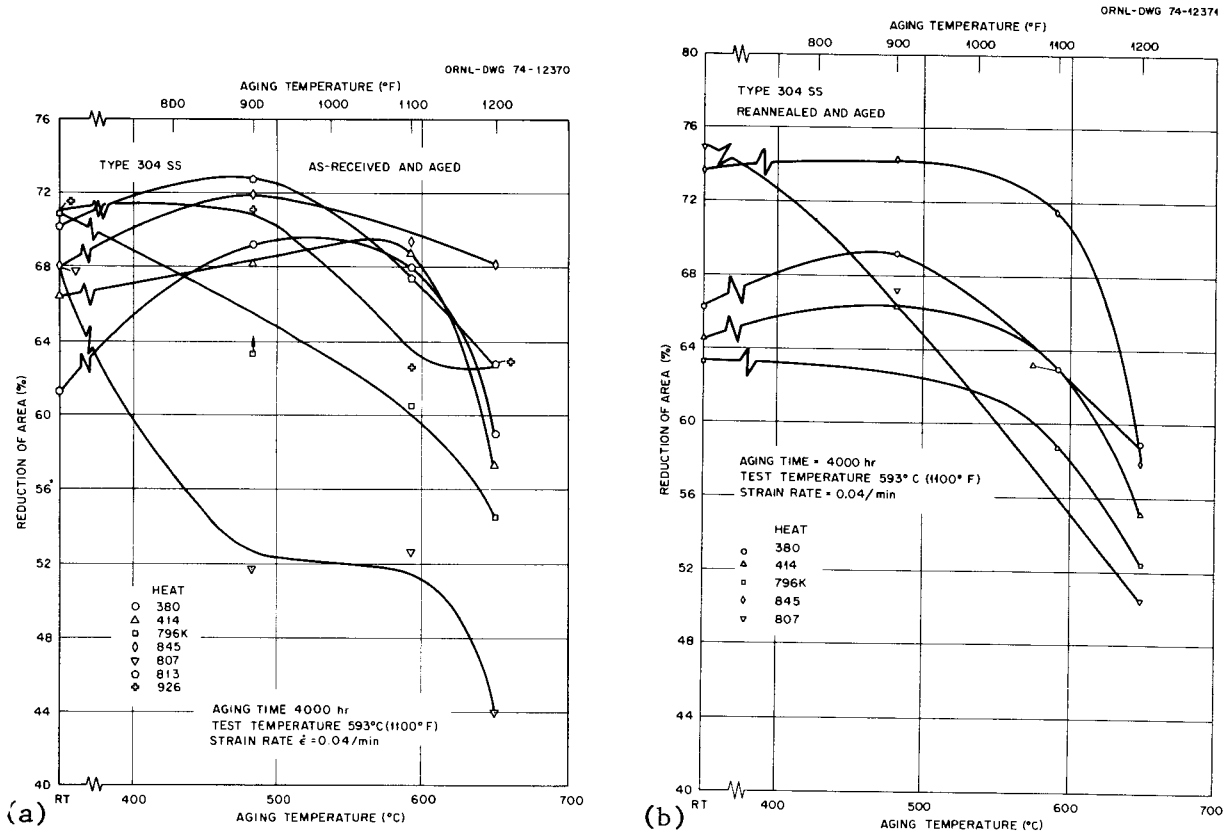

Fig. 3.41. Effect of Aging Temperature on Reduction of Area for Several Heats of Type 304 Stainless Steel, Aged for 4000 hr and Tested at 593°C (1100°F). (a) As received and aged. (b) Reannealed and aged.

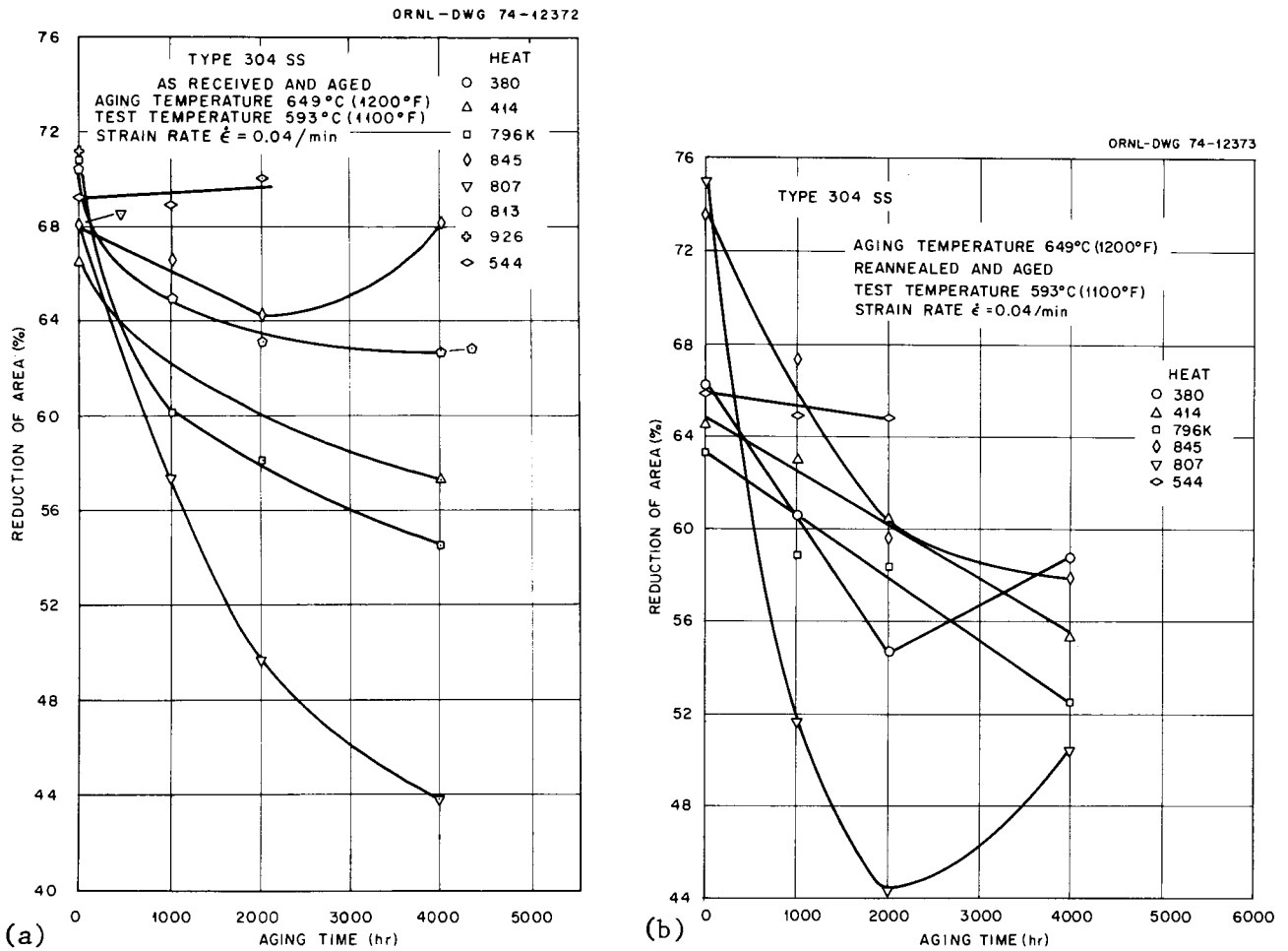

Fig. 3.42. Effect of Aging Time on Reduction of Area for Several Heats of Type 304 Stainless Steel, Aged at 649°C (1200°F) and Tested at 593°C (1100°F). (a) As received and aged. (b) Reannealed and aged.

identified by a magnetic etching technique as δ-ferrite. On aging, these areas start transforming to another phase, shown as black areas in Fig. 3.38(c) and (d). Magnetic etching and color staining techniques showed that the black areas are sigma phase, whereas some light areas among the black areas are untransformed δ-ferrite. Sigma phase has been reported[17,18] to impair ductility. Thus the loss in reduction of area on aging for heat 807 has been associated with the sigma phase. The greater amount of decrease in ultimate tensile strength on aging for this heat is also thought to be associated with sigma phase.

Tensile results from HEDL on aged types 304 and 316 stainless steel are available[1] for aging 3050 hr at 427, 482, 538, 593, and 649°C (800, 900, 1000, 1100, and 1200°F) and testing at 538, 593, and 649°C (1000, 1100, and 1200°F). The ORNL and HEDL results on uniform elongation are plotted together in Figs. 3.43 and 3.44. The ORNL data used for comparison were on heat 845 of type 304 and heat 613 of type 316 stainless steel. Both these heats were quite similar in chemical composition to heats used by HEDL. One important difference between the ORNL and HEDL data is that HEDL values of uniform elongation in the unaged condition were far lower than ORNL data. The HEDL data on type 304 stainless steel show a decrease in uniform elongation for an aging temperature of 427°C (800°F), increase for 482°C (900°F) and a decrease for 538°C (1000°F) and higher. The HEDL data for type 316 stainless steel showed no change on aging even at 649°C (1200°F). The ORNL data on type 304 stainless steel showed little or no decrease for an aging temperature of 482°C (900°F), whereas considerable decrease was observed for aging at 593 and 649°C (1100–1200°F). The ORNL data on type 316 stainless steel showed losses in uniform elongation for all three aging temperatures. The decrease was from 46 to 25%, and greatest for an aging temperature of 649°C (1200°F).

The major difference in testing conditions for the two laboratories was the strain rate. HEDL used a strain rate of 0.0018/min, as opposed to 0.04/min used by ORNL. Steichen and Paxton,[19] in a report on the effect of strain rate on the mechanical properties of austenitic stainless steels, have shown that uniform elongation for type 304 stainless steel shows the following behavior:

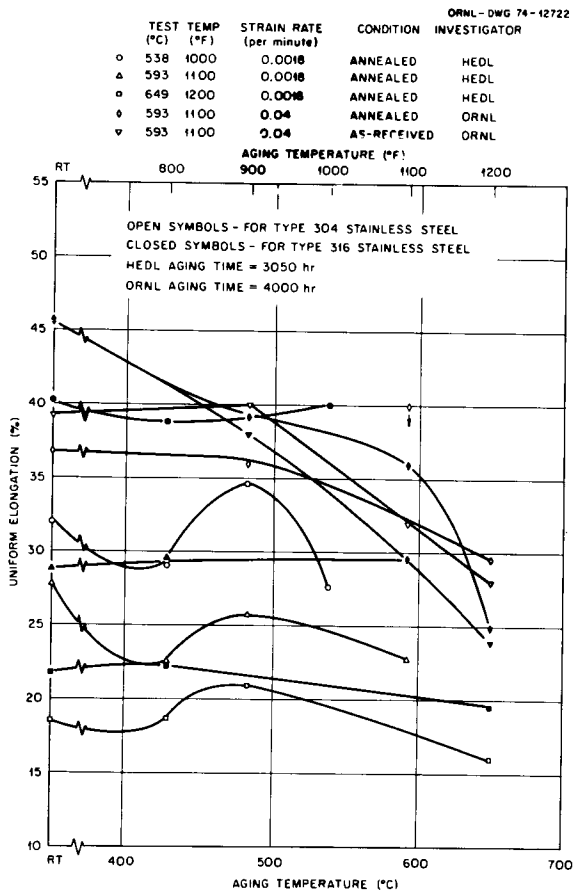

Fig. 3.43. Effect of Aging and Test Temperatures on Uniform Elongation of Types 304 and 316 Stainless Steel. Comparison of ORNL and HEDL data.

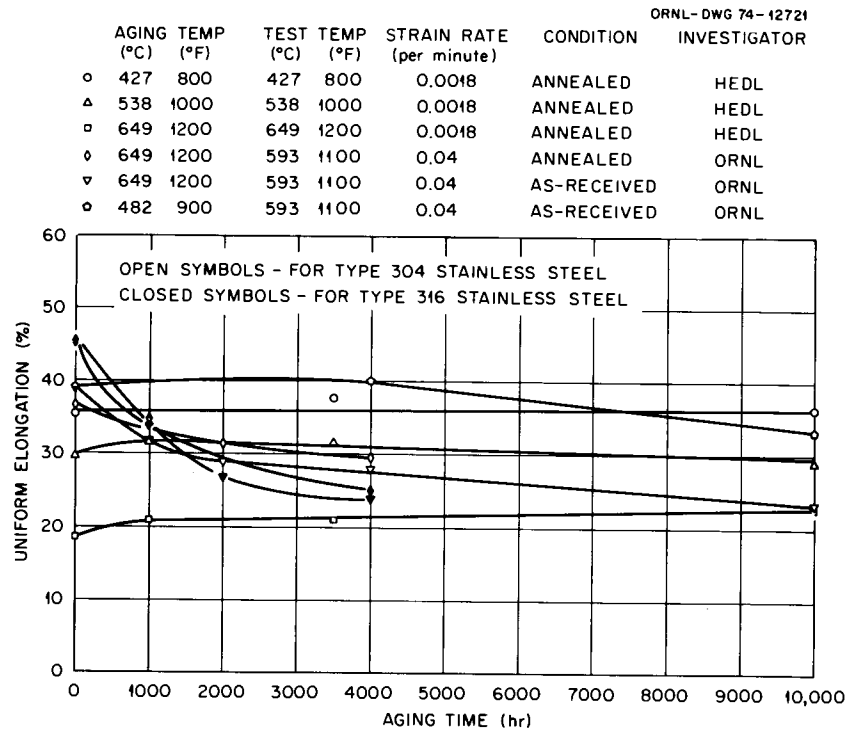

Fig. 3.44. Effect of Aging Time and Test Temperature on Uniform Elongation of Types 304 and 316 Stainless Steel. Comparison of ORNL and HEDL data.

1. At test temperatures below 538°C (1000°F), uniform elongation is lower for a strain rate of 0.044/min than for 0.0018/min.

2. At test temperatures above 538°C (1000°F), uniform elongation is higher for a strain rate of 0.044/min than for 0.0018/min.

3. Total elongation also shows a similar but more pronounced reversal in strain rate effect at a test temperature of 538°C (1000°F).

Thus, the lower values at 593°C (1100°F) observed[1] by HEDL for annealed types 304 and 316 stainless steel must be associated with the lower strain rate than that used by ORNL. The ORNL data[20] on strain-rate dependence of uniform and total elongations for unaged and aged reference heat of type 304 stainless steel are shown in Figs. 3.45 and 3.46. The figures show that the strain-rate dependence of the aged material is opposite to that for the unaged material. Furthermore, at a strain rate of approximately 10^{-5}/sec aging is not expected from Fig. 3.45 to produce any change in uniform elongation. The strain rate used by HEDL was 3×10^{-5}/sec, which from Fig. 3.45 is expected to produce a small reduction in uniform elongation, in excellent agreement with the data.

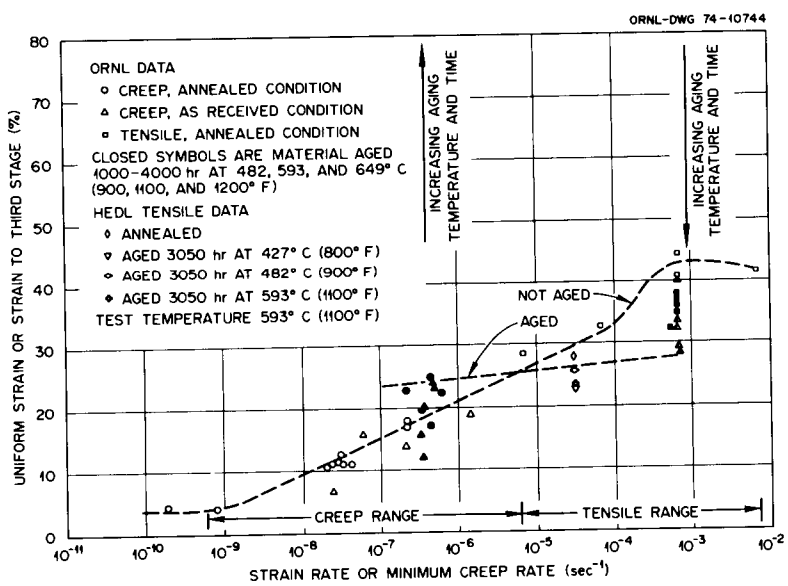

Fig. 3.45. Effect of Thermal Aging on Uniform Elongation During Creep and Tensile Testing of Reference Heat (9T2796K) of Type 304 Stainless Steel. Strain in third stage is 0.2% offset from onset of third stage.

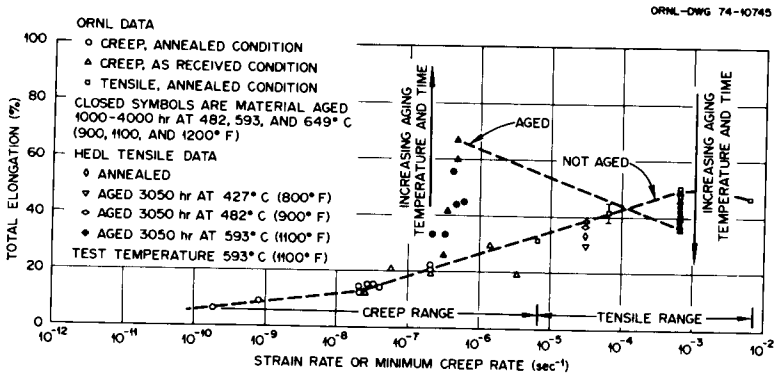

Fig. 3.46. Effect of Thermal Aging on Total Elongation During Creep and Tensile Testing of Reference Heat (9T2796K) of Type 304 Stainless Steel.

The strain-rate dependence of total elongation for aged material, Fig. 3.46, appears much stronger than that of uniform elongation. The strain rate for no change in total elongation on aging is about 10^{-4}/sec, as compared with 10^{-5}/sec for the uniform elongation. Thus, HEDL results on total elongation are expected to show no change to an increase in total elongation on aging. HEDL observed an increase in total elongation and stated, "it is interesting to note that the data at 649°C (1200°F) for type 304 stainless appears to reflect the increased tensile elongation resulting from thermal aging at this temperature." Now, we have shown that ORNL results showing a decrease and HEDL results showing no change or increase in uniform and total elongation are just a consequence of different strain rates. The question that remains unanswered is as to why the strain-rate dependence of uniform and total elongations for the aged material shows an opposite effect.

3.2.2.5.2 Creep Properties. The ORNL data on the effect of thermal aging on the short-term creep properties of several heats of type 304 stainless steel were reported previously.[20,21] The changes on aging in time to rupture and onset of third-stage creep are shown as functions of corresponding changes in ultimate tensile strength in Fig. 3.47. It can be noted that the time to rupture follows the same trend as ultimate tensile strength. For example, the decrease in ultimate tensile strength followed a corresponding decrease in time to rupture and time to onset of third-stage creep. The high-nitrogen heat (121) is an exception to this general behavior.

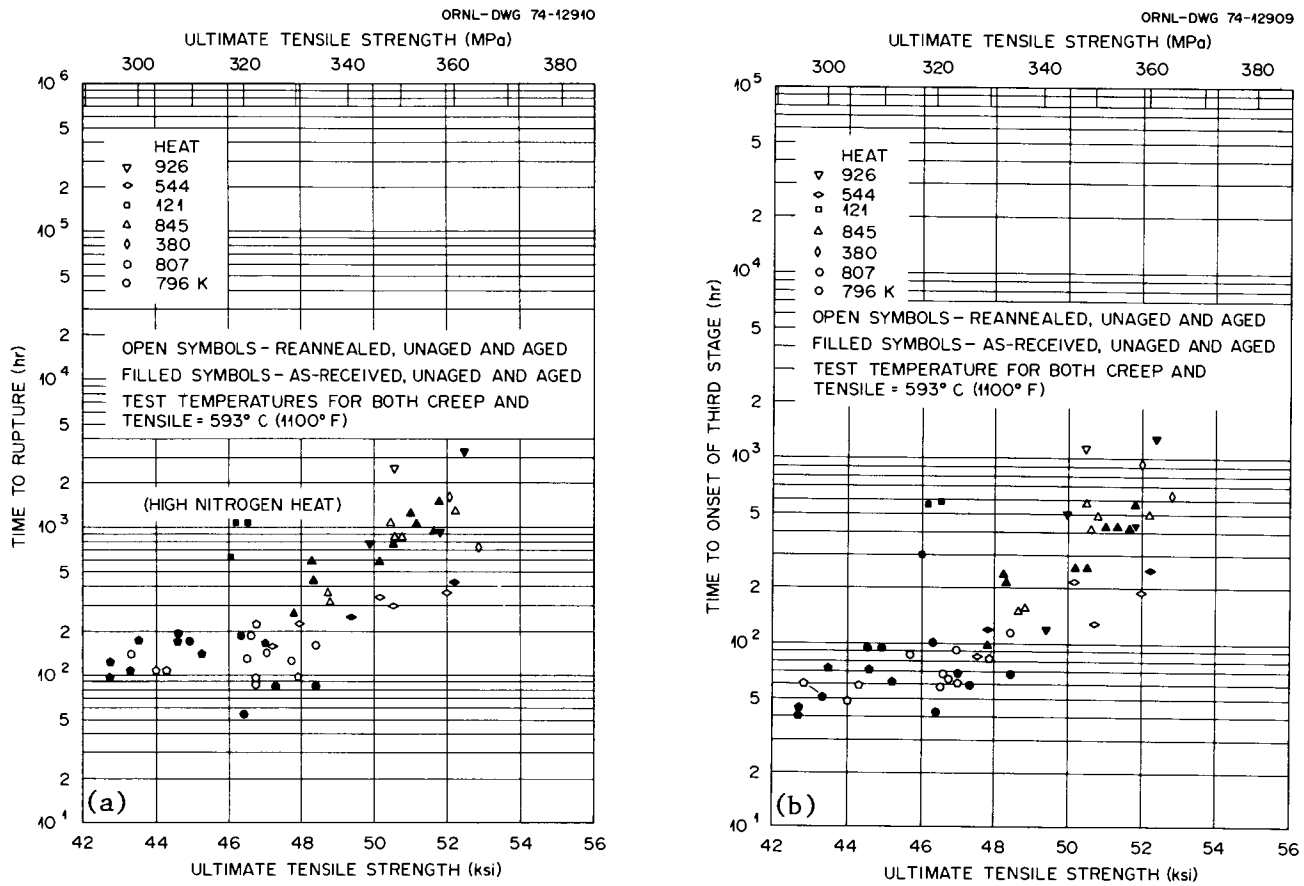

Fig. 3.47. Relation Between Creep and Short-Term Tensile Properties of Several Heats of Types 304 Stainless Steel in Both Unaged and Aged Conditions. (a) Time to rupture and (b) time to onset of third-stage creep as functions of ultimate tensile at the creep temperature.

In addition to the short-term creep tests, several long-term creep tests are also in progress on the aged material. Figure 3.48 compares the creep tests on annealed specimens and specimens that had been annealed and then aged for 4000 hr at 482°C (900°F). It can be noted that the test on the annealed specimen had ruptured after 4554 hr, whereas the test on the aged specimen has gone 6400 hr and is still continuing. The aged specimen showed a slight decrease in loading strain, but the strain accumulated during primary creep is larger. The progress on this and other long-term creep tests on the aged material will be reported next quarter.

3.2.2.5.3 Microstructure. The creep curves on heat 926 were presented last quarter[21] to show the effect of aging temperature for an aging time of 10,000 hr. The creep curve shown for unaged material was for the reannealed condition, whereas the other curves were for material aged in

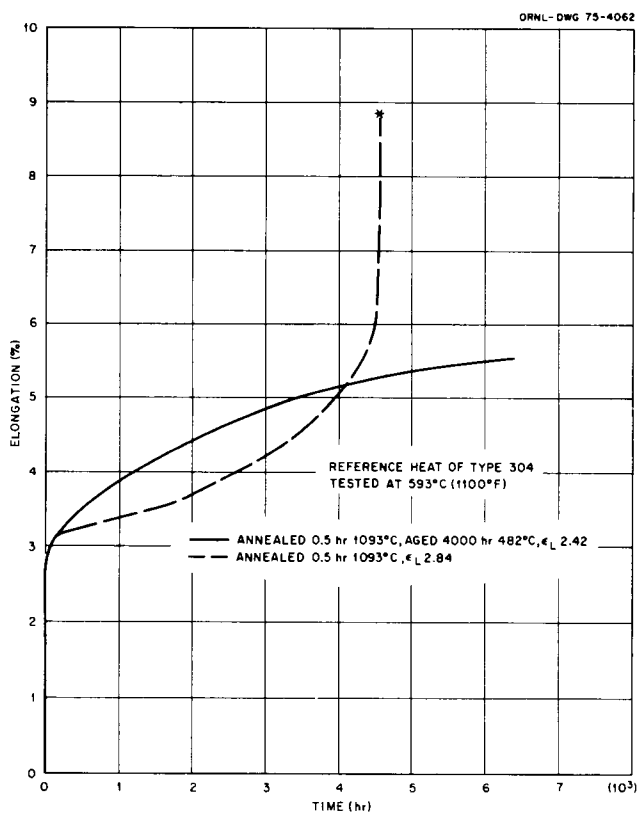

Fig. 3.48. Comparison Between Creep Curves of the Annealed and Annealed-and-Aged Reference Heat of Type 304 Stainless Steel.

the as-received condition. Therefore, a creep test was completed for an unaged specimen in the as-received condition. The updated creep curves showing the effect of reannealing and 10,000 hr thermal aging are presented in Fig. 3.49. The general comments presented earlier[21] on the effect of aging on creep data remain unchanged, except that Fig. 3.49 now shows that reannealing also lowers the time to rupture.

The macro- and micrographs of the unaged and aged specimens are presented in Figs. 3.50 through 3.52. The increase in rupture elongation and reduction of area on thermal aging are obvious from Fig. 3.50. The microstructures in Fig. 3.51 show grain boundary cavities for the unaged specimen and one aged for 10,000 hr at 482°C (900°F). The microstructures in Fig. 3.52 show twin boundary cavitation for specimens aged for 10,000 hr at 593 and 649°C (1100 and 1200°F). The comparison of microstructures in Figs. 3.51 and 3.52 shows that the transition from grain to twin boundary cavitation starts at an aging temperature of 593°C (1100°F). Furthermore,

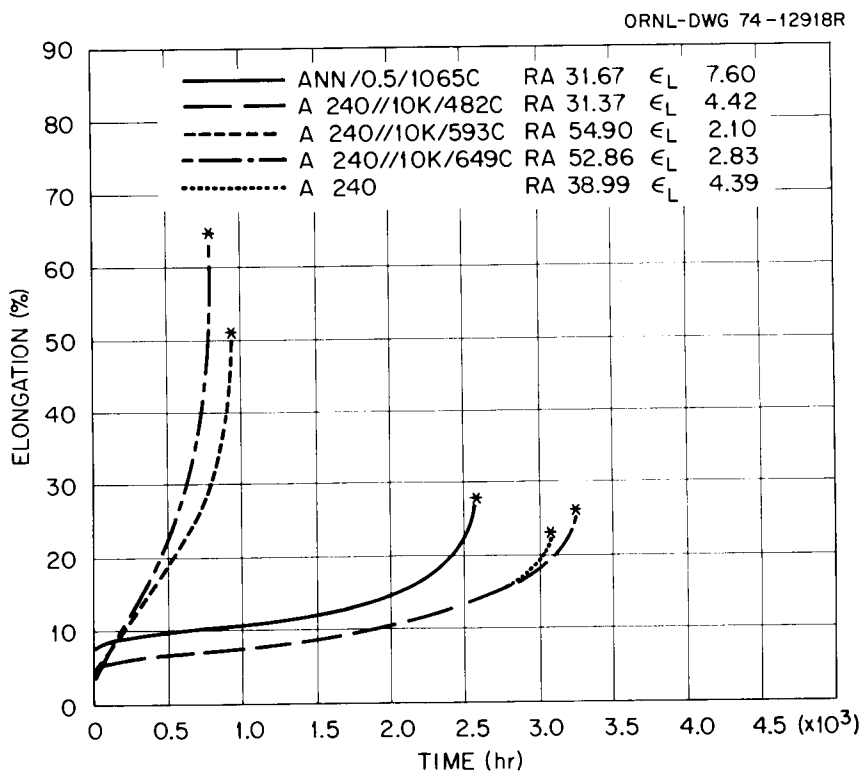

Fig. 3.49. Effect of Aging Temperature on Creep Curves for Heat 926 of Type 304 Stainless Steel. Creep tests were performed at 593°C (1100°F) and 30 ksi (207 MPa). 10K stands for aging time of 10,000 hr.

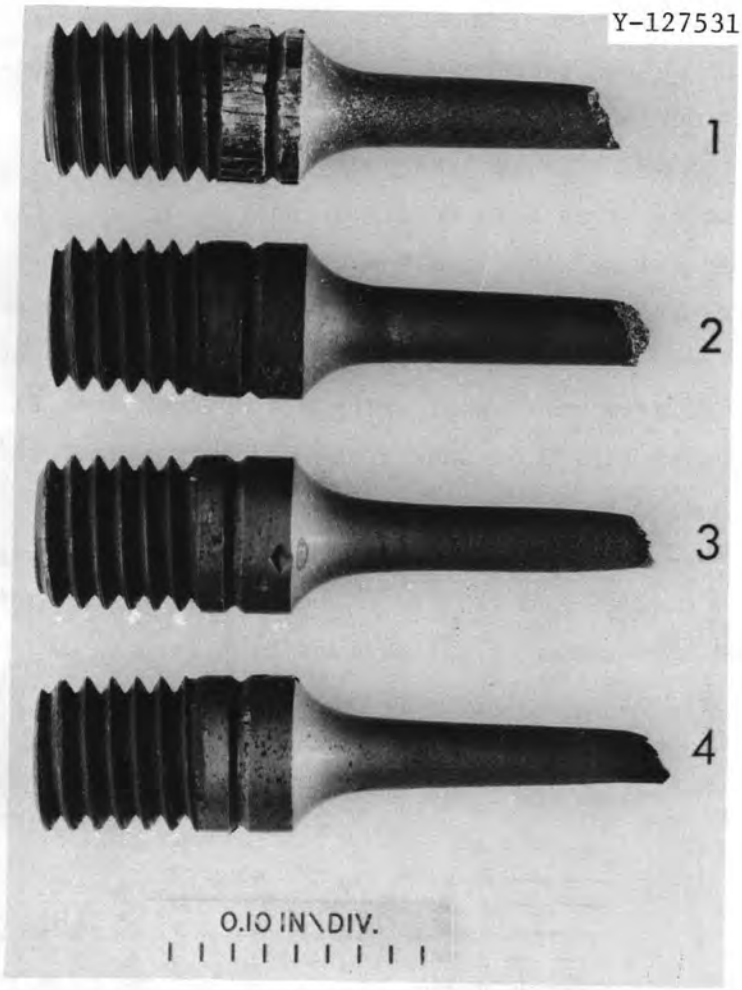

Fig. 3.50. Ruptured Creep Specimens of Heat 926 of Type 304 Stainless Steel Tested at 593°C (1100°F) and 30 ksi (207 MPa). Specimens 1 through 4 are as received and as received-and-aged for 10,000 hr at 482, 593, and 649°C (900, 1100, and 1200°F), respectively. Note the increase in ductility on aging.

this transition in cavitation is associated with a large reduction in time to rupture, as seen in Fig. 3.49, and a large increase in rupture elongation and reduction of area, shown in Figs. 3.49 and 3.50. The twin boundary cavitation in Fig. 3.52 is associated with extensive grain matrix deformation, as indicated by elongated grains, whereas grain boundary cavitation in Fig. 3.51 is associated with relatively small grain matrix deformation.

High-magnification micrographs of twin boundary cracks are presented in Fig. 3.53. The possible nucleation of the twin boundary crack at the junction of incoherent and coherent parts of the twin is shown in Fig. 3.53(a). The micrograph in (b) shows the propagation of the cavity,

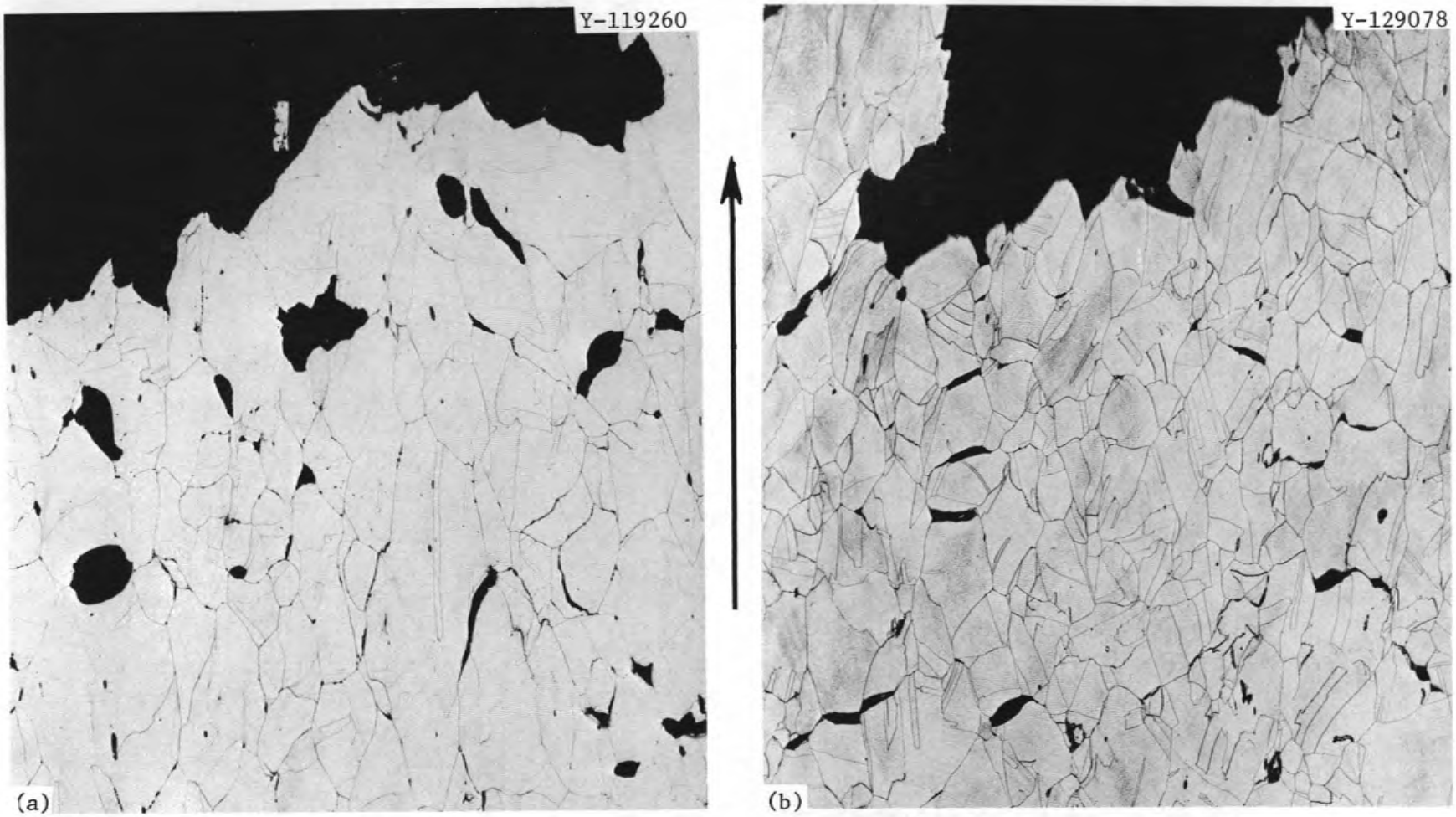

Fig. 3.51. Microstructure of the Fracture Ends of Creep Specimens of Heat 926 of Type 304 Stainless Steel Tested at 593°C (1100°F) and 30 ksi (207 MPa). 100×. Arrow indicates direction of applied stress. (a) Annealed and creep tested. (b) Aged at 482°C (900°F) for 10,000 hr. Note grain boundary cavitation.

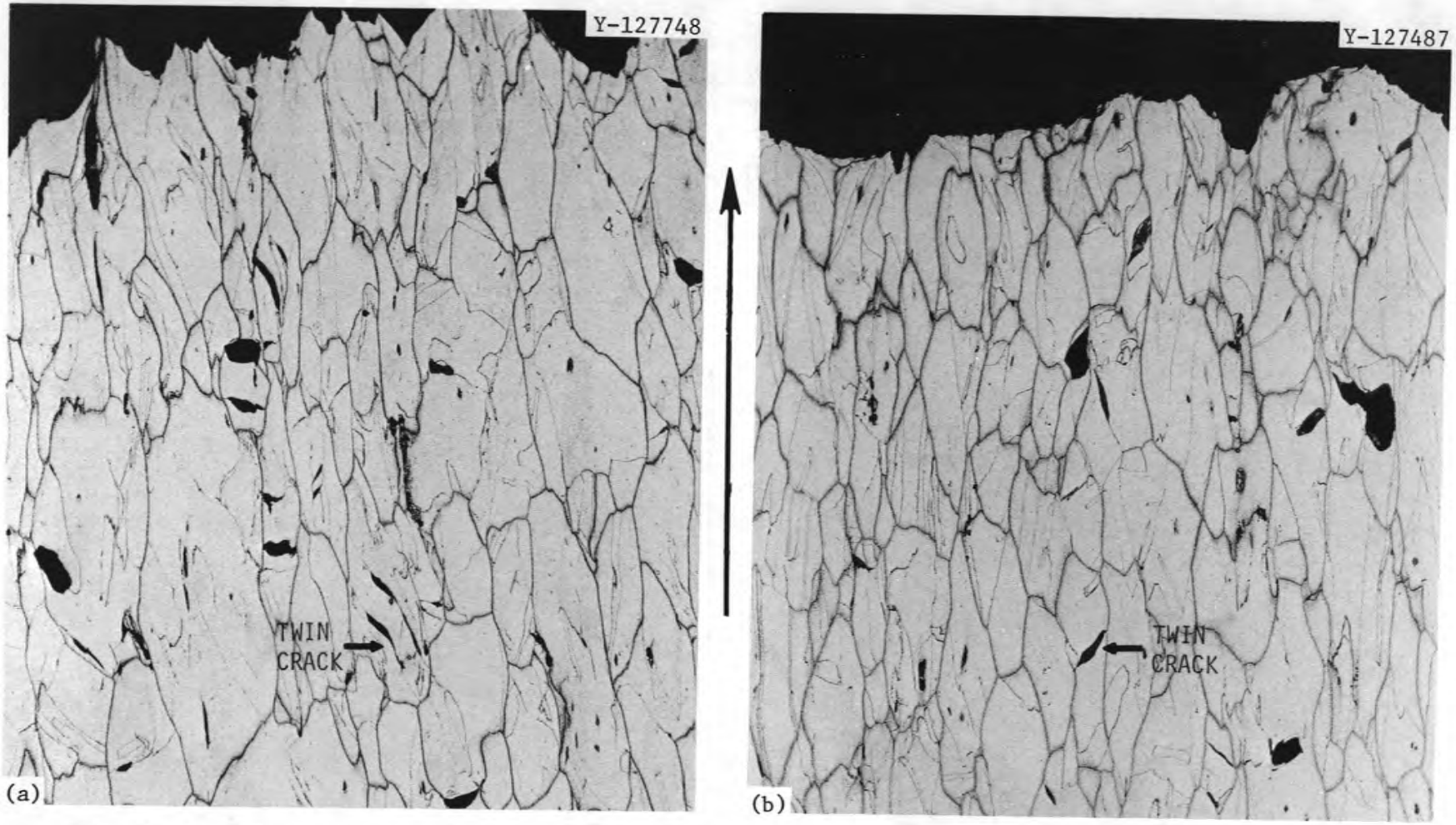

Fig. 3.52. Microstructure of the Fracture Ends of Creep Specimens of Heat 926 of Type 304 Stainless Steel Tested at 593°C (1100°F) and 30 ksi (207 MPa). 100×. Arrow indicates the direction of applied stress. (a) Aged at 593°C (1100°F) for 10,000 hr. (b) Aged at 649°C (1200°F) for 10,000 hr. Note the twin boundary cracking in both micrographs.

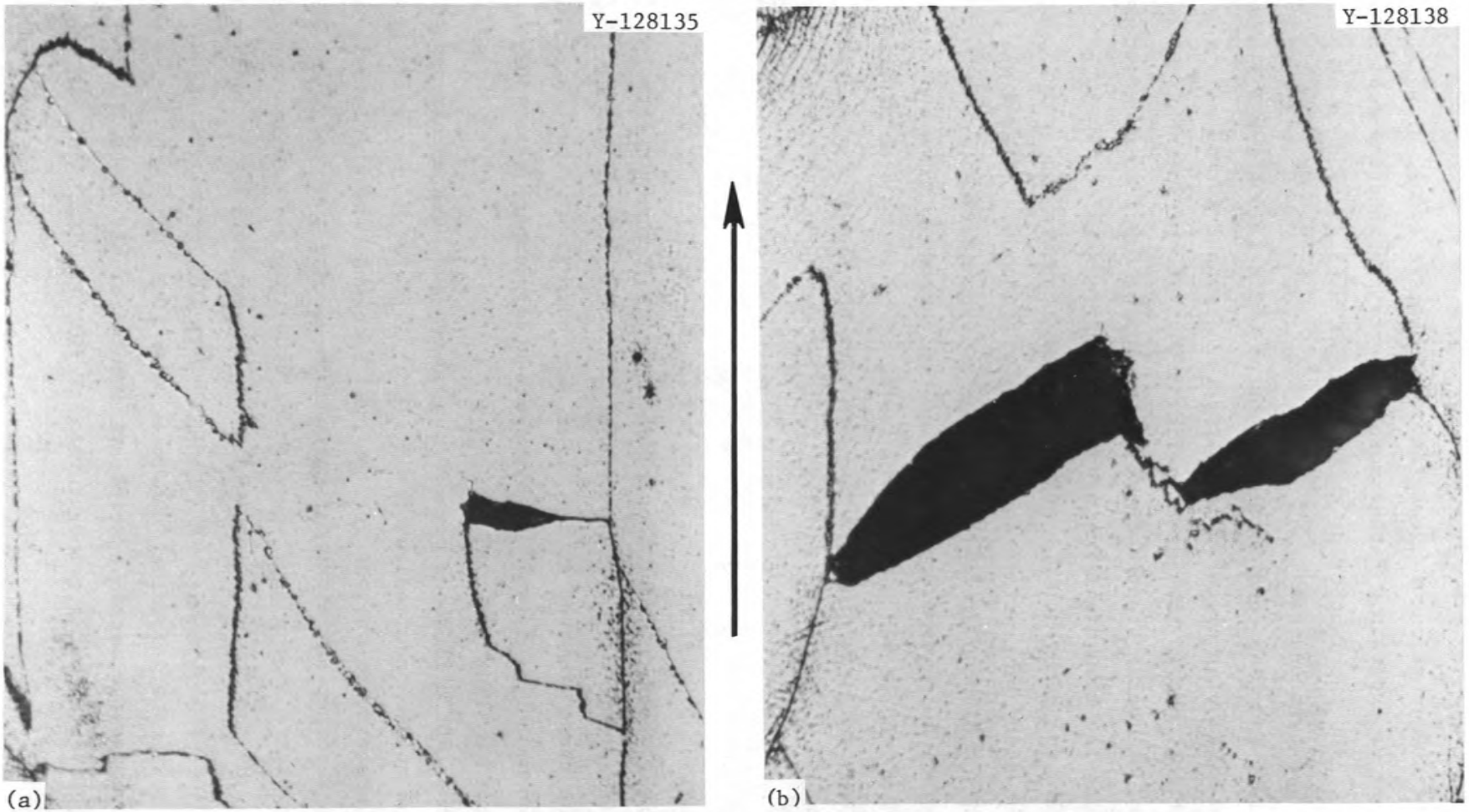

Fig. 3.53. Micrographs of the Creep Specimen of Heat 926 of Type 304 Stainless Steel Aged for 10,000 hr at 649°C (1200°F) and Tested at 593°C (1100°F) at 30 ksi (207 MPa). Arrow indicates direction of applied stress. 1000×. (a) Twin cavity nucleated at intersection of incoherent-coherent twin junction. (b) Twin crack propagated along the coherent twin.

nucleated at the junction of incoherent and coherent twins, along the coherent part of the twin. Furthermore, the grain boundaries (which are incoherent), like the incoherent part of the twin, also tend to stop the propagation of twin cracks.

The creep specimen aged for 10,000 hr at 649°C (1200°F) was also examined in a scanning electron microscope. A typical set of scanning electron micrographs is presented in Fig. 3.54. The micrographs show two twin cracks, one being stopped from propagating by the incoherent steps of the twin. The more significant observation from Fig. 3.54 is the difference in the nature of the precipitate at the twin and grain boundaries. The grain boundary precipitate appears more continuous, compared with a spotty or discontinuous precipitate at the twin boundaries.

Transmission electron micrographs on the unaged specimen and one aged for 10,000 hr at 649°C are shown in Fig. 3.55. The precipitate particle sizes and densities were measured for the annealed and aged specimens and are summarized in Table 3.7. It can be noted again from Fig. 3.55 that the precipitate is more continuous at the grain boundaries of the aged specimen compared with the unaged specimen. It should also be noted that no precipitate was observed at the twin boundaries of the annealed creep specimen. The precipitate size and density in the matrix and precipitate size at the grain boundary of the aged specimen are much greater than those observed in the annealed specimen. The ORNL precipitate size data on heat 926 of type 304 stainless steel compare remarkably with those reported by Etienne et al.[22]

One important difference between the unaged and aged specimens is that for the unaged specimen the precipitate particles nucleate and grow during the creep test, whereas for the aged specimens the precipitate was present before creep and might have grown some during the creep test. The matrix precipitate in the aged specimen results in precipitation hardening, as evidenced by the increase in yield strength (see Fig. 3.37) and decrease in the loading strain (Fig. 3.49). For the unaged specimen, the grain boundary precipitate initiates[22] approximately 10 hr after the start of the test, whereas the matrix precipitate initiates only about 500 hr after the start of the test at a temperature of 593°C (1100°F). For the unaged

Y-130424

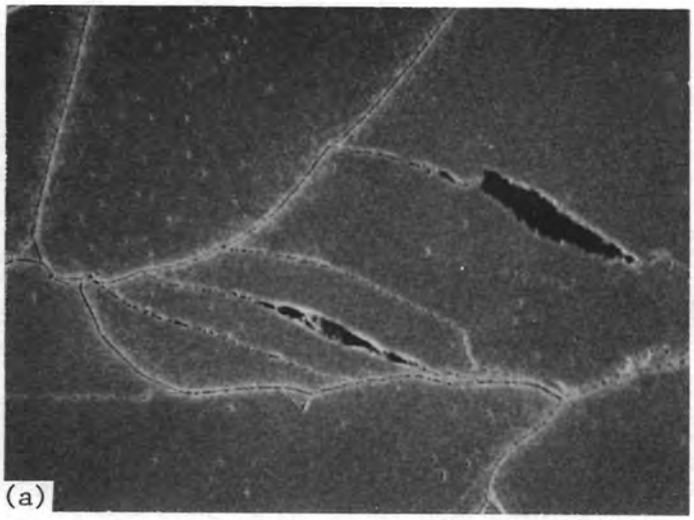

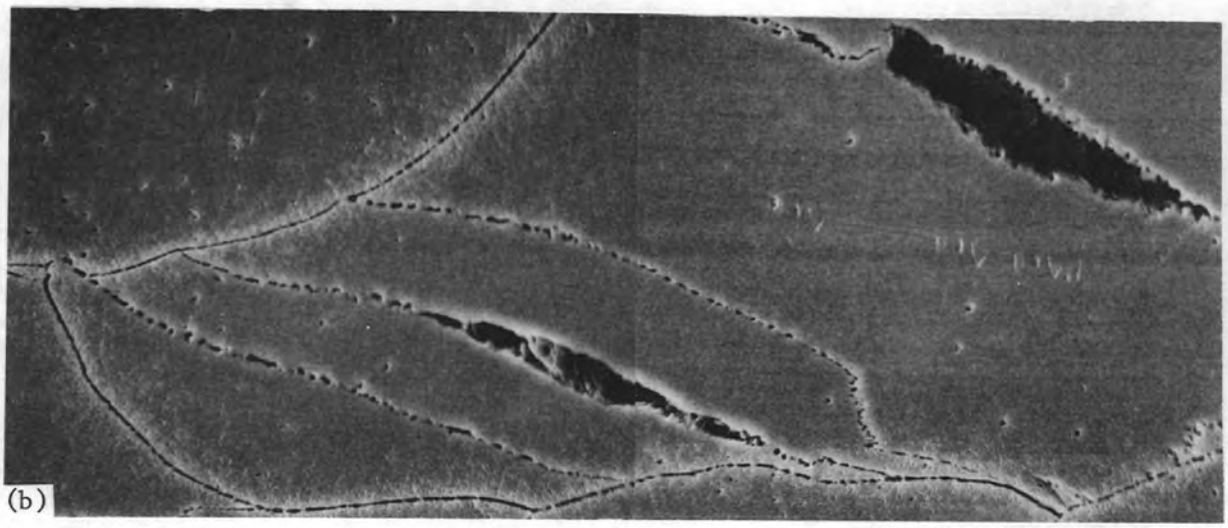

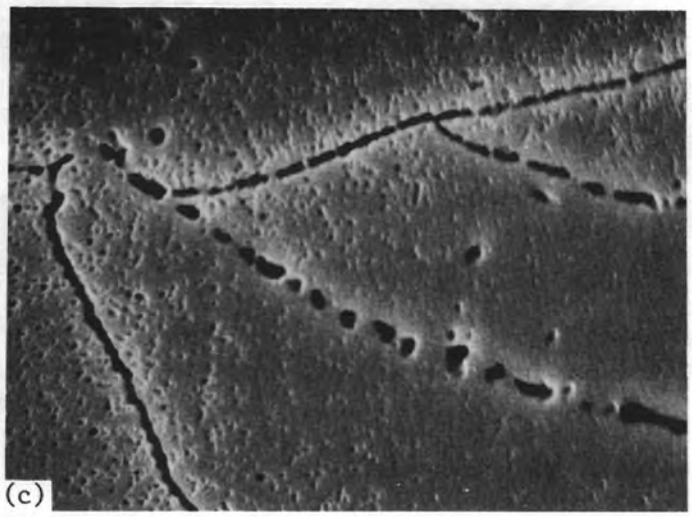

Fig. 3.54. Scanning Electron Micrograph from Creep Specimen of Heat 926 of Type 304 Stainless Steel, Aged for 10,000 hr at 649°C (1200°F) and Tested at 593°C (1100°F). (a) Twin cracks, 500×. (b) Twin crack stopped by incoherent segments, 1000×. (c) Difference in precipitate distribution at grain and twin boundaries, 3000×.

Fig. 3.55. Electron Micrographs from Buttonheads of Creep Specimens of Heat 926 of Type 304 Stainless Steel. (a) Annealed, tested 2580 hr at 593°C (1100°F). (b) Aged for 10,000 hr at 649°C (1200°F), tested 780 hr at 593°C (1100°F). Note the difference in precipitate at twin and grain boundaries.

Table 3.7. Summary of Precipitate Data for Heat 926 of Type 304 Stainless Steel

Temperature, °C(°F)		Time, hr		Precipitate Character at Various Locations						Reference
				Matrix		Grain Boundary		Twin Boundary		
Aging	Test	Aging	Test	Size (μm)	Density (cm^{-3})	Size (μm)	Density (cm^{-1})	Size (μm)	Density	
	593(1100)		2,580	0.069	5.7×10^{12}	0.35	4.8×10^{4}	a	a	ORNL
	593(1100)		~2,580	0.020	b	~0.30	b	b	b	c
649(1200)	593(1100)	10,000	780	0.130	4.3×10^{13}	1.26	1.15×10^{4}	0.20	b	ORNL
	649(1200)		~11,000	0.05–0.10	b	1.0	b	b	b	c

[a]None observed.

[b]Not measured or reported.

[c]C. F. Etienne, W. Dortland, and H. B. Zeedijk, "On the Capability of Austenitic Stainless Steel to Withstand Cyclic Deformation During Service at Elevated Temperature," Paper Presented at the International Conference on Creep and Fatigue in Elevated Temperature Applications, Philadelphia, September 1973, and Sheffield UK, April 1974.

specimen of heat 926 tested at 593°C (1100°F) and 30 ksi (207 MPa), the second-stage creep starts at approximately 350 hr (Fig. 3.49). Thus, nucleation and growth of matrix precipitate particles must be occurring during the second-stage creep of the unaged specimen.

Ansel and Weertman[23] developed a dislocation creep model for the effect of dispersed particles on steady-state creep. The basis of the theory involves the climb of mobile dislocations over particles and their annihilation by dislocations of opposite sign on neighboring parallel slip planes. According to the Ansell and Weertman model, minimum creep rate is given by

$$\dot{\varepsilon}_m = 6\tau^4 D_s \lambda^2 / dG^3 kT \ , \tag{19}$$

where τ = applied shear stress,

D_s = self-diffusion coefficient,

λ = interparticle spacing,

d = particle diameter, and

G = shear modulus.

For identical test conditions, the ratio of the minimum creep rate in aged and unaged conditions can be expressed as

$$\frac{\dot{\varepsilon}_m(\text{aged})}{\dot{\varepsilon}_m(\text{unaged})} = \frac{\lambda_A^2 \cdot d_{UA}}{d_A \lambda_{UA}^2} \ . \tag{20}$$

The interparticle spacing can be related to the particle size and density by the relation

$$\lambda = 1/\sqrt{Nd} \ . \tag{21}$$

Combining Eq. (21) with (20) gives:

$$\frac{\dot{\varepsilon}_m(\text{aged})}{\dot{\varepsilon}_m(\text{unaged})} = \frac{N_{UA} d_{UA}^2}{N_A d_A^2} \ . \tag{22}$$

Substituting values of particle size and density from Table 3.7 into Eq. (22) yields $\dot{\varepsilon}_m(\text{aged})/\dot{\varepsilon}_m(\text{unaged}) \approx 1/27$, as opposed to a value of approximately 19 observed in the present investigation. Such a large difference between theory and experimental data can be rationalized only if Eq. (19) is valid in a different particle size and spacing range than that observed in the present investigation or such mechanism is not applicable here. Qualitatively, we expect the carbides nucleating and growing during the second-stage creep of the unaged specimen to anchor the dislocations and impede recovery effectively.[24] Such a process would decrease the creep rate and thus increase the time to rupture. For the aged specimen carbides exist before testing. Although they increase the yield strength, they prevent the formation of dislocation substructure and thus may accelerate dislocation recovery and minimum creep rate. The above suggestions are consistent with the results of Garofalo et al.,[25] where prestrain followed by precipitation led to a 25-fold increase in the time to rupture.

The initiation of intergranular cavitation requires the presence of the following:[26]

1. grain-boundary sliding,
2. high intragranular flow strength,
3. nonwetting inclusions (oxides etc.) at the grain boundaries,
4. impurity segregation at grain boundaries preventing grain boundary migration,
5. brittle film formation at the grain boundaries, and
6. denudation phenomenon in alloys

and absence of the following:

1. grain-boundary migration,
2. high cohension between the particle and matrix,
3. a phase change, and
4. recrystallization.

Garofalo[26] investigated the influence of grain boundary precipitate morphology on the intergranular cavitation of type 316 stainless steel. For the annealed condition small closely spaced carbide particles are precipitated at the grain boundaries at 593°C (1100°F). No grain

boundary migration is possible under these conditions; the elongation at rupture is low and the fracture totally intergranular. The present results for heat 926 of type 304 stainless steel show small (0.35-μm) closely spaced particles (0.21 μm apart) after tests at 593°C (1100°F) and 30 ksi (207 MPa). The fracture under these conditions was intergranular, Fig. 3.51(a), with a rupture elongation of 28.0%. Thus, it is quite possible that intergranular cavitation in heat 926 occurred by a mechanism suggested by Garofalo for type 316 stainless steel tested under similar conditions.

Garofalo[26] pretreated type 316 stainless steel for 24 hr at 816°C (1500°F) before testing at 593°C (1100°F). This pretreatment increased rupture life and elongation. The increase in time to rupture was suggested to have resulted from the grain boundary migration that occurred during pretreatment. The pretreatment was thought to have spheroidized the precipitate, as compared with the fine precipitate formed in the annealed material during testing at 593°C (1100°F). The fracture behavior of the pretreated specimen was still intergranular, but no cracks were observed along the precipitate-matrix interface. The lack of cracks along the precipitated particle was considered as the possible result of strong adherence between the matrix and the particles. In the present investigation, thermal aging for 10,000 hr at 649°C (1200°F) increased the grain boundary precipitate particle size from 0.35 μm in the unaged condition to 1.26 μm and particle spacing from 0.21 to 0.87 μm. Contrary to the results of Garofalo, the time to rupture decreased by 75%, and no intergranular cavities were observed. Instead, the cavities were all along the twin boundaries (Figs. 3.52—3.54). The absence of grain boundary cavities may be the result of the following conditions produced by thermal aging:

1. Intragranular flow strength was lower than that of grain boundaries. The intragranular deformation, ε_g, was calculated by the following relation:[27]

$$\varepsilon_g = \left(\frac{\ell}{w} \cdot \frac{w_0}{\ell_0}\right)^{2/3} - 1 , \qquad (23)$$

where ℓ_0/w_0 and ℓ/w are the average length-to-width ratios in the annealed and deformed specimens, respectively, ℓ being measured parallel and w transverse to the stress axis. The calculated value of ε_g was 75%, which compared extremely well with the true measured ductility of 75.3%, thus indicating that total deformation was all intragranular.

2. Coarse precipitates in the aged specimen might have resulted in grain-boundary migration, as observed by Garofalo[26] in pretreated type 316 stainless steel.

3. The coarse precipitate at the grain boundaries of the aged specimen might have more cohesion with the matrix than the fine precipitate at the twin boundaries of the aged specimen and at grain boundaries of the unaged specimen. Such a possibility is suggested because cavitation was observed at the location of small precipitate particles (grain boundaries of the unaged tested specimen and twin boundaries of the aged tested specimens).

All above-mentioned factors might be operating to prevent grain-boundary cracking.

Greenwood et al.[28] investigated the intergranular cavitation in stressed metals (copper, α-brass, and magnesium) containing annealing twins and showed that no cavities were associated with twin boundaries. Hull and Rimmer[29] investigated cavitation in copper and pointed out that voids do not form on twin boundaries even when the boundaries are transverse to the applied stress. The only observation where twin cracks have been reported in type 304 stainless steel is by Michel, Nahm, and Moteff.[30] Specimens showing twin cracks had been tested at 649°C (1200°F) and a strain rate of 8.3×10^{-5}/sec. The average strain rate at which twin cavities were observed in the present investigation varied from 1.6 to 1.9×10^{-7}/sec. Furthermore, specimens showing twins were aged for 10,000 hr at 593 and 649°C (1100 and 1200°F) and both tested at 593°C (1100°F). Although the strain rate used in present investigation was 0.002 times that used in the investigation of Michel et al.,[30] the twin cavities in both cases were maximum for boundaries inclined between 30 and 90° to the direction of the applied stress, whereas only few cavities occurred at angles less than 30°. Such an observation is quite consistent with the results[26] on distribution of grain boundary cavities.

The observation that many cracks occur along the maximum shear stress axis, and they are distributed similarly to grain boundary cavities, suggests that the twin-boundary sliding may be a possible cause for cavity nucleation.

The coherent part of the annealing twin (where cracks have been observed) is bounded by {111} planes. In contrast, short incoherent steps and terminations are crystallographically more complicated.[31] The schematic diagram in Fig. 3.56 can be used to explain the twin boundary cavitation. The coherent parts of the twin, AB and CD, contain the {111} planes, on which slip (twin boundary sliding) can occur under the shear component of the applied stress. The incoherent part of the twin remains immobile because of its crystallography (it does not contain a plane for easy slip) and the stress acting on it, which is essentially zero.

Now consider the coherent twin component AB, trying to slide under the shear stress component. The segment AB is stopped at points A and B, thus building up stresses, which can relax only by opening cavities at the intersection of AB and BC or AB and the grain boundary. The precipitate particles present at the sliding twin boundary can help relax the stress by nucleating cavities at the weak cohesion particle, as suggested by Harris[31] for particles at the sliding grain boundaries.

The examples of cavity opening at the intersection of coherent and incoherent twin boundaries are shown in Figs. 3.53 and 3.54. The twin boundary cavities on boundaries transverse to the stress axis can probably form by vacancies produced at the boundary because of the tension across it. For a stress σ_p on the particle on the boundary, vacancy supersaturation[24] is given by

$$C/C\mathrm{eq} = \exp(\sigma_p \Omega/kT) \quad . \tag{24}$$

For an applied stress of 30 ksi (207 MPa) at a test temperature of 593°C (1100°F), a vacancy supersaturation of approximately 1.6 can exist at the precipitate particle. Hull and Rimmer[29] calculated the growth rate of cavities on the basis of vacancy condensation on nonwetting particles.

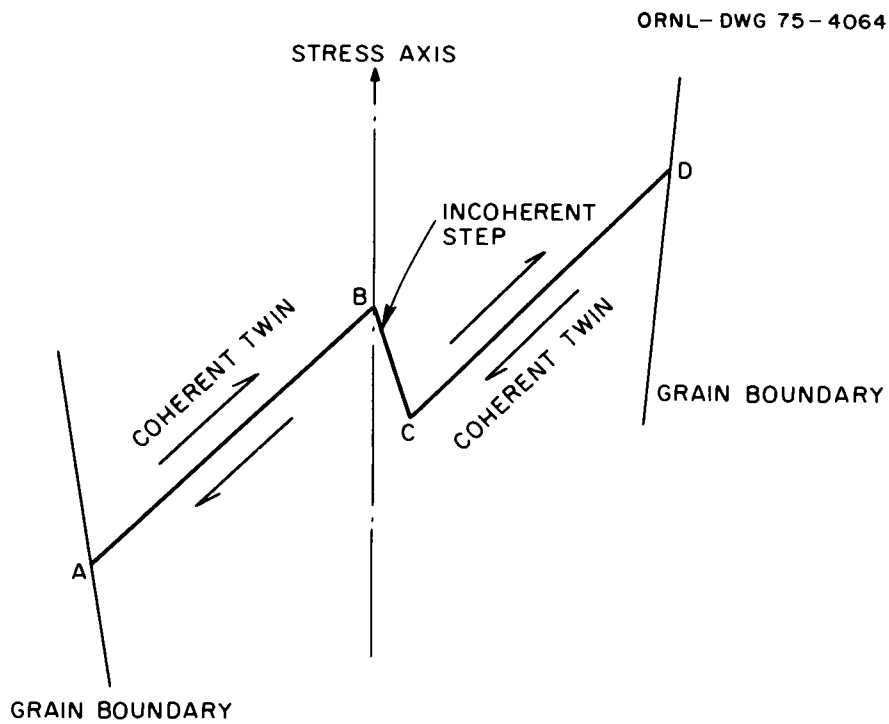

Fig. 3.56. Schematic Showing Possible Mechanism for Twin-Boundary Cracking.

3.2.3 Materials Behavior in Support of Development and Evaluation of Failure Criteria for Materials — M. K. Booker

Current elevated-temperature design rules contain specific stress limits for the prevention of failure due to time-dependent deformation.[32] These limits are obtained from (1) the stress to cause rupture in time t (rupture strength); (2) the stress to cause onset of tertiary creep in time t (stable creep strength); and (3) the stress to cause a total membrane strain (elastic, plastic, and creep) of 1% in time t. This last limit is due to the currently recommended 1% strain limit.

The fact that this strain limit is merely a broad, general value, not expressed as a function of temperature or stress, is caused by the scatter inherent in creep ductility data, which makes direct analysis difficult. Still, strain limits can be important,[33] and therefore should be addressed. Therefore, the objective of this effort is to explore and develop analytical expressions for correlating and extrapolating long-term ductility indices. An indirect parametric method, based on that suggested by Goldhoff,[34] for

analysis of creep ductility data was presented earlier, along with preliminary results.[35,36] This method also provides predictions for stress to rupture and stress to tertiary creep.

Briefly, the method for parametric analysis of creep ductility data consists of expressing a given ductility criterion as a product of a time and a creep rate. Then, each of these two quantities is separately treated by standard parametric techniques. Criteria currently being considered include:

$$\text{plasticity resource } e_s = \dot{e}_m t_r \ , \tag{25}$$

$$\text{engineering creep strain to tertiary creep } e_3 = \dot{e}_3 t_3 \ , \tag{26}$$

$$\text{true creep strain to tertiary creep } \varepsilon_3 = \dot{\varepsilon}_3 t_3 \ , \tag{27}$$

$$\text{total engineering creep elongation to rupture } e_T = \dot{e}_r t_r \ , \tag{28}$$

$$\text{true rupture ductility } \varepsilon_T = \dot{\varepsilon}_r t_r \ , \tag{29}$$

where $\dot{e}_m$ = minimum creep rate,
$\dot{e}_3$ = average engineering creep rate to tertiary creep,
$\dot{\varepsilon}_3$ = average true creep rate to tertiary creep,
$\dot{e}_r$ = average engineering creep rate to rupture,
$\dot{\varepsilon}_r$ = average true strain rate to rupture,
t_r = rupture life, and
t_3 = time to tertiary creep.

These quantities have been defined previously,[36] with one exception: ε_3 is the true creep strain to tertiary creep, and is therefore given by $\varepsilon_3^T - \varepsilon_l$, where ε_3^T is the total true strain to tertiary creep and ε_l is the true loading strain, since true strains are additive. Meanwhile, e_3 is calculated by $e_3^T - e_l$, although this relationship is not strictly valid since engineering strains are not additive. Therefore ε_3 is not given by 100 $\ln(1 + e_3)$ as reported in ref. 36, but rather by

$$\varepsilon_3(\%) = 100[\ln(1 + e_3 + e_l) - \ln(1 + e_l)] \ , \tag{30}$$

where e_3 = engineering creep strain to tertiary creep and

e_l = engineering loading strain.

These creep time and creep rate quantities may be treated by any one of a number of standard parametric techniques. Methods being used currently include the Orr-Sherby-Dorn,[37] Larson-Miller,[38] and Manson-Succop[39] time-temperature parameters, and the minimum commitment method.[40] These latter two methods are empirical, and therefore their applicability can be judged only by how well they describe a given data set. The first two, however, can be derived for rupture life from the Arrhenius rate equation,[41] and the assumption that

$$\dot{e}_m t_r = \text{constant} \ . \tag{31}$$

However, the present results show this assumption to be false, so it is probably better to view these methods as empirical as well. Therefore, application of these methods to quantities like $\dot{e}_3$, $\dot{\varepsilon}_3$, $\dot{e}_r$, $\dot{\varepsilon}_r$, etc. depends only on whether the predictions from the methods are consistent with the data. Results from the Orr-Sherby-Dorn (O-S-D) and Manson-Succop (M-S) methods will be presented here for types 304 and 316 austenitic stainless steels.

Table 3.8 summarizes the four heats of type 304 stainless steel and the heat of type 316 stainless steel being investigated. Partial results for the 1-in. (25-mm)[42] and 2-in. (51-mm)[43] plates of heat 9T2796 and the 0.275-in. (7.0-mm) rod[44] have been reported previously.[35,36] Note, however, that some results reported here for the 2-in. plate of heat 9T2796 and for heat 55697 are slightly different than those reported previously. These differences are because two questionable rupture life data points have been deleted for heat 55697, and 1 data point has been deleted and a new one added for the 2-in. plate of heat 9T2796.

Table 3.9 summarizes the results of the parametric analysis of the seven quantities under consideration: t_r, t_3, $\dot{e}_m$, $\dot{e}_3$, $\dot{\varepsilon}_3$, $\dot{\varepsilon}_r$, and $\dot{e}_r$.

Table 3.8. Characteristics of Materials Being Investigated

Heat	Ref.	Product Form	Content, wt %										
			C	Mn	P	S	Si	Cr	Ni	Co	Mo	Cu	N
			Type 304 Stainless Steel										
9T2796	42	1-in. plate	0.051	1.37	0.041		0.4	18.5	9.87	0.1	0.3	0.24	0.031
9T2796	43	2-in. plate	0.047	1.22	0.029	0.012	0.47	18.5	9.58	0.05	0.10	0.10	0.031
55697[a]	44	0.275-in. rod	0.052	1.1	0.011	0.01	0.52	18.92	9.52	0.035	0.12	0.10	0.052
8043813	45	1-in. plate	0.062	1.87	0.04	0.0043	0.48	17.8	8.95	0.20	0.32	0.20	0.033
ASTM A240, 479		Plate, rod	0.08[b]	2.0[b]	0.045[b]	0.03[b]	1.0[b]	17–19	8–10				
			Type 316 Stainless Steel										
332990	44	0.275-in. rod	0.052	1.72	0.012	0.02	0.38	17.8	13.55	0.14	2.33	0.20	0.041
ASTM A240, 479		Plate, rod	0.08[b]	2.0[b]	0.045[b]	0.03[b]	1.0[b]	16–18	10–14		2–3		

[a]Incorrectly reported as 3/8-in.-diam bar in ref. 36.

[b]Maximum permitted.

Table 3.9. Comparison of Orr-Sherby-Dorn and Manson-Succop[a] Correlations for the Quantities Involved in Calculating Failure Criteria for Types 304 and 316 Stainless Steel

Heat	Data Points Used	Optimized Constants		Sum of Squared Residuals[b]		Residual Mean Square[c]	
		O-S-D Q	M-S D	O-S-D	M-S	O-S-D	M-S
			Rupture Life, t_r				
9T2796 1 in.	58	1.874×10^4	−0.02094	0.784	1.636	0.0148	0.0309
9T2796 2 in.	20	2.0199	−0.024694	0.17813	0.21701	0.0119	0.0145
55697	42	1.7236	−0.023054	0.85159	0.84874	0.0230	0.0229
8043813	24	2.6709	−0.029226	0.45176	1.0466	0.0238	0.0551
332990	39	1.9852	−0.025079	0.80472	0.79418	0.0237	0.0234
			Time to Tertiary Creep, t_3				
9T2796 1 in.	63	1.8711×10^4	−0.020898	1.9527	3.3078	0.0337	0.0570
9T2796 2 in.	20	2.1089	−0.02583	0.53213	0.55371	0.0355	0.0369
55697	38	1.852	−0.024636	1.3005	1.4363	0.0394	0.0435
8043813	23	2.7752	−0.030142	0.54927	1.1491	0.0305	0.0638
332990	38	2.0788	−0.025914	0.96756	1.2094	0.0366	0.0366
			Minimum Creep Rate, $\dot{e}_m$				
9T2796 1 in.	58	-2.3857×10^4	0.026231	1.7795	5.4315	0.0336	0.1025
9T2796 2 in.	20	−2.7036	0.032933	0.48395	0.61949	0.0323	0.0413
55697	42	−2.3224	0.031067	0.8524	0.83727	0.0230	0.0226
8043813	24	−3.2695	0.035578	1.396	2.7945	0.0735	0.1471
332990	39	−2.5629	0.032003	0.79071	1.7551	0.0233	0.0516
			Average Engineering Creep Rate to Tertiary Creep, $\dot{e}_3$				
9T2796 1 in.	63	-2.3203×10^4	0.025716	1.256	4.6047	0.0217	0.0794
9T2796 2 in.	20	−2.8333	0.034506	0.32481	0.47696	0.0217	0.0318
55697	38	−2.2075	0.029408	0.72616	0.79615	0.0220	0.0241
8043813	23	−3.1262	0.033763	1.14	2.347	0.0633	0.1304
332990	38	−2.5398	0.031442	0.91896	1.8133	0.0278	0.0549
			Average True Creep Rate to Tertiary Creep, $\dot{\varepsilon}_3$				
9T2796 1 in.	63	-2.2705×10^4	0.02491	1.0849	3.8961	0.0187	0.0672
9T2796 2 in.	20	−2.8157	0.034293	0.32384	0.47368	0.0216	0.0316
55697	38	−2.195	0.02924	0.71469	0.78888	0.0217	0.0239
8043813	23	−3.1023	0.033512	1.0854	2.2592	0.0603	0.1255
332990	38	−2.5207	0.031213	0.86141	1.7238	0.0261	0.0522
			Average True Strain Rate to Rupture, $\dot{\varepsilon}_T$				
9T2796 1 in.	52	-2.121×10^4	0.023383	1.0034	2.4818	0.0213	0.0528
9T2796 2 in.	20	−2.4606	0.030088	0.46103	0.51561	0.0307	0.0344
8043813	24	−2.9813	0.32503	0.83046	1.8504	0.0437	0.0974
			Average Engineering Creep Rate to Rupture, $\dot{e}_T$				
9T2796 1 in.	58	-2.1968×10^4	0.024275	0.76324	2.697	0.0144	0.0509
9T2796 2 in.	20	−2.721	0.033248	0.36576	0.44576	0.0244	0.0297
55697	41	−2.222	0.029744	1.6613	1.5635	0.0461	0.0423
8043813	24	−3.0723	0.033483	0.75182	1.8646	0.0396	0.0981
332990	37	−2.4753	0.031204	1.7053	2.2016	0.0533	0.0688

[a] O-S-D = Orr-Sherby-Dorn; M-S = Manson Succop.

[b] Sum of squared residuals ; $\Sigma(\log y\text{calc.} - \log y\text{exp.})^2 = \Sigma R^2$

[c] Residual mean = $\Sigma R^2/(n-\nu)$ where n = number of data points, ν = number of degrees of freedom of model. Here $\nu = 5$.

Several features are immediately obvious from Table 3.9. First, the results confirm that the current analysis is indeed valid in that parametric methods do give satisfactory correlation of all quantities involved. In fact, all quantities can be correlated with practically equal precision, although in a few cases the M-S results are relatively poor. The residual mean squares given in Table 3.9 are expressed in terms of the logarithms of the predicted quantities for two reasons: (1) the models used are expressed in terms of logarithms, and (2) using logarithms makes the absolute values of all seven quantities approximately the same. Therefore, comparisons can be made among the various residual mean squares, even though they have not been corrected for the mean values of the data involved. Second, the O-S-D results are better in almost every case and are never significantly worse on the basis of the residual mean squares. (Note: for purposes of the present investigation, the major criterion for "fitting" the data is that the predicted isothermals "go through" the experimental data. For design purposes, this criterion is probably sufficient, since it guarantees that predicted values will approximate real values. However, subtle inflections, "dips," etc. in the experimental isothermals would probably not be well described by the current parametric techniques, which tend to yield only smooth isothermals with slowly changing slopes. Even the use of a cubic log stress dependence, as done here, would probably not prevent this shortcoming, and indications that it does exist, at least for the 1-in. plate of heat 9T2796, have been reported.[42]) Finally, the variations in the so-called optimized constants for the two parameters support the contention that these constants have no real physical meaning, but are merely regression constants. This result is not unexpected for the M-S parameter, but Q in the O-S-D parameter is supposedly related to an activation energy (in this case, the O-S-D activation energy would be $4.6Q$ as a result of the form of the parameter used here). Activation energies calculated from the O-S-D results are indeed of reasonable magnitudes, but the variations in these energies show no consistent trends. Furthermore, (1) the quantities involved here ($\dot{e}_r$, $\dot{\varepsilon}_r$, $\dot{e}_3$, etc.) are of such a nature that the meaning of an activation energy in most cases is unclear, and (2) each "optimized constant" is but one of five

regression constants involved in fitting the models to the data. After Manson and Mendelson,[46] the models are expressed as

$$\text{(O-S-D)}\ \log y - Q/RT = b_0 + b_1 \log \sigma + b_2(\log \sigma)^2 + b_3(\log \sigma)^3 \ , \quad (32)$$

$$\text{(M-S)}\ \log y + DT = a_0 + a_1 \log \sigma + a_2(\log \sigma)^2 + a_3(\log \sigma)^3 \ . \quad (33)$$

Least squares fits of these models to the data force an intermingling of the effects of the constants involved, which makes it difficult to give physical meaning to any one.

Table 3.10 summarizes the results obtained for 10^4- and 10^5-hr creep-rupture strengths and stable creep strengths of the materials under investigation.

The table is self-explanatory, but a few comments are warranted.

1. Both plates of heat 9T2796 and the rod of 55697 are of similar strength, while heat 8043813 is relatively strong[45] for type 304 stainless steel. These results are in agreement with findings of the ORNL heat-to-heat variation program.[42,47]

2. Heat 332990 of type 316 stainless steel,[44] as expected, displays better strength than most of the type 304 stainless steel, although it has about the same strength as heat 8043813. The type 316 stainless steel data from Garofalo et al.[48] will be analyzed next quarter.

3. For heat 9T2796 long-term predictions that the stable creep strength is greater than the rupture strength, while unrealistic, reflect the data in that long-term tests indicate an increase in t_3 as a fraction of t_r for these two heats. This increase forces the unexpected behavior of the predicted isothermals.

Figure 3.57 shows the 10^5-hr rupture strength for type 304 stainless steel in comparison with the results given by Smith[49] and the minimum values[32] from Code Case 1592.

Figures 3.58 through 3.63 illustrate the calculations of the creep times and creep rates that go into the formulation of the various ductility criteria being considered. Several explanations of the data used are necessary. These include:

Table 3.10. Predicted Creep-Rupture Strengths and Stable Creep Strengths for Types 304 and 316 Stainless Steel

Temperature (°C)	Temperature (°F)	Prediction Method[a]	10^4-hr Strength, ksi(MPa) Creep Rupture	10^4-hr Strength, ksi(MPa) Stable Creep	10^5-hr Strength, ksi(MPa) Creep Rupture	10^5-hr Strength, ksi(MPa) Stable Creep
		Heat 9T2796 1-in. (25-mm) Plate Type 304				
538	1000	O-S-D	25.8(178)	24.3(168)	19.1(131)	17.4(120)
		M-S	23.0(159)	21.4(148)	16.7(115)	15.1(104)
593	1100	O-S-D	16.4(113)	14.8(102)	11.5(79)	10.3(71)
		M-S	15.8(109)	14.3(99)	11.4(79)	10.2(70)
649	1200	O-S-D	10.2(70)	9.2(63)	7.0(48)	6.6(46)
		M-S	10.7(74)	9.7(67)	7.6(52)	7.1(49)
704	1300	O-S-D	6.7(46)	6.4(44)	4.7(32)	4.8(33)
		M-S	7.3(50)	6.8(47)	5.2(36)	5.2(36)
		Heat 9T2796 2-in. (51-mm) Plate Type 304				
538	1000	O-S-D	26.1(180)	26.1(180)	19.2(132)	18.9(130)
		M-S	24.3(168)	24.2(167)	17.6(121)	17.1(118)
593	1100	O-S-D	15.8(109)	14.8(102)	11.2(77)	10.7(74)
		M-S	15.7(108)	14.7(101)	11.3(78)	10.8(74)
649	1200	O-S-D	9.8(68)	9.4(65)	7.4(51)	7.6(52)
		M-S	10.0(69)	9.6(66)	7.6(52)	7.8(54)
704	1300	O-S-D	7.0(48)	7.3(50)	5.5(38)	6.2(43)
		M-S	7.0(48)	7.3(50)	5.6(39)	6.3(43)
		Heat 55697 0.275-in. (7.0-mm) Rod Type 304				
538	1000	O-S-D	26.4(182)	25.8(178)	19.2(132)	17.3(119)
		M-S	26.1(180)	25.4(175)	19.2(132)	17.2(119)
593	1100	O-S-D	17.0(117)	13.9(96)	11.6(80)	8.7(60)
		M-S	17.6(121)	14.7(101)	12.6(89)	9.6(66)
649	1200	O-S-D	10.7 (74)	7.8(54)	7.1(49)	5.7(39)
		M-S	11.4(79)	8.4(58)	8.3(57)	6.2(43)
		Heat 8043813 1-in. (25-mm) Plate Type 304				
538	1000	O-S-D	38.9(268)	38.2(263)	32.6(225)	32.0(221)
		M-S	35.6(245)	34.8(240)	28.5(196)	27.7(191)
593	1100	O-S-D	26.1(180)	25.2(174)	20.6(142)	19.9(137)
		M-S	24.8(171)	23.7(163)	19.8(137)	18.9(130)
649	1200	O-S-D	16.6(114)	15.6(108)	12.9(89)	11.8(81)
		M-S	17.3(119)	16.4(113)	14.3(99)	13.7(94)
704	1300	O-S-D	11.1(77)	9.8(68)	8.9(61)	7.5(52)
		M-S	12.9(89)	12.3(85)	11.1(77)	10.6(73)
		Heat 332990 0.275-in. (7.0-mm) Rod Type 316				
538	1000	O-S-D	37.0(255)	35.5(245)	28.8(199)	27.2(188)
		M-S	35.4(244)	33.6(232)	28.0(193)	26.2(181)
593	1100	O-S-D	24.8(171)	22.7(157)	18.6(128)	16.8(116)
		M-S	25.6(177)	23.6(163)	20.1(139)	18.4(127)
649	1200	O-S-D	16.4(113)	14.6(101)	11.4(79)	10.4(72)
		M-S	18.1(125)	16.3(112)	13.6(94)	12.2(84)
704	1300	O-S-D	10.3(71)	9.5(66)	b	6.6(46)
		M-S	11.9(82)	10.7(74)	b	7.0(48)

[a]O-S-D = Orr-Sherby-Dorn; M-S = Manson-Succop.

[b]Not available.

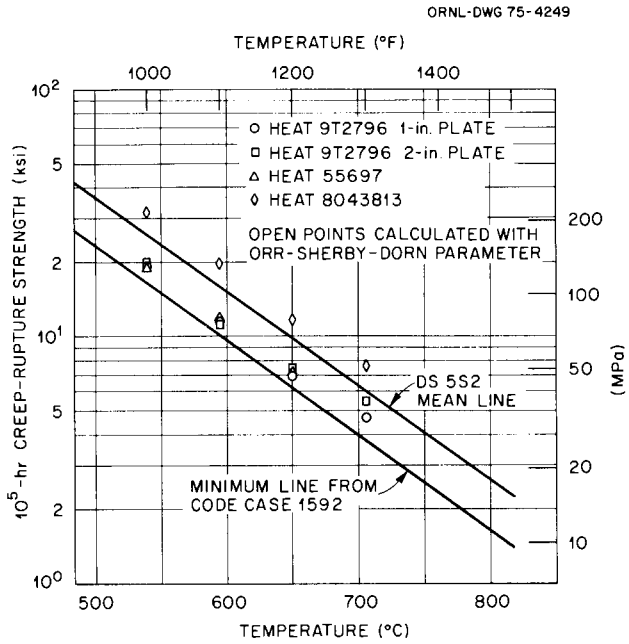

Fig. 3.57. Comparison of Predicted Creep-Rupture Strengths for Type 304 Stainless Steel with Results from DS 5S2 and Code Case 1592.

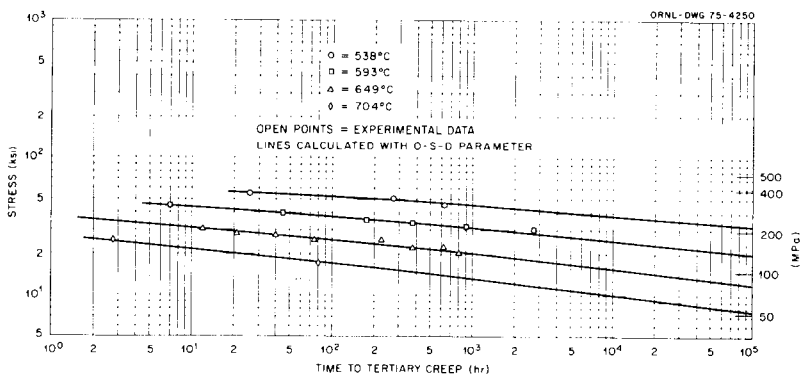

Fig. 3.58. Time to Tertiary Creep for Type 304 Stainless Steel Heat 8043813.

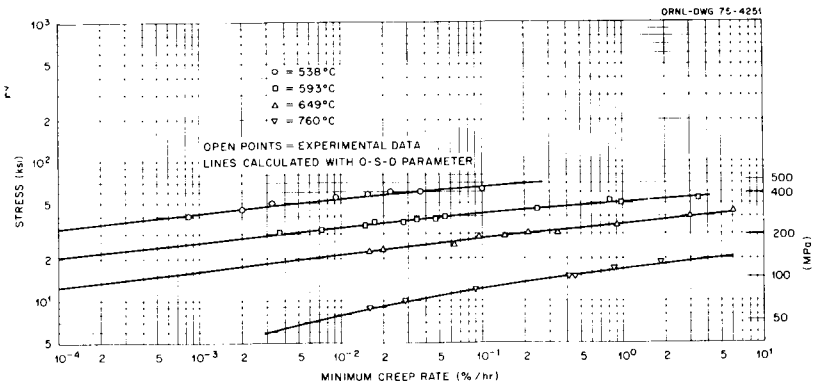

Fig. 3.59. Stress-Minimum Creep Rate Isothermals for Type 316 Stainless Steel Heat 332990.

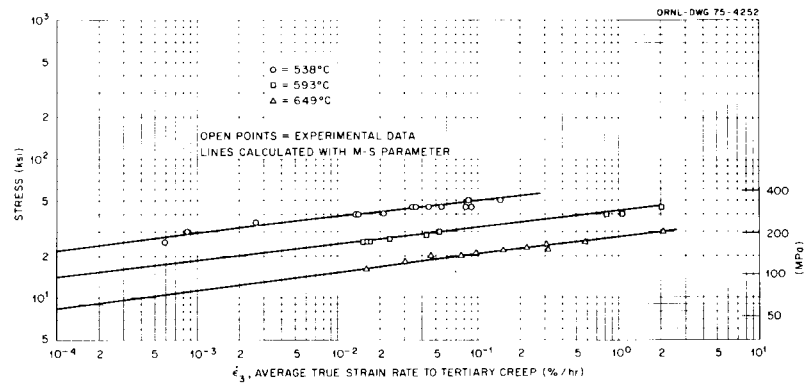

Fig. 3.60. Average True Strain Rate to Tertiary Creep Isothermals for Type 304 Stainless Steel Heat 55697.

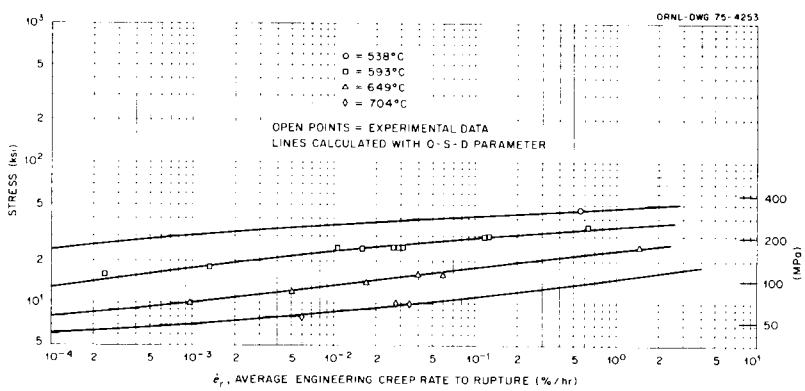

Fig. 3.61. Average Engineering Creep Rate to Rupture Isothermals for Type 304 Stainless Steel Heat 9T2796 2-in. (51-mm) Plate.

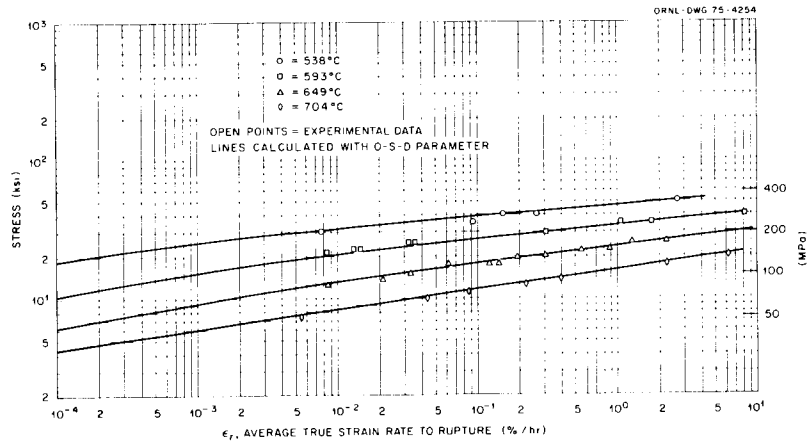

Fig. 3.62. Average True Strain Rate to Rupture Isothermals for Type 304 Stainless Steel Heat 9T2796, 1-in. (25-mm) Plate.

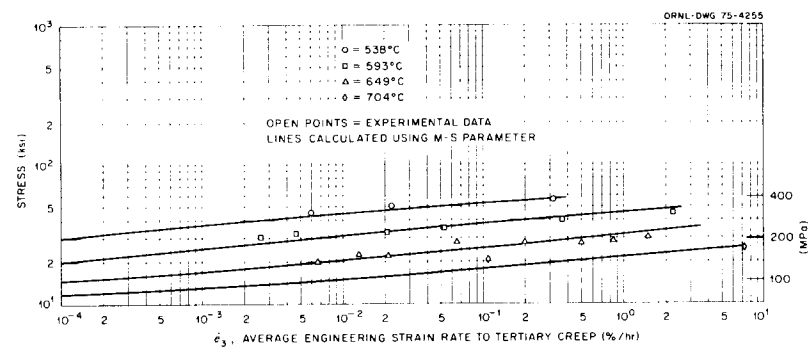

Fig. 3.63. Average Engineering Strain Rate to Tertiary Creep Isothermals for Type 304 Stainless Steel Heat 8043813.

Heat 9T2796, 1- and 2-in. plate, heat 8043813 — onset of tertiary creep determined by 0.2% offset method.

Heat 55697, heat 332990, onset of tertiary creep determined by first deviation from linear secondary creep line.

Representative plots of the various ductility correlations are shown in Figs. 3.64 through 3.68. As expected, the data show considerable scatter. The decrease in scatter obtained by plotting creep times and creep rates separately rather than plotting creep ductility directly is considerable. In reality, the creep rates involved are nothing more than ductility values normalized to time. Therefore, it is seen that the

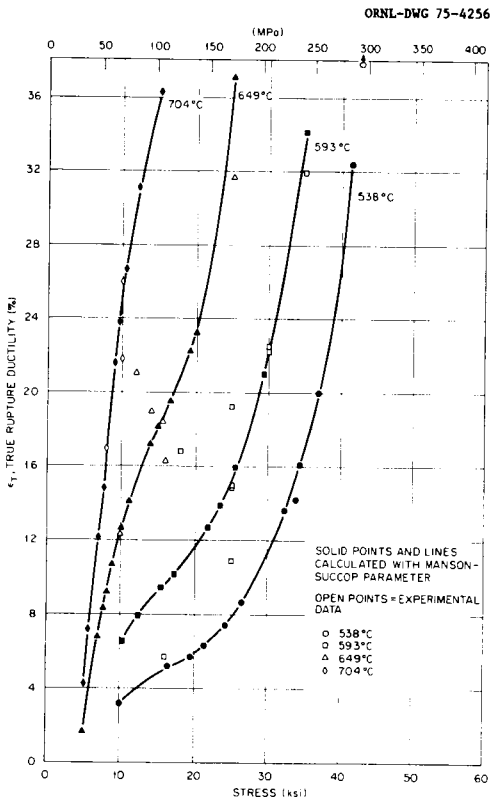

Fig. 3.64. True Rupture Ductility Versus Stress for Type 304 Stainless Steel Heat 9T2796 2-in. (51-mm) Plate.

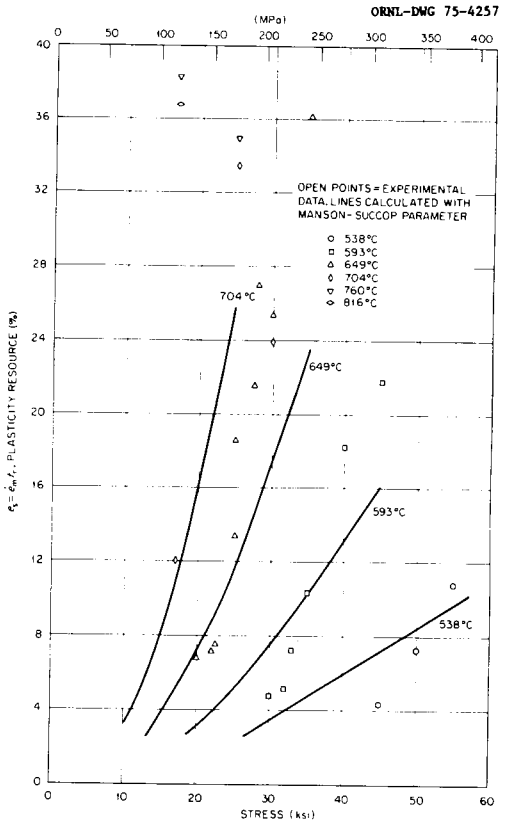

Fig. 3.65. Plasticity Resource Versus Stress for Type 304 Stainless Steel Heat 8043813.

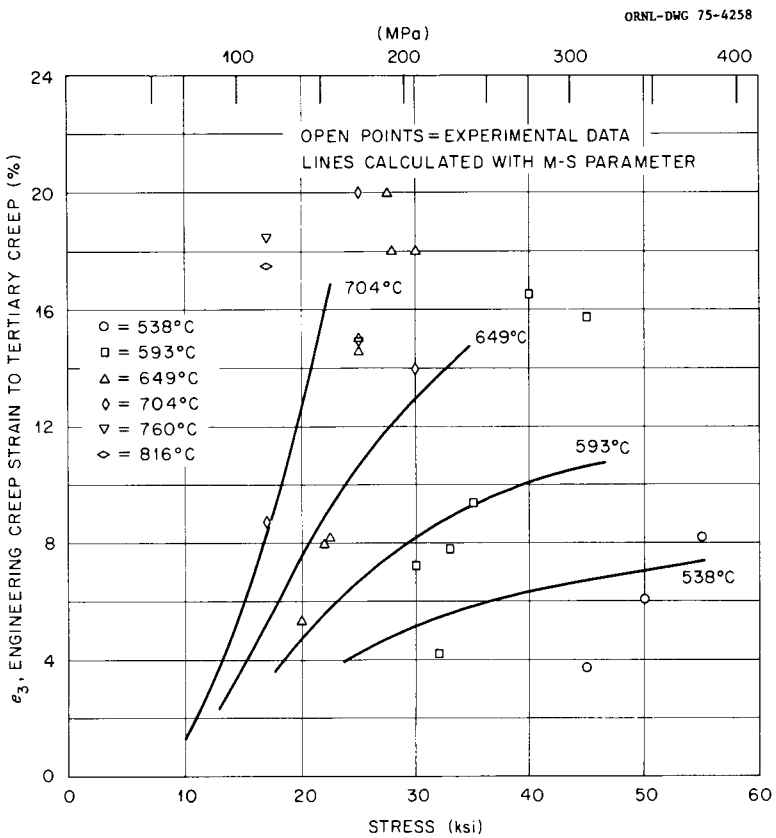

Fig. 3.66. Engineering Creep Strain to Tertiary Creep Versus Stress for Type 304 Stainless Steel, Heat 8043813.

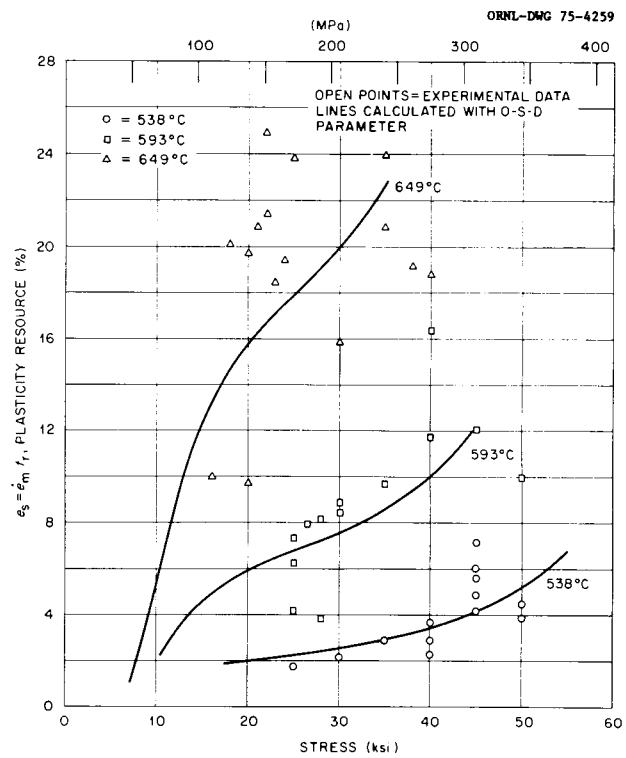

Fig. 3.67. Plasticity Resource Versus Stress for Type 304 Stainless Steel, Heat 55697 0.275-in. (7.0-mm) Rod.

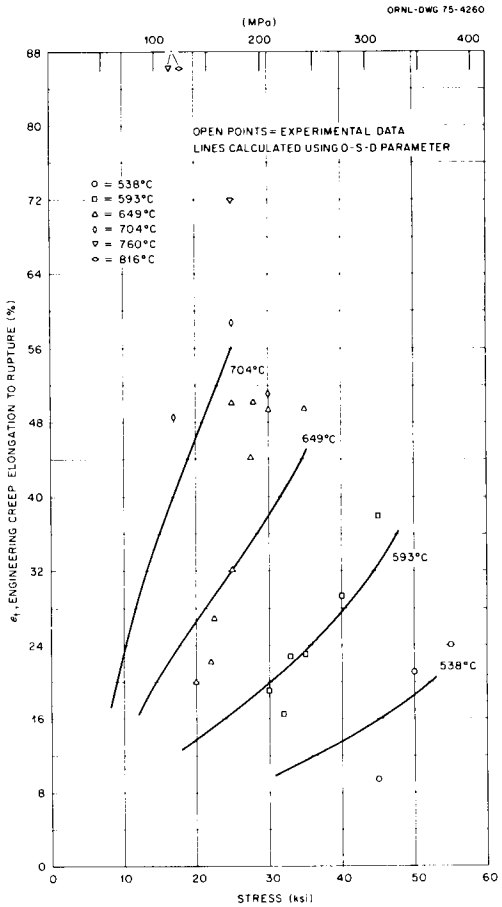

Fig. 3.68. Engineering Creep Elongation to Rupture Versus Stress for Type 304 Stainless Steel, Heat 8043813.

scatter commonly seen in ductility data is largely related simply to variations in rupture time or time to tertiary creep, as the case may be. From this viewpoint, the current parametric method for the estimation of creep ductility has even greater validity. Indeed, the calculated values obtained from the parametric analysis method do seem to describe general trends in the data. These trends, while somewhat difficult to describe in a precise quantitative manner, are nonetheless clear. In general, one can say that for types 304 and 316 austenitic stainless steels, ductility increases with increasing temperature and/or uniaxial stress level, especially in the range 538 to 704°C (1000—1300°F). Furthermore, these trends are evident for all five criteria studied. Tables 3.11 through 3.14 summarize the 10^2-, 10^3-, 10^4-, and 10^5-hr creep ductility predictions for

Table 3.11. Plasticity Resource for Types 304 and 316 Stainless Steel

Temperature (°C)	Temperature (°F)	Prediction Method[a]	Predicted Plasticity Resource, %, for Rupture Time 10^2hr	10^3hr	10^4hr	10^5hr
		Heat 9T2796 1-in. (25-mm) Plate Type 304				
538	1000	O-S-D	2.58	2.43	2.21	1.90
		M-S	2.65	2.97	2.95	2.62
593	1100	O-S-D	5.88	5.21	4.36	3.41
		M-S	5.85	5.71	4.98	3.96
649	1200	O-S-D	11.34	9.29	7.13	5.20
		M-S	11.12	9.54	7.47	5.50
704	1300	O-S-D	18.44	14.02	10.18	7.29
		M-S	18.06	13.99	10.24	7.34
		Heat 9T2796 2-in. (51-mm) Plate Type 304				
538	1000	O-S-D	1.50	1.48	1.26	0.92
		M-S	1.63	1.70	1.46	1.05
593	1100	O-S-D	4.70	3.66	2.55	1.84
		M-S	4.67	3.73	2.60	1.85
649	1200	O-S-D	9.57	6.61	5.08	4.81
		M-S	9.48	6.52	4.89	4.43
704	1300	O-S-D	16.01	12.86	12.80	15.37
		M-S	16.41	13.08	12.76	15.00
		Heat 55697 0.275-in. (7.0-mm) Rod Type 304				
538	1000	O-S-D	4.04	2.91	2.38	2.00
		M-S	4.07	2.96	2.44	2.01
593	1100	O-S-D	7.89	6.64	5.37	3.05
		M-S	7.69	6.43	5.14	3.06
649	1200	O-S-D	16.89	13.11	6.52	1.29
		M-S	17.18	12.95	6.74	2.00
		Heat 8043813 1-in. (25-mm) Plate Type 304				
538	1000	O-S-D	8.85	6.41	4.41	2.87
		M-S	8.93	6.84	4.80	3.09
593	1100	O-S-D	12.51	8.10	4.96	2.94
		M-S	12.47	8.30	5.13	3.09
649	1200	O-S-D	13.92	8.25	4.93	3.18
		M-S	13.93	8.42	5.13	3.27
704	1300	O-S-D	13.76	8.56	5.96	4.54
		M-S	13.87	8.67	5.72	3.98
		Heat 332990 0.275-in. (7.0-mm) Rod Type 316				
538	1000	O-S-D	3.24	3.25	2.90	2.35
		M-S	3.28	3.73	3.39	2.70
593	1100	O-S-D	8.77	7.40	5.71	4.09
		M-S	8.81	7.57	5.82	4.16
649	1200	O-S-D	17.16	12.83	8.97	6.04
		M-S	16.80	12.50	8.72	5.85
704	1300	O-S-D	26.93	18.62	12.53	b
		M-S	26.38	18.08	12.05	b

[a]O-S-D = Orr-Sherby-Dorn; M-S = Manson-Succop.

[b]Not available.

Table 3.12. Engineering Creep Strain to Tertiary Creep for Types 304 and 316 Stainless Steel

Temperature (°C)	Temperature (°F)	Prediction Method[a]	Predicted Strain, %, for Time to Tertiary Creep 10^2hr	10^3hr	10^4hr	10^5hr
		Heat 9T2796 1-in. (25-mm) Plate Type 304				
538	1000	O-S-D	2.68	2.26	1.79	1.37
		M-S	2.71	2.54	2.10	1.66
593	1100	O-S-D	4.59	3.56	2.74	2.30
		M-S	4.57	3.74	2.95	2.48
649	1200	O-S-D	6.75	5.28	4.65	4.90
		M-S	6.68	5.30	4.54	4.45
704	1300	O-S-D	9.67	8.71	9.41	12.04
		M-S	9.47	8.26	8.28	9.70
		Heat 9T2796 2-in. (51-mm) Plate Type 304				
538	1000	O-S-D	1.08	1.37	1.17	0.59
		M-S	1.25	1.64	1.30	0.60
593	1100	O-S-D	4.82	2.92	1.27	0.92
		M-S	4.80	2.94	1.30	0.92
649	1200	O-S-D	6.27	3.17	3.28	5.96
		M-S	6.20	3.12	3.01	5.02
704	1300	O-S-D	8.22	10.30	20.98	56.67
		M-S	8.49	10.63	20.87	54.24
		Heat 55697 0.275-in. (7.0-mm) Rod Type 304				
538	1000	O-S-D	3.20	4.52	3.81	1.46
		M-S	3.26	4.59	3.77	1.44
593	1100	O-S-D	8.60	5.25	1.46	0.57
		M-S	8.45	5.37	1.62	0.55
649	1200	O-S-D	6.80	1.73	0.97	1.60
		M-S	6.77	1.82	0.87	1.02
		Heat 8043813 1-in. (25-mm) Plate Type 304				
538	1000	O-S-D	7.03	6.16	5.29	4.39
		M-S	7.12	6.56	5.82	4.78
593	1100	O-S-D	9.68	7.95	6.10	4.16
		M-S	9.65	8.17	6.25	4.24
649	1200	O-S-D	10.92	7.51	4.33	1.98
		M-S	10.98	7.72	4.87	2.85
704	1300	O-S-D	8.58	4.23	1.63	0.51
		M-S	9.11	5.45	3.08	1.69
		Heat 332990 0.275-in. (7.0-mm) Rod Type 316				
538	1000	O-S-D	2.60	2.78	2.34	1.65
		M-S	3.26	4.59	3.77	1.44
593	1100	O-S-D	5.86	4.38	2.92	2.09
		M-S	8.45	5.37	1.62	0.55
649	1200	O-S-D	7.71	5.12	3.82	4.16
		M-S	6.77	1.82	0.87	1.02
704	1300	O-S-D	8.86	7.11	9.09	27.92
		M-S	2.29	1.55	2.29	5.43

[a]O-S-D = Orr-Sherby-Dorn; M-S = Manson-Succop.

Table 3.13. True Rupture Ductility for Types 304 and 316 Stainless Steel

Temperature (°C)	Temperature (°F)	Prediction Method	Predicted Strain (%) for Rupture Time 10^2hr	10^3hr	10^4hr	10^5hr
		Heat 9T2796 1-in. (25-mm) Plate Type 304				
538	1000	O-S-D	32.54	20.56	14.82	12.14
		M-S	32.48	20.45	15.69	13.69
593	1100	O-S-D	27.18	20.83	17.95	16.30
		M-S	27.22	21.37	18.86	17.10
649	1200	O-S-D	29.39	26.00	23.42	18.44
		M-S	29.26	26.11	23.54	19.18
704	1300	O-S-D	36.41	32.50	24.75	13.88
		M-S	36.00	32.23	26.63	15.93
		Heat 9T2796 2-in. (51-mm) Plate Type 304				
538	1000	O-S-D	33.68	14.27	7.46	4.95
		M-S	32.39	13.64	7.46	5.22
593	1100	O-S-D	21.04	12.64	9.39	7.30
		M-S	21.08	12.69	9.44	7.26
649	1200	O-S-D	22.31	17.37	12.85	7.67
		M-S	22.32	17.26	12.74	7.78
704	1300	O-S-D	30.48	21.64	12.21	5.51
		M-S	31.12	21.67	12.24	5.61
		Heat 8043813 1-in. (25-mm) Plate Type 304				
538	1000	O-S-D	62.34	46.14	35.61	28.64
		M-S	62.21	46.56	37.10	31.07
593	1100	O-S-D	60.98	49.22	40.91	33.86
		M-S	60.98	50.25	42.58	35.26
649	1200	O-S-D	69.08	57.36	44.91	30.82
		M-S	68.98	57.95	46.25	34.35
704	1300	O-S-D	76.94	55.83	34.46	18.03
		M-S	77.14	58.96	41.95	28.06

Table 3.14. Total Engineering Creep Strain to Rupture for Types 304 and 316 Stainless Steel

Temperature (°C)	Temperature (°F)	Prediction Method[a]	Predicted Strain, %, in Rupture Time 10^2hr	10^3hr	10^4hr	10^5hr
		Heat 9T2796 1-in. (25-mm) Plate Type 304				
538	1000	O-S-D	7.98	7.15	6.73	6.55
		M-S	7.98	7.95	8.13	8.19
593	1100	O-S-D	12.44	11.94	11.66	10.90
		M-S	12.34	12.62	12.62	11.69
649	1200	O-S-D	20.05	19.49	17.63	13.46
		M-S	19.74	19.57	17.80	14.05
704	1300	O-S-D	30.57	27.16	20.10	11.75
		M-S	30.06	26.88	20.68	13.06
		Heat 9T2796 2-in. (51-mm) Plate Type 304				
538	1000	O-S-D	10.75	4.32	2.18	1.41
		M-S	10.57	4.33	2.34	1.60
593	1100	O-S-D	9.95	5.82	4.21	3.09
		M-S	9.94	5.90	4.27	3.07
649	1200	O-S-D	15.50	11.64	7.96	4.16
		M-S	15.47	11.49	7.78	4.16
704	1300	O-S-D	29.06	18.81	9.19	3.45
		M-S	30.16	18.93	9.21	3.52
		Heat 55697 0.275-in. (7.0-mm) Rod Type 304				
538	1000	O-S-D	6.24	5.18	5.66	5.83
		M-S	6.26	5.27	5.79	5.81
593	1100	O-S-D	12.85	14.51	12.60	3.10
		M-S	12.40	13.95	12.35	4.28
649	1200	O-S-D	32.90	24.42	3.79	0.02
		M-S	33.59	24.49	5.63	0.24
		Heat 8043813 1-in. (25-mm) Plate Type 304				
538	1000	O-S-D				
		M-S	20.41	17.00	14.26	11.96
593	1100	O-S-D	20.32	16.20	13.01	10.53
		M-S	26.18	21.98	18.35	15.05
649	1200	O-S-D	26.31	21.31	17.36	14.16
		M-S	33.97	28.07	22.70	17.96
704	1300	O-S-D	34.06	27.79	22.50	17.85
		M-S	42.42	33.84	26.48	20.40
		Heat 332990 0.275-in. (7.0-mm) Rod Type 316				
538	1000	O-S-D	5.76	6.46	6.66	6.36
		M-S	5.78	7.29	7.59	7.02
593	1100	O-S-D	16.31	16.12	14.71	12.28
		M-S	16.37	16.22	14.45	11.79
649	1200	O-S-D	35.17	31.05	24.90	17.30
		M-S	34.53	29.65	23.40	16.85
704	1300	O-S-D	60.34	47.25	31.36	0.00
		M-S	59.52	45.47	31.30	0.00

[a]O-S-D = Orr-Sherby-Dorn; M-S = Manson-Succop.

five criteria for the six heats used, as calculated with the Orr-Sherby-Dorn and Larson-Miller parameters. (The behavior of ε_3 is in every case the same as that of e_3. Therefore, only the more familiar quantity will be discussed henceforth.)

As can be seen from the tables, ductility often also tends to decrease as a function of rupture time or time to tertiary creep. This effect is, of course, because lower stresses give longer lives. However, the temperature dependence is somewhat clouded since higher temperatures correspond to lower stresses for given lives. Thus the data in Tables 3.11 through 3.14, while at constant lives, correspond to different stresses for different temperatures. Still, for design purposes, it is desirable to know how much strain a component can endure in a given time. Figure 3.69 illustrates the variation of predicted 10^5-hr creep ductility with temperature, while Fig. 3.70 illustrates the variation in the 20-ksi (138-MPa) creep ductility.

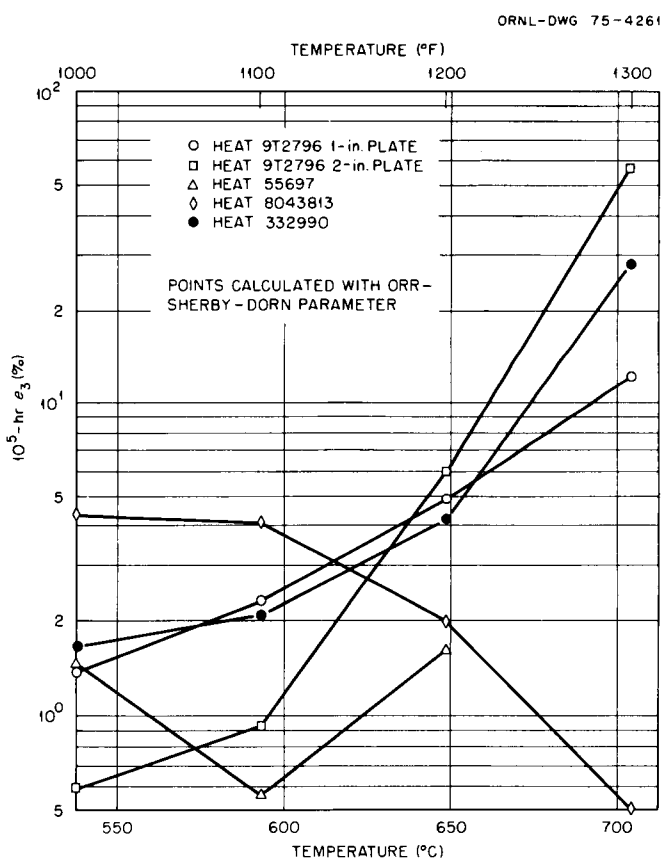

Fig. 3.69. Variation of 10^5-hr Creep Strain to Tertiary Creep with Temperature for Types 304 and 316 Stainless Steel.

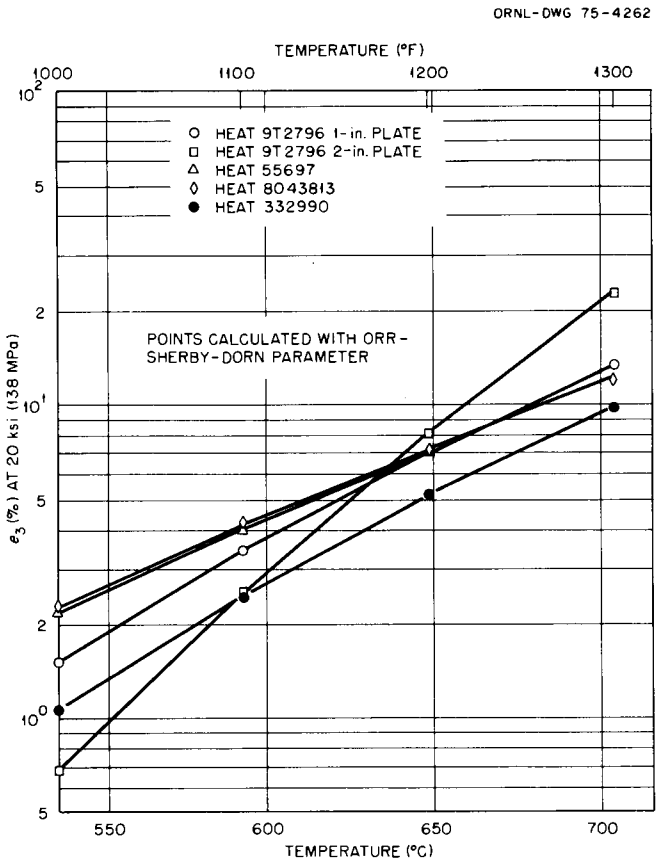

Fig. 3.70. Variation of Creep Strain to Tertiary Creep with Temperature at 20-ksi (138-MPa) Creep Stress for Types 304 and 316 Stainless Steel.

Despite isolated instances of erratic predictions (especially for heats 332990 and 55697), the calculated ductility values are reasonable and consistent for each of the individual heats. An analysis of the variations among the different heats is now under way and will be presented in a later report. Perhaps more important, however, is the question of how to use such results in an evaluation of possible design strain limits. Clearly, the variations in the data are dangerously large, but the creep rate and creep time isothermals are quite smooth. Thus, a method for estimating lower limits on ductility is suggested as follows. It has been shown that

$$\text{Ductility} = \text{creep rate} \times \text{creep time} \ , \qquad (34)$$

for various ductilities, rates and times. Moreover, since the creep rates and creep times that make up the ductility criteria form smooth

isothermals, lower limits can be set on each of these quantities, say t_D and $\dot{e}_D$. Thus, a design ductility prediction could be made by

$$\text{Ductility}_{\text{design}} = t_D \times \dot{e}_D \ .$$

Application of this approach is now under way, and results should be available soon.

One of the major problems involved in evaluating time-dependent behavior is the lack of data. The presently reported data sets were chosen specifically for completeness, but in general only rupture life and, to a lesser extent, minimum creep rate have been available in the past. This situation probably reflects earlier design rules, which required the stress to cause rupture in 10^5 hr and the stress to cause a minimum creep rate of 10^{-5}/hr as design limits. However, perhaps because of the advent of the high-temperature LMFBR, elevated-temperature design rules are now more specific in their application to time-dependent behavior, as discussed above. Thus, more specific data are suddenly needed. One way to improve this situation would be to find expressions for less available quantities in terms of more available quantities. For instance, time to tertiary creep may be formulated[47,50] as a function of rupture life by use of a relationship of the form

$$t_3 = A t_r^{\beta} \ , \tag{35}$$

where A and β are constants. Values of A and β determined for types 304 and 316 stainless steel are shown in Table 3.15, while Figs. 3.71 and 3.72 illustrate the relationship, including upper and lower central tolerance limits.[51] Meanwhile, time to tertiary creep has also been treated by standard parametric techniques, and the independent parametric predictions for t_3 and t_r agree well with the relationship given in Eq. (35).

Creep ductility data are probably the scarcest of all. In fact, one major advantage of the use of e_s as a ductility criterion is simply that data for t_r and $\dot{e}_m$ are available. (Although the meaning of e_s is unclear, it can still be useful for comparisons etc.) Thus, it would be extremely

Table 3.15. Constants for the Tertiary Creep Relationship $t_3 = At_r^{\beta}$

Stainless Steel Type	Constants	
	A	β
304[a]	0.752	0.977
304	0.685	0.968
316	0.526	1.004

[a]Onset of tertiary creep defined by 0.2% offset method. Otherwise, onset of tertiary creep is defined by first deviation from linear secondary creep.

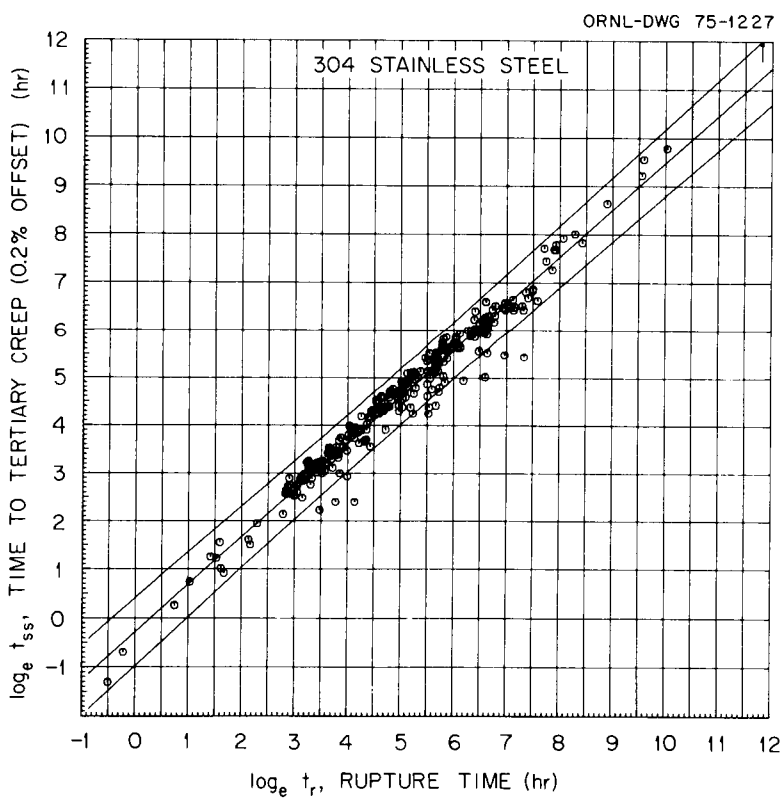

Fig. 3.71. Time to Tertiary Creep (0.2% Offset) as a Function of Rupture Time for Type 304 Stainless Steel.

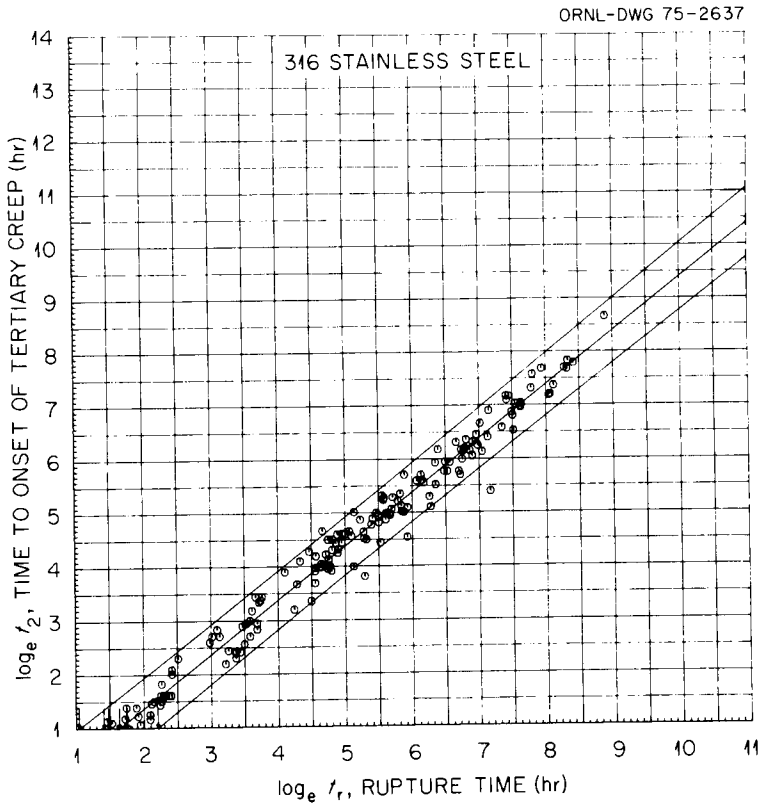

Fig. 3.72. Time to Tertiary Creep as a Function of Rupture Time for Type 316 Stainless Steel.

useful to be able to express other ductility criteria in terms of e_s or other available quantities. In this vein, a relationship of the type

$$e_s = t_r^{1-\beta}(e_3 - e_t)/A \ , \tag{36}$$

has been derived.[36] Here A and β are the same as in Eq. (35), and e_t is the creep strain to secondary creep (primary creep strain); (e_t does *not* include loading strain, and is incorrectly shown in Fig. 3.53 of ref. 36.)

Unfortunately, this equation has two unknowns, e_3 and e_t, and therefore can predict neither. However, it does provide a method for estimating $e_3 - e_t$, henceforth to be referred to as e_2, the "secondary creep strain". Rewriting Eq. (36) as

$$e_m t_r = t_r^{1-\beta}(e_2)/A \ , \tag{37}$$

the relationship becomes

$$e_2 = A\dot{e}_m t_r^{\beta} , \tag{38}$$

or

$$e_2 = \dot{e}_m t_3 , \tag{39}$$

which is, of course, merely the definition of e_2. In cases where the primary component is relatively small, e_2 may provide a useful estimate of the "usable strain" that a material can endure. In fact, for the 1-in. plate of heat 9T2796, Swindeman[52] has reported that the primary strain is vitally constant and about equal to 1%. Thus, an immediate application for Eq. (38) is apparent, in that it allows one to estimate e_3 only from $\dot{e}_m$ and t_r. [Even better estimates could be obtained from Eq. (39), of course, if data for t_r were available.] Estimates of this type are currently being developed.

Attempts at determining interrelationships among failure criteria will continue, as will application of a parametric method for the estimation of creep ductility. Application of these concepts to actual design will be stressed, including the evaluation of lower limit values.

3.2.4 Material Data Processing — M. K. Booker and C. O. Stevens

The computerized system for the in-house acquisition, analysis, storage, and retrieval of mechanical properties data is continuing to function, expand, and improve. Efforts during this past quarter have been concentrated on expanding the data base for the Mechanical Properties Data Storage and Retrieval System (DSRS), and on expanding the Automatic Data Acquisition System (ADAS), including software development.

As described in previous reports[53,54] DSRS is a flexible computerized system, which offers many advantages over manual handling of data. These advantages include:

1. Data can be located quickly and easily, eliminating the danger of lost or misplaced tests. An extensive system of safeguards prevents

data from being "lost" in the system, and the remarkable flexibility of the ORLOOK program[55] makes searches for data on the system quick and efficient.

2. The system offers virtually limitless possibilities for the handling of data in it. Once stored in the DSRS on-line disk file, data can be accessed by any number of programs that display, sort, or analyze the data. For example, a particular subset of data on file can be isolated, then output in graphical[56] or tabular[57] formats. The use of ADTABL,[57] the program that provides tabular output, has been improved this quarter by addition of the ADSØRT program.[58] ADSØRT sorts data according to specified DSRS identifiers.[54] For example, one might sort a given subset of tensile data first by temperature, then by strain rate within each temperature, then by tensile strength within each strain rate, etc. Running ADSØRT and ADTABL as consecutive job steps then allows one to receive tabular output sorted in whatever manner is desired. Access of data on file by statistical and numerical programs to provide curve fits, measures of scatter, etc. could also be easily accomplished. In fact, all the power and flexibility of modern digital computers can be made easily available to enable the analyst to treat the data in whatever fashion he desires. Clearly, such power is far beyond what might be accomplished by manual data handling.

3. Programs developed to process raw test output (strip charts, etc.) and to calculate relevant DSRS identifiers greatly decrease the time involved in such analysis, as well as making more extensive analysis possible. The TENSIS program[59] for the analysis of tensile data has been described previously.[54] Figures 3.73 through 3.75 illustrate graphical output from TENSIS for engineering stress-strain and true stress-strain curves. (The numbers to the right of the plots indicate DSRS test number.) During this quarter, a similar program called FATIGUE has been developed[60] for the analysis of fatigue data. FATIGUE takes input values of divisions on chart paper (as well as test characteristics such as divisions to load conversion factors, specimen diameter, temperature, etc.) and outputs tables of data, punched cards for input to DSRS, punched cards for use in analytical programs, and plots of data. Plots include stress range,

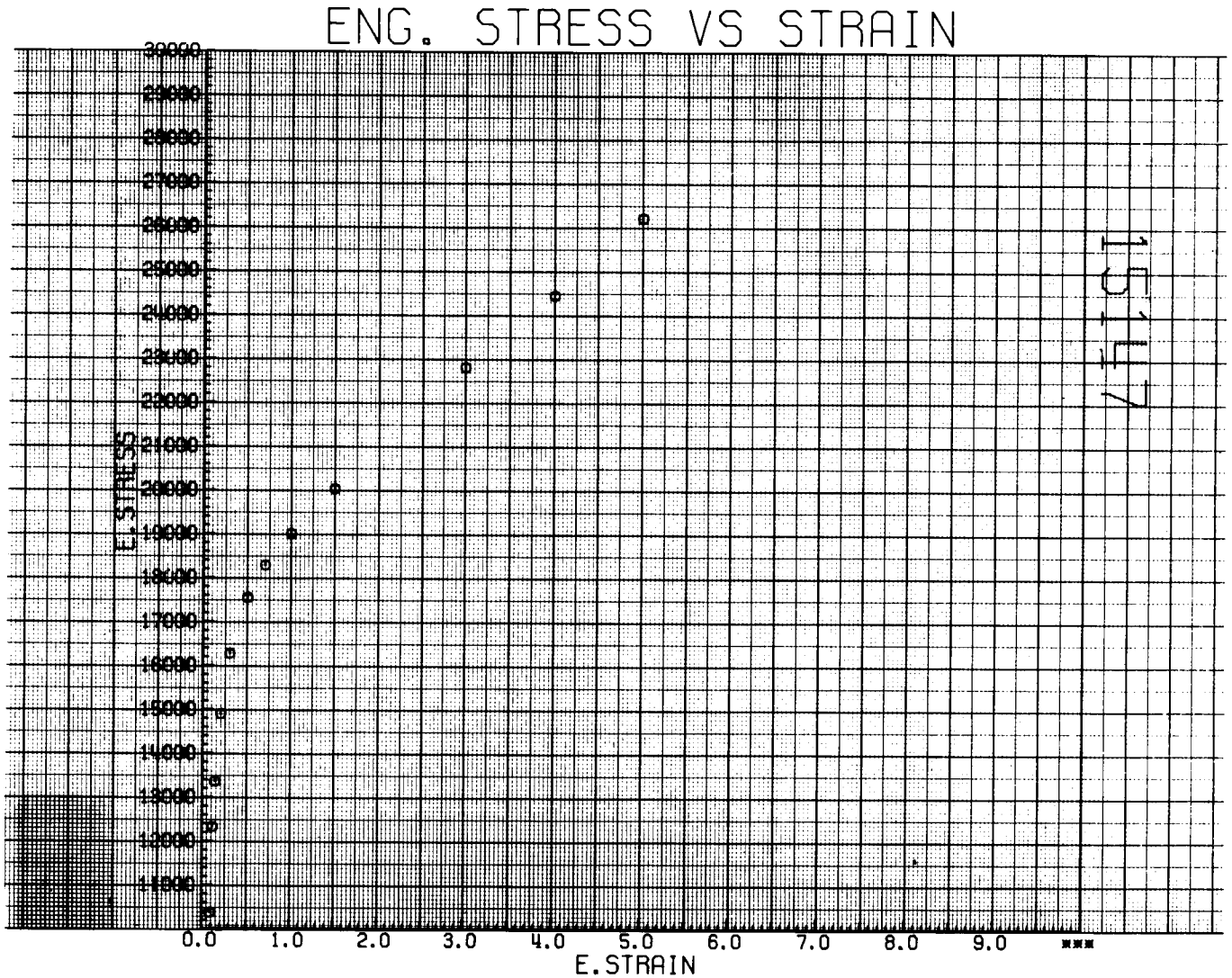

Fig. 3.73. TENSIS Engineering Stress-Strain Plot.

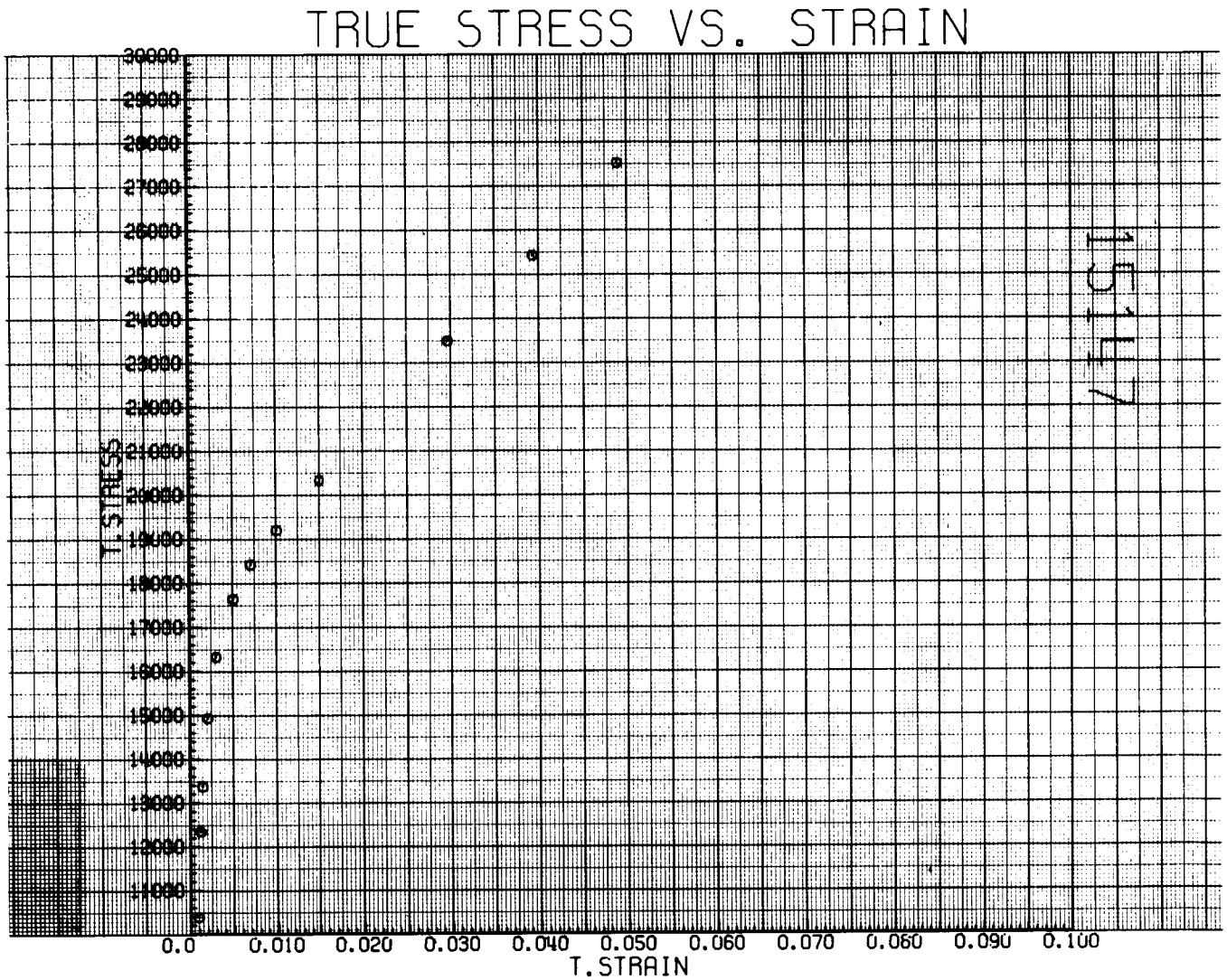

Fig. 3.74. TENSIS True Stress-Strain Plot.

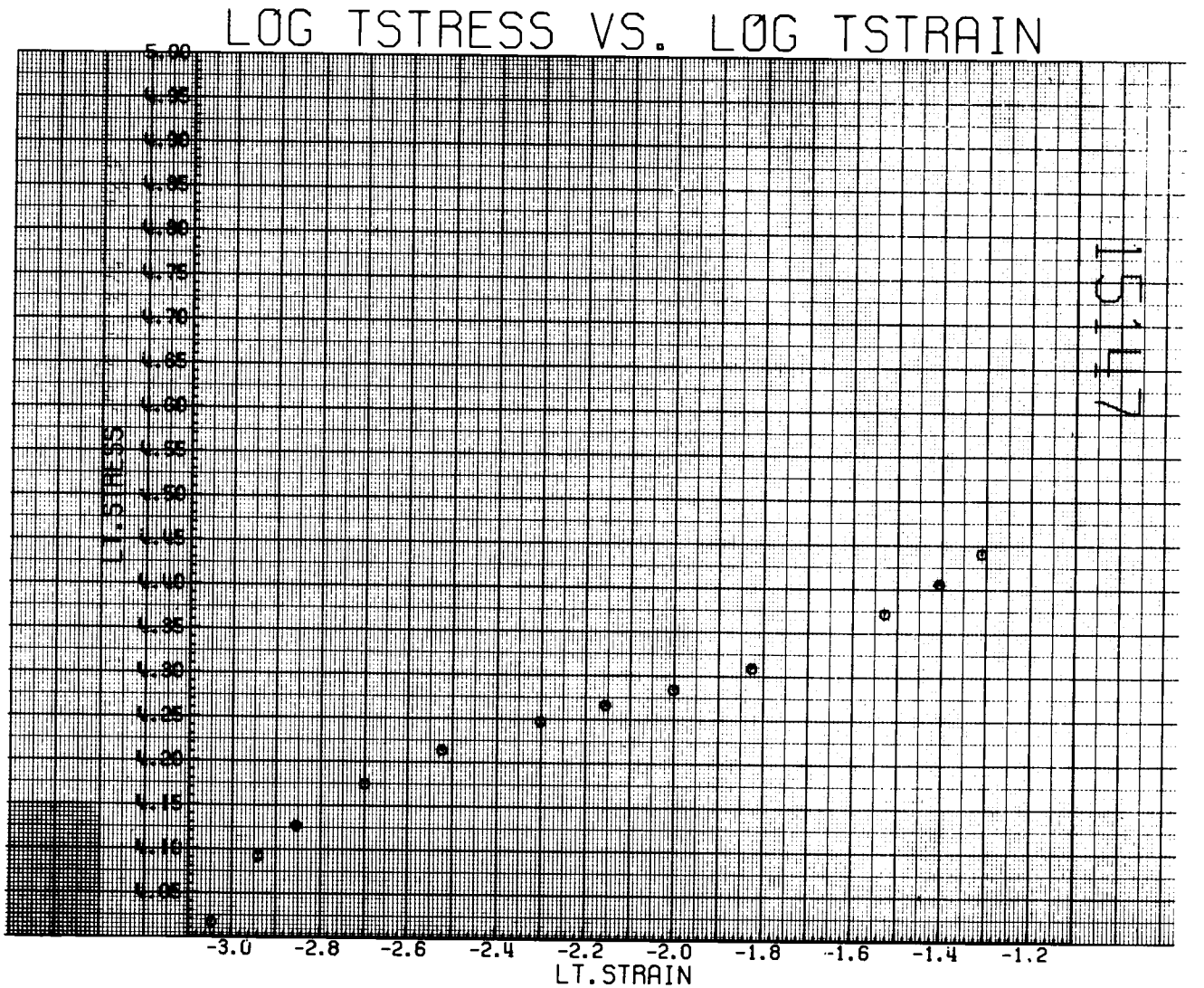

Fig. 3.75. TENSIS Log-Log True Stress-Strain Plot.

tensile-compressive stress amplitudes, mean stress, "relaxed" stress (stress at the end of a relaxation period or hold time), and plastic strain range versus cycle fraction (N/N_f). Currently FATIGUE treats only strain-controlled tests with hold times, but it is being modified for more flexibility.

4. The extensive documentation planned for DSRS helps ensure standardization and uniformity of input data. Such standardization is especially important for computerized data management, but it is also a general benefit in that mechanical-property-related definitions and procedures often vary widely. Thus, DSRS can provide a unifying influence. When complete, DSRS documentation will include:

a. *DSRS Thesaurus* contains definitions of "identifiers" or terms labelling data in DSRS. Periodic updates and memos of DSRS-related news are issued to all system users.

b. *Standard Procedures Manual for the Determination of DSRS Identifers* gives accepted standard methods for determining quantities to be input to DSRS from raw test output.

c. *User's Guide for a Mechanical Properties Data Storage and Retrieval System* contains detailed information on how to put data in and get data out, including descriptions of the use of ADPLØT, ADTABL, TENSIS, FATIGUE, and other system services.

5. A centralized collection center for mechanical properties data would ensure that the best available data base is used in establishing correlations for design applications. At present, with data being obtained at various laboratories and reported (if at all) in various places, it is difficult to bring together all available data for a particular task. Data collected but never used are, of course, worthless.

The only disadvantage of DSRS has been that, being a new system, it suffers from a shortage of data, which decreases its usefulness for specific applications. To remedy this situation, and to implement advantage 5 above, a second DSRS data base has been established[54] for data from sources outside ORNL. A special effort has been made during this quarter to input data to this system in order to develop a useful, working data base

for nuclear materials. Emphasis has been placed on types 304 and 316 stainless steel, 2 1/4 Cr-1 Mo steel, Inconel Alloy 718, and Incoloy Alloys 800 and 800H. Tables 3.16 and 3.17 show a breakdown of data currently on file in DSRS.

Extension of computerized data management to the collection of experimental data is embodied in the Automatic Data Acquisition System (ADAS). Figure 3.76 presents a schematic diagram of the flow of information through ADAS for the computerized acquisition of creep data. Briefly, the functions of the components shown are:

1. *Digitrend* receives analog (voltage) signals corresponding to load and extension measurements from each creep test and converts these signals into coded on-off pulses.

2. *Digital recorder interface* gathers information from the clock and the Digitrends and relays them onward. It also relays signal to Digitrend to initiate printed output of data there in the event of a breakdown in the system.

3. *Clock* keeps time for the creep tests being monitored. In the event of a power failure, the clock continues to operate on battery power.

Table 3.16. Mechanical Properties Supplemental Data Base — Data Summary

Material	Number of Individual Tests		
	Tensile	Creep	Fatigue
2 1/4 Cr-1 Mo	41	134	205
316 SS		171	112
304 SS		45	
Inconel 718	156	176	208
Incoloy 800	235	167	
A 533-B	77		
1 Cr-1 Mo-1/4 V	1		4
Incoloy 800H	385	440	
Total	895	1133	529
Total Tests — 2557			

Table 3.17. Mechanical Properties ORNL Data Base — Data Summary

Material	Number of Individual Tests					
	Tensile	Creep	Fatigue	Impact	Slow Bend	Relaxation
304 SS	810	377				11
316 SS	158	48				
2 1/4 Cr-1 Mo	375	74		73	18	
Incoloy 800	102					
308 SS	75	14				
Hastelloy X	34					
9 Cr-1 Mo	18					
INOR-8		122				
Other	190	26		83	38	
Total	1762	669		156	56	11
Total Tests — 2646						

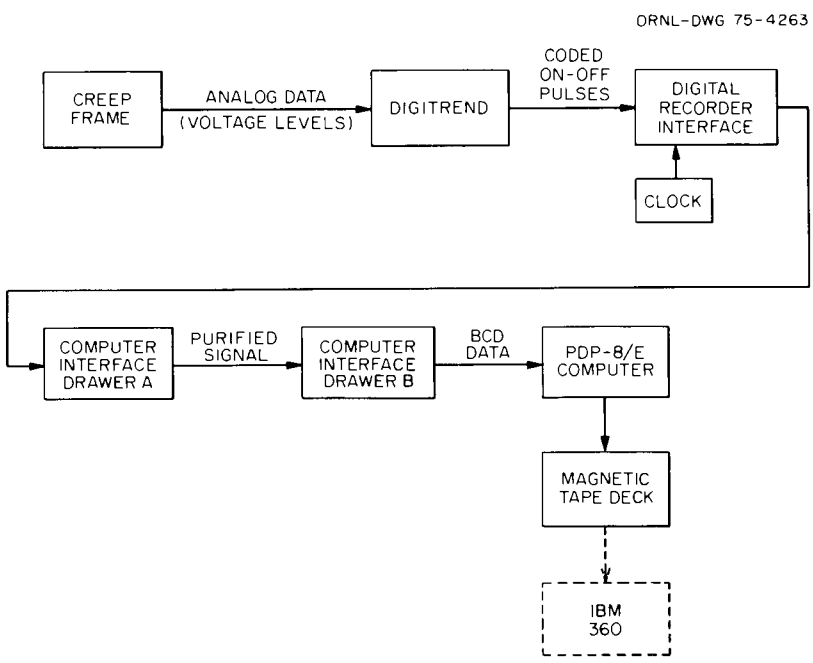

Fig. 3.76. Schematic Diagram of the Automatic Data Acquisition System.

4. *Computer interface drawer A* acts as a sort of filter to eliminate "noise" and static from the electronic signal received from the digital recorder interface.

5. *Computer interface drawer B* converts signal to a binary coded decimal (BCD) format readable by the computer and relays this converted signal to the computer.

6. *PDP-8/E computer* accepts input data and writes it in a special format on a seven-track magnetic tape in the magnetic tape drive.

7. *Magnetic tape drive* records data read by ADAS on magnetic tape, which is transmitted to the ORNL computer center for analysis by the IBM 360 computers there.

Development of a software system through which the ADAS tapes can be analyzed by the IBM 360 computers is continuing. The data from the tapes, which contain voltages representing load and extension, time readings, and temperature readings is read in, converted to actual stresses, strains, test times, and degrees, and stored on a disk file. A second disk file contains test descriptive characteristics (material, heat, specimen description, etc.) and can be updated through direct teletype access or through the input of card decks. Interaction with this second disk file through the PROMPT F4 computer program[61] will enable the user to request from the teletype tabular printouts of data from a given test, plots of data, etc. Data and test information will be directly transferred to DSRS through this same program once a test is complete. (DSRS contains test summary characteristics, not actual data points. The actual data points from a complete test will be written on magnetic tape and stored for future use.) This system could be extended to include analytical steps such as curve fits to creep curves, etc. Thus the advantages of ADAS will be extended to include enhanced analytical capabilities as well increased experimental efficiency.

3.2.5 Elastic Properties of Engineering Materials — J. P. Hammond

The purpose of this program is to measure and correlate the dynamic and static elastic constants for reactor materials of interest, giving specific attention to temperature and other significant test variables.

The major progress in this program has been in the development and improvement of data gathering and analysis. This work is reported in detail elsewhere[62] and in summary here along with some results on the static Young's modulus of 2 1/4 Cr-1 Mo steel.

3.2.5.1 Elastic Properties Determined by Dynamic Tests — J. P. Hammond and M. W. Moyer*

Dynamic (sonic) elastic constants are being established at room and elevated temperatures. During the last quarter superior procedures of data taking were incorporated and an improved computer program was prepared. Measurements on annealed 2 1/4 Cr-1 Mo and 9 Cr-1 Mo steels, 75%-cold-reduced 2 1/4 Cr-1 Mo steel and type 304 stainless steel, the same two alloys 75% cold-reduced and annealed, solution-annealed type 304 stainless steel and Incoloy 800H, and age-hardened Inconel 718 base metal and weld deposit await data processing. Specimens are ready for testing or in preparation for several other materials.

3.2.5.2 Elastic Properties Determined by Static Tests — J. P. Hammond

Equipment has been assembled for static modulus measurements on 2 1/4 Cr-1 Mo steel heat 20017 and type 304 stainless steel heat 9T2796 using three strain-sensing devices: weldable resistance strain gages, linear variable differential transformers, and laser diffractometers. A welding procedure was qualified[62] for attaching strain gages to 2 1/4 Cr-1 Mo steel.

The test matrix developed for the two materials calls for simultaneous measurements using the resistance strain gages with each of the other two techniques. So far Young's modulus has been measured only with the dual LVDT technique on isothermally annealed 2 1/4 Cr-1 Mo steel containing 0.136% C. The results are given in Table 3.18.

---

*Laboratory Development, Y-12.

Table 3.18. Static Young's Modulus Values Obtained in Preliminary Tests on Isothermally Annealed 2 1/4 Cr-1 Mo Steel Containing 0.136% C by Use of Extensometer with Two High-Sensitivity LVDTs

Nominal Strain Rate in Gage (sec^{-1})	Measured Values of Young's Modulus at Each Temperature					
	Room Temperature[a]		480°C (900°F)[a]		595°C (1100°F)[b]	
	(psi)	(GPa)	(psi)	(GPa)	(psi)	(GPa)
0.004	28.52×10^6	196.6	22.3×10^6[b]	154	18.05×10^6	124.5
	28.52	196.6			17.98	124.0
	29.42	202.8			18.33	126.4
	28.52	198.2				
	28.75 av	198.2			18.12 av	124.9
0.04	29.42	202.8	23.77	163.9	19.38	133.6
	29.05	200.3	24.64	169.9	18.91	130.4
	29.79	205.4	23.83	164.3	20.20	139.3
	29.69	204.7	24.64	169.9	20.03	138.1
	29.49 av	203.3	24.22 av	167.0	19.63 av	135.3
0.4	29.99	206.8	25.30	174.4	19.22	132.5
	30.07	207.3	26.00	179.3	19.30	133.1
	30.07	207.3	25.24	174.0	19.54	134.7
	29.88	206.0	25.03	172.6	19.62	135.3
	30.00 av	206.8	25.39 av	175.1	19.42 av	133.9

[a]Determined by chord method (ASTM E 231-69) for stress to 2400 psi (16.55 MPa), $\varepsilon = 80 \times 10^{-6}$, unless otherwise noted.

[b]Determined by chord method for stresses to 5000 psi (34.47 MPa), $\varepsilon = 170 \times 10^{-6}$.

3.3 MECHANICAL AND METALLURGICAL BEHAVIOR OF WELDMENTS FOR LMFBR — P. Patriarca, G. M. Slaughter, W. R. Martin, and C. R. Brinkman

3.3.1 Creep and Creep-Rupture Characterization of Type 16-8-2 Stainless Steel Weld Metal — R. T. King, G. M. Goodwin, and E. Bolling

Recent data compilations have been prepared on the creep and creep-rupture behavior of type 16-8-2 stainless steel weld metal,[63,64] including analyses of data from the ORNL Weld Development Program and available data from other sources. Characterization of 16-8-2 welds made with commercial filler metals is continuing. Recent results from a series of such test welds are reported below. The preparation and history

of these welds were presented previously.[65] The test welds include those identified as V-79, V-80, V-81, V-82, V-83, V-84, V-86, V-87, and V-89. These test welds represent a total of five combinations of welding electrode or wire, process, and welding parameters.

The test welds were made in 13-mm-thick (0.5-in.) type 316 stainless steel plate. The end preparation for all welds was identical to that used[63,64] for welds V-66 to V-74. Some of the welding parameters are given in Table 3.19.

Longitudinal all-weld-metal specimens had a 31.7-mm-long by 6.3-mm-diam (1.25 by 0.25 in.) gage, with the center line located about 5 mm (0.2 in.) below the weld surface. The method of fabricating these specimens is identical to that used[63,64] for welds V-66 through V-74. The specimens were creep tested at 649°C (1200°F) at stresses that were selected to produce rupture times to several thousand hours; test techniques were identical to those used for welds V-66 through V-74, except that extensometers were attached at the specimen shoulders rather than directly to the gage sections.

Table 3.19. Welding Parameters Used in Preparation of 16-8-2 Test Welds[a]

Test Weld	Process	Welding		Number of Passes[b]
		Voltage (V)	Current (A)	
V-79,80	Manual GTA	17–18	~170	11
V-81,82	Manual SMA	25–30	130–140[c]	18
V-83,84	Manual SMA	13–14	70	14
V-86,87	Manual GTA	15–18	170[d]	10
V-88,89	Automatic GTA (stringer bead)	13–14	70	2 or 3

[a]All used 0.125-in.-diam (3.2-mm) wire or electrode; interpass temperature was below 107°C (225°F).

[b]Exclusive of root passes.

[c]Second pass made at 110–120 A.

[d]Second pass made at 130 A, third pass made at 140 A.

The test results are summarized in Table 3.20. They include strain on loading, strain during first-stage creep, strain during second-stage creep (both by departure from linearity and the 0.2% offset strain method), and associated tertiary creep strains. The rupture strain was determined by direct measurement on the fractured sample, except where inaccuracies of measurement led to extensometer strains in excess of measured strains. The reduction of area was computed on the assumption that the projection of the fracture surface is an ellipse. The rupture time is used to compute several quantities, including the average creep rate, the ratio of time to the end of first-stage creep to the time to rupture, and the ratio of the time to tertiary creep to the time to rupture. The real or minimum second-stage creep rate and the average creep rate during second-stage creep to the onset of tertiary creep by the 0.2% offset strain method are also given.

Several important observations for these 16-8-2 weld tests and test conditions include the following:

1. The sum of the first- and second-stage creep strains is predominantly less than 2%, and several values less than 1% were recorded. This is important, because of the present strain limits imposed on weld metal in ASME Code Case 1592. By far, most of the creep strain that occurs in type 16-8-2 weld metal for these test conditions occurs during tertiary creep.

2. The 16-8-2 automatic (stringer bead) welds V-88 and V-89 exhibit decreasing reductions of area and total elongations with increasing rupture time. These values extrapolate to the nil-ductility level in about 10,000 hr. Importantly, this behavior also occurred in automatic welds V-66 through V-74, which were made by torch oscillation techniques (weave) with the same batch of weld wire.[63,64] For the test conditions that were explored, about a 2000 psi (14 MPa) higher stress was required to cause rupture in a given time for the weave technique welds than for the stringer bead welds.

3. The rupture times for 16-8-2 weld metal range from values high in the range expected[63] for type 316 stainless steel base metal, to values low in that range.

Table 3.20. Creep and Creep-Rupture Behavior of Type 16-8-2 Weld Metal

Weld	Stress (ksi)	Stress (MPa)	Strain, % Loading ε_L	$\varepsilon_{Stage\ I}$	$\varepsilon_{Stage\ II}$ Real	$\varepsilon_{Stage\ II}$ Offset	$\varepsilon_{Stage\ III}$ Real	$\varepsilon_{Stage\ III}$ Offset	Rupture ε_r	Reduction of Area (%)	Rupture Time, t_r (hr)	ε_r/t_r	t_I/t_r [a]	t_{III}/t_r [b]	$\dot{\varepsilon}_{Stage\ II}$ Real	$\dot{\varepsilon}_{Stage\ II}$ Offset
Manual GTA — McKay Heat 71370																
V79, 80	25.0	172	0.32	0.29	0.577	1.05	52.1	51.6	53.3	52.6	1630.6	0.033	1.34×10^{-2}	0.217	1.73×10^{-3}	2.11×10^{-3}
	28.0	193	0.42	0.20	0.66	1.42	35.6	34.9	36.9	51.7	396.5	0.093	1.03×10^{-2}	0.132	2.72×10^{-2}	2.94×10^{-2}
	30.0	207	~0.5	~0.2	~1.4	~1.9	39.6	39.1	41.7	50.8	171.9	0.24	5.8×10^{-3}	0.144	$\sim7.5\times10^{-2}$	$\sim8.0\times10^{-2}$
Manual SMA — McKay Commercial DC Lime, Heat 73804																
V81, 82	22.0	152	0.27	0.24	0.48	0.95	36.6	36.1	37.6	52.2	1485.7	0.25	2.08×10^{-2}	0.32	1.73×10^{-3}	2.14×10^{-3}
	25.0	172	0.32	0.21	0.99	1.57	42.4	41.8	43.9	44.9	844.5	0.052	7.7×10^{-3}	0.33	4.86×10^{-3}	5.72×10^{-3}
	28.0	193	~0.12	~0.2	~0.27	0.57	44.2	43.9	44.4	50.3	138.5	0.32	2.4×10^{-2}	0.13	3.7×10^{-2}	3.93×10^{-2}
	46.7	322	c	c	>25	>25	~2	~2	36.6	55.9	0.4	91.5	c	c	~92.6	
	30.0	207	0.47	0.33	0.53	1.64	38.6	37.5	39.9	54.7	132.0	0.30	1.8×10^{-2}	0.18	6.8×10^{-2}	7.9×10^{-2}
Manual SMA — McKay Commercial AC-DC, Heat 73804																
V83, 84	25.0	172	0.365	0.198	0.73	1.1	30.9	30.5	32.2	56.8	954.6	0.034	8.69×10^{-3}	0.62	1.56×10^{-3}	1.96×10^{-3}
	28.0	193	0.35	0.34	0.67	1.04	16.7	16.4	18.1	44.5	810.6	0.022	3.1×10^{-2}	0.64	1.77×10^{-3}	2.10×10^{-3}
	30.0	207	0.58	0.41	~0.27	~0.4	37.3	37.0	38.6	49.6	81.0	0.48	1.48×10^{-2}	0.105	$\sim5.6\times10^{-2}$	$\sim5.5\times10^{-2}$
Manual GTA — Arcos 1/8-in.-diam (3-mm) Heat D1309T301[d]																
V86, 87	25.0	172	0.17	0.08	0.27	0.56	21.6	21.3	22.2	47.4	767.7	0.029	6.5×10^{-3}	0.59	8.4×10^{-4}	1.25×10^{-3}
	28.0	193	0.50	0.73	0.62	1.42	21.2	20.4	23.0	33.7	262.1	0.088	8.6×10^{-2}	0.57	9.2×10^{-3}	1.11×10^{-2}
	30.0	207	1.64	2.0	1.85	2.61	19.4	21.3	24.9	40.3	175.3	0.14	1.33×10^{-1}	0.62	2.7×10^{-2}	3.09×10^{-2}
Automatic GTA — Champion Heat 58691, 0.045-in. (1.14-mm) Wire (Stringer Bead)																
V88, 89	22.0	152	0.23	0.31	0.3	0.56	19.0	18.7	19.8	31.0	722.6	0.027	3.8×10^{-2}	0.39	1.7×10^{-3}	2.2×10^{-3}
	25.0[e]	172	0.12	{0.22 10.8	{0.16 0.7	0.59	{13.8 2.7	13.4	14.3	34.6	1267.2	0.011	{1.89×10^{-2} 0.42	{0.15 0.997	{2.53×10^{-3} 9.5×10^{-4}	3.57×10^{-3}
	25.0	172	0.27	0.23	0.92	1.5	35.2	34.6	36.6	50.2	176.8	0.21	2.1×10^{-2}	0.34	2.3×10^{-2}	2.7×10^{-2}
	28.0	193	0.38	0.29	0.75	1.07	39.6	39.3	41.0	56.6	68.6	0.60	3.5×10^{-2}	0.26	6.2×10^{-2}	7.0×10^{-2}

[a] Time to end of first-stage creep divided by time to rupture.

[b] Time to onset of tertiary creep divided by time to rupture.

[c] Data inadequate for determination.

[d] 0.001% B, 0.019% P, 0.01% Ti, 0.42% Si.

[e] The unusual curve shape for this test has two local minima in strain rate. Values corresponding to both are provided.

3.3.2 Effect of Thermal Aging on the Creep and Creep-Rupture Behavior of CRE Type 308 Stainless Steel SMA Welds — R. T. King and E. Bolling

Work is in progress to obtain design data on the creep and creep-rupture of type 308 stainless steel weld metal. We have previously summarized[66] the results of creep tests on type 308 welds with controlled residual elements (CRE) that are prototypic of the longitudinal seam and girth welds in the FFTF.

Thermal aging of whole cross sections of these same welds at 482, 593, and 649°C (900, 1100, and 1200°F) is in progress. Aging at 482 and 593°C is intended to cover portions of the anticipated operating temperature range for LMFBRs, while aging at 649°C is performed to accelerate sigma phase formation. Base metal was trimmed to within 1 1/2 in. (3.8 cm) of the weld center line. The aging was performed in air furnaces that were continuously monitored. Aging to 4000 and 10,000 hr has been completed, and specimens aged to 20,000 hr will be available for testing in a few weeks. Other sections will be aged to 50,000 hr. Some tensile test data on these aged welds have already been presented.[67]

After the weld cross sections were aged, they were sectioned and made into longitudinal all-weld-metal specimens in the same manner as their unaged counterparts.[68] Selected specimens were then creep tested by the same techniques that were used for unaged specimens,[69,70] except that extensometers were mounted on the specimen shoulders rather than on the gage section.

The creep and creep-rupture data for aged and unaged specimens are summarized in Tables 3.21, 3.22, and 3.23. Terms were defined previously.[66]

For the data that are now available, there is no significant effect of aging at either 593 or 649°C. However, for weld metal aged at 482°C, significant and consistent reductions of rupture life occurred at all stress levels that were explored, regardless of the location in the weld from which the specimens were cut. (Rupture times were decreased to 0.1 to 0.2 times the values for unaged material.) The corresponding reduction of stress to cause rupture in a given time is about 5000 to 7000 psi (34–48 MPa). This observation is consistent with reductions in the ultimate tensile strength that were previously reported[67] and may be related to observed[67] changes in microstructure that occur during aging.

Table 3.21. Effect of Aging at 482°C (900°F) on the Creep Behavior of Type 308 CRE Stainless Steel Weld Metal at 482°C (900°F)

Stress (ksi)	Stress (MPa)	Aging Time (hr)	Strain, %							Strain Rate, %/hr			Reduction of Area (%)	Rupture Time, t_r (hr)	$\frac{t_{III}}{t_r}$	t_I (hr)	Specimen	Test
			Loading ε_L	$\varepsilon_{Stage\ I}$	$\varepsilon_{Stage\ II}$ Real	$\varepsilon_{Stage\ II}$ Offset	$\varepsilon_{Stage\ III}$ Real	$\varepsilon_{Stage\ III}$ Offset	Rupture ε_r	$\dot{\varepsilon}_{Stage\ II}$ Real	$\dot{\varepsilon}_{Stage\ II}$ Offset	ε_r/t_r						
									L1 Specimens									
55.0	379	0	12.16	~0	0.11	0.365	23.74	23.54	36.16	5.53×10^{-4}	1.22×10^{-3}	0.0414	57.7	873.0	0.34	~0	FF17-1	FFC-58
		4,000							21.4					~0		~0	FF65-1	FFC-89
50.0	345	0	5.84	0.01	0.26	0.367	18.17	18.06	24.28	4.33×10^{-4}	4.59×10^{-4}	0.0126	52.3	1921.9	0.42	~0	FF15-12	FFC-49
		4,000	8.93	3.16	5.92	7.91	18.2	16.2	36.2	5.2×10^{-2}	5.4×10^{-2}	0.127	42.1	384.7	0.61	24.9	FF65-9	FFC-102
		10,000	11.7	4.32	8.78	10.68	8.1	6.2	32.9	6.5×10^{-2}	6.9×10^{-2}	0.133	45.6	247.1	0.74	27.7	FF66-31	FFC-139
45.0	310	0	1.65	0.08	0.17	0.581	19.2	18.79	21.6	9.19×10^{-4}	1.4×10^{-3}	0.00319	31.7	6764.7	0.06	200	FF17-2	FFC-24[a]
				(3.94)	(1.5)	(1.7)	(14.5)	(14.3)	21.6	(1.0×10^{-3})	(1.07×10^{-3})				(0.59)	(~2500)		
		4,000	6.1	6.8	5.68	8.57	15.5	12.6	34.1	9.88×10^{-3}	1.02×10^{-2}	0.018	48.8	1886.0	0.62	329.7	FF65-10	FFC-140
		10,000	6.13	7.3	4.05	6.08	17.9	15.9	35.4	9.4×10^{-3}	9.7×10^{-3}	0.020	43.4	1795.4	0.57	402.5	FF66-32	FFC-141
									L2 Specimens									
52.5[b]	362	4,000	5.44	~1.35	~8.3		~12.7		23.1	~0.1		0.37	35.6	62.9	~0.7	~2.1	FF65-8	FFC-103
		10,000	5.75	3.0	5.3	7.0	11.8	10.1	25.9	8.3×10^{-2}	8.6×10^{-2}	0.16	46.96	158.6	0.63	18.6	FF66-34	FFC-146
50.0	345	0	2.8	~0	0.5	0.767	24.62	24.35	27.92	1.33×10^{-3}	1.80×10^{-3}	0.0117	56.3	2394.6	0.18	~0	FF17-3	FFC-6
		4,000	5.0	1.87	3.12	4.58	15.6	14.1	23.7	1.56×10^{-2}	1.64×10^{-2}	0.037	26.8	630.5	0.56	75.0	FF65-7	FFC-95
		10,000	3.9	1.47	2.25	3.25	23.2	22.2	30.8	1.66×10^{-2}	1.77×10^{-2}	0.070	52.6	438.2	0.48	25.9	FF66-37	FFC-142
									L3 Specimens									
55.0	379	0	9.24	0.05	0.78	1.00	16.97	16.75	27.04	7.28×10^{-3}	9.34×10^{-3}	0.076	35.9	353.9	0.40	3.0	FF84-5	FFC-79
		4,000	7.66	c	c	c	c	c	22.2	c	c	1.15		19.2	c	c	FF65-5	FFC-156

[a]The unusual curve shape for this test has two local minima in strain rate. Values corresponding to both are provided.

[b]Test on unaged specimens yet to be run.

[c]Data not sufficient for reasonable determination of values.

Table 3.22. Effect of Aging at 593°C (1100°F) on the Creep Behavior of Type 308 Stainless Steel Weld Metal at 593°C (1100°F)

Stress (ksi)	Stress (MPa)	Aging Time (hr)	Strain, %							Strain Rate, %/hr			Reduction of Area (%)	Rupture Time, t_r (hr)	t_{III}/t_r	t_I (hr)	Specimen	Test
			Loading ε_L	$\varepsilon_{Stage\ I}$	$\varepsilon_{Stage\ II}$ Real	$\varepsilon_{Stage\ II}$ Offset	$\varepsilon_{Stage\ III}$ Real	$\varepsilon_{Stage\ III}$ Offset	Rupture ε_r	$\dot{\varepsilon}_{Stage\ II}$ Real	$\dot{\varepsilon}_{Stage\ II}$ Offset	ε_r/t_r						
										L1 Specimens								
33.0	228	0	0.69	1.46	7.05	8.36	26.56	25.1	35.8	2.47×10^{-1}	2.53×10^{-1}	0.488	49.9	73.3	0.52	5.0	FF17-22	FFC-18
		4,000	0.95	0.34	3.1	4.7	30.54	28.9	33.6	5.36×10^{-2}	5.7×10^{-2}	0.18	59.3	186.1	0.46	2.2	FF69-1	FFC-90
		10,000	0.31	1.24	5.5	7.45	34.3	32.3	41.3	0.26	0.26	0.48	50.8	86.2	0.35	1.8	FF69-32	FFC-144
30.0	207	0	~2.0	8.25	3.75	4.53	12.24	11.46	26.2	5.77×10^{-2}	6.04×10^{-2}	0.111	54.6	236.4	0.59	65	FF17-29	FFC-16[a]
		4,000	2.28	1.1	7.43	9.43	33.6	31.6	41.0	0.99	1.04	2.03	53.2	20.2	0.47	0.5	FF69-9	FFC-104
		10,000	0.78	1.1	3.6	4.8	49.5	48.4	53.2	5.67×10^{-2}	6.36×10^{-2}	0.19	53.5	272.2	0.29	4.5	FF69-39	FFC-145
28.0	193	0	0.29	1.37	0.84	1.08	25.18	24.9	27.7	1.5×10^{-3}	1.95×10^{-3}	0.0148	58.1	1873.9	0.40	164	FF15-22	FFC-73
		4,000	0.50	1.27	3.07	4.08	45.7	44.7	50.6	2.72×10^{-2}	2.73×10^{-2}	0.083	66.9	606.9	0.29	25.6	FF69-10	FFC-147
		10,000	0.55	1.05	4.73	5.22	53.9	53.4	60.2	4.56×10^{-2}	4.62×10^{-2}	0.139	62.5	433.5	0.29	12.0	FF69-40	FFC-148
										L2 Specimens								
35.0	241	0	0.44	0.31	4.25	6.81	27.64	25.08	30.64	9.4×10^{-1}	9.7×10^{-1}	0.804	60.3	38.1	0.20	0.5	FF15-18	FFC-63
		4,000	0.56	1.07	1.14	2.19	34.2	33.2	37.0	9.5×10^{-2}	1.0×10^{-1}	0.44	56.3	84.9	0.33	6.85	FF69-7	FFC-106
		10,000	0.39	0.43	1.01	1.87	24.4	23.5	26.2	1.8×10^{-2}	2.1×10^{-2}	0.13	55.5	197.2	0.50	10.2	FF69-34	FFC-149
33.0	228	0	0.34	1.46	2.2	2.93	19.92	19.19	23.92	8.8×10^{-3}	9.44×10^{-3}	0.0392	35.5	610.2	0.59	50	FF15-14	FFC-60
		4,000	0.53	0.47	0.89	1.86	39.2	37.3	41.2	3.6×10^{-2}	3.8×10^{-2}	0.17	50.7	235.4	0.28	17.3	FF69-8	FFC-150
		10,000	0.51	1.76	2.75	4.68	27.0	25.0	32.0	1.03×10^{-2}	1.08×10^{-2}	0.049	56.9	651.6	0.76	65.9	FF69-37	FFC-151
30.0	207	0	0.249	0.28	0.69	0.91	20.48	20.26	21.7	3.7×10^{-4}	4.9×10^{-4}	0.0049	53.1	4446.3	0.54	50.0	FF15-4	FFC-56
		4,000	0.015	0.21	0.67	1.10	19.7	19.3	20.6	3.39×10^{-4}	4.2×10^{-4}	0.0047	44.0	4389.9	0.61	42	FF69-33	FFC-154
		10,000	0.395	0.33	0.77	1.52	27.6	26.8	29.1	4.1×10^{-3}	4.6×10^{-3}	0.034	60.6	854.4	0.41	23.2	FF69-38	FFC-152
										L3 Specimens								
33.0	228	0	0.4	0.35	1.25	1.81	19.44	18.88	21.44	8.06×10^{-3}	9.06×10^{-3}	0.0485	52.2	441.9	0.51	25.0	FF17-25	FFC-15
		4,000	1.5	0.5	1.7	2.37	31.0	30.2	34.6	2.12×10^{-2}	2.28×10^{-3}	0.13	59.4	265.2	0.43	10.2	FF69-5	FFC-159

[a]Step loaded.

Table 3.23. Effect of Aging at 640°C (1200°F) on the Creep Behavior of Type 308 CRE Stainless Steel Weld Metal at 649°C (1200°F)

Stress (ksi)	Stress (MPa)	Aging Time (hr)	Strain, %							Strain Rate, %/hr			Reduction of Area (%)	Rupture Time, t_r (hr)	t_{III}/t_r	t_I (hr)	Specimen	Test
			Loading ε_L	$\varepsilon_{Stage\ I}$	$\varepsilon_{Stage\ II}$ Real	$\varepsilon_{Stage\ II}$ Offset	$\varepsilon_{Stage\ III}$ Real	$\varepsilon_{Stage\ III}$ Offset	Rupture ε_r	$\dot{\varepsilon}_{Stage\ II}$ Real	$\dot{\varepsilon}_{Stage\ II}$ Offset	ε_r/t_r						
									L1 Specimens									
28.0	193	0	<0.2	0.05	0.25	0.46	37.58	37.38	38.08	1.67×10^{-2}	2.92×10^{-2}	1.614	54.4	23.6	0.68	0.25	FF15-1	FFC-8
		4,000	0.4	0.3	1.8	2.8	44.9	43.9	47.4	~1.0	~1.0	2.4	55.7	19.7	0.18	0.7	FF20-2	FFC-107
		10,000	0.35	0.27	1.35	2.25	38.7	37.8	40.7	0.5	0.55	2.1	61.0	19.3	0.23	0.3	FF20-12	FFC-109
22.0	152	0	0.197	1.111	0.26	0.53	44.03	43.76	43.30	8.11×10^{-4}	1.30×10^{-3}	0.0552	64.0	785.0	0.52	~0	FF15-21	FFC-55
		4,000	0.3	0.39	0.56	1.31	36.5	35.8	37.8	1.77×10^{-2}	2.19×10^{-2}	0.14	64.9	268.6	0.16	10.3	FF20-9	FFC-153
									L2 Specimens									
28.0	193	0	0.25	0.15	0.6	0.95	19.79	19.19	20.79	1.24×10^{-2}	1.56×10^{-2}	0.213	59.6	97.5	0.64	2.0	FF15-17	FFC-57
		4,000	0.19	0.12	0.67	0.89	42.3	42.1	43.3	8.7×10^{-2}	8.8×10^{-2}	1.06	59.0	40.9	0.34	1.0	FF20-4	FFC-108
		10,000	0.21	0.10	0.57	1.01	41.1	40.6	42.0	6.2×10^{-2}	7.2×10^{-2}		56.8	42.6	0.34	0.5	FF20-14	FFC-110
									L3 Specimens									
30.0	207	0	0.52	0.56					13.6			2.65	62.0	13.6	a	~1	FF83-6	FFC-160
		4,000	0.5	0.2	0.85	1.82	34.4	33.5	35.3	0.198	0.24	1.50	62.0	23.5	0.35	0.7	FF20-6	FFC-161
28.0	193	0	0.3	0.4	0.55	1.0	35.65	35.2	36.2	7.7×10^{-3}	9.5×10^{-3}	0.179	59.9	201.2	0.55	5.0	FF83-5	FFC-158
		4,000	0.41	0.19	0.42	0.65	19.7	19.4	20.1	2.2×10^{-3}	3.8×10^{-3}	0.105	61.3	191.0	0.60	3.8	FF20-5	FFC-157

[a]Insufficient data for analysis.

3.3.3 Creep-Rupture Behavior of Gas Tungsten-Arc Types 308, 316, and 16-8-2 Stainless Steel Welds Made with Special Filler Materials — D. P. Edmonds and E. Bolling

Previous work[70–72] has shown that minor additions of B, P, and Ti to shielded metal-arc (SMA) type 308 stainless steel weldments result in improved creep strength and long-time creep ductility. We are trying to improve the creep behavior of types 308, 316, and 16-8-2 stainless steel gas tungsten-arc welds, by adding varying amounts of the same elements to the filler wire. Creep-rupture testing of the first iteration of these materials is in progress, although most of it is completed at this time. The preliminary results of this testing are shown in Tables 3.24 through 3.26.

All the test welds were made in 1/2-in.-thick (13-mm) stainless steel plates, by use of a 75°-included angle V-groove joint. The type 308 welds were made in type 304 plates, and the types 316 and 16-8-2 welds were made in type 316 plates. Almost all the welds were made with the manual GTA process, with the only exception being the type 16-8-2 welds made with Champion heat 58691 (see Table 3.26) filler wire, which were made automatically with Astro-Arc equipment. The manual welds were made by stringer bead techniques, with average welding conditions of 190 A current and 17 V (direct current straight polarity, DCSP). The automatic welds used both stringer and weave bead techniques, with average conditions of 180 A current and 10 V (DCSP). All welds used pure argon shielding gas.

All-weld-metal buttonhead specimens with a 0.13-in.-diam by 1.13-in.-long (3.2- by 28.6-mm) gage section parallel to the welding direction were machined from each test weld. The center of each specimen coincides with the middle of the weld at a distance about 0.2 in. (5 mm) below the top surface of the weld. These specimens were tested at 649°C (1200°F) in air, at stress levels intended to produce rupture times ranging from a few hours to several thousand hours. The load was applied gradually by mechanical and/or hydraulic devices. Extensometers mounted on the grips were used to monitor creep strains to within ±1%, with the total elongation and reduction of area being measured directly by fitting the fractured specimens together. Rupture data only are considered in this report.

Table 3.24. Creep-Rupture Properties of Manual Gas Tungsten-Arc Type 308 Stainless Steel Weldments at 649°C (1200°F)

Weld Number	Supplier	Heat or Composition Aim	Stress (ksi)	Stress (MPa)	Time to Rupture (hr)	Total Elongation (%)	Total Reduction of Area (%)
V-5, 6	Arcos	Commercial D1717-3082	25.0	172	26.6	18.8	29.3
			25.0	172	24.0	20.6	24.4
			20.0	138	115.4	11.6	14.7
			20.0	138	143.5	7.9	20.7
			14.0	110	927.0	2.7	6.1
V-14	ORNL	Special, remelted D1717-3082	20.0	138	164.7	8.8	14.6
			16.0	110	733.0	3.6	10.0
			14.0	97	1630.1	3.6	4.8
V-16	ORNL	Special, 0.007% B, 0.045% P	20.0	138	432.4	12.1	25.1
			16.0	110	1980.0	6.3	13.0
V-15	ORNL	Special, 0.5% Ti	25.0	172	100.3	28.8	64.6
			20.0	138	991.0	35.8	66.1
			18.0	124	2083.5	38.1	63.4
V-7	ORNL	Special, 1% Ti	25.0	172	62.4	51.8	80.9
			20.0	138	321.9	22.3	51.7
			16.0	110	2415.6	34.0	66.5
V-8	ORNL	Special, 0.007% B	25.0	172	40.2	39.1	47.5
			20.0	138	262.2	18.8	24.1
			16.0	110	1198.7	4.6	11.2
V-13	ORNL	Special, 0.015% B	20.0	138	495.1	6.3	15.3
			16.0	110	1634.5	5.5	8.4
V-12	ORNL	Special, 0.045% P	20.0	138	215.2	10.0	21.7
			16.0	110	922.0	4.3	9.2
V-9	ORNL	Special, 0.060% P	25.0	172	26.5	28.2	42.6
			20.0	138	190.4	13.4	22.4
			16.0	110	1091.7	6.4	6.7
V-10	ORNL	Special, no Si	25.0	172	11.35	37.5	80.7
			20.0	138	25.0	13.6	40.4
			14.0	97	936.7	25.4	36.6
V-11	ORNL	Special, 0.60% Si	25.0	172	15.65	32.7	62.1
			16.0	110	357.4	33.1	50.8
			14.0	97	1496.6	15.4	44.7
V-130, 131	ORNL	Special, 0.5% Ti, 0.006% B 0.042% P	30.0	207	59.1	42.5	64.5
			28.0	193	74.2	46.6	70.5
			25.0	172	422.4	29.4	60.9
			22.0	152	1168.9	34.3	66.8

Table 3.25. Creep-Rupture Properties of Manual Gas Tungsten-Arc Type 316 Stainless Steel Weldments at 649°C (1200°F)

Weld Number	Supplier	Heat or Composition Aim	Stress (ksi)	Stress (MPa)	Time to Rupture (hr)	Total Elongation (%)	Total Reduction of Area (%)
V-1,2	McKay	20281	25.0	172	451.1	6.5	22.7
			25.0	172	408.8	4.7	26.4
			22.0	152	1078.3	4.3	24.9
			20.0	138	2824.6	3.9	3.1
V-44	ORNL	Special, 0.29% Ti	25.0	172	696.7	6.8	21.7
			22.0	152	1210.2	3.3	14.3
V-116,117	ORNL	Special, 0.006% B, 0.042% P	Not weldable — hot cracking problem				
V-122,129	ORNL	Special, 0.006% B, 0.042% P, 0.5% Ti	40.0	276	20.2	12.1	64.0
			35.0	241	369.4	11.7	56.4
			30.0	207	4716.7	15.0	47.7
V-123,124	ORNL	Special, 0.5% Ti	45.0	310	0.8	16.0	52.5
			40.0	276	9.0	21.2	62.8
			35.0	241	1330.7	14.6	44.0
V-126,128	ORNL	Special, 1.0% Ti	40.0	272	48.4	18.3	47.4
			35.0	241	116.4	40.0	54.2
			30.0	207	474.5	10.8	38.3

Creep-rupture properties of the type 308 stainless steel test welds are given in Table 3.24. The first two weld types in the table (V-5 and -6, -14) are typical of standard type 308 GTA welds, with reasonable creep strength and low creep ductility. Varying additions of B, P, Ti, and Si noticeably affected the creep properties. The addition of 0.007% B, 0.045% P (V-16); 0.015% B (V-13); 0.045% P (V-12); and 0.060% P (V-9) to the deposit yielded only minor increases in strength and ductility. Additions of 1% Ti (V-7) and 0.007% B (V-8) to the deposit substantially increased both strength and ductility. Addition of 0.60% Si (V-11) or no silicon (V-10, actual deposit had a higher silicon content than typical type 308 deposits) to the deposit produced little change in strength

Table 3.26. Creep-Rupture Properties of Gas Tungsten-Arc Type 16-8-2 Stainless Steel Weldments at 649°C (1200°F)

Weld Number	Supplier	Heat or Composition Aim	Stress (ksi)	Stress (MPa)	Time to Rupture (hr)	Total Elongation (%)	Total Reduction of Area (%)
V-55,56	Champion	45209 30-mil (0.76-mm) wire	28.0	193	358.5	12.5	50.6
			25.0	172	791.6	11.9	55.6
			22.0	152	3204.9	8.2	14.6
			30.0	207	127.2	26.5	44.5
V-57,58	Reid-Avery Armco	39048, 45-mil (114-mm) wire	28.0	193	126.9	22.0	51.6
			25.0	172	328.5	16.6	64.5
			23.5	162	843.9	27.6	47.2
			22.0	152	817.7	14.9	48.8
			21.0	145	1775.4	10.9	27.4
V-78, 46	Champion	56004	28.0	193	28.3	34.9	68.4
			25.0	172	74.6	18.9	45.7
			25.0	172	190.4	29.6	47.7
			25.0	172	97.1	25.6	67.8
			22.0	152	84.2	21.6	53.6
			20.0	138	1339.3	21.7	56.3
			20.0	138	431.8	34.4	73.0
			18.0	124	1204.0	43.7	54.8
V-66–74, 85,88,89[a]	Champion	58691	28.0	193	68.6	41.0	56.6
			25.0	172	176.8	36.6	50.2
			25.0	172	78.0	27.8	51.9
			25.0	172	104.3	62.9	52.7
			25.0	172	1267.2	14.3	34.6
			22.0	152	722.6	19.8	31.0
			20.0	138	765.6	47.6	
			18.0	124	1703.2	29.8	41.5
			16.0	110	5671.8	23.7	28.4
V-79,80	McKay	71370	30.0	207	171.9	41.7	50.8
			28.0	193	396.5	36.9	51.7
			25.0	172	1630.6	53.3	52.6
V-90	ORNL (Remelt Champion wire)	0.50% Si, 8.5% Ni	25.0	172	97.1	25.6	67.8
			20.0	138	431.8	34.4	72.9
			18.0	124	1204.0	43.7	54.8
V-86,87	Arcos	D1309T 301 Mod	30.0	207	175.3	24.9	40.3
			28.0	193	262.1	23.0	33.7
			25.0	172	767.7	22.2	47.4
V-114,115	Arcos	Reference Heat 2367-R-16-8-2	28.0	193	107.1	55.0	64.5
			25.0	172	3602.4	40.1	63.3
			25.0	172	513.0	30.1	70.0
V-118,125	ORNL	Special, 0.5% Ti	35.0	241	342.0	6.2	15.9
			30.0	207	1010.8	5.9	7.8
			28.0	193	1812.3	3.3	4.7
V-119,127	ORNL	Special, 1.0% Ti	35.0	241	128.9	12.1	42.7
			30.0	207	888.5	7.1	18.8
			28.0	193	>2100[b]		
V-120,132	ORNL	Special, 0.5% Ti, 0.006% B, 0.042% P	28.0	193	2684.2	10.5	71.7
			28.0	193	1165.0	9.3	12.8
			25.0	172	2463.1	6.2	16.0
			25.0	172	>5000[b]		
V-121,133	ORNL	Special, 0.006% B, 0.042% P	28.0	193	>500[b]		
			25.0	172	>600[b]		

[a]Automatic welds, all others manual.

[b]Indicates test in progress.

(decrease in strength at higher stresses) with a substantial increase in ductility. Superior creep strengths and ductilities were obtained from the 0.5% Ti (V-15) and the 0.5% Ti, 0.006% B, 0.042% P (V-130, -131) deposits, with the latter type deposit having the best properties. Additional testing will be done to more fully characterize the type 308 stainless steel deposits with 0.5% Ti, 0.006% B, and 0.042% P.

Creep-rupture properties of the type 316 stainless steel test welds are given in Table 3.25. The welds made with the McKay bare wire heat 20281 (V-1, -2) have typical type 316 weld metal creep properties. (Notice that the creep ductility decreases very rapidly as time to rupture, t_r, increases.) Additions of 0.006% B and 0.042% P (V-116, -117) produced a bare wire that is not weldable because of hot-cracking problems. The cracks are caused by the high concentration of low-melting materials and the low level of ferrite in the deposit. Additions of 0.29% Ti (V-44) to the deposit yielded slightly higher creep strength than the standard type 316 deposit, with no increase in ductility. However, the creep strength and ductility are increased with the addition of 1.0% Ti (V-126, -128), moderate increase; 0.5% Ti (V-123, -124), greater increase; and 0.006% B, 0.042% P, 0.5% Ti (V-122, -129), greatest increase. From the results of this iteration, it is seen that additions of 0.5% Ti, 0.042% P, and 0.006% B to type 316 GTA welds produce the greatest enchancement of creep properties.

Listed in Table 3.26 are the creep-rupture properties of welds made with several commercial heats along with ORNL test heats of type 16-8-2 stainless steel wire. A comparison of the limited creep-rupture data available in the tables shows that standard type 16-8-2 GTA welds have far superior creep strength to standard type 308 welds and equal or inferior strengths to standard type 316 welds. Also, the type 16-8-2 GTA welds have far superior creep ductility and do not appear to be as susceptible to long-time embrittlement as types 308 and 316. Because creep testing of the modified ORNL welds is incomplete at this time, they cannot be compared with the commercial type 16-8-2 welds. However, from the one group of data that is complete (weld V-118, -125), it appears that the addition of 0.5% Ti increases the creep strength, but decreases

the ductility. A more detailed analysis of the effect of B, P, and Ti on the creep properties of type 16-8-2 GTA welds cannot be made until testing is completed.

3.4 MECHANICAL PROPERTIES OF STEAM GENERATOR AND HEAT EXCHANGER MATERIALS — C. R. Brinkman

3.4.1 Strain Rate Effects on the Tensile Properties of Annealed 2 1/4 Cr-1 Mo Steel — R. L. Klueh

Last quarter[73] we reported on the high-strain-rate tensile properties of annealed 2 1/4 Cr-1 Mo steel. Tests were conducted at 25, 454, 510, and 566°C (75, 850, 950, and 1050°F) at strain rates of 0.16, 1.6, 16, and 144/sec. During this quarter, we completed tests at the same strain rates at 204 and 371°C (400 and 700°F). The results of these tests are shown in Table 3.27. Tests have also been completed over the temperature range 25 to 566°C (75—1050°F) at 2.67×10^{-6}/sec (0.0002/min), the lowest strain rate tensile tests we have yet conducted. The results for these tests are shown in Table 3.28. All tests were made on the commercial 1-in. (25-mm) plate, B&W heat 20017, in the annealed condition. With the completion of these tests and those previously completed,[74] we can now represent the variation of the tensile properties over a strain rate range of eight orders of magnitude.

Figures 3.77 through 3.80 show three-dimensional representations of the 0.2% yield strength, ultimate tensile strength, total elongation, and reduction of area over the entire strain rate range of 2.67×10^{-6} to 144/sec and from 25 to 566°C (75—1050°F). To better show the behavior of the yield strength and ultimate tensile strength, Fig. 3.81 shows the results as functions of strain rate at the six test temperatures, and Fig. 3.82 shows the results as a function of temperature at four strain rates. In addition to the yield stress and ultimate tensile strength, Figs. 3.81 and 3.82 show the stress at strains of 2 and 5%.

Except at room temperature, Figs. 3.77 and 3.81 show that the yield stress is little affected by strain rate. At room temperature [Fig. 3.81(a)], there is little effect up to about 0.1/sec, after

Table 3.27. Engineering Tensile Properties of Annealed 2 1/4 Cr-1 Mo Steel at High Strain Rates

Strain Rate (sec^{-1})	Strength, ksi(MPa)			Elongation (%)	Reduction of Area (%)
	0.2% Yield	Ultimate Tensile	Fracture		
		204°C (400°F)			
0.16	34.3(237)	66.2(460)	44(300)	24.3	68
1.6	37.6(259)	68.2(470)	42(290)	24.9	70
16	35.4(244)	71.2(490)	42(290)	27.3	72
144	38.0(262)	73.6(508)	41(280)	27.4	72
		371°C (700°F)			
0.16	37.4(258)	68.0(469)	50(340)	17.8	58
1.6	35.4(244)	65.4(454)	47(320)	19.3	65
16	30.4(210)	64.0(441)	44(300)	19.0	62
144	32.8(226)	63.6(439)	39(270)	23.0	71

Table 3.28. Engineering Tensile Properties of Annealed 2 1/4 Cr-1 Mo Steel at 2.67×10^{-6}/sec (0.0002/min)

Temperature		Strength, ksi (MPa)			Elongation (%)	Reduction of Area (%)
(°C)	(°F)	0.2% Yield	Ultimate Tensile	Fracture		
25	75	35.2(242)	71.0(490)	42.9(295)	28.0	68.6
204	400	33.8(233)	71.2(491)	49.6(342)	21.0	63.9
371	700	33.3(230)	81.7(563)	51.7(357)	20.6	60.5
454	850	32.8(226)	72.6(501)	30.5(210)	23.8	67.2
510	950	29.9(206)	50.9(351)	14.4(99)	35.8	83.8
538	1000	27.5(190)	38.9(268)	9.3(64)	30.6	86.6
566	1050	25.3(174)	30.3(209)	5.9(41)	56.7	88.4
593	1100	21.0(145)	24.0(165)	4.9(34)	59.0	86.2

ORNL-DWG 75-5482

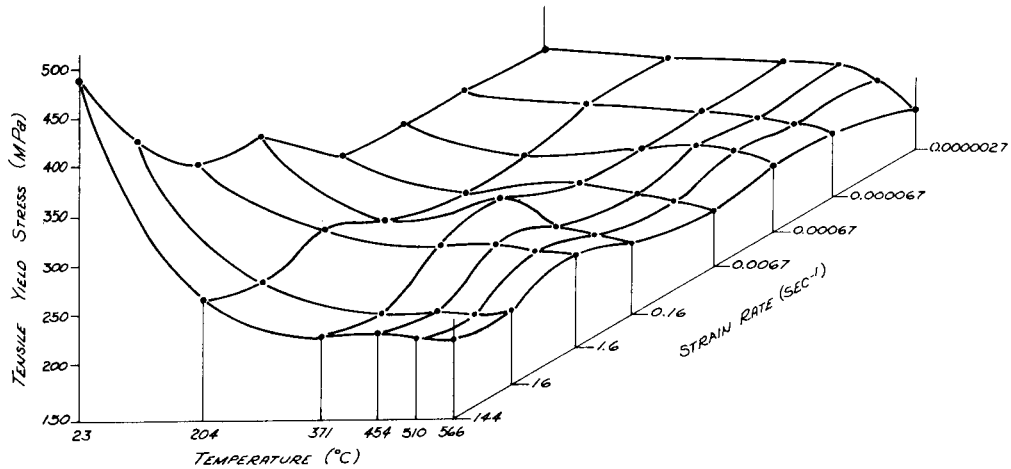

Fig. 3.77. Yield Strength of 2 1/4 Cr-1 Mo Steel as a Function of Temperature and Strain Rate.

ORNL-DWG 75-5483

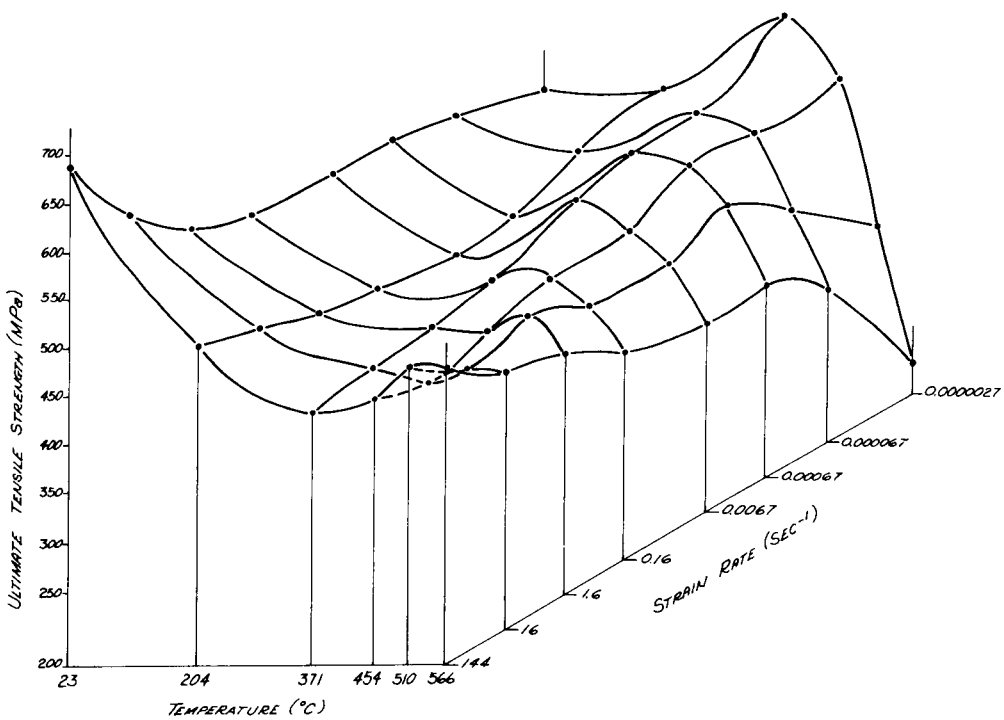

Fig. 3.78. Ultimate Tensile Strength of 2 1/4 Cr-1 Mo Steel as a Function of Temperature and Strain Rate.

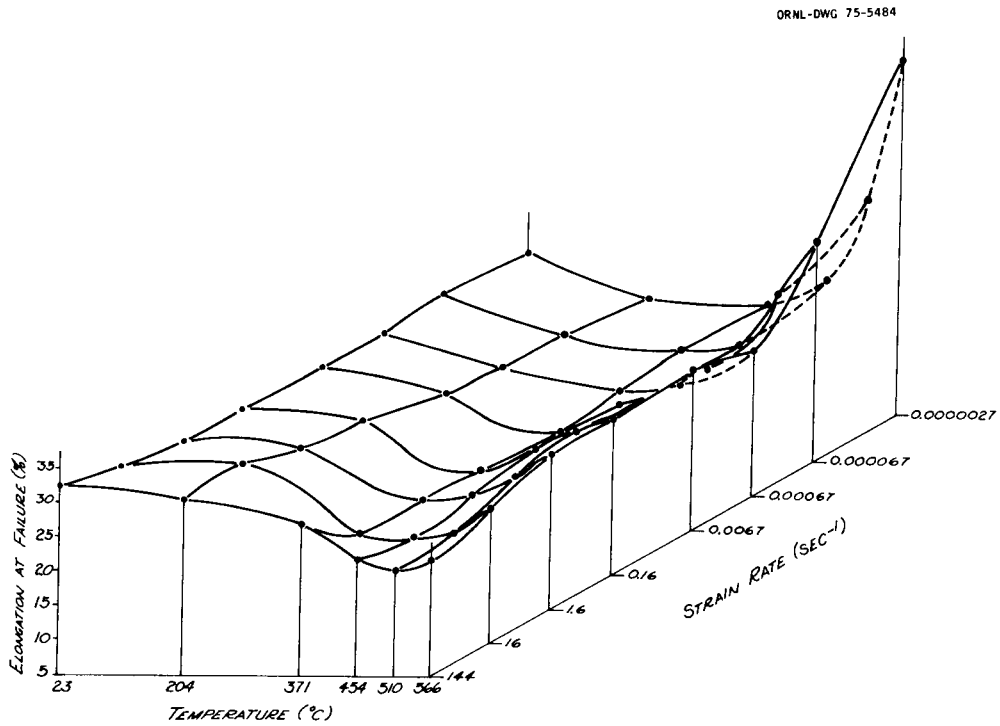

Fig. 3.79. Total Elongation of 2 1/4 Cr-1 Mo Steel as a Function of Temperature and Strain Rate.

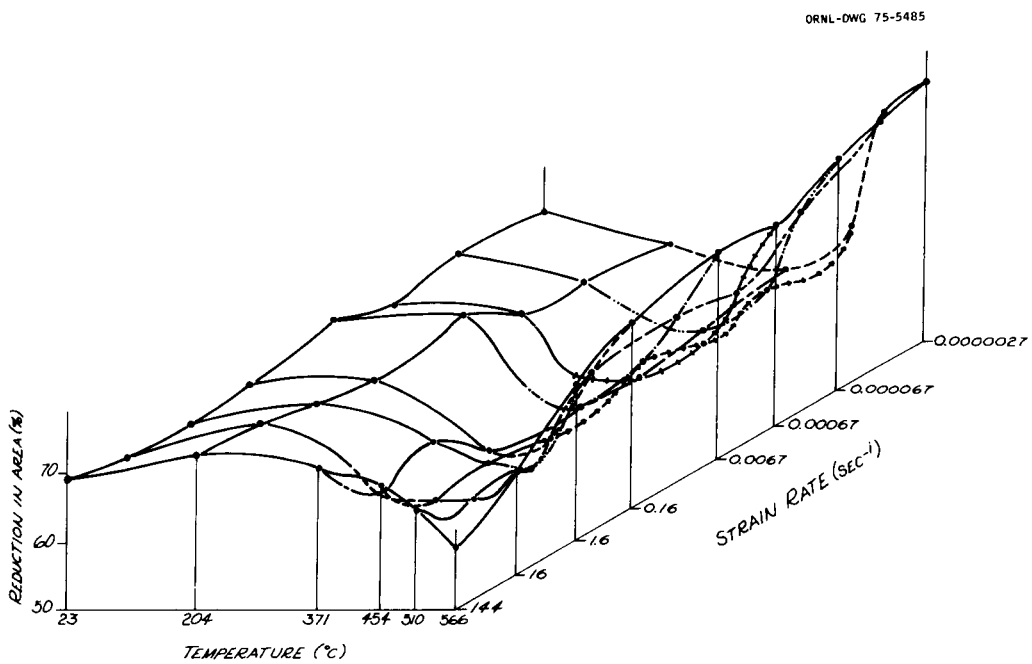

Fig. 3.80. Reduction of Area of 2 1/4 Cr-1 Mo Steel as a Function of Temperature and Strain Rate.

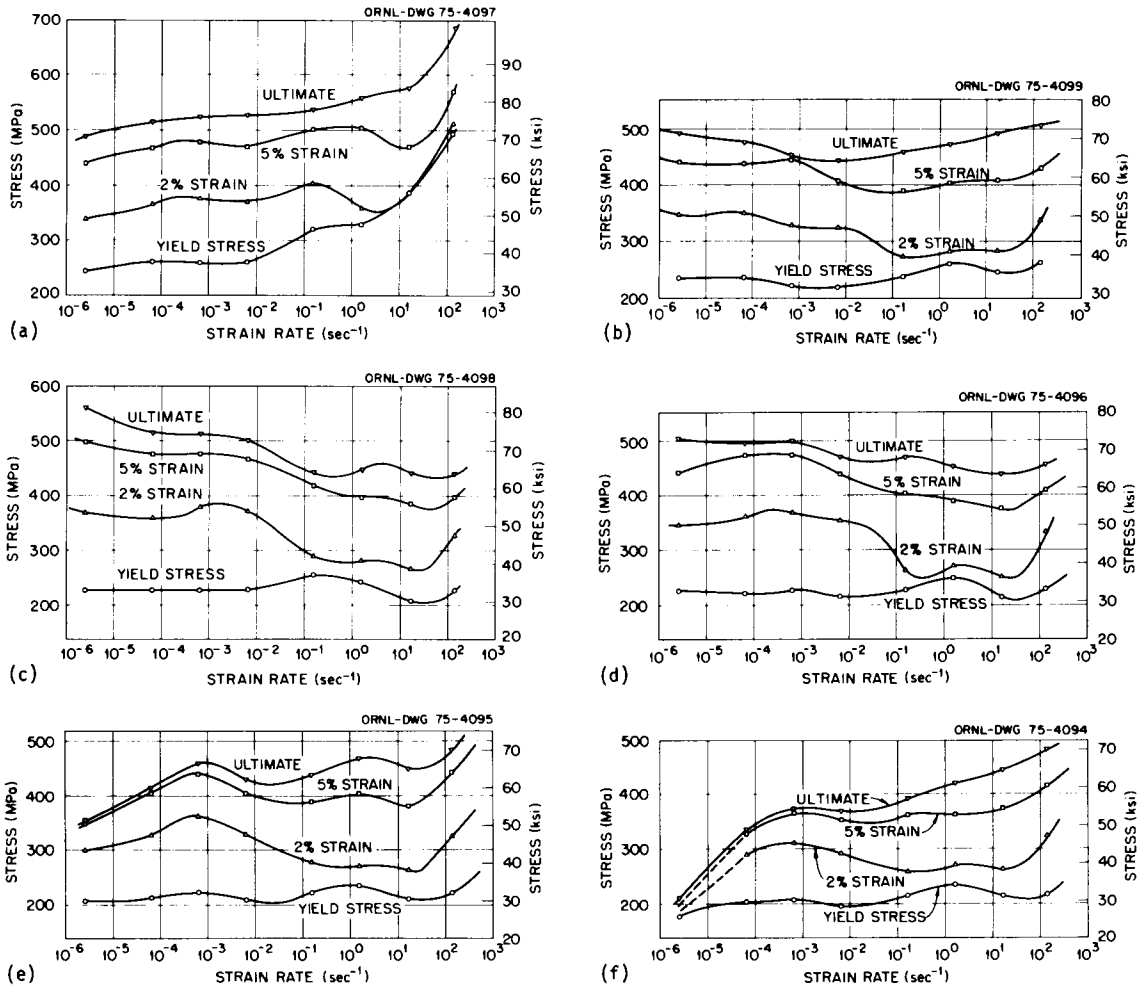

Fig. 3.81. The Yield Stress, Ultimate Tensile Strength, and Stress for 2 and 5% Strain as Functions of Strain Rate at (a) 25°C (75°F), (b) 204°C (400°F), (c) 371°C (700°F), (d) 454°C (850°F), (e) 510°C (950°F), and (f) 566°C (1050°F).

which yield stress increases rapidly with increasing strain rate. The only other effect of strain rate is an apparent local maximum in the yield stress in the range 0.01 to 10/sec above 204°C. The maximum peak height occurs at 371°C (700°F) [Fig. 3.81(c)]. This is verified by examination of the yield stress-temperature representation in Figs. 3.82(b) and (c), where a peak is observed near 371°C (700°F). Figure 3.82 also shows the effect of strain rate on the peak, as no peak is observed at 2.67×10^{-6} and 144/sec, only at the two intermediate strain rates.

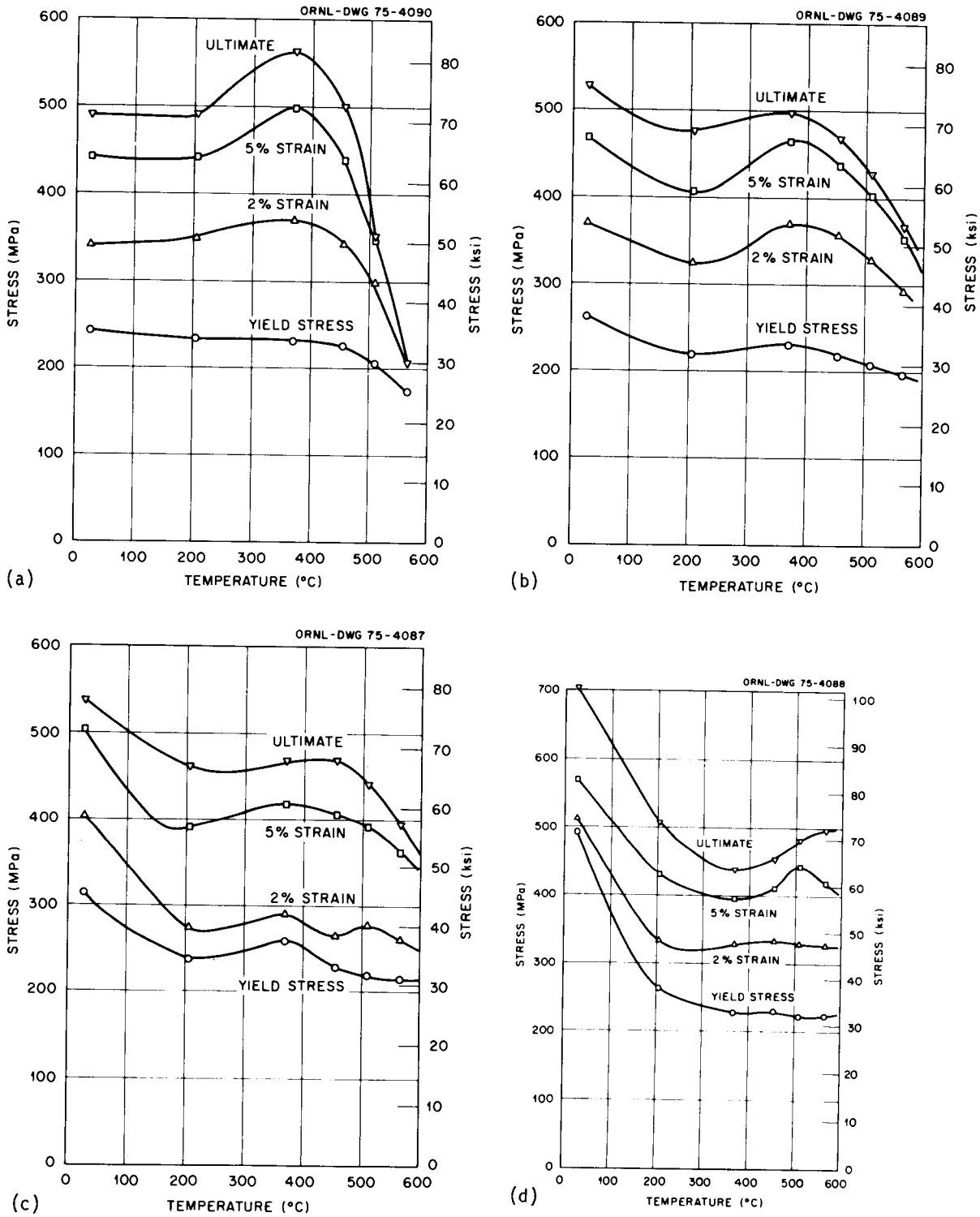

Fig. 3.82. Yield Stress, Ultimate Tensile Strength, and Stress for 2 and 5% Strain as Functions of Temperature at (a) 2.67×10^{-6}/sec, (b) 6.67×10^{-3}/sec, (c) 0.16/sec, and (d) 144/sec.

The effect of strain rate on the ultimate tensile strength, Fig. 3.78, is quite complicated. As with yield stress, the room-temperature behavior shows a considerable strain rate effect: at strain rates above 0.16/sec, there is a large increase in tensile strength with increasing strain rate; at lower strain rates, the increase is much slighter. At 204°C (400°F), Fig. 3.81(b), there is an apparent minimum at about 10^{-2}/sec, with tensile strength decreasing with increasing strain rate below and increasing above. At 371°C (700°F), Fig. 3.81(c), the ultimate tensile strength rather continuously decreases with increasing strain rate. The behavior at 454°C (850°F) is ill defined, Fig. 3.81(d), showing a plateau at the three lowest strain rates, followed by a nominally decreasing tensile strength with increasing strain rate. As the strain rate is decreased at 510°C (950°F), Fig. 3.81(e), there is little change in the strength until 6.67×10^{-4}/sec, after which the strength decreases. Finally, at 566°C (1050°F), Fig. 3.81(f), there is a continuous decrease in strength with decreasing strain rate.

From the ultimate tensile strength — temperature relationships shown in Fig. 3.82, two types of behavior can be distinguished. First, as the strain rate is decreased at 510 and 566°C (950 and 1050°F), there is a large decrease in strength, the effect increasing with increasing temperature; this is the expected strain rate behavior. Second, there is a dynamic strain-aging peak, where the tensile strength goes through a maximum. Comparison of the ultimate tensile strength curves in Fig. 3.81 shows that the lower the strain rate, the higher the strength. Furthermore, as the strain rate increases, the decreased peak occurs at higher and higher temperatures. At the highest strain rate, 144/sec, the peak appears to occur near 566°C.

Dynamic strain aging is the result of interactions of solutes (e.g., carbon and nitrogen), with dislocations. The increase in the temperature of the maximum with increasing strain rate is a reflection of the increased diffusion rate of the solutes with increased temperature (i.e., at the highest temperatures for the high strain rate, the solutes that lead to dislocation locking can diffuse rapidly enough to enhance the strength).

Strain rate effects on fracture stress (not shown graphically) are qualitatively similar to effects on ultimate tensile strength. At 25°C (75°F), there is a gradual increase in fracture stress with increasing strain rate. At 454, 510, and 566°C (850, 950, and 1050°F) the fracture strength decreases as strain rate decreases, the drop-off in strength becoming greater, the higher the temperature. For the intermediate temperatures of 204 and 371°C (400 and 700°F), the fracture strength increases with decreasing strain rate, the increase being greater at 371°C.

The effect of strain rate on total elongation, Fig. 3.79, reflects the effect of strain rate on the ultimate tensile strength. That is, a relatively high strength was accompanied by a relatively low total elongation. From 2.67×10^{-6} to 1.6/sec, the specimens tested at 371°C (700°F) had the lowest elongation, followed by those tested at 454°C (850°F), a reflection of the strength peaks at low strain rate, Fig. 3.82. Only at 510 and 566°C (950 and 1050°F) did the total elongation (at a given temperature) show significant change over the eight orders of magnitude in strain rate. At these temperatures the elongation increased with decreasing strain rate: from 18 to 37% at 510°C and 20 to 56% at 566°C. The behavior of the reduction of area, Fig. 3.80, paralleled that for the total elongation.

Uniform elongation (not shown graphically) showed relatively little effect of strain rate. Only at the lowest strain rate, 2.67×10^{-6}/sec, and the two highest temperatures, 510 and 566°C (950 and 1050°F), was there a noticable decrease in the uniform elongation with decreasing strain rate.

The general trends in properties discussed above are well illustrated by examining the selected engineering stress-strain curves shown in Fig. 3.83. Curves are shown for four strain rates at three temperatures. The large increase in strength properties above 0.16/sec at 25°C (75°F) (Fig. 3.81) is rather obvious when the upward displacement of the 144/sec curve is noted in Fig. 3.83(a). The relationship of strain rate and the peak in the ultimate tensile strength-temperature curve of Fig. 3.81 is evident in Fig. 3.83(b) and (c). At 371°C (700°F), the highest

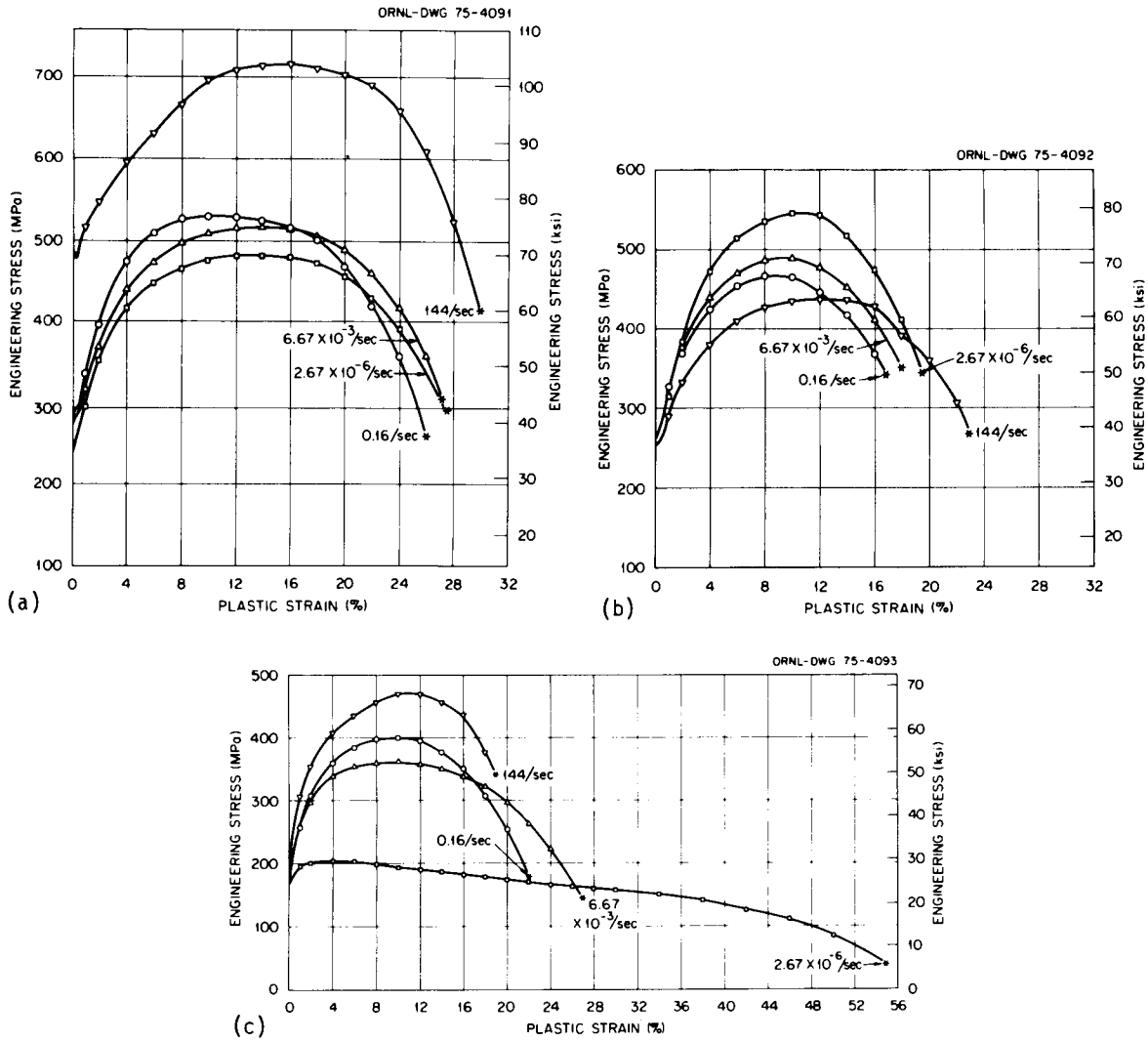

Fig. 3.83. Engineering Stress-Strain Curves for Plastic Deformation for Strain Rates of 2.67×10^{-6}, 6.67×10^{-3}, 0.16, and 144/sec at (a) 25°C (75°F), (b) 371°C (700°F), and (c) 566°C (1050°F).

stress-strain curves correspond to the lowest strain rates. In line with the shift of the peak to higher strain rates at the higher temperatures, Fig. 3.83(c) shows that at 566°C (1050°F) the trend reverses to restore the highest stress-strain curves to the highest strain rates. Figure 3.83(c) also displays the increased elongation with decreasing strain rate and increasing temperature (Fig. 3.79). With the exception of the low-strain-rate test at 566°C, all the stress-strain curves have similar shapes, especially when just the portion of the curve up to the ultimate tensile strength is considered. Hence, we expect that the plastic

behavior of the high-strain-rate tests can be represented analytically by the Voce equation,[75] as was done previously for the low-strain-rate tests.[76]

At room temperature, a yield point with its accompanying Luder's strain at the lower yield was observed at strain rates of 1.6, 16, and 144/sec. This gives rise to the merging of the yield stress and stress for 2% strain curves in Fig. 3.81; that is, the Luder's strain exceeds 2%. At 6.67×10^{-3} and 0.16/sec, an inflection point was noted in the stress-strain curves in the strain range in which a yield point would be expected. Above 25°C a yield point was noted only at 144/sec and was quite distinct for all tests conducted at that strain rate up to 454°C.

In all cases, visual examination of the fractured specimens indicated that a ductile cup-cone failure occurred. Likewise, metallography revealed that the failures were of a ductile transgranular mode. There was no evidence of any intergranular failure.

3.4.2 Effect of Sodium on Mechanical Properties of 2 1/4 Cr-1 Mo Steel — R. L. Klueh and J. M. Leitnaker

We have completed our metallurgical studies on the MSA-decarburized 2 1/4 Cr-1 Mo steel,[77-79] and a report has been issued.[80] A summary follows.

Specimens of 2 1/4 Cr-1 Mo steel that had been decarburized in sodium or aged in an inert atmosphere for 26,500 hr at 566°C (1050°F) were metallurgically examined with optical and transmission electron microscopy. The carbide particle density of the decarburized and aged specimens was considerably less after 26,500 hr than after 10,000 hr, with the density in the aged specimen being considerably greater than that in the decarburized specimen. For the aged specimen, the density decrease was a result of Ostwald ripening, and the total amount of carbide was not noticeably affected. Decarburization, however, resulted in a gradient in carbide density, with the smallest density near the surface.

Carbides were electrolytically extracted and identified by x-ray diffraction. From the before-test material, which was in the annealed condition and had a ferrite-pearlite microstructure, 1.4 wt % carbide

was obtained. This sample contained M_3C, $M_{23}C_6$, and M_6C, with $M_{23}C_6$ constituting the major portion. In the aged specimen, 2.3 wt % of precipitate was extracted and contained 60% M_6C, the balance $M_{23}C_6$. The decarburized specimen contained two regions with different carbide contents. The first 20% of the 0.063-in.-thick (1.6 mm) specimen yielded 1.3 wt % precipitate, which contained 94% M_6C, the balance $M_{23}C_6$. The interior of the specimen contained 1.6 wt % precipitate, 86% M_6C.

From the observations of these studies, the following conclusions were made:

1. The kinetics of decarburization is quite complicated and cannot be separated from the aging process.

2. The aging process and the subsequent removal of molybdenum from solid solution to form molybdenum-rich carbides may, in the limit, have as much effect on the creep properties as decarburization does.

Creep-rupture tests at 510 and 566°C (950 and 1050°F) are now being made on the decarburized and aged specimens to determine the effect of these processes on creep.

3.4.3 Heat-to-Heat Variation of 2 1/4 Cr-1 Mo Steel — R. L. Klueh

Last quarter[81] we reported on tensile studies of two small sections of forgings manufactured by the vacuum arc remelt (VAR) process, one produced by the Jorgensen Company, the other by the Coulter Company. We also obtained a small piece of plate manufactured by the electroslag remelt (ESR) process (trade name Lukens Lectrefine) by Lukens Steel Corporation. The tests reported last quarter were conducted on specimens that had been given identical isothermal anneals: 1 hr at 927°C (1700°F), furnace cooled to 704°C (1300°F) and held for 2 hr, then furnace cooled to room temperature. During this quarter, we tested these same materials in the as-received (normalized-and-tempered) condition.

Buttonhead specimens were tested at a crosshead speed of 0.05 in./min (1.27 mm/min, nominal strain rate of 0.0444/min) at 25, 204, 371, 454, 510, and 566°C (75, 400, 700, 850, 950, and 1050°F). The results are shown in Table 3.29. In Fig. 3.84 the yield stress and ultimate tensile

Table 3.29. Tensile Properties of As-Received 2 1/4 Cr-1 Mo Steel Forgings

Test Temperature		Strength, ksi (MPa)		Elongation, %		Reduction of Area (%)
(°C)	(°F)	Yield	Ultimate Tensile	Uniform	Total	
			Jorgensen (VAR)			
25	75	47.1(325)	77.3(533)	9.4	17.9	66.9
204	400	43.7(301)	67.3(464)	7.5	14.8	66.0
371	700	42.8(295)	69.9(482)	6.9	12.2	49.8
454	850	42.3(292)	63.7(439)	6.3	13.4	45.3
510	950	38.5(265)	55.6(383)	6.3	18.3	64.2
566	1050	36.4(251)	45.9(316)	5.0	21.7	73.9
			Coulter (VAR)			
25	75	52.3(361)	76.5(527)	13.4	22.3	60.6
204	400	43.3(299)	67.3(464)	10.2	18.3	72.2
371	700	38.4(265)	71.4(492)	8.8	14.9	60.1
454	850	38.2(263)	66.0(455)	8.8	16.1	65.6
510	950	33.6(232)	60.4(416)	9.8	18.7	65.6
566	1050	34.7(239)	51.1(352)	10.1	23.9	80.5
			Lukens (ESR)			
25	75	52.9(365)	82.6(570)	9.6	18.4	73.9
204	400	47.4(327)	72.6(501)	8.1	16.3	73.1
371	700	46.7(322)	74.4(513)	6.9	13.5	61.0
454	850	44.9(310)	68.6(473)	6.5	15.8	66.9
510	950	43.7(301)	61.8(426)	6.1	18.2	77.1
566	1050	39.4(272)	51.6(356)	6.4	22.3	82.6

strength are shown as functions of temperature, and in Fig. 3.85 the uniform elongation, total elongation, and reduction of area are shown as functions of temperature.

As expected, the strength of the as-received material is somewhat greater than that of the same material after an isothermal anneal. Likewise, the isothermal anneal increased the ductility of the material. These materials as received are being prepared for metallographic examination.

Last quarter[81] we gave the composition as reported by an outside laboratory. Because of the unusually high oxygen concentration reported

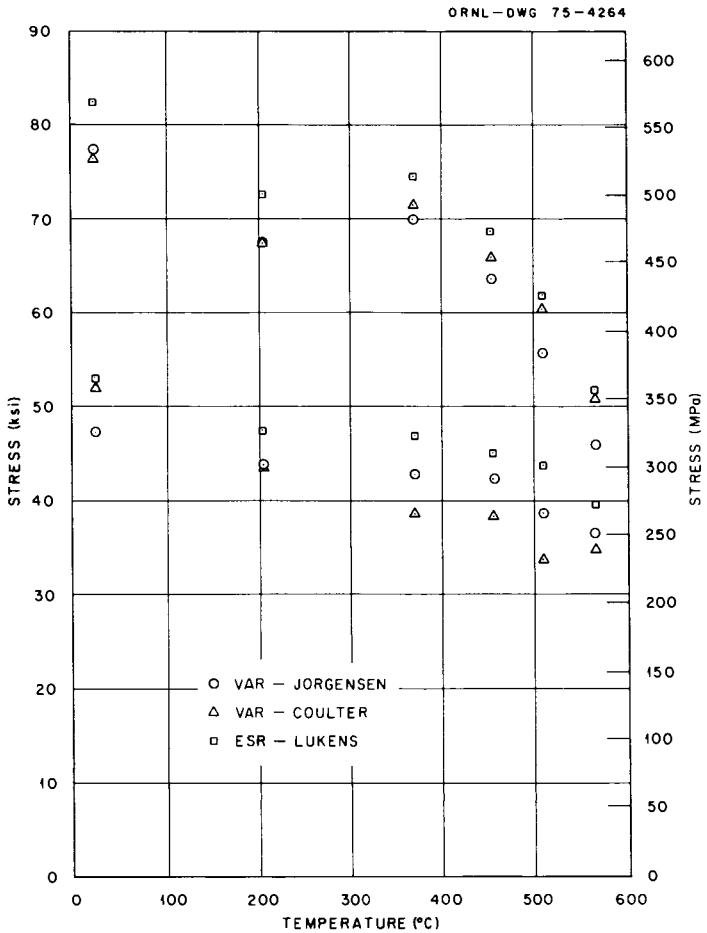

Fig. 3.84. The Yield Stress and Ultimate Tensile Strength as Functions of Temperature for the Jorgensen VAR, Coulter VAR, and Lukens ESR 2 1/4 Cr-1 Mo Steel Forgings, As Received.

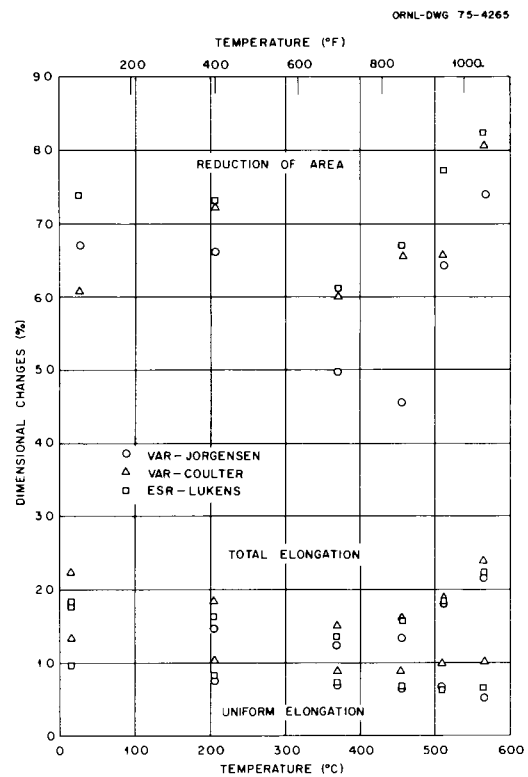

Fig. 3.85. The Uniform Elongation, Total Elongation, and Reduction of Area as Functions of Temperature for the Jorgensen VAR, Coulter VAR, and Lukens ESR 2 1/4 Cr-1 Mo Steel Forgings, As Received.

for the Jorgensen heat, we redetermined the oxygen, nitrogen, and carbon for all three heats. The nitrogen and carbon values were similar to those previously reported. The oxygen, however, was considerably below the concentrations previously reported. Instead of the 1200, 60, and 80 ppm O previously reported, values of 25, <1, and <1 ppm were determined for the Jorgensen, Coulter, and Lukens heats, respectively. These values are more in line with what is expected for these materials.

3.4.4 Fatigue Behavior of 2 1/4 Cr-1 Mo Steel — C. R. Brinkman, M. K. Booker, J. P. Strizak, W. R. Corwin, J. M. Leitnaker, and J. L. Frazier*

Fatigue testing of 2 1/4 Cr-1 Mo steel in the annealed condition continued over the range room temperature to 538°C (1000°F). The objectives of this effort are to collect (1) sufficient continuous low- and high-cycle fatigue data to establish ASME design curves for this material, (2) sufficient hold time and frequency variation data to formulate creep-fatigue design rules and to define strain aging phenomena, (3) adequate data covering the influence of material melting practice, heat treatment, and chemical or minor cold-work (heat-to-heat) variations, and (4) data covering other effects, such as thermal aging, mean stress, environment, notch behavior, crack growth rates, and biaxiality. Considerable data have been collected in support of the first objective, and progress in this area will be discussed in detail in this report. Tests presently under way will fulfill the second objective and progress to date is presented.

Details concerning specific materials, heat treatments, specimen designs, and test methods have been discussed previously.[82] However, an additional heat (heat 3P5601) of 2 1/4 Cr-1 Mo has been added to this program, and its composition is compared in Table 3.30 with previously tested material. Results reported herein were obtained from four test laboratories: Mar-Test, Battelle Memorial Institute — Columbus, Oak Ridge National Laboratory, and the Oak Ridge Y-12 Plant.

Additional strain- and load-controlled data were obtained by courtesy of General Atomic Company.[83] The chemical composition of the material tested in the GA program is compared with the ORNL heats in Table 3.30.

---

*Oak Ridge Y-12 Plant.

Table 3.30. Chemical Analysis of the 2 1/4 Cr-1 Mo Steel

Product Form	Heat	Chemical Composition, wt %								ASTM Grain Size
		C	Mn	Si	Cr	Mo	Ni	S	P	
Plate	20017	0.135	0.57	0.37	2.2	0.92	0.16	0.016	0.012	4–5
Pipe	1	0.145	0.53	0.40	2.18	0.94	0.30	0.019	0.014	7–8
Pipe	2	0.11	0.47	0.35	2.89	0.96	0.26	0.009	0.013	4–5
Pipe	3 (27479)	0.11	0.35	0.23	2.42	0.92	0.04	0.025	0.008	7–8
Plate	3P5601	0.119	0.35	0.27	2.30	0.96	0.20	0.022	0.009	5

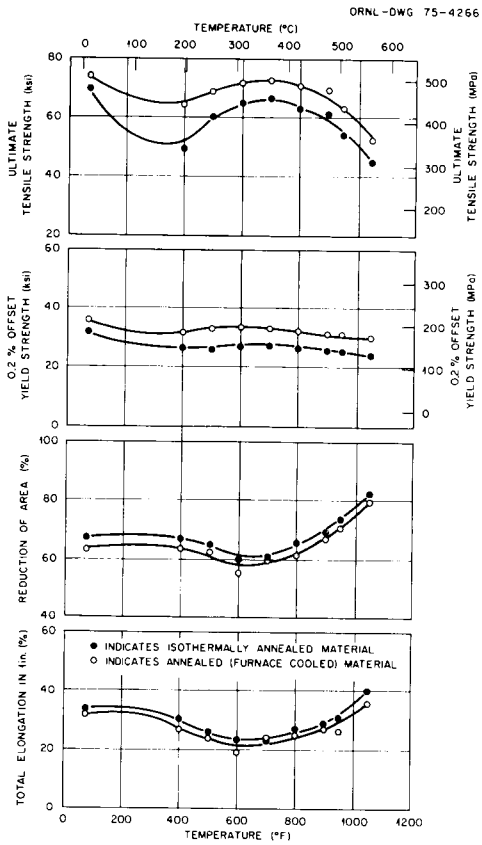

Fig. 3.86. Tensile Properties of 2 1/4 Cr-1 Mo Steel Heat 3P5601 Tested at a Strain Rate of 6.67 × 10^{-4}/sec.

Results from tensile tests conducted on heat 3P5601 are plotted in Fig. 3.86. Comparisons are made between tensile properties of this heat in both the annealed (furnace cooled) and the isothermally annealed[82] condition. Indications of strain aging in the intermediate temperature range are apparent.

3.4.4.1 Low- and High-Cycle Fatigue

Continuous cycling fatigue tests were continued at 316 and 371°C (600 and 700°F). Tests conducted at 316°C were high cycle load controlled and were run at a frequency of 20 Hz to help substantiate the estimated high-cycle life predictions based on the results of strain-controlled tests. The data are plotted in Fig. 3.87 on semilog coordinates in order to expand the abscissa scale. The solid line drawn through the strain-controlled data and extrapolated to 10^8 cycles to failure was obtained by summing the best-fit equations for the elastic and plastic components. Thus the total strain range can be expressed as

$$\Delta\varepsilon_t = \Delta\varepsilon_p + \Delta\varepsilon_e \ , \tag{40}$$

$$\Delta\varepsilon_t = AN_f^{-a} + BN_f^{-b} \ . \tag{41}$$

However, because of the bilinearity of the plastic strain range line when plotted on log-log coordinates, values of the constants A and a depend on strain range, as indicated in Table 3.31. Figure 3.87 shows the scatter in the results of the load-controlled tests to be quite high, as was the case for the 427°C (800°F) tests previously shown.[84] However, this can be attributed to the variable strain amplitude resulting from cyclic hardening and softening, as indicated by periodic extensometer measurements made during the tests and plotted in Fig. 3.87. One of the load-controlled tests (Test C) was step loaded several times following cycle numbers of about 10^7 cycles until failure occurred. The results obtained to date indicate the high-cycle fatigue life to be quite sensitive to variable strain amplitude loading when various increments of plastic strain are introduced throughout the cycle life.

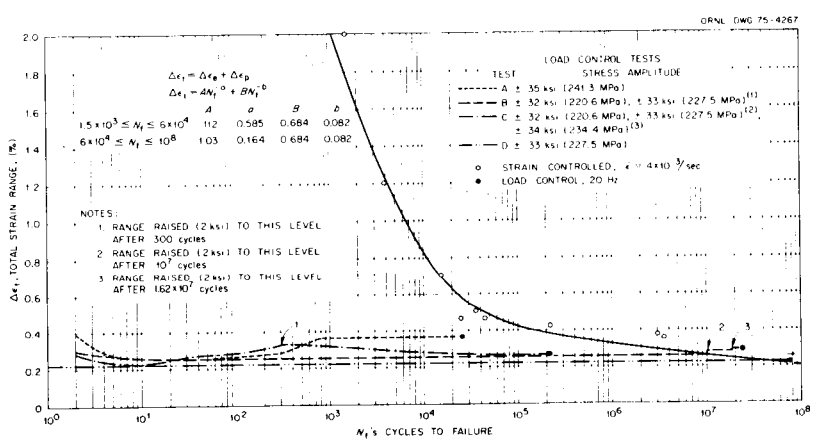

Fig. 3.87. Total Strain Range Versus Cycles to Failure for 2 1/4 Cr-1 Mo (Heat 20017) Isothermally Annealed. All tests were conducted at 316°C (600°F) in either strain or load control as indicated. Variable strain range associated with some of the load controlled tests is also shown.

A number of strain-controlled tests were conducted at 371°C (700°F), and the results are compared in Fig. 3.88. Best fit lines were again drawn through the elastic and plastic components, and bilinearity was

Table 3.31. Values for the Elastic and Plastic Strain Range Constants for Strain-Controlled Tests Conducted at a Strain Rate of 4×10^{-3}/sec

Temperature (°C)	Temperature (°F)	N_f Range (cycles)	Values of Constants in $\Delta\varepsilon_t = AN_f^{-a} + BN_f^{-b}$			
			A	a	B	b
Room		$\leq 6 \times 10^5$	112	0.585	0.684	0.082
315	600	$<6 \times 10^4$	112	0.585	0.684	0.082
		$>6 \times 10^4$	1.03	0.164	0.684	0.082
371	700	$<10^5$	102	0.683	0.713	0.081
		$>10^5$	0.214	0.063	0.713	0.081
427	800	$<1.8 \times 10^4$	166	0.661	0.407	0.031
		$>1.8 \times 10^4$	8.23	0.349	0.407	0.031
539	1000	$<1 \times 10^4$	263	0.756	0.440	0.048
		$>1 \times 10^4$	16.3	0.439	0.440	0.048
593	1100	$<7.5 \times 10^3$	210.6	0.744	0.445	0.064
		$>7.5 \times 10^3$	3.768	0.284	0.445	0.064

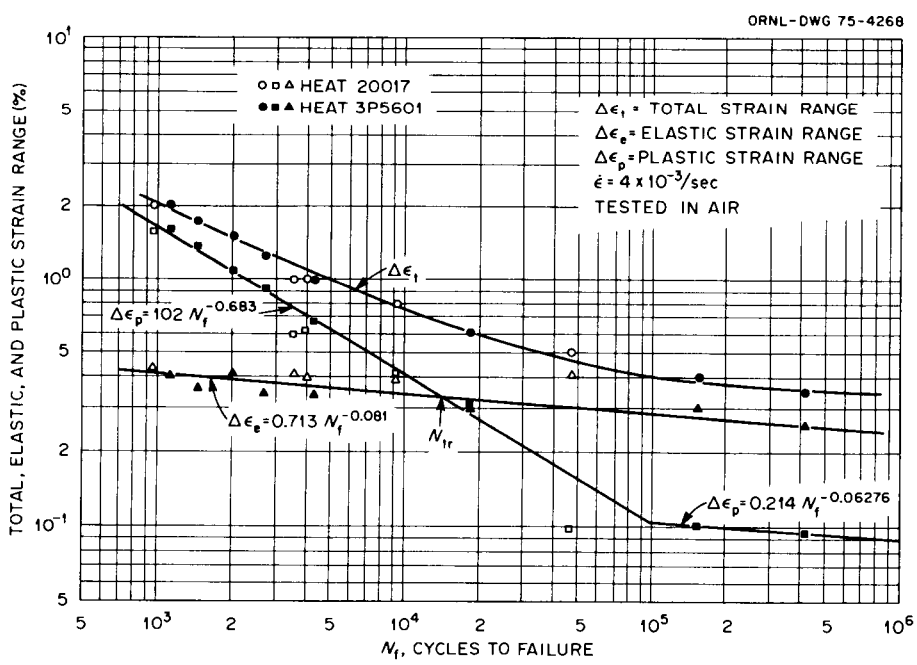

Fig. 3.88. Total Elastic and Plastic Strain Range Versus Cycles to Failure for 2 1/4 Cr-1 Mo Steel (Isothermally Annealed) at 371°C (700°F), Showing Transition Fatigue Life, N_{tr}.

indicated for the plastic component as shown. Values for the constants in Eq. (41) above for the range from room temperature to 593°C (1100°F) are summarized in Table 3.31. The GA 593°C (1100°F) data are plotted in Fig. 3.89.

Cycling specimens from the two heats in strain control at 371°C (700°F) resulted in initial rapid (primary) hardening followed by either gradual (secondary) hardening, softening, or near stability as cycling continued as evidenced by changes in load required to maintain the prescribed total axial strain range, $\Delta\varepsilon_t$, a constant. The amount of secondary hardening or softening depended upon $\Delta\varepsilon_t$, as was shown for other temperatures, with a tendency toward continuous hardening at the higher strain ranges, say 2%, and softening at lower strain ranges as shown in Fig. 3.90.

Figure 3.91 compares the total strain range versus cycles to failure lines generated from data obtained over the temperature range of 316 to 427°C (600–800°F). The plots show that the 371°C data fall generally between the two temperature extremes. Several compressive hold time and lower strain-rate continuous cycling fatigue tests were also conducted at 371°C

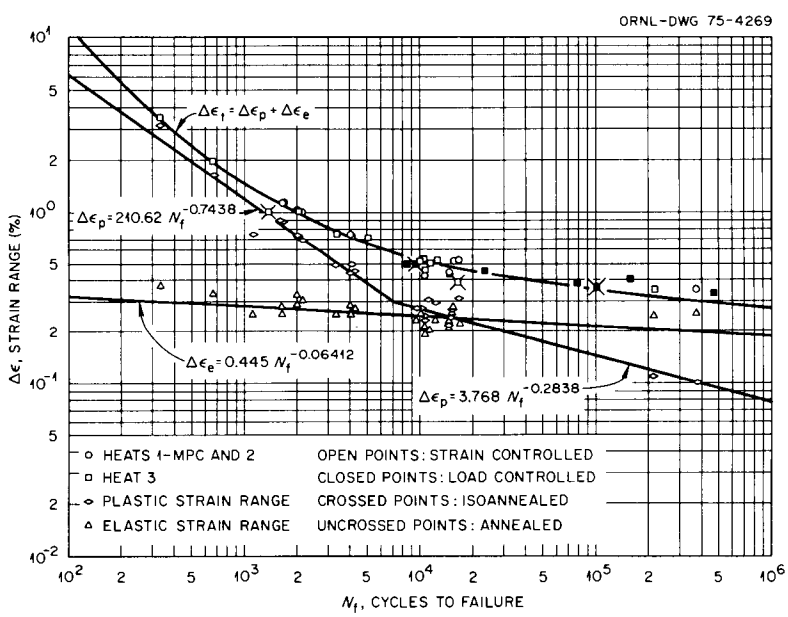

Fig. 3.89. Total, Elastic, and Plastic Strain Range Versus Cycles to Failure for 2 1/4 Cr-1 Mo Steel (Annealed and Isothermally Annealed) at 593°C (1100°F). Best fit lines for plastic and elastic strain ranges and the sum of these lines for the total strain range are shown.

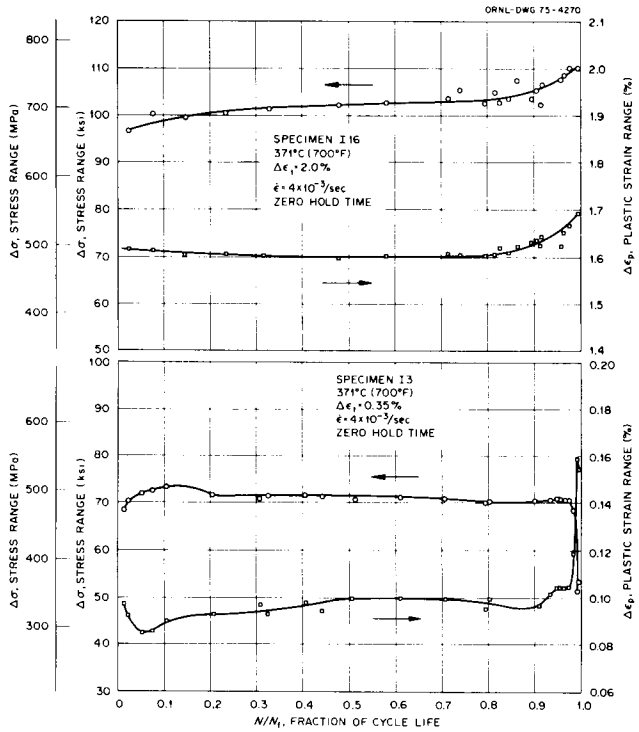

Fig. 3.90. Stress and Plastic Strain Ranges as Functions of Fraction of Cyclic Life for Isothermally Annealed 2 1/4 Cr-1 Mo Steel, Heat 3P5601, at 371°C (700°F).

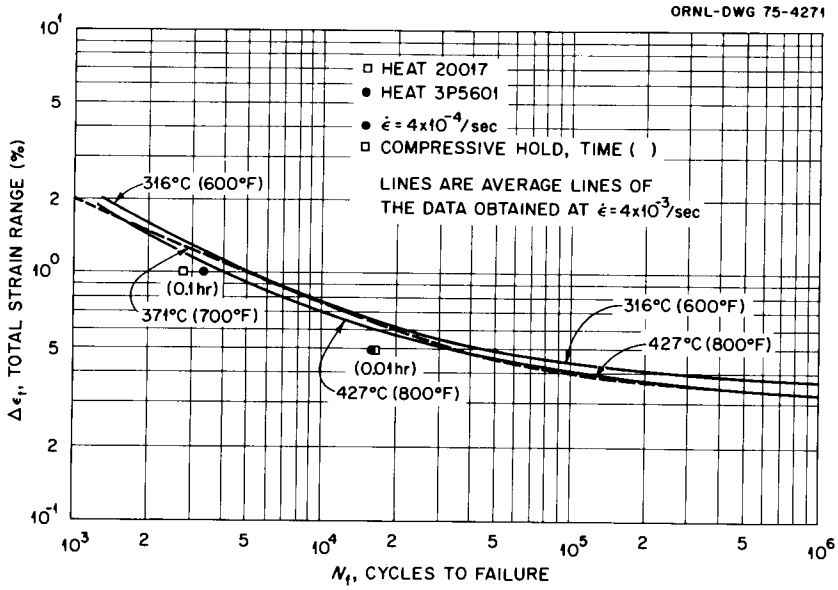

Fig. 3.91. Total Strain Range Versus Cycles to Failure for 2 1/4 Cr-1 Mo Steel, Isothermally Annealed.

to determine the influence of dynamic strain aging on fatigue life. The data shown in Fig. 3.91 indicate a degradation in fatigue life with decreasing strain rate achieved by either hold periods or a lower cyclic frequency.

Cyclic stress-strain curves were obtained with $N_f/2$ values of the stress range and are compared in Fig. 3.92 with monotonic curves obtained for the two heats undergoing testing at 371°C (700°F). Comparison of the overall fatigue lives of these two heats (see Fig. 3.88) shows little difference in their behavior at this temperature. However, for identical heat treatments some differences in both cyclic and monotonic flow response on loading are apparent from the plots given in Fig. 3.92. Further, some of the specimens (M series) from heat 20017 apparently received a slightly different heat treatment than the others in that they showed increased hardening upon cyclic deformation as shown in Fig. 3.92. Metallographic examination and hardess (R_B 73 ± 2) determinations, however, failed to detect any appreciable differences. These observations confirm previous tentative conclusions concerning the sensitivity of the cylic hardening response to heat treatment, heat-to-heat variations, etc. Stress amplitude ($\Delta\sigma/2$) is plotted in Fig. 3.93 against plastic strain amplitude ($\Delta\varepsilon_p/2$) obtained from these tests.

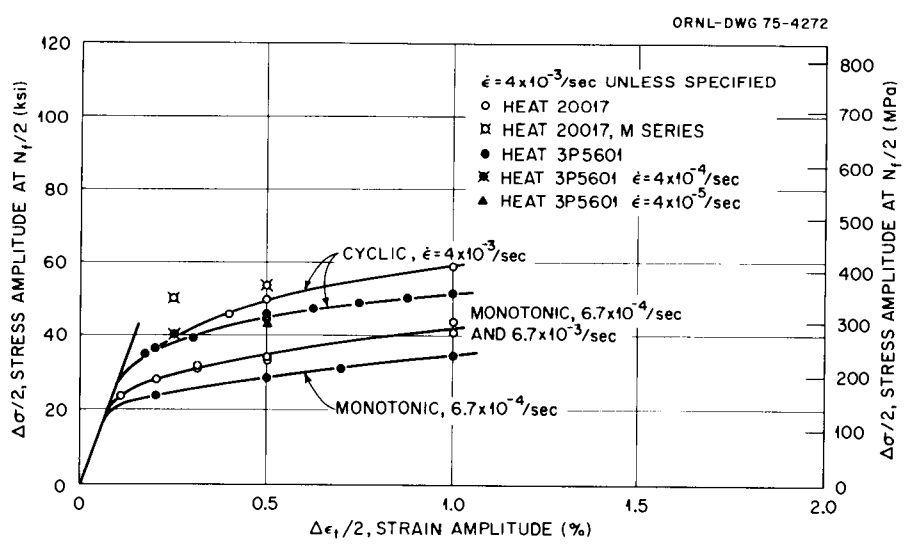

Fig. 3.92. Comparison of the Cyclic and Monotonic Stress-Strain Curves for Isothermally Annealed 2 1/4 Cr-1 Mo Steel at 371°C (700°F).

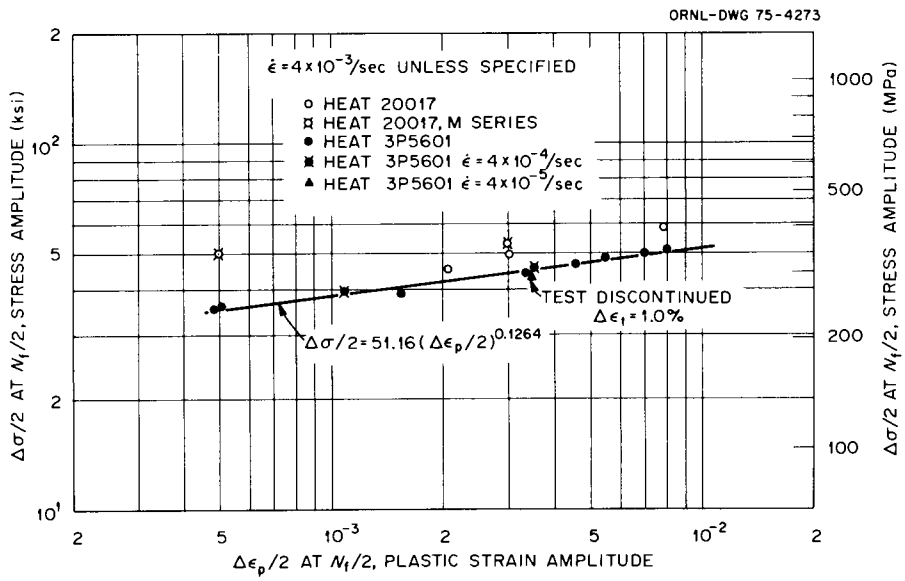

Fig. 3.93. Stress Amplitude as a Function of Plastic Strain Amplitude for Two Heats of 2 1/4 Cr-1 Mo Steel.

A summary plot of both the half-life ($N_f/2$) stress and plastic strain range as functions of temperature for several total strain ranges ($\Delta\varepsilon_t$) is given in Fig. 3.94. The plots of these independent variables indicate only slight temperature sensitivity [excluding dynamic strain aging effects at 371°C (700°F)] until temperatures above about 427°C (800°F) are obtained. Strain aging in the range 316 to 427°C (600–800°F) complicates the high-cycle fatigue life in that material tested at 316°C shows superior resistance to fatigue compared with the same material tested at room temperature, as shown in Fig. 3.95. To simplify this problem for design purposes, we decided to base the room temperature to 427°C (800°F) design curve on the 427°C data. The best fit line from the 427°C data plot reported previously[84] has been replotted in Fig. 3.96 with the available data from room temperature to 371°C (700°F) to show that it is indeed conservative with respect to the lower temperature data. This conservatism, however, may not be the case at lower frequencies or strain rates, where strain aging has been shown to reduce fatigue life. Proposed ASME design curves covering the range from room temperature to 593°C (1100°F) were constructed as reported previously[84] and are compared in Fig. 3.97. Equations for these lines have also been reported previously.[84]

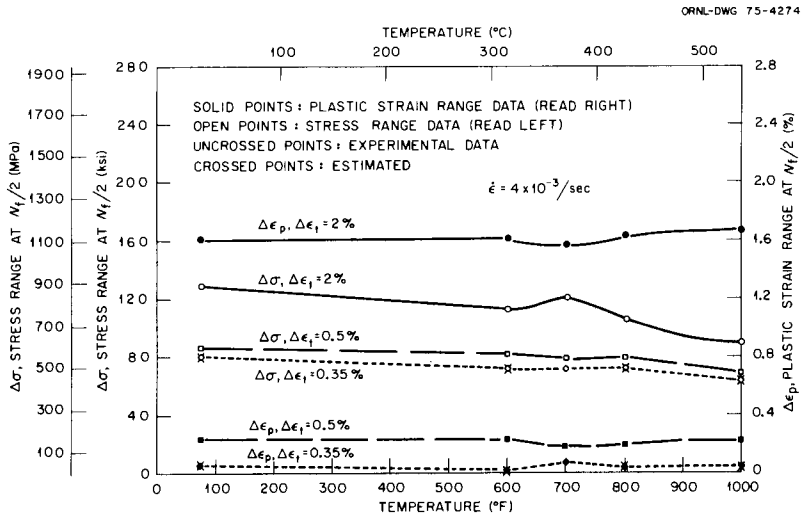

Fig. 3.94. Stress and Plastic Strain Ranges at $N_f/2$ as Functions of Temperature at Several Total Strain Ranges ($\Delta\varepsilon_t$).

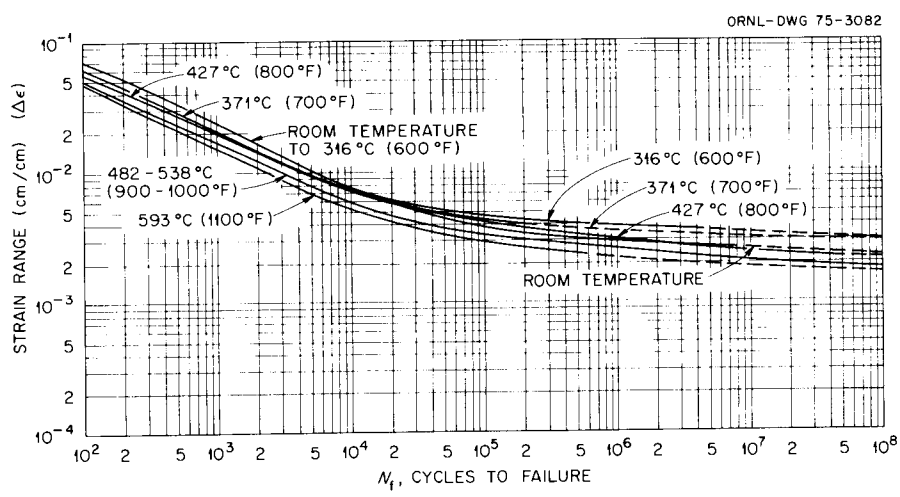

Fig. 3.95. Best Fit Fatigue Curves for Annealed and Isothermally Annealed 2 1/4 Cr-1 Mo Steel. $\dot{\varepsilon} \approx 4 \times 10^{-3}$/sec.

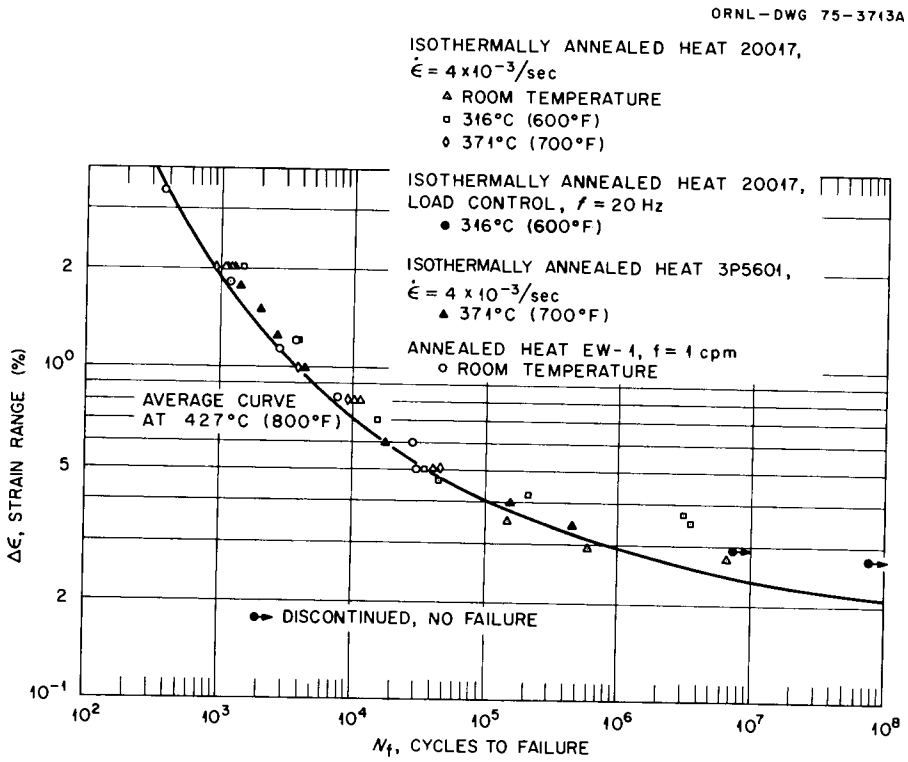

Fig. 3.96. Comparison of the Best Fit 427°C (800°F) Fatigue Curve with Lower Temperature Data. $\dot{\varepsilon} = 4 \times 10^{-3}$/sec.

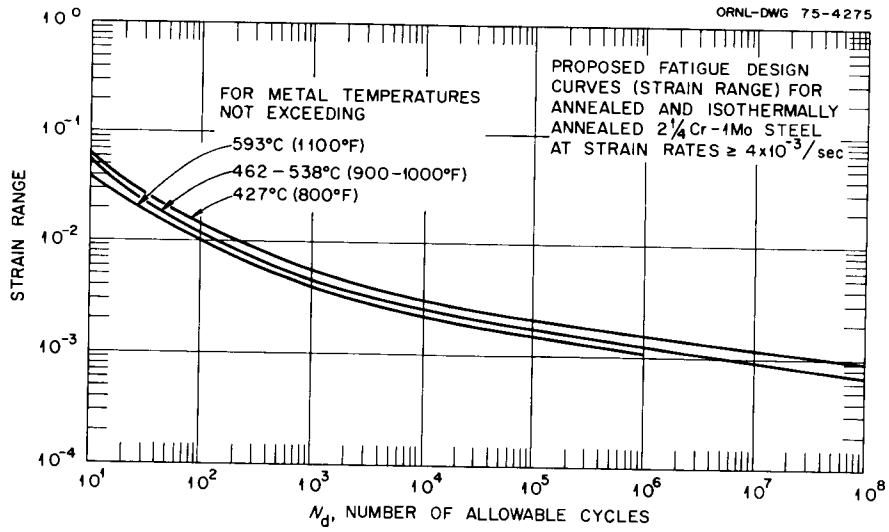

Fig. 3.97. Proposed ASME Fatigue Design Curves for 2 1/4 Cr-1 Mo Steel in the Annealed Condition for Temperatures Indicated.

3.4.4.2 Creep-Fatigue Interactions

Continuous cycling strain-controlled fatigue tests conducted with either tensile or compressive hold periods are also under way. These tests are necessary to define the design creep-fatigue curves. Figure 3.98 contains the results of hold time tests conducted to date over the range from 371 to 539°C (700–1000°F). In these plots cycle life reduction factors and changes in the plastic strain range are compared for various strain ranges and temperatures as functions of hold time. The cycle life reduction factor is defined as the ratio of the cycles to failure, N_h, for a given strain range, temperature, and hold time divided by the corresponding cycles to failure, N_f, from a test conducted under identical conditions without a hold time. The interim data were plotted this way so that the reader might compare the influence of various hold times, both tensile and compressive, on the fatigue life in tests conducted at various strain ranges and temperatures. From these plots the following preliminary conclusions concerning the behavior of 2 1/4 Cr-1 Mo steel were made:

1. There is a deleterious hold-time effect at all temperatures considered. However, the hold-time effect at 371°C (700°F) appears to be due to strain aging rather than creep, since the value of the $N_f/2$ plastic strain range actually decreases in comparison with the similar no-hold-time test.

2. The hold-time effect is greater at lower strain ranges (i.e., $\Delta\varepsilon_t$ = 0.4 or 0.5%) than at higher strain ranges. At low strain ranges compressive hold times seem to be more deleterious than the corresponding tensile hold times. Since compressive effects do occur in elevated-temperature design this finding has engineering significance and, therefore, compressive hold-time tests have been emphasized.

3. Over the temperature range and hold times employed to date, very short hold times (e.g., 0.01 hr) had a marked influence on the low-strain-range fatigue life of this material. Low strain ranges and fairly low temperatures have been particularly emphasized to date in order to obtain data approaching actual design conditions and to provide the data base for comparison with predictions based on data taken at higher temperatures and higher strain ranges.

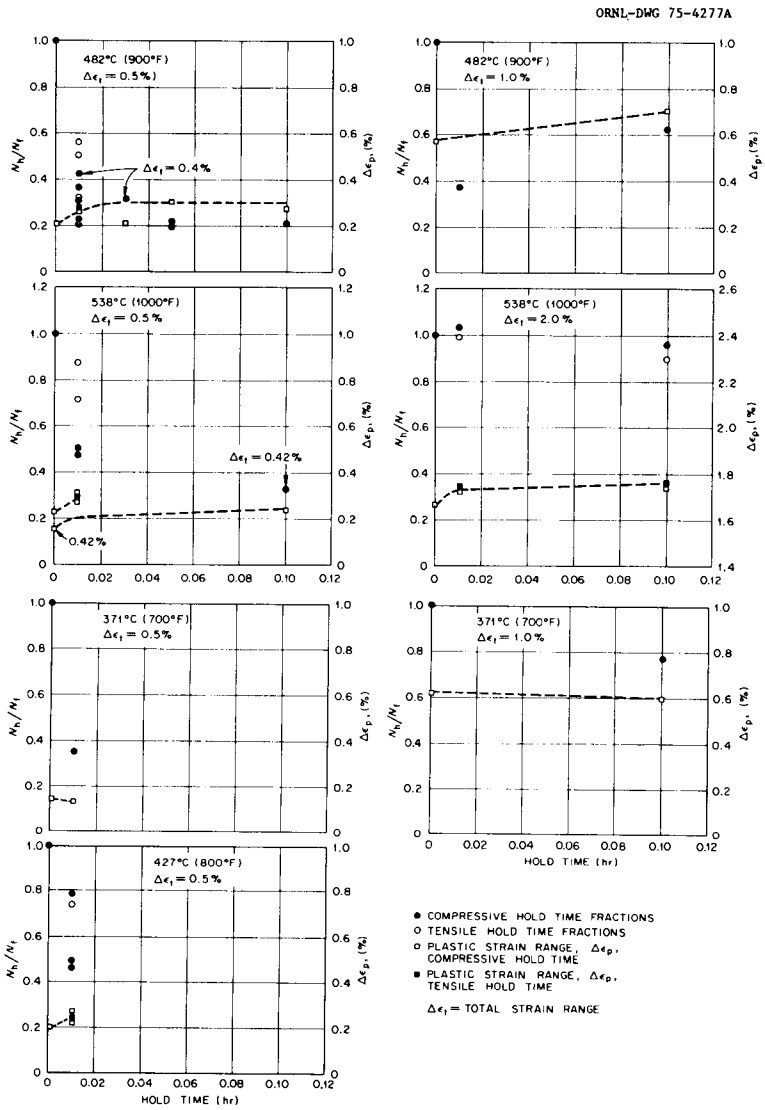

Fig. 3.98. Cyclic Life Reduction Factors for Several Strain Ranges as Functions of Strain-Controlled Hold Times (Compressive or Tensile) at Four Temperatures. N_h = cyclic life with indicated hold time. N_f = cyclic life without hold time.

Figure 3.99 compares peak stresses and plastic strain ranges achieved as functions of fraction of cycle life for specimens tested with and without hold times for similar test conditions. At low strain ranges there is a considerable apparent drop in the peak stress range introduced as a consequence of the hold times at this temperature. Also, the plastic strain range shows a marked increase.

The particularly damaging effect of compressive hold periods is somewhat contrary to earlier findings[85] on other materials, and requires investigation. One suggestion[86] has been that compressive holds tend to create a mean tensile stress and thus enhance crack propagation, leading to decreased cyclic life. An investigation of this effect, however, has shown no noticeable trend in this direction for the current data, as shown in Fig. 3.100 for two different temperatures.

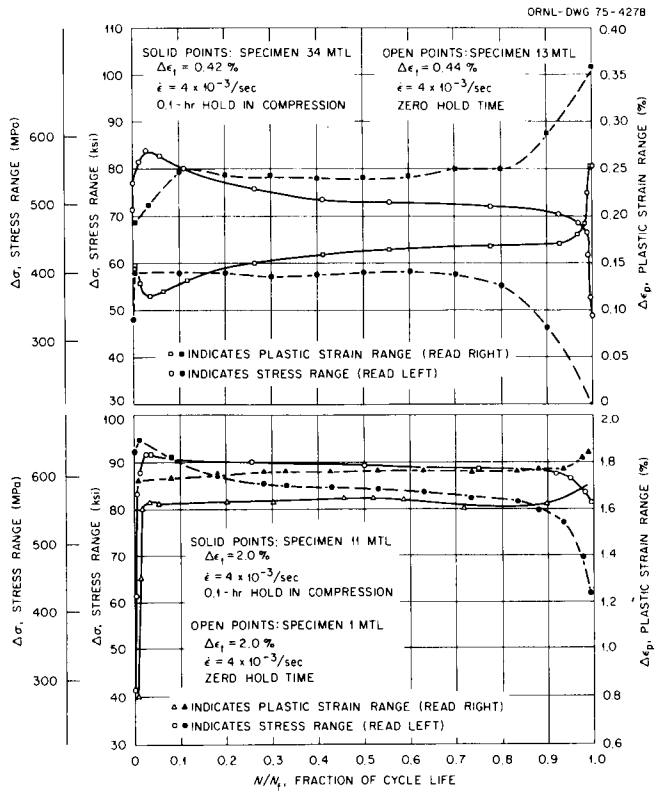

Fig. 3.99. Stress and Plastic Strain Ranges as Functions of Fraction of Cyclic Life for 2 1/4 Cr-1 Mo Steel (Isothermally Annealed) at 538°C (100°F). Tests conducted with and without hold times are compared.

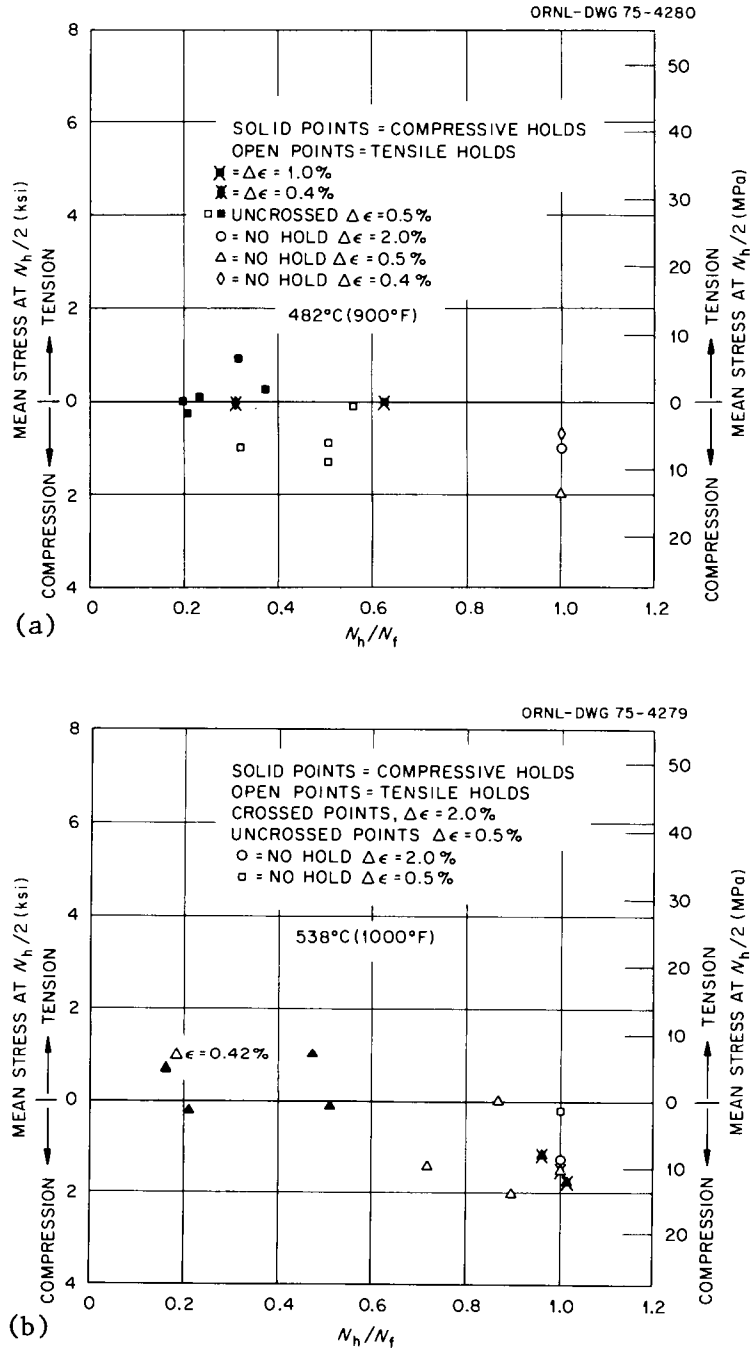

Fig. 3.100. Half-Life Mean Stresses for Isothermally Annealed 2 1/4 Cr-1 Mo Steel Heat 20017. (a) At 482°C (900°F). (b) At 538°C (1000°F).

3.4.4.3 Creep-Fatigue Data Analysis

Several methods for the analysis of creep-fatigue data have been proposed, including the strain range partitioning approach,[87] the linear summation of damage approach,[88] the frequency modification approach,[89] the ductility exhaustion approach,[90] and several others. Most methods, however, require a complete spectrum of data, including a range of hold times, strain ranges, etc. However, data obtained in the current program are as yet incomplete, making analysis by these latter methods difficult. Interim results have been obtained, however, by the methods of strain range partitioning and linear summation of damage.

The linear summation of damage approach is that currently used for actual design.[32] Briefly, the method consists of separately identifying creep and fatigue "damage fractions." If these two types of damage fractions combine linearly, then the sum of the two damage fractions should be equal to unity:

$$D_c + D_F = 1 \ , \tag{42}$$

where

$$D_c = \Sigma \Delta t / t_r = \text{creep damage fraction} \ , \tag{43}$$

$$D_F = N_h / N_f = \text{fatigue damage fraction} \ . \tag{44}$$

Here, N_h is the number of cycles to failure with hold times and N_f is the number of cycles to failure that would have been expected with no hold time. At 427°C (800°F) N_f was determined from actual data at a given strain range, while 538°C (1000°F) data were used to establish N_f at both 538 and 482°C (900°F). For the calculation of creep damage, D_c, Δt is the time increment at a given stress and t_r is the expected rupture life (taken from the *NSM Handbook*) at that stress and test temperature. In the present case, the calculation of creep damage is complicated, however, by the fact that the hold times are strain controlled, and thus the stress relaxes during each hold period. Therefore the term $\Delta t / t_r$ for each cycle must be evaluated by integration over the relaxation curve so that the creep damage in one cycle becomes

$$D_c^1 = \int_0^{t_r} dt/t_r \ , \tag{45}$$

where t_r is now the rupture life expressed as a function of the continuously changing stress.

The integrals in Eq. (45) have been evaluated by first fitting a Gittus-type equation[91] to the relaxation curves, such that

$$\ln(\sigma_0/\sigma) = At^{\alpha} \ , \tag{46}$$

where σ_0 = maximum stress, σ = a stress somewhere on the relaxation curve corresponding to time t, A,α = constants. Solving this equation for stress as a function of time yields the relationship

$$\sigma = \exp(\ln \sigma_0 - At^{\alpha}) \ . \tag{47}$$

Equation (47) then allows the integral in Eq. (45) to be evaluated numerically by Simpson's rule by use of a model for t_r previously developed[92] at ORNL. The entire analysis is performed by means of the DAMAGE computer program.[93]

This integration technique involves knowledge of actual relaxation curves, and cannot readily be performed separately for each cycle. An approximation was therefore used. The procedure was to perform the integration on a representative relaxation curve obtained at the half-life ($N_f/2$) and to multiply the creep damage during this cycle by the total number of cycles to failure, such that

$$D_c = N_h \int dt/t_r \ . \tag{48}$$

It should be noted that Campbell,[88] in a similar analysis of type 304 stainless steel, defined failure as the point at which the stress range had decreased 5% from its stabilized value rather than actual specimen separation. For fatigue damage, this definition makes no significant difference, since N_h and N_f would both be defined in this way. For creep

damage calculations performed to date, the damage per cycle is so small (10^{-6}–10^{-4}) that there is again no meaningful difference. Actual specimen separation was used here to be consistent with previous work[84] in the current program.

Figure 3.101 shows a "damage summation diagram" calculated for results obtained to date at 427, 482, and 538°C (800, 900, and 1000°F) by the above technique, while Fig. 3.102 shows the result of life predictions obtained by rewriting Eq. (42) as

$$N_{\mathrm{PRED}} = N_f(1 - D_c) \ . \tag{49}$$

Tests involving tensile holds are correlated well by this technique, while the correlation for tests involving compressive holds is considerably less effective. Such a result is not surprising since the data used to establish

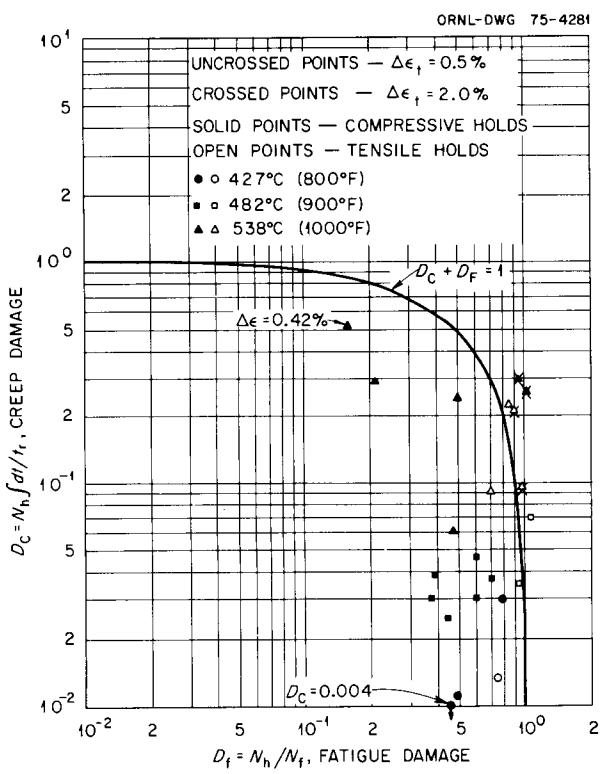

Fig. 3.101. Results of Linear Summation of Damage Analysis of Hold-Time Fatigue Data for Isothermally Annealed 2 1/4 Cr-1 Mo Steel.

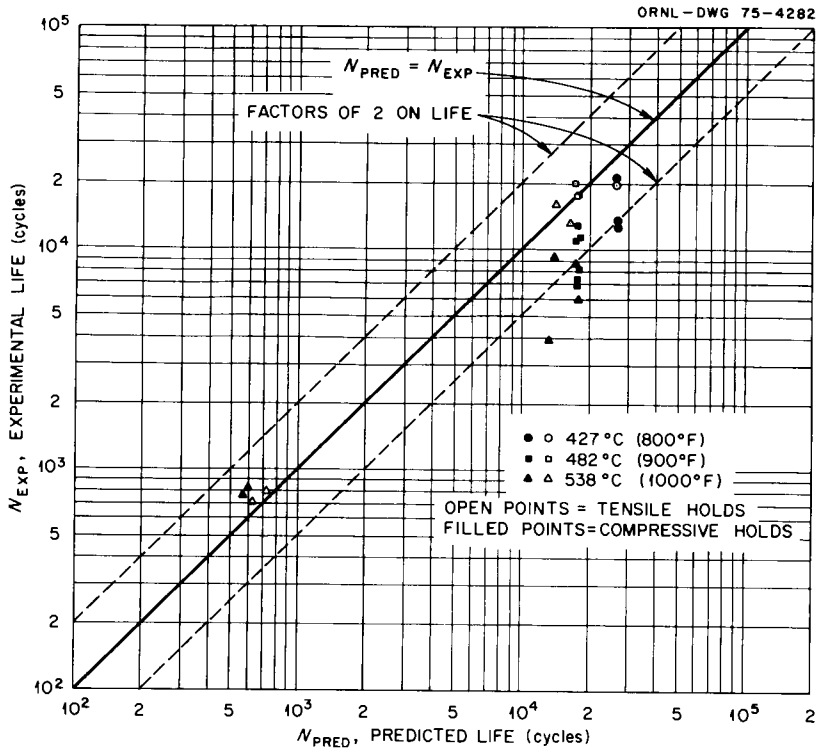

Fig. 3.102. Comparison of Experimental Hold-Time Fatigue Lives with Predicted Lives Calculated by the Linear Summation of Damage Approach.

the t_r values were all from tensile creep-rupture tests. Meaningful correlation of tests involving compressive or combined tensile-compressive holds would probably require data from cyclic creep-rupture tests such as those reported by Halford.[94]

For design applications, the values of t_r and N_f in Eqs. (43) and (44) are replaced by t_D and N_D, where t_D and N_D are design limits on rupture life and fatigue life, respectively. Thus, the design damage criterion becomes

$$\Sigma \frac{\Delta t}{t_D} + \frac{N_n}{N_D} < 1 \ . \tag{50}$$

Calculations of damage using this rule will be reported next quarter.

The strain range partitioning approach involves partitioning the plastic strain range traversed by a cycling specimen into four types:

$\Delta\varepsilon_{pp}$ = tensile plastic strain reversed by compressive plastic strain,

$\Delta\varepsilon_{cc}$ = tensile creep strain reversed by compressive creep strain,

$\Delta\varepsilon_{cp}$ = tensile creep strain reversed by compressive plastic strain,

$\Delta\varepsilon_{pc}$ = tensile plastic strain reversed by compressive creep strain.

Here, "plastic" strain is defined as time-independent inelastic strain, while "creep" strain is defined as time-dependent inelastic strain.

Test results obtained to date at 427, 482, and 538°C (800, 900, and 1000°F) include either tensile or compressive hold periods at constant strain. Thus, in this case, the types of strain involved are $\Delta\varepsilon_{pp}$, $\Delta\varepsilon_{cp}$, and $\Delta\varepsilon_{pc}$ only, where $\Delta\varepsilon_{cp}$ and $\Delta\varepsilon_{pc}$ are defined by

$$\Delta\varepsilon = \Delta\sigma_r/E \ , \tag{51}$$

where $\Delta\sigma_r$ is the total change in stress due to relaxation and E is Young's modulus at test temperature.

Application of the strain range partitioning approach involves two steps. First, "life relationships" must be formulated whereby $\Delta\varepsilon_{pp}$, $\Delta\varepsilon_{cp}$, and $\Delta\varepsilon_{pc}$ are related respectively to N_{pp}, N_{cp}, and N_{pc}, where N_i is the expected cycle life of a specimen cycled in pure $\Delta\varepsilon_i$ strain. Formulation of a life relationship for $\Delta\varepsilon_{pp}$-N_{pp} was reported previously.[84] However, the present data do not involve enough different strain ranges or enough creep strain to enable formulation of $\Delta\varepsilon_{cp}$-N_{cp} and $\Delta\varepsilon_{pc}$-N_{pc} relationships. Such relationships for annealed 2 1/4 Cr-1 Mo steel, which were generated at high strain ranges, have been reported previously.[87] Thus, the present approach was to use our $\Delta\varepsilon_{pp}$-N_{pp} relationship[84] and $\Delta\varepsilon_{pc}$-N_{pc} and $\Delta\varepsilon_{cp}$-N_{cp} relationships reported by Manson et al.[87]

Once the life relationships are established, the next step is to formulate a damage rule to predict cyclic lives for tests involving mixtures of the various types of strain. One approach might be to again formulate a linear rule such that

$$D_{pp} + D_{cp} + D_{pc} + D_{cc} = 1 \ , \tag{52}$$

where, for example, D_{cp} is a "damage fraction" calculated for $\Delta\varepsilon_{cp}$ strain by

$$D_{cp} = N/N_{cp} \ . \tag{53}$$

However, recent experience has suggested that an "interaction damage rule"[95] is more appropriate.[96] Employing this rule, for example, D_{cp} would be given by

$$D_{cp} = \frac{\Delta\varepsilon_{cp}}{\Delta\varepsilon_{\text{inel}}} \left(\frac{N}{N_{cp}} \right) \ , \tag{54}$$

where $\Delta\varepsilon_{\text{inel}}$ is the total inelastic strain range and N_{cp} is the life corresponding to a pure $\Delta\varepsilon_{cp}$ strain equal to $\Delta\varepsilon_{\text{inel}}$.

In the present analysis, the interaction damage rule has been used, although the relationships taken from Manson et al.[87] had been established by the linear damage rule. Such an approach requires caution, but it turns out that the values of $\Delta\varepsilon_{cp}$ and $\Delta\varepsilon_{pc}$ from the linear rule technique[87] are of the same order of magnitude as the $\Delta\varepsilon_{\text{inel}}$ values for the present data, while the $\Delta\varepsilon_{\text{inel}}$, $\Delta\varepsilon_{cp}$, and $\Delta\varepsilon_{pc}$ values from ref. 87 are generally somewhat higher than those for the present data. Therefore, the current technique of summing damage by the interaction rule using the linearly determined[87] life relationships has an advantage in that it makes extrapolation of the life relationship line unnecessary.

With the life relationships and the damage summation rule established, the remaining step is "simply" to determine $\Delta\varepsilon_{pp}$, $\Delta\varepsilon_{cp}$, and $\Delta\varepsilon_{pc}$ for a given test. Here again, in the present analysis, values have been obtained from a representative cycle at $N_f/2$. For example, in a test with a tensile hold period, $\Delta\varepsilon_{cp}$ is defined by Eq. (51) and $\Delta\varepsilon_{pp}$ is given by

$$\Delta\varepsilon_{pp} = \Delta\varepsilon_{inel} - \Delta\varepsilon_{cp} \ . \tag{55}$$

However, there is somewhat of a complication in the determination of $\Delta\sigma$. At the beginning of a hold period, the stress undergoes a sudden rapid decrease ($\Delta\sigma_i$) followed by a period of more gradual decrease. Diercks[97] has attributed such a decrease for type 304 stainless steel to a strain-rate effect caused by a sudden change from the ramp strain rate to the zero strain rate of the hold period, and has thus suggested that the strain

$$\varepsilon_{in} = \Delta\sigma_{in}/E \ , \tag{56}$$

might be considered plastic rather than creep strain. Furthermore, there is some indication that plastic strains accumulated during relaxation and creep strains are not equivalent.[97] The current results have been obtained by treating the entire plastic strain due to relaxation as creep, but the effect is being examined closely. Life predictions obtained by the strain range partitioning approach are shown in Fig. 3.103. All predictions are within a factor of 2 on life, and are considerably better than those obtained through the linear summation of damage method (Fig. 3.102). If the strain ε_{in} were plastic rather than creep, the predictions should be overconservative. Indeed, there is some tendency to underpredict, although several lives were overpredicted.

Analysis by these two methods will continue, including attempts to identify creep failure behavior under cyclic conditions and a further investigation of the plastic strain increase during relaxation. Also, analysis by other techniques will begin as more data become available. Thus, both descriptions of material behavior and comparisons of analytical methods will be obtained.

3.4.4.4 Microstructural Studies of Fatigue Specimens

In order to understand the softening and hardening behavior that occurs as a function of temperature and strain range as well as to characterize microstructural changes that occur during dynamic strain aging, transmission electron microscopy studies (TEM) have been initiated. These studies are

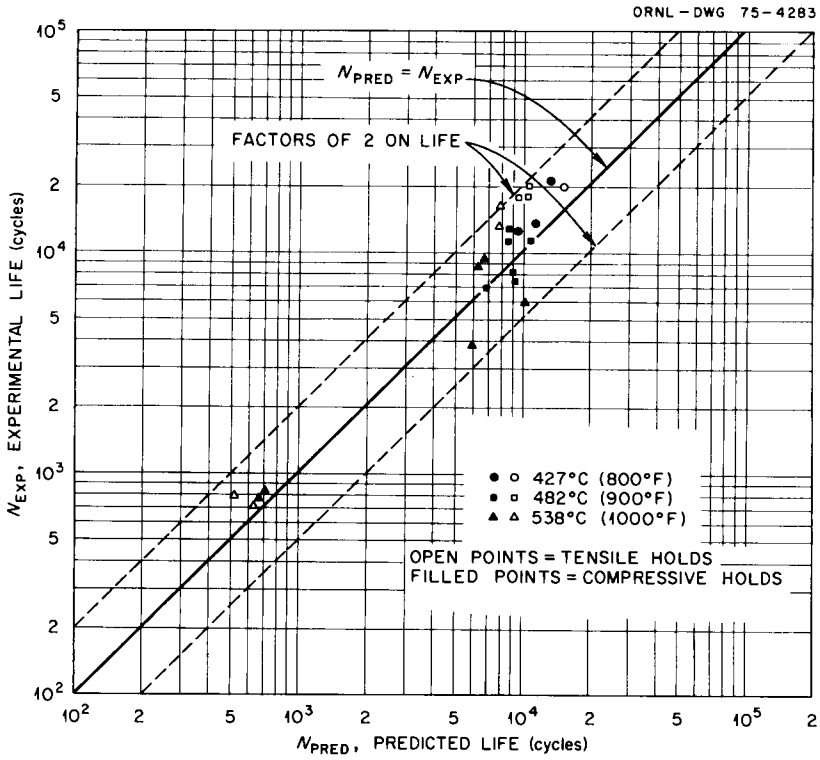

Fig. 3.103. Comparison of Experimental Hold-Time Fatigue Lives with Predicted Lives Calculated by the Strain Range Partitioning Approach.

being conducted on material adjacent to the fracture (fatigue) surface (minimum diameter of the hourglass specimen), as well as at various positions remote from the fatigued section for comparison.

To date we have examined two specimens that were fatigued at 427°C (800°F). Specimen 18MTL and 31MTL were tested at total strain ranges of 2 and 0.36%, respectively. Specimen 18MTL cyclically hardened initially quite rapidly (primary hardening) and then continued to harden at a decreasing rate throughout most of test, while specimen 31MTL hardened rapidly during the first few cycles and then softened at a decreasing rate throughout the remainder of the test.[82] Cyclic softening at all temperatures results in deviations from the Coffin-Manson law for linearity of plastic strain range versus cyclic life when plotted on log-log coordinates.

Transmission electron micrographs taken of various samples from specimen 31MTL (0.36%) at increasing distances from the fatigue fracture surface are shown in Figs. 3.104 and 3.105. Micrographs of specimen 18MTL (2%) are shown in Fig. 3.106. Figure 3.107 shows a region in the head of

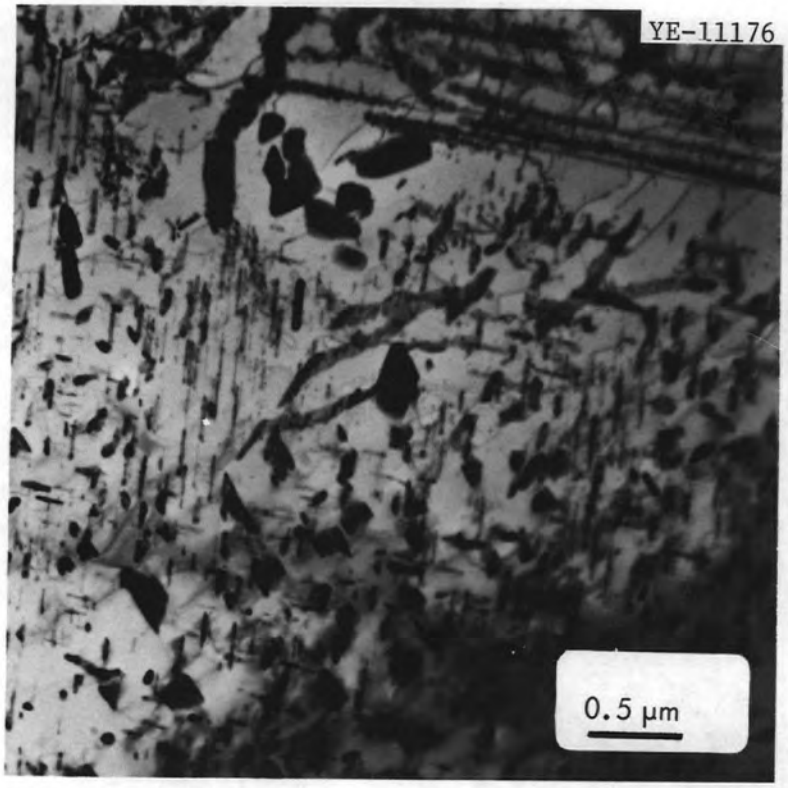

Fig. 3.104. Representative Areas from a High-Cycle Fatigue Specimen (31 MTL) 0.027 in. (0.69 mm) from Fracture Surface.

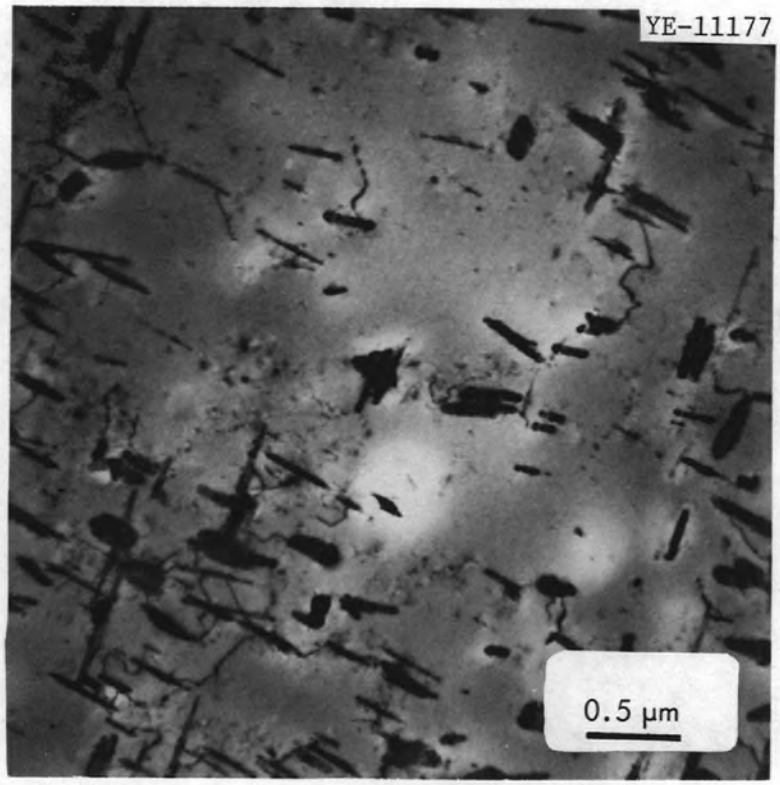

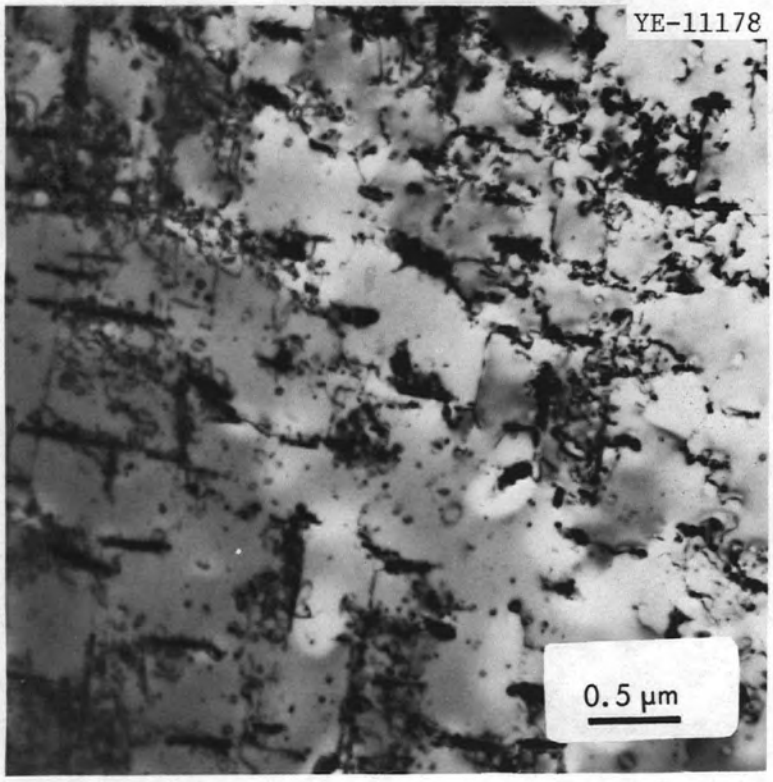

Fig. 3.105. Representative Areas from a High-Cycle Fatigue Specimen (31 MTL) 0.081 in. (2.06 mm) from Fracture Surface.

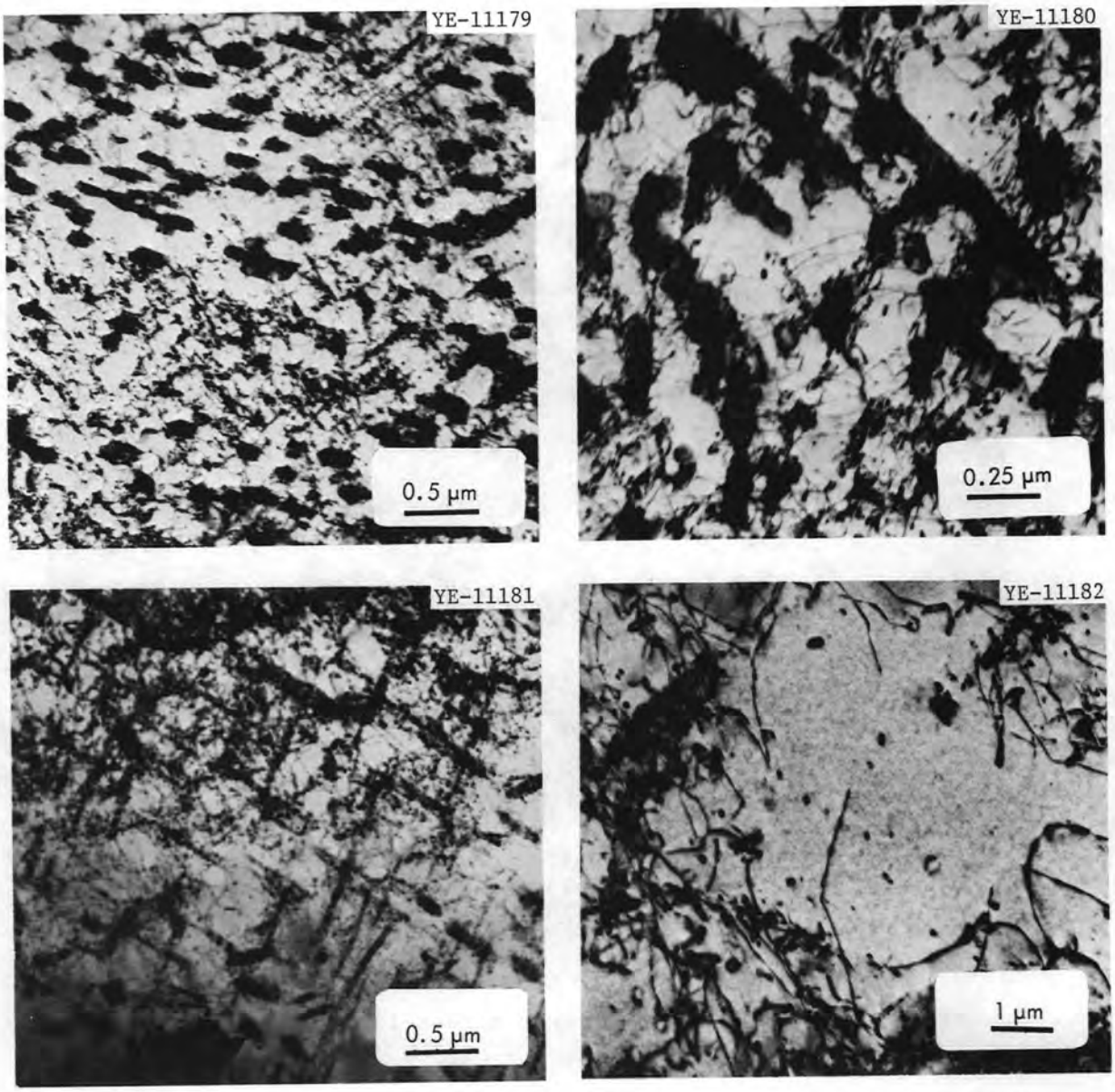

Fig. 3.106. Representative Areas from a Low-Cycle Fatigue Specimen (18 MTL) 0.054 in. (1.37 mm) from Fracture Surface.

the specimen that saw no plastic straining during the fatigue tests. These electron micrographs show a complex precipitate morphology and distribution, with some dislocation-precipitate interaction, which is particularly apparent in the high-strain-range test specimen in Fig. 3.107.

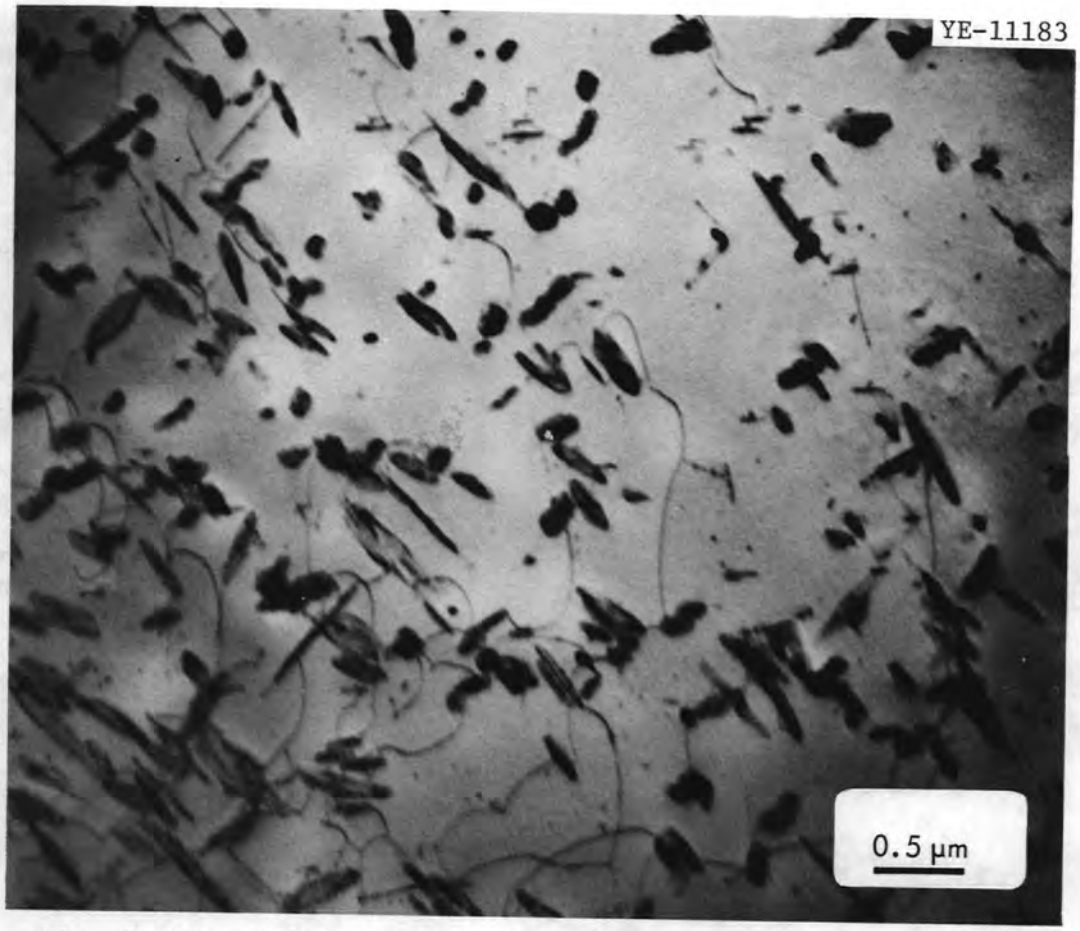

Fig. 3.107. Region from Unstressed Specimen Showing Dislocation Structure in Region with Comparable Precipitate Density to Fig. 3.106.

3.4.4.5 Subcritical Crack Growth of 2 1/4 Cr-1 Mo Steel

The effects of temperature, mean stress level, frequency, and environment on 2 1/4 Cr-1 Mo steel are being studied by use of five electrohydraulic closed-loop test systems. Specimen configurations include compact tension (CT), wedge opening load (WOL), and center notch (CN). The material used in this study to date has been heat 20017 in the isothermally annealed condition. Its mechanical properties have been reported in previous quarterlies.

The room-temperature subcritical crack growth data are presented in the standard form of a plot of da/dn vs ΔK in Fig. 3.108. All tests were conducted at ratios of minimum to maximum stress (R) of 0.05. The growth rates at room temperature show no significant dependence on frequency over

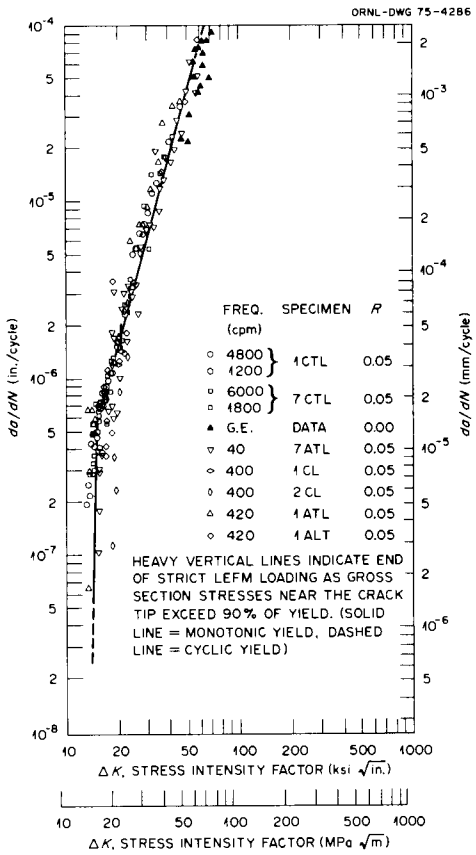

Fig. 3.108. Fatigue-Crack Growth Data for 2 1/4 Cr-1 Mo Steel in Air at Room Temperature.

2 1/2 decades. This is as expected since at room temperature aging and creep effects are minimal or nonexistant. Also presented in Fig. 3.108 for comparison are data obtained by General Electric[98] on 2 1/4 Cr-1 Mo steel, which show very good agreement with the ORNL data.

Elevated-temperature testing has been performed at 510 and 593°C (950 and 1100°F). At these higher temperatures, which are within the creep range, there is a noticeable effect of frequency. As seen in Fig. 3.109, decreasing the frequency at 593°C from 40 to 4 cpm markedly increases the crack growth rate at a given ΔK. Less pronounced but still noticeable is the slight shift in the 510°C data between frequencies of 40 and 300 cpm. Recent testing done by Johnson[99] at a frequency of 0.25 cpm indicated a larger effect, although some allowance is required for the slightly higher test temperature of 524°C (975°F).

An attempt was made to normalize the data at different temperatures using a correction for the changing Young's modulus with increasing temperature. Speidel[100] has recently shown success using such an approach

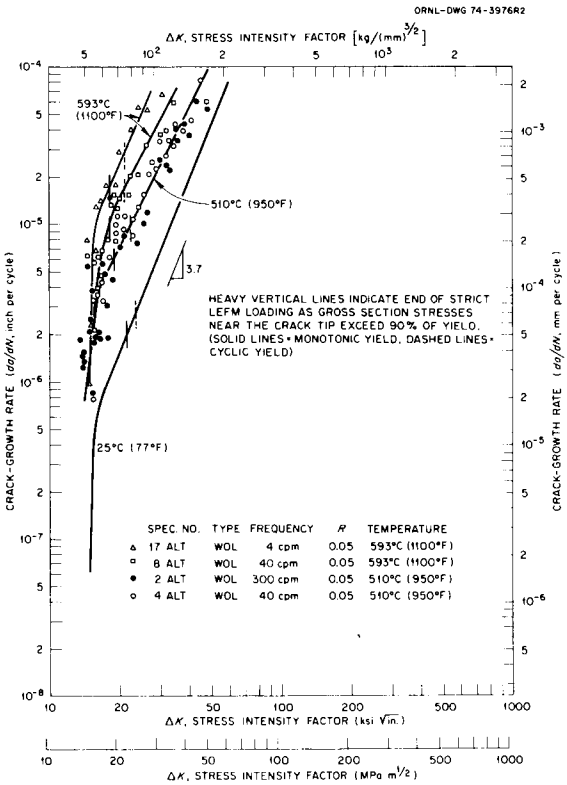

Fig. 3.109. Effects of Temperature and Frequency on Fatigue Crack Propogation of 2 1/4 Cr-1 Mo Steel in Air.

to normalize crack growth data on 12 different materials at room temperature. He plotted da/dn as a function of $\Delta K/E$ with E corresponding to the particular material tested. He reduced the scatter of da/dn at a given ΔK from several orders of magnitude to less than one.

In this case, attempting to normalize the ΔK-da/dn data for 2 1/4 Cr-1 Mo steel obtained at several temperatures by $E(RT)/E(T)$, while resulting in some consolidation of the data, still showed the data to fall into distinct temperature bands, with 593°C (1100°F) still showing the highest growth rates. One possibility for this is the increasing importance of monotonic crack extension due to creep and environmental (air) effects at the higher temperatures.

Few of the components of reactor systems manufactured from this material and subject to cyclic loading will operate at zero mean stress. Therefore, mean stress effects must be accounted for and R ratio studies were conducted. The results of a number of tests at 510°C (950°F) are shown in Fig. 3.110. Since frequency effects at 510°C are important, only those data points at similar test frequencies are reported. The summary

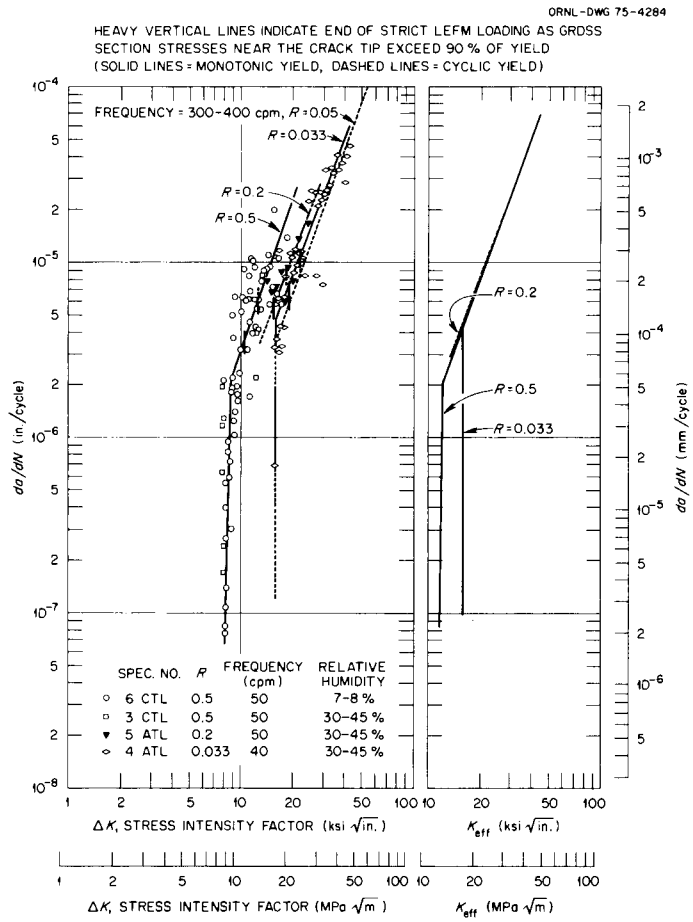

Fig. 3.110. Effect of Stress Ratio on Fatigue-Crack Propagation of 2 1/4 Cr-1 Mo Steel at 510°C (950°F) in Air.

line for R = 0.05 at higher frequency is shown for comparison. As can be seen from the main figure, the rate of crack growth increases markedly with increasing mean stress.

Barsom[101] has recently examined the effect of stress ratio R on the threshold ΔK value, ΔK_{Th} for crack propagation for several materials. He showed a clear dependence of decreasing ΔK_{Th} with increasing R, above an R ratio of about 0.1. This same trend is exhibited by the ORNL data, although the actual values of ΔK_{Th} found were roughly twice those predicted by Barsom.

The ORNL data were reanalyzed with the concept of effective stress intensity factor used by Walker.[102] The effective stress intensity factor, K_{eff}, is given by:

$$K_{eff} = K_{max}(1 - R)^m ,$$

where m varies with the material. Using a value of m = 0.5 gave the results shown in the inset of Fig. 3.110. The higher growth rates were effectively normalized with K_{eff}; however, the lower rates below the knee of the curve clearly were not.

The effect of a steam environment at 510°C (950°F) and atmospheric pressure on crack growth rates is presently being investigated. To date testing has been performed at 200 cpm, where effects of a steam environment are minimal (Fig. 3.111). Comparative tests at 4 cpm are presently under way.

Current and future tests will continue to investigate R ratio effects at room and elevated temperatures and further effects of frequency in air and steam at elevated temperature. Testing at 371°C (700°F) will be initiated, as will comparative high-temperature testing in vacuum for an environmental effects base line.

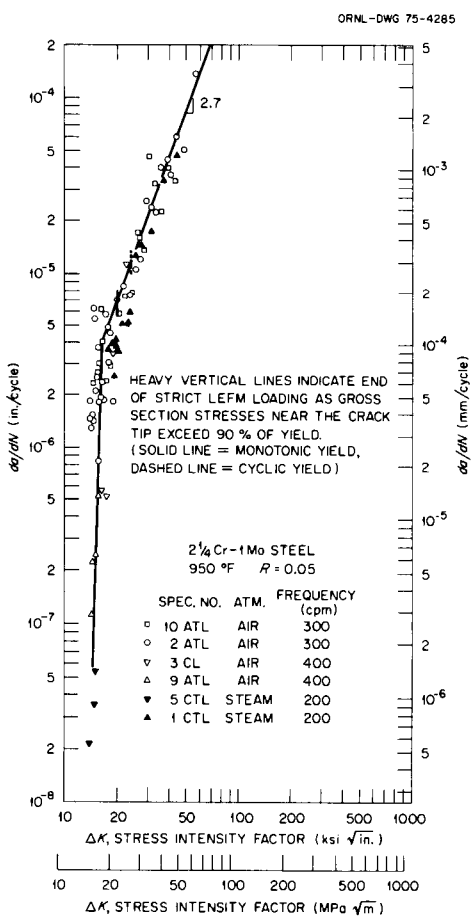

Fig. 3.111. Effect of Steam on Fatigue-Crack Propagation of 2 1/4 Cr-1 Mo Steel at 510°C (950°F).

3.4.5 Mechanical Property Correlations of 2 1/4 Cr-1 Mo Steel for LMFBR Steam Generators — M. K. Booker and T. L. Hebble*

Correlations for Charpy impact energy and ductile-brittle transition temperature for annealed 2 1/4 Cr-1 Mo steel are nearing completion. In addition, previously reported[103] results for 0.2% yield strength and ultimate tensile strength have been revised to include additional data obtained from the ORNL mechanical properties Data Storage and Retrieval System (DSRS).[54]

As previously reported,[104] the model used to express impact energy as a function of temperature is of the form

$$Y = A[1 - e^{-B(T - C)^2}] \ , \tag{57}$$

where Y = impact fracture energy,

T = temperature, and

A,B,C = constants estimated by the method of least squares.

The nine data sets treated by this model are shown in Table 3.32. Variations in properties among the data sets are so large that each data set had to be treated separately to obtain meaningful results. Values of the constants A, B, and C for the various data sets are shown in Table 3.33, while Table 3.34 displays values of temperatures at which the various data sets display predicted impact fracture energies of 10 and 20 J (14 and 28 ft-lb).

Ultimate tensile strength (UTS) and 0.2% yield strength (YS) have been expressed as cubic polynomials in temperature, such that

$$Y = a_0 + a_1T + a_2T^2 + a_3T^3 \ , \tag{58}$$

where Y = UTS or YS,

T = temperature, and

a_0,a_1,a_2,a_3 = constants evaluated by the method of least squares.

---

*Mathematics Research Staff.

Table 3.32. Data Sets Used in Analysis of Impact Energy

Data Set	Reference	Heat Treatment	Product Form	Carbon (%)
KB-1	a	Annealed	Plate	0.135
KB-2	a	Stress relieved	Plate	0.135
KB-3	a	Annealed	Plate	0.135
KB-4	a	Aged 1000 hr 510°C	Plate	0.135
CE-1	a	Annealed	Plate	0.10
CE-2	a	Annealed	Plate	0.10
GA-1	b	Annealed	Pipe	0.145
GA-2	b	Isothermally annealed	Pipe	0.11
GA-3	b	Isothermally annealed	Pipe	0.135

[a]D. A. Canonico and W. J. Stelzman, Oak Ridge National Laboratory, private communication.

[b]J. R. Ellis and D. I. Roberts, General Atomic Corporation, private communication.

Table 3.35 gives the revised estimates for the constants a_0, a_1, a_2, and a_3, while Figs. 3.112 and 3.113 show the actual data plotted with lines of expected value and upper and lower central tolerance limits.

3.4.6 Mechanical Properties of Weld-Overlaid Stainless Steel Forging — R. L. Klueh

During this quarter, we completed a series of tests at 538°C (1000°F) on composite specimens that contained both weld metal and forging in the gage section of the test specimen. The results of these tests are given in Table 3.36. Since the tensile properties of these specimens were similar to those of the weld metal,[105] the creep-rupture results were compared with those for the weld metal. For all stresses, the composite specimens had the longest rupture times; the difference appeared to become larger as the stress was lowered. The minimum creep rates were not compared, since it is difficult to determine the correct gage length to use for composite specimens (i.e., deformation is not uniform in the reduced section, since most of the deformation occurred in the weld metal). Visual inspection

Table 3.33. Least Squares Estimates of Coefficients for Impact Energy Model

Data Set	Coefficients (Standard Deviations)			Residual Standard Errors	Number of Observations
	Upper Shelf Energy, *A* (J)	*B*	Lower Temperature Limit, *C* (°C)		
KB-1	164 (±7)	0.000317 (±0.000112)	−36 (±7)	16.3	15
KB-2	218 (±9)	0.000131 (±0.000061)	−48 (±14)	20.6	12
KB-3	111 (±7)	0.000178 (±0.000113)	−29 (±17)	10.6	6
KB-4	201 (±13)	0.000077 (±0.000029)	−63 (±15)	18.7	11
CE-1	145 (±4)	0.000223 (±0.000053)	−39 (±6)	5.8	6
CE-2	227 (±20)	0.000093 (±0.000063)	−45 (±24)	26.5	6
GA-1	98 (±29)	0.000032 (±0.000026)	−90 (±26)	5.1	14
GA-2	82 (±4)	0.000629 (±0.000168)	4 (±4)	9.3	16
GA-3	184 (±166)	0.000022 (±0.000032)	−57 (±24)	8.0	16

Table 3.34. Impact Energy (10 and 20 J) Temperatures for 2 1/4 Cr-1 Mo Steel

Data Set	Temperature, °C	
	10 J	20 J
KB-1	−21.7	−15.5
KB-2	−29.4	−21.3
KB-3	−6.2	4.2
KB-4	−36.8	−25.6
CE-1	−21.3	−13.4
CE-2	−23.2	−13.7
GA-1	−32.5	−6.0
GA-2	18.8	25.5
GA-3	−6.2	15.9

Table 3.35. Least Squares Estimates of Coefficients in Equation for Ultimate Tensile Strength and Yield Strength

Coefficient[a]	Value, Metric Units[b]		Value, English Units[c]	
	UTS	YS	UTS	YS
a_0	527	263	79.3	39
a_1	−1.03	−0.315	-9.61×10^{-2}	−0.0281
a_2	4.54×10^{-3}	9.39×10^{-4}	2.17×10^{-4}	4.46×10^{-5}
a_3	-5.83×10^{-6}	-1.08×10^{-6}	-1.45×10^{-7}	-2.69×10^{-8}

[a]In equation property $Y = a_0 + a_1T + a_2T^2 + a_3T^3$.

[b]Y in MPa, T in °C.

[c]Y in ksi, T in °F.

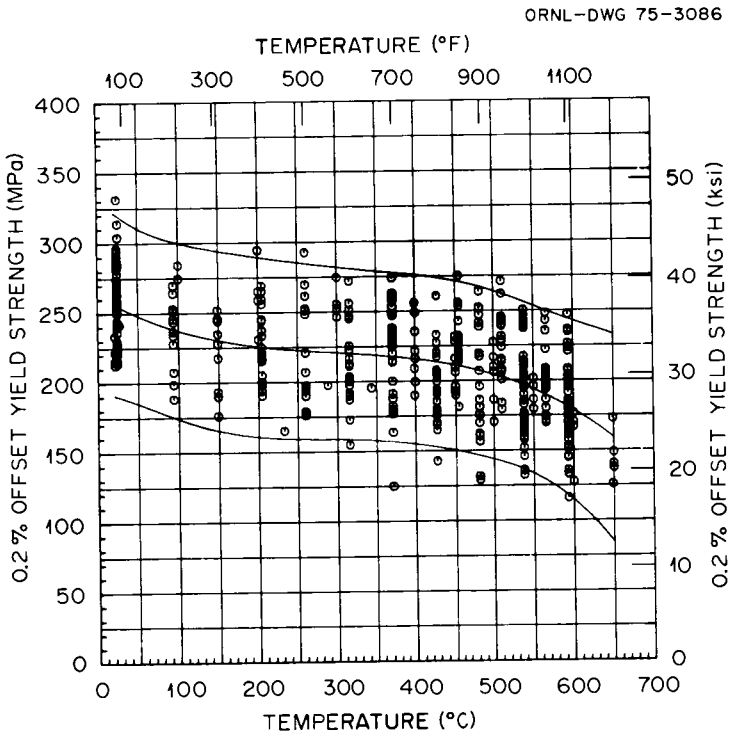

Fig. 3.112. Yield Strength (0.2% Offset) as a Function of Temperature for Annealed 2 1/4 Cr-1 Mo Steel. Lines show expected value from the equation and upper and lower central tolerance limits.

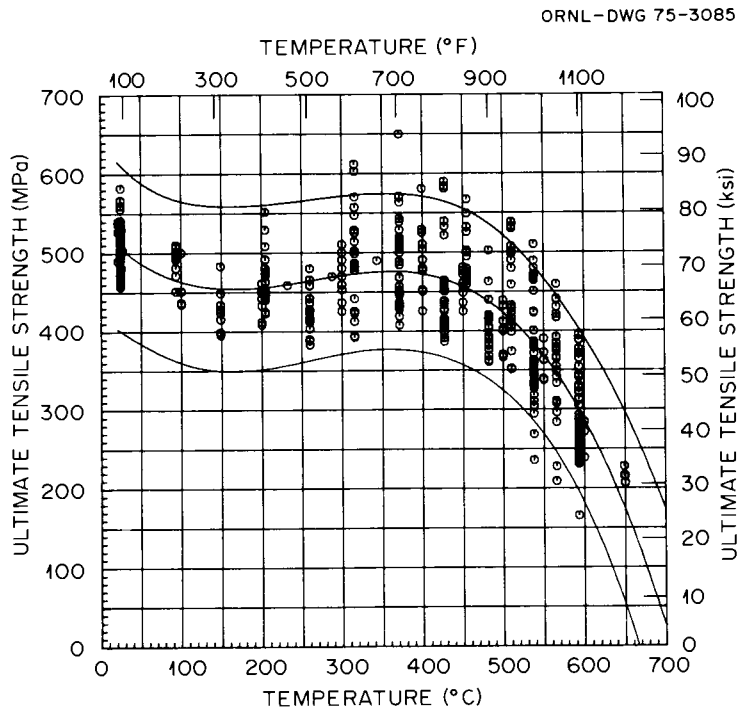

Fig. 3.113. Ultimate Tensile Strength as a Function of Temperature for Annealed 2 1/4 Cr-1 Mo Steel. Lines show expected value from the equation and upper and lower central tolerance limits.

Table 3.36. Creep-Rupture Properties of Composite Types 304 and 308 Stainless Steel Specimens at 538°C (1000°F).

Stress (ksi)	Stress (MPa)	Rupture Life (hr)	Elongation (%)	Reduction of Area (%)	Minimum Creep Rate (%/hr)
55	379	26.4	28.5	60.7	0.208
50	345	144.8	17.3	17.1	0.0275
47.5	328	219.0	21.8	54.9	0.0204
45	310	617.7	12.4	10.8	0.00412
42.5	299	2210.4			

indicated that all specimens necked and failed in the weld metal. Selected specimens are being prepared for metallographic examination.

With the exception of several long-time tests still in progress, the experimental part of our creep-rupture program is complete. This program consisted of tests made at 482, 538, and 593°C (900, 1000, and 1100°F) on tangential and radial (relative to the axis of the forging cylinder) specimens taken from the weld metal and from forging adjacent to the interface between the weld metal and the forging.[106-109] Two types of axial specimens were also tested: specimens taken from as-forged material and specimens taken across the fusion line. In the following, the results of these studies will be discussed.

The previous microhardness and tensile studies determined that the overlaying process affected the underlying forging.[105] A strengthening (in terms of increased microhardness and yield strength) was observed; the strengthening was not confined to a superficial distance from the interface; a depth of about 0.8 in. (20 mm) was affected, the microhardness progressively decreasing with distance from the fusion line. The creep and rupture properties were also affected by the overlay process.

In Figs. 3.114 and 3.115 the creep rupture data for the overlay weld metal and the two types of forging specimens are compared at 593 and 538°C (1100 and 1000°F), respectively. At both temperatures, the forging adjacent to the fusion line is slightly stronger than the forging that

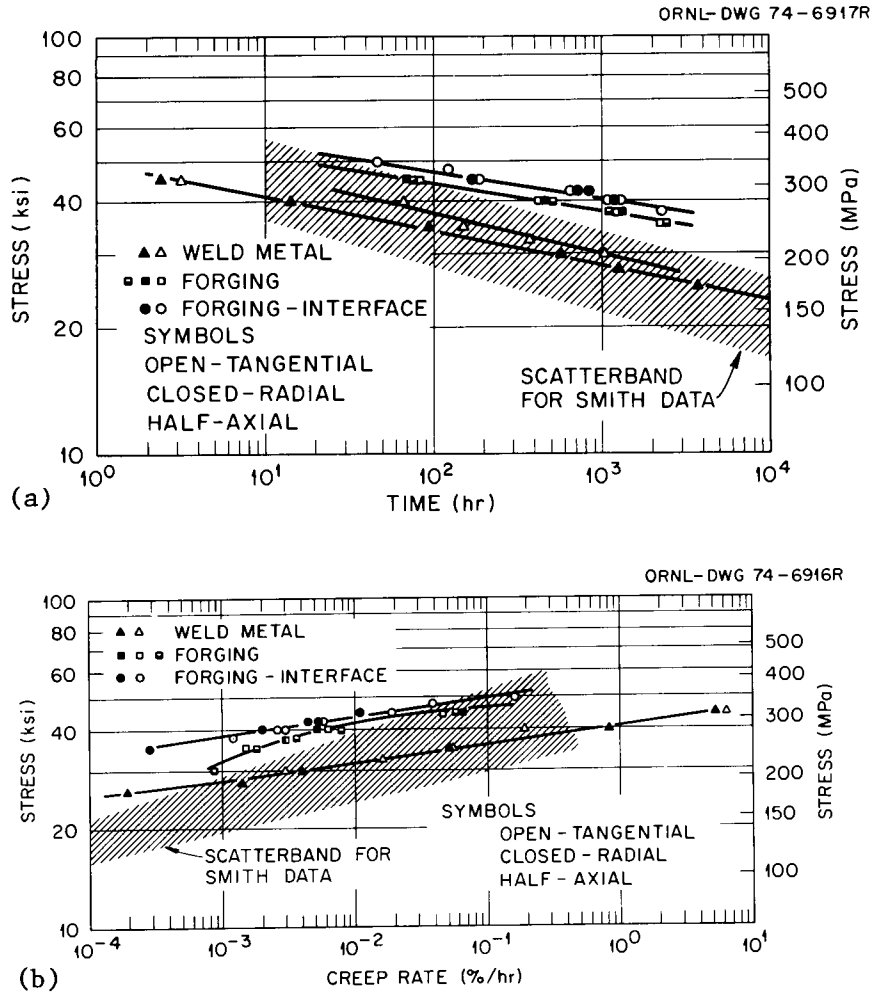

Fig. 3.114. A Comparison of the 593°C (1100°F) Creep-Rupture Properties of the Type 304 Stainless Steel Forging, Type 308 Stainless Steel Weld Metal, and Type 304 Stainless Steel Forging Adjacent to the Overlay-Forging Fusion Line. (a) Rupture life. (b) Minimum creep rate. Also shown is the scatter band for the data compiled by Smith for type 304 stainless steel.

was some distance from the fusion line and unaffected by the overlay process; at 538°C the difference becomes greater as the rupture stress decreases. Both types of forging specimens are considerably stronger than the weld metal.

Also shown in Figs. 3.114 and 3.115 is a summary of data compiled by Smith[49] for the creep-rupture strengths of a large number of heats of wrought type 304 stainless steel in the form of plate, bar, and pipe. For Smith's data at 593°C (1100°F), a scatter band is shown in Fig. 3.114.

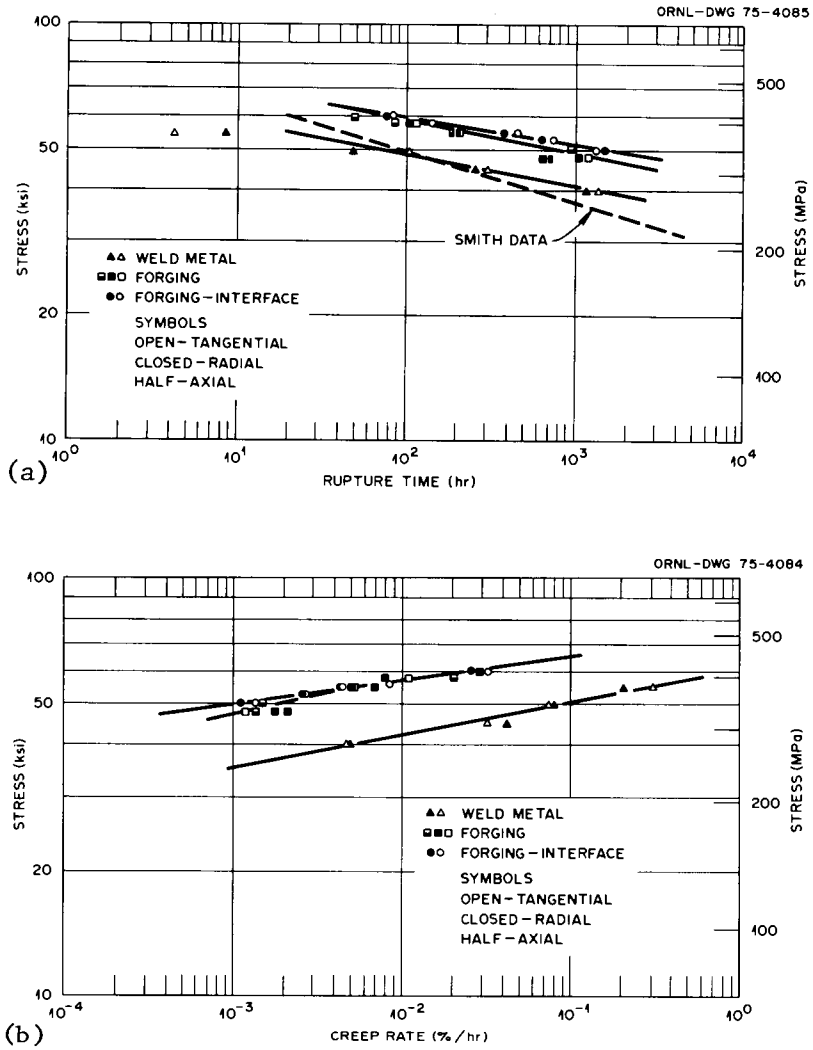

Fig. 3.115. A Comparison of the 538°C Creep-Rupture Properties of the Type 304 Stainless Steel Forging, Type 308 Stainless Steel Weld Metal, and Type 304 Stainless Steel Forging Adjacent to the Overlay-Forging Fusion Line. (a) Rupture life. (b) Minimum creep rate. Also shown is a line for the data compiled by Smith for type 304 stainless steel.

At 538°C (1000°F), Smith has but six data points, and the line through these points is shown in Fig. 3.115. Smith has no data at 482°C (900°F). A similar compilation of stainless steel weld metal data has been published by Vorhees and Freeman,[110] but no data are given for type 308 stainless steel at 482, 538, and 593°C.

It is seen in Fig. 3.114(a) that the creep-rupture strengths at 593°C (1100°F) for the type 304 stainless steel — as forged and immediately adjacent to the fusion line — are somewhat greater than the average of

those given by Smith[49] and slightly greater than Smith's maximum. A similar conclusion applies at 538°C (1000°F). The tensile properties for this forging also fell on the upper edge of the scatter band given by Smith. The weld metal properties fall near the center of the Smith scatter band at 593°C and slightly above the Smith data at 538°C.

The only type 308 stainless steel weld metal data for comparison is that of King, Stiegler, and Goodwin,[70] who determined the creep-rupture properties of submerged-arc welds of type 308 stainless steel weld metal in which the residual elements boron, titanium, and phosphorus had been controlled. They tested the type 308 CRE (controlled residual elements) stainless steel at 482, 566, 593, and 649°C (900, 1050, 1100, and 1200°F); at 566 and 649°C, the type 308 CRE stainless steel had strength properties as good as or better than those given by Voorhees and Freeman.[110] When the creep-rupture data for the overlay weld metal were compared with the King, Stiegler, and Goodwin[70] data at 482 and 593°C, it was found that the overlay is as strong as or stronger than the type 308 CRE stainless steel.

In Figs. 3.116 and 3.117 the elongation and reduction of area are shown as functions of rupture life for the tests at 593 and 538°C (1100 and 1000°F), respectively. The curves shown are meant only to represent the trend of the data (these are visual fits). For the weld metal, separate curves were required for the radial and tangential specimens, whereas the ductility of the specimens from the two forging locations was independent of orientation. For the tests at 593°C (Fig. 3.116) the ductility of the weld metal — both radial and tangential orientations — decreased with rupture life (decreasing stress) and appeared to approach a single curve at long times. Forging from both locations displayed a minimum in ductility with increasing rupture life. At 538°C (Fig. 3.117), a similar trend is evident, though the minimum observed for the type 304 stainless steel at 593°C is not evident (this may mean that it occurs at longer rupture times than those measured in this study).

The primary motivation for the development of the type 308 CRE stainless steel was improved ductility, which King, Stiegler, and Goodwin[70] were able to demonstrate. A comparison with their data at 593°C (1100°F) indicates that the type 308 CRE stainless steel is more ductile. For rupture times of about 450 and 3000 hr, the total elongation of type 308 CRE stainless

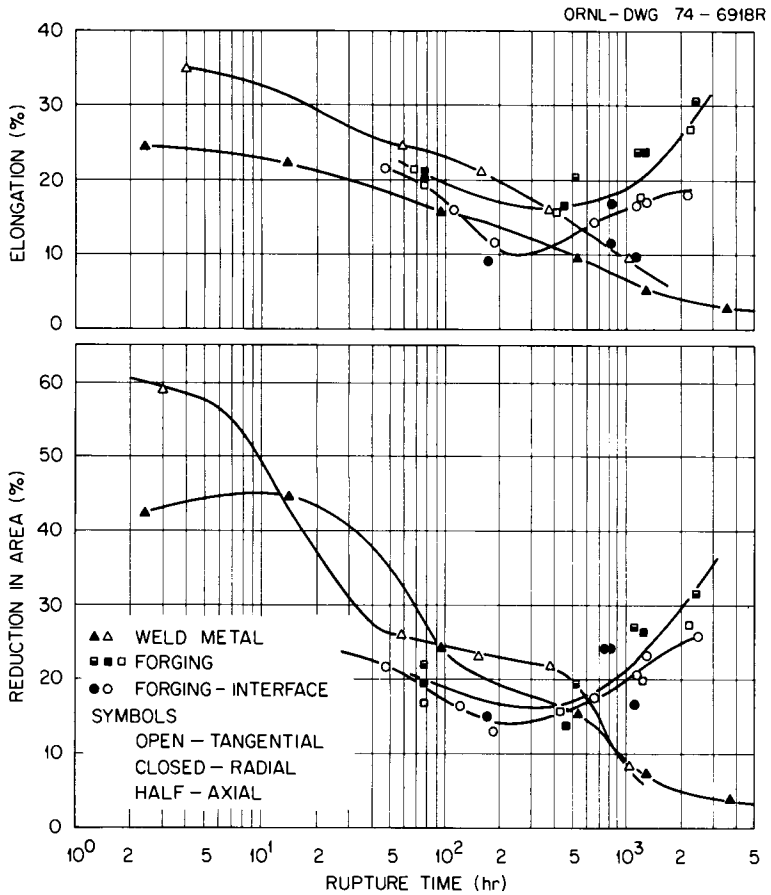

Fig. 3.116. Comparison of the Total Elongations and Reductions of Area at 593°C (1100°F) of the Type 304 Stainless Steel Forging, Type 308 Stainless Steel Weld Metal, and Type 304 Stainless Steel Forging Adjacent to the Overlay-Forging Fusion Line.

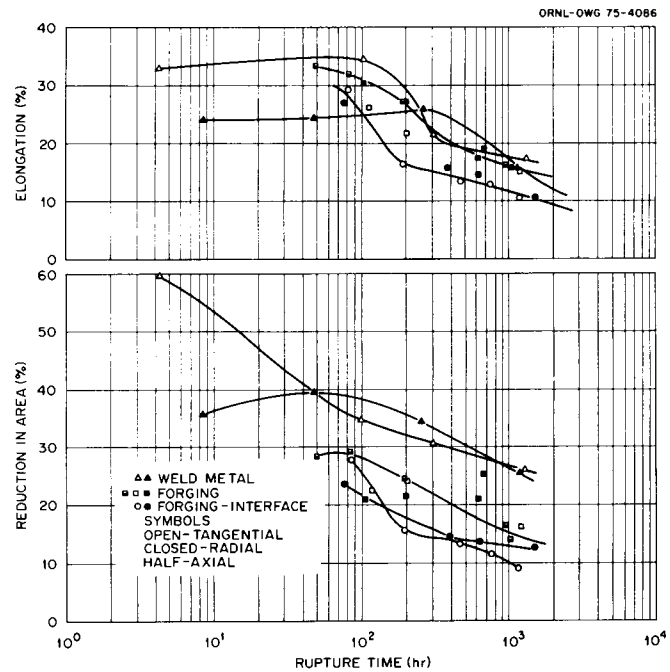

Fig. 3.117. Comparison of the Total Elongations and Reductions of Area at 538°C (1000°F) of the Type 304 Stainless Steel Forging, Type 308 Stainless Steel Weld Metal, and Type 304 Stainless Steel Forging Adjacent to the Overlay-Forging Fusion Line.

steel was 22 and 13%, respectively, which compares with the total elongations of the overlay weld metal of 15 and 4% at 450 and 3700 hr, respectively.

The observed advantage in creep strength for the forging immediately adjacent to the fusion line over the forging at some distance from the fusion line is consistent with the yield strength advantage noted previously. We concluded[105] that this strengthening effect must be the result of stresses generated in the forging by shrinkage of the weld metal during solidification. This strengthening effect has a greater influence than the "annealing" due to the heating cycle during welding.

With transmission electron microscopic examination of the microstructure of the type 304 stainless steel at various distances from the fusion line, we found that the dislocation density immediately adjacent to the fusion line was much higher than it was in forging well-removed from the fusion line, an indication of the stresses generated during welding. Furthermore, the dislocation density decreased in the vicinity of the fusion line as samples were taken further from the fusion line, which agrees with the microhardness results.[105]

It was observed — especially from the curves of stress versus minimum creep rate — that the properties of the as-forged material and that immediately adjacent to the fusion line differ less for the high-stress tests (short rupture life); the deviation in properties increases as the stress decreases. This can be explained in terms of the initial dislocation densities. The higher the creep stress, the greater is the plastic deformation introduced when the test is started. For a high-stress test, the larger number of dislocations introduced into the material during loading swamps the effect of the dislocations introduced by the overlay process. At lower loading stresses, the dislocations introduced by the overlay process have a much greater effect, since they make up a greater proportion of the total dislocation structure. Thus, the greater deviation of properties at the low stresses.

3.5 HIGH-TEMPERATURE DESIGN — J. M. Corum and C. E. Pugh

3.5.1 Exploratory Studies in Support of Structural Design Methods

3.5.1.1 Characterization of the Product Forms of the Reference Heat of Type 304 Stainless Steel — R. W. Swindeman and V. K. Sikka

Creep-rupture characterization testing has been completed for nearly all the product forms of the reference heat (9T2796) of type 304 stainless steel. The status is summarized in Table 3.37, while secondary creep rate and rupture data at 593°C (1100°F) are plotted in Fig. 3.118. Data at 35, 30, and 25 ksi (241, 207, and 172 MPa) were fitted to a power law, by least squares, and used to calculate the 1000-hr rupture strength and the 10^{-2}%/hr creep strength. Rupture strengths, reported in Table 3.38, range from 22.7 ksi (156 MPa) for 2-in. (51-mm) plate to 24.47 ksi (169 MPa) for the 2 1/2-in. (64-mm) cold-drawn pipe. The relative strengths of the different products depend, to a certain extent, on variables associated with experimental techniques. For example, the 1000-hr rupture strength obtained from data of the Babcock and Wilcox[111] study of the hot-rolled 5/8-in. (16-mm) bar (item 18) is 24.3 ksi (167 MPa), which is substantially greater than the 23.1 ksi (159 MPa) observed by us. Strength differences appear to be associated with differences in heat-treating methods, which may produce differences in grain size or carbide distribution. This is particularly true for the hot-rolled 5/8- and 1-in. (16- and 25-mm) bar materials (items 18 and 19), which seem to develop a duplex grain size[111] after reannealing at 1093°C (2000°F) for 0.5 hr. We are examining other bar products to see if they suffer similar problems.

The cold-drawn 5/8-in. (16-mm) bar (item 23) does not seem to be a problem. Microstructures produced by reannealing at temperatures between 1010 and 1120°C (1850—2048°F) show that grain size differences are scarcely detectable. Further, no significant differences in the yield strengths can be detected. To further examine the sensitivity of the creep strength to heat-treating variables several specimens were reannealed at 1050°C (1922°F) and tested at 593°C (1100°F). Data, included in the graph for this product form in Fig. 3.118, were about the same as data produced by testing specimens reannealed at 1093°C (2000°F). Some of this material has been shipped to the University of Cincinnati for further testing.

Table 3.37. Status of Creep-Rupture Tests[a] on Different Product Forms of the Reference Heat of Type 304 Stainless Steel (Heat 9T2796)

Item	Form	Size[b] (in.)	Size[b] (mm)	Designation	Tests Completed
4	Plate	3/8	9.5	L	All
5	Plate	1/2	12.7	J	All
6	Plate	3/4	19	H	All
7	Plate	1	25	M	All
8	Plate	2	51	K	All
10	Pipe	4 sched 160	102	B	All
11	Pipe	8 sched 80	203	A	All
15	Pipe	2 1/2 OD (CD)	64	D	All
51[c]	Pipe	2 1/2 OD (HR)	64	C	All
18	Bar	5/8 (HR)	16	R	All
19	Bar	1	25	T	(1), (2), (3)
20	Bar	1 3/4	44	G	(1), (2), (3), (5)
21	Bar	1 7/8	48	F	(1), (2), (3), (5)
22	Bar	4 1/2	114	E	All
23	Bar	5/8 (CD)	16	S	(1), (2), (3)

[a]Tests at 593°C (1100°F) and (1) 35 ksi (241 MPa); (2) 30 ksi (207 MPa); (3) 25 ksi (172 MPa); (4) 15 ksi (103 MPa); (5) 12.5 ksi (86 MPa).

[b]CD = cold drawn; HR = hot rolled.

[c]Gun-drilled bar.

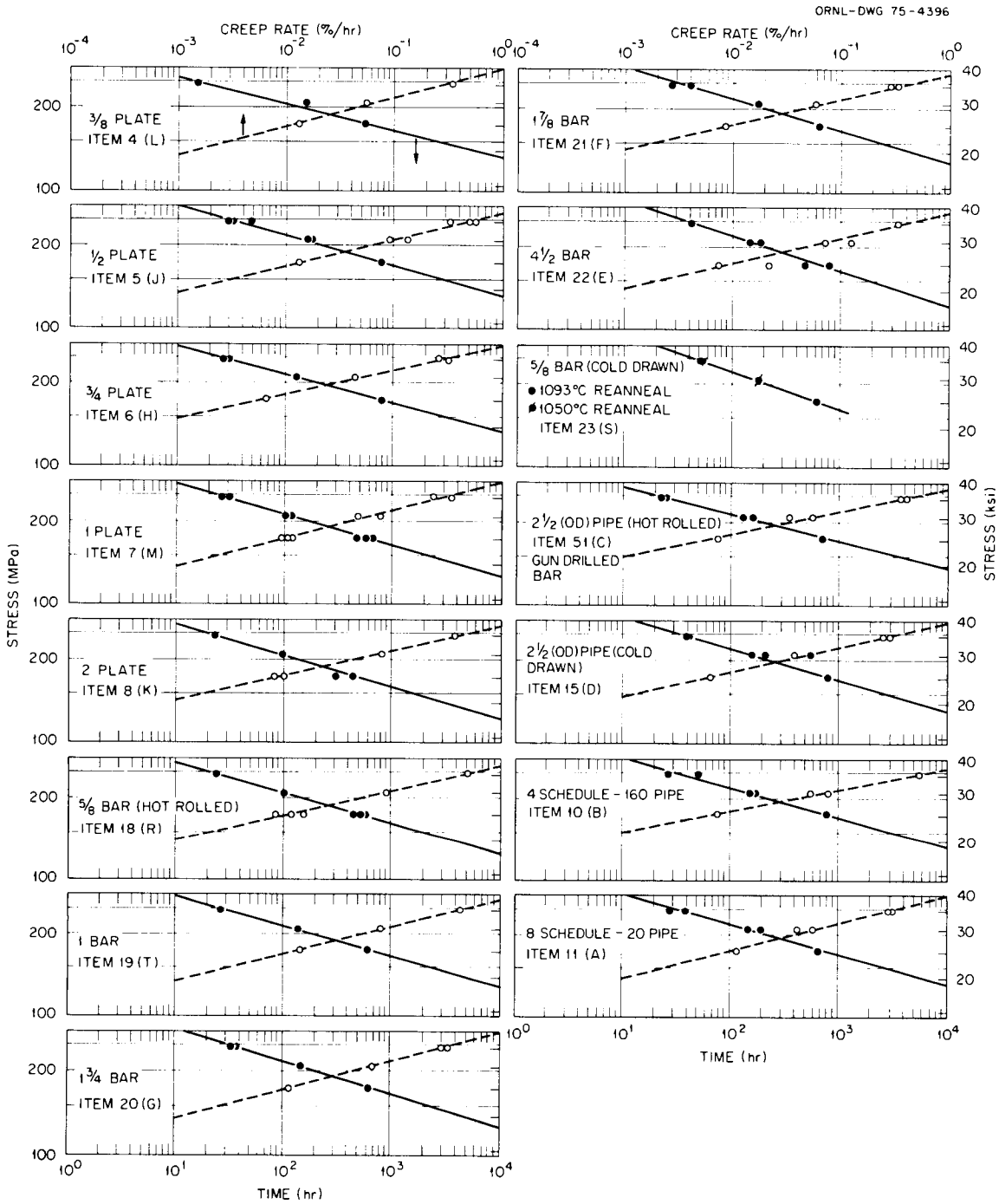

Fig. 3.118. Rupture and Creep Rate Characterization Data at 593°C (1100°F) for the Reference Heat (9T2796) of Type 304 Stainless Steel.

Table 3.38. Summary of Creep-Rupture Characterization of Different Product Forms of the Reference Heat of Type 304 Stainless Steel

Item, Designation	1000-hr Rupture Strength		10^{-2} %/hr Creep Strength	
	ksi	MPa	ksi	MPa
4, L	23.97	165	24.58	169
5, J	24.16	166	24.37	168
6, H	24.34	168	26.10	180
7, M	23.27	160	24.98	172
8, K	22.70	156	25.36	175
10, B	24.46	169	25.73	177
11, A	24.43	168	26.02	179
15, C	23.10	159	24.74	170
51, D	24.47	169	26.02	179
18, R	23.10	159	24.74	170
19, T	23.72	163	24.28	167
20, G	23.67	163	24.77	171
21, F	23.93	165	25.47	175
22, E	23.49	162	24.34	168
23, S	23.4	161	24.8	171

3.5.1.2 Tensile Testing of 1-in. (25-mm) Plate of the Reference Heat of Type 304 Stainless Steel — R. W. Swindeman

The purposes for tensile testing the reference heat (9T2796) of type 304 stainless steel are to (1) characterize the material relative to other heats of type 304 stainless steel, (2) provide the stress-strain data required to establish the monotonic yield and flow behavior necessary to analyze the results of structural tests, and (3) explore the extent and nature of the rate dependence of the monotonic yield and flow strength. The basic tensile behavior of the 1-in. (25-mm) plate has been presented elsewhere,[112] and recent work has involved the exploration of flow behavior under changing temperature and strain rate conditions. The Voce equation has been shown capable of representing the true-stress true-strain curve over a broad range of testing conditions, and we hope that

this equation can be developed as a link between tensile and creep behavior. The model, developed elsewhere,[112] is being evaluated by comparing the results of ultralow-strain-rate tests against the behavior predicted by the model. A comparison is shown in Fig. 3.119 for a test at 482°C (900°F) and a strain rate averaging 4.3×10^{-8}/sec. The model dearly predicts a higher ultimate strength and uniform elongation than actually developed; hence, it appears that additional testing at temperatures in the regime 427 to 538°C (800–1000°F) will be required before the ultralow-strain-rate behavior can be fully understood. Further information concerning the relationships between tensile and creep behavior is provided in the next section.

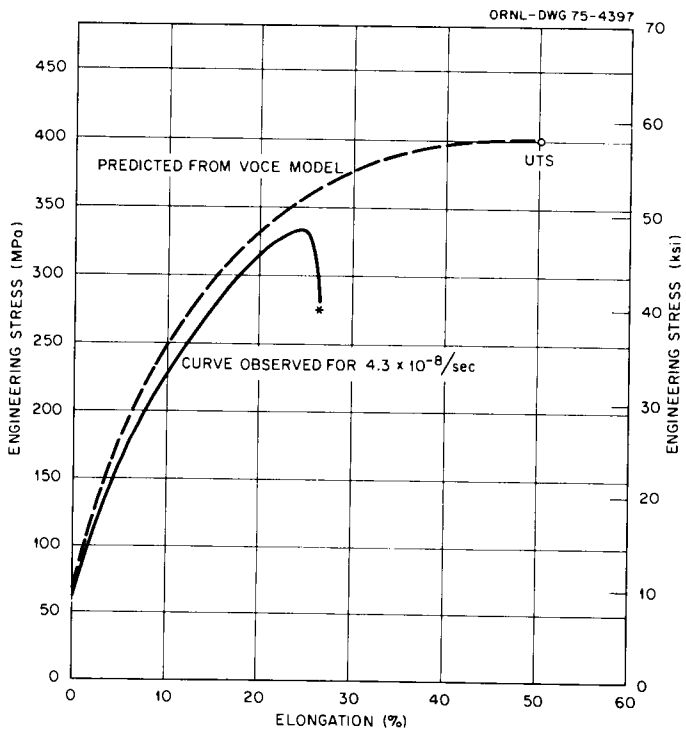

Fig. 3.119. Tensile Curve for Type 304 Stainless Steel at 482°C (900°F) at an Ultralow Strain Rate. Test was terminated by an intergranular failure after 1670 hr.

3.5.1.3 Creep-Rupture Testing of the 1-in. (25-mm) Plate of the Reference Heat of Type 304 Stainless Steel — R. W. Swindeman

A summary report concerning creep-rupture correlations for the 1-in. (25-mm) plate of the reference heat (9T2796) of type 304 stainless

steel is being prepared. The fit of several time-temperature parameters to engineering stress-rupture data has been reported previously,[42] and in this report we consider data in the form of modulus-compensated true stresses. In earlier studies [42] stresses were adjusted to reflect true stresses by using the strain at the inflection point of the creep curve. Here, to be consistant with workers at the University of Cincinnati, we use the strain that represents the sum of the loading, transient, and one-half of the linear component. Thus:

$$\sigma = S(1 + \varepsilon_p + \varepsilon_t + \dot{\varepsilon}_S t_R/2) \tag{59}$$

where σ is true stress, S is engineering stress, ε_p is loading strain, ε_t is transient strain, $\dot{\varepsilon}_S$ is secondary creep rate, and t_R is rupture life. Creep-rupture data are plotted in Fig. 3.120, while a fit of the Barrett-Ardell-Sherby[113] parameter to the data is shown in Fig. 3.121. In contrast to the fit of the Orr-Sherby-Dorn parameter to engineering data,[42] the Barrett-Ardell-Sherby parameter exhibits only slight curvature in the master curve. To explore this in more detail, we examined the high-stress short-time behavior by using data produced in a tensile test. True-stress versus true-strain data are shown in Fig. 3.122 for tensile tests at 538 and 704°C (1000 and 1300°F). Included are data from Diercks and Burke[114] on the same heat of type 304 stainless steel but in the aged condition. At 704°C, the strain is clearly accumulated between the ultimate strength and the rupture strength at nearly constant stress. Thus, the time between the ultimate and fracture is roughly equivalent to the rupture life, t_R, of a "true stress" creep test. Also under these conditions, the Voce constant,[112] σ_∞, is roughly equivalent to the true flow stress. Thus, we should be able to plot σ_∞ against t_R as a short-time creep-rupture point. It is far from obvious that the treatment is applicable at 538°C, however, since the material fails before σ_∞ is achieved. Nonetheless, a plot of σ_∞ versus t_R pairs is shown in Fig. 3.123 and includes data to 538°C. The line through the data represents the master curve replotted from Fig. 3.121, and the near-linear behavior appears valid up to some fairly high stress levels. It has been shown,[112]

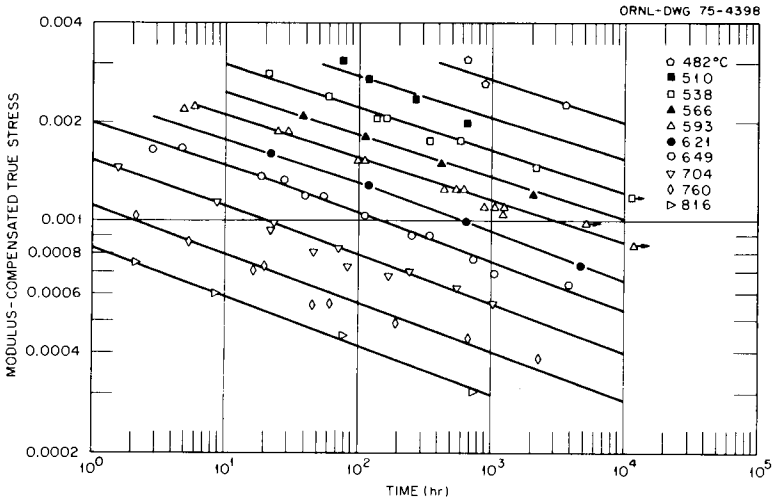

Fig. 3.120. Modulus-Compensated True Stress Plotted Against Rupture Life for Type 304 Stainless Steel (Heat 9T2796).

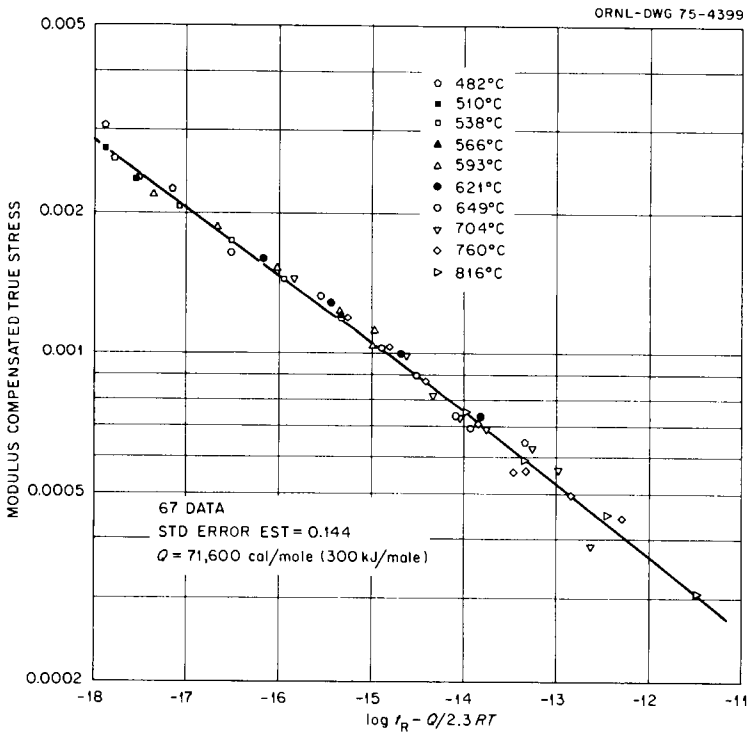

Fig. 3.121. Fit of the Barrett-Ardell-Sherby Parameter to Rupture Data for Type 304 Stainless Steel (Heat 9T2796).

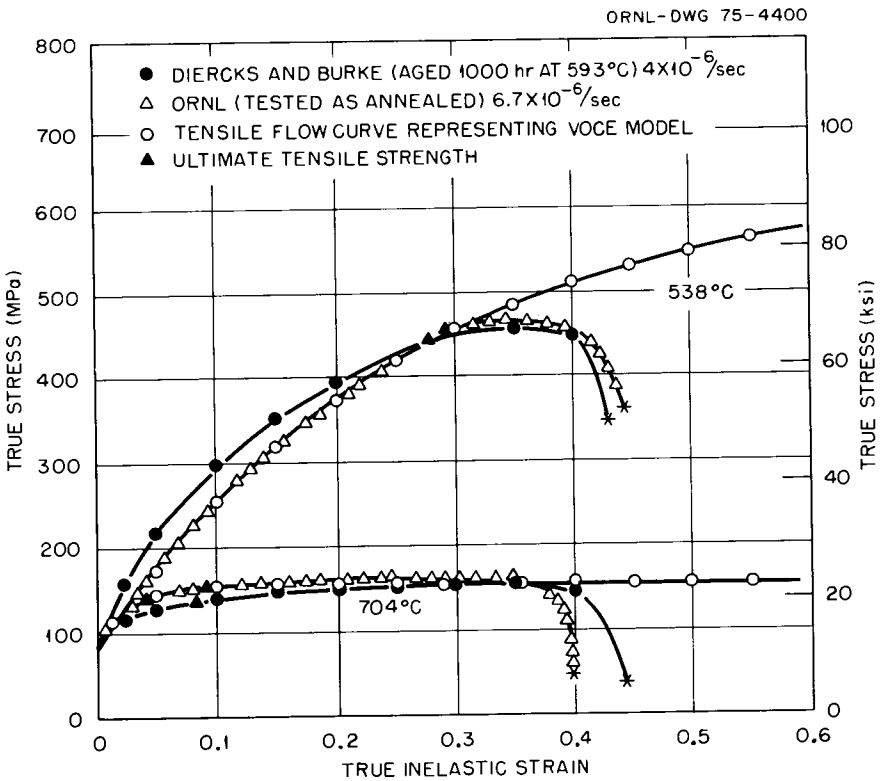

Fig. 3.122. True-Stress True-Strain Tensile Curves for Type 304 Stainless Steel (Heat 9T2796).

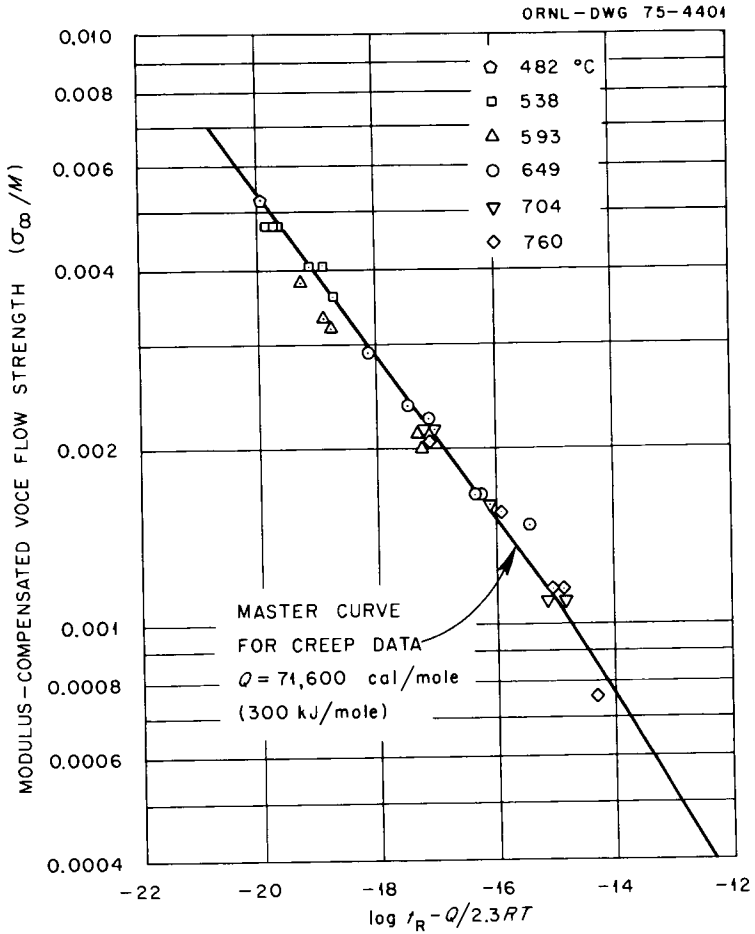

Fig. 3.123. Correlation of Rupture Data Based on Tensile Tests with the Master Curve Based on the Fit of the Barrett-Ardell-Sherby Parameter to Creep-Rupture Data.

however, that type 304 stainless steel shows a critical strain rate at which the σ_∞ values diminish with increasing strain rate. Data taken from tests in this regime do not plot on the curve shown in Fig. 3.123.

Correlations of the linear strain component are also being attempted on the basis of modulus-compensated true stresses. At temperatures between 482 and 649°C (900–1200°F) it appears that the "true" linear strain component, ε_ℓ, is sensitive to temperature and, to a first approximation, can be represented by the relation:

$$\varepsilon_\ell = (1/K) f(\sigma/M) e^{-Q/RT}$$

where K is a constant, $f(\sigma/M)$ is some function of modulus-compensated true stress, R is the gas constant, T is absolute temperature, and Q is an activation energy near 35,000 cal/mole (146 kJ/mole). Data for two heats of type 304 stainless steel are plotted in Fig. 3.124.

3.5.1.4 Strain Cycling Tests of Type 304 Stainless Steel — R. W. Swindeman

No contribution for this reporting period.

3.5.1.5 Exploratory Testing of 2 1/4 Cr-1 Mo Steel — R. W. Swindeman and R. L. Klueh

One additional relaxation test (SA-211A) on 2 1/4 Cr-1 Mo steel at 510°C (950°F) was initiated during this reporting period. Data are shown with previously reported data in Fig. 3.125. The latest test, started near 30 ksi (207 MPa), relaxed more slowly than the test (SA-207A) started near 39 ksi (269 MPa), and the two relaxation curves actually cross near 100 hr. The reason for this behavior is not known, and additional testing would be desirable before any conclusions are drawn.

The creep-plasticity test at 510°C (950°F) reported last quarter was continued into this reporting period. After 1300 hr emphasis was placed on cyclic creep behavior, rather than creep-plasticity behavior, and about 30 cycles of 48 hr duration were introduced at ±18 ksi

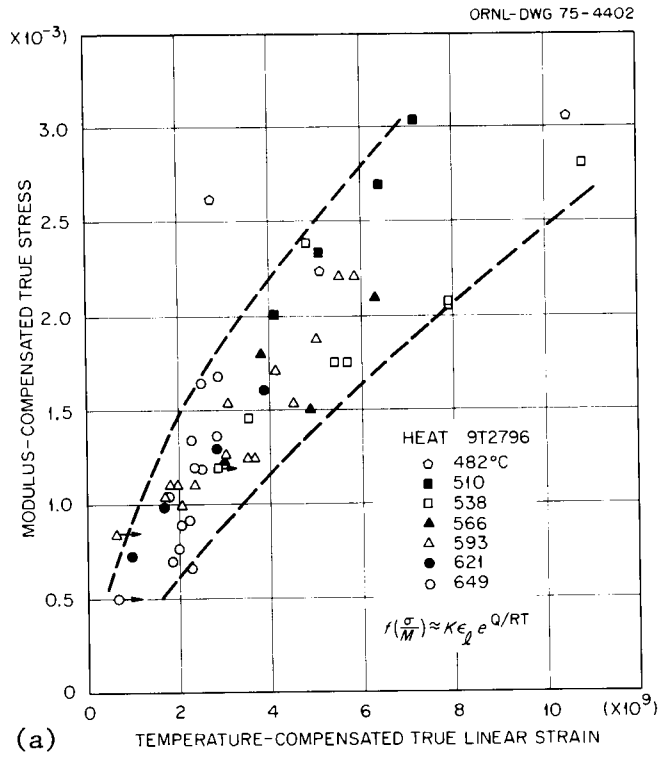

(a)

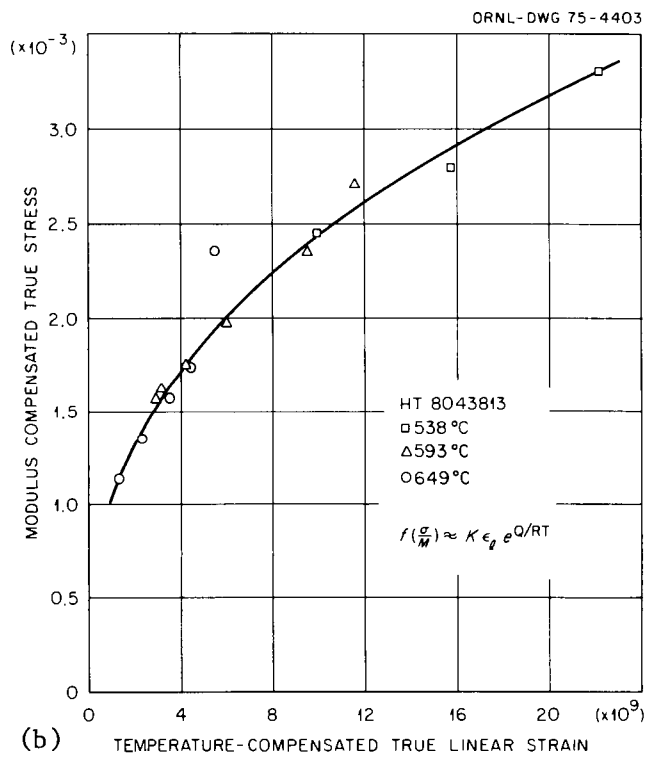

(b)

Fig. 3.124. Temperature-Compensated True Linear Strain Data for Type 304 Stainless Steel. (a) Heat 9T2796. (b) Heat 8043813.

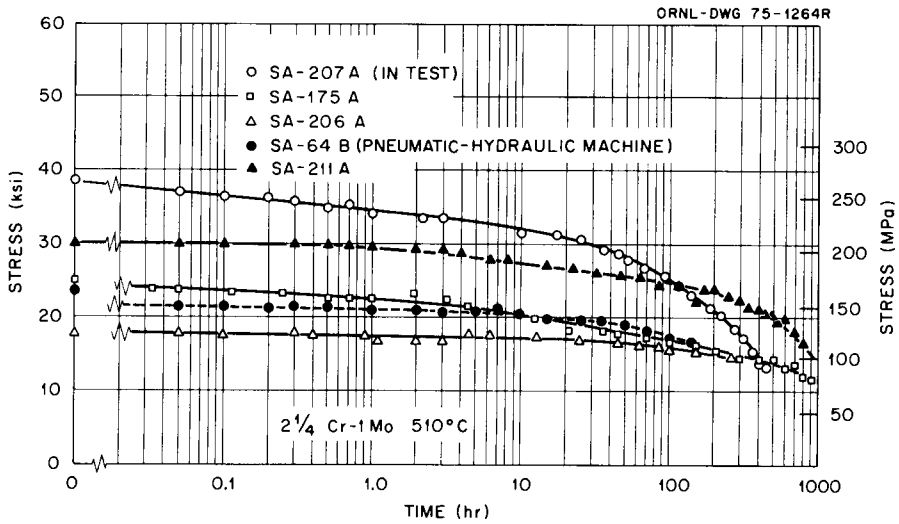

Fig. 3.125. Relaxation Curves for 2 1/4 Cr-1 Mo Steel at 510°C (950°F).

(±124 MPa) or +25/−18 ksi (+172/−124 MPa). Our most significant observation concerned the influence of the tensile stress on the compressive creep component. This is illustrated in Fig. 3.126, where portions of the cyclic curves are shown for the two stress ratios mentioned above.

It appears that the compressive creep component is significantly greater after tensile creep at 25 ksi (172 MPa) than after creep at 18 ksi (124 MPa).

3.5.2 Investigations of Creep Failure Under Uniaxial and Multiaxial Conditions — C. C. Schultz, Babcock and Wilcox

3.5.2.1 Constant-Load Uniaxial Tests

Figure 3.127 shows the creep strain-time results for tests BWR-9 (18 ksi), BWR-11 (17 ksi), and BWR-7 (16 ksi), the only tests of the original constant-load uniaxial tests shown in Table 3.39 that are still in progress. The estimated rupture times for these three stress levels, based on an extrapolation of a linear least-squares fit of the log stress—log rupture time data in Table 3.39, are 21,500, 37,400, and 67,400 hr respectively. Based on time to onset of tertiary creep, rupture in test BWR-9 is expected to occur very near the estimated time, while in test BWR-11 rupture is expected to occur in considerably less time than was estimated.

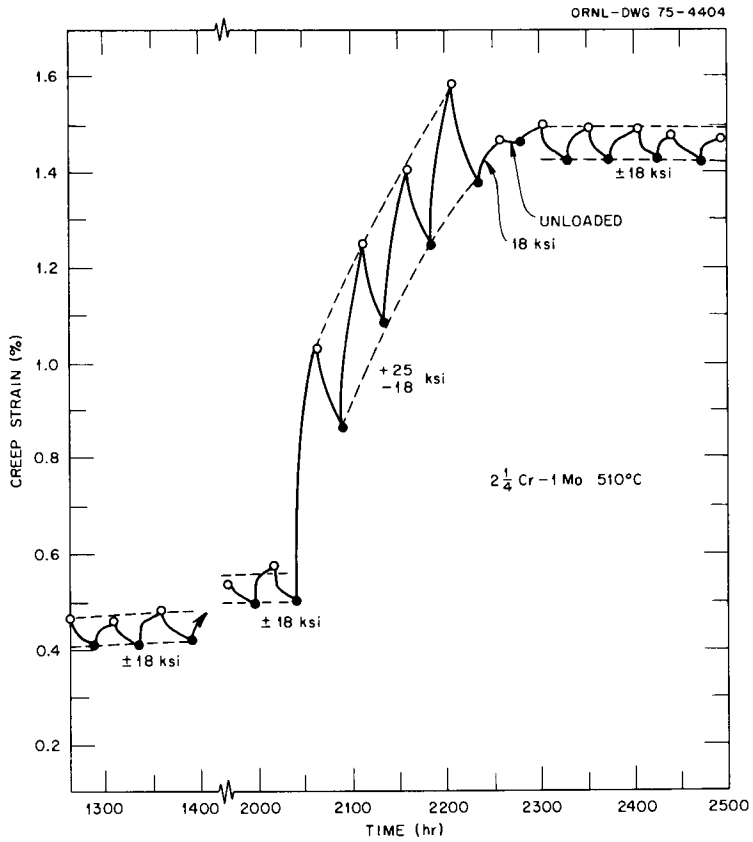

Fig. 3.126. Influence of the Tensile Creep Component on the Compressive Component for 2 1/4 Cr-1 Mo Steel at 510°C (950°F). (Elastic components are not included.) Stresses: 18 ksi = 124 MPa, 25 ksi = 172 MPa.

3.5.2.2 Step-Load Uniaxial Tests

The initial series of step-load uniaxial tests was completed during the previous reporting period.[115] The calculated life fractions reported in Table 3.40 have been modified to reflect a more recent curve fit (linear log-log least squares) and extrapolation of the constant-load data. The adjustments are small in all cases.

3.5.2.3 Interrupted Uniaxial Tests

The six interrupted uniaxial tests (all at 19.5 ksi) are shown in Table 3.41 and Fig. 3.128. The specimen in test BWI-3 ruptured during the previous reporting period.[115] The original intent of this test series was to terminate pairs of tests at different life fractions for destructive

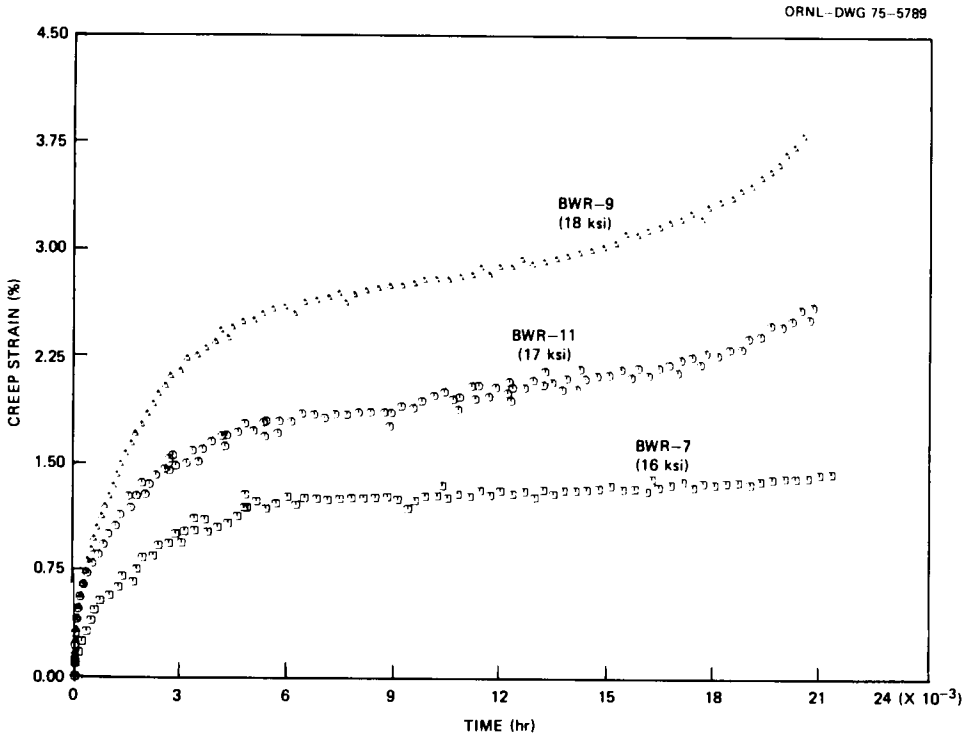

Fig. 3.127. Constant Uniaxial Load Creep-Rupture Tests (in Progress). Loaded as Shown at 593°C (1100°F). Type 304 Stainless Steel (Heat 9T2796) 5/8-in. Bar.

testing. From each pair, one specimen was to be used for metallographic examination and one for a short-time tensile test to failure. It was anticipated that the creep response of all specimens would be similar, so that the examination of different specimens at different life fractions would be a reasonable approximation to the desired examination of a single specimen at different points in its life. The data of Fig. 3.128 suggest treating these six tests as two separate groups, one consisting of tests BWI-1, BWI-2, and BWI-4, and the other of tests BWI-3, BWI-5, and BWI-6. Plans are to let test BWI-2 proceed to failure; test BWI-1 will be terminated for metallographic examination. Test BWI-4 will be terminated at initiation of tertiary creep (estimated from the data of tests BWI-1 and BWI-2) for short-time tensile testing to failure at 593°C (1100°F). In the second group of tests, test BWI-3 has ruptured. Tests BWI-5 and BWI-6 will be terminated near initiation of tertiary creep (estimated

Table 3.39. Constant-Load, Uniaxial Rupture Tests
[Type 304 Stainless Steel (Heat 9T2796); 593°C (1100°F)]

Test No.	Specimen No.	Stress (ksi)	Total Strain on Loading[a] (%)	Time to Secondary Creep (hr)	Minimum Creep Rate (%/hr)	Time to Tertiary Creep[b] (hr)	Intercept Creep Strain[c] (%)	Test Time[d] (hr)	Fracture Elongation[e] (%)	Reduction in Area (%)
BWC-1	7-15	30	5.0					187 R	19.0	30.5
BWR-1	7-1	30	7.80					138 R	21.5	32.9
BWC-2	2-22	28	6.35	40	0.016	195	0.50	227 R	13.0	20.4
BWR-2	2-1	28	5.75	40	0.022	230	0.65	368 R	16.5	29.0
BWR-13	7-13	28	6.57	60	0.023	215	0.88	276 R	16.5	18.9
BWC-9	7-25	28	4.25	85	0.021	330	1.16	415 R	18.3	25.2
BWC-3[f]	7-28	25	4.20	80	0.0065	500	0.45	667 R	12.7	12.0
BWR-3	7-8	25	3.90	100	0.0079	585	0.71	948 R	17.0	23.2
BWC-4	2-28	22	4.00	175	0.0014	1,400	0.60	2,130 R	10.7	13.7
BWR-4	7-7	22	3.30	160	0.0030	1,170	0.72	2,026 R	12.5	16.6
BWC-5[g]	2-15	20						D		
BWC-5B	2-16	20	1.83	5000	0.000165	8,700	1.84	9,584 R	10.5	12.0
BWR-5[h]	2-14	20	2.02					4,842 D		
BWR-14	2-9	20	2.02	3200	0.00044	5,800	1.88	6,868 R	8.5	13.1
BWC-10	7-18	20	1.58	4000	0.00021	8,000	2.30	9,450 R	9.3	14.3
BWR-6	7-14	19	1.48	6000	0.000073	13,500	2.90	17,547 R	9.5	12.6
BWR-9	7-11	18	1.15	7500	0.000036	18,000	2.40	20,200 I		
BWR-11[i]	2-12	17						94 D		
BWR-11B	2-10	17	1.35	6000	0.000033	20,000	1.60	20,300 I		
BWR-7	2-4	16	0.60					20,900 I		

[a]All specimens were step loaded at 1.87-ksi increments, except test BWC-5B, which was step loaded at 1.49-ksi increments.

[b]Time to tertiary creep based on the 0.2% offset from the minimum rate line.

[c]Intercept creep strain does not include the elastic and initial plastic components.

[d]R = rupture; D = discontinued; I = in test.

[e]Elongation over 3 in. in BWC series; over 2 in. in BWR series.

[f]Failure occurred near end of gage length.

[g]Temperature excursion to 704°C (1300°F) prior to loading; replaced by test BWC-5B.

[h]Temperature excursion to 749°C (1380°F) at 4842 hr; terminated.

[i]Temperature excursion at 704°C (1300°F) at 94 hr; replaced by test BWR-11B.

Table 3.40. Step-Load Uniaxial Rupture Tests, Type 304 Stainless Steel (Heat 9T2796), 593°C (1100°F)

Test No.	Specimen No.	Stress (ksi)	Total Strain on Loading (%)	Time at Load (hr)	Life Fraction[a] (%)	Fracture Elongation[b] (%)	Reduction in Area (%)
BWC-6	2-17	16	0.42	3,871	6		
		25		136	15		
		20		9,251	120		
				13,258 R	141	9.0	16.0
BWR-10	2-11	16	1.05	3,871	6		
		25		136	15		
		20		5,655	73		
				9,662 R	94	11.5	17.8
BWC-7	2-18	17	1.00	3,699	10		
		25		136	15		
		20		5,066	66		
				8,901 R	91	12.0	20.6
BWR-8	2-5	17	0.88	3,703	10		
		25		136	15		
		20		8,901	115		
				12,740 R	140	11.0	13.8
BWC-8	7-16	18	2.05	5,071	24		
		25		136	15		
		20		5,420	70		
				10,627 R	109	8.0	15.5
BWR-12	7-12	18	1.68	4,897	23		
		25		136	15		
		20		3,996	52		
				9,029	90	11.5	17.2
BWLF-5	2-25	20	2.06	503	7		
		25		198	22		
		20		5,246	68		
				5,947 R	97	12.5	17.0
BWLF-5B	2-21	21	2.62	500	10		
		25		200	23		
		21		1,236	26		
				1,936 R	59	10.3	15.9
BWLF-6	7-22	21	3.11	500	10		
		25		200	23		
		21		1,214	25		
				1,914 R	58	10.5	14.8
BWLF-7	2-26	21	2.60	750	16		
		25		136	15		
		21		2,003	42		
				2,889 R	73	12.3	20.5
BWLF-8	7-23	21	1.85	750	16		
		25		136	15		
		21		3,711	77		
				4,597 R	108	12.3	15.4
BWLF-9	7-24	21	2.55	1,014	21		
		25		136	15		
		21		1,816	38		
				2,966 R	74	18.0	16.5
BWLF-10	2-27	21	2.47	1,006	21		
		25		136	15		
		21		2,286	48		
				3,428 R	84	16.0	18.2

[a]Based on average time to rupture as determined from a linear log-log least squares curve fit of the constant-load data.

[b]Elongation over 3 in. in BWC and BWLF series; over 2 in. in BWR series.

Table 3.41. Interrupted Uniaxial Tests, Type 304 Stainless Steel (Heat 9T2796), 593°C (1100°F)

Test No.	Specimen No.	Stress (ksi)	Total Strain on Loading[a] (%)	Time to Secondary Creep (hr)	Minimum Creep Rate (%/hr)	Time to Tertiary Creep[b] (hr)	Intercept Creep Strain[c] (%)	Test Time[d] (hr)	Fracture Elongation[e] (%)	Reduction in Area (%)
BWI-1	6-4	19.5	0.98	5600	0.00008	13,000	3.3	15,000 I		
BWI-2	6-5	19.5	1.07	5400	0.00010	13,000	3.2	15,000 I		
BWI-3	6-6	19.5	1.50	4800	0.00019	9,000	3.2	11,608 R	11.0	13.3
BWI-4	6-1	19.5	0.98					8,100 I		
BWI-5	6-2	19.5	1.65					8,100 I		
BWI-6	6-3	19.5	1.30					8,100 I		

[a]All specimens were step loaded at 1.87-ksi increments.

[b]Time to tertiary creep based on the 0.2% offset from the minimum rate line.

[c]Intercept creep strain does not include the elastic and initial plastic components.

[d]R = rupture; I = in test.

[e]Elongation over 2-in. gage length.

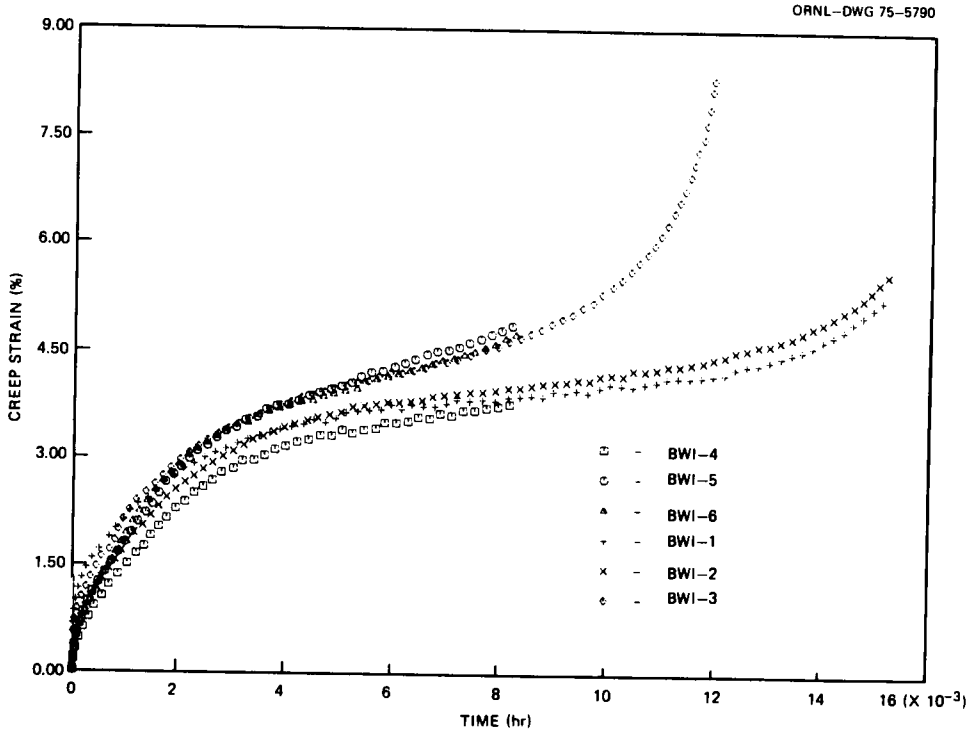

Fig. 3.128. Comparison of Uniaxial Load Tests at 19.5 ksi and 593°C (1100°F), Type 304 Stainless Steel (Heat 9T2796) 5/8-in. Bar. All Data from Load Train Motion.

from the data of test BWI-3) for metallographic examination and tensile testing. The grain size of all six specimens will be determined.

3.5.2.4 Biaxial Test

The pressure inlet line in test BWTR-3 was replaced,[115] and a subsequent helium leak test was negative. The specimen will be reloaded to the original equal biaxial tension of 21.85 ksi.

3.5.2.5 Loading Strains

The total strain on loading has not been reported for the BWR and BWI series tests, since measurements of only the full load train motion are normally obtained. To obtain this information, which is now included in Tables 3.39 to 3.41, we have assumed that the load-deflection response of these machines is linear throughout the full load range, so that any nonlinearity is the result of specimen plasticity. Several of the 2-in. gage length threaded specimens have recently been tested with extensometers

over the gage length and have shown this to be an acceptable procedure. Also note in Tables 3.39 and 3.40 that the total strain on loading for many of the BWC and BWLF series tests has been adjusted from previously reported values. This is due to the fact that resistance to plastic flow has frequently been observed during the final load increment, as shown in Fig. 3.129. This resistance was found with both measuring systems (gage length and load train measurements), so it is not the result of an extensometer malfunction. The values now reported in Tables 3.39 and 3.40 are based on an extrapolation of the data as shown in Fig. 3.129. Contrary to what might be expected, this resistance to flow is not rapidly overcome during subsequent creep flow.

3.5.2.6 Inconsistent Microstructure

During this reporting period significant effort was directed to the preparation of a topical report summarizing our findings with respect to the inconsistent microstructure that we have observed in the 5/8-in.-diam

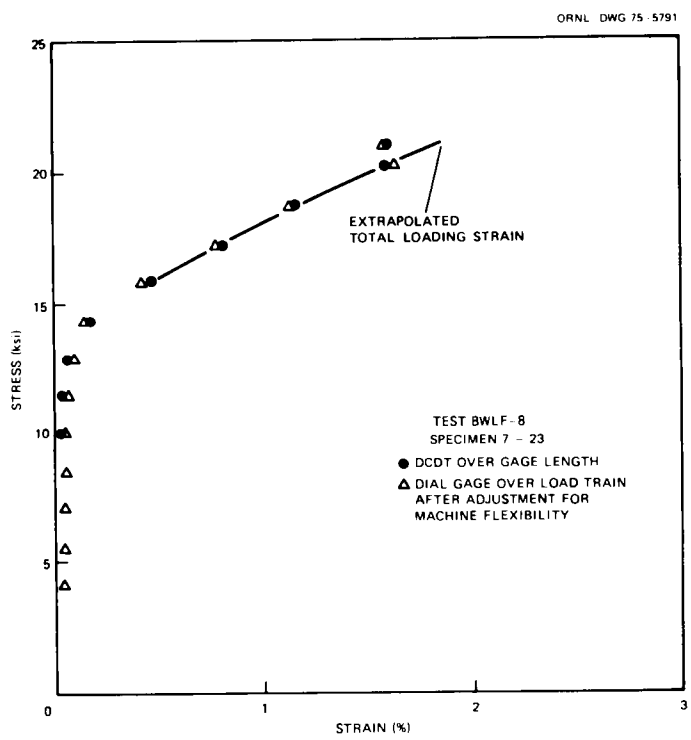

Fig. 3.129. Temporary Resistance to Flow During Loading.

hot-rolled bar product form (heat 9T2796)[116] and the observed differences in creep response between our two types of uniaxial creep testing machines.[117] A draft of that portion of the topical report concerning the inconsistent microstructure was completed and submitted to ORNL for review. The preparation of the remainder of the report is still in progress.

Significant conclusions have been reached concerning the microstructural instabilities. The instability[111] referred to is the formation, during the laboratory reanneal, of a heterogeneous duplex grain structure such as that shown in Fig. 3.130. Similar structures in the same product form of heat 9T2796 have been observed at both ORNL and at Argonne National Laboratory. In addition, the same structure has been observed in the 1-in.-diam hot-rolled bar at the Westinghouse Research and Development Laboratory.

A review of the B&W uniaxial data has led B&W to the conclusion that these variations in structure contribute significantly to the observed scatter in both the constant-load and step-load time-to-rupture data.

3.5.2.7 Machine/Specimen Differences

Test BWC-10 (20 ksi), which was part of B&W's investigation of the apparently different creep strain-time responses exhibited by the two types of uniaxial testing machines and specimens, ruptured during this reporting period. The purpose of this test was to determine if significant strain localization occurred prior to initiation of tertiary creep. To evaluate this effect, the specimen had extensometers over the full 3-in. gage length and over the center 2 in. of the gage length, as well as a dial gage monitoring the full load train motion. The failure occurred at the attachment location of the 3-in. gage length extensometers with a reduction in area of 14.3%. A similar local reduction in area (9.6%) existed near the center of the gage length. Nominally the reduction of area was under 4% in the rest of the specimen. The creep strain-time data as determined from the three methods of measurement are shown in Fig. 3.131. (The load train data actually extend to approximately 6.3%.) Although the data have not been fully evaluated, it is apparent that the strain, as determined within the center 2 in. of the gage length, attained a lower minimum rate than the strain as determined over the full 3-in. gage

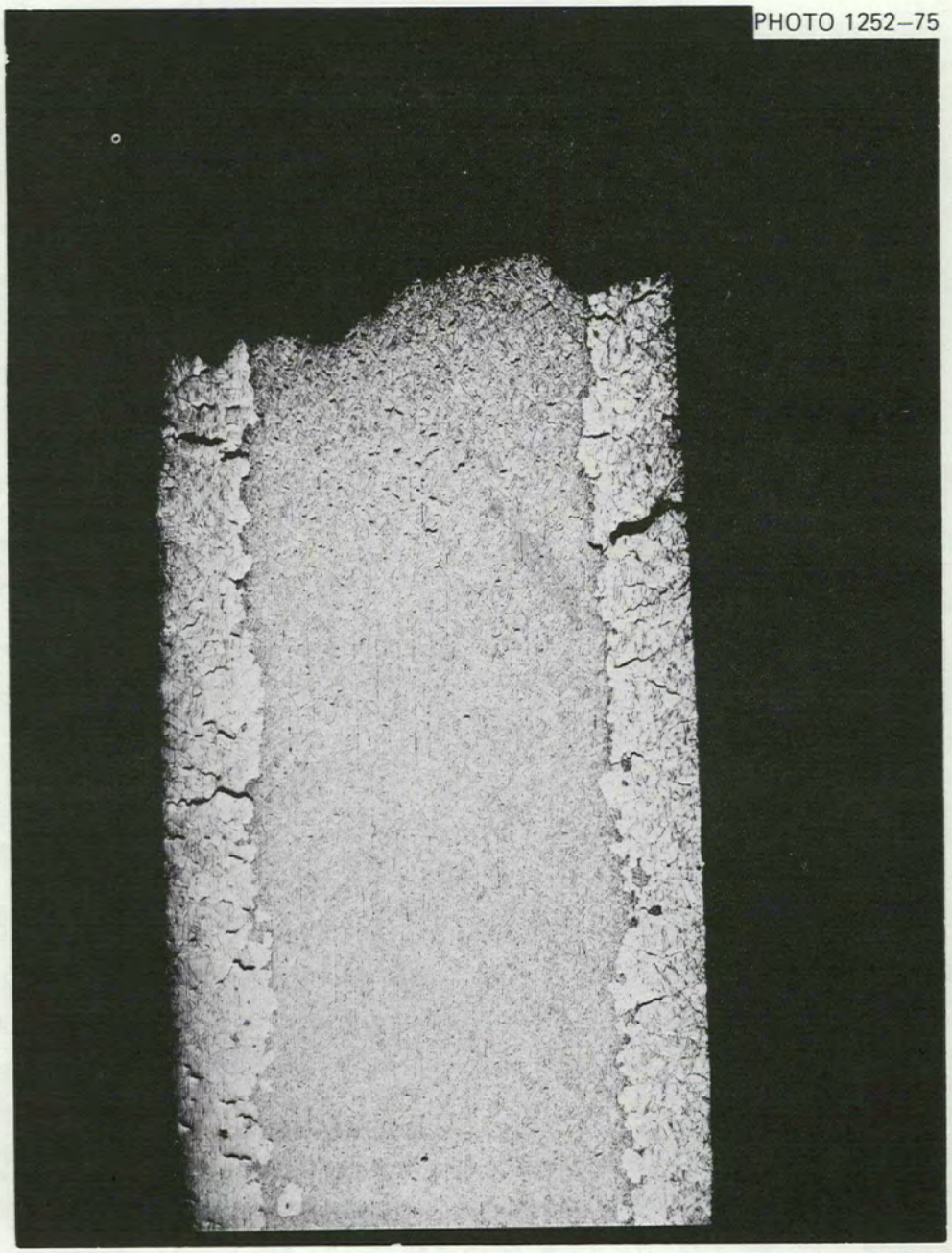

(10x)

Fig. 3.130. Heterogeneous Duplex Grain Structure Typical of That Observed in the Uniaxial Test Specimens. Longitudinal Section, Specimen 2-26, Test BWLF-7.

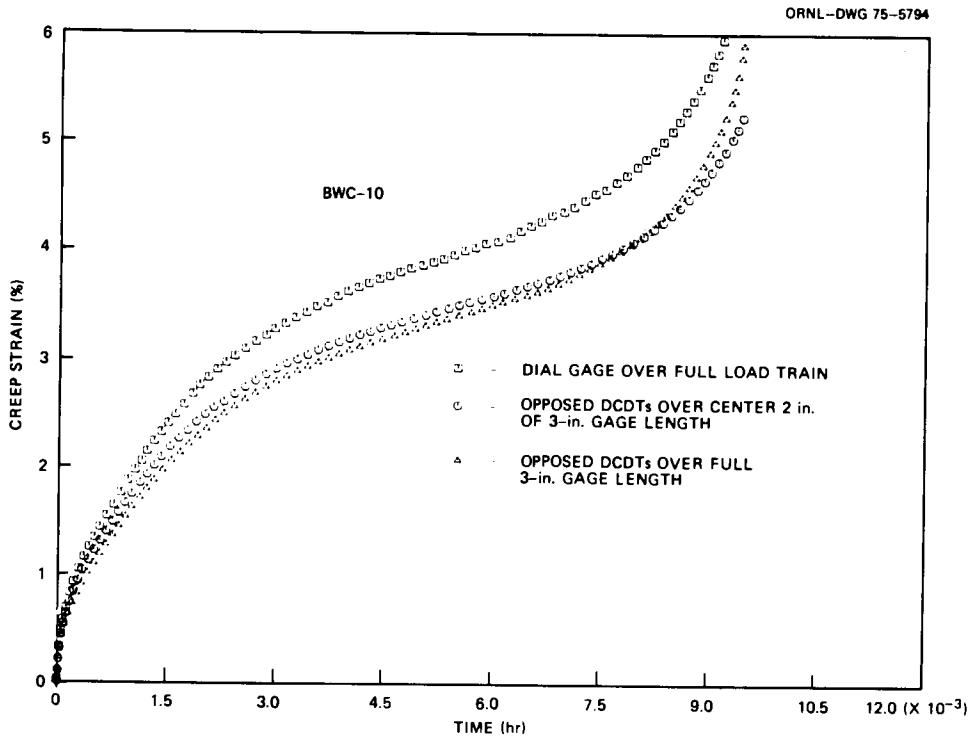

Fig. 3.131. Constant Uniaxial Load Creep-Rupture Test to Evaluate Localization of Strain in 3-in. Buttonhead Creep Machine Specimen. Loaded at 20 ksi and 593°C (1100°F). Type 304 Stainless Steel (Heat 9T2796) 5/8-in. Bar.

length. This would indicate that strain localization occurred prior to the attainment of a minimum creep rate over the full gage length.

Figure 3.132 shows the results of six tests that were conducted at 20 ksi, two of which had different reannealing times. Test BWR-5 was previously terminated at 4842 hr because of overheating. For that test the strain-time data were determined by load train motion; only the data prior to overheating are reported. The strain-time data for the other tests were determined by actual gage length displacement. The 2-in. specimens in Fig. 3.132 consistently show higher creep strain and strain rate, and shorter rupture time than the 3-in. specimens, although there are also large differences for specimens of the same type. We are now planning to investigate machine/specimen differences using an in-house heat of 304 stainless steel with uniform grain size.

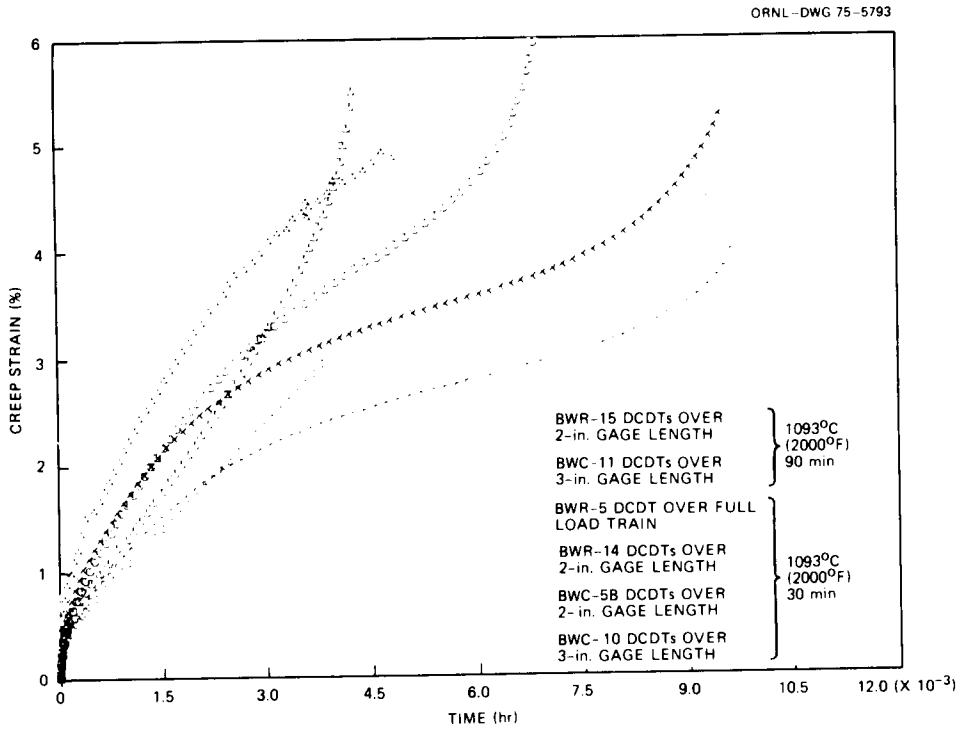

Fig. 3.132. Comparison of Uniaxial Load Creep-Rupture Tests at 20 ksi and 593°C (1100°F). Reannealed as Indicated. Type 304 Stainless Steel (Heat 9T2796) 5/8-in. Bar.

3.5.2.8 Modified Reanneal

It was previously reported[111] that a modification to the reanneal had been devised to alleviate the problem of grain size variability. The modification was to extend the time, at 2000°F, from 30 to 90 min. Verification of the adequacy of this treatment was made on three separate occasions by reannealing, for an additional 60 min, specimens which were known to have heterogeneous duplex grain structures following the initial 30-min anneal. It has now been established that this modified reanneal is not adequate. Four specimens which had received the additional 60-min anneal were subjected to creep-rupture testing, two at 20 ksi and two at 25 ksi (see Table 3.42). Three of these specimens have since ruptured, and photomicrographs are available for the two specimens as shown in Fig. 3.133. Specimen 7-19 attained a reasonably uniform grain size estimated at ASTM 1-2. Specimen 7-2 retained the heterogeneous structure, with the core grains an estimated ASTM 4 size and the outer grains an estimated ASTM 0 size. After this experience, it is B&W's opinion that any reanneal

Table 3.42. Uniaxial Constant-Load Rupture Tests on Specimens Reannealed at 1093°C (2000°F) for 90 min

Test No.	Specimen No.	Stress (ksi)	Total Strain on Loading[a] (%)	Time to Secondary Creep (hr)	Minimum Creep Rate (%/hr)	Time to Tertiary Creep[b] (hr)	Intercept Creep Strain[c] (%)	Test Time[d] (hr)	Fracture Elongation[e] (%)	Reduction in Area (%)
BWR-15	2-3	20	2.50	225	0.00088	3000	0.50	4240 R	10.5	10.9
BWC-11	2-19	20	2.90	500	0.00066		0.43	3600 I		
BWC-13	7-19	25	5.30	135	0.0049	405	0.42	467 R	10.0	16.0
BWR-16	7-2	25	4.80	70	0.0090	250	0.50	284 R	11.5	21.1

[a]All specimens were step loaded at 1.87-ksi increments.

[b]Time to tertiary creep based on the 0.2% offset from the minimum rate line.

[c]Intercept creep strain does not include the elastic and initial plastic components.

[d]R = rupture; I = in test.

[e]Elongation over 3 in. in BWC series; over 2 in. in BWR series.

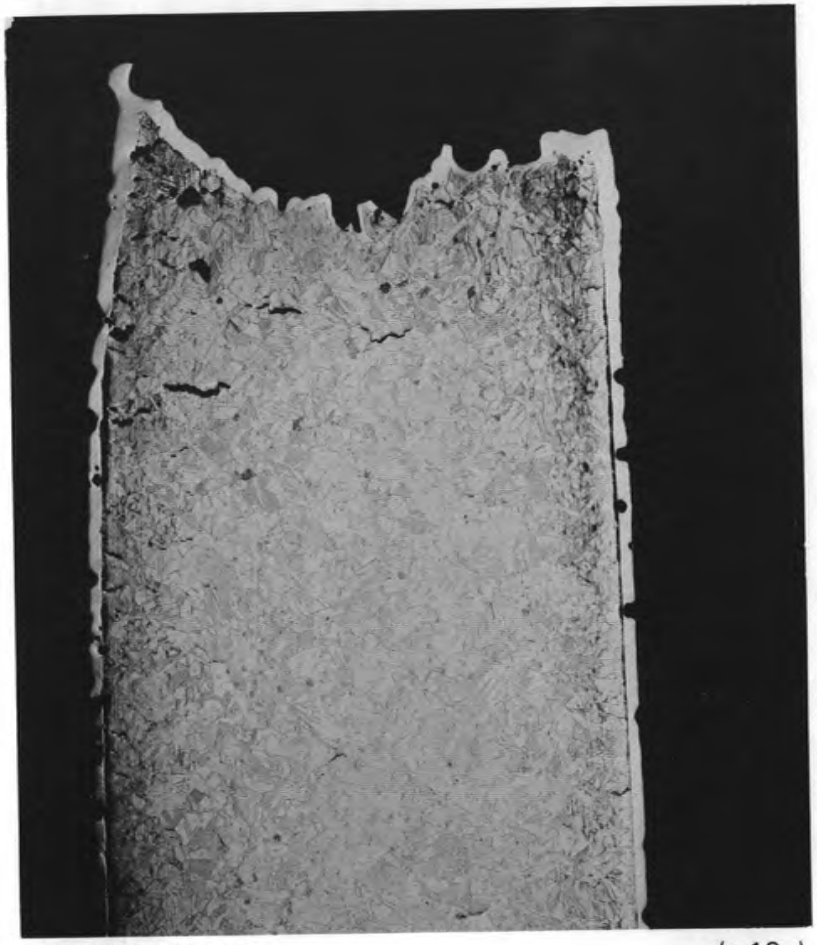

SPECIMEN 7-19
TEST BWC-13

(≈10x)

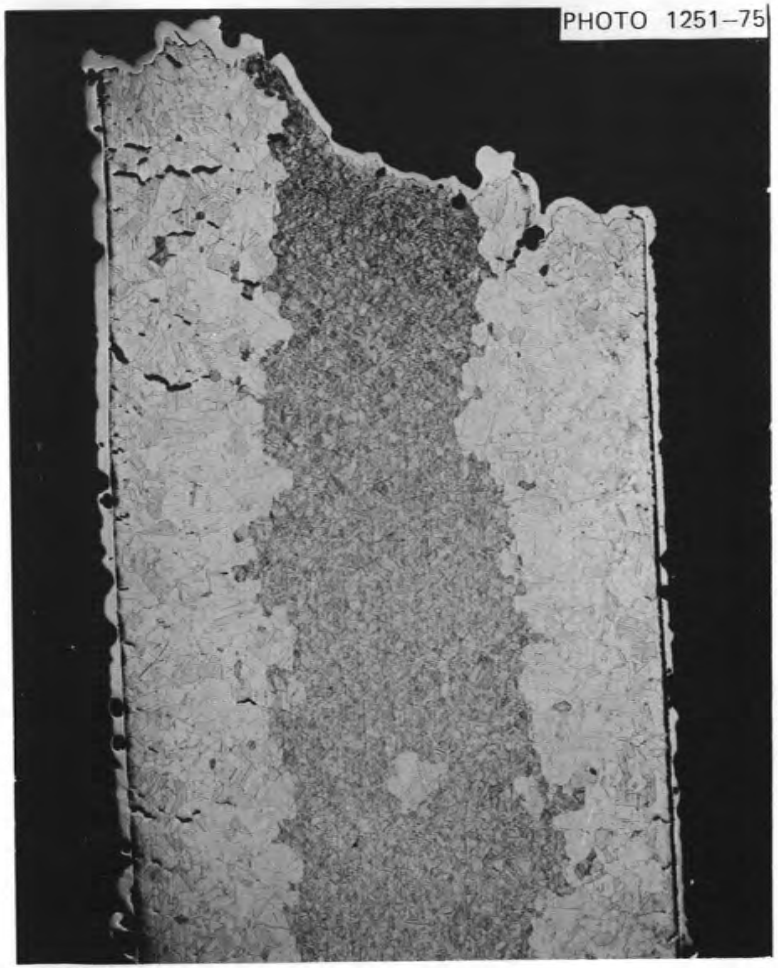

SPECIMEN 7-2
TEST BWR-16

(≈10x)

Fig. 3.133. Longitudinal Sections (Oxalic Etch) of Uniaxial Specimens Ruptured at 25 ksi at 593°C (1100°F). Type 304 Stainless Steel (Heat 9T2796) 5/8-in. Bar. Reannealed for Total of 90 min at 1093°C (2000°F).

procedure that would effectively eliminate the inconsistent grain structure would, in all likelihood, result in such excessively large grains as to invalidate the utility of the resulting data. As a result, alternate product forms for B&W's use in future uniaxial tests are being reviewed.

The creep strain-time response of the two tests at 20 ksi (BWC-11 and BWR-15) are included in Fig. 3.132. Again, the 2-in. threaded specimen shows a higher secondary creep rate than the 3-in. buttonhead specimen. The additional 60 min of annealing also resulted in a more prominent period of steady-state creep than was observed in the other tests at 20 ksi. Figure 3.134 compares the creep at 25 ksi of the two specimens reannealed for 90 min to that of two specimens reannealed for 30 min.

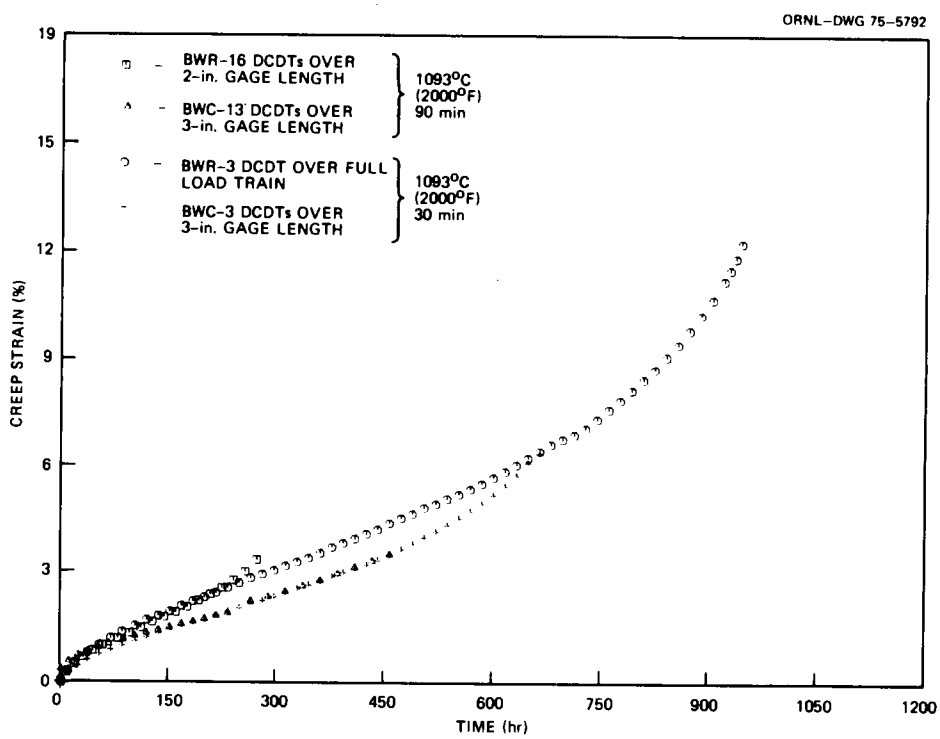

Fig. 3.134. Comparison of Uniaxial Creep-Rupture Tests Loaded at 25 ksi and 593°C (1100°F). Reannealed as Indicated. Type 304 Stainless Steel (Heat 9T2796) 5/8-in. Bar.

3.6 MECHANICAL PROPERTIES OF HTGR STEAM GENERATOR AND PRIMARY CIRCUIT MATERIALS — P. L. Rittenhouse

The goals of this program are (1) the determination of the long-term compatibility of HTGR steam-cycle plant alloys with their environment and (2) the compilation and analysis of materials design data for commercial HTGRs. The achievement of these goals involves mechanical property testing (i.e. tensile, creep, low-cycle fatigue, and crack growth) of HTGR alloys at temperatures and in environments (helium and steam) appropriate to their anticipated uses.

3.6.1 Tensile Testing — A. B. Boatwright, W. R. Corwin, and P. L. Rittenhouse

Tensile tests from 22 through 871°C (72—1600°F), have been completed on 1/2-in. (13-mm) Hastelloy X plate (heat 2600-3-4986). Results of these tests, shown in Table 3.43, are consistent with literature values for the properties of this alloy. Most of the tests were conducted at a strain rate of 0.4%/min through yielding and then at a higher rate (1.6%/min) to failure, but some later tests were run to failure at the lower rate. The property most affected by the use of the constant lower strain rate seems to be the reduction of area (e.g., note that at 760°C (1400°F) elongations exceeding 99% are found with the constant strain rate, compared with below 60% with the other).

Testing of Hastelloy S to a matrix identical to that for Hastelloy X has been completed, and data reduction and analysis are in progress.

3.6.2 Environmental Creep Testing — A. B. Boatwright and P. L. Rittenhouse

The matrix of current environmental creep tests is shown in Table 3.44. All tests in progress (Frames I-160, -161, -162, -168, and -169) are operating with the premix gas supply at a pressure of 1.1 to 1.3 atm (0.11—0.13 MPa). Nominal composition of the gas is 275 μatm (27.8 Pa) H_2, 30 μatm (3.0 Pa) CH_4, 12 μatm (1.2 Pa) CO, and 10—25 μatm (1.0—2.5 Pa) H_2O. Test times to date range from 1000 to 1100 hr.

Environmental tests in Frames I-163, -164, and -165 (see Table 3.44) are constructed, and tests for I-166 and -167 are now being built. All will be supplied by the dynamic-mix system, which is currently being

Table 3.43. Tensile Properties of Hastelloy X

Test	Temperature		Tensile Strength, ksi(MPa)		Elongation (%)	Reduction of Area (%)
	(°C)	(°F)	0.2% Yield	Ultimate		
14892	22	72	52.0(358)	110.5(762)	50.5	59.8
14893	22	72	50.6(349)	110.8(764)	51.5	59.2
14894	22	72	50.8(350)	110.8(764)	51.9	61.4
14895	149	300	42.1(290)	98.9(682)	51.1	60.6
14899[a]	149	300	41.8(288)	97.3(671)	51.5	59.8
14896	288	550	36.0(248)	96.0(662)	52.8	57.9
14897	288	550	35.4(244)	94.4(651)	53.7	55.9
14814	288	550	35.5(245)	95.2(656)	54.4	55.4
14813	427	800	32.4(223)	91.0(627)	56.5	56.9
14813	427	800	34.0(234)	91.2(629)	49.8	
14809	482	900	28.0(193)	90.4(623)	59.0	43.6
14810	482	900	34.0(234)	90.2(622)	55.9	38.4
14811	482	900	31.8(219)	90.1(621)	58.4	48.2
14807	538	1000	34.6(239)	85.8(592)	49.9	40.9
14808	538	1000	32.1(221)	86.5(596)	48.8	31.4
14804	593	1100	31.9(220)	84.9(585)	53.3	40.9
14805	593	1100	32.4(223)	85.1(587)	53.1	41.9
14806	593	1100	33.7(232)	84.3(581)	51.5	43.0
14802	649	1200	31.1(214)	73.6(507)	39.7	35.9
14803	649	1200	30.9(213)	73.6(507)	39.7	39.4
14799[a]	704	1300	32.4(223)	61.6(425)	48.5	41.7
14800	704	1300	31.2(215)	65.5(452)	37.3	33.6
14801	704	1300	30.8(212)	66.7(460)	37.6	35.9
14790[a]	760	1400	31.2(215)	46.4(320)	73.3	99.7
14791[a]	760	1400	31.5(217)	62.2(429)	75.6	99.7
14796	760	1400	31.5(217)	55.8(385)	66.6	55.8
14798	760	1400	29.9(206)	55.2(381)	68.1	57.0
14792[a]	816	1500	32.1(221)	34.9(241)	87.2	99.4
14793[a]	816	1500	33.7(232)	34.8(240)	72.2	99.7
14794[a]	816	1500	33.5(231)	34.5(238)	74.6	99.8
14795	816	1500	30.9(213)	34.9(241)	81.2	81.4
14797	816	1500	32.7(225)	41.7(288)	86.0	69.6
14815[a]	871	1600	23.4(161)	24.0(165)	79.8	88.9
14898[a]	871	1600	23.6(163)	24.3(168)	84.4	88.2

[a]Constant strain rate of 0.4%/min through failure; all other tests at this rate through yielding and then 1.6%/min.

Table 3.44. Matrix of Current Environmental Creep Tests

Test Frame	Material	Test Temperature		Stress	
		(°C)	(°F)	(ksi)	(MPa)
I-160[a]	2 1/4 Cr-1 Mo	593	1100	10	69
I-161	2 1/4 Cr-1 Mo	538	1000	15	103
I-162	Hastelloy X	704	1300	20	138
I-163	9 Cr-1 Mo	538	1000	15	103
I-164	2 1/4 Cr-1 Mo	482	900	25	172
I-165	2 1/4 Cr-1 Mo	538	1000	15	103
I-168[a]	2 1/4 Cr-1 Mo	593	1100	10	69
I-169[a]	2 1/4 Cr-1 Mo	593	1100	10	69

[a]Tests in triplicate to check reproducibility of results.

calibrated. The desired level of impurities added to the helium for these tests will be 1500 μatm (150 Pa) H_2, 50 μatm (5.0 Pa) CH_4, 450 μatm (45 Pa) CO, and 50 μatm H_2O. Moisture injection may be required to achieve the 50 μatm level, and this feature, although planned, has yet to be added to the system. The calibrations now in progress will give us our system "equilibrium" water vapor levels. If these levels are too low relative to that desired, the tests could be started with supply from the premix system.

3.6.3 Subcritical Crack Growth Studies — W. R. Corwin and J. L. Frazier*

Tests are being conducted on 2 1/4 Cr-1 Mo steel in steam at 510°C (950°F) at a variety of frequencies. At the first frequency investigated (200 cpm), the effects of the steam environment are minimal. However, if anything, there seems to be a slight enhancement of crack propagation relative to testing in air. Since the size of this effect is quite small (possibly within a reasonable scatter band for such testing), additional tests — currently under way — will be necessary to verify that steam

*Oak Ridge Y-12 Plant.

accelerates crack propagation. As a larger effect would be expected at lower testing frequencies, the next set of tests will be run at 4 cpm instead of 200 cpm.

Mechanical difficulties have been encountered with the electro-hydraulic closed-loop test machine that is equipped for crack propagation testing in simulated HTGR helium. The environmental supply and control system has functioned well, but major overhaul of the mechanical controls has been necessary. A limited amount of testing has been performed in helium at 510°C (950°F), but results are insufficient to permit conclusions.

3.6.4 Fatigue Life Testing — J. P. Strizak

The MTS system is now capable of load-, displacement-, and axial strain-controlled fatigue testing in air. (A simple computer is used in conjunction with a diametral extensometer on an hourglass-shaped specimen and a load cell to calculate axial strain.) Work is continuing to permit use of the system in strain-controlled tests in simulated HTGR primary coolant helium. Connections have been made to the helium supply and control system; design of specimen grip modifications and an environmental chamber are presently under way. Currently the unit is being used to establish base-line data in air.

3.7 REFERENCES

1. A. J. Lovell, J. D. Blackburn, and J. J. Holmes, "Effect of Prior Creep Deformation on the Residual Tensile Properties of Unirradiated Austenitic Stainless Steels," *Quart. Progr. Rep. Irradiation Effects on Reactor Structural Materials, August–October 1970*, WHAN-FR-40-1, pp. 8.4–8.14.
2. M. M. Paxton, *Effect of Prior Creep Strain on Residual Mechanical Properties of 20% Cold Worked Type 316 Stainless Steel (RM 30)*, HEDL-TME 72-153 (January 1973).
3. C. E. Beck, *The Effect of Prior Creep on the Mechanical Properties of Al Clad 2024-T3 Aluminum Alloy Sheet*, WADC Technical Note 55-49 (September 1955).

4. J. V. Gluck, H. R. Voorhees, and J. M. Freeman, *Effect of Prior Creep on Mechanical Properties of Aircraft Structural Metals*, WADC Technical Report 57-150, Pt. 1 (February 1958).

5. L. Modfin, G. E. Greene, and N. Halsey, *Effects of Creep on Tensile Properties of 2024-T3 Clad Aluminum Alloy Sheet and Riveted Joints*, National Bureau of Standards Report 4863 (1957).

6. K. O. Bogardus et al., "Effects of Prior Creep on the Tensile Properties of Cold-Worked Unalloyed Aluminum," pp. 1-17—1-29 in *Joint International Conference on Creep, ASME and ASTM*, American Society for Mechanical Engineers and American Society for Testing and Materials (1973).

7. R. W. Swindeman, *The Mechanical Properties of INOR-8*, ORNL-2780 (January 1961).

8. V. D. Scott, F. G. Scott, and A. D. Wilcox, "Model for Loss of Static Strength Caused by the Presence of Microcracks," *J. Inst. Met.* 101: 315—19 (October 1973).

9. I. R. McLauchlin, "The Effect of Long Aging Treatments on Steady State Creep in 20% Cr-25 Ni, Nb-Stablized Stainless Steel," *Met. Sci.* 8: 247—52 (1974).

10. P. G. Stone, "The Effect of Carbon, Nitrogen, and Boron on Elevated-Temperature Properties, " pp. 505—13 in *High Temperature Properties of Steels* (Proceedings of the joint conference organized by the British Iron and Steel Research Association and the Iron and Steel Institute, April 4—7, 1966) Iron and Steel Institute, London, 1967.

11. T. Shinoda, T. Matsuo, and R. Tanaka, "Method for Improving the Creep Strength in Austenitic Heat-Resisting Steel," paper presented at International Conference on Creep and Fatigue in Elevated Temperature Applications, Philadelphia, September 1973 and Sheffield, UK, April 1974.

12. V. K. Sikka, E. Lee, and E. B. Patton, "Mechanical Property Characterization of Type 304 Stainless Steel Reference Heat," *Mechanical Properties Test Data for Structural Materials Quart. Progr. Rep. Jan. 31, 1975*, ORNL-5104, pp. 116—19, 128—31.

13. G. V. Smith, *Supplemental Report on the Elevated Temperature Properties of Chromium-Molybdenum Steels (An Evaluation of 2 1/4 Cr-1 Mo Steel), ASTM Data Ser. Publ.* DS 6-S2, American Society for Testing and Materials, Philadelphia, March 1971.

14. R. Vishwanathan, "Strength and Ductility of 2 1/4 Cr-1 Mo Steels in Creep at Elevated Temperatures," *Met. Technol.* 1: 284–94 (June 1974).

15. G. N. Emmanuel, W. E. Leyda, and E. J. Rozic, "Versatility of 2 1/4 Cr-1 Mo as a Pressure Vessel Material," pp. 78–123 in *Symposium on 2 1/4 Cr-1 Mo Steel in Pressure Vessels and Piping,* ed. by A. O. Schaefer, American Society of Mechanical Engineers, New York, 1971.

16. V. K. Sikka, E. Lee, and E. B. Patton, "Effect of Aging on Tensile and Creep Properties of Type 304 Stainless Steel," *Mechanical Properties Test Data for Structural Materials Quart. Progr. Rep. Jan. 31, 1975,* ORNL-5104, pp. 131–38.

17. G. J. Guarnieri, J. Miller, and F. J. Vawter, "The Effect of Sigma Phase on the Short-Term High-Temperature Properties of 25 Cr-20 Nickel Stainless Steel," *Trans. Amer. Soc. Met.* 42: 981–1007 (1950).

18. E. O. Hall and S. H. Algie, "The Sigma Phase," *Metall. Rev.* 11: 61–88 (1966).

19. J. M. Steichen and M. M. Paxton, *Interim Report: Effect of Strain Rate on Mechanical Properties of Austenitic Stainless Steels,* HEDL-TME-71-56 (May 1971).

20. V. K. Sikka, E. Lee, and E. B. Patton, "Heat-to-Heat Variation of Mechanical Properties of Types 304 and 316 Stainless Steel," *Mechanical Properties Test Data for Structural Materials Quart. Progr. Rep. Oct. 31, 1974,* ORNL-5103, pp. 119–47.

21. V. K. Sikka, E. Lee, and E. B. Patton, "Tensile Properties," *Mechanical Properties Test Data for Structural Materials Quart. Progr. Rep. Jan. 31, 1975,* ORNL-5104, pp. 139–54.

22. C. F. Etienne, W. Dortland, and H. B. Zeedijk, "On the Capability of Austenitic Steel to Withstand Cyclic Deformation During Service at Elevated Temperature," paper presented at International Conference on Creep and Fatigue in Elevated Temperature Applications, Philadelphia, September 1973 and Sheffield, UK, April 1974.

23. G. S. Ansell and J. Weertman, *Trans. AIME* 215:838 (1959), as cited by McLean, *Rep. Progr. Phys.* 29(Part I): 1–33 (1966).

24. D. McLean, "The Physics of High Temperature Creep in Metals," *Rep. Progr. Phys.* 29(Part I): 1–33 (1966).

25. F. Garofalo, F. von Gemmingen, and W. F. Domis, "The Creep Behavior of an Austenitic Stainless Steel as Affected by Carbides Precipitated on Dislocations," *ASM (Amer. Soc. Metals) Trans. Quart.* 54: 430–44 (1961).

26. F. Garofalo, *Fundamentals of Creep and Creep-Rupture in Metals*, Macmillan, New York, 1965.

27. F. Garofalo, *Ductility*, American Society for Metals, Metals Park, Ohio, 1968, pp. 87–129.

28. J. N. Greenwood, D. R. Miller, and J. W. Suitter, "Intergranular Cavitation in Stressed Metals," *Acta Metall.* 2: 250–58 (1954).

29. D. Hull and D. E. Rimmer, "The Growth of Grain-Boundary Voids Under Stress," *Phil. Mag.* 4: 673–87 (1959).

30. D. J. Michel, H. Nahm, and J. Moteff, "Deformation Induced Twin Boundary Crack Formation in Type 304 Stainless Steel," *Mater. Sci. Eng.* 11: 97–102 (1973).

31. J. E. Harris, "An Analysis of Creep Ductility of Magnox AL80 and Its Implications," *J. Nucl. Mater.* 15: 201–07 (1965).

32. *Interpretations of the ASME Boiler and Pressure Vessel Code, "Case 1592,"* American Society of Mechanical Engineers, New York, 1974.

33. G. T. Yahr, *High-Temperature Structural Design Methods for LMFBR Components Quart. Progr. Rep. Mar. 31, 1974*, ORNL-4977, pp. 181–84.

34. R. M. Goldhoff, "A Method for Extrapolating Rupture Ductility," pp. 82–94 in *Elevated Temperature Testing Problem Areas, ASTM Spec. Tech. Publ.* 488, American Society for Testing and Materials, Philadelphia, 1971.

35. M. K. Booker, "Materials Behavior in Support of Development and Evaluation of Failure Criteria for Materials," *Mechanical Properties Test Data for Structural Materials Quart. Progr. Rep. Oct. 31, 1974*, ORNL-5103, pp. 148–57.

36. M. K. Booker, "Materials Behavior in Support of Development and Evaluation of Failure Criteria for Materials," *Mechanical Properties Test Data for Structural Materials Quart. Progr. Rep. Jan. 31, 1975*, ORNL-5104, pp. 166–81.

37. R. L. Orr, O. D. Sherby, and J. E. Dorn, "Correlations of Rupture Data for Metals at Elevated Temperatures," *Trans. Amer. Soc. Met.* 46: 113 (1954).

38. F. R. Larson and J. Miller, "A Time-Temperature Relationship for Rupture and Creep Stresses," *Trans. ASME* 74. 765–75 (1952).

39. S. S. Manson and G. Succop, "Stress-Rupture Properties of Inconel 700 and Correlation on the Basis of Several Time-Temperature Parameters," pp. 40–46 in *Symposium on Metallic Materials for Service at Temperatures Above 1600°F, ASTM Spec. Tech. Publ.* 174, American Society for Testing and Materials, Philadelphia, 1956.

40. S. S. Manson and C. R. Ensign, *A Specialized Model for Analysis of Creep-Rupture Data by the Minimum Commitment, Station Function Approach*, NASA-TM-X-52999 (1970).

41. J. Burke, *The Kinetics of Phase Transformations in Metals*, Pergamon Press, Oxford, 1965, p. 22.

42. R. W. Swindeman, "Exploratory Studies in Support of Structural Design Methods," *Mechanical Properties Test Data for Structural Materials Quart. Progr. Rep. Oct. 31, 1974*, ORNL-5103, pp. 241–60.

43. V. K. Sikka, E. Lee, and E. B. Patton, "Creep and Rupture Properties of the 2-in. (51-mm) Plate of Reference Heat," *Mechanical Properties Test Data for Structural Materials Quart. Progr. Rep. Jan. 31, 1974*, ORNL-5104, pp. 115–19.

44. L. D. Blackburn, Hanford Engineering Development Laboratory, private communication, November, 1973.

45. R. W. Swindeman and C. E. Pugh, *Creep Studies on Type 304 Stainless Steel (Heat 8043813) Under Constant and Varying Loads*, ORNL-TM-4427 (June 1974).

46. S. S. Manson and A. Mendelson, *Optimization of Parametric Constants for Creep-Rupture Data by Means of Least Squares*, NASA-Memo 3-10-59E (1959).

47. V. K. Sikka, H. E. McCoy, M. K. Booker, and C. R. Brinkman, "Heat-to-Heat Variation in Creep Properties of Types 304 and 316 Stainless Steels," submitted for presentation at the 2nd National Congress on Pressure Vessels and Piping, 1975 ASME Summer Meeting, June 23–27, 1975.

48. F. Garofalo et al., "Creep and Creep-Rupture Relationship in an Austenitic Stainless Steel," *Trans. AIME* 221: 310–19 (1961).

49. G. V. Smith, *An Evaluation of the Yield, Tensile, Creep, and Rupture Properties of Wrought 304, 316, 321, and 347 Stainless Steels at Elevated Temperatures, ASTM DATA Ser. Publ.* DS 5-S2, American Society for Testing and Materials, Philadelphia, February 1969.

50. M. K. Booker and V. K. Sikka, "Interrelationships Between Creep Life Criteria for Four Nuclear Structural Materials," to be presented at 1975 annual meeting, American Nuclear Society, New Orleans, Louisiana, June 1975.

51. G. T. Lieberman and R. G. Miller, Jr., "Simultaneous Tolerance Intervals in Regression," *Biometrika* 50: 165 (1963).

52. R. W. Swindeman, "Creep Testing of 1-in. Plate of Type 304 Stainless Steel Heat 9T2796," *Mechanical Properties Test Data for Structural Materials Quart. Progr. Rep. Jan. 31, 1975,* ORNL-5104, pp. 240–47.

53. M. K. Booker and C. O. Stevens, "Structural Materials Information Center," *Mechanical Properties Test Data for Structural Materials Quart. Progr. Rep. Oct. 31, 1974,* ORNL-5103, pp. 158–61.

54. Ibid., *Jan. 31, 1975,* ORNL-5104, pp. 182–85.

55. V. A. Singletary, *An On-Line Conversational Retrieval System for Orchis Text-Orientated Data Based User's Manual,* ORNL-4951 (April 1974).

56. R. L. Stephenson, "ADPLOT," unpublished computer program.

57. V. A. Singletary, "ADTABL," unpublished computer program.

58. F. Hamrnerling, "ADSØRT," unpublished computer program.

59. M. K. Booker and B.L.P. Booker, "TENSIS," unpublished computer program.

60. M. K. Booker and B.L.P. Booker, "FATIGUE," unpublished computer program.

61. D. N. Clark, "PROMPT.F4," unpublished computer program.

62. J. P. Hammond, *Fuels and Materials Development Program Quart. Progr. Rep. Mar. 31, 1975*, ORNL-TM-4940, in press.

63. R. T. King, N. C. Cole, R. G. Berggren, and G. M. Goodwin, "Properties and Structure of 16-8-2 Stainless Steel Weld Metal," paper to be presented at ASME Piping and Pressure Vessel Conference, San Francisco, Calif., June, 1975, to be published.

64. R. T. King, N. C. Cole, R. G. Berggren, and G. M. Goodwin, "Properties and Structure of 16-8-2 Stainless Steel Weld Metal," *Mechanical Properties Test Data for Structural Materials Quart. Progr. Rep. Jan. 31, 1974*, ORNL-4948, p. 230–53.

65. N. C. Cole, "Stainless Steel Welding Development," *Fuels and Materials Development Program Quart. Progr. Rep. Dec. 31, 1973*, ORNL-TM-4524, pp. 117–29.

66. R. T. King and E. Bolling, "Creep and Creep-Rupture Properties of Type 308 CRE Stainless Steel Weld Metal From the FFTF Vessel Test Welds," *Mechanical Properties Test Data for Structural Materials Quart. Progr. Rep. Apr. 30, 1974*, ORNL-4963, pp. 140–43.

67. R. T. King and J. O. Stiegler, "Effects of Thermal Aging on the Properties and Structure of Type 308 CRE Stainless Steel Weld Metal," *Fuels and Materials Development Program Quart. Progr. Rep. Sept. 30, 1973*, ORNL-TM-4405, pp. 155–62.

68. R. T. King, R. E. Adams, and G. M. Goodwin, "Tensile Properties of FFTF Vessel Test Weldments," *Fuels and Materials Development Program Quart. Progr. Rep. Mar. 31, 1972*, ORNL-TM-3797, pp. 210–20.

69. R. T. King and G. M. Goodwin, "Tensile Properties," *Fuels and Materials Development Program Quart. Progr. Rep. Dec. 31, 1971*, ORNL-TM-3703, p. 209.

70. R. T. King, J. O. Stiegler, and G. M. Goodwin, *Creep Properties of a Type 308 Stainless Steel Pressure Vessel Weld with Controlled Residual Elements*, ORNL-TM-4131 (May 1973).

71. N. C. Binkley, R. G. Berggren, and G. M. Goodwin, "Effects of Slight Compositional Variations on Type E308 Electrode Deposits," *Weld. J. (Miami)* 53(2): 91-s–95-s (February 1974).

72. J. O. Stiegler, R. T. King, and G. M. Goodwin, "Effect of Composition on Fracture Characteristics and Creep Ductility of Type 308 Stainless Steel Weld Metal," paper presented at Materials Division, ASME Winter Annual Meeting, Detroit, Nov. 12–15, 1973, to be published in special American Society of Mechanical Engineers publication.

73. R. L. Klueh, "High-Strain Rate Tensile Properties of Annealed 2 1/4 Cr-1 Mo Steel," *Fuels and Materials Development Program Quart. Progr. Rep. Dec. 31, 1974,* ORNL-TM-4878, pp. 30–34.

74. R. L. Klueh, "Cyclic Creep of Decarburized 2 1/4 Cr-1 Mo Steel Tubes," *Fuels and Materials Development Program Quart. Progr. Rep. Mar. 31, 1974,* ORNL-TM-4620, pp. 33–35.

75. E. Voce, *J. Inst. Met.* 74: 537 (1948).

76. R. L. Klueh, "Tensile Properties of 2 1/4 Cr-1 Mo Steel," *Fuels and Materials Development Program Quart. Progr. Rep. Sept. 30, 1974,* ORNL-TM-4726, pp. 48–59.

77. R. L. Klueh, "Effect of Sodium on the Mechanical Properties of 2 1/4 Cr-1 Mo Steel," *Fuels and Materials Development Program Quart. Progr. Rep. June 30, 1974,* ORNL-TM-4688, pp. 50–55.

78. Ibid., *Sept. 30, 1974,* ORNL-TM-4726, pp. 59–61.

79. R. L. Klueh and J. M. Leitnaker, "Effect of Sodium on Mechanical Properties of 2 1/4 Cr-1 Mo Steel," *Fuels and Materials Development Program Quart. Progr. Rep. Dec. 31, 1974,* ORNL-TM-4878, pp. 41–47.

80. R. L. Klueh and J. M. Leitnaker, *An Analysis of the Decarburization and Aging Processes in 2 1/4 Cr-1 Mo Steel,* ORNL-TM-4799 (March 1975).

81. R. L. Klueh, "Heat-to-Heat Variation of 2 1/4 Cr-1 Mo Steel," *Fuels and Materials Development Program Quart. Progr. Rep. Dec. 31, 1974,* ORNL-TM-4878, pp. 35–40.

82. C. R. Brinkman, J. P. Strizak, and C. O. Stevens, "Fatigue Behavior of 2 1/4 Cr-1 Mo Steel," *Mechanical Properties Test Data for Structural Materials Quart. Progr. Rep. Oct. 31, 1974,* ORNL-5103, pp. 220–31.

83. J. R. Ellis, General Atomic Company, personal communications.

84. C. R. Brinkman, M. K. Booker, and J. P. Strizak, "Fatigue Behavior of 2 1/4 Cr-1 Mo Steel," *Mechanical Properties Test Data for Structural Materials Quart. Progr. Rep. Jan. 31, 1975,* ORNL-5104, pp. 220–31.

85. C. E. Jaske, J. S. Perrin, and H. Mindlin, "Low Cycle Fatigue of Reactor Structural Materials," *React. Technol.* 15(3): 185–207 (Fall 1972).

86. L. F. Coffin, Jr., "Fatigue at High Temperature-Prediction and Interpretation," *Proc. Inst. Mech. Eng. London* 188: 109–27 (September 1974).

87. S. S. Manson, G. R. Halford, and M. H. Hirschberg, *Creep-Fatigue Analysis by Strain-Range Partitioning*, NASA-TM-X-67838 (1971).

88. R. D. Campbell, "Creep Fatigue Interaction Correlation for 304 Stainless Steel Subjected to Strain-Controlled Cycling with Hold Times at Peak Strain," *J. Eng. Ind.* 887–92 (1971).

89. L. F. Coffin, Jr., "Predictive Parameters and Their Application to High Temperature, Low Cycle Fatigue," pp. 643–54 in *Proc. Int. Conf. Fract. 2nd, 1969*, Chapman and Hall, London.

90. J. F. Polhemus, C. E. Spaeth, and W. H. Vogel, "Ductility Exhaustion Model for Prediction of Thermal Fatigue and Creep Interaction," pp. 625–35 in *Fatigue at Elevated Temperatures, ASTM Spec. Tech. Publ.* 520, American Society for Testing and Materials, Philadelphia, 1972.

91. J. H. Gittus, "Implications of Some Data on Relaxation Creep in Nimonic 80 A," *Phil. Mag.* 9: 749 (1964).

92. M. K. Booker, T. L. Hebble, D. O. Hobson, and C. R. Brinkman, "Mechanical Property Correlations for 2 1/4 Cr-1 Mo Steel in Support of Nuclear Reactor System Design," paper to be presented at the Third International Conference on Structural Mechanics in Reactor Technology, London, 1975.

93. M. K. Booker and B.L.P. Booker, "DAMAGE," unpublished computer program.

94. G. R. Halford, *Cyclic Creep-Rupture Behavior of Three High-Temperature Alloys*, NASA-TN-D-6309 (1971).

95. S. S. Manson, "The Challenge to Unify Treatment of High Temperature Fatigue — A Partisan Proposal Based on Strainrange Partitioning," pp. 744–75 in *Fatigue at Elevated Temperatures, ASTM Spec. Tech. Publ.* 520, American Society for Testing and Materials, Philadelphia, 1972.

96. G. R. Halford, NASA Lewis Research Center, private communications.

97. D. R. Diercks, "Strain-Range-Partitioning Analysis of Tension-Hold-Time Data for Type 304 Stainless Steel," *Mechanical Properties Test Data for Structural Materials Quart. Progr. Rep. Jan. 31, 1975*, ORNL-5104, pp. 3–13.

98. A. J. Brothers, *Fatigue Crack Growth in Nuclear Reactor Piping Steels*, GEAP-5607 (March 1968).

99. R. G. Johnson, Department of Aerospace Engineering, Mechanical Engineering, and Engineering Mechanics, University of Alabama, private communication, July 1974.

100. M. O. Speidel, "Fatigue Crack Growth at High Temperatures," in *High Temperature Materials in G&S Turbines*, ed. by P. R. Sahm and M. O. Speidel, Elsevier Scientific Publishing Company, 1974.

101. J. M. Barsom, *Fatigue Behavior of Pressure-Vessel Steels*, WRC Bulletin 194, Welding Research Council, May 1974.

102. E. K. Walker, "An Effective Strain Concept for Crack Propagation and Fatigue Life with Specific Applications to Biaxial Stress Fatigue," p. 225 in *Proc. Air Force Conf. Fatigue and Fracture of Aircraft Structures and Materials*, H. A. Wood et al., eds. AFFDL-TR-70-144 (1970).

103. D. O. Hobson and T. L. Hebble, "Yield and Ultimate Tensile Strength," *Mechanical Properties Test Data for Structural Materials Quart. Progr. Rep. July 31, 1974*, ORNL-4998, p. 224.

104. M. K. Booker and T. L. Hebble, "Mechanical Properties Correlations of 2 1/4 Cr-1 Mo Steel for LMFBR Steam Generators," *Mechanical Properties Test Data for Structural Materials Quart. Progr. Rep. Jan. 31, 1975*, ORNL-5104, pp. 231–36.

105. R. L. Klueh and D. A. Canonico, *Elevated-Temperature Tensile Strength and Microstructure of a Weld-Overlaid Type 304 Stainless Steel Forging*, ORNL-TM-4521 (May 1974).

106. R. L. Klueh, "Nondestructive Testing," *Fuels and Materials Development Program Quart. Progr. Rep. Mar. 31, 1974*, ORNL-TM-4620, pp. 49–53.

107. R. L. Klueh, "Mechanical Properties of Weld-Overlaid Stainless Steel," *Fuels and Materials Development Program Quart. Progr. Rep. June 30, 1974*, ORNL-TM-4688, pp. 68–74.

108. R. L. Klueh, "Mechanical Properties of Weld-Overlaid Forging," *Mechanical Properties Test Data for Structural Materials Quart. Progr. Rep. Oct. 31, 1974,* ORNL-5103, pp. 236–40.

109. Ibid., *Jan. 31, 1975,* ORNL-5104, pp. 236–39.

110. H. R. Voorhees and J. W. Freeman, *The Elevated-Temperature Properties of Weld-Deposited Metal and Weldments, ASTM Spec. Tech. Publ.* 226, American Society for Testing and Materials, Philadelphia, 1958.

111. C. C. Schultz, "Investigations of Creep Failure Under Uniaxial and Multiaxial Conditions," *Mechanical Properties Test Data for Structural Materials Quart. Progr. Rep. Oct. 31, 1974,* ORNL-5103, pp. 260–85.

112. R. W. Swindeman, "Representation of the High-Temperature Tensile Behavior of Reannealed Type 304 Stainless Steel by the Voce Equation," ASME paper 74-WA/Mat-7 presented at the ASME Winter Annual Meeting, New York, Nov. 17–22, 1974.

113. C. R. Barrett, A. J. Ardell, and O. D. Sherby, "Influence of Modulus on the Temperature Dependence of the Activation Energy for Creep at High Temperature," *Trans. Met. Soc. AIME* 230: 200–04 (1964).

114. D. R. Diercks and W. F. Burke, "Elevated-Temperature True-Stress True-Strain Tensile Behavior of AISI Type 304 Stainless Steel," pp. 19–30 in *Symposium on Elevated Temperature Properties of Austenitic Stainless Steels* (held June 24–28, 1974 at Miami Beach, Florida), ed. by A. O. Scharfer, American Society of Mechanical Engineers, New York, 1974.

115. C. C. Schultz, "Investigation of Creep Failure Under Uniaxial and Multiaxial Conditions," *Mechanical Properties Test Data for Structural Materials Quart. Progr. Rep. Jan. 31, 1975,* ORNL-5104, pp. 256–68.

116. Ibid., *Jan. 31, 1974,* ORNL-4948, pp. 285–315.

117. Ibid., *Oct. 31, 1973,* ORNL-4936, pp. 180–83.

118. Ibid., *Oct. 31, 1974,* ORNL-5103, pp. 260–85.

4. NAVAL RESEARCH LABORATORY

Contribution not received in time for inclusion in this issue; it will be included in the subsequent report.

5. HANFORD ENGINEERING DEVELOPMENT LABORATORY

Contribution not received in time for inclusion in this issue; it will be included in the subsequent report.

6. WESTINGHOUSE ADVANCED REACTORS DIVISION

E. C. Bishop

6.1 INTRODUCTION

The program being performed at Westinghouse Advanced Reactors Division (ARD) is entitled "Validation of High Temperature Design Methods and Criteria" (189a No. 04165). Two of the tasks in this program are "Basic Specimen Testing" and Tubular Specimen Testing." The objective of these tasks is to design and test specimens of increasing complexity to determine the inelastic behavior and strain tolerances of Types 304 and 316 stainless steel under complex stress distributions. This report covers the work performed during the period from December 1 to February 28, 1975.

6.2 BASIC SPECIMEN TESTING - N. J. Ettenson, M. Manjoine (Westinghouse Research Laboratories)

A variety of specimen designs have been selected for this task, as shown in Table 6.1 and Figure 6-1. Data obtained to date are presented in Table 6.2.

6.2.1 Uniaxially Loaded Specimen Models with Nonuniform Gage Section

6.2.1.1 Test Piece Description (304 SS Heat 9T2796)

Types C and D test piece designs, as shown in Table 6.1, are used for this part of the test program.

6.2.1.2 Current Results

The circumferentially notched round bar, D-6 (see Figure 6-1), has two notched sections. Both notches were stressed at 20 ksi (138 MPa) at 1100°F for 4023 hours, at which time visual examination revealed fine cracks in the oxide that had formed at the roots of the notches. The specimen was halved; one notched section, D6-1, will be used for metallographic examination and the other, D6-2, was reloaded at 20 ksi (138 MPa). D6-2 has now completed 9500 hours without an instability in the deflection rate. This time is about double the rupture time for that expected under

TABLE 6.1

MODEL TYPES

Specimens From Base Material[a]

Code Designation	Description[b]
A.	Plane Stress Specimen 1/3 x 2/3 x 3 in. (8.5 x 17 x 76.2 mm) gage section.
B.	Plate Specimen 1/3 x 10/3 x 3 in. (8.5 x 85 x 76.2 mm) gage section.
C.	Plate Specimen with Central Hole of 1/3 in. (8.5 mm) Diameter, 1/3 x 10/3 x 3 inc. (8.5 x 85 x 76.2 mm) plate section.
D.	Round Circumferentially Notched Specimen, Major Diameter = 0.96 in. (24.4 mm), Minor Diameter = 0.64 in. (16.2 mm), K_t = 4, Root Radius = 0.018 in. (0.46 mm), Two nearly identical notches in specimen.
E.	Plate Specimen in bending and tension, 1/3 x 10/3 x 2 in. (8.5 x 85 x 50.8 mm) plates section, eccentric load
F.	Designation generally refers to failure or fracture; therefore, it is not used to identify a type of model.
G.	Plane Strain Specimen 1/3 x 10/3 x 1 in. (8.5 x 85 x 25.4 mm) gage section. Ends constrained in transverse direction
H.	Biaxially Loaded Notched Plates, Wedge-opening-loaded Plates with 1/3 in. (8.5 mm) Diameter Notch.

Specimen With Welds

BTW - B-type plate specimen with transverse weld at mid-length of gage section.

BAW - B-type plate specimen with axial weld at center of gage section.

CTW - C-type specimen with hole through transverse weld.

CAW - C-type specimen with hole through axial weld.

DTW - D-type specimen with notch root in transverse weld.

DZTW - D-type specimen with notch root at weld fusion line of heat affected zone.

GTW - G-type specimen with transverse weld at mid-gage length.

GAW - G-type specimen with axial weld at center of gage section.

(a) Type 304 SS (HT9T2796) annealed at 2000°F.

(b) Reference Figure 6-1.

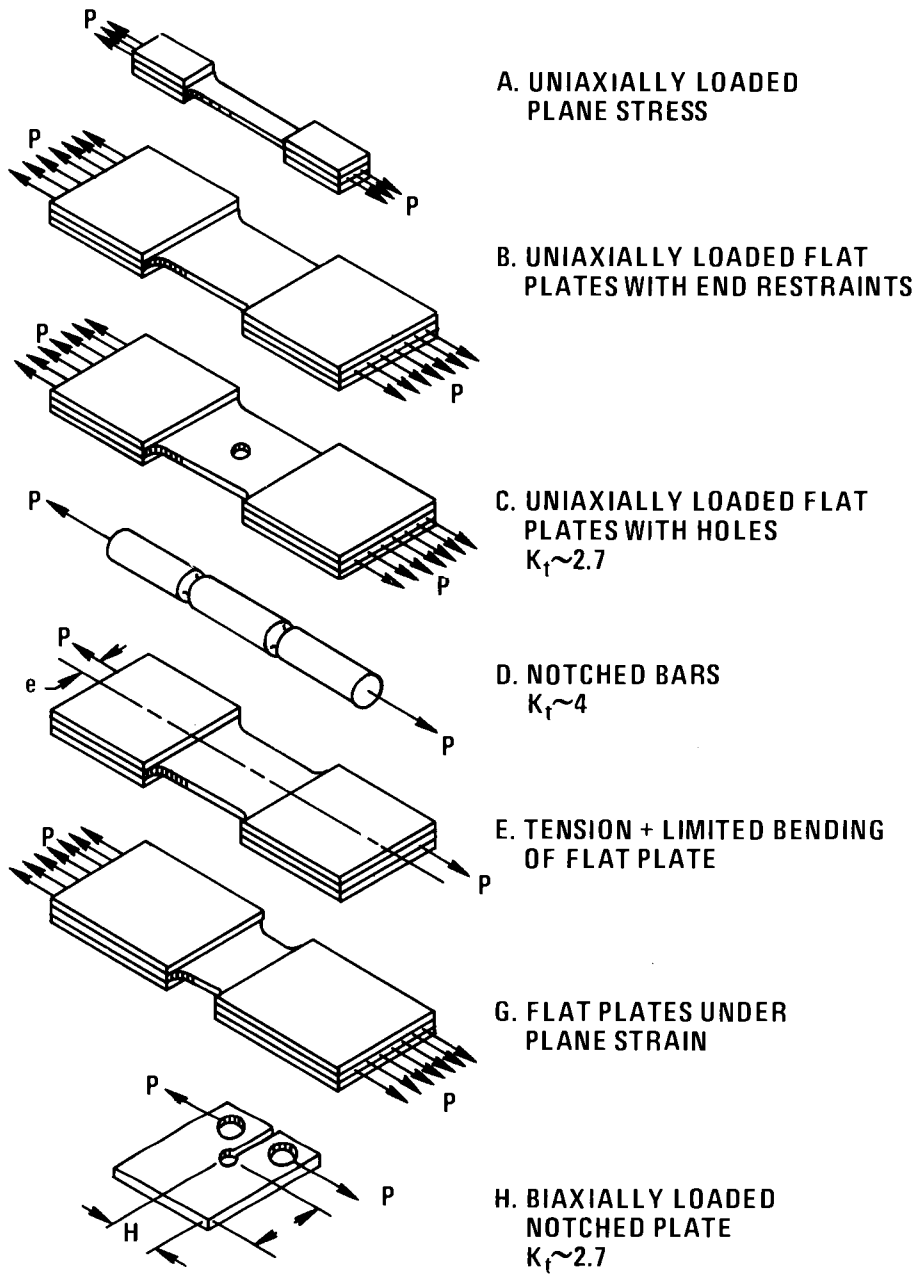

Figure 6.1 Basic Specimen Types

7518 - 1

TABLE 6.2

SUMMARY OF CREEP DATA FOR MODELS OF TYPE 304 STAINLESS STEEL* AT 1100°F (593°C)

Loading Data			Creep Data					
		Plastic	Creep	Increment		Accumulated		Permanent
Stress		Strain	Rate	Strain	Time	Strain	Time	Strain
(ksi)	(MPa)	(%)	(%/hr)	(%)	(hr)	(%)	(hr)	(%)
A1, GAGE SECTION 1/3 x 2/3 x 3 in. (8.5 x 17 x 76.2 mm)								
21.0	144.8	4.66	2.2×10^{-3}	1.10	303	1.10	303[a]	5.76
			2.2×10^{-3}	0.89	403	1.99	706[a]	6.65
						3.47	1250[b]	8.13
						3.65	1270[c]	8.31
						7.34	1826[d]	12.0
A2 (STEP-LOADED TEST)								
10.0	69.95	0.215	8.5×10^{-5}	0.228	2180	0.228	2180[a]	0.443
			6.2×10^{-5}	0.028	405	0.256	2585[e]	0.471
11.0	75.84	0	8.6×10^{-5}	0.124	1349	0.380	3934[e]	0.595
12.5	86.19	0	2.0×10^{-4}	0.213	1002	0.593	4936[e]	0.808
15.0	103.4	0.014	2.5×10^{-4}	0.811	1848	1.40[a]	6784[e]	1.619
21.0	144.8	0.646	4.5×10^{-3}	14.80	2800	16.20	9584	17.07
				1.05[b]	200	17.25	9784	18.12
				12.90	1266[h]	30.15	11050	31.02
						--	4266[m]	--
B1, GAGE SECTION, 1/3 x 10/3 x 3 in. (8.5 x 85 x 76.2 mm)								
21.0	144.8	5.34	1.4×10^{-3}	1.76	666	1.76	666[a]	7.10
			7.6×10^{-4}	1.03	1005	2.79	1671[a]	8.13
			1.7×10^{-3}	--	--	--	3000[c]	--
				1.72	1587	4.51	3258[a]	9.85[g]
						5.33	3487	--
						--	3525[h]	--
B2 (STEP-LOADED TEST)								
10.0	68.95	0.273[i]	8.6×10^{-5}	0.31	1044	0.31	1644[a]	0.58
j			9.0×10^{-5}	0.17	1462	0.45	3106[e]	0.72
11.0	75.84	0	1.1×10^{-4}	0.16	1804	0.61	4910[e]	0.88
12.5	86.19	0	2.0×10^{-4}	0.33	1364	0.94	6274[e]	1.21
15.0	103.4	0.051	4.7×10^{-4}	1.00	1302[a]	1.93	7576[e]	1.98
21.0	144.8	1.880	8.4×10^{-3}	7.50	720	9.43	8296	11.64
				5.28[b]	604	14.71	8900	16.92
				3.69[h]	239	18.40	9139	20.61
				--	--	--	1563[m]	--

Loading Data			Creep Data					
		Plastic	Creep	Increment		Accumulated		Permanent
Stress		Strain	Rate	Strain	Time	Strain	Time	Strain
(ksi)	(MPa)	(%)	(%/hr)	(%)	(hr)	(%)	(hr)	(%)
G1, GAGE SECTION, 1/3 x 10/3 x 1 in. (8.5 x 85 x 25.4 mm)								
25.0	172.4	4.25	1.8×10^{-2}	2.1	47[a]	2.1	47	6.35
			7.2×10^{-3}	2.8	268[a]	4.9	315	9.1
			1.4×10^{-2}	--	--	6.5	420[c]	10.7
				--	170[a]	7.6	485[g]	11.8
				--	83	11.6	568[h]	--
G1, DATA FROM WELDABLE STRAIN GAGES (Middle, 5/8 in. Gage Section)								
25.0	172.4	2.00	2.6×10^{-2}	0.88	47[a]	0.88	47	2.47
			2.5×10^{-3}	1.12	268[a]	2.00	315	4.00
			7×10^{-3}	0.90	170[a]	2.90[c]	485[g]	4.90
			--	0.65	83	3.55	568[h]	5.60
G2 (STEP-LOADED TEST)								
21.0	144.8	0.43	3.9×10^{-4}	1.34	1195[a]	1.34	1195	1.77
			1×10^{-4}	0.83	5520[a]	2.17	6715[e]	2.60
25.0	172.4	0.01	2.3×10^{-3}	1.80	700	3.97	7415	4.41
			4.6×10^{-3}	2.50	450[c]	4.67	7865	6.90
				4.43	283[a]	6.60	8148	11.33
				--	1837[k]	--	8552[d]	--
C1, 1/3 x 10/3 x 3 in. (8.5 x 85 x 76.2 mm), CENTRAL HOLE, 1/3 in. (8.5 mm) Dia.								
23.3[k]	160.6	8[n]	1.2×10^{-2n}	1.7[n]	100	1.7[n]	100	8.7[n]
						2.0	125[c]	10.0
							138[d]	
C2, 1/3 x 10/3 x 3 in. (8.5 x 85 x 76.2 mm), CENTRAL HOLE, 1/3 in. (8.5 mm) Dia.								
10.0[k]	68.95	0.14[n]		0.62[n]	2808[a]	0.62	2808[e]	0.76[n]
11.0	75.84	0		0.40	1290	1.02	4098[e]	1.16
12.5	85.68	0		0.50	1300[a]	1.52	5398[e]	1.66
15.0	103.4	0.28		0.82	1148	2.34	6546[e]	2.76
18.0	124.1	0.06		3.31	1630[a]	5.65	8176	6.13
			1.1×10^{-3n}	0.89	791[a]	6.54	8967	7.02
			1.1×10^{-3n}	1.05	944[a]	7.59	9911	8.07
			9.3×10^{-4n}	1.25	1345[a]	8.84	11256	9.32
			2.2×10^{-3n}	1.54	942[c]	10.38	12198	10.86
				5.0	520	15.4	12718[d]	15.9
							6172[m]	
C3, 1/3 x 10/3 x 3 in. (8.5 x 86 x 76.2 mm), CENTRAL HOLE, 1/3 in. (8.5 mm) Dia.								
21.0[k]	144.8	4.4[n]	2.3×10^{-3}n	1.5[n]	310	1.5[n]	310[g]	5.9[n]
				0.3	28	1.8	338[c]	
				2.3	59	4.1	397[h]	8.5

Loading Data			Creep Data					
Stress		Plastic Strain	Creep Rate	Increment		Accumulated		Permanent Strain
(ksi)	(MPa)	(%)	(%/hr)	Strain (%)	Time (hr)	Strain (%)	Time (hr)	(%)
E1, TENSION PLUS BENDING, 1/3 x 10/3 x 2 in. (8.5 x 8.5 x 50.8 mm)								
20.0	137.9	7.77nv	1.2×10^{-2}	1.1nv	94	1.1nv	94[a]	8.27nv
±13.0[w]	± 89.64		3.5×10^{-3}	2.27	648	3.27	742[s]	11.54
				0.63	167	4.0	909[s]	12.17
				0.58	168	4.58	1077[s]	12.75
				0.57	168	5.15	1245[s]	13.32
				0.46	115	5.16	1360[a]	13.18
				0.79	262	6.40	1622[s]	14.51
			3.0×10^{-3}	0.58	190	6.98	1812[s]	15.15
				0.65	215	7.63	2027[s]	15.80
				0.90	263	8.53	2290[s]	16.70
				0.49	190	9.02	2481[s]	17.19
				0.52	171	9.54	2652[s]	17.71
				0.77	237	10.31	2889[s]	18.48
				1.81	238	12.12	3127[h]	20.29
E2, TENSION PLUS BENDING								
18.0	124.1	6.25nv		0.47[nv]	23	0.47[nv]	23	6.72[nv]
±11.7w	±80.7		1.2×10^{-3}	2.52	1317[a]	2.99	1340	9.24
						4.17	2486[f]	
MODELS WITH WELDS								
BAW-1, B-TYPE WITH CENTRAL AXIAL WELD								
25.0	172.4	0.25[n]	8.3×10^{-3}	4.35[n]	477[a]	4.35	477	4.60[g]
			1.1×10^{-2}	8.32	765	12.67	1242	12.92
			1.5×10^{-2}	3.42	216	16.09	1458	16.34
				2.35	71	18.44	1529	18.69
							1532[d]	
CAW-1, C-TYPE WITH CENTRAL AXIAL WELD								
18.0[k]	124.1	0.33[n]				0.94[n]	6647[f]	
DWT-1, NOT STARTED								
DWT-2, ROUND NOTCHED BAR, NOTCH AT CENTER OF WELD								
25.0	172.4				5183		5183[e]	0.16[t]
28.0	193.0				2000[f]		7183[f]	
DZTW-1, CIRCUMFERENTIAL NOTCH AT HAZ								
25.0	172.4						978[d]	0.39[t]

	Loading Data			Creep Data					
					Increment		Accumulated		
	Stress (ksi)	Stress (MPa)	Plastic Strain (%)	Creep Rate (%/hr)	Strain (%)	Time (hr)	Strain (%)	Time (hr)	Permanent Strain (%)
D1-1, NOTCHED BAR D = 0.96 in. (24.4 mm) Dia., d = 0.64 in. (16.2 mm) Dia., r = 0.19 in. (0.46 mm)									
	30.0	206.8	2.6[t]		0.3[t]	137	0.3[t]	137	2.9[t]
					0.2	102	0.5	239[g]	3.1[u]
D1-2									
	30.0	206.8	2.2[t]		0.26[t]	137	0.26[t]	137	2.46[t]
					0.22	113	0.48	250[c]	2.68
							10.92	305[d]	13.12
D2-1 NOTCHED BAR									
	25.0	172.4	0.009[r]				0.006[r]	1371[g]	0.15[r]
								1371	2.17[t]
D2-2									
	25.0	172.4	0.009[r]				0.006[r]	1240[c]	
								1371[d]	5.3[t]
D3-1 and 2 NOTCHED BAR									
	21.0	144.8	0.002[r]					5499[h]	1.52[t]
D4-1 and 2 NOTCHED BAR									
	10.0	68.95	0			406		406[e]	
	11.0	75.84				477		883[e]	
	12.5	85.68				434		1317[e]	
	15.0	103.4				404		1721[e]	
	21.0	144.8	0.001[r]		0.004[r]	433		2154[e]	
	25.0	172.4	0.003[r]		0.033[r]	1581[g]		3735[u]	1.73[t]
D4-2[u]									
	25.0	172.4			0.93[t]	1323		5058	2.66
						2904[m]			
D5-1 NOTCHED BAR									
	23.0	158.4				1681[g]		1681[u]	1.8[t]
D5-2									
	23.0	158.4				1681		1681	1.69[t]
						150		1831[d]	2.83
D6-1 NOTCHED BAR									
	20.0	137.9			1.0[t]	4023[g]	1.0[t]	4023[g]	1.0[t]
D6-2									
	20.0	137.9			0.94[t]	4023	0.94[t]	4023[u]	0.94[t]
								9493[f]	

Loading Data			Creep Data					
Stress		Plastic Strain	Creep Rate	Increment		Accumulated		Permanent Strain
(ksi)	(MPa)	(%)	(%/hr)	Strain (%)	Time (hr)	Strain (%)	Time (hr)	(%)
GAW-1, G-TYPE WITH CENTRAL AXIAL WELD								
23.0	158.6	0.1[n]	5.1×10^{-3}	1.56[n]	188	1.56[n]	188	1.65[n]
			4.2×10^{-3}	1.93	452[a]	3.59	640	3.69[n]
			5.3×10^{-3}	1.64	307[a]	5.13	947	5.23
			5.3×10^{-3}	2.0	379[a]	7.13	1326[g]	7.23
				2.21	456[a]	9.34	1782	9.44
				3.17	576[a]	12.54	2758	12.62
				4.69	528[a]	17.21	2886	17.31
				8.20	210	25.41	3096[d]	25.51
BTW-1, B-TYPE, CENTRAL TRANSVERSE WELD								
21.0	144.8	0.17[n]	3.2×10^{-3}	1.29[n]	339[a]	1.29[n]	339	2.47[n]
			3.2×10^{-3}	2.35	718[a]	3.64	1057[g]	3.82
				1.25	474[a]	4.89	1531	5.07
						5.67	1724	
							1734[d]	
GTW-1, G-TYPE, CENTRAL TRANSVERSE WELD								
25.0	172.4	0.09[n]	4.7×10^{-3}	1.62[n]	240[a]	1.62[n]	240	1.71[n]
					208		448[d]	

*HT9T2796, annealed 2000°F (1094°C)

[a]Interrupted for photographic measurement

[b]Transition at 0.2% offset

[c]Transition at double minimum rate

[d]Rupture, R

[e]Stress raised (step-loaded test)

[f]Test in progress

[g]Crack initiated

[h]Test terminated, crack tearing

[i]Strain gage average, bending noted

[j]Specimen rotated 180° to investigate bending

[k]Net section stress

[m]Time at final stress

[n]Average overall strain

[p]Test in preparation

[q]Specimen to be sectioned to determine damage.

[r]Deflection of notch, inches (25.4 mm)

[s]Unload-load cycle

[t]True strain = $l_n(Ao/A)$

[u]Test interrupted, 1/2 of specimen continued

[v]Higher stress side

[w]Nominal elastic bending stress

a plane stress condition. The test will be interrupted at 10,000 hours for inspection.

6.2.2 Eccentrically Loaded Specimens With Uniform Gage Section (304 SS Heat 9T2796)

6.2.2.1 Test Piece Description

Type E test piece design, as shown in Table 6.1, is used for this part of the test program.

6.2.2.2 Current Results

A second test was started on the E-type specimen, an eccentrically loaded plate shown in Figure 6-1, at an average stress of 18 ksi (124.1 MPa). The eccentricity of the load on this specimen, E-2, was kept the same as the previously tested specimen, E-1, at 0.36 inch (9.1 mm) offset from the centerline. The E-2 test has been in progress for 2486 hours.

The nominal elastic bending stress at loading was 11.7 ksi (80.7 MPa). The plastic strains on loading were again high; that for the higher stressed side was 6.49 percent. From the strain measurements of the grid of specimen E-1, an alternate location for a strain gage was selected for E-2 to measure a lower transverse strain at a position nearer to the end of the uniform section.

The creep curves for E-2 are given in Figure 6-2 for the overall strains as measured by the clip gages and for that indicated by the strain gage. Because of the strain gradient, the strain gage measures the integrated lateral strain. In Figure 6-2 it can be seen that this strain is much lower than the overall strain on the lower stressed side. Because of the lower strains on loading and during creep, the strain gage has continued to indicate throughout the test. It will therefore be possible to estimate the bending strain and stress during the planned load cycling for this test. The gradual decreasing creep rate, evident from the creep curves of Figure 6-2, indicates that the bending stresses are decreasing with time or creep strain. The creep rate on the higher stressed side at 1340 hours was $1.2 \times 10^{-3}\%h^{-1}$ which is much higher than that estimated

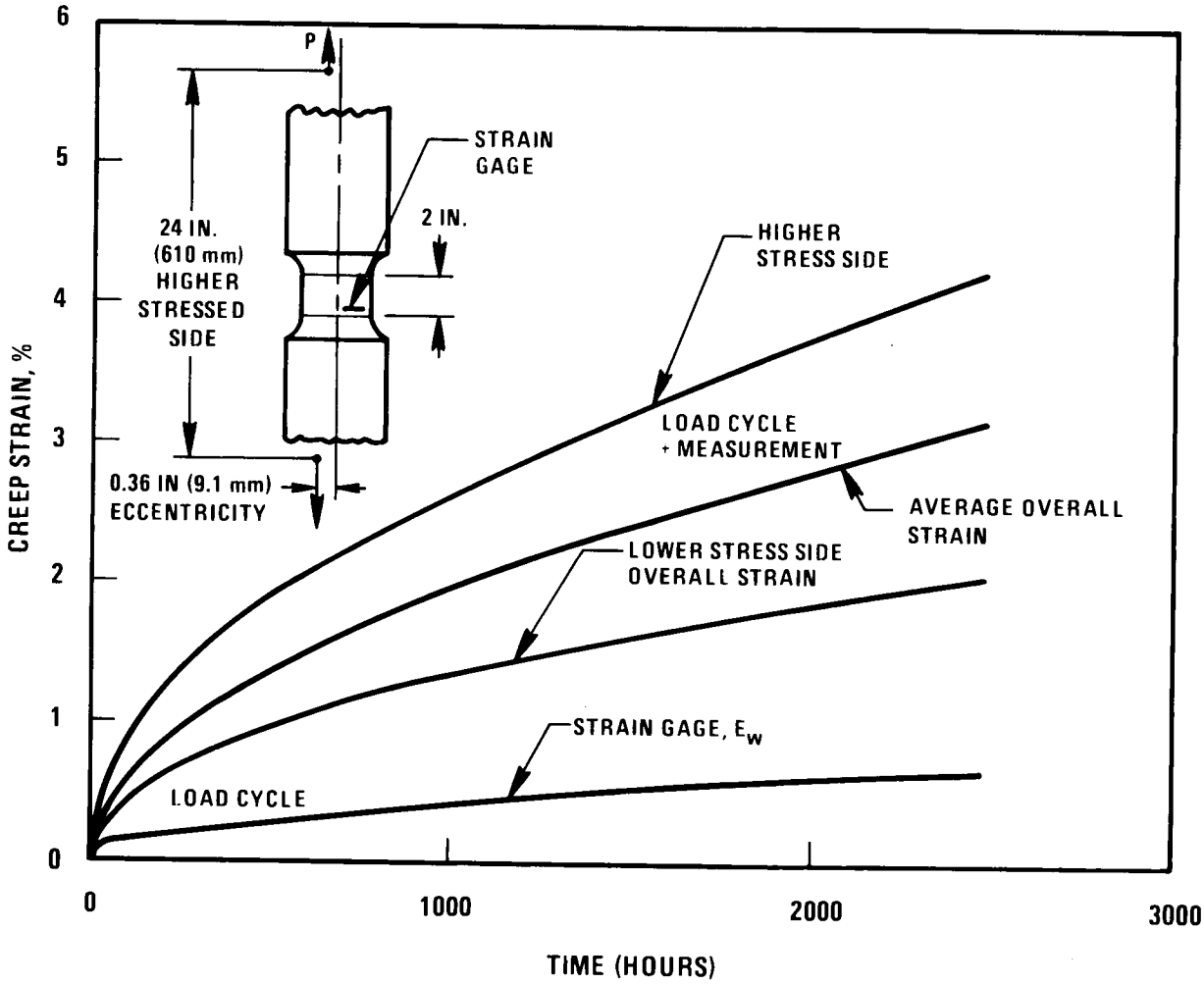

Figure 6.2 Creep Data for Model E 2, 18 ksi Average Stress Plus Bending

7518 - 2

for plane stress of 18 ksi ($3.5 \times 10^{-4}\%h^{-1}$). The test was interrupted at 1340 hours for photographic examination of the surface grid pattern.

6.2.3 Specimens with Welds (304 SS, Heat 9T2796)

6.2.3.1 Test Piece Description

The test piece designs used for this part of the program are described in Table 6.1.

6.2.3.2 Current Results

Specimen CAW-1 (see Table 6.1 and Figure 6-1) is a plate specimen with a central hole entirely within the axial weld. This specimen is still in progress after 6647 hours at a net section stress of 18 ksi (124.1 MPa). The overall deflection rate is now $9 \times 10^{-5}\%h^{-1}$, which is lower than that estimated for the gross stress of 16.2 ksi under plane stress for the base plate. The rupture curves for base plate and all weld metal are given in Figure 6-3. The current life of CAW-1 is plotted on this figure at the net section stress as point "C_A."

Specimen DTW-2 (Table 6.1) was interrupted after 5183 hours at 25 ksi (172.4 MPa). The notch, with a K_t of 4, is positioned so that the root is entirely with the central part of the weld metal. No cracks were visible at this time, which is over double the rupture life estimated for all weld metal unnotched specimens (Figure 6-3). The stress was then raised to 28 ksi (193 MPa) and has been in progress for over 2000 hours, which is nearly four times the rupture life estimated for an all weld metal unnotched specimen (Figure 6-3).

All of the tests on welds are plotted by code in Figure 6-3. Additional tests are planned to enable a better comparison with the base and weld metal properties. The limited data obtained to date indicate that the rupture strength of the transverse weld is lower than that of the base metal. This is primarily due to the lower strength of the heat affected zone. The strength of the weld metal is higher than that of the plate, so that an axial weld in a plate does increase the strength of the composite.

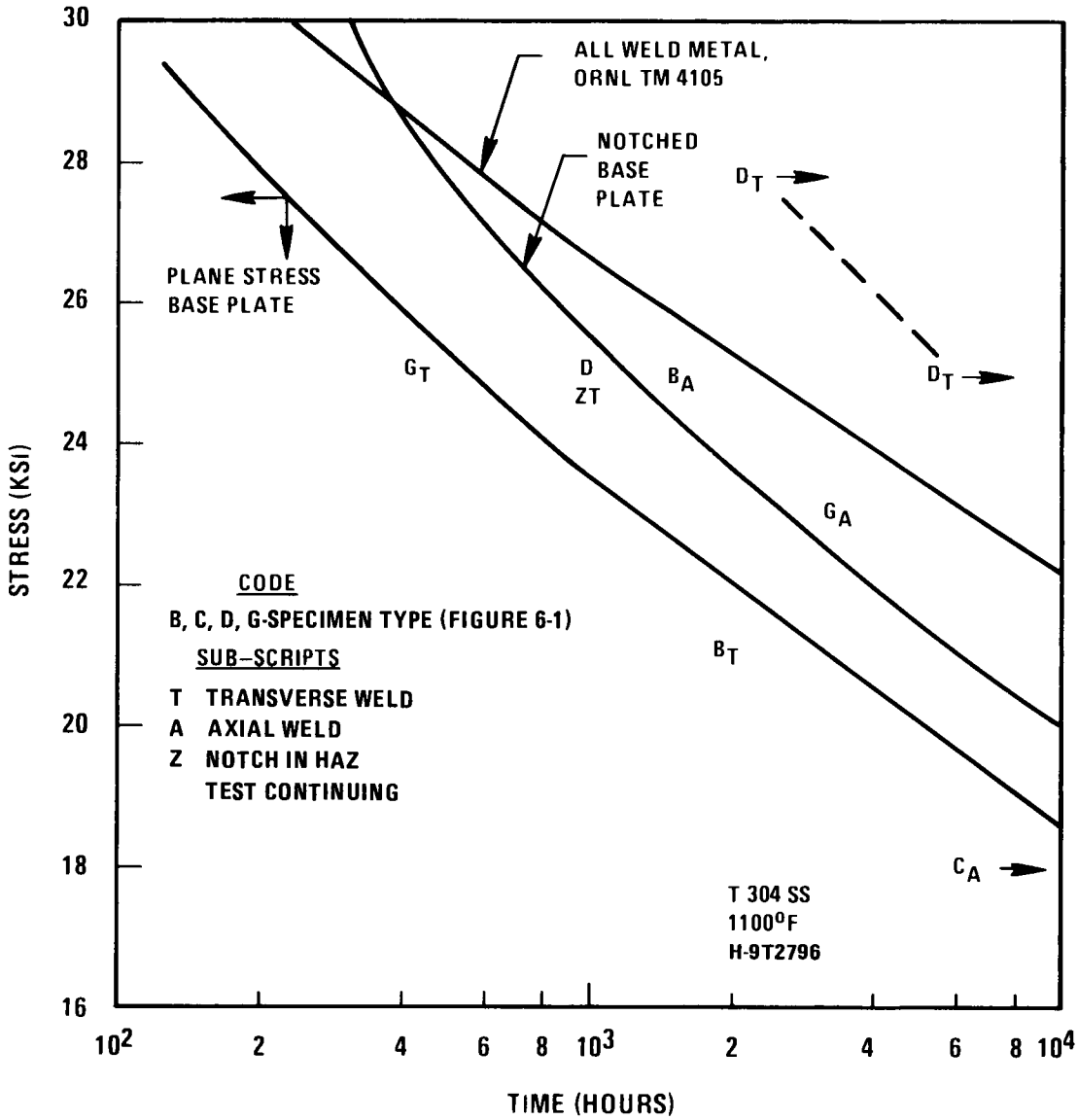

Figure 6.3 Comparison of Rupture Data of Specimens with Welds

7518 - 3

6.3 TUBULAR SPECIMEN TESTING - K. C. Thomas, P. C. S. Wu, A. K. Dhalla

6.3.1 Test Piece Description

The tubular test pieces used in this program are Type 304 stainless steel, Heat 9T2796, of 1.8-inch OD, 1.6-inch ID, and 8.7-inch length. However, thinner wall (1.7-inch OD and 1.6-inch ID) test pieces are planned for use in future tests to reduce the stress variation through the wall thickness during multiaxial testing.

6.3.2 Test Matrix

Following the completion of uniaxial Test No. 3F, the test matrix shown in Table 6.3 has been completed. Continued progress was made on the multiaxial, variable load (step-loaded) test matrix for the Type 304 stainless steel tubular specimens. The basis for each test was given in a previous report.[1] Currently, Test No. 13 was completed. However, due to the difficulties encountered in specimen fabrication, new specimens were not available to initiate Test Nos. 14 and 15.

Significant progress was made on the post-test Type 304 stainless steel tubular specimen test matrix shown in Table 6.4 This matrix was designed to utilize the machine time which became available due to the unexpected delay in delivery of Type 304 stainless steel test specimens and the Type 316 stainless steel pipe product form. The rationale for this post-test program has been discussed previously.[1]

6.3.3 Test Equipment, Specimens, and Measurement

6.3.3.1 Test Equipment

The strain measuring system, including five SLVC capacitive-type strain transducers, was instrumented and calibrated for the newly installed creep units. The performance of furnace controllers and the temperature distribution for these new creep units were also determined to be satisfactory. Heise pressure gages are being installed on each of the creep units so that the testing pressure of each creep unit can be monitored individually.

TABLE 6.3

TYPE 304 STAINLESS STEEL TUBULAR SPECIMEN CREEP TEST - UNIAIXIAL CONSTANT LOAD

Test No.	Nominal Test Temperature (°F)	Wall Thickness (0.001 Inch)	Axial Stress (psi)	Test Hours Accumulated	Axial Loading Strain (%)	Axial Creep Strain[a] (%)	Total Axial Strain (%)
1B	1100	50	25,000	241.5	0.7988	3.5572	4.3660
2A	1100	100	10,000	2016.0	0.0490	0.0697	0.1187
2B	1100	100	10,000	2000.0	0.0780	0.0880	0.1660
3A	1100	100	20,000	336.0	- - -	0.9591	- - -
3B	1100	100	20,000	1990.0	0.1783	2.7468	2.9251
3C	1100	100	7,700	2002.0	0.0461	0.0534	0.0995
3D	1100	100	5,000	1721.0	0.0253	0.0089	0.0342
3F	1100	100	15,000	1556.0	0.4855	1.1224	1.1710

(a) Average of two readings.

TABLE 6.4

TYPE 304 SS TUBULAR SPECIMEN CREEP TEST - POST-TEST MATRIX

Test No.	Effective Stress, σ_e (ksi)	Specimen History[a] Stress Ratio (σ_θ/σ_z)	Axial Load (lb)	Internal Pressure (psi)	Post Test Plan	Current Status
2A	10.0	0.0	5340	0	(b)	(i)
3C	7.7	0.0	4112	0	(b)	(i)
4A	10.0	2.0	323	1209	(c)	(i)
3B	20.0	0.0	10681	0	(d)	(j)
9	20.0	1.5	2018	2668	(d)	(j)
12	20.0	1.0	5340	2353	(d)	(j)
11	15.0	1.0	4005	1574	(d)	(k)
7A	10.0	1.5	1211	1180	(d)	(k)
2B	10.0	0.0	5340	0	(e)	(k)
3D	5.0	0.0	2670	0	(f)	(k)
10	10.0	1.0	2670	1049	(e)	(k)
1A[g]	25.0	0.0	6872	0	(h)	(j)
1B	25.0	0.0	6872	0	(h)	(j)
3A	20.0	0.0	10681	0	(h)	(j)
4	10.0	2.0	323	1207	(h)	(j)
6	20.0	2.0	0	2717	(h)	(j)
7	10.0	1.5	1212	1180	(h)	(j)
8	15.0	1.5	1515	2000	(h)	(j)

* Priority of testing is indicated by the order of listing in the table.
(a) All specimens tested at 1100°F for about 2000 hours.
(b) Tensile test to failure.
(c) Pressurize to failure.
(d) Creep-rupture test under the same prior creep test condition.
(e) Specimen step-loaded to effective stress levels of 15 and 20 ksi, respectively, for a period of 500 hours at each stress level.
(f) Specimen step-loaded to effective stress levels of 10, 15, and 20 ksi, respectively, for a period of 500 hours at each stress level.
(g) Test terminated due to over-temperature.
(h) Microstructural characterization.
(i) To be initiated.
(j) Test completed.
(k) Test in progress.

6.3.3.2 Test Specimens

Fabrication of additional Type 304 stainless steel test specimens is progressing satisfactorily after serious delay due to dimensional tolerance outage. The vendor has agreed to replace all rejected specimens. Two tubular samples were rough machined before the end plugs and extensometer tabs were welded. Currently, these samples are being final machined after the weld inspection and they will be ready for testing during the early part of the next report period.

Five 10-inch length, 2.5 inch OD x 0.562 inch wall thickness Type 304 stainless steel pipe sections have been heat treated according to the reference annealing procedure (one-half hour at 2000°F and cooled at a rate to avoid any appreciable precipitation of carbides). These materials will be used to fabricate additional tubular specimens for the additional Type 304 stainless steel test matrix proposed in Table 6.5.

A purchase order has been placed to ORNL requesting shipment of the reference heat Type 316 stainless steel pipe product form. At the present time, the delivery date of this material is still uncertain. Consequently, fabrication of test specimens made of this material cannot be scheduled.

6.3.3.3 Test Measurements and Data Records

Step-loading multiaxial creep Test No. 13 was terminated after the intended 2000-hour test period under various effective stress levels ranging from 10,000 to 20,000 psi. Measurements obtained for this test were stored in the semiautomatic data acquisition system developed specifically for the tubular specimen testing program. Currently, the computer program is being modified so that literature values will be plotted at all stress levels to compare with the present results.

The current status of the post-test matrix is shown in Table 6.4. Results obtained from the metallographical studies are discussed below.

6.3.3.4 Microstructural Characterization of the Post-Test Specimens

During the work meeting held at ORNL on August 8, 1974 between ARD and ORNL personnel to discuss creep test techniques, a decision was made to microstructurally evaluate some of the post-test samples. As a follow-up to this decision, the post-test matrix (shown in Table 6.4) was defined,

TABLE 6.5

TYPE 304 SS TUBULAR SPECIMEN CREEP TEST - ADDITIONAL MULTIAXIAL CONSTANT LOAD

Test No.	Nominal Test Temp. (°F)	Axial Load (lbs)	Nominal Internal Pressure (psi)	Nominal Effective Stress (psi)	Nominal Principal Stress-Ratio σ_r/σ_z	Test Time (hrs)	Average[a] Loading Strain, %		Nominal Average Creep Strain[a], %			
							Axial	Hoop	Radial	Hoop	Axial	Effective
4A	1100	323	1209.5	10,000	2.0	1965.7	0.01048	0.02174	-0.12711	0.12466	0.00245	0.14536
5	1115	484	1814.3	15,000	2.0	1998.0	0.09208	0.08499	-0.57795	0.54670	0.03125	0.64996
6[c]	1100	0	2716.9	20,000	2.0	762.0	0.13321	2.71103	-2.12850	2.16000	-0.03150	2.47000
7A	1100	1211	1180.0	10,000	1.5	1648.0	0.04240	0.03521	-0.02101	0.01360	0.00741	0.02110
7[b]	1100	1211	1180.0	10,000	1.5							
8	1100	1515	2000.0	15,000	1.5	2009.3	0.19414	0.80047	-0.84800	0.71900	0.12900	0.91300
9[d]	1100	2018.6	2668.4	20,000	1.5	573.4	0.00541	0.02334	-3.7460	3.31000	0.43600	4.09000
10	1100	2670	1049.4	10,000	1.0	2033.8	0.04363	0.01994	-0.06130	0.03890	0.03330	0.06000
11	1100	4005	1574.0	15,000	1.0	2012.9	0.03288	0.07339	-0.48900	0.21100	0.27800	0.47200
12[d]	1100	5340.7	2353.0	20,000	1.0	1096.5	1.82117	0.99892	-2.82000	1.56000	1.26000	2.79000
16[e]	1100	1619.9	757.6	12,500	1.0	2000.0						
17	1100	612.3	859.0	12,500	1.5	2000.0						
18	1100	0.000	874.8	12,500	2.0	2000.0						
19	1100	2267.8	1060.6	17,500	1.0	2000.0						
20	1100	857.1	1202.6	17,500	1.5	2000.0						
21	1100	0.000	1224.6	17,500	2.0	2000.0						

(a) The axial loading strain is the average of two readings.
The loop strain is the average of three readings.

(b) Test terminated due to instability of the strain measuring system.

(c) Sample ruptured after 808 hours under the test condition.

(d) Test terminated because the sample has already reached tertiary creep stage.

(e) Tests 16 to 21 are proposed to provide additional data at the stress levels specified.
Testing schedule for these specimens depends on the availability of machine time.

and currently the metallographic examination of the post-test specimens defined in the table has been completed.

The specimen history and the results obtained from metallographic characterization are summarized in Table 6.6. Hardness measurements were made on each specimen along the longitudinal and transverse directions. The general positions at which the hardness measurements were made are shown in Figure 6.4. No significant difference was observed between the longitudinal and transverse measurements. The variation was less then 5 percent in all cases. The average hardness value obtained for each specimen is given in Table 6.6.

Preliminary correlation of the hardness value with the effective stress level for each specimen is shown in Figure 6.5. Except for the thin walled specimens, 1A and 1B, a linear relationship seems to prevail between the hardness and the effective stress values for the other specimens. It is also noted that the hardness for a given specimen seems to have primarily resulted from the initial loading strain for a given effective stress and is independent of the creep strain. However, additional work has to be done in order to confirm this relationship.

Grain size distribution and cracking characteristics of the test specimens were determined at the areas shown in Figure 6-4. The results obtained are summarized in Table 6.6. Intergranular cracks were observed in all specimens except in the case of Test Nos. 4 and 7, which were terminated shortly after initiation. Transgranular cracking was observed only in the case of Test 1B, in which the specimen was ruptured after 241 hours under 25,000 psi axial stress. The ASTM grain size determined for each specimen is given in the same table. The grain size of the test material in the annealed condition, one-half hour at 2000°F, has a grain size ranging from 1 to 2, while it is seen in Table 6.6 that the grain size for the post-test specimens ranges from 2 to 5. The significance of this observation is currently being evaluated.

Microstructural examination of the specimen from multiaxial creep Test No. 12 was also performed. The specimen, previously creep tested under 20,000 psi effective stress with a stress ration ($\sigma_{hoop}/\sigma_{axial}$) of 1.0 for 1096 hours at 1100°F, developed numerous pin-hole leaks after 351 hours during subsequent rupture test under the same conditions. It

TABLE 6.6

TEST CONDITIONS AND METALLOGRAPHIC ANALYSES FOR POST-TEST CREEP SPECIMENS[a]

Test No.	Effective Stress (ksi)	Stress Ratio	Axial Load	Internal Pressure (psi)	Test Time (Hours)	Hardness Rockwell A 60 kg	Intergranular Cracks of 1 to 2 Grain Length	Transgranular Cracks of 1 to 2 Grain Length	ASTM Average Grain Size of Center of Section Longitudinal			ASTM Average Grain Size of Center of Section Tranverse		
							T = transverse section L = longitudinal section		Top	Middle	Bottom	Top	Middle	Bottom
Uniaxial Cases														
1A[b]	25	---	6872	---	17	30	L		5	4	4-1/2	4-1/2	4	4-1/2
1B	25	---	6872	---	241	40	L [d]	T	4	4	4	3-1/2	4	4
3A	20	---	10681	---	336	49	L		4-1/2	4-1/2	4	4	4	4-1/2
3B	20	---	---	---	1990	50								
Multiaxial Cases														
4[c]	10	2	323	1207	43	42			3	3-1/2	2	3	3	2
7[c]	10	1.5	1211	1180	47	43			3-1/2	3	3	3	3-1/2	3-1/2
8	15	1.5	1515	2000	2009	47	I		4-1/2	4-1/2	4	4-1/2	4-1/2	4

(a) All specimens have 0.100 inch wall thickness except specimens 1A and 1B which have 0.050 inch wall thickness. All specimens tested at 1100°F.

(b) Test terminated due to overheating.

(c) Test terminated due to malfunction of strain measuring system.

(d) Many 1 grain depth intergranular outside surface cracks, a few similar cracks on inside surface.

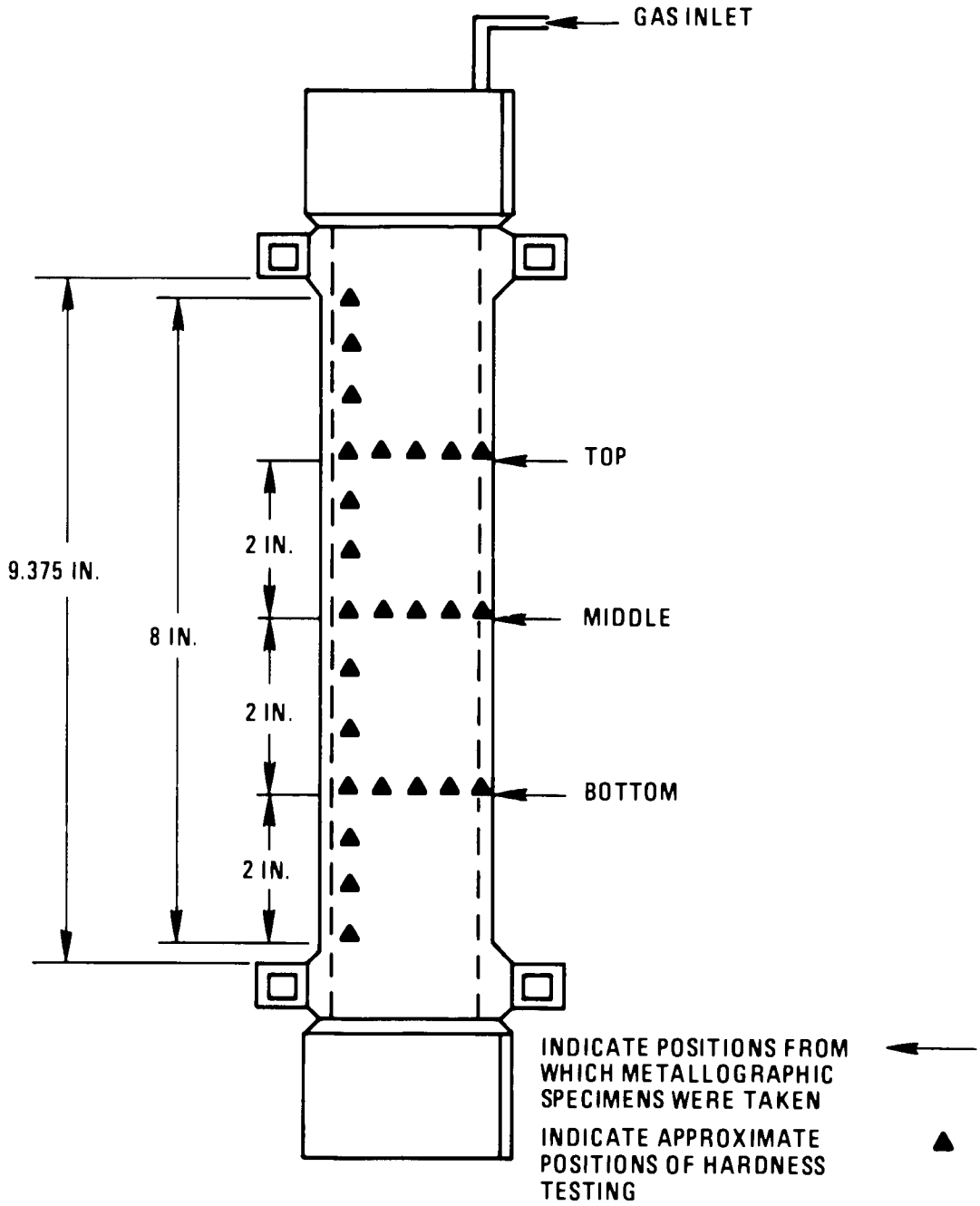

Figure 6.4 Schematic Diagram of Creep Specimen

7518 - 4

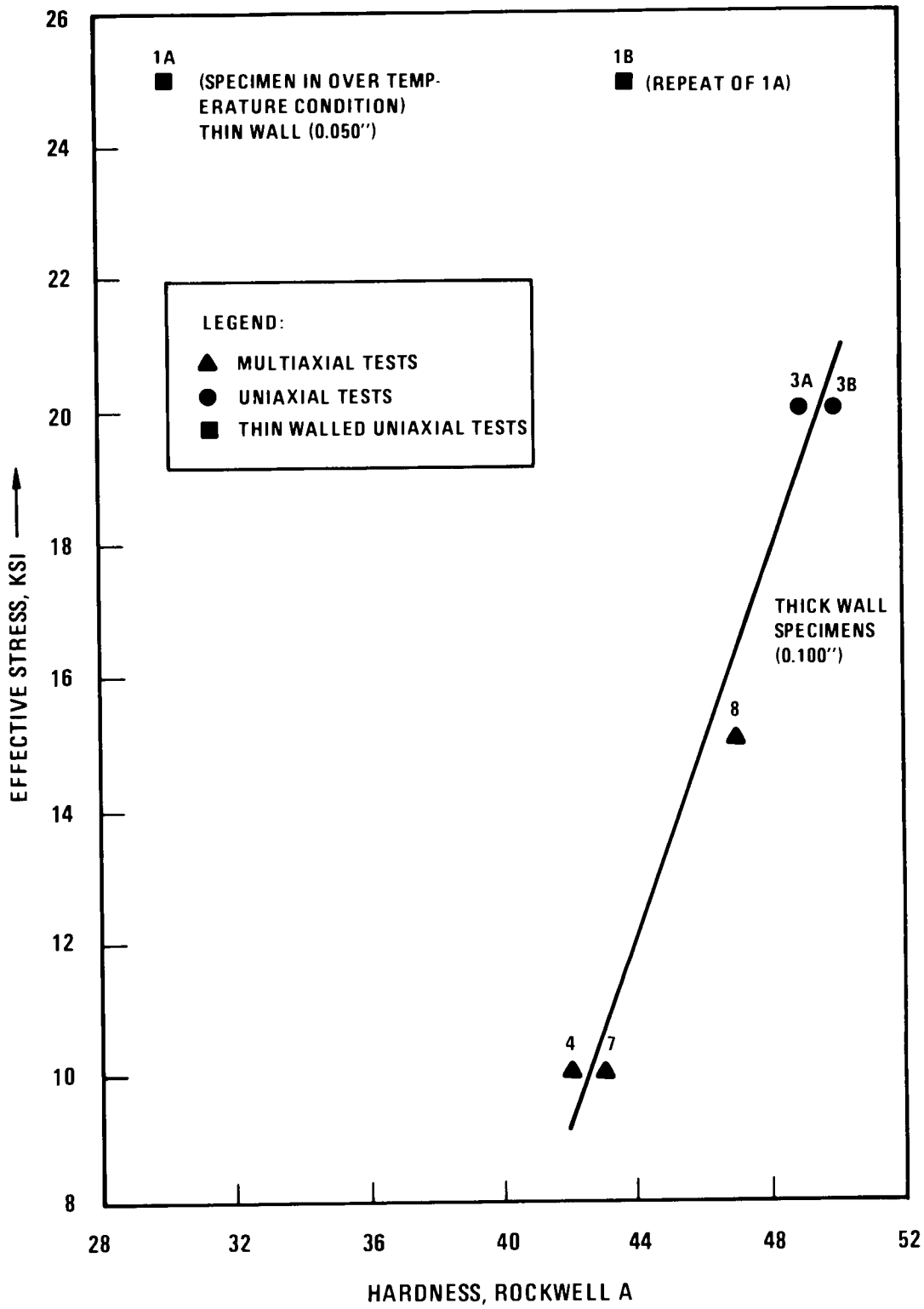

Figure 6.5 Effective Stress Versus Hardness for Creep of 304 Stainless Steel

was noted from the fracture appearance that cracks developed on both outside and inside surfaces. However, a larger amount of cracking occurred on the outside surface. Severe grain boundary separation was observed in both longitudinal and transverse sections, which is consistent with the test conditions. It is important to note that the cracks propagated predominantly in a direction perpendicular to the maximum principal stress in both cases. In addition, it is believed that some of the cracks must be interconnected, which in turn caused the leakage.

Compared to the sample burst reported previously[2] for a specimen tested under similar conditions with a stress ratio of 2.0, the failure mode for internal pressurization multiaxial creep rupture tests appears to depend on the stress ratio. Simple rupture or burst will most likely occur in specimens with higher stress ratios, while pin-hole leakage will happen in the case of lower stress ratios.

6.3.4 Data Reduction

The basic data reduction is continuing. The calculations involved were presented previously.[3] This includes the calculation of equivalent constant test conditions of temperature and pressure and equivalent uniform and constant effective strain. In addition, the effective axial gage length was also determined. Preliminary results on the uniaxial creep test measurements were presented in the previous report.[4]

The effective strain versus time relationship derived from the multiaxial creep measurements are fitted according to the following equation.

$$\varepsilon - \varepsilon_L = \varepsilon_t \left(1-e^{-rt}\right) + \dot{\varepsilon}_m t \qquad (1)$$

where: ε = total strain (in/in)

ε_L = initial loading strain (in/in)

t = test time (hrs)

ε_t, r, and $\dot{\varepsilon}_m$ are constants

Three constants in Equation (1) were obtained for each effective stress level by using the computer program CREEP-FIT transmitted from

ORNL. The values of the three constants for effective stress level are tabulated in Table 6.7.

In Figures 6-6 to 6-9, the three constants, ε_t, r, and $\dot{\varepsilon}_m$, derived for the multiaxial creep tests are plotted as a function of stress.

It is encouraging to note that the minimum creep rate, $\dot{\varepsilon}_m$, for the multiaxial creep tests does seem to follow a linear relationship with respect to the effective stress. Consequently, a very good estimate of the minimum creep rate, $\dot{\varepsilon}_m$, can be made within the stress range shown in Figures 6-6 and 6-7. However, a nonlinear relationship was observed for the same parameters for the uniaxial creep tests reported previously. Additional analyses are required to further clarify these relationships.

It is noted in Figures 6-8 and 6-9 that, in general, the data show a linear relationship between log ε_t versus log σ and log r versus log σ, respectively. However, the occurrence of the deviation, shown at the 10,000 psi and 20,000 psi stress levels, is not yet known; work is being initiated to examine this discrepancy.

6.4 REFERENCES

1. "Validation of High Temperature Design Methods and Criteria, Quarterly Progress Report for Period Ending November 30, 1974," WARD-HT-3045-8, March 1974 (Availability: USERDA Technical Information Center).
2. "Validation of High Temperature Design Methods and Criteria, Quarterly Progress Report for Period Ending August 31, 1974," WARD-HT-3045-7, November 1974. (Availability: USERDA Technical Information Center).
3. "Validation of High Temperature Design Methods and Criteria, Quarterly Progress Report for Period Ending November 30, 1973," WARD-HT-3045-4, March 1974. (Availability: USERDA Technical Information Center).
4. "Validation of High Temperature Design Method and Criteria, Quarterly Progress Report for Period Ending May 31, 1974," WARD-HT-3045-6, August 1974. (Availability: USERDA Technical Information Center).

TABLE 6.7

ε_t, r and $\dot{\varepsilon}_m$ DERIVED FOR MULTIAXIAL CREEP TESTS

Test No.	Test Temperature (°F)	Total Test Time (hours)	Internal Pressure (psi)	Axial Load (lb)	Effective Stress (psi)	Stress Ratio	ε_t	r	$\dot{\varepsilon}_m$
4A4	1100	1965.7	1209.5	323	10,000	2.0	0.1350	0.2010	0.550×10^{-5}
5-5	1115	1998	1814	484	15,000	2.0	0.2960	0.0204	0.178×10^{-3}
10-9	1100	2033	1049	2670	10,000	1.0	0.0332	0.0294	0.170×10^{-4}
11-10	1100	2012	1575	4005	15,000	1.0	0.2410	0.0121	0.125×10^{-3}
8-13	1100	2000	2000	1515	15,000	1.5	0.4250	0.0207	0.250×10^{-3}
12-14	1100	2000	2353	5340	20,000	1.0	0.0121	0.00275	0.120×10^{-2}
9-23	1100	573	2668	2018	20,000	1.5	0.9180	0.1620	0.457×10^{-2}
6-22	1100	808	2717	0	20,000	2.0	1.7300	0.00134	0.139×10^{-2}

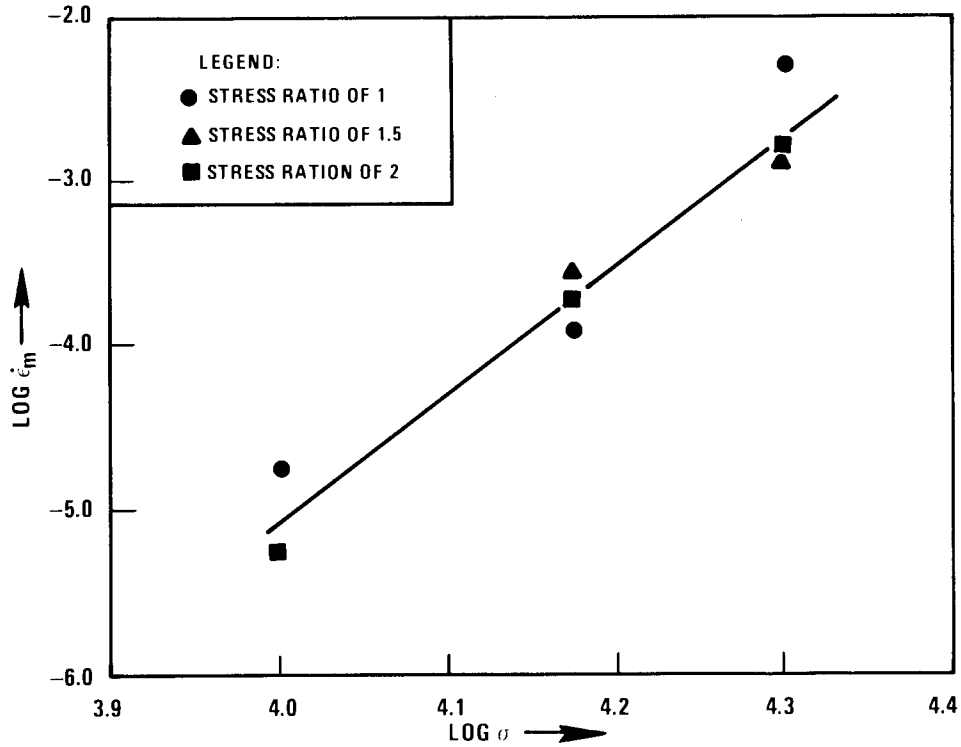

Figure 6.6 $\dot{\epsilon}_m$ as a Function of Stress for Multiaxial Creep Test

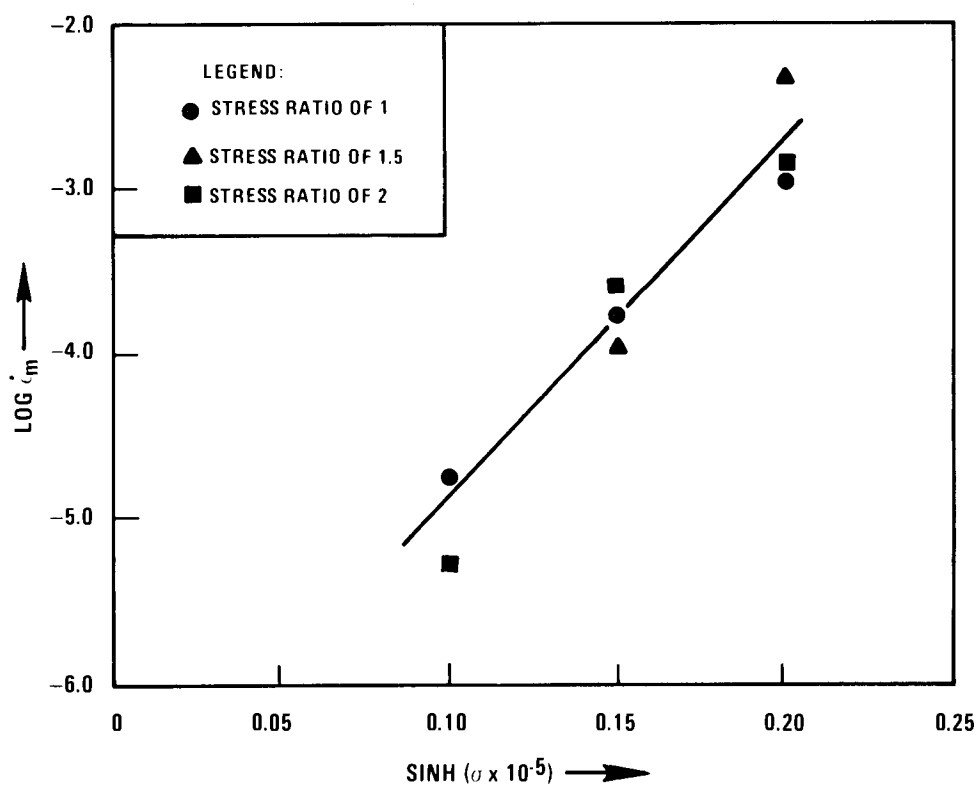

Figure 6.7 $\dot{\epsilon}_m$ as a Function of Stress for Multiaxial Creep Test

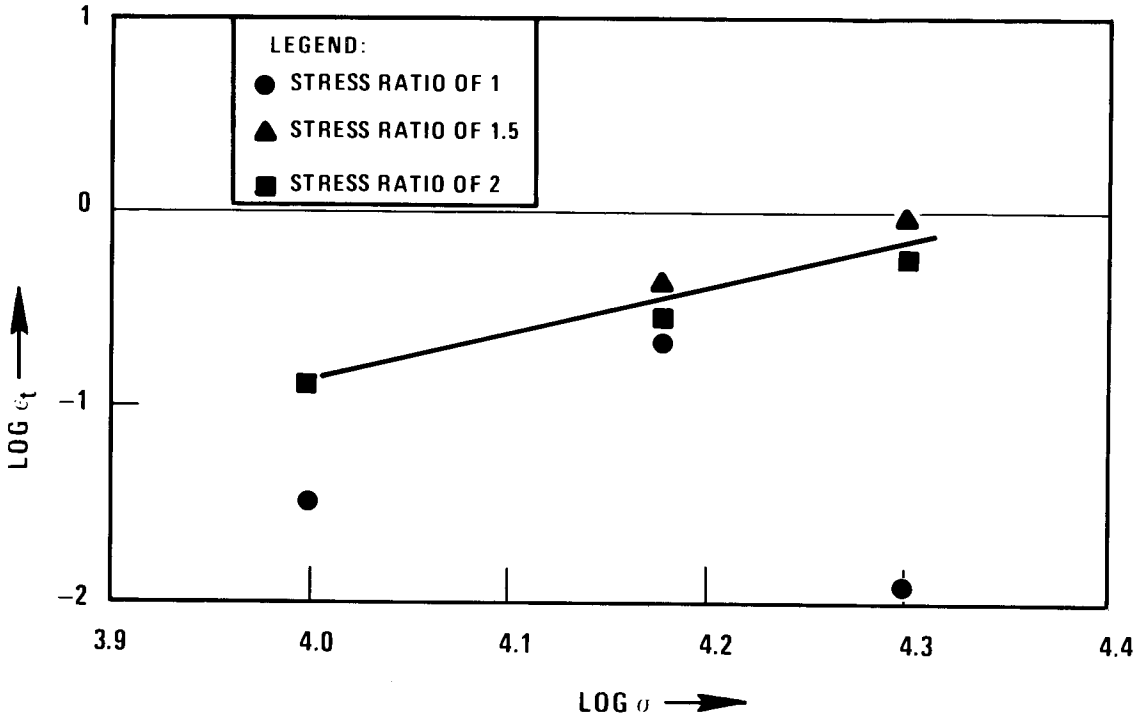

Figure 6.8 ε_t as a Function of Stress for Multiaxial Creep Test

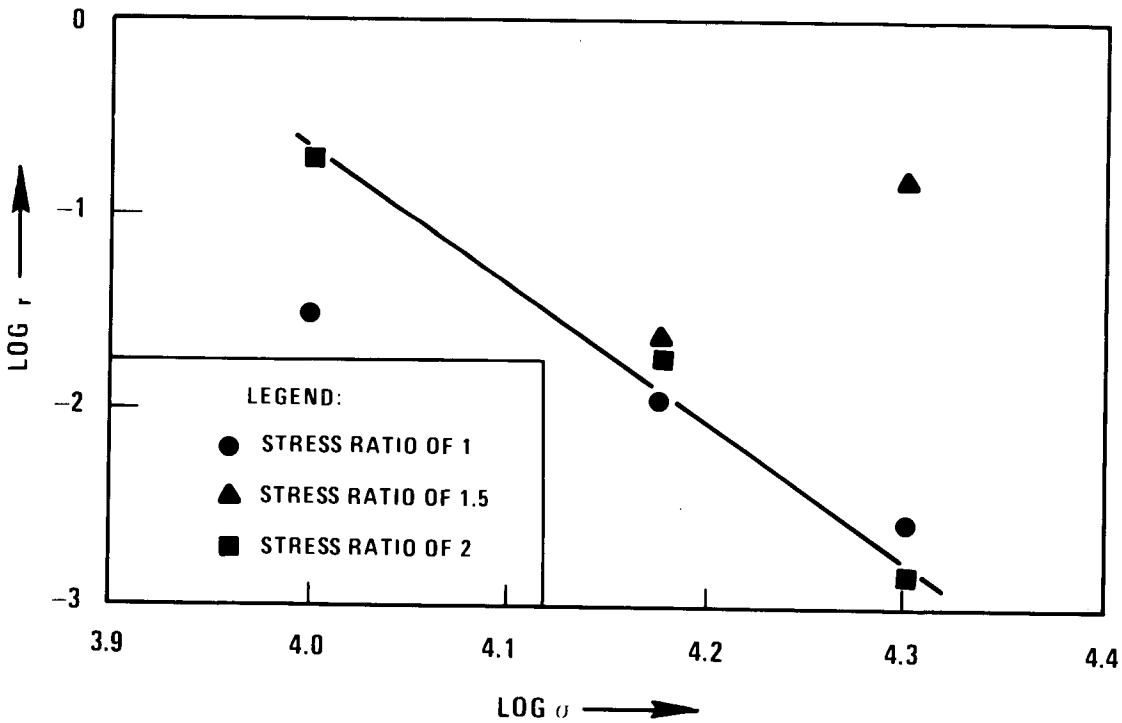

Figure 6.9 r as a Function of Stress for Multiaxial Creep Test

7518-8,9

7. UNIVERSITIES

7.1 UNIVERSITY OF CINCINNATI – J. Moteff

7.1.1 Introduction

The objective of this program is to (a) evaluate the time, temperature and stress-dependent mechanical properties of reactor structural materials, (b) determine the relationship of these properties to the microstructure and (c) show the contribution of the microstructure to the internal stress fields and the subsequent influence on microcracking and the grain boundary sliding behavior during the normal plastic deformation at elevated temperatures. Special consideration is being given to operating conditions typical of nuclear reactor applications, including the knowledge that the radiation environment can influence the substructure of these metals, a circumstance which can lead to significant changes in the conventional mechanical property behavior.

7.1.2 Experimental Program

Transmission electron microscopy has been used to study the deformation substructure resulting from creep, fatigue and tensile deformation at elevated temperatures. Creep and tensile data from ORNL (Heat Number 9T2796) was further evaluated through analysis in preparation for the correlation of the macroscopic deformation properties with the corresponding microstructure. Creep tests are continuing on 304 Stainless Steel specimens in which the stress level is abruptly changed to another value during time on test at elevated temperatures

and then subsequently terminated following a given strain and/or steady state creep rate for TEM evaluation of the substructure. A family of creep tests were performed on 304 stainless steel in which the tests were terminated at different strain levels for a TEM evaluation of the substructure developments as a function of the creep life. The preliminary TEM results are now presented. A family of fatigue tests on 304 stainless steel conducted at ANL under a Thesis Parts Program were completed and the electron microstructure is nearing completion and will be presented in the next progress report.

The influence of plastic deformation at elevated temperatures on sub-grain misorientation angles and also the effect of fatigue test temperatures on second phase particles in alloy Incoloy 800 are nearing completion and some preliminary results are presented.

Work is continuing on the creep-rupture studies on three alloys obtained from the National Alloy Development Program (NADP) and the results are presented in the NADP Progress Reports.

7.1.2.1 Characterization of the Creep and Tensile Substructure of 304 Stainless Steel, Reference Heat 9T2796

(R. Bhargava)

The characterization of the substructure of the tensile and creep tested specimens of AISI 304 stainless steel (Reference Heat 9T2796) is nearing completion. During the analysis

of relationships of deformation rate, stress and temperature for 304 stainless steel[1] it was observed that for the specimens tested in tensile mode at very high strain rates, viz., 8.33×10^{-2} sec^{-1}, the temperature compensated deformation rate, Z, increases at a much faster rate with the modulus compensated stress parameter, σ_T/E than predicted by the Equation [2]. The transmission electron microscope examinations were performed to characterize the substructure and some preliminary information is presented. Figure 1 shows some typical substructures that were developed for the specimens RP201, RP202, RP206, and RP208. These were tested in tension at a strain rate of 8.33×10^{-2} sec^{-1} and temperatures of 538, 593, 650, and 704°C, respectively. At lower temperatures, the substructural features bear close resemblance to the dynamic conditions that are present during these high strain rate tensile tests. Note the patches of incomplete cell walls in Figure 1(b). A more detailed explanation is presented elsewhere[2,3] and will be reported in future progress reports.

The substructural features of all the specimens with test conditions resulting in an effective temperature compensated deformation rate spanning eleven orders of magnitude are being evaluated. In Figure 2 the average subgrain or cell intercept, λ, is plotted versus a modulus compensated true stress parameter, σ_T/G. At modulus compensated stress levels below about 6×10^{-3}, the substructure takes the form

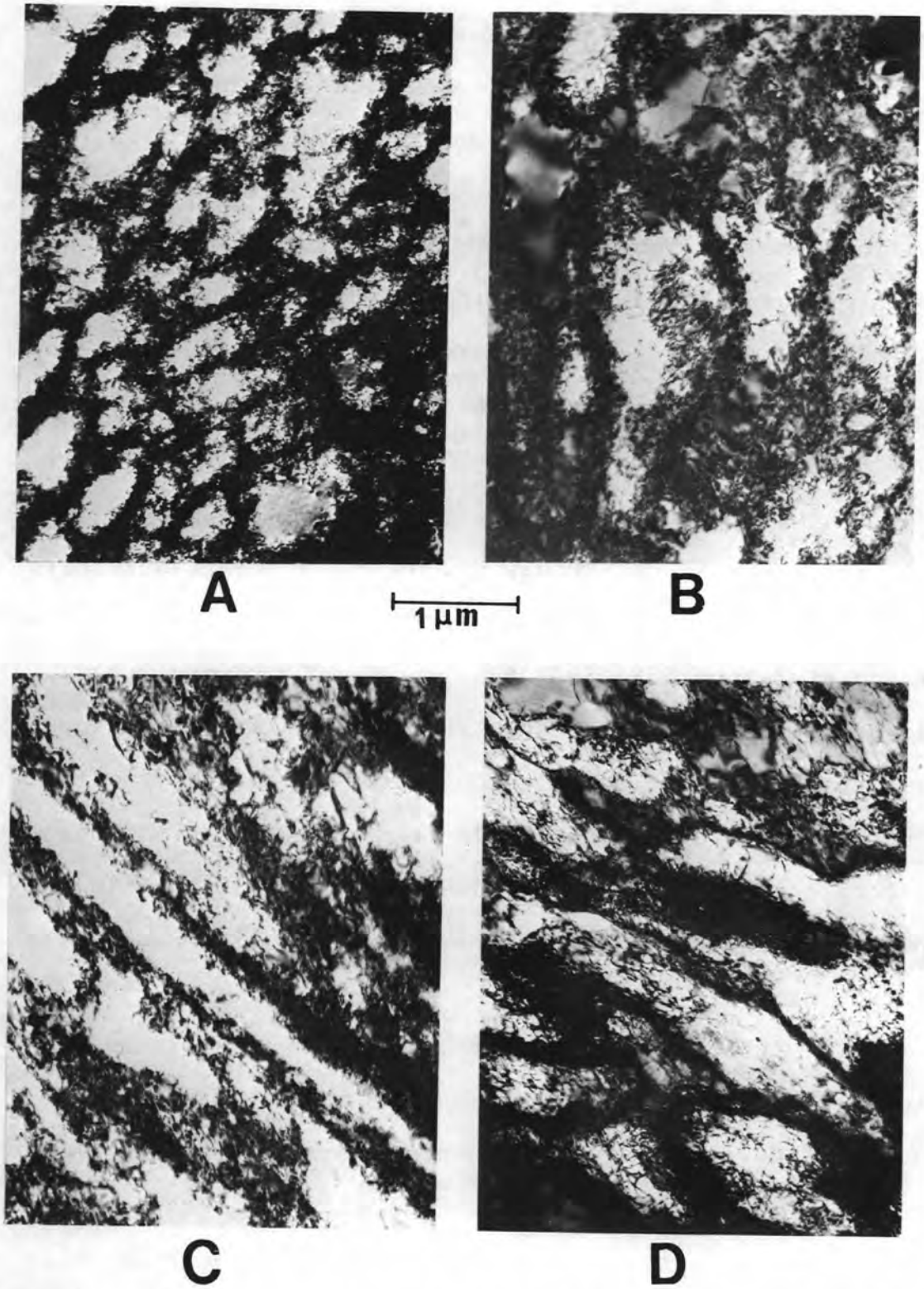

Fig. 7.1 Typical Photomicrographs of the Substructures Developed in Tension at a Strain Rate of 8.33×10^{-2} sec^{-1}, (a) 538°C (b) 593°C (c) 650°C (d) 704°C. (AISI 304 Stainless Steel, Reference Heat 9T2796)

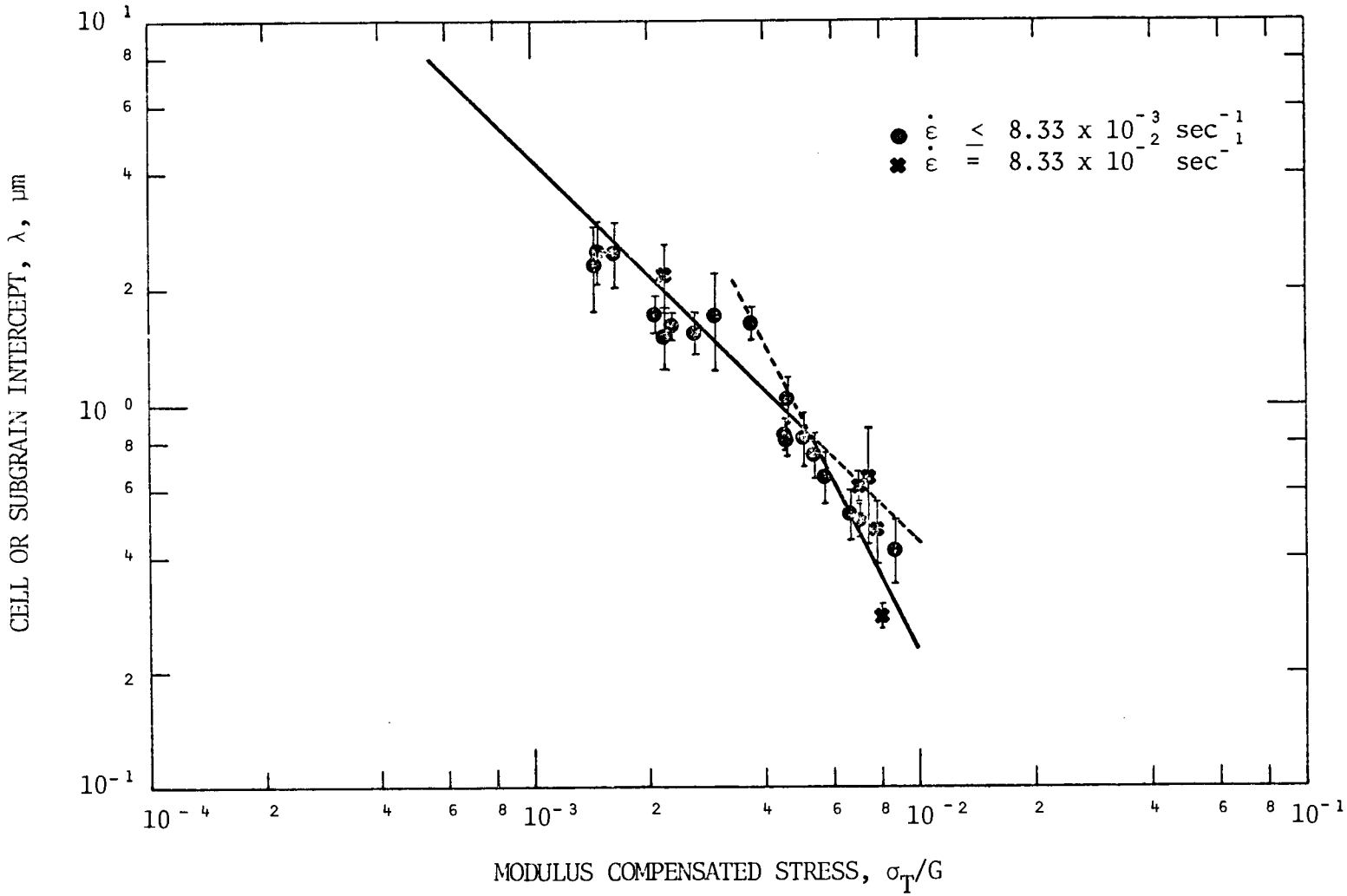

Fig. 7.2 Plot of Cell or Subgrain Intercept Versus Modulus Compensated Stress of AISI 304 Stainless Steel tested in Creep and Tension. (Reference Heat No. 9T2796)

of well defined subgrains with the size, λ in microns, varying as

$$\lambda = 16\ b(\sigma_T/G)^{-1} \qquad [1]$$

where σ_T is the true stress, G is the appropriate shear modulus and b is the Burgers vector taken normally to be equal to 2.54×10^{-8} cm. At stress levels higher than this apparent initial value, cells are formed with the size-stress relationship being given by

$$\lambda = 9 \times 10^{-2}\ b(\sigma_T/G)^{-2} \qquad [2]$$

This sort of behavior has been observed by earlier investigators[4-8]. Future progress reports will include the further developments during this program.

7.1.2.2 Characterization of the Substructure During Early Stages of Creep of 304 Stainless Steel (R. K. Bhargava)

The substructural characterization of the specimens[1] tested in creep at 704°C was performed and some of the preliminary results will be presented here. Figure 3 shows the typical micrographs of the substructure developed during the various stages of creep deformation. Also included is the substructure before testing for comparison. The dislocation density before testing was estimated at $(7.4 \pm 0.4) \times 10^8$ cm^{-2}. On loading, the dislocation density increases to a value of $7.14 \pm 0.84) \times 10^9$ cm^{-2}. The photo micrograph (RUC-6) shows some loops, stacking faults and some tangled and free dislocations. In the early primary stage (RUC-3), the dislocation density increases to $(9.94 \pm 0.86) \times 10^9$ cm^{-2}. The typical

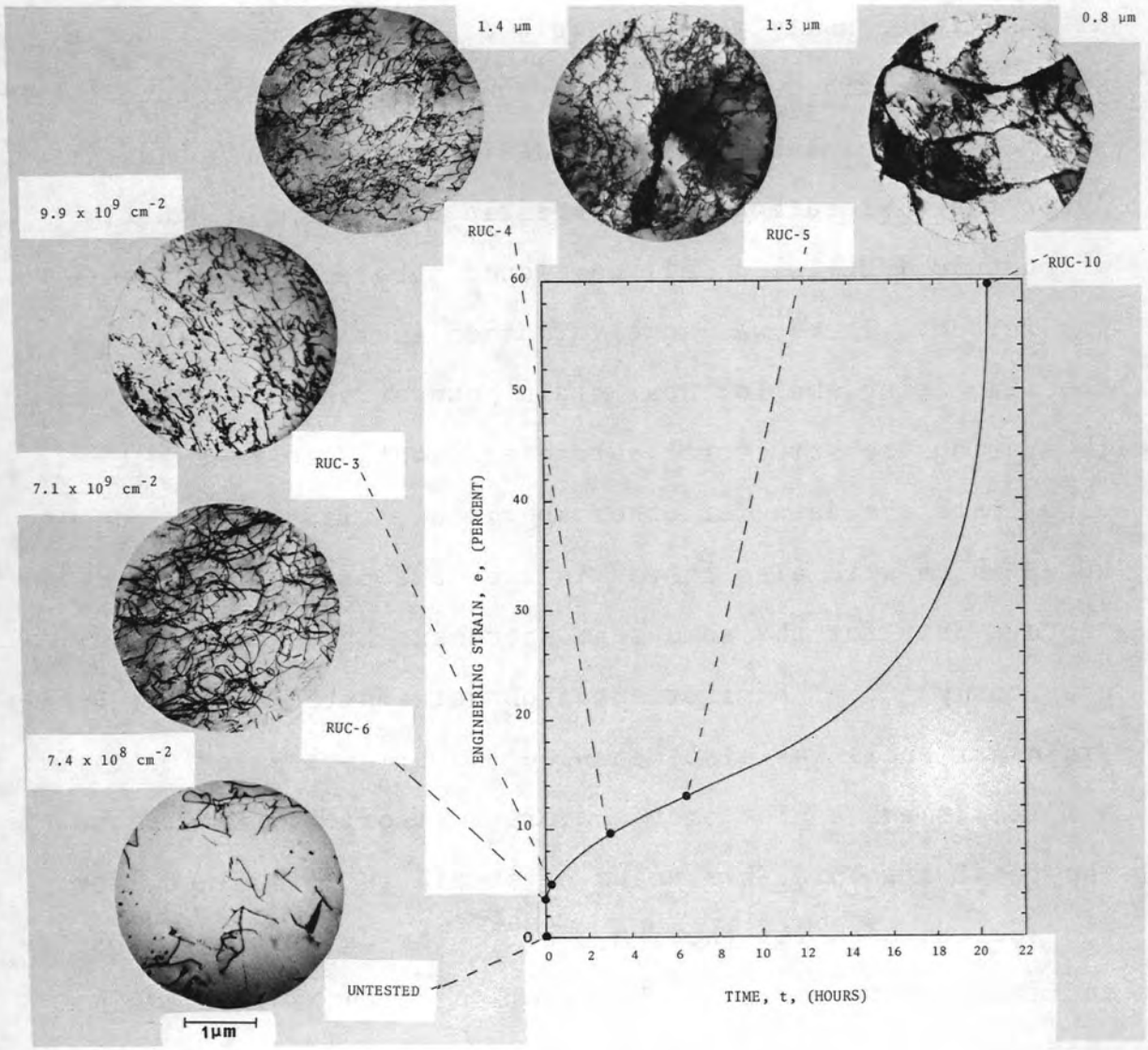

Fig. 7.3 Strain Behavior in 304 Stainless Steel as a Function of Time During Creep at 704°C with Corresponding Substructures. (Stress 17.58 $kg \cdot mm^{-2}$)

substructure consists of more tangles with some localized tendency to form cells. In the late primary stage (RUC-4), the tendency to form cells became more prevalent. The total dislocation density remained more or less the same. During steady state creep (RUC-5), the substructure started to take on the shape of subgrains with definite subgrain boundaries. Again the dislocation density remained the same. Finally at rupture (RUC-10) a well developed subgrain substructure was formed. There was some variation in the subgrain size, the size being smaller near grain boundaries. Table I lists the various substructural parameters that were measured. It also lists the data for other specimens, viz., RUC-1, RUC-9, RUC-8 which were also tested in the same program. The creep rupture data for the same test specimens have been reported previously[1]. The misorientation between the adjacent subgrains or cells was also measured and are presented in Figure 4. This shows a plot of the average misorientation versus the total strain. This value of strain is determined from the section used for the TEM study. The data from this study indicates an increase in the misorientation as the strain increases. After the secondary stage has developed the increase in misorientation angle is less apparent and it tends to reach a saturation value. The average subgrain intercept, λ, is plotted versus the modulus compensated true stress, σ_T/G in Figure 5. For comparison the relationship determined for the reference heat 9T2796 is also shown (See Figure 2).

TABLE 7.1

SUBSTRUCTURE DATA FROM 304 STAINLESS STEEL (UC HEAT G8607) CREEP TESTS AT 704°C

Specimen Number[a]	True Stress[b] σ_T kg · mm^{-2}	Modulus Compensated True Stress[c] σ_T/E	σ_T/G	Average Cell or Subgrain Intercept λ, μm	Average Dislocation Density ρ, cm^{-2}	Cell or Subgrain Misorientation θ, Degrees
RUC-1	13.09	0.91×10^{-3}	2.36×10^{-3}	1.62 ± 0.24	N.M.[d]	0.63 ± 0.31
RUC-9	23.26	1.61×10^{-3}	4.19×10^{-3}	1.34 ± 0.54	$(9.68 \pm 1.52)\times10^{9}$	0.63 ± 0.21
RUC-10	26.22	1.82×10^{-3}	4.72×10^{-3}	0.84 ± 0.12	$(9.96 \pm 1.20)\times10^{9}$	0.85 ± 0.27
RUC-6	18.14	1.26×10^{-3}	3.27×10^{-3}	N.O.[d]	$(7.14 \pm 0.84)\times10^{9}$	N.O.[d]
RUC-3	18.44	1.28×10^{-3}	3.32×10^{-3}	N.O.[d]	$(9.94 \pm 0.86)\times10^{9}$	N.O.[d]
RUC-4	19.04	1.32×10^{-3}	3.43×10^{-3}	1.37 ± 0.22	$(9.84 \pm 1.96)\times10^{9}$	0.36 ± 0.25
RUC-5	20.36	1.41×10^{-3}	3.66×10^{-3}	1.29 ± 0.18	$(10.28 \pm 0.60)\times10^{9}$	0.44 ± 0.19
RUC-8	35.92	2.49×10^{-3}	6.47×10^{-3}	0.51 ± 0.04	$(15.78 \pm 2.14)\times10^{9}$	N.M.[d]

[a] Specimens RUC-9, RUC-10, RUC-8 were tested till Rupture and the rest were stopped at intermediate strain levels.

[b] Ture Stress $\sigma_T = \sigma_A (1 + e)$ where σ_A is the applied stress and e is calculated from the cross section of the foil for TEM.

[c] Elastic Modulii at 704°C ($E = 14.4 \times 10^3$, $G = 5.55 \times 10^3$ kg·mm^{-2}).

[d] The error indicates the 95 percent confidence level (σ, ρ among the plates and θ among the measurements). N.O. (not observed), N.M. (not measured).

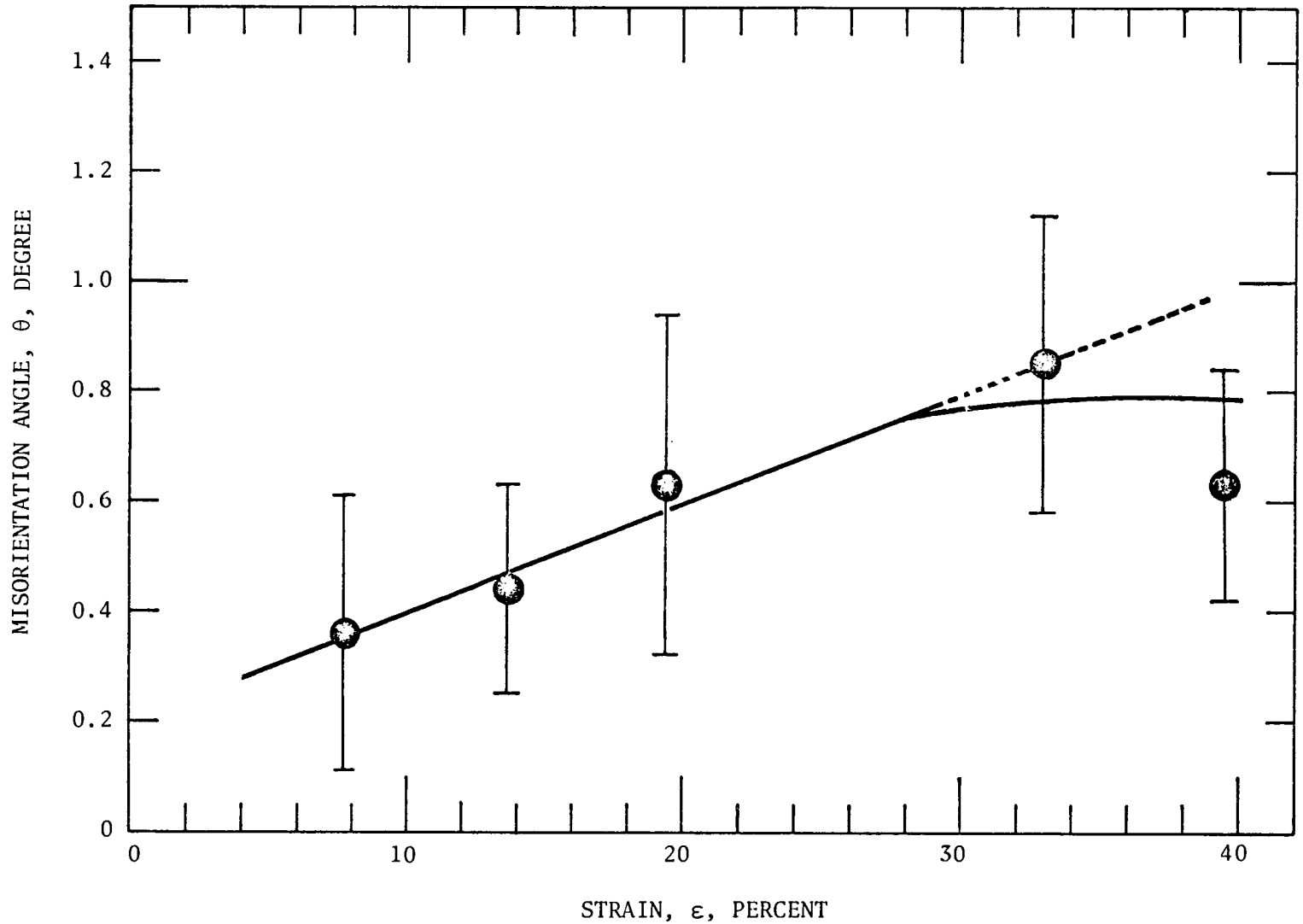

Fig. 7. 4. Plot of the Misorientation Angle versus the Strain of AISI 304 Stainless Steel (Heat No. G8607) Creep Tested at 704°C.

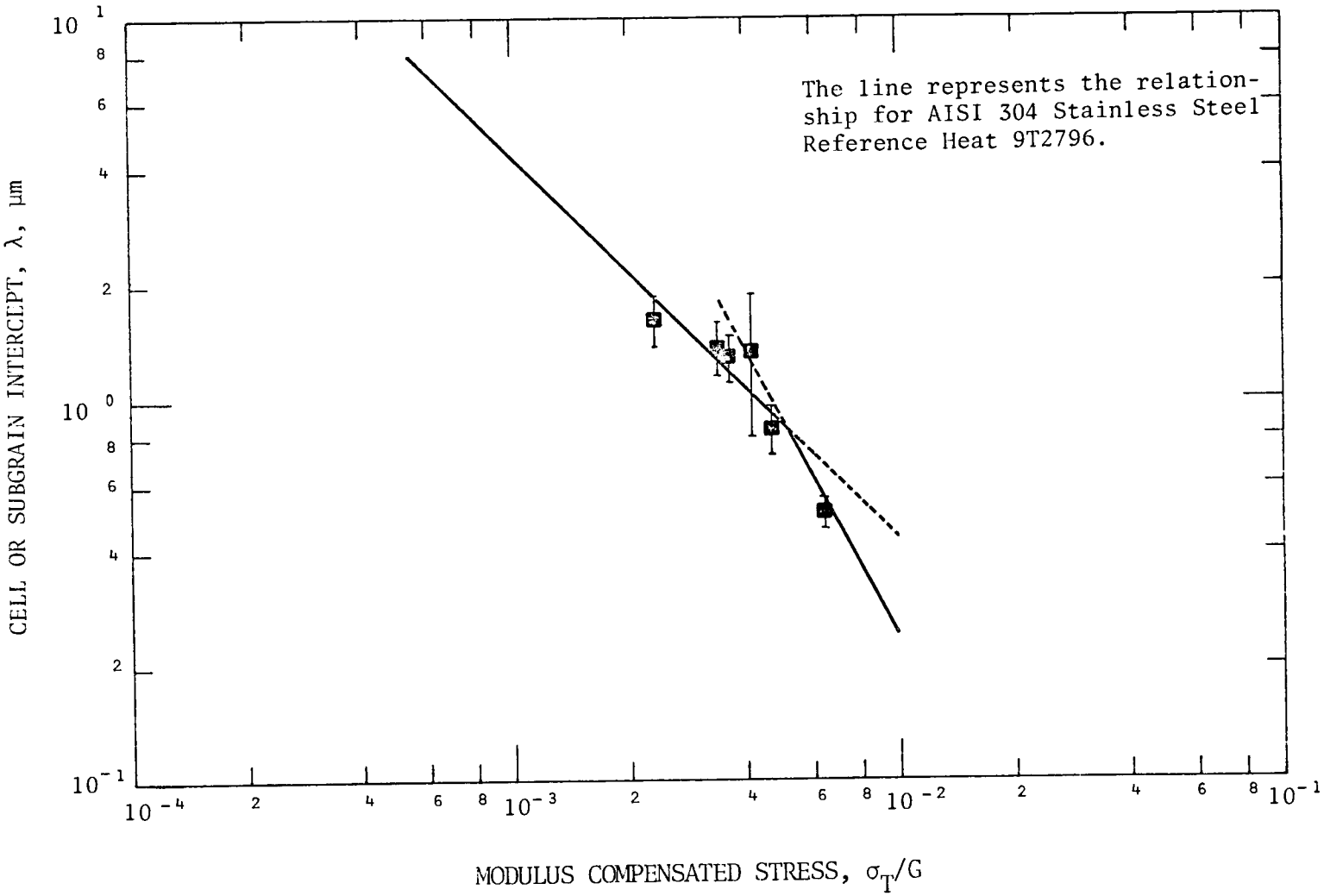

Fig. 7.5 Plot of cell or Subgrain Intercept versus Modulus Compensated Stress. (AISI 304 Stainless Steel, U.C. Heat No. G8607).

7.1.2.3 Change in Stress Experiments on 304 Stainless Steel, Reference Heat 9T2796 (R. Bhargava)

A program to perform some special creep tests on the Reference Heat 9T2796 of AISI 304 stainless steel was initiated at the University of Cincinnati[1]. A set of 8 creep tests were performed. All the tests were performed at 650°C. The stress history of the tests is provided in Table II. All the specimens were heated from room temperature slowly and allowed to soak at the test temperature for a period of about 10 hours. The strain measurements were made by using an extensometer attached to the shoulders of the specimens. The strain was monitored by a LVDT capable of reading up to 5 μin. extension over a gage length of 1.25 inches. The temperature measurements were made by attaching two chromel-alumel thermocouples, one to the bottom and one to the top of the gage portion. The temperature was maintained constant over the entire test duration and to within ± 1°C during the period when the stress changes were made. The stress changes were accomplished by removing the load from the load pan taking precautions to avoid large oscillations of the weight train. A continuous plot of the elongation was recorded on a x-y recorder with a sweep function.

Specimen RP301 was tested at 17.58 kg mm^{-2} (25,000 psi) till rupture. Specimen RP303 was crept at 17.58 kg mm^{-2} (25,000 psi) into a steady state region and then the load was removed to give an effective true stress of 15.08 kg mm^{-2}

TABLE 7.2

DATA FROM CHANGE IN STRESS[a] EXPERIMENTS DURING CREEP OF 304 STAINLESS STEEL (Reference Heat 9T2796) AT 650°C

Specimen Number[b]	Before Change: Applied Stress σ_A, $(kg \cdot mm^{-2})$	Before Change: True Stress σ_T, $(kg \cdot mm^{-2})$	After Change: Applied Stress σ_A, $(kg \cdot mm^{-2})$	After Change: True Stress σ_T, $(kg \cdot mm^{-2})$	Creep Rate $\dot{\varepsilon}$ (sec^{-1}): Before	Creep Rate $\dot{\varepsilon}$ (sec^{-1}): After[c]
RP 301	17.58	19.34	---	---	1.80×10^{-6}	---
RP 303	17.58	18.84	14.06	15.08	1.82×10^{-6}	1.19×10^{-7}
RP 314	17.58	18.90	11.85	12.73	1.84×10^{-6}	3.93×10^{-8}
RP 313	17.58	18.89	10.42	11.19	1.73×10^{-6}	3.72×10^{-9}
RP 306	21.09	23.46	15.36	17.09	1.07×10^{-5}	2.00×10^{-7}
RP 304	21.09	23.57	14.06	15.71	1.09×10^{-5}	8.89×10^{-8}
RP 307	21.09	23.71	10.03	11.27	1.13×10^{-5}	4.70×10^{-9}
RP 305	21.09	23.62	6.88	7.70	1.13×10^{-5}	N.M.

(a) Change in stress was made by removing load from the pan after a steady state creep was reached. (RP 301 is an exception).

(b) After a positive creep rate was obtained subsequent to the change in stress, the tests were terminated with the exception of RP 303 and RP 301 which were run till rupture.

(c) RP 307 and RP 305 showed a negative creep immediately after stress change. The creep rates were measured after a forward creep began in all specimens.

and allowed to creep till rupture at the reduced stress. The creep rate before and after the stress changes were measured and are also reported in Table II. For all other specimens the indicated stress changes were made and the resulting creep rates were determined. Specimens RP307 and RP305 showed a negative creep immediately following the change in stress. After some time, the forward creep began again. All these tests were stopped after a measurement of forward creep rates were made. The specimens were allowed to cool under load to freeze the dislocation substructure. More work is being done to determine the internal stresses and other creep parameters. The characterization of the dislocation substructure has also been started and the developments will be reported in future progress reports.

7.1.2.4 Subgrain Misorientation Observation in Incoloy 800 Tested in the Fatigue Mode (H. Nahm)

Since the degree of crystal lattice misorientation between adjacent cells or subgrains is believed to play an important role in the deformation behavior of polycrystalline solids, it is considered important to describe the technique used in this analysis.

The origin and mechanism of Kikuchi pattern formation is a complex phenomenon involving both elastic and inelastic electron scattering. However, its geometry is useful for the determination of the exact orientation of the electron beam with respect to the crystal lattice and the direction and

magnitude of Kikuchi pattern shift can be used to study the nature of the misorientation among the subgrains or cells. Kikuchi patterns from each cell or subgrain was obtained by using the selected area aperture in the 200 kV transmission electron microscope.

In order to convert Kikuchi pattern shift to misorientation angle, the scale factor was calculated from the relationship:

$$S.F. = D/2\theta_B \qquad [3]$$

where D is the distance between the Kikuchi pair measured from the photographic plates and θ_B is Bragg's angle. Using the camera constant for the chosen diffraction condition at 200 kV, the scale factor was found to be 15.02 mm/degree.

Figure 6 illustrates the details of misorientation between subgrains occurred in fatigued Incoloy 800 (2K35). Figure 6-a is the electron micrograph showing the subgrains, Figure 6-b the schematics identifying each subgrain, and Figure 6-c shows the misorientation angles with respect to the subgrain 1 in a polar plot. The correction for image rotation is made so that Figure 6-c is consistent with Figure 6-a or 6-b. The Kikuchi shift is expressed in vector notation. Therefore, the tilt axis is perpendicular to each of the respective radius vectors. The misorientation between any two selected subgrains can be obtained from Figure 6-c by connecting the extremeties of the respective radius vectors, and this was shown to be consistent with experimental

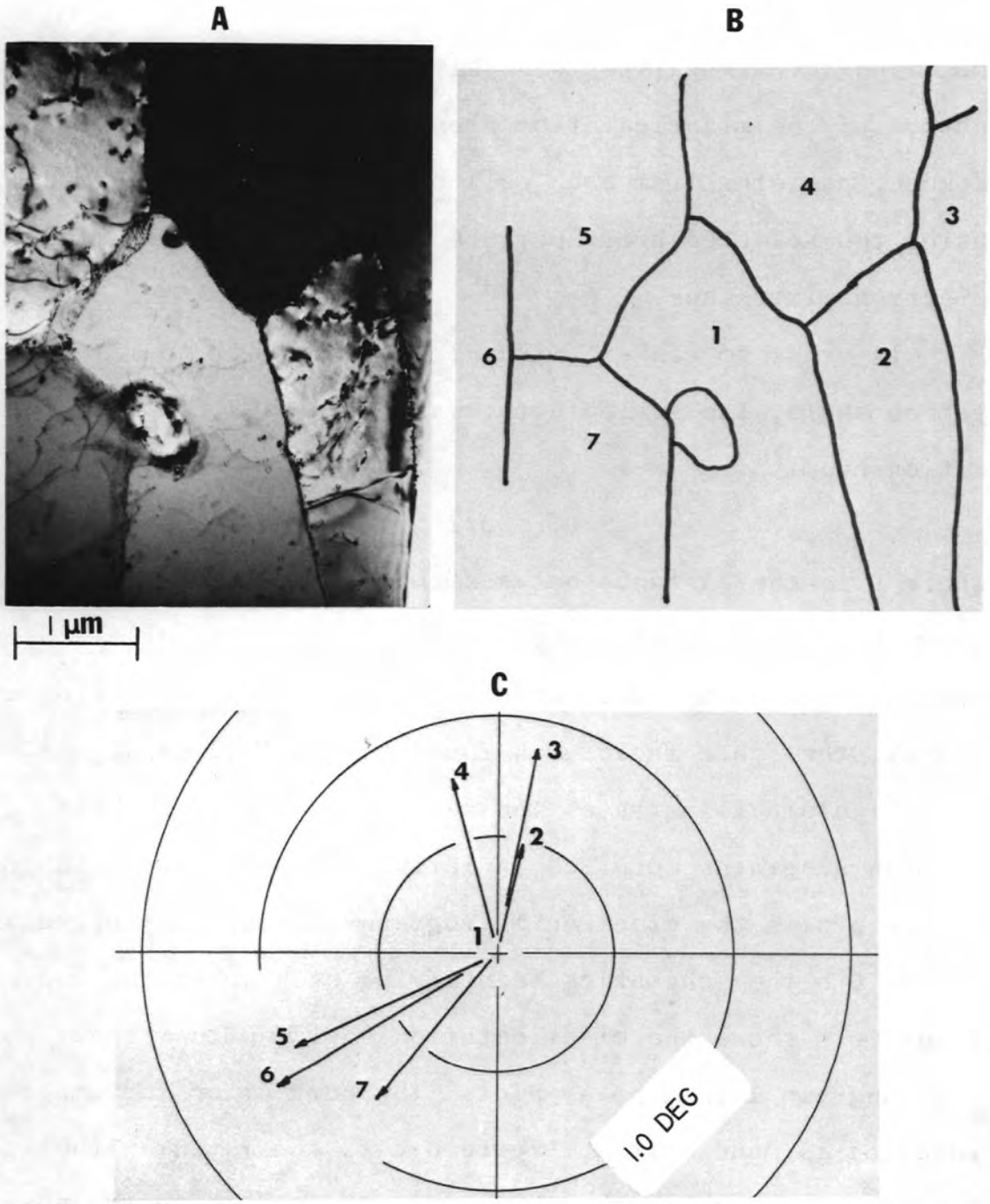

Fig. 7.6 Display Showing the Details of Misorientation Between Subgrains Occurred in Fatigued Incoloy 800 (2K35).
(a) The Electron Micrograph showing the Subgrains.
(b) The Schematics Identifying each Subgrain.
(c) The Misorientation Angles with Respect to Subgrain 1 in a Polar Plot.

observations. It was also found that the misorientation angle was, in general, not more than several times the largest one between adjacent subgrains across the entire grain. This observation implies that the misorientation angle is of an alternating nature, increasing and decreasing over several subboundary walls across the entire subgrains within the grain boundaries. The average misorientation angle between adjacent subgrains which are shown in Figure 6 is about 0.59 degrees.

It is interesting to note that the misorientation angles between the cells is much smaller than that between the well developed subgrains. For instance, the adjacent cells shown in Figure 7 have an average misorientation of about 0.18 degrees. This microstructure was obtained from a specimen of Incoloy 800 (2Q40) tested in the fatigue mode at elevated temperature.

The equation

$$\rho_{SB} = 3\theta/b\lambda' \qquad [4]$$

was used to calculate the dislocation density ρ_{SB} of the subgrain boundary walls such as that shown in Figures 6 & 8. Here θ is the misorientation angle between adjacent subgrains, b is the Burgers vector, λ' is the subboundary diameter. Care should be taken not to use this relationship for the analysis of dislocations in the regions of the apparent cell walls since the boundary dislocation density can in many instances be underestimated.

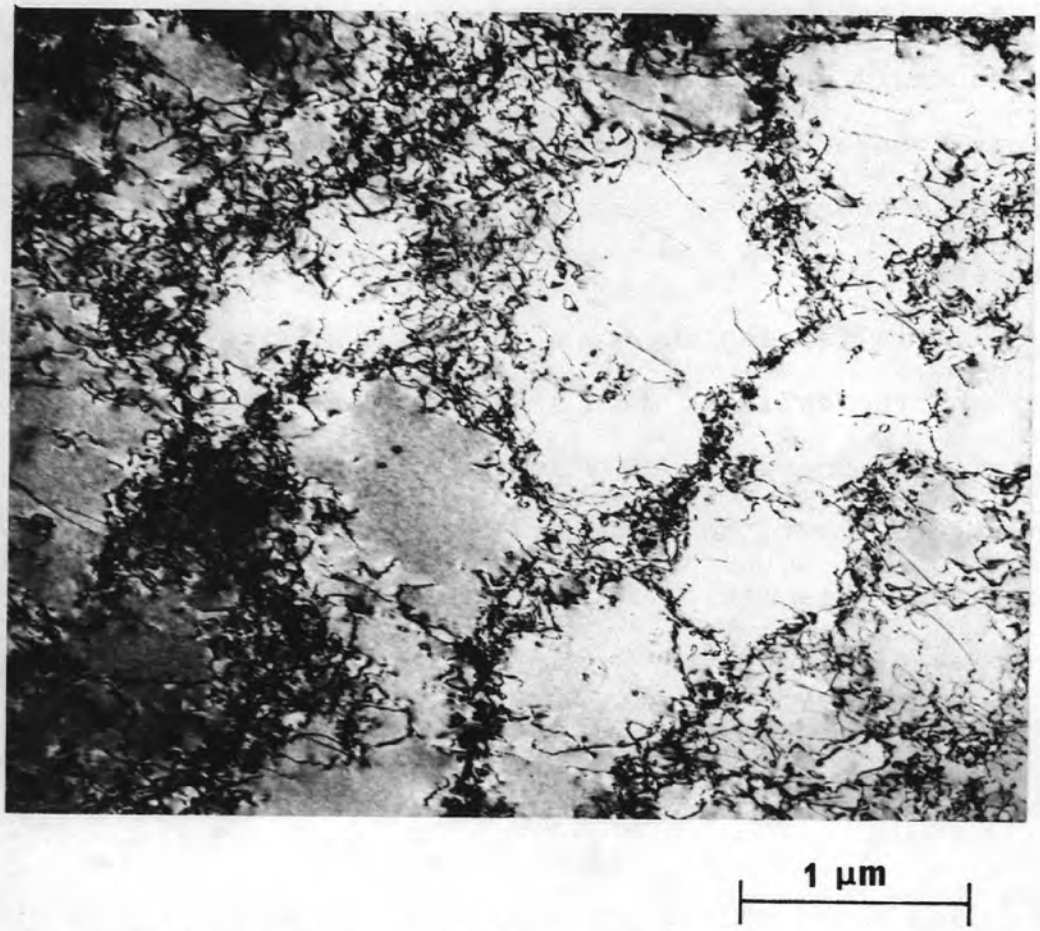

Fig. 7.7 Electron Micrograph Showing Cells With Misorientation Angle Between Adjacent Cells of 0.18 Degree in Fatigued Incoloy 800 (2Q40).

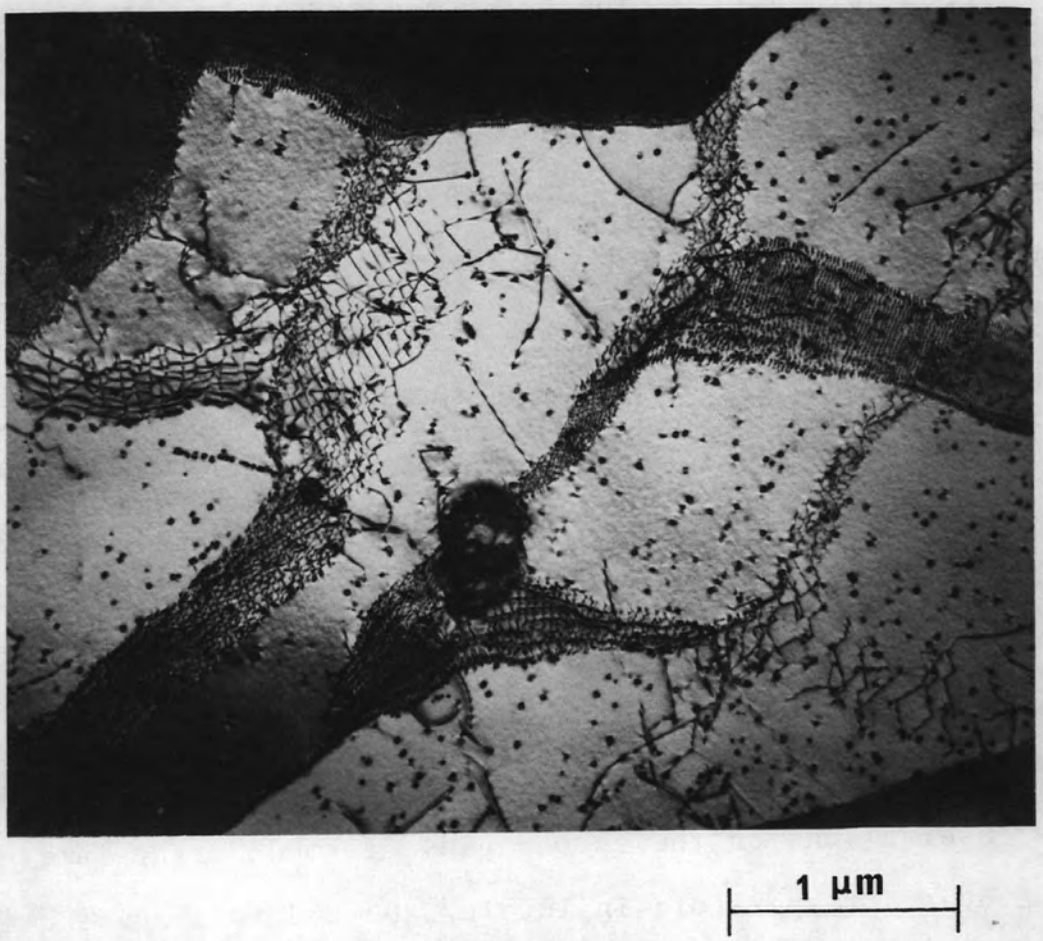

Fig. 7.8 Electron Micrograph Showing Subgrains With Misorientation Angle Between Adjacent Subgrains of 0.37 Degree in Fatigued Incoloy 800 (2B26).

7.1.2.5 Second Phase Particles and Their Influence on the Mechanical Behavior of Incoloy 800 Tested in the Fatigue Mode (H. Nahm)

From both diffraction pattern analysis and high resolution dark field microscopy, second phase particles can be identified and their nature, such as coherency, shape, size, number density and other parameters may be examined in considerable detail. When the diffraction pattern indicates the existence of second phase, a diffracted electron beam from the second phase is tilted such that the beam coincides with the objective axis of the microscope. This procedure is called "high resolution dark field analysis" because the corresponding image contrast becomes equivalent to that of bright field microscopy. The details of this technique is available elsewhere[9].

The purpose of this section is to report the results of TEM observations on the second phase formed during fatigue at elevated temperature in Incoloy 800 and to discuss briefly the possible influences of these second phase particles on the fatigue properties.

In general, the three types of precipitates, γ', $M_{23}C_6$ and presumably a TiN precipitate were confirmed through transmission electron microscopy. The presence of γ' was believed to strongly influence the cyclic stress strain response and are present only at the lower test temperatures. The other two precipates, formed at all testing temperatures

were interpreted to be responsible for the enhancement in the resistance to the fatigue crack propagation and to the creep-fatigue interaction of Incoloy 800 at elevated temperature.

The gamma prime precipitate, γ', was found in only one specimen (2I9) which was fatigue tested at a frequency of 4×10^{-4} sec^{-1} with the strain range of 0.5% at 538°C. The fatigue failure occurred at 23,510 cycles (163.3 hours). Even though it was observed in one particular testing condition, γ' is believed to form during fatigue at the lower temperatures of 538°C and 650°C. This will be further discussed later. The evidence for γ' formation with $M_{23}C_6$ was given in Figure 9b and 9c. Even though the diffracted beams from γ' are apparent in this figure, the distinct image contrast of the γ' phase was not observable through either bright or dark field microscopy. This could be due to the severe strain field arising from both the high dislocation density and/or precipitates in the matrix. The small white spots in Figure 9a could possibly be γ', but this would only be a conjecture.

It was, however, possible to resolve the image of $M_{23}C_6$ in this test specimen (2I9) by the use of dark field microscopy. This is shown in Figure 10. Figure 10a is the bright field and 10b the corresponding dark field micrograph taken after tilting the diffracted beam from the $M_{23}C_6$ phases. This micrograph is a good example to demonstrate the advan-

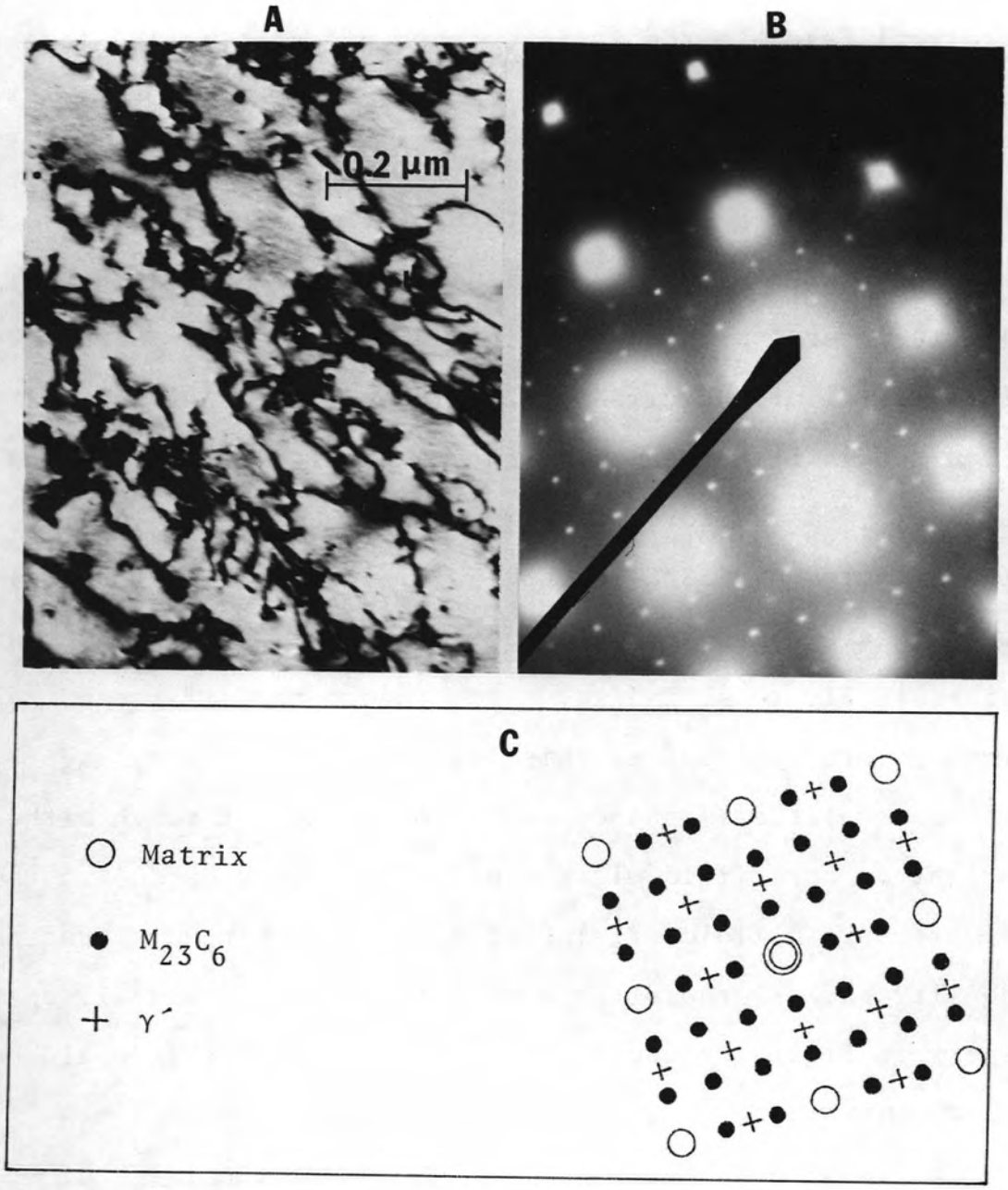

Fig. 7.9 Electron Micrographs Showing γ´ and $M_{23}C_6$ in Fatigued Incoloy 800 (219, T = 538°C, $\dot{\varepsilon} = 4 \times 10^{-4}$ sec^{-1}, $\Delta\varepsilon_t = 0.50\%$, $N_f = 23{,}510$ cycles, $t_f = 163.3$ hours).

tages of high resolution dark field microscopy. The preferential formation of $M_{23}C_6$ along the dislocation band is clearly visible in Figure 10b.

An example of identifying two different types of second phase particles is depicted in Figure 11. Figure 11a is the bright field, Figure 11b the dark field from TiN particles which were tentatively identified and 11c the dark field micrograph for the $M_{23}C_6$ phase. This is schematically shown in Figure 11d.

In order to show the effect of these precipitates on the cyclic stress strain behavior of Incoloy 800, all the data reported by Conway et. al.[10] were plotted and presented in Figure 12. These specimens are now being studied in terms of dislocation substructure at this laboratory. The saturation stresses taken at each half fatigue life are plotted as a function of the plastic strain range for each test temperature for the two different strain rates which were used. In general, the saturation stress can be represented as an equation in the form:

$$\Delta\sigma = A(\Delta Ep)^m \qquad [5]$$

where $\Delta\sigma$ is the saturation stress at half fatigue life

A is the cyclic strength coefficient

ΔEp is the plastic strain range

and m is the cyclic strain hardening exponent.

The saturation stress is decreased as the strain rate is decreased and the cyclic strength coefficient, m, is found

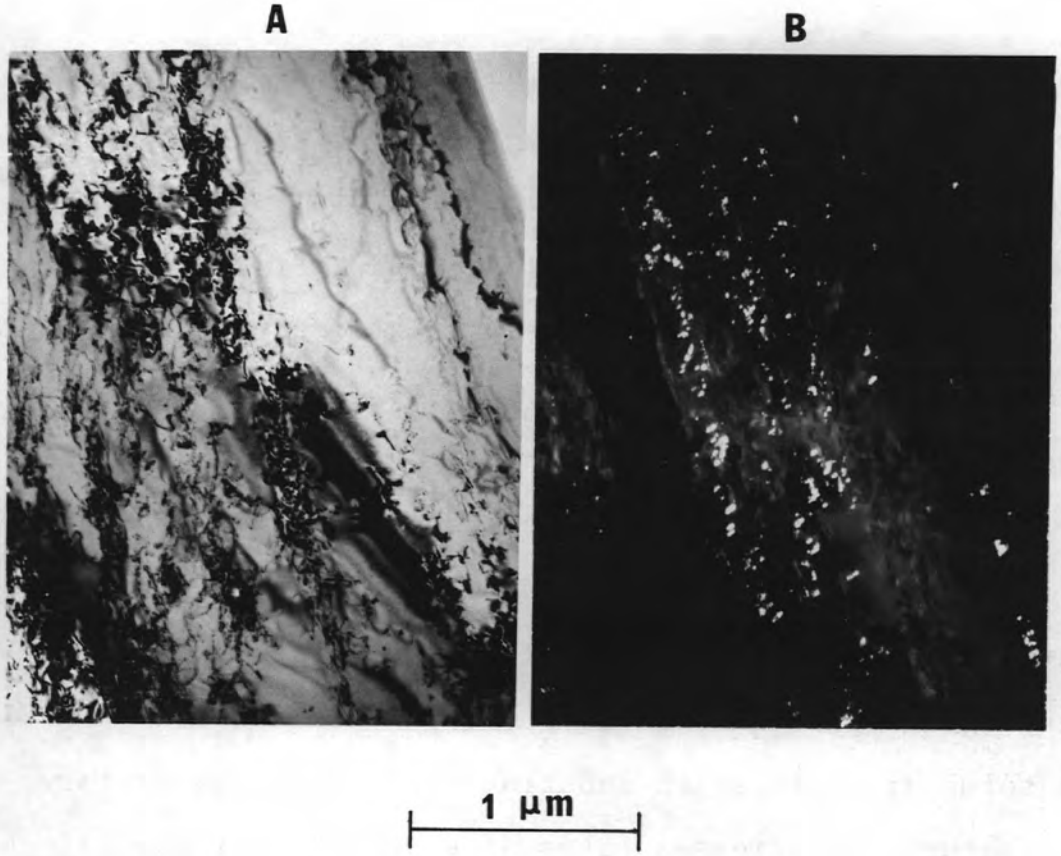

Fig. 7.10 Electron Micrographs showing $M_{23}C_6$ in the Fatigued Incoloy 800 (2I9, T = 538°C, $\dot{\varepsilon} = 4 \times 10^{-4}$ sec^{-1}, $\Delta\varepsilon_t = 0.5\%$, $N_f = 23{,}510$ cycles, $t_f = 163.3$ hours) by High Resolution Dark Field Microscopy: (a) Bright Field (b) Dark Field Using a Diffracted Beam from $M_{23}C_6$.

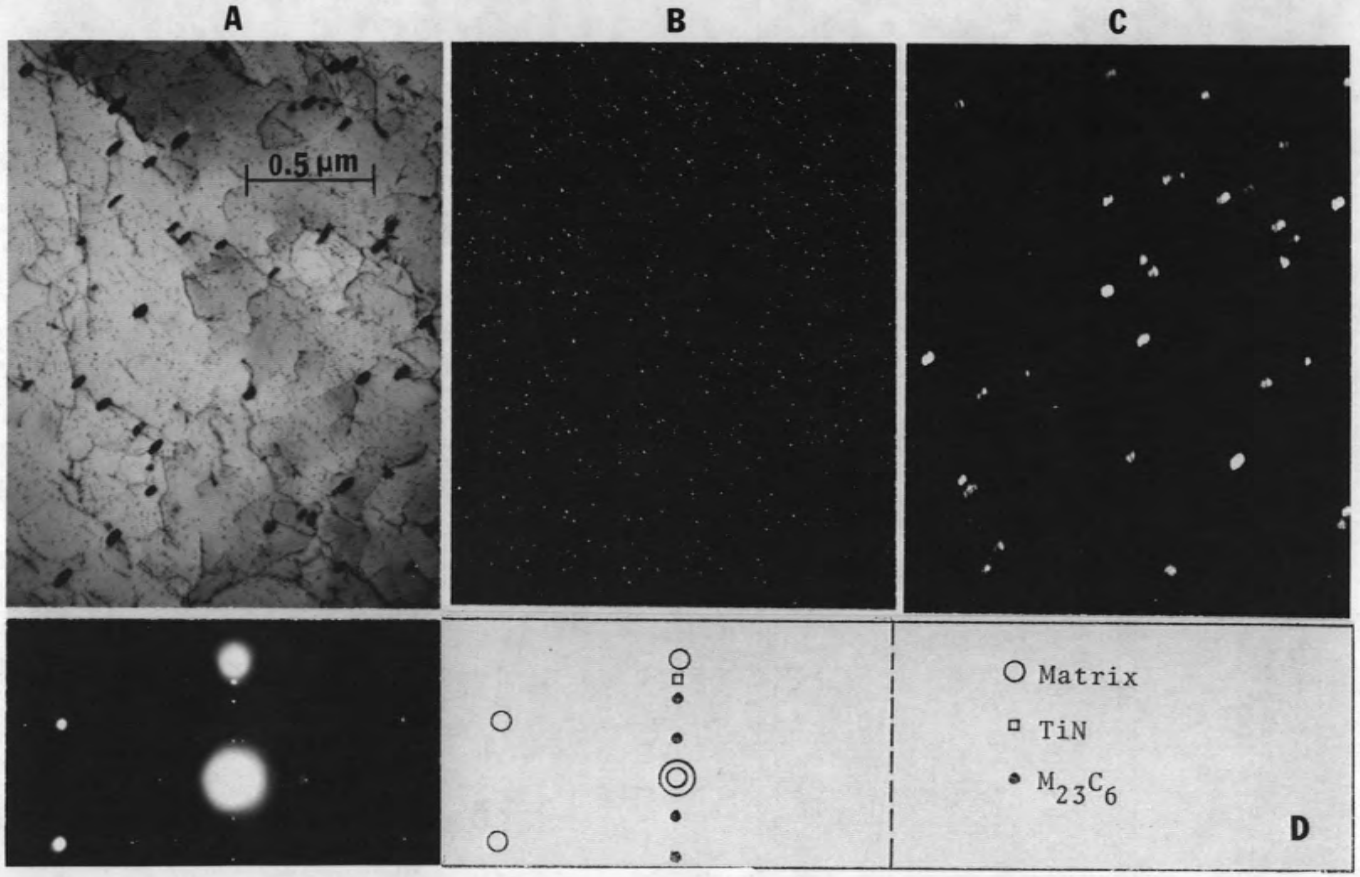

Fig. 7.11 A Set of Micrographs Showing the Identification of Second Phases in Fatigued Incoloy 800: (a) Bright Field (b) and (c) High Resolution Dark Field From Diffracted Beams of TiN and $M_{23}C_6$, respectively as depicted in (d). (2N14: $T = 649°C$, $\dot{\varepsilon} = 4 \times 10^{-4}\ sec^{-1}$, $\Delta\varepsilon_t = 0.99\%$, $N_f = 1{,}414$ cycles, $t_f = 19.63$ hours)

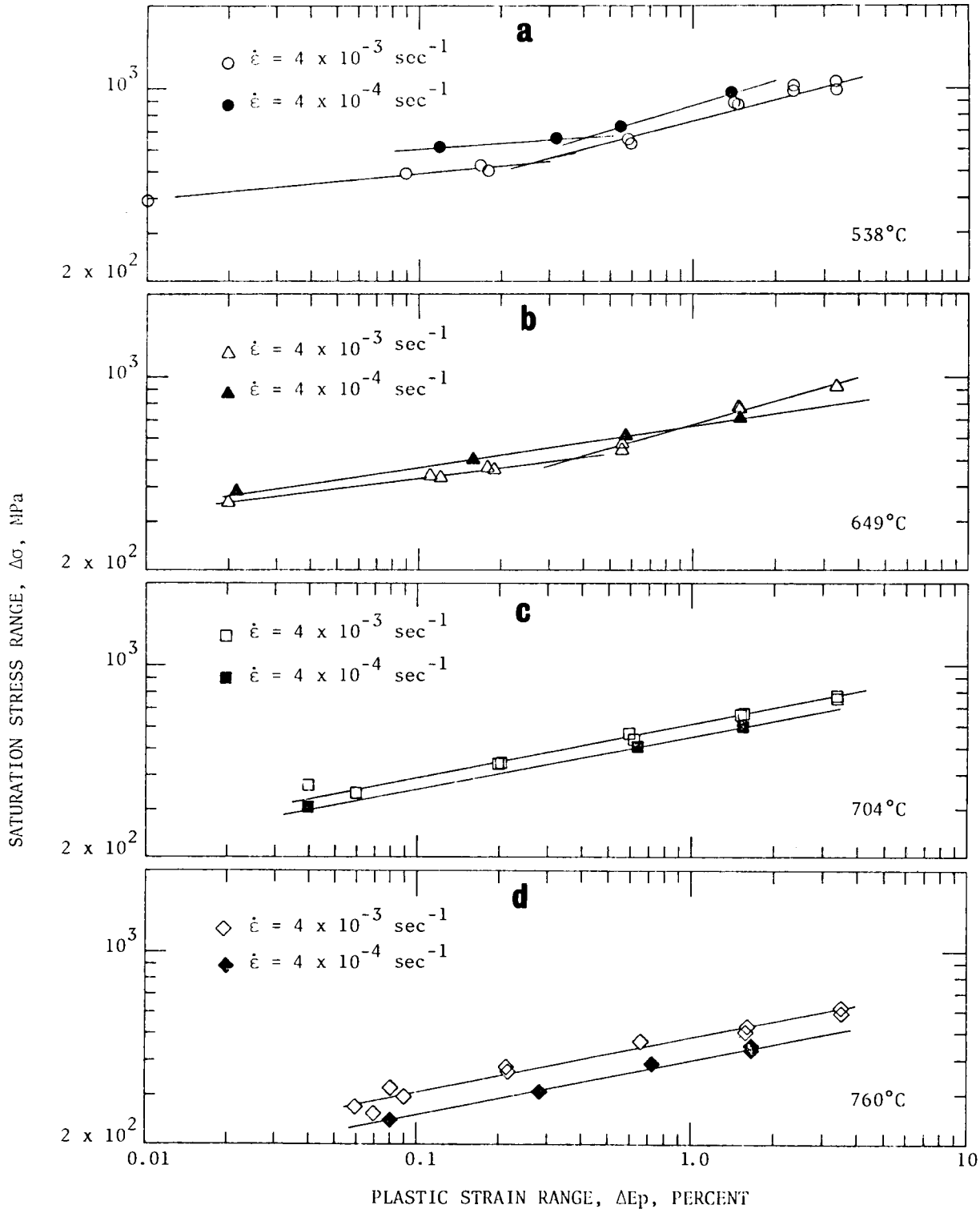

Fig. 7.12 Plot of Cyclic Stress Range Versus Plastic Strain Range of Incoloy 800 Tested in Low Cycle Fatigue for Various Test Temperatures.

to remain close to 0.2 for those specimens tested at 704°C and 760°C irrespective of the change in strain rate. There is a change only in the cyclic strength coefficient. This is generally true in the sense that the flow stress increases when the deformation rate is increased in elevated temperature plastic deformations.

An anomalous behavior in the cyclic stress strain relationship, however, can be noted at test temperatures of 538°C and 650°C. Not only is the saturation stress increased as the strain rate is decreased from 4×10^{-3} sec^{-1} to 4×10^{-4}, but the cyclic strain hardening exponent, m, tends to split into two regions as shown in Figure 12. This circumstance is more pronounced in the case of those specimens tested at a small plastic strain range ($\Delta Ep \leq 0.4\%$) and having relatively long fatigue lives at 538°C.

This unusual phenomenon appears to be mainly due to the presence of γ' phases which form during fatigue at these low temperatures. There are two reasons supporting this view: a) γ' formation was observed only at low temperatures while $M_{23}C_6$ and TiN were found at all the testing temperatures, and b) γ' was reported to form approximately in the range of 560 to 620°C over the exposure time of 100 hours[11]. Other possibilities, although remote, can be that the coherent precipitates of TiN or $M_{23}C_6$ could contribute to this deviation in the cyclic stress strain behavior.

Incoloy 800 has been known to have superior mechanical

properties with respect to creep-fatigue interaction[12] as well as better fatigue crack propagation properties[13] when compared to the other austenitic stainless steels. These observed enhancements of the elevated temperature mechanical properties in Incoloy 800 could be again attributed to the effect of the uniform dispersion of TiN in the matrix. Work is continuing in the evaluation of the microstructure with the mechanical behavior of Incoloy 800.

7.1.3 REFERENCES

1. ORNL 5104, "Mechanical Properties Test Data for Structural Materials" Quarterly Progress Report for Period ending January 31, 1975, pp. 303-312.

2. R. K. Bhargava, Ph.D. Thesis, University of Cincinnati, (In Preparation).

3. R. K. Bhargava, R. W. Swindeman, and J. Moteff, To be presented at the ASME Winter Annual Meeting, Houston, Texas, November 30 - December 5, 1975. (In Preparation)

4. V. K. Sikka, H. Nahm, and J. Moteff, Accepted for publication in Materials Science and Engineering Journal (1975).

5. C. M. Young and O. D. Sherby, Journal of Iron and Steel Institute, 211, 1973, pp. 640-647.

6. C. C. Yu, M.S. Thesis, University of Cincinnati, 1973.

7. K. D. Challenger and J. Moteff, Scripta Met., 6, 1972, pp. 155-160.

8. R. K. Bhargava, Unpublished research at University of Cincinnati.

9. Hirsh et. al. "Electron Microscopy of Thin Crystals", Butterworths (London) 1971, p. 295.

10. J. B. Conway, J. T. Berling, and R. H. Stentz, Met. Trans., 3 (1972) p. 1633.

11. "Incoloy Alloy 800" Huntington Alloy Products Division, The International Nickel Company, Inc., (1973) p. 11.

12. C. E. Jaske, H. Mindlin and J. S. Perrin, ASTM STP 520 (1973) 365.

13. L. A. James, Trans. ASME, J. Eng. Mat. Tech., (1974) Paper No. 74-Mat-7, page 1.

7.2 UNIVERSITY OF CALIFORNIA, LOS ANGELES — K. Ono, A. J. Ardell, and A. S. Tetelman

7.2.1 Microstructure and High Temperature Deformation of Cr-Mo Steels for LMFBR Heat Exchanger (P. A. Chalco, K. Ono, S. Y. Hsu, and S. L. Wang)

7.2.1.1 Introduction

We have examined microstructural variations as a function of time and temperature, and the concomitant effects on mechanical behavior in 2-1/4Cr-1Mo steels of different carbon content. The microstructural variation in Alloys L (0.009%C), I(0.03%C) and H(0.12%C) has been reported previously,[1,2] as well as the creep behavior of these alloys.[3] In addition to the three alloys, we have received a piece of low carbon 2-1/4Cr-1Mo steel (0.021%C) plate (1" x 10" x 10") also from ORNL, to be referred to as alloy M. It is interesting to note that the strain burst phenomenon during stress changes was almost non-existent in this material. The reason for the absence is not understood at this time.

In this report, discussions on the creep behavior of these alloys are presented in conjunction with their respective microstructural characteristics. Creep behavior at intermediate stresses appears to be best explained in terms of the climb of dislocation loops pinched off around carbide particles.

7.2.1.2 Microstructure-Creep Properties Correlation

Based on the microstructural observations,[1,2] the alloy steels that have been tested in creep can be classified as two-phase materials. In the analysis of the observed creep behavior,[3] we must consider the creep-strengthening contributions of the matrix, as well as the second-phase particles. We will discuss the temperature dependence and subsequently the stress dependence of the observed creep behavior of Cr-Mo steels.

7.2.1.3 Temperature Dependence of Creep

Creep deformation is a thermally activated process and the steady state creep rate can be described by an Arrhenius relation as follows:

$$\dot{\epsilon}_s = A \exp(-Q_c/RT) \qquad (1)$$

where A is a constant and is a function of creep stress. Q_c is the activation energy for creep, R is the gas constant and T is the absolute temperature. Most of the experimental evidence for single phase materials indicates that Q_c is about the same as the activation energy for self-diffusion, Q_d, at elevated temperatures ($T \sim 0.5\ T_m$). This suggests that at high temperatures, the operating creep mechanisms in these materials are dependent on the self-diffusion of atoms in the matrix. The temperature dependence of the creep rate is thus related to the temperature dependence of the self-diffusion

coefficient, D, so that $\dot{\epsilon}_s/D = A/D_o$, where D_o is the pre-exponential factor.

A number of observations have been reported where Q_c exhibits anomalously high values in comparison to Q_d. For example, Q_c is equal to $3Q_d$ for TD Nickel[4] and $4\text{-}12Q_d$ for SAP-type alloys.[5] In Aℓ-3.2% Mg alloy, Borch et al.[4] found a peak in the value of Q_c (at about $T \approx 0.35\ T_m$) which reached a maximum value of $\sim 2Q_d$. However, it is still unknown at present the cause of such high values of Q_c, although some models have been discussed. For example, Borch et al.[5] suggested that the high values of Q_c were caused by the segregation of solute atoms at dislocations while these rest at barriers. The possibility that the solute segregation occurred on moving dislocations was ruled out since Q_c was not equal to the activation energy for diffusion of Mg in Aℓ. In reference to this work, Phillips[6] has argued that the strain induced precipitation at dislocations is very much expected from the equilibrium phase diagram of this alloy. This would cause strong locking of dislocations and consequently high values of Q_c. This view has been shared by other investigators, many of whom have confirmed the strain induced precipitation of particles at dislocations during high-temperature deformation.[7,8,9]

A third mechanism, which could also lead to high values of Q_c, is based on the interaction between substitutional-interstitial (S-I) solute atom pairs and moving dislocations.[10-12] In this case, Q_c would be equal to the activation energy of diffusion of the S-I pairs.

Such quantity is not known but is expected to be higher than that of each solute. This concept which is known as the S-I effect, is a modification of dynamic strain aging and has been observed in solid solutions of α-Fe.[11]

There are no diffusion data available for 2-1/4Cr-1Mo steels. For the present analysis, these data must be approximated from similar alloys or from pure α-Fe. Askill[13] has reviewed the self-diffusion data published for pure metals and alloys. The closest alloy composition to the present Cr-Mo steels is 4.0%Cr-0.2%C steel. Q_c = 69 Kcal/mole and D_o = 4 $cm^2 sec^{-1}$ are given for this steel in the temperature range of 1100-1250°C. The temperature range is well above the Curie temperature, T_c (780°C) for iron and its dilute alloys. Since D has different values above and below T_c,[14] we cannot use the above diffusion data for our materials. Instead, we choose the self-diffusion data for α-Fe, below T_c, as a first order approximation. The accepted values of Q_c and D_o for α-Fe, are Q_c = 60 Kcal/mole and D_p = 2 cm^2 sec^{-1}, respectively.[13]

By using the value of D for α-Fe, at the corresponding temperature the logarithm of $\dot{\epsilon}_s/D$ (for Alloy H, N&T) was plotted as a function of log σ, as shown in Fig. 1. Actually, the shear modulus, G, is a function of temperature, and generally the stress should be divided by G for such an analysis. However, according to a recent study of the temperature dependence of G in 2-1/4Cr-1Mo steel,[15] in the 850-1050°F temperature range, G varies only ~4%.

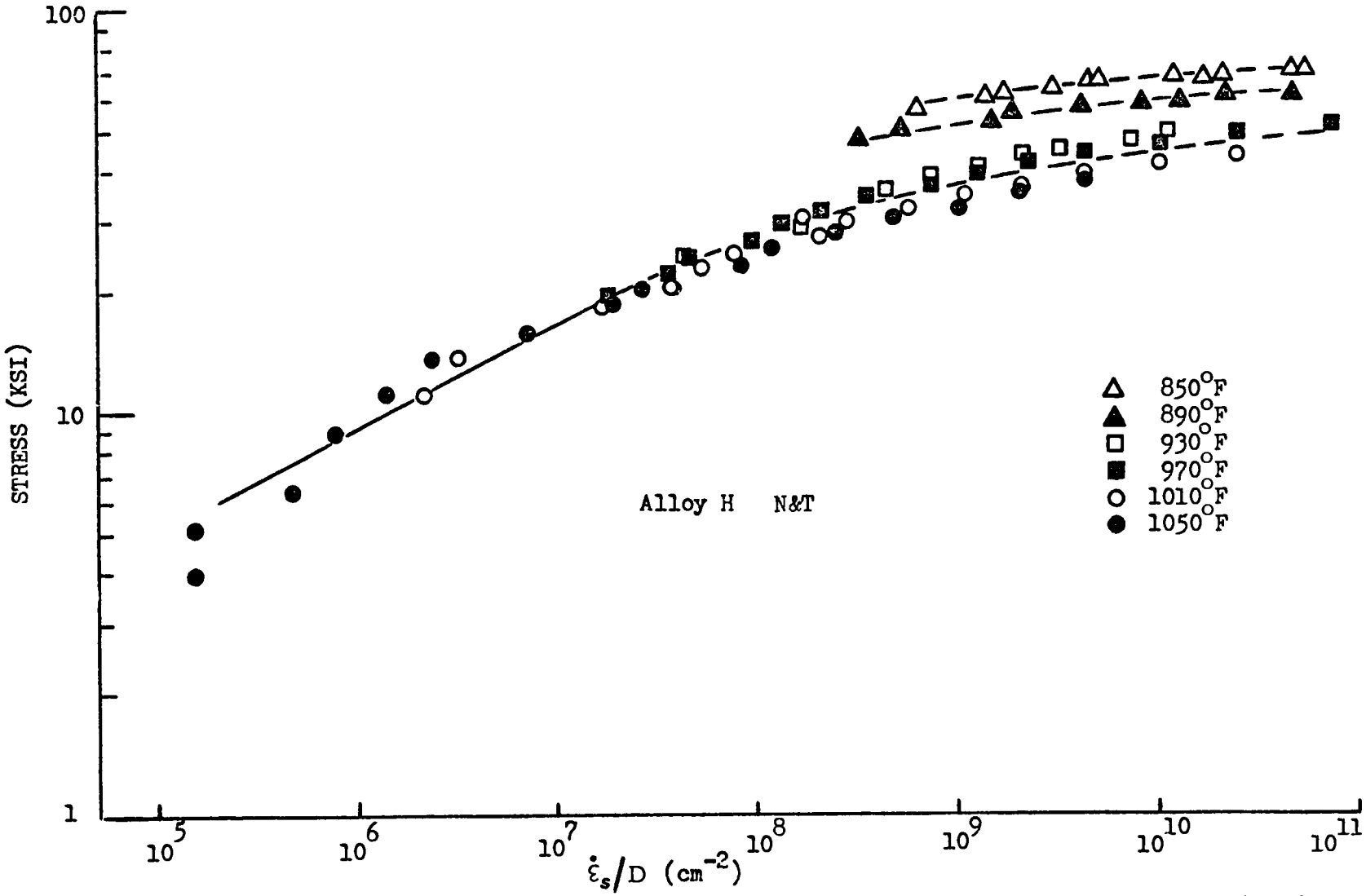

Figure 1 Diffusion-Compensated Steady State Creep Rate as a function of Stress for Normalized and Tempered (1300°F, 1hr.) Alloy H

This correlation is negligible and does not affect the essential features of the data in Fig. 1. It can be seen in Fig. 1 that at temperatures ranging from 930-1050°F, the change in $\dot{\epsilon}_s$ due to a different temperature can be correlated directly to a corresponding variation in the value of D, because all the data points can be fitted approximately into a single curve. This observation strongly suggests that at these temperatures, $Q_c \approx Q_d$. The only reported value of Q_c for 2-1/4Cr-1Mo steel is 55 Kcal/mole.[16] This is very close to that of Q_d in α-Fe.

At 850 and 890°F, the present data yield Q_c = 190 ± 10 Kcal/mole, which is over three times the Q_c value observed in the 930-1050°F range. Based on the microstructure observations, it is very likely that such high values of Q_c are due to the precipitation of second-phase particles on dislocations during creep deformation, since, almost invariably, the dislocations found in tempered materials were observed to be decorated by very fine, closely spaced precipitates. However, more thin-film TEM studies on crept specimens are needed to confirm this hypothesis. We cannot rule out the possibility that either substitutional solute atoms or S-I atom pairs interact with dislocations during creep at temperatures where high values of Q_c were observed. However, this possibility would be much harder to establish than the previous one by experiment. In any case, more studies are needed to clarify the cause of the observed high values of Q_c.

7.2.1.4 Stress Dependence of Creep

Extensive creep studies have shown that the steady state creep rate exhibits several stress dependencies.[14] These are usually different at low, intermediate, and high-stress levels. At low and intermediate stresses, the following power-law relation is observed to be obeyed:

$$\dot{\epsilon}_s = B\,\sigma^n \qquad (2)$$

where B is a temperature dependent constant and n is the stress exponent. As the applied stress increases, the power-law expression breaks down, and several different stress dependencies have been used to describe the high stress creep. Even at these high stresses, however, it is possible to refer to the apparent values of n, i.e., $n = d \log \dot{\epsilon}_s / d \log \sigma$, within a narrow range of creep rates.

In $\log \dot{\epsilon}_s$ vs. $\log \sigma$ plots (Figs. 1-6 in ref. 3), three regions of stress dependence were observed, which we have labeled high, intermediate, and low-stress creep regions. We define the intermediate stress region as that in which the stress exponent has the value of $\sim$4. The data could have been fitted with a line corresponding to n as high as 5, but not much less than 4. This stress region was generally well established and it was between 5 and 20 Ksi, depending on the alloy condition. Since the yield strength of N&T materials in the 850-1050°F temperature range has been reported[17] to be 20-30 Ksi for Alloys L and I, and 55-60 Ksi for Alloy H, the intermediate stress range is always below the yield strength of these materials.

The low-stress region is defined as that region where the data deviate from n = 4 to a lower value of n. The value of n in this region was not well established since an insufficient number of data points were available. However, a deviation from n = 4 appears to have occurred. This deviation was observed mainly in Alloy H (long-term tempered) at about 7 Ksi. However, for other materials, this deviation was not found even at stresses as low as 4 Ksi. In a manner similar to the low-stress region, the high-stress region was defined as the region where the data deviated from n = 4 to higher values of n. This region appeared in every single material tested and was characterized by high values of n (up to ~ 40) which increased with an increasing stress. At higher temperatures such as 1050°F, the high-stress region was first observed at stresses below the yield strength at this temperature. For example, in Alloy H (N&T) which has a yield strength of 55 Ksi at 1050°F, the high-stress region started at ~20 Ksi. On the other hand, at 850°F, the high stress region was observed at stresses comparable to the yield strength. For the same material as above, the high-stress region was located above 56 Ksi, which is very close to the observed yield strength (58 Ksi).

In the following discussion, we will analyze our data according to the apparent changes in the stress dependence of $\dot{\epsilon}_s$. In each case, we will present the available creep theories, and evaluate their applicability to the experimental results of the present investigation.

7.2.1.4.1 High-Stress Creep. In the case of dispersion hardened materials, the power-law relation [Eq. (2)] has been observed even at stresses above the yield strength, as in the case of a Ni-2ThO_2 material,[4,18] tested at 850-1100°C. The observed values of n, however, are very high. In the case of TD Nickel, n is 40[4] and for SAP materials it is over 10[19] although a value of 4 has also been reported.[20] It has not been possible to account for such values of n. One possible approach to reconcile the observation with available creep theories is to introduce the concept of effective stress, σ^*. The effective stress is defined as $\sigma - \sigma_i$, where σ_i is the internal stress. In this treatment, $\dot{\epsilon}_s$ is considered as a power function of the effective stress σ^* as follows

$$\dot{\epsilon}_s \propto \sigma^{*n} \tag{3}$$

thereby reducing the apparent value of n via Eq. (2) to the range of 3-7. There is sufficient evidence in single-phase materials showing that even at temperatures above 0.5 T_m, the ratio σ^*/σ can be much lower than 1.[21,22] In some cases, it can be as low as 0.4,[23] depending on the applied stress. Dispersion hardened alloys are expected to have large internal stresses due to the dispersed particles. Consequently, the ratio σ^*/σ can have low values. However, this has not been shown experimentally. Thus, it remains to be established whether the concept expressed above can account for the observed high values of n in dispersion hardened alloys in terms of available

creep theories predicing n of 3 to 4.5. Such an investigation will require mainly the measurement of the internal stress during creep at a given stress and temperature.

The effective stress concept was tested as follows: Using the present data, the value for the internal stress was estimated from Eq. (2), by setting n equal to 4.5 which corresponds to Weertman's dislocation climb model.[24] The results of the calculation based on the experimental values of $\dot{\epsilon}_s$ obtained for Alloy H (N&T) at 850, 890 and 930°F are shown in Fig. 2 in which the calculated effective stresses $\sigma^* = \sigma - \sigma_i$ are plotted against $\dot{\epsilon}_s$. It can be seen that although the value of n = 4.5 is observed over a limited range of high stresses, the stress exponent n in terms of σ^* becomes progressively small as the value of the applied stress approaches that of the internal stress. In addition, it can be seen in Fig. 2 that the temperature dependence of $\dot{\epsilon}_s$ is altered in contradiction to what is normally observed. A more systematic study is needed where a direct measurement of σ_i (as a function of stress and temperature) should be made, so that the applicability of $\dot{\epsilon}_s = f(\sigma^*)$ can be tested more properly. However, the present result cannot be explained in terms of the effective stress concept with a fixed value of σ_i.

It is possible that at high stresses the $\dot{\epsilon}_s$ (σ) data can be fitted into an empirical exponential form of:

$$\dot{\epsilon}_s = A' \exp(c\,\sigma) \qquad (4)$$

where A' can C are constants. In single-phase materials most of the

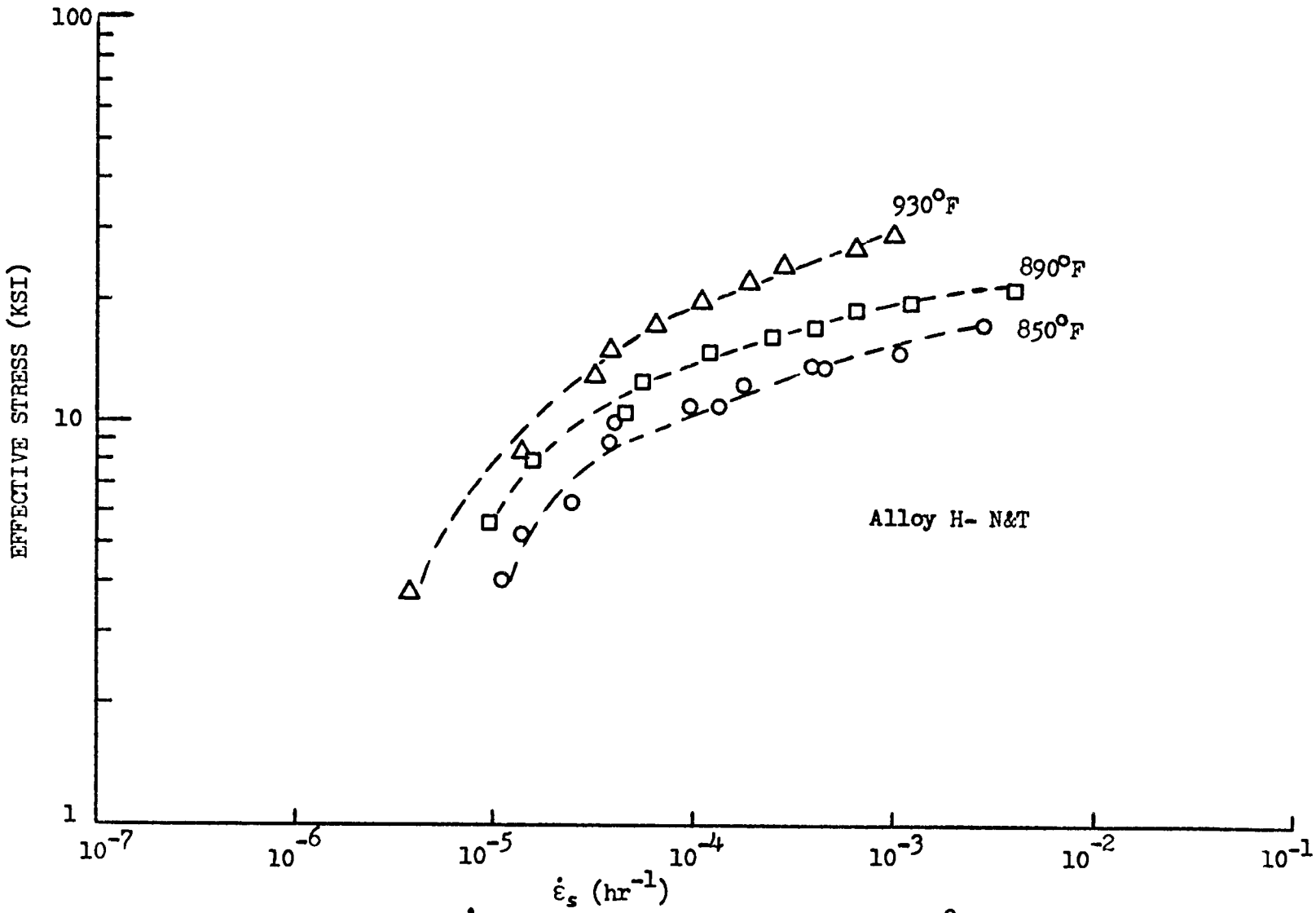

Figure 2 Effective Stress vs $\dot{\varepsilon}_s$ for Normalized and Tempered (1300°F, 1hr.) Alloy H

high-stress $\dot{\epsilon}_s(\sigma)$ data can be fitted into such a relation, which was first proposed by Garofalo.[23]

Various theories have also been proposed, which associated high-stress creep with the presence of a high vacancy concentration. The most common are the theories of Weertman,[24] and Barrett and Nix.[25] The first is based on dislocation climb and the second one is based on the nonconservative motion of jogs in screw dislocations.

The $\dot{\epsilon}_s$ values predicted by these two equations are, for Weertman's theory:

$$\dot{\epsilon}_s = A''D\,\sigma^2 \sinh B\sigma^{2.5} \tag{5}$$

and for Barrett and Nix's theory:

$$\dot{\epsilon}_s = A'''D^{\,3.5} \sinh (B'\sigma) \tag{6}$$

where A', A"', B, and B' are constants. As shown by Sherby and Burke,[14] all three equations can describe the observed high-stress creep data. In order to show the applicability of these three equations to our experimental data, we have plotted log $\dot{\epsilon}_s$ vs. σ for Alloy H (N&T) in Fig. 3. Also shown in this figure is a dashed line, corresponding to $\dot{\epsilon}_s/D = 10^9$, above which the power-law creep equation has been found to break down in a large variety of materials. It can be seen that at 1010 and 1050°F the stress dependence of the minimum creep rate obeys an exponential form at all the stress levels, since a straight line fits the data for these temperatures. At 850, 890, and 970°F, the exponential form is obeyed at high stresses, while the data is insufficient to determine the applicability of the exponential

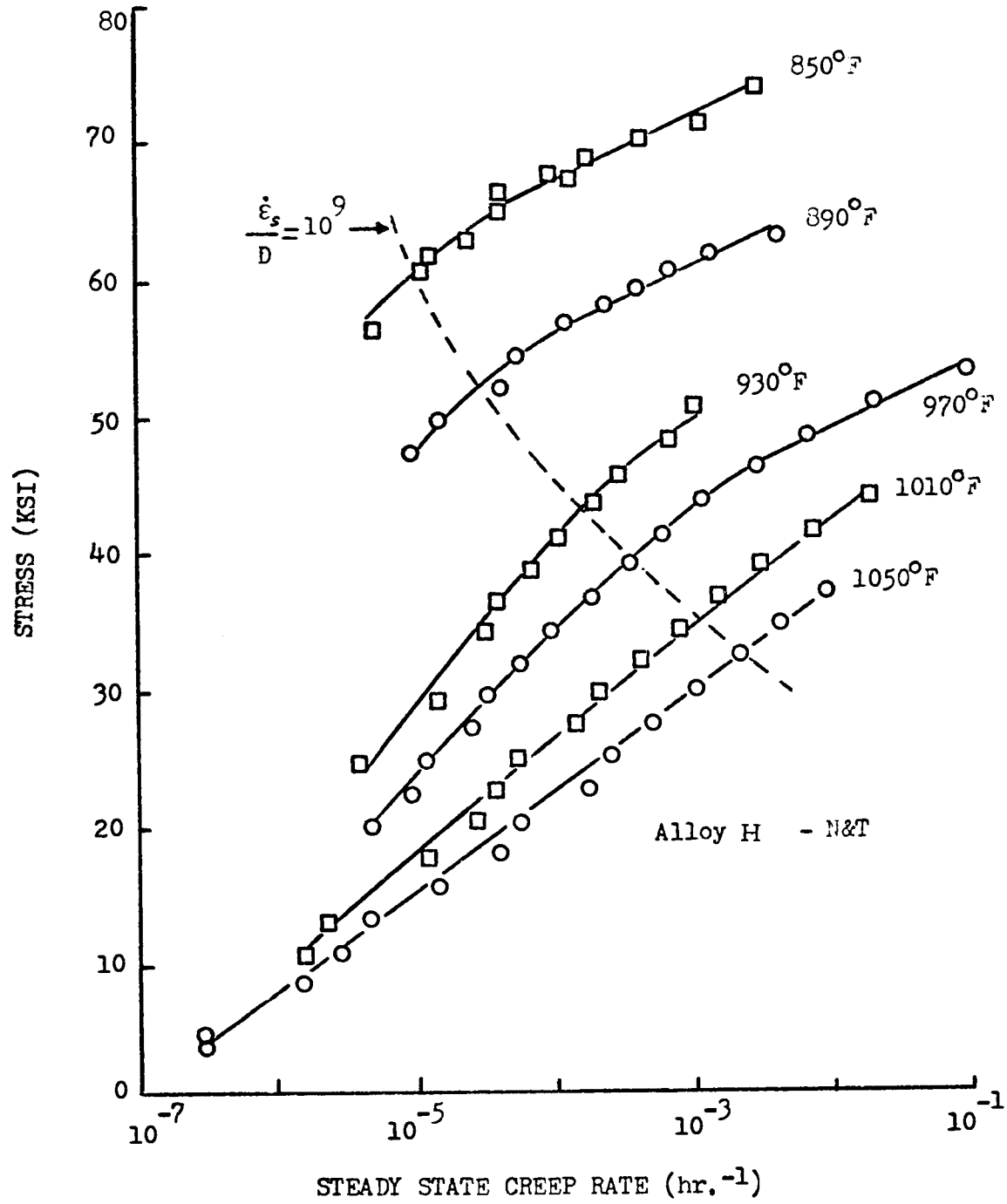

Figure 3 Log $\dot{\varepsilon}_s$ vs σ for Normalized and Tempered (1300°F, 1hr) Alloy H

form at 930°F. These observations indicate that the exponential creep law can describe the experimental data. Since, as mentioned before, both Weertman's theory and Barrett-Nix's theory [Eqs. (5) and (6)] predict a stress dependence of $\dot{\epsilon}_s$, which is very close to that of the exponential form, it is likely that either of these two theories can be applicable to explain the present creep data. However, we observed that $Q_c \gg Q_d$ at 850 and 890°F, which cannot be explained by the above three theories which predict that $Q_c = Q_d$.

Ansell and Weertman[26] have developed the only quantitative theory for creep of dispersion hardened alloys, in which $\dot{\epsilon}_s$ is given by three different relations according to the stress range. We will discuss later the low and intermediate stress cases, but at stresses above

$$\sigma_{cr} = (GkT/2\lambda b^2)^{1/2}, \tag{7}$$

the steady state creep rate is given as follows:

$$\dot{\epsilon}_s = \frac{\pi \gamma D \sigma^2}{G^2 b^2 h} \exp\left(\frac{2 \gamma b^2 \sigma^2}{G\, kT}\right), \tag{8}$$

where λ is the interparticle spacing and h is the total height climbed by a dislocation. h is approximated as the average particle diameter. This equation was obtained by considering the rate of climb of dislocation loops formed around particles which is the same approach they followed in the intermediate stress range, except that the velocity of climb is given by a different relation in each case. It appears that this theory has not been tested at all, but it has

been mentioned very often in the literature.

In order to examine the applicability of this theory to our experimental data the log $\dot{\epsilon}_s/\sigma^2$ was plotted against σ^2 in Fig. 4 for Alloy H (N&T) tested at 850°F. A good correlation was observed between Eq. (8) and our experimental data, since a straight line fitted the data above 65 Ksi. However, this theory contains some area of disagreement with experiment. These are: a) the predicted $\dot{\epsilon}_s$ value (at σ = 50 Ksi, λ = 1000Å) is 3.4 x 10^{-4} hr^{-1} and is slightly higher than the observed value of $\sim 10^{-6}$ hr^{-1}; b) the predicted value of σ_{cr} [Eq. (7)] above which this model is proposed to apply was too high ($\sim$380 Ksi); and c) the predicted value of Q_c for this theory should be equal to $Q_d - 2\lambda b^2 \sigma^2/G \simeq Q_d$ which is too low in comparison to our experimental observation ($Q_c > Q_d$ at 850°F).

In summary, the high stress creep data can be described by an exponential creep law or either of the two most common theories for high stress creep [Eqs. (5) and (6)]. On the other hand, the theory that relates $\dot{\epsilon}_s$ to σ^* (instead of σ) failed to explain our experimental results when the internal stress was assumed to be independent of the applied stress. The Ansell-Weertman theory described correctly the stress dependence of $\dot{\epsilon}_s$, but the predicted critical stress, above which this creep mechanism is supposed to operate was found to be much higher than the creep stresses used; and also, the Q_c predicted by this theory was much lower than the observed value of Q_c. Within the limited scope of our investigation, we cannot establish with certainty which creep mechanism is in control of $\dot{\epsilon}_s$ at high stresses.

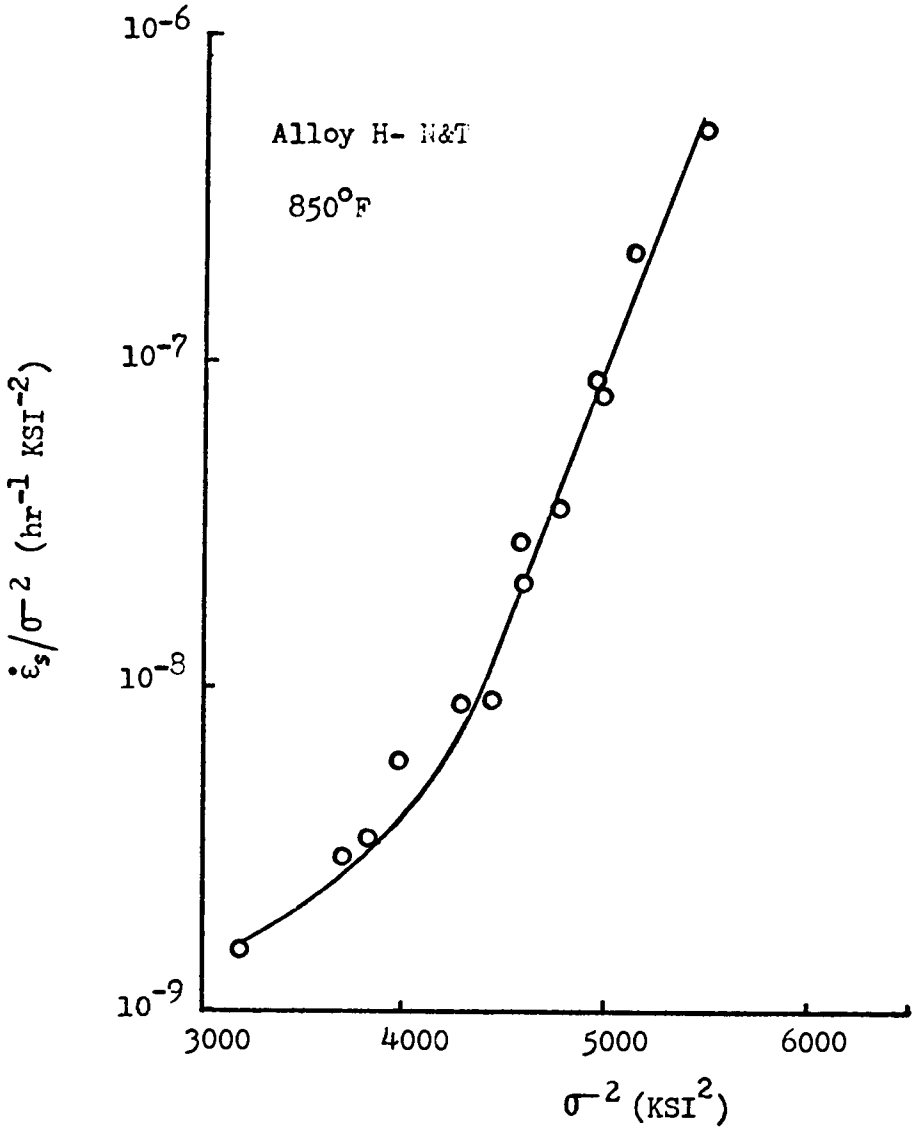

Figure 4 Log $\dot{\varepsilon}_s/\sigma^2$ vs σ^2 for Normalized and Tempered (1300°F, 1 hr.) Alloy H

7.2.1.4.2 Intermediate-Stress Creep. In this stress range, the power-law applies regularly to creep of single-phase materials. Generally, two different values of n are observed. In solid solutions classified as class I, n = 3 is found, while in class II materials, n = 4.5. Several theories have been proposed to account for the creep behavior of these alloys at these stresses. The two most common (and widely accepted) theories are the ones proposed by Weertman[24] for the case when n = 3 (microcreep) and n = 4.5 (dislocation climb). Dilute alloys of iron are generally classified as class II alloys.[14] For class II materials, the following equation can be used to estimate values of $\dot{\epsilon}_s$,[27]

$$\epsilon_s = \frac{ADGb}{RT} \left[\frac{\sigma}{G}\right]^n \qquad (9)$$

where A is a dimensionless constant equal to 7.3×10^{14} for α-iron, and n is equal to 4.5. The value of A is not expected to change appreciably for such dilute alloys as a 2-1/4Cr-1Mo steel if it behaves as a single-phase material. Furthermore, Eq. (9) is not expected to depend on the microstructure of the material.

The Ansell-Weertman theory[26] for creep in two-phase material predicts the stress dependence of ϵ_s as

$$\epsilon_s = \pi \sigma^4 \lambda^2 D/8\sqrt{2}\, h\, G^3\, RT \qquad (10)$$

for an intermediate stress range $\sigma_{cr} \geq \sigma \geq Gb/\lambda$. The theory assumes that at intermediate stresses, the dislocations are forced past

particles by pinching off loops around the particles, and that the rate controlling process for creep is the rate of climb of the loops by stress aided diffusion.

Let us now evaluate the predictions of the above two creep theories and compare with the creep data of Alloys H, I, and L. First, consider the stress exponent, n. Weertman theory predicts n = 4.5, while Ansell-Weertman theory predicts n = 4. Since the observed experimental values of n at intermediate stresses was 4 to 5, either of the two creep mechanisms can explain the observed n. Next, we consider the activation energy Q_c. Both theories predict that $Q_c = Q_d$. Our experimental results indicate that $Q_c \approx Q_d$, and therefore it is not possible to distinguish between the two. The only parameter that appears to indicate a significant difference, is the values of $\dot{\epsilon}_s$ predicted by the theories. In the case of Weertman's model (n = 4.5), the value of A for the case of a ternary Fe-2-1/4Cr-1Mo alloy was taken as that of pure α-iron, assuming that the presence of such small amounts of Cr and Mo in the α-Fe will not affect appreciably the value of A. For an applied stress equal to 10 Ksi and T = 1050°F, $\dot{\epsilon}_s/D$ values were calculated for Alloy H in the N&T condition. The results were as follows:

	$\dot{\epsilon}_s/D$
a) Dislocation climb (n=4.5)	2×10^{14}
b) Ansell-Weertman (n=4)	1.5×10^{5}
c) Experimentally obs. value	$\sim 10^{6}$

Here, λ and h for the Ansell-Weertman theory are taken from the microstructural examination and are equal to 0.16 μm and 600Å,

respectively. Clearly, this result indicates the preference of the Ansell-Weertman theory.

Still another argument in favor of the Ansell-Weertman model is the fact that this model predicts a change in creep rate for alloys having a different particle size and distribution. Such variations in $\dot{\epsilon}_s$ were observed during the creep study of Alloys H, I, and L.

To show this point, we have combined all the $\dot{\epsilon}_s$ vs. σ (Figs. 1-6 in ref. 3) into Figs. 5 and 6 for N&T and long-term tempered materials, respectively. We have also plotted in Figs. 7 and 8 the $\dot{\epsilon}_s$ values calculated by the Ansell-Weertman theory at intermediate and low stresses (low-stress creep will be discussed later). The characteristic values for particles used for this calculation are shown in Table 1. As noted earlier, no change in $\dot{\epsilon}_s$ is expected due to a change in the particle dispersion characteristics according to the Weertman theory of dislocation climb. A comparison of Figs. 5 and 7, and Figs. 6 and 8, show that the Ansell-Weertman model predicts correctly the relative creep strength of Alloy H as compared to that of Alloys L and I, at intermediate stresses. Therefore, we conclude that, at intermediate stresses, the rate controlling process of creep in the precipitation hardened mateirals, Alloys H, I, and L, is the climb of loops present around particles as proposed by Ansell and Weertman.

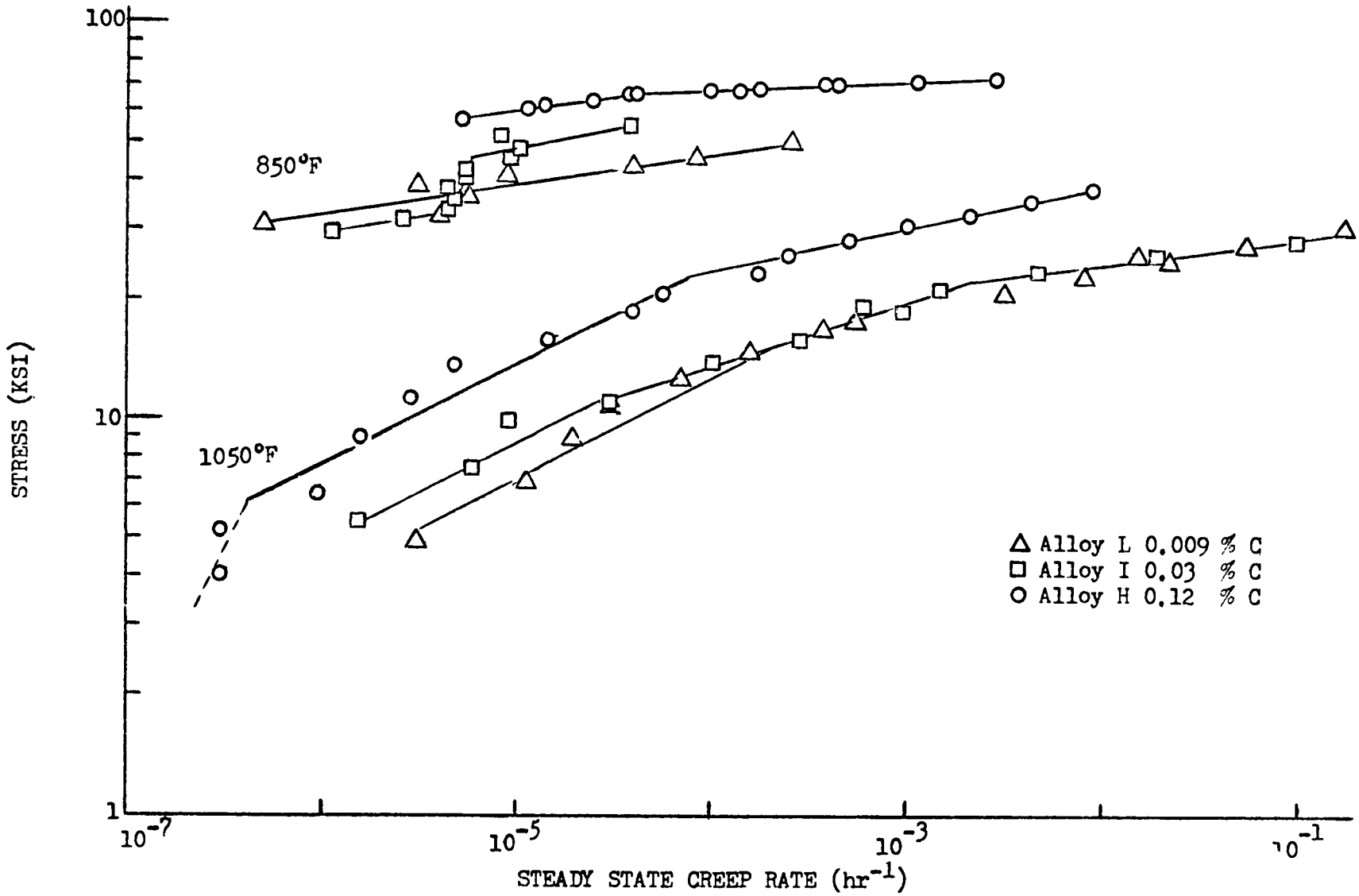

Figure 5 Creep Stress vs Steady State Creep Rate of Normalized and Tempered (1300°F, 1hr) 2¼ Cr-1Mo Steels

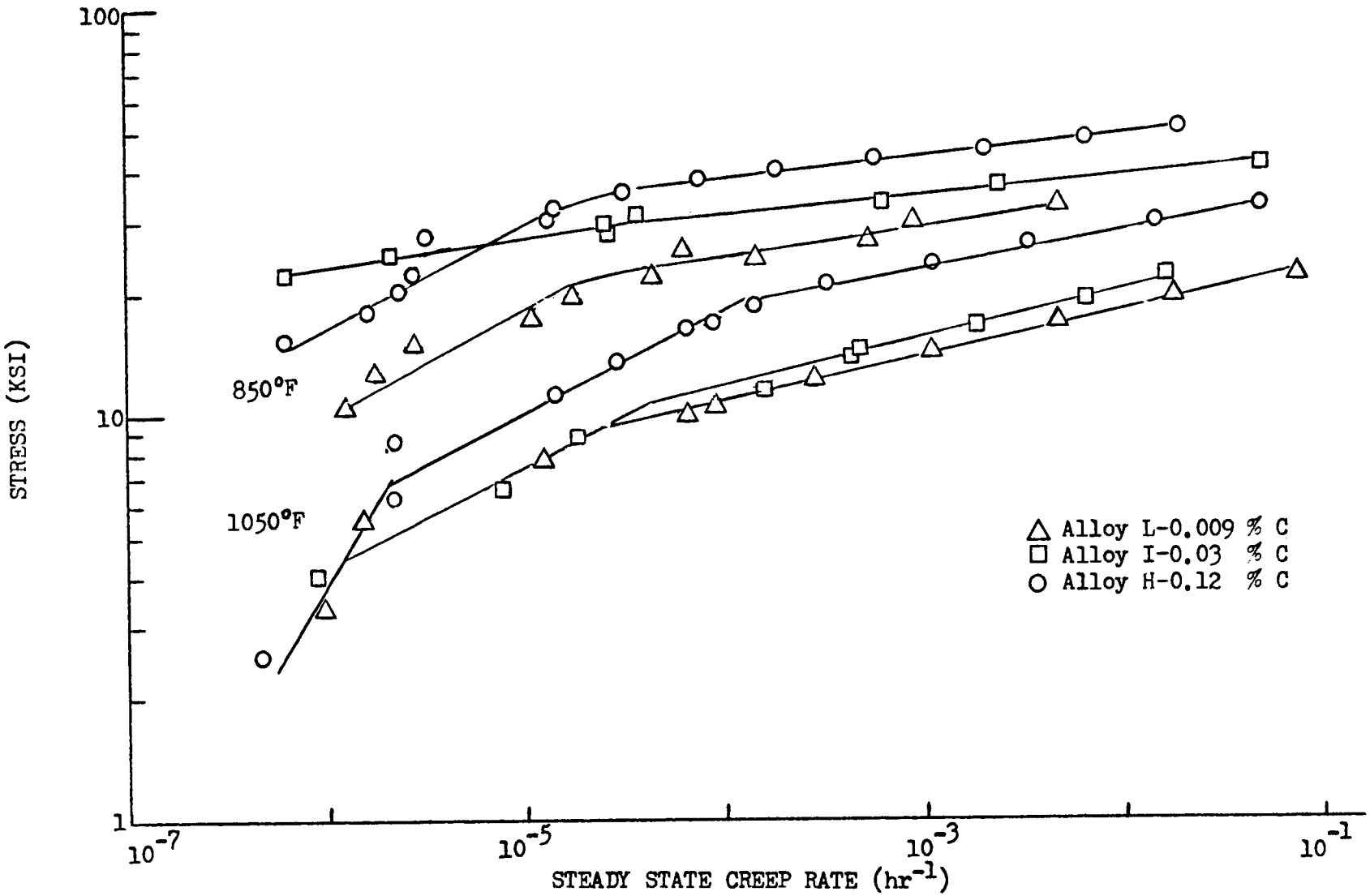

Figure 6 Creep Stress vs Steady State Creep Rate of Normalized and Tempered (1300°F, 1 hr.) 2¼ Cr-1Mo Steels, Tempered at 1050°F for 12 Months

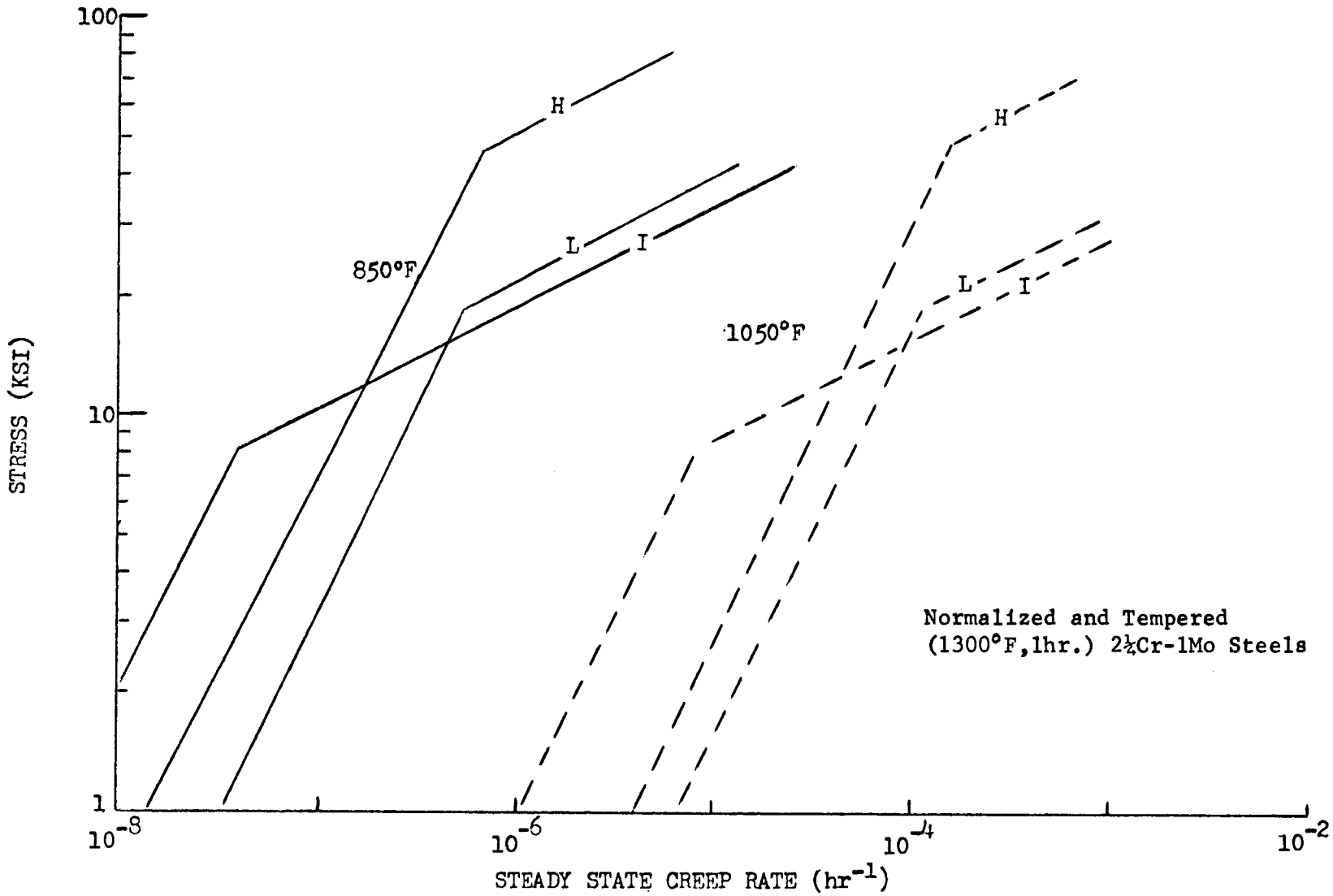

Figure 7 Creep Rates Predicted by Weertman's Theory for Creep in Dispersion Strengthened Alloys

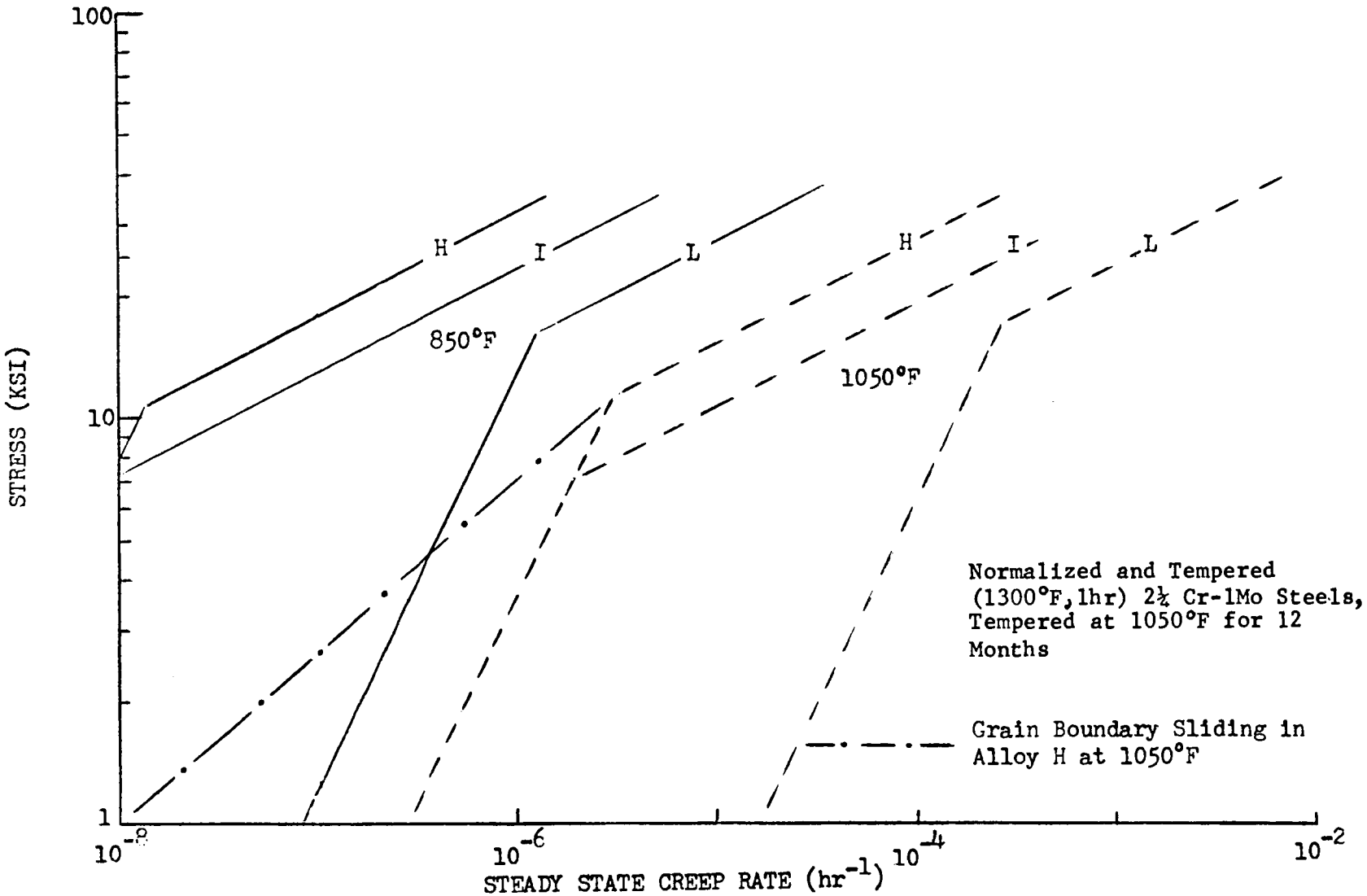

Figure 8 Creep Rates Predicted by Weertman's Theory for Creep in Dispersion Strengthened Alloys

TABLE 1

Particle Characteristics for Alloys H, I, and L

Alloy	Condition			
	N&T*		LTT**	
	λ (μm)	h(Å)	λ(μm)	h(Å)
L	0.5	400	0.76	250
I	1.1	1,000	1.1	2,000
H	0.16	600	0.65	2,000

N&T* : Normalized and tempered

LTT**: Long-term-tempered

λ : Interparticle spacing

h : Particle diameter

7.2.1.4.3 Low-Stress Creep. In this stress range, the creep data we have obtained is limited to a few data points. However, as shown in Fig. 6, these data suggest n to be much lower than 4 in this stress region. In Fig. 6, a line having n = 1 was drawn to illustrate such possibility, although it is not possible to establish clearly the existence of such low-n region or the exact value of n. More extensive creep data must be obtained at low stresses, as this range is technology most important.

7.2.1.5 References

1. Ono, K., et al. UCLA-34P177-21, June 1974.

2. Chalco, P.A. and K. Ono, ORNL-4963, June 1974.

3. Chalco, P.A., et al. ORNL-5103, Dec. 1974.

4. Wilcox, B.A. and A.H. Clauer, "Creep of Thoriated Nickel Above and Below $0.5T_m$," Trans. Met. Soc. AIME, Vol. 236, pp. 570-580, 1966.

5. Borch, N.R., et al. "Activation Energies for Creep of An Alpha Solid Solution of Magnesium and Aluminum," Trans. ASM, Vol. 52, pp. 511-513, 1960.

6. Phillips, V.A., Discussion of Pager Listed as Ref. 5, Trans. ASM, Vol. 52, pp. 511-513, 1960.

7. Woodhead, J.H. and A.G. Quarrell, "The Role of Carbides in Low-Alloy-Creep Resisting Steels," JISI, Vol. 203, pp. 605-620, 1965.

8. Raffo, P.L., "Dynamic Strain Aging During the Creep of a Mo-Ti-C Alloy," Trans. ASM, Vol. 62, pp. 846-851, 1969.

9. Woodford, D.A. and S.G. Glover, "The Creep of a Low-Alloy Ferritic Steel," JISI, Vol. 201, pp. 873-875.

10. Argent, B.B., et al., "Creep of Ferritic Steels," JISI, Vol. 208, pp. 830-843, 1970.

11. Leslie, W.C., et al., "Serrated Yielding and Flow in Substitutional Solid Solutions of Alpha Iron," Proceedings of the Third International Conference on the Strength of Metals and Alloys, Cambridge, England, August 20-25, 1973, Vol. 1, pp. 11-15.

12. Momma, K., "On the Influences of Alloying Elements Upon the Hot Hardness of Low Alloy Steels," Nippon Kinzoku Gakkai-shi, Vol. 29, pp. 191-196, 1965.

13. Askill, J., "A Bibliography on Tracer Diffusion in Metals and Alloys," ORNL-3795, 1965.

14. Serby, O.D. and P.M. Burke, "Mechanical Behavior of Crystalline Solids at Elevated Temperature," Prog. Mat. Sci., Vol. 13, pp. 325-390, 1968.

15. Dews, T.W. and W.R. Martin, "Mechanical Properties of 2-1/4 Cr-Mo Steel for Design; Elastic Properties," Mechanical Properties Test Data for Structural Materials, Quarterly Progress Report, Oak Ridge National Laboratory, ORNL-4948, March 1974, p. 262.

16. Bauer, A.A., Discussion of Paper Listed as Ref. 28, Proceedings of a Symposium on Low Carbon and Stabilized 2-1/4% Chromium 1% Molybdenum Steels, Cleveland, Ohio, October 1970, ASM, Metals Park, Ohio, 1973, pp. 113-118.

17. Klueh, R.L., "Mechanical Properties of LMFBR Steam Generator," Private Communication.

18. Wilcox, B.A. and A.H. Clauer, "The Role of Grain Size and Shape in Strengthening of Dispersion Hardened Nickel Alloys," Acta Met., Vol. 20, pp. 743-757, 1972.

19. Meyers, C.L., et al., "Relation of Properties to Structure in Sintered Aluminum Powder," J. Australian Inst. Metals, Vol. 8, pp. 171-183, 1963.

20. Ansell, G.S., "Theory of Strengthening Due to Precipitate Phases," Precipitation from Iron Base Alloys, AIME Metallurgical Society Conferences, Vol. 28, Gordon and Breach, New York, 1965, --. 231-279.

21. Cuddy, L.J., "Internal Stresses and Structures Developed During Creep," Met. Trans., Vol. 1, pp. 395-401, 1970.

22. Kuchavova, K., et al., "Effective Stress in Steady State Creep in an Al-5.5 at % Mg Solid Solution," Acta Met., Vol. 22, pp. 465-472, 1974.

23. Garofalo, F., "An Empirical Relation Defining the Stress Dependence of Minimum Creep Rate in Metals," Trans. Met. Soc. AIME, Vol. 227, pp. 351-355.

24. Weertman, J., "Steady-State Creep of Crystals," J. Applied Physics, Vol. 28, pp. 1185-1188, 1975.

25. Barret, C.R. and W.D. Nix, "A Model for Steady State Creep Based on the Motion of Jogged Screw Dislocations," Acta Met., Vol. 13, pp. 1247-1258, 1965.

26. Ansell, G.S. and J. Weertman, "Creep of a Dispersed-Hardened Aluminum Alloy," Trans. Met. Soc. AIME, Vol. 215, pp. 838-843, 1959.

27. Ashby, M.F., "A First Report on Deformation-Mechanism Maps," Acta Met., Vol. 20, pp. 887-897, 1972.

28. Sponseller, D.L., et al., "Effects of Low Carbon Contents and Exposures to Liquid Sodium on Elevated-Temperature Behavior of

2-1/4% Cr-1%Mo Steel," Proceedings of a Symposium on Low Carbon and Stabilized 2-1/4% Chromium - 1% Molybdenum Steels, Cleveland, Ohio, October 1970, ASM, Metals Park, Ohio, 1973, pp. 73-112.

8. GENERAL ELECTRIC COMPANY

D. Weinstein

8.1 INTRODUCTION

The principal objective of mechanical properties testing at the General Electric Company is to characterize the behavior of 2¼Cr-1Mo and austenitic stainless steels in sodium environments relevent to LMFBR steam generators and intermediate heat transport systems. Under conditions predicted for the intermediate sodium system of the CRBRP, 2¼Cr-1Mo will lose carbon to the system and be weakened. The carbon will tend to carburize and embrittle stainless steel components in other portions of the system. The effects of a carburizing environment on creep rupture properties of Type 316 stainless steel will be evaluated along with an assessment of creep-fatigue interactions. In addition, studies of fatigue crack propagation rates in carburizing sodium will be performed in order to assess environmental effects under pertinent intermediate sodium loop loading conditions. The loss of carbon from 2¼Cr-1Mo steel components can result in increased creep rates of the decarburized surface layer with the possibility of ratchetting under cyclic straining. These effects will be evaluated for base metal and weld metal in a decarburizing sodium environment.

8.2 MECHANICAL PROPERTIES OF STAINLESS STEEL IN CARBURIZING SODIUM- J. F. Copeland

8.2.1 Background

The objective of this program is to experimentally verify and supplement ASME Code design values for austenitic stainless steels to be used in LMFBR Intermediate Heat Transport Systems (IHTS). The effects of sodium carburization on creep rupture lives and deformation rates will be evaluated, as well as the influence of creep-fatigue interaction and of tension hold time at peak stresses (30 min). The effect of environment and other design-related parameters on the fatigue crack propagation rate will be determined in high carbon sodium using a fracture mechanics

approach. Frequency (0.5 and 0.05 cpm) and hold time (1 min) effects will be determined over a range of ΔK values in air and in carburizing sodium. This study will include the influence of continuous carburization in sodium at a crack tip during load cycling and stressing since even a very thick component could conceivably be degraded by this mechanism. A possible mechanism for the influence of carburizing sodium on crack initiation and propagation is illustrated in Figure 8-1. Such data will be utilized for assessing and ensuring the integrity of LMFBR IHTS components in carburizing liquid sodium environments.

Initial tests will be performed on Type 316 stainless steel at 950°F in carbon-saturated sodium after approximately 1000 hours specimen pre-exposures. The degree of carburization expected[1] is a case depth of about 5 mils with a surface carbon content of approximately 1 to 1.5 wt%. This carburization corresponds to that expected (Figure 8-2)[2] for the 30-year CRBR IHTS design life with a 2¼Cr-1Mo steel carbon source. GE analysis of bimetallic sodium test loops (Steam Generator Test Rig,[3] PA-15 Loop 3,[4,5] B&W Model Steam Generator,[6] and EBR-II secondary sodium system vent-lines[2]) has verified that such surface carburization of stainless steel components does occur.

Two types of tests will be performed, in addition to initial material characterizations: a) tubular creep and creep-fatigue tests that give rupture times, deformation rates, and rupture ductilities, and b) ASTM E399 fracture mechanics bend tests to give fatigue crack propagation rates. Under a), specimens shown in Figure 8-3, will be filled with sodium and a carbon source and sealed prior to testing. Control specimens will be filled with argon. For part b), testing will be performed in flowing sodium (Loop A, previously employed in carburization studies). Control tests will be performed in air. Cyclic frequency will be low and will include the determination of hold-time effects. The first phase of the program with these two tests is shown in Tables 8-1 and 8-2. It is currently projected that Phase I will be completed by December 31, 1975. In addition, work on weldments will initiate at the start of FY76. Phase I of the program concentrates on producing relevant design-related data as quickly as possible. This is accomplished by accelerated carburization

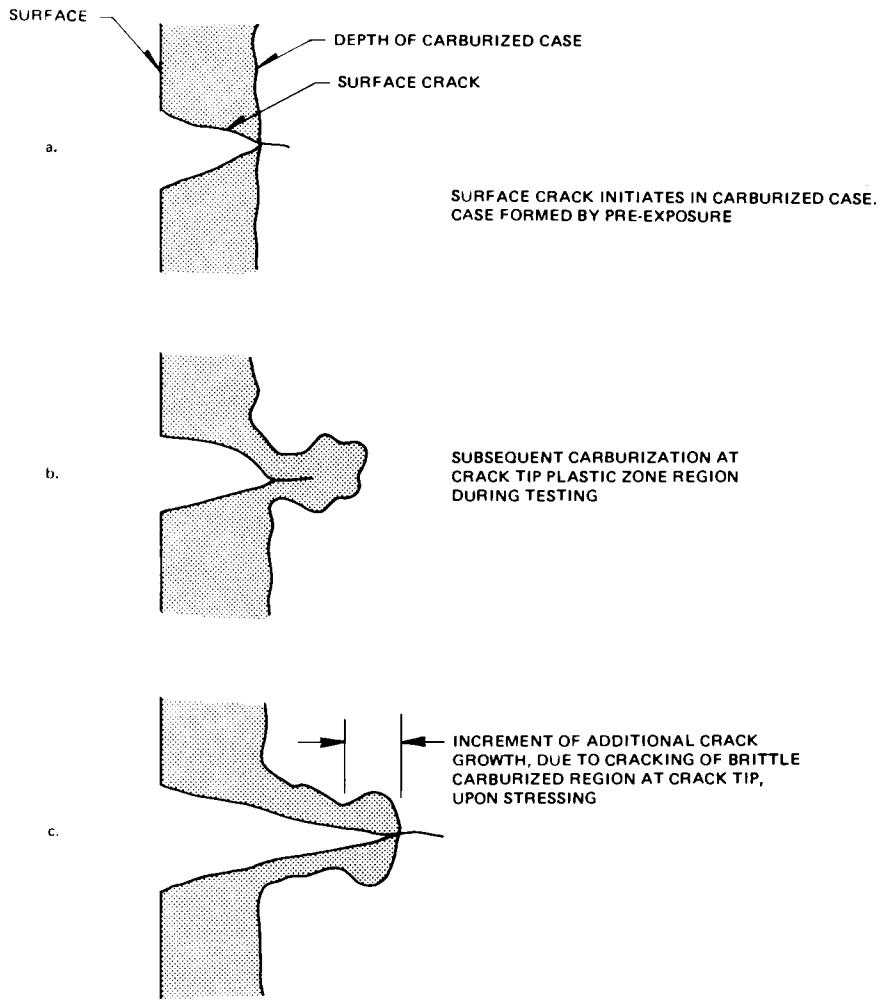

Figure 8.1 Schematic Representation of the Mechanism of Crack Initiation and Growth for Fatigue Specimens Carburized by Pre-Exposure and Tested in Carburizing Environment. Effects on Both Crack Initiation and Propagation, Since the Crack is Always Growing Through Carburizing Material Exposed to Sodium.

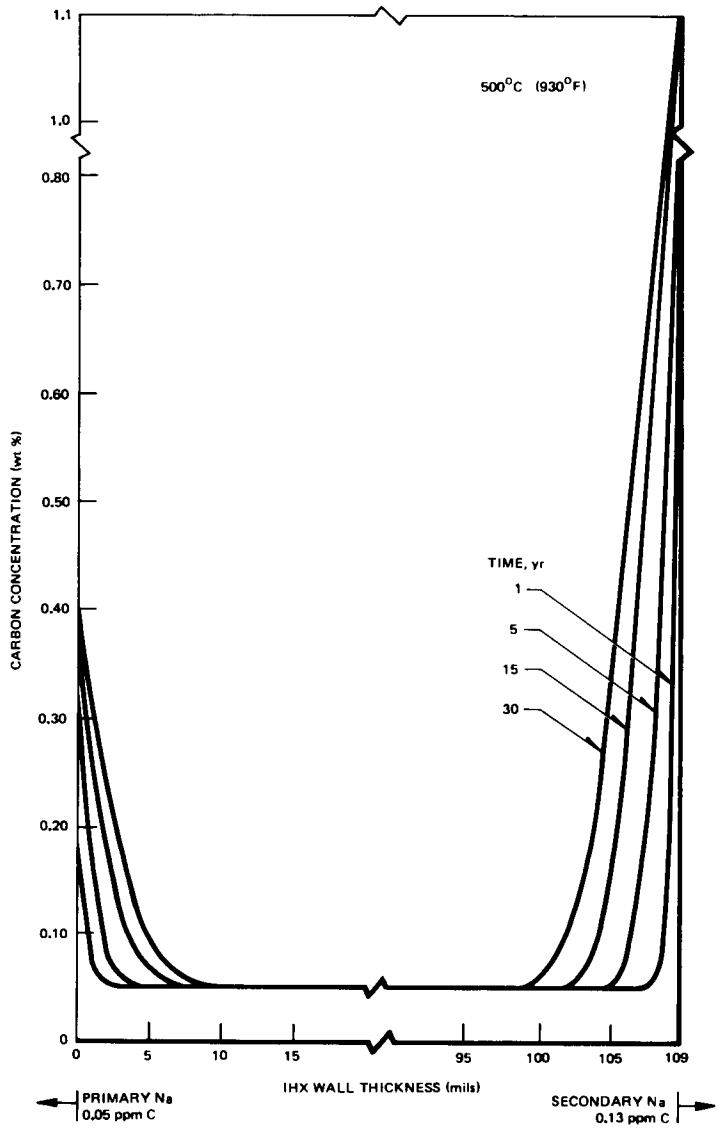

Figure 8.2 Carbon Concentration-Distance Profiles Across Type 304 Stainless Steel IHX Piping After Exposure to Primary-and Secondary-System Sodium Containing 0.05 and 0.13 ppm Carbon, Respectively, for up to 30 yr at 500°C. ANL NEG No. MSD-58582; REF 2.

Table 8.1 Phase I Test Matrix - Annealed Type 316 Uniaxial Tubular Creep-Fatigue Tests (950°F)

	Approximate Test Duration (hr.)				Purpose
	30	300	1500	3000	
Uniaxial Tests - Creep Mach. (Na/C source inside tube)					
1. Control - Argon Creep-fatigue $\Delta\sigma$ = +10ksi, 1cph.	X	X	X	X	Control
2. Na/C Creep-fatigue, $\Delta\sigma$ = +10ksi, 1cph.	X	X	X	X	C-effect
3. Na/C Creep	X	X	X	X	Creep contribution
4. Na/C Creep-fatigue, $\Delta\sigma$ = +10ksi, 1cph. 30 min. hold at peak stress	X	X	X	X	Hold time

*cph - cycles per hour

$\Delta\sigma$ - range of stress overload

Table 8.2 Phase I Test Matrix - Annealed Type 316 Fatigue Crack Propagation Tests (950°F)

$\Delta K = \Delta P\ f(a)$

ΔK = stress intensity factor range
ΔP = loading range ($\sim$0 to P max.)-0.5 in. thick bend tests
a = crack length

ΔP(lb) =	500	750	1000	1250	1500	1750	2250
ΔK avg.(ksi$\sqrt{in.}$) =	10	15	20	25	30	35	45
$\sim$cycles($\times 10^3$),(for Δa=0.06") =	10	10	10	5	3.3	2.5	1.25
$\sim$test time at 0.5 cpm (da) =	8.5	8.5	8.5	4	3	2	1
$\sim$test time at 0.05 cpm (da) =	85	85	85	40	30	20	10
A. Control (Air)							
1. 0.5 cpm - zero hold =	X	X	X	X	X	X	X
2. 0.5 cpm -1 min.hold =	X	X	X	X	X	X	X
3. 0.05 cpm - zero hold =		X		X	X	X	X
4. 0.05 cpm -1 min.hold =		X		X	X	X	X
B. Na with 1050 C Source							
1. 0.5 cpm - zero hold =	X	X	X	X	X	X	X
2. 0.5 cpm -1 min.hold =	X	X	X	X	X	X	X
3. 0.05 cpm - zero hold =		X		X	X	X	X
4. 0.05 cpm -1 min.hold =		X		X	X	X	X

(by using a maximum carbon potential source) before and during the test. Additionally, load cycle frequencies and test times will be a compromise between actual operating conditions and the conditions required to produce test results. As a result of Phase I, extrapolations with regard to load frequency and test time may be performed. The effect of carburization on these mechanical properties of Tp. 316 will be established for Phase I conditions. Critical extrapolations may subsequently be verified by longer term and lower frequency data, where deemed necessary.

As stated, the tubular creep and creep-fatigue results from this study will be compared to ASME Code Case 1592 minimum stress-to-rupture values for Tp. 316 (Table I - 14.6 B and Fig. I - 14.6 B of C.C. 1592). Creep strains will also be compared with available control data. In this way, the influence of a high carbon sodium environment on rupture stress and creep rate can be evaluated. A control run for creep-fatigue (line 1. in Table 8-1) will be performed in air environment with argon-filled tubular specimens. This data will be compared with similar data from sodium/carbon filled, precarburized specimens. Using available stress rupture and fatigue data this creep-fatigue data may also be normalized to produce life fraction information. This life fraction data may then be utilized according to the philosophy of the accumulative damage equation (Equation 5 of Appendix T, C.C. 1592) and compared to the current creep-fatigue damage curve for Tp. 316 (Fig. T-1420-2, C.C. 1592). Thus, the influence of environment on creep-fatigue interaction may be determined, both by the control run and by comparison with the ASME damage curve. The rupture strains will be evaluated to assure that they surpass the strain limits for inelastic analysis (1, 2, and 5%) set forth in T-1310 of Code Case 1592, even with a carburized case.

The fracture mechanics crack propagation data from this study will show the influence of a carburizing sodium environment on the number of cycles to leak or failure for a pipe or other component with an assumed pre-existing flaw. The assumption of a pre-existing flaw in a component is expecially valid in this situation, since it may be produced at relatively low strains in a carburized case. It would then proceed to grow upon subsequent cycling. Such crack growth data provides pertinent

input to another study[7] at GE, the Probabilistic Assessment of a LMFBR Pipe Break - 189 No. 13854. This study essentially utilizes the basic crack growth equation of fracture mechanics

$$\frac{da}{dN} = C\ (\Delta K_{eff})^n \qquad \text{Eqn. 8-1}$$

to predict the chance of a flaw growing to a size sufficient for the onset of a leak or pipe break. In Eqn. 8-1, da/dN is the instantaneous crack extension per fatigue cycle, ΔK_{eff} is the effective range of stress intensity factor for each cycle, and C and n are data correlation constants. The data from subtask C will evaluate the influence of IHTS environment and other pertinent parameters (hold time and frequency) to determine the values of the correlation parameters C and n in Eqn. 8-1. Since a fracture mechanics approach will be used in this program, the crack growth data can be applied to components of any size and geometry, as long as their behavior is essentially elastic and the stress intensity factor relationships are known for them.

The preliminary characterization of the Tp. 316 test material for this study was performed. Chemical composition and tensile test results, presented in Tables 5.3 and 5.4, satisfy ASME specifications and indicate no material irregularities.

8.2.2 Current Progress

Five Satec creep machines at GE have been modified to allow automatic load increases and data accumulation. The load perturbations (to simulate transient stress situations) are accomplished by timer-activated gas cylinders which raise and lower trays containing the additional weight. These trays are attached to the load pans of the creep machines and have been calibrated to produce the required load increases (+ 10 ksi., currently). The load increases are performed once per hour and are programmed to give both zero hold times (∿ 5 second up-ramp and 5 second down-ramp) and 30 minute hold times. Specimen extension data will be collected automatically from an IKL electronic digital dial indicator on

Table 8.3 Type 316 Stainless Steel Annealed Test Material Characterization-Chemical Composition (wt. %)

	C	Mn	P	S	Si	Cu	Ni	Cr	Mo	N
					1/4 Schedule 80 pipe [(a) Tests]					
Ladle	0.056	1.63	0.029	0.015	0.56	0.08	13.32	17.24	2.40	-
Check	0.055	1.63	0.018	0.010	0.70	0.05	13.40	17.47	2.67	0.038
					5/8 in. Plate [(b) Tests]					
Ladle	0.042	1.66	0.015	0.008	0.60	-	13.40	17.50	2.69	-
Check	0.053	1.59	0.009	0.013	0.54	0.06	13.37	17.22	2.37	0.050

Table 8.4 Type 316 Stainless Steel Annealed Test Material Characterization-Tensile Tests

	0.2% Y.S. (ksi.)	U.T.S. (ksi.)	% El. (2")	% R.A.
1/4 in. Schedule 80 Pipe [(a) Tests]*				
Room Temperature	39.4	90.4	50.0	55.3
	43.5	88.7	44.0	48.5
950°F	25.1	69.4	28.5	36.3
	24.0	71.2	32.5	36.6
5/8 in. Plate [(b) Tests]**				
Room Temperature	38.0	88.7	45.9	77.0
	39.3	89.4	53.6	77.4
950°F	21.1	70.6	36.5	66.4
	21.8	74.1	41.3	61.3

* 0.34 inch O.D. x 0.020 inch wall x 2 inch reduced section
** 0.25 inch Dia. x 2 inch reduced section

each test piece. These extension indicators possess an excellent combination of accuracy, stroke, and stability. They provide electronic signals which are then recorded as digital deformation data with a printer. Deformation data is currently collected every 30 minutes, once at the steady creep load and once at the peak load for each creep-fatigue cycle. These test system modifications have been essentially completed, and the machines are now being operated.

Two low cycle fatigue test pot facilities have been designed to perform crack propagation tests. One pot will be connected to Loop A, containing a carbon source, in order to evaluate fatigue crack propagation rates in flowing high carbon sodium at 950°F. The other test facility will produce control data by testing in air at 950°F. These test chambers each consist of a section of 10 inch diameter stainless steel pipe sealed at the ends with a cap and flange. Each chamber allows for the concurrent testing of three fracture mechanics, three-point bend specimens (0.5 inch thick). The specimens are each loaded by a ram inserted through the top of the flange and sealed with a bellows. Load control is achieved by an in-line load cell on each ram. These loads will be calibrated prior to testing. Loading will be achieved by a gas cylinder on each ram. The cycling rates will initially be 0.5 and 0.05 cycles per minute. Zero and one minute hold times will be produced, and the load ratio R, of minimum to maximum load, will be approximately 0.05. Each test will be run for approximately 1000 to 10,000 cycles. At this time the specimen will be withdrawn and examined on the sides for crack extension. It is expected that crack extension will be on the order of 50 mils. If the anticipated crack extension is achieved, the specimen will be broken in half to more thoroughly examine the progress of the crack front. The increment of crack growth, Δa, will be divided by the number of fatigue cycles, ΔN, in order to compute the average crack growth rate $\Delta a/\Delta N$. For a small increment of crack growth, $\Delta a/\Delta N$ approximates da/dN, and ΔK is calculated from the average crack length for the increment.[8] These fatigue test facilities are currently being fabricated. Completion of machining is now scheduled for April 30, 1975, with an additional month required for assembly and incorporation into Loop A.

Twenty-four Tp. 316 tubular creep specimens, as shown in Fig. 8-3, have been fabricated and filled with sodium and a carbon source or argon in order to satisfy the matrix in Table 8-1. Twenty of these have been aged at 950°F for 1000 hours. Ten specimens have been sent to Battelle-Columbus for testing according to parts 1 and 3 of Table 8-1. This testing was initiated in February 1975. Four argon specimens have been tested at high stresses, and a fifth argon specimen has been running for about 1000 hours. These preliminary results indicate data scatter. Therefore, additional specimens have been prepared and are presently being aged, prior to sending to Battelle. Two sodium-filled specimens are also now being tested at Battelle and have been running for more than 300 hours. Testing of the specimens for parts 2 and 4 of Table 8-1 was initiated at GE in March 1975. Preliminary results should be available in the next month.

Fifty Tp. 316 fatigue bend specimens have been fabricated, and half of these have been fatigue precracked. Aging of 11 of these precracked specimens in air, and of 13 precracked specimens in Loop A with a carbon source, was initiated in late March 1975. Tp. 304 foils are being used to monitor the carburization in Loop A during this aging. The 1000 hour aging will be complete in May 1975. This has been planned to interface with the incorporation of the fatigue test facility into Loop A in May.

The test matrix in Table 8-1 should be completed by late August 1975. Preliminary results indicating the effect of sodium environment should be available by June 30, 1975.

The major accomplishments for FY75 with regard to the crack propagation program will be the completion of the test facility. It is hoped that several sets of the higher frequency data (0.5 cpm) can be generated in June 1975, in order to check out the equipment and provide preliminary data guidelines. It is projected that the matrix in Table 8-2 will be completed by December 31, 1975. Additionally, preparation and testing of Tp. 316 weldments will be initiated in FY76.

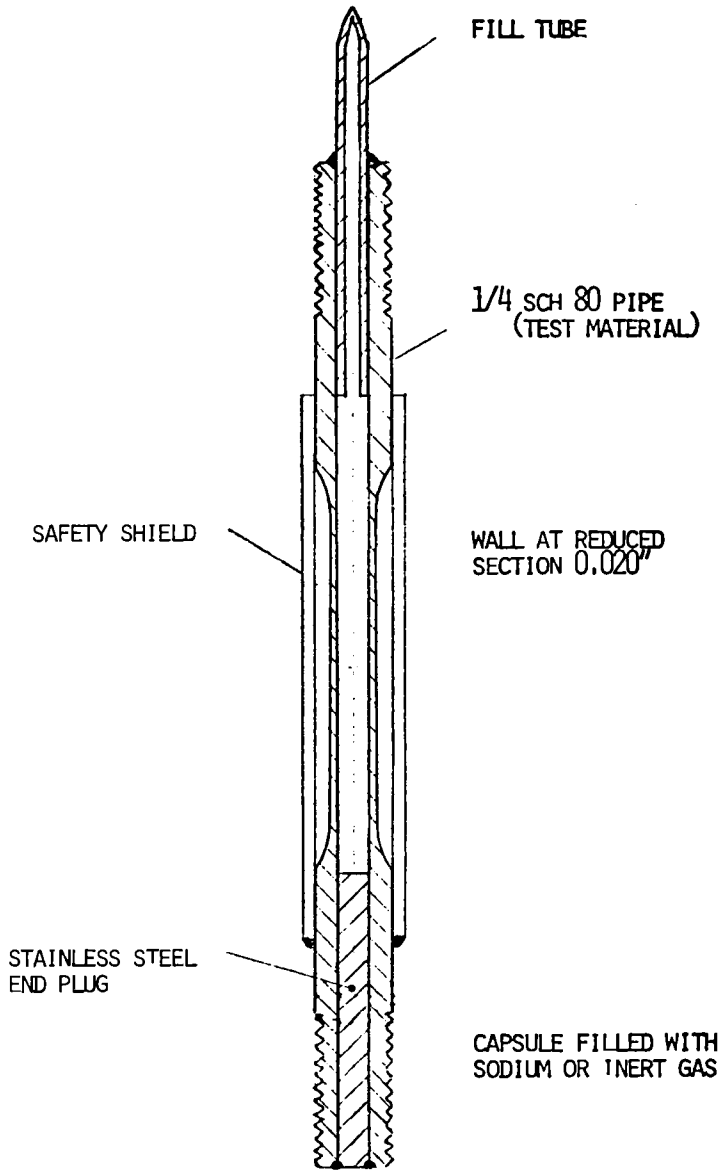

Figure 8.3 Uniaxial Creep/Fatigue Specimen

8.3 DECARBURIZATION KINETICS AND DESIGN METHODS VERIFICATION TESTING - G. J. Licina

8.3.1 Background

The selection of 2¼Cr-1Mo steel as the reference alloy for sodium-heated steam generators was based primarily upon its immunity to stress corrosion cracking in chloride or caustic contaminated environments and its proven fabricability.[9] One of the major concerns with the use of this material for sodium applications is its susceptibility to decarburization during service. Early analyses assumed that relatively thin sections, such as steam generator tubing, would completely decarburize during the LMFBR lifetime, with concomitant severe design stress penalties necessarily imposed.[10] In addition to the assumed carbon losses, the potential for severe carburization of stainless steel components in the loop was also recognized as a potential difficulty.

In the absence of an acceptable theoretical model for decarburization of 2¼Cr-1Mo steel, an approach introduced by Armijo and Krankota[11] was used to analyze the results obtained from many different experiments.[4,12-29] This technique treats carbon loss data as if it were corrosion data; that is, the loss of carbon per unit area is described as a function of time. A parabolic time dependence has been observed which suggests that the decarburization process is diffusion controlled. The decarburization rate constants, K*, from all available data were fit to an Arrhenius type expression for design use. Figure 8-4 shows the results of this analysis. The "data class" and the weighting applied to each class are defined in the NSM Handbook entry for decarburization of 2¼Cr-1Mo steel.[30] Based upon the upper limit curve given in Figure 8-4, estimates of carbon loss and associated design stress penalties can be made for steam generator components. These predictions of decarburization kinetics

---

*Where K is defined by:

$$K = \frac{gm^c}{cm^2 - sec^{\frac{1}{2}}}$$

$$M \quad \left(\frac{gm^c}{cm^2}\right) = Kt^{\frac{1}{2}}$$

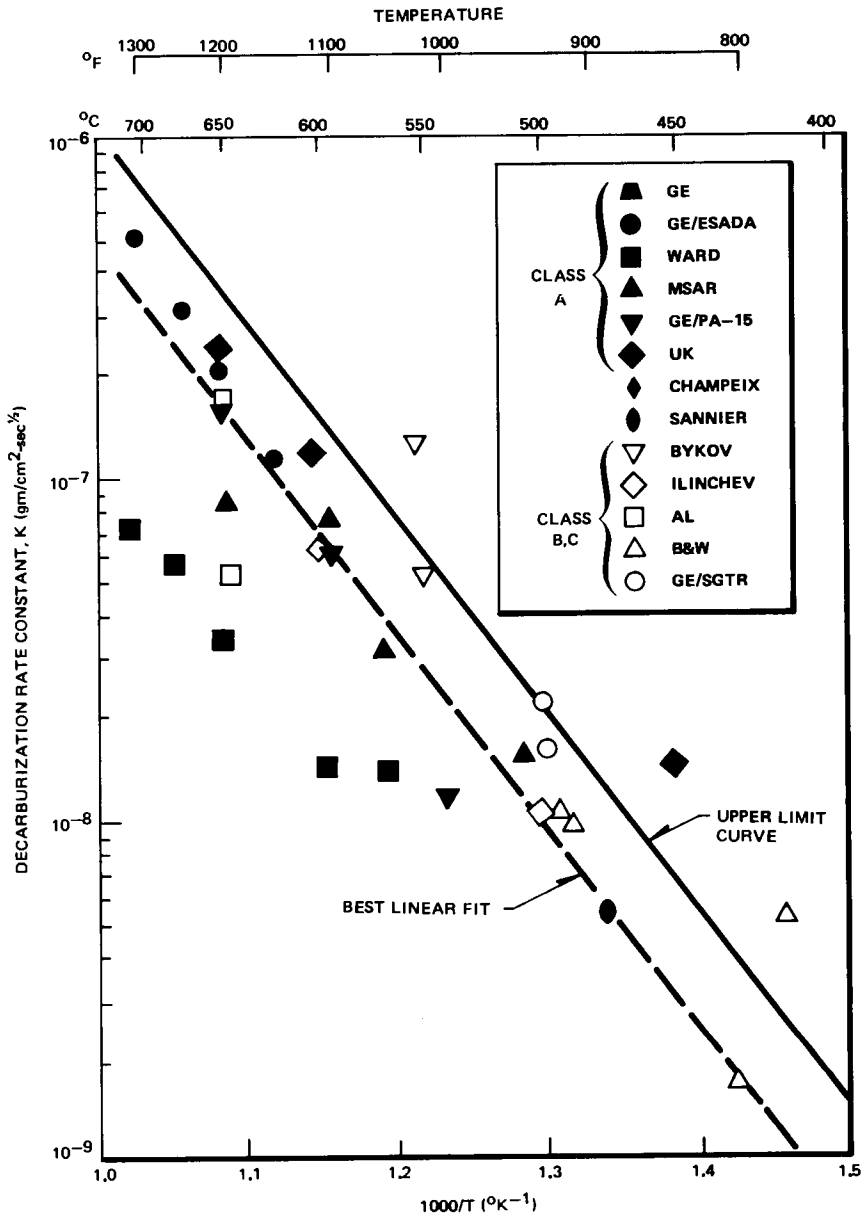

Figure 8.4 Decarburization Rate Constants for All Investigations

indicate that steam generator tubes would not be expected to lose more than 300 ppm carbon in the design life of the CRBRP. Only a small design stress penalty (<10%) is associated with this loss. While the handbook approach suggests that decarburization kinetics are too slow to yield a carbon loss at end-of-life of greater than 300 ppm for CRBRP steam generator tubing,* WARD experiments, utilizing thin foils, imply that the "equilibrium" carbon content of 2¼Cr-1Mo in 950°F sodium will be approximately 700-900 ppm.[14] The design stress penalty associated with these predictions of carbon loss can be accomodated.

Design analysis for high temperature components requires a consideration of creep/fatigue interaction to accomodate the effects of transient loading. A recent study has provided creep/fatigue interaction information for 2¼Cr-1Mo[31] under conditons of uniform microstructure (i.e. no decarburized surface layer) with no ratcheting strains permitted. Steam generator tubes will experience cyclic loading with the potential to accumulate ratcheting strains, and with a weaker surface layer, as compared to the bulk metal. Interrupted creep tests on 2¼Cr-1Mo pipe, tubing, and weld metal are being undertaken to assess the effects of such loading on partially decarburized material. Uniaxial tests will be performed on sodium-filled and inert gas-filled pipe samples in order to characterize the effect of stress cycling on creep strains. Tubing and all-weld-metal tubes will be internally pressurized in sodium and argon environments to assess the effects of creep/fatigue on rupture life in a decarburizing environment. Description of the samples, test facilities, and test matrix is included in earlier reports.[32,33]

8.3.2 Current Progress

Construction of the test facility for biaxial creep/fatigue interaction testing, Decarburization Pot #2, is nearly complete. Modification of uniaxial creep testing machines to incorporate load interruption and automatic strain recording has been completed. The initial run on this facility has begun.

---

*Tubing specification sets initial carbon levels of 700-1100 ppm.

8.4 REFERENCES

1. LMFBR Heat Exchanger Materials Development Program, Second Quarterly Report, September - November 1972, AEC Contract AT(04-3)-189, PA-60, December 1972 (GEAP-13919-2).
2. R. B. Snyder, K. Natesan and T. F. Kassner, "A Generalized Method of Computing Carbon-Diffusion Profiles in Austenitic Stainless Steels Exposed to a Sodium Environment," ANL-8015, AEC Contract W-31-109-Eng-38, June 1973.
3. J. L. Krankota, "Carburization of Stainless Steel Rupture Discs in SGTR," GE letter report, August 1, 1974.
4. M. C. Rowland and D. E. Plumlee, "Sodium Mass Transfer: XXII - Metallurgical Examination of the Test Loops," GEAP-4838 (Oct., 1965).
5. Summary Report - Sodium Mass Transfer Program: "Effects of Sodium Exposure on the Corrosion and Strength of Stainless Steel," GE-FBRD, August 1971 (GEAP-10394).
6. D. W. Koch, P. J. Kovach, BAW-1280-37 (June, 1966).
7. S. L. Derby, "Probabilistic Assessment of a LMFBR Pipe Break," Draft of portion of Task 13 Quarterly Report, Contract No. AT(04-3)-893, Task 13, 189 No. 13854, GE, Sunnyvale, CA, March 17, 1975.
8. L. A. James, "Fatigue-Crack Propagation Behavior of Incoloy 800 at Elevated Temperatures," ASME Paper No. 74-Mat-7, Presented at ASME Pressure Vessel and Piping Conference in Miami Beach, Fla., June 24-28, 1974.
9. G. J. Licina and J. F. Copeland, "A Review of 2¼Cr-1Mo Steel for Steam Generator Applications in the Clinch River Breeder Reactor," GEAP-20589 (August, 1974).
10. "Task VI Final Report, Vol. 4, Steam Generator Development," NEDC-13655 (Oct. 1970).
11. J. L. Krankota and J. S. Armijo, "Decarburization Kinetics of Low Alloy Ferritic Steels in Sodium," Met Trans., 3, pp. 2515-2523, (Sept., 1972).
12. J. M. Scott, et. al., "Sodium Heated Steam Generator Model Tests at SGTR: Volume 1," GEAP-10580-1, (June, 1972).

13. J. L. Krankota and J. S. Armijo, "The Kinetics of Decarburization of 2¼%Cr-1%Mo Steel in Sodium," Nuc Tech., 24 (November, 1974).

14. "Sodium Technology Program - Component Materials Compatibility," WARD-NA-3045-11 (August, 1974).

15. D. E. Plumlee, R. W. Lockhart, and L. E. Pohl, "Sodium Mass Transfer: XVIII - Studies of Carbon Movement in Pumped Sodium Test Loops," GEAP-4834 (June, 1965).

16. M. C. Rowland, et al., "Sodium Mass Transfer: XIX - Long-Term Exposure Effects in a Bimetallic Type 316 Stainless Steel - 2¼Cr Test Loop," GEAP 4835 (April, 1965).

17. L. H. Kirschler, R. H. Hiltz, and S. J. Rodgers, MSAR 64-81 (July, 1964).

18. L. H. Kirschler, R. H. Hiltz, and S. J. Rodgers, MSAR 69-42 (April, 1969).

19. L. H. Kirschler, R. H. Hiltz, and S. J. Rodgers, MSAR 69-207 (October 1969).

20. L. Champeix and O. Konovaltschikoff, Proceedings of the International Conference on Sodium Technology, pp. 93-103, ANL-USAEC Report ANL-7520-Part 1, (Nov., 1968).

21. J. Sannier, et al, Report on BNES Conference on Corrosion and Effects of Environment on Materials Properties in Nuclear Systems, pp. 137-147, London (July, 1971).

22. G. Ilinchev, CEMA Symposium of Atomic Power Stations with Fast Reactors - Volume I (Obninsk), pp. 462-477, Joint Publications Research Service, Washington, D. C. (July, 1969).

23. W. J. Anderson, G. J. Sheffield, and J. Birkle, NAA-SR-7544 (Nov., 1963).

24. L. H. Kirschler, R. H. Hiltz, and S. J. Rodgers, MSAR 72-286, (December, 1972).

25. V. N. Bykov, et al., "The Problems of Corrosion Resistance of Structural Materials In Sodium," CEMA Symposium of Atomic Power Stations with Fast Reactors (Obninsk) Volume I, pp. 426-461 (July, 1969).

26. A. Thorley, B. Longson, and J. Prescott, "Effect of Exposure to Sodium on the Mechanical Properties and Structure of Some Ferritic, Austenitic and High Nickel Alloys," TRG Report 1909 C (1969).

27. D. W. Koch, P. J. Kovach, BAW-1280-37 (June, 1966).

28. S. Ohta, "2¼Cr-1Mo-Nb Steel: A New Steel for Steam Generator Tubes of Sodium Cooled Fast Breeder Reactors," Central Research Lab Kobe Steel. Ltd. (in Reactor Steels Studies in Japan UCLA-34 pp. 177-179).

29. J. Motz, Zeit. Fur Metallkunde, Vol. 55, pp. 489-494, (1964).

30. Nuclear Systems Materials Handbook, Decarburization of 2¼Cr-1Mo Steel (January, 1975).

31. R. M. Curran and B. M. Wundt, "A Study of Low-Cycle Fatigue and Creep Interactions in Steels at Elevated Temperatures," to be published.

32. Steam Generator Materials Engineering - First Quarterly Report, GEAP 14029-1 (Oct., 1971).

33. Steam Generator Materials Engineering - Second Quarterly Report, GEAP 14029-2.

INDEX

Test	Material	Page
Chemical Analysis		
	type 314 SS	96
	2 1/4 Cr-1 Mo	199–200; 201
Creep Test Data		
Base-Line Data		
	type 304 SS bar	252–255; 260–266; 285–295
	type 304 SS plate	67–70; 285–295
	type 304 SS tube	232–241; 297–310
	type 304 SS welded bar	295–296
	type 304 SS welded plate	295–296
	type 308 SS welded metal	182–187; 232–241
	type 308 SS weld metal, aged	178–181
	type 316 SS tube	370–381
	type 316 SS weld metal	182–187
	type 16-8-2 weld metal	174–177; 182–187
	2 1/4 Cr-1 Mo weld metal	384
Correlations		
	type 304 SS	101–102; 141–164; 246–251
	type 316 SS	141–164
	2 1/4 Cr-1 Mo	341–364
Effect of Aging		
	type 304 SS	124–127
Effect of Composition		
	type 304 SS	95–101

Test	Material	Page
Creep Test Data (Continued)		
Effect of Cycling		
	type 316 SS tube	369–381
	2 1/4 Cr-1 Mo tube, weld metal	384
Effect of Hold Time		
	type 316 SS	369–381
Effect of Load Change		
	type 304 SS	322–324
Effect of Product Form		
	type 304 SS	242–245
Effect of Sodium Exposure		
	type 304 SS	52–61
	type 316 SS tube (carburizing)	369–381
	2 1/4 Cr-1 Mo weld metal	384
Effect of Strain Cycling		
	2 1/2 Cr-1 Mo	215–222; 251–253
Heat-to-Heat Variation		
	type 304 SS	91–95
Interrupted Tests		
	type 304 SS	253–258
Step-Load Tests		
	type 304 SS	253–256
Strain Limits		
	type 304 SS	141–164
	type 316 SS	141–164
Cyclic Testing		
	type 304 SS	21–32
	high-purity SS	32–51
	2 1/4 Cr-1 Mo	200–230; 251–253
Fatigue Test Data		
Cyclic Fatigue Test Data		
	2 1/4 Cr-1 Mo	200

Test	Material	Page
Fatigue Test Data (Continued)		
Effect of Hold Time		
	2 1/4 Cr-1 Mo	211–222
Effect of Microstructure		
	high-purity SS	32–51
Effect of Strain Rate		
	type 304 SS	21–32
Effect of Sodium Expsoure		
	type 316 SS	61–64
	type 316 SS plate	369–81
Effect of Surface Roughness		
	type 304 SS	21–32
Load-Controlled Tests		
	2 1/4 Cr-1 Mo	202–210
Strain-Controlled Tests		
	2 1/4 Cr-1 Mo	202–205
Crack Growth Rate Data		
	type 304 SS	21–32
	high-purity SS	32–51
	2 1/4 Cr-1 Mo	226–230
Base-Line Data		
	type 316 SS plate	370–381
Effect of Environment		
	2 1/4 Cr-1 Mo	230
Effect of Frequency		
	type 316 SS plate	370–381
Effect of Hold Time		
	type 316 SS plate	316–381
Effect of Microstructure		
	high-purity SS	32–51
Effect of Stress Intensity Factor		
	type 316 SS plate	370–381

Test	Material	Page
Impact Energy Correlation		
	2 1/4 Cr-1 Mo	231–235
Microstructure		
	type 304 SS, aged	117
	type 304 SS, creep tested	126–141; 259–261; 265; 316–321
	type 304 SS, tensile tested	312–316
	type 316 SS	108–110
	2 1/4 Cr-1 Mo, fatigue tested	221–226
	Incoloy 800, fatigue tested	324–328
Relaxation		
	2 1/4 Cr-1 Mo	250
Tensile Test Data		
Base-Line Data		
	Hastelloy X	267–268
	2 1/4 Cr-1 Mo	202
Correlations		
	2 1/4 Cr-1 Mo	231–235
Effect of Aging		
	type 304 SS	112–124
Effect of Annealing		
	type 304 SS	102–113
	type 316 SS	102–113
Effect of Heat Treatment		
	Inconel 718	11–17
	Inconel 718 weldments	15–20
Effect of Prior Creep		
	type 304 SS	72–91
	literature review	68–72
Effect of Prior Fatigue		
	types 304 and 316 SS	2–11

Test	Material	Page
Tensile Test Data (Continued)		
Effect of Strain Rate		
	type 304 SS	245–246
	2 1/4 Cr-1 Mo	187–196
Heat-to-Heat Variation		
	2 1/4 Cr-1 Mo	197–200

ORNL-5105
UC-79b, -h, -k
(Liquid Metal Fast
Breeder Reactors)

INTERNAL DISTRIBUTION

(3) Central Research Library
ORNL — Y-12 Technical Library
Document Reference Section
(10) Laboratory Records Department
Laboratory Records, ORNL RC
ORNL Patent Office
R. J. Beaver
R. G. Berggren
J. J. Blass
M. K. Booker
C. R. Brinkman
D. A. Canonico
J. Corum
W. R. Corwin
F. L. Culler
J. E. Cunningham
J. H. DeVan
D. P. Edmonds
G. Fee
M. H. Fontana
W. R. Gall
B. L. Greenstreet
J. C. Griess, Jr.
J. P. Hammond
W. O. Harms
R. L. Heestand
(5) M. R. Hill
D. O. Hobson
F. J. Homan
H. Inouye
P. R. Kasten
J. F. King
R. T. King
R. L. Klueh
K. C. Liu
C. T. Liu
A. L. Lotts
(20) W. R. Martin
W. J. McAfee
H. E. McCoy
H. C. McCurdy
C. J. McHargue
J. Merkle
P. Patriarca
S. Peterson
H. Postma
C. E. Pugh
P. L. Rittenhouse
D. N. Robinson
T. Roche
J. L. Scott
Myrtleen Sheldon
V. K. Sikka
G. M. Slaughter
W. J. Stelzman
J. P. Strizak
R. W. Swindeman
D. B. Trauger
T. N. Washburn
J. R. Weir, Jr.
G. D. Whitman
T. Yahr
W. C. Leslie (consultant)
John Moteff (consultant)
Hayne Palmour III (consultant)
J. W. Prados (consultant)
N. E. Promisel (consultant)
G. V. Smith (consultant)
D. F. Stein (consultant)

EXTERNAL DISTRIBUTION

USERDA DIVISION OF REACTOR RESEARCH AND DEVELOPMENT, Washington, DC 20545

(2) Director

USERDA OAK RIDGE OPERATIONS OFFICE, P.O. Box E, Oak Ridge, TN 37830

Research and Technical Support Division
Director, Reactor Division

USERDA TECHNICAL INFORMATION CENTER, Office of Information Services, P.O. Box 62, Oak Ridge, TN 37830

(309) For distribution as shown in TID-4500 Distribution Category, UC-79b (Fuels and Materials Engineering Development); UC-79h (Structural Materials and Design Engineering); UC-79k (Components)

☆U. S. GOVERNMENT PRINTING OFFICE: 1975-748-189/223